Heat and Mass Transfer

Kuo-Tsung Yu
Xigang Yuan

Introduction to Computational Mass Transfer

With Applications to Chemical Engineering

Second Edition

EXTRAS ONLINE

Springer

Heat and Mass Transfer

More information about this series at http://www.springer.com/series/4247

Kuo-Tsung Yu · Xigang Yuan

Introduction to Computational Mass Transfer

With Applications to Chemical Engineering

Second Edition

Springer

Kuo-Tsung Yu
School of Chemical Engineering
and Technology
Tianjin University
Tianjin
People's Republic of China

Xigang Yuan
School of Chemical Engineering
and Technology
Tianjin University
Tianjin
People's Republic of China

Additional material to this book can be downloaded from http://extras.springer.com.

ISSN 1860-4846 ISSN 1860-4854 (electronic)
Heat and Mass Transfer
ISBN 978-981-10-2497-9 ISBN 978-981-10-2498-6 (eBook)
DOI 10.1007/978-981-10-2498-6

Library of Congress Control Number: 2013957426

Printed on acid-free paper

This Springer imprint is published by Springer Nature
The registered company is Springer Nature Singapore Pte Ltd.
The registered company address is: 152 Beach Road, #22-06/08 Gateway East, Singapore 189721, Singapore

Preface

With the rapid development and continuing advances of computer technologies and numerical computation, many new multidisciplinary research areas have emerged, including computational chemistry, computational physics, computational biology, and others. It is recognized that computational methodology has now became one of the three basic methodologies of conducting scientific and engineering research, along with theoretical investigation and experimental studies.

In the 1970s, the cross-disciplinary studies of fluid dynamics and numerical computation had led to the new research area of computational fluid dynamics (CFD). This multidisciplinary development later on extended to heat transfer; and consequently the field of computational heat transfer (CHT) or numerical heat transfer (NHT) was introduced. The establishment of these two new research areas has helped scientists and engineers solve many difficult problems, such as the prediction of flow and heat transfer behaviors in engineering design and applications.

Nevertheless, what chemical engineers deal with includes not only fluid flows and heat transfer but also mass transfer and chemical reactions. The detailed information of mass transfer, especially the concentration distribution, is essential to the design and the assessment of chemical equipment as it serves as the basis in evaluating the process effectiveness or efficiency. The conventional approach to predict the concentration field is by the empirical method which is not only unreliable but also lacking of theoretical foundation. Thus a rigorous method for accurate predictions needs to be investigated.

Mass transfer processes are complicated, usually involving turbulent flow, heat transfer, multiple phases, chemical reactions, unsteady operation, as well as the influences from internal construction of the equipment and many other factors. To study such a complicated system, we propose a novel scientific computing framework in which all the relevant equations on mass transfer, fluid dynamics, heat transfer, chemical reactions, and all other influencing factors are involved and solved numerically. This is the main task and research methodology of computational mass transfer (CMT).

Moreover, all mass transfer processes involve the diffusion through the interface between adjacent phases. Interfacial effects, such as the Marangoni convection and the Rayleigh convection, cannot be ignored. Therefore, the study of interfacial effects is another important aspect of CMT.

In recent years, we explored in this new area on the closure of the differential turbulent mass transfer equation by proposing the two-equation $c'^2 - \varepsilon_{c'}$ model and the Reynold's mass flux (fluctuating mass flux) $u'c$ model. Our approach has been successfully applied to various chemical processes and equipments, including distillation, absorption, adsorption, catalytic reaction, and fluidized chemical processes. The interfacial behaviors of mass transfer were also studied by both simulations and experiments.

This book is chiefly based on our published research work and graduate dissertations in the area of CMT. The purpose of writing this book is first to serve as a textbook for the graduate course titled "Introduction to the Computational Mass Transfer", offered to the graduate students of Chemical Engineering discipline in Tianjin University; and second as a reference book for those who are interested in this area.

The contents of this book can be divided into two parts. The first part, Process Computation, involves the prediction of concentration, velocity, and temperature distributions in chemical engineering equipment. The second part, Interface Computation, concerns the prediction of interfacial effect on mass transfer behaviors.

Chapter 1 of this book covers the basic equation and models of computational mass transfer. Chapters 2–6 present the application of computational mass transfer to discuss the process computation of various gas–liquid contacting and catalytic reaction as well as fluidized processes and equipment in chemical engineering. Chapters 7 and 8 deal with the multi-component mass transfer and concentration behavior near interface. Chapters 9 and 10 introduce the computation of Marangoni and Rayleigh convections and their influence on mass transfer by using respectively differential equations and the lattice Boltzmann method.

The research works presented in this book were performed in the State Key Laboratory for Chemical Engineering at Tianjin University under the support of Chinese National Science Foundation (contract number 20136010, 20736005, and 91434204). The help and encouragement from the Chemical Engineering Research Center of Tianjin University is acknowledged.

We warmly welcome any suggestions, discussions, and criticism on this book.

Tianjin, China
December 2015

Kuo-Tsung Yu
Xigang Yuan

Contents

Chapter 1
Basic Models of Computational Mass Transfer

Abstract The computational mass transfer (CMT) aims to find the concentration profile in a process equipment, which is the most important basis for evaluating the process efficiency, as well as, the effectiveness of an existing mass transfer equipment. This chapter is dedicated to the description of the fundamentals and the recently published models of CMT for obtaining simultaneously the concentration, velocity and temperature distributions. The challenge is the closure of the differential species conservation equation for the mass transfer in turbulent flow. Two models are presented. The first is a two-equation model termed as $\overline{c'^2} - \varepsilon_{c'}$ model, which is based on the Boussinesq postulate by introducing an isotropic turbulent mass transfer diffusivity. The other is the Reynolds mass flux model, in which the variable covariant term in the equation is modeled and computed directly, and so it is anisotropic and rigorous. Both methods are proved to be validated by comparing with experimental data.

Keywords Computational mass transfer (CMT) · Reynolds averaging · Closure of time-averaged mass transfer equation · Two-equation model · Turbulent mass transfer diffusivity · Reynolds mass flux model

Nomenclature

c	Instantaneous mass concentration of species i, kg m^{-3}
	Molar concentration of species i in Sect. 1.4.2, mol s^{-3}
c_t	Total molar concentration of component i per m^3, mol m^{-3}
C	Time average concentration, kg m^{-3}
C^+	Dimensionless concentration
c'	Fluctuating concentration, kg m^{-3}
$\overline{c'^2}$	Variance of fluctuating concentration, kg^2 m^{-6}
D	Molecular diffusivity, m^2 s^{-1}
D_e	Effective mass diffusivity, m^2 s^{-1}
D_t	Isotropic turbulent mass diffusivity, m^2 s^{-1}
$\mathbf{D}_t$	Anisotropic turbulent mass diffusivity, m^2 s^{-1}
g	Gravity acceleration, m s^{-2}
$[I]$	Identity matrix, dimensionless

K.-T. Yu and X. Yuan, *Introduction to Computational Mass Transfer*,
Heat and Mass Transfer, DOI 10.1007/978-981-10-2498-6_1

Table 1.1 Influence of $\overline{u_i'c'}$ on mass transfer for different processes

Process	S_n	$\left(\frac{\partial \overline{u_i'c'}}{\partial x_i}\right)$	$S_{\text{comb}} = \left(-\frac{\partial \overline{u_i'c'}}{\partial x_i}\right) + S_n$	Process concentration profile and $\overline{u_i'c'}$ profile	Influence on mass transfer
Absorption	+	−	$S_{\text{comb}} > S_n$	Consistent	Favorable
Desorption (regeneration)	−	−	$S_{\text{comb}} < S_n$	Not consistent	Unfavorable
Adsorption	+	+	$S_{\text{comb}} < S_n$	Not consistent	Unfavorable
Desorption (regeneration)	−	+	$S_{\text{comb}} > S_n$	Consistent	Favorable

[a]Absorption process characterized by decreasing concentration profile
Desorption (regeneration) process characterized by increasing concentration profile

J_{w}	Mass flux at wall surface, kg m^{-2} s^{-1}
k	Fluctuating kinetic energy, m^2 s^{-2}
	Mass transfer coefficient, m s^{-1}
$[k]$	Matrix of mass transfer coefficients, m s^{-1}
l	Characteristic length, m
p'	Fluctuating pressure, kg m^{-1} s^{-2}
P	Time average pressure, kg m^{-1} s^{-2}
Pe	Peclet number
r_{c}	Ratio of fluctuating velocity dissipation time and fluctuating concentration dissipation time
S	Source term
Sc	Schmidt number
Sc_{t}	Turbulent Schmidt number
t	Time, s
T'	Fluctuating temperature, K
$\overline{T'^2}$	Variance of fluctuating temperature, K^2
T	Time average temperature, K
u	Instantaneous velocity of species i, m s^{-1}
u'	Fluctuating velocity, m s^{-1}
u_τ	Frictional velocity, m s^{-1}
u^+	Dimensionless velocity, m s^{-1}
U, V, W	Time average velocity in three directions, m s^{-1}
y^+	Dimensionless distance, m
α_{t}	Turbulent thermal diffusivity, m^{-1} s^{-1}
δ	Thickness of fluid film, m
ε	Dissipation rate of turbulent kinetic energy, m^2 s^{-3}
$\varepsilon_{c'}$	Dissipation rate of concentration variance, kg^2 m^{-6} s^{-1}
ε_t	Dissipation rate of temperature variance, K^2 s^{-1}
μ	Viscosity, kg m^{-1} s^{-1}
μ_{t}	Turbulent viscosity, kg m^{-1} s^{-1}

ν_e	Effective turbulent diffusivity, $m^2\ s^{-1}$
ρ	Density, kg m^{-3}
τ_μ, τ_c, τ_m	Characteristic time scale, s
τ_w	Near wall stress, kg $m^{-1}\ s^{-2}$

In many chemical engineering processes, the concentration profile is chiefly concerned as it is the basis for calculating the mass transfer efficiency. The conventional way to predict the concentration profile is using some simple but unreliable methods. The recent development of computation mass transfer (CMT) as described in this book provides a rigorous basis for dependable predictions of both concentration profile and the effectiveness of the mass transfer process as well as the interfacial effects on mass transfer efficiency.

The chemical process equipment involving mass transfer is always accompanied with fluid flow and heat transfer to form a complicated transport system. The model equations of mass transfer inevitably include fluid flow and heat transfer. Yet such large differential equation system is unclosed, and the method of closure is also a task to be tackled.

The process of mass transfer is realized by the mass transport from interfacial surface to the bulk fluid. Thus, the computational mass transfer covers the following two parts

- **Process computation**: It aims at finding the local and the overall (whole equipment) concentration as well as velocity and temperature distributions and also their relevant parameters, which are essential in scale-up, better design and assessment the efficiency of mass transfer equipment. The basic models, namely, the $\overline{c'^2} - \varepsilon_{c'}$ model and Reynolds mass flux model, for this computation are introduced in this chapter.
- **Interface computation**: It aims at predicting the influence of interfacial effect on the mass transfer, such as Marangoni convection and Rayleigh convection. Such effects may lead to the increase of the separation efficiency. Besides, the investigation of interfacial behaviors is also the basic step to understand the details of mass transferred from one phase to the other. This part of computation is described in the last two chapters of this book.

1.1 Equation of Mass Conservation and Its Closure

For the low Reynolds number flow (no turbulence) with mass transfer, the conversation equation of a mass species (component substance) is known to be

$$\frac{\partial c}{\partial t} + \frac{\partial}{\partial x_i}(u_i c) = \frac{\partial}{\partial x_i}\left(D\frac{\partial c}{\partial x_i}\right) + S_n \tag{1.1}$$

where c is the mass concentration of component species n (hereafter the subscript n is omitted for simplifying the notation); u_i is the velocity of fluid ($i = i, j, k$); $u_i c$ is the mass flux of component species n; D is the molecular diffusivity of component species n; S_n is the source term of species mass transferred from adjacent phase to the phase concerned or the species mass generated from chemical reaction. Note that the unit of mass concentration c in this chapter is kg m^{-3} except in Sect. 1.4.2. In some literatures, the concentration is also expressed as mass fraction c_{mf}; the conversion is $c = \rho c_{\mathrm{mf}}$ where ρ is the density of the mixture.

In chemical engineering practice, the mass transfer equipments, such as distillation, absorption and many others, are operated under turbulent flow condition. The u_i and c in Eq. (1.1) becomes instantaneous value and their fluctuating character should be considered.

Similar to the average concept in CFD (readers are referred to Appendix 1 for detail of CFD), the instantaneous concentration c can be resolved into time-average concentration C and fluctuating concentration c':

$$c = C + c'$$

Also as given in Appendix 1,

$$u_i = U_i + u_i'$$

Substitute foregoing relationship to Eq. (1.1) and take time-average of each term, and note that

$$\overline{u_i c} = \overline{(U_i + u_i')(C + c')} = U_i C + \overline{U_i c'} + \overline{u_i' C} + \overline{u_i' c'}$$

Since the average fluctuating quantity $\overline{c'} = 0$ and $\overline{u_i'} = 0$, both $\overline{U_i c'}$ and $\overline{u_i' C}$ are equal to zero, we have

$$\overline{u_i c} = \overline{(U_i + u_i')(C + c')} = U_i C + \overline{u_i' c'} \tag{1.2}$$

or

$$\overline{u_i' c'} = \overline{u_i c} - U_i C \tag{1.2a}$$

Substitute to Eq. (1.1) and after time-averaging yields the following form under turbulent condition:

$$\frac{\partial C}{\partial t} + \frac{\partial \left(U_i C + \overline{u_i' c'}\right)}{\partial x_i} = \frac{\partial}{\partial x_i}\left(D \frac{\partial C}{\partial x_i}\right) + S_n$$

which can be written as:

$$\frac{\partial C}{\partial t}+\frac{\partial U_i C}{\partial x_i}=\frac{\partial}{\partial x_i}\left(D\frac{\partial C}{\partial x_i}-\overline{u_i'c'}\right)+S_n \tag{1.3}$$

or

$$\frac{\partial C}{\partial t}+\frac{\partial U_i C}{\partial x_i}=\frac{\partial}{\partial x_i}D\frac{\partial C}{\partial x_i}-\frac{\partial \overline{u_i'c'}}{\partial x}+S_n \tag{1.3a}$$

The left sides of the foregoing equations represent, respectively, the increasing rate of time-averaged C and mass flux U_iC with respect to time t and coordinate x_i. The first term on the right side represents the molecular diffusion; the second term represents the turbulent diffusion in terms of $-\overline{u_i'c'}$ gradient which is unknown.

The term $-\overline{u_i'c'}$ (or its equivalent $-\rho\overline{u_i'c_{\mathrm{mf}}'}$) resembles the Reynolds stress $-\rho\overline{u_i'u_j'}$ and Reynolds heat flux $-\rho\overline{u_i'T'}$, and thus we may call it as Reynolds mass flux for the convenience of terminology. The negative Reynolds mass flux, $-\left(-\overline{u_i'c'}\right)=\overline{u_i'c'}$, is called fluctuating mass flux hereafter as it is frequently appeared in the model calculation.

Since concentration is scalar quantity, $-\overline{u_i'c'}$ implies only three unknown quantities ($-\overline{u_i'c'}$, $-\overline{u_j'c'}$, $-\overline{u_k'c'}$). If U_i can be found by CFD, Eq. (1.3) involves four unknowns (C, $-\overline{u_i'c'}$, $-\overline{u_j'c'}$, $-\overline{u_k'c'}$); yet only three equation can be written from Eq. (1.3), it is unclosed and insufficient to obtain solution.

There are two categories of mathematical models for closing Eq. (1.3).

(1) **Turbulent mass diffusivity models**: This category of models is conventional, which features to evaluate the unknown $-\overline{u_i'c'}$ in terms of a new variable: the turbulent mass diffusivity D_{t}. The following models belong to this category:

- Turbulent Schmidt number model
- Inert tracer model
- Two-equation ($\overline{c'^2}-\varepsilon_{c'}$) model.

(2) **Reynolds mass flux models**: This category of models features to solve the unknown $-\overline{u_i'c'}$ directly instead of in terms of D_{t}. This category of models includes

- Standard Reynolds mass flux model
- Hybrid Reynolds mass flux model
- Algebraic Reynolds mass flux model.

1.2 Turbulent Mass Diffusivity Model

Similar to the Boussinesq's postulate in CFD, the unknown $-\overline{u_i'c'}$ can be set to be proportional to the gradient of C:

$$-\overline{u_i'c'} = D_t \frac{\partial C}{\partial x_i} \tag{1.4}$$

where D_t is the proportional coefficient and conventionally called it as turbulent mass diffusivity of species n (subscript n is omitted hereafter for simplifying the notation), which is still an unknown pending to find out. It should be pointed out that the D_t in Eq. (1.4) is isotropic in spite of $\frac{\partial C}{\partial x_i}$ is directional.

From Eq. (1.4), the fluctuating mass flux $\overline{u_i'c'}$ can be also expressed as proportional to the negative gradient of C as follows:

$$\overline{u_i'c'} = D_t\left(-\frac{\partial C}{\partial x_i}\right) \tag{1.4a}$$

In chemical engineering literature, Eq. (1.4a) is usually referred to as the well known Fick's law, which states that the mass flux flow is proportional to the negative concentration gradient due to the fact that the flow of mass flux is from high to the low concentration, or the flow of any mass flux should be in the direction of negative concentration gradient.

Substituting Eq. (1.4) to Eq. (1.3), we have

$$\frac{\partial C}{\partial t} + \frac{\partial U_i C}{\partial x_i} = \frac{\partial}{\partial x_i}(D + D_t)\frac{\partial C}{\partial x_i} + S_n \tag{1.5}$$

If U_i can be found from CFD, there are only two unknown variables in foregoing equation: C and D_t. The closure of Eq. (1.5) relies on the evaluation of D_t.

1.3 Conventional Turbulent Mass Diffusivity Model

1.3.1 Turbulent Schmidt Number Model

By considering the analogy between mass transfer and fluid flow, the turbulent mass diffusivity D_t may be analogous to the turbulent diffusivity (eddy diffusivity) ν_t ($\nu_t = \frac{\mu_t}{\rho}$) and independent of concentration. In other words, D_t is solely proportional to the turbulent diffusivity ν_t, and can be represented by a dimensionless ratio, called turbulent Schmidt number, which is defined as $Sc_t = \frac{\nu_t}{D_t} = \frac{\mu_t}{\rho D_t}$, i.e. $D_t = \frac{1}{Sc_t}\frac{\mu_t}{\rho}$.

In the literature, Sc_t is usually assumed to be a constant ranging from 0.5 to 1.2 for different processes and operating conditions. Although this is the simplest way

to obtain D_t, yet the correct value of Sc_t is hard to guess. Moreover, the relationship between D_t and μ_t is complicated as seen from Eq. (1.4) for D_t and Eq. (1.7) for μ_t; the assumption of constant Sc_t throughout the process and equipment cannot be proved and remains questionable.

1.3.2 Inert Tracer Model

Instead of assuming Sc_t, many authors employed the inert tracer technique to measure the time average concentration C of an inert tracer in a simulator to find the D_t experimentally. They customary used the turbulent Peclet number Pe_t to express their experimental result. Pe_t is defined as $Pe_t = \frac{UL}{D_t}$, where U is the superficial or time-averaged fluid velocity and L is the characteristic length. The experimental Pe_t is usually reported as either a constant or as an empirical equation involving some constructional or operational variables, such as characteristic dimensions, Reynolds number and others. Nevertheless, the D_t determined by inert tracer technique without mass transfer (denoted by $D_{t,tracer}$) is entirely different from that with mass transfer as seen by comparing the following two species mass conservation equations from Eq. (1.5)

For the inert tracer process without mass transfer

$$\frac{\partial C}{\partial t} + \frac{\partial U_i C}{\partial x_i} = \frac{\partial}{\partial x_i}\left(D + D_{t,tracer}\right)\frac{\partial C}{\partial x_i}$$

For the process with mass transfer

$$\frac{\partial C}{\partial t} + \frac{\partial U_i C}{\partial x_i} = \frac{\partial}{\partial x_i}\left(D + D_t\right)\frac{\partial C}{\partial x_i} + S_n$$

Obviously, by comparing the foregoing two equations, D_t and $D_{t,tracer}$ is not equal; the difference between them is depending on the value of the source term S_n, which represents the amount of species mass to be transferred in the process.

In view of the drawbacks of foregoing models in applying Sc_t or using experimental correlation obtained by the inert tracer technique, some dependable models have been recently developed to overcome such insufficiency as shown in subsequent sections.

1.4 $\overline{c'^2} - \varepsilon_c$ Model (Two-Equation Model)

The investigation on using the $\overline{c'^2} - \varepsilon_c$ two-equation model to calculate D_t was undertaken in recent years and had been applied with success to distillation, chemical absorption, adsorption, and catalytic reactor [1–11].

From the general concept of diffusion, the diffusivity is proportional to the diffusion velocity times the diffusion length. The former, representing by characteristic fluctuating velocity, can be proportional to $k^{0.5}$, here k is the average fluctuating kinetic energy ($k = \frac{1}{2}\overline{u_i' u_i'}$, see Appendix 1). The latter, fluctuating diffusion length, can be considered to be the product of characteristic fluctuating velocity $k^{0.5}$ and fluctuating dissipation time τ_m. Then we have $D_t \propto k^{0.5}\left(k^{0.5}\tau_m\right)$. The τ_m is referred to both the dissipation time of the characteristic velocity τ_μ and the fluctuating concentration τ_c. Since τ_μ and τ_c are not equal, we may take their geometric average τ_m, i.e. $\tau_m = \sqrt{\tau_\mu \tau_c}$.

As we know, $\tau_\mu = k/\varepsilon$, and similarly we may let $\tau_c = \overline{c'^2}/\varepsilon_{c'}$, where $\overline{c'^2} = \overline{c'c'}$ is the variance of average fluctuating concentration (dimension $\mathrm{kg}^2\ \mathrm{m}^{-6}$), and $\varepsilon_{c'}$ is its dissipation rate (dimension $\mathrm{kg}^2\ \mathrm{m}^{-6}\ \mathrm{s}^{-1}$) so as both k/ε and $\overline{c'^2}/\varepsilon_{c'}$ have the dimension of "time" (t).

From the foregoing relationship, we obtain the following equation for calculating D_t:

$$D_t = C_{c0} k \left(\frac{k\overline{c'^2}}{\varepsilon \varepsilon_{c'}}\right)^{\frac{1}{2}} \tag{1.6}$$

where C_{c0} is a proportional constant. Since k and ε can be calculated by corresponding equations given by Eqs. (A1.11a) and (A1.13a), respectively, in Appendix 1 for CFD, while $\overline{c'^2}$ and $\varepsilon_{c'}$ can be evaluated by the equations given in subsequent sections.

It is important to note that the ratio of $\frac{k}{\varepsilon} / \frac{\overline{c'^2}}{\varepsilon_{c'}}$ had been studied experimentally and found to be varying under different conditions [12–14]. Thus D_t as given by Eq. (1.6) is a variable coefficient.

1.4.1 The $\overline{c'^2}$ and $\varepsilon_{c'}$ Equations

(1) **Exact $\overline{c'^2}$ equation**

Substituting Eq. (1.2) to Eq. (1.1) and subtracting Eq. (1.3), we have the transport equation for the fluctuating concentration c' as follows:

$$\frac{\partial c'}{\partial t} + \frac{\partial U_i c'}{\partial x_i} = \frac{\partial}{\partial x_i}\left(D\frac{\partial c'}{\partial x_i}\right) - \frac{\partial}{\partial x_i}\left(u_i' C + u_i' c' - \overline{u_i' c'}\right) \tag{1.7}$$

Multiply both sides by $2c'$ and take the average, i.e.,

$$\overline{2c'\left[\frac{\partial c'}{\partial t} + \frac{\partial}{\partial x_i}(U_i c')\right]} = \overline{2c'\left[\frac{\partial}{\partial x_i}\left(D\frac{\partial c'}{\partial x_i}\right) - \frac{\partial}{\partial x_i}(u_i' C + u_i' c' - \overline{u_i' c'})\right]} \tag{1.8}$$

The left side of the foregoing equation can be written as

$$\overline{2c'\left[\frac{\partial c'}{\partial t} + \frac{\partial}{\partial x_i}(U_i c')\right]} = \frac{\partial(\overline{c'^2})}{\partial t} + \frac{\partial}{\partial x_i}(U_j \overline{c'^2})$$

For the simplification of the right side, let us note that according to the following derivation

$$\frac{\partial^2(c'^2)}{\partial x_i \partial x_i} = \frac{\partial}{\partial x_i}\left[\frac{\partial(c'^2)}{\partial x_i}\right] = \frac{\partial}{\partial x_i}\left[2c'\frac{\partial c'}{\partial x_i}\right] = 2\left[\frac{\partial c'}{\partial x_i}\frac{\partial c'}{\partial x_i} + c'\frac{\partial^2 c'}{\partial x_i}\right]$$

and after rearranging we can get the following relationship:

$$2c'\frac{\partial^2 c'}{\partial x_i \partial x_i} = \frac{\partial^2(c'^2)}{\partial x_i \partial x_i} - 2\frac{\partial c'}{\partial x_i}\frac{\partial c'}{\partial x_i}$$

Take the average of the foregoing equation and multiply by D, also define the dissipation rate of fluctuating concentration variance $\varepsilon_{c'}$ to be

$$\varepsilon_{c'} = D\overline{\frac{\partial c'}{\partial x_i}\frac{\partial c'}{\partial x_i}} \tag{1.9}$$

Then the first term on the right side of Eq. (1.8) takes the following form:

$$\overline{2c'\left[\frac{\partial}{\partial x_i}\left(D\frac{\partial c'}{\partial x_i}\right)\right]} = D\left[\frac{\partial^2 \overline{c'^2}}{\partial x_i \partial x_i} - 2\overline{\frac{\partial c'}{\partial x_i}\frac{\partial c'}{\partial x_i}}\right] = D\frac{\partial^2 \overline{c'^2}}{\partial x_i \partial x_i} - 2\varepsilon_{c'}$$

For the second term, since $\frac{\partial u_i'}{\partial x_i} = 0$, it becomes

$$\overline{-2c'\frac{\partial}{\partial x_i}(u_i' C)} = \overline{-2c'\left[C\frac{\partial u_i'}{\partial x_i} + u_i'\frac{\partial C}{\partial x_i}\right]} = -2\overline{c'C\frac{\partial u_i'}{\partial x_i}} - 2\overline{c'u_i'}\frac{\partial C}{\partial x_i} = -2\overline{c'u_i'}\frac{\partial C}{\partial x_i}$$

For the third term, due to

$$\frac{\partial}{\partial x_i}(-u_i' c'^2) = -\left[2u_i' c'\frac{\partial c'}{\partial x_i} + c'^2\frac{\partial u_i'}{\partial x_i}\right] = -2c'\frac{\partial u_i' c'}{\partial x_i}$$

we obtain

$$\overline{-2c'\frac{\partial}{\partial x_i}(u_i'c')} = -\frac{\partial}{\partial x_i}\left[\overline{u_i'c'^2}\right]$$

The fourth term can be neglected, i.e.,

$$\overline{2c'\frac{\partial}{\partial x_i}(\overline{u_i'c'})} = 0$$

After the foregoing arrangement, the exact equation of $\overline{c'^2}$ takes the following form:

$$\frac{\partial(\overline{c'^2})}{\partial t} + \frac{\partial}{\partial x_i}(U_i\overline{c'^2}) = \frac{\partial}{\partial x_i}\left[D\frac{\partial\overline{c'^2}}{\partial x_i} - \overline{u_i'c'^2}\right] - 2\overline{u_i'c'}\frac{\partial C}{\partial x_i} - 2\varepsilon_{c'} \tag{1.10}$$

The first term on the right side of the foregoing equation represents the transport of $\overline{c'^2}$ due to molecular motion and turbulent fluctuation; the second term represents the production of fluctuating mass flux due to average concentration gradient; the third term represents the dissipation. Equation (1.10) should be further modeled to suit computation as shown in subsequent section.

(2) **Modeling of $\overline{c'^2}$ equation**

Similar to the Boussinesq postulate or Fick's law, the $\overline{u_i'c'^2}$ and $\overline{u_i'c'}$ on the right side of Eq. (1.10) can be considered proportional to the corresponding negative gradients as shown below

$$\overline{u_i'c'^2} = \frac{D_\mathrm{t}}{\sigma_{c'^2}}\left(-\frac{\partial\overline{c'^2}}{\partial x_i}\right)$$
$$\overline{u_i'c'} = D_\mathrm{t}\left(-\frac{\partial C}{\partial x_i}\right)$$

where $\sigma_{c'^2}$ is correction factor, usually taken as 1. Then the modeled $\overline{c'^2}$ equation becomes

$$\frac{\partial\overline{c'^2}}{\partial t} + \frac{\partial U_i\overline{c'^2}}{\partial x_i} = \frac{\partial}{\partial x_i}\left[\left(D + \frac{D_\mathrm{t}}{\sigma_{c'^2}}\right)\frac{\partial\overline{c'^2}}{\partial x_i}\right] - 2D_\mathrm{t}\left(\frac{\partial C}{\partial x_i}\right)^2 - 2\varepsilon_{c'} \tag{1.11}$$

The foregoing equation still involves two unknown quantities: D_t and $\varepsilon_{c'}$; the evaluation of $\varepsilon_{c'}$ is given in subsequent section.

(3) **Exact $\varepsilon_{c'}$ equation**

Differentiate Eq. (1.1) with respect to x_k to get

$$\frac{\partial}{\partial t}\left(\frac{\partial c}{\partial x_k}\right)+\frac{\partial}{\partial x_k}\left[\frac{\partial}{\partial x_i}(u_i c)\right]=D\frac{\partial^2}{\partial x_i \partial x_i}\left(\frac{\partial c}{\partial x_k}\right)$$

Multiply by $2D\partial C/\partial x_k$ to obtain

$$\begin{aligned}&\frac{\partial}{\partial t}\left(D\frac{\partial c}{\partial x_k}\frac{\partial c}{\partial x_k}\right)+u_i\frac{\partial}{\partial x_i}\left(D\frac{\partial c}{\partial x_k}\frac{\partial c}{\partial x_k}\right)+2D\frac{\partial u_i}{\partial x_k}\frac{\partial c}{\partial x_k}\frac{\partial c}{\partial x_i}\\&\quad=D\frac{\partial^2}{\partial x_i x_i}\left(D\frac{\partial c}{\partial x_k}\frac{\partial c}{\partial x_k}\right)-2D^2\frac{\partial^2 c}{\partial x_k \partial x_i}\frac{\partial^2 c}{\partial x_i x_k}\end{aligned}\tag{1.12}$$

Substituting $u_i = U_i + u_i'$ and $c = C + c'$ to the foregoing equation and taking the time average, we have

$$\begin{aligned}&\frac{\partial}{\partial t}\left(D\frac{\partial C}{\partial x_k}\frac{\partial C}{\partial x_k}\right)+\frac{\partial}{\partial t}\left(D\overline{\frac{\partial c'}{\partial x_k}\frac{\partial c'}{\partial x_k}}\right)+U_i\frac{\partial}{\partial x_i}\left(D\frac{\partial C}{\partial x_k}\frac{\partial C}{\partial x_k}\right)+U_i\frac{\partial}{\partial x_i}\left(D\overline{\frac{\partial c'}{\partial x_k}\frac{\partial c'}{\partial x_k}}\right)\\&\quad+2D\frac{\partial}{\partial x_i}\left[u_i'\overline{\frac{\partial c'}{\partial x_k}}\frac{\partial C}{\partial x_k}\right]+D\frac{\partial}{\partial x_i}\left(u_i'\overline{\frac{\partial c'}{\partial x_k}\frac{\partial c'}{\partial x_k}}\right)+2D\frac{\partial U_i}{\partial x_k}\frac{\partial C}{\partial x_i}\frac{\partial C}{\partial x_k}+2D\overline{\frac{\partial u_i'}{\partial x_k}\frac{\partial c'}{\partial x_k}}\frac{\partial C}{\partial x_i}\\&\quad+2D\overline{\frac{\partial u_i'}{\partial x_k}\frac{\partial c'}{\partial x_i}}\frac{\partial C}{\partial x_k}+2\rho D\overline{\frac{\partial c'}{\partial x_i}\frac{\partial c'}{\partial x_k}}\frac{\partial U_i}{\partial x_k}+2D\overline{\frac{\partial u_i'}{\partial x_k}\frac{\partial c'}{\partial x_i}\frac{\partial c'}{\partial x_k}}=D\frac{\partial^2}{\partial x_i \partial x_i}\left(D\frac{\partial C}{\partial x_k}\frac{\partial C}{\partial x_k}\right)\\&\quad+D\frac{\partial^2}{\partial x_i \partial x_i}\left(D\overline{\frac{\partial c'}{\partial x_k}\frac{\partial c'}{\partial x_k}}\right)-2D^2\frac{\partial^2 C}{\partial x_k \partial x_i}\frac{\partial^2 C}{\partial x_i \partial x_k}-2D^2\overline{\frac{\partial^2 c'}{\partial x_k \partial x_i}\frac{\partial^2 c'}{\partial x_i \partial x_k}}\end{aligned}\tag{1.13}$$

Differentiate Eq. (1.3) with respect to x_k, then multiply by $2D\frac{\partial C}{\partial x_k}$ and take the time average, we get

$$\begin{aligned}&\frac{\partial}{\partial t}\left(D\frac{\partial C}{\partial x_k}\frac{\partial C}{\partial x_k}\right)+U_i\frac{\partial}{\partial x_i}\left(D\frac{\partial C}{\partial x_k}\frac{\partial C}{\partial x_k}\right)+2D\frac{\partial U_i}{\partial x_k}\frac{\partial C}{\partial x_i}\frac{\partial C}{\partial x_k}\\&\quad=D\frac{\partial^2}{\partial x_i \partial x_i}\left(D\frac{\partial C}{\partial x_k}\frac{\partial C}{\partial x_k}\right)-2D^2\frac{\partial^2 C}{\partial x_k \partial x_i}\frac{\partial^2 C}{\partial x_i \partial x_k}-2D\frac{\partial}{\partial x_i}\left[u_i'\overline{\frac{\partial c'}{\partial x_k}}\frac{\partial C}{\partial x_k}\right]\\&\quad\quad-2D\overline{\frac{\partial u_i'}{\partial x_k}\frac{\partial c'}{\partial x_i}}\frac{\partial C}{\partial x_k}\end{aligned}\tag{1.14}$$

Subtracting Eq. (1.14) from Eq. (1.13) and noting that $\varepsilon_{c'} = D\overline{\frac{\partial c'}{\partial x_i}\frac{\partial c'}{\partial x_i}}$, we have the following exact transport equation of $\varepsilon_{c'}$:

$$\frac{\partial \varepsilon_{c'}}{\partial t}+\frac{\partial U_i \varepsilon_{c'}}{\partial x_i}=\frac{\partial}{\partial x_i}\left(D\frac{\partial \varepsilon_{c'}}{\partial x_i}-\overline{\varepsilon_{c'}u_i'}\right)-2D\overline{\frac{\partial u_i'}{\partial x_k}\frac{\partial c'}{\partial x_k}\frac{\partial C}{\partial x_i}}$$
$$-2D\overline{\frac{\partial c'}{\partial x_i}\frac{\partial c'}{\partial x_k}}\frac{\partial U_i}{\partial x_k}-2\rho D\overline{u_i'\frac{\partial c'}{\partial x_k}}\frac{\partial^2 C}{\partial x_i \partial x_k}-2D^2\overline{\frac{\partial^2 c'}{\partial x_k \partial x_i}\frac{\partial^2 c'}{\partial x_i \partial x_k}}-2D\overline{\frac{\partial u_i'}{\partial x_k}\frac{\partial c'}{\partial x_i}\frac{\partial c'}{\partial x_k}} \tag{1.15}$$

The first term on the right side of the foregoing equation represents the molecular and turbulent diffusion of $\varepsilon_{c'}$; the second, third and fourth terms represent, respectively, the production of $\varepsilon_{c'}$ by average concentration gradient, average velocity gradient and velocity fluctuation; the fifth and sixth terms represent the dissipation. Equation (1.15) should be further modeled to the form suitable for numerical computation as shown below.

(4) **Modeling of $\varepsilon_{c'}$ equation**

Let $\overline{u_i'\varepsilon_{c'}}$ be proportional to the negative gradient of $\varepsilon_{c'}$

$$\overline{u_i'\varepsilon_{c'}}=-\frac{D_\mathrm{t}}{\sigma_{\varepsilon_{c'}}}\frac{\partial \varepsilon_{c'}}{\partial x_i}$$

where $\sigma_{\varepsilon'}$ is a correction factor, usually letting $\sigma_{c'}=1$ except for some special cases. Thus the first term on the right side of Eq. (1.15) can be modeled as follows:

$$\frac{\partial}{\partial x_i}\left(D\frac{\partial \varepsilon_{c'}}{\partial x_i}-\overline{\varepsilon_{c'}u_i'}\right)=\frac{\partial}{\partial x_i}\left(D+\frac{D_\mathrm{t}}{\sigma_{\varepsilon_{c'}}}\right)\frac{\partial \varepsilon_{c'}}{\partial x_i}$$

The second term can be considered proportional to the product of $\overline{c'u_i'}$ and the concentration gradient $\frac{\partial C}{\partial x_i}$. According to the modeling rule, the dimension of a term before and after modeling should be equal, the proportional coefficient is set to be $C_{c1}\frac{\varepsilon_{c'}}{\overline{c'^2}}$ where C_{c1} is constant and $\frac{\varepsilon_{c'}}{\overline{c'^2}}$ represents the dimension $(1/t)$. Then we have

$$-2D\overline{\frac{\partial u_i'}{\partial x_k}\frac{\partial c'}{\partial x_k}}\frac{\partial C}{\partial x_i}=-C_{c1}\frac{\varepsilon_{c'}}{\overline{c'^2}}\overline{c'u_i'}\frac{\partial C}{\partial x_i}$$

The third term can be considered proportional to the product of $\overline{u_i'u_j'}$ and the velocity gradient $\frac{\partial U_i}{\partial x_j}$; the proportion coefficient is equal to $C_{c2}\frac{\varepsilon_{c'}}{k}$ from the modeling rule of dimensional equality as follows:

$$-2D\overline{\frac{\partial c'}{\partial x_i}\frac{\partial c'}{\partial x_k}}\frac{\partial U_i}{\partial x_k}=-C_{c2}\frac{\varepsilon_{c'}}{k}\overline{u_i'u_j'}\frac{\partial U_i}{\partial x_i}$$

The fourth term can be modeled as

$$-2D\overline{u_i'\frac{\partial c'}{\partial x_k}\frac{\partial^2 C}{\partial x_i \partial x_k}} = -DD_t\left(\frac{\partial^2 C}{\partial x_i \partial x_i}\right)^2$$

The fifth term can be considered proportional to $\varepsilon_{c'}^2$; the proportional coefficient is $C_{c3}\frac{1}{\overline{c'^2}}$ from the dimension equality of modeling rule, so that

$$-2D^2\overline{\frac{\partial^2 c'}{\partial x_k \partial x_i}\frac{\partial^2 c'}{\partial x_i \partial x_k}} = -C_{c3}\frac{\varepsilon_{c'}^2}{\overline{c'^2}}$$

The sixth term can be considered proportional to $\varepsilon_{c'}$ as follows and the proportional coefficient is $C_{c4}\frac{\varepsilon}{k}$ accordingly.

$$-2D\overline{\frac{\partial u_j'}{\partial x_k}\frac{\partial c'}{\partial x_i}\frac{\partial c'}{\partial x_k}} = -C_{c4}\frac{\varepsilon\varepsilon_{c'}}{k}$$

With all modeling terms, Eq. (1.15) becomes

$$\begin{aligned}\frac{\partial \varepsilon_{c'}}{\partial t} + \frac{\partial U_i \varepsilon_{c'}}{\partial x_i} = \frac{\partial}{\partial x_i}\left[\left(D + \frac{D_t}{\sigma_{\varepsilon_{c'}}}\right)\frac{\partial \varepsilon_{c'}}{\partial x_i}\right] - C_{c1}\frac{\varepsilon_{c'}}{\overline{c'^2}}\overline{u_j'c'}\frac{\partial C}{\partial x_i} \\ - C_{c2}\overline{u_i'u_j'}\frac{\partial U_i}{\partial x_i}\frac{\varepsilon_c}{k} - C_{c3}\frac{\varepsilon_{c'}^2}{\overline{c'^2}} - C_{c4}\frac{\varepsilon\varepsilon_{c'}}{k} - DD_t\left(\frac{\partial^2 C}{\partial x_i \partial x_i}\right)^2\end{aligned}$$

Since the value DD_t is very small, the term $DD_t\left(\frac{\partial^2 C}{\partial x_i \partial x_i}\right)^2$ can be neglected. The final modeling form of $\varepsilon_{c'}$ equation is as follows (*modeling form 1*):

$$\begin{aligned}\frac{\partial \varepsilon_{c'}}{\partial t} + \frac{\partial U_i \varepsilon_{c'}}{\partial x_i} = \frac{\partial}{\partial x_i}\left[\left(D + \frac{D_t}{\sigma_{\varepsilon_c}}\right)\frac{\partial \varepsilon_{c'}}{\partial x_i}\right] - C_{c1}\frac{\varepsilon_{c'}}{\overline{c'^2}}\overline{u_j'c'}\frac{\partial C}{\partial x_i} \\ - C_{c2}\overline{u_i'u_j'}\frac{\partial U_i}{\partial x_i}\frac{\varepsilon_c}{k} - C_{c3}\frac{\varepsilon_{c'}^2}{\overline{c'^2}} - C_{c4}\frac{\varepsilon\varepsilon_{c'}}{k}\end{aligned} \tag{1.16}$$

Sun et al. [4] further simplified the second and third terms of Eq. (1.16) to be

$$C_{c1}\frac{\varepsilon_{c'}}{\overline{c'^2}}\overline{u_j'c'}\frac{\partial C}{\partial x_i} + C_{c2}\overline{u_i'u_j'}\frac{\partial U_i}{\partial x_i} = C_{c1}\frac{\varepsilon_{c'}^2}{\overline{c'^2}}\left(\frac{\partial C}{\partial x_i}\right)^2$$

Then $\varepsilon_{c'}$ equation becomes (*modeling form 2*)

$$\frac{\partial \varepsilon_{c'}}{\partial t}+\frac{\partial U_i \varepsilon_{c'}}{\partial x_i}=\frac{\partial}{\partial x_i}\left[\left(D+\frac{D_t}{\sigma_{\varepsilon_c}}\right)\frac{\partial \varepsilon_{c'}}{\partial x_i}\right]-C_{c1}D_t\frac{\varepsilon_{c'}}{\overline{c'^2}}\left(\frac{\partial C}{\partial x_i}\right)^2-C_{c3}\frac{\varepsilon_{c'}^2}{\overline{c'^2}}-C_{c4}\frac{\varepsilon\varepsilon_{c'}}{k} \tag{1.17}$$

After a number of calculations, it was found [4] that the $C_{c4}\frac{\varepsilon\varepsilon_{c'}}{k}$ term is much greater than the $C_{c3}\frac{\varepsilon_{c'}^2}{\overline{c'^2}}$ term, and the neglect of the later do not affect substantially the simulated result. Thus $\varepsilon_{c'}$ equation can be further simplified to (*modeling form 3*)

$$\frac{\partial \varepsilon_{c'}}{\partial t}+\frac{\partial U_i \varepsilon_{c'}}{\partial x_i}=\frac{\partial}{\partial x_i}\left[\left(D+\frac{D_t}{\sigma_{\varepsilon_{c'}}}\right)\frac{\partial \varepsilon_{c'}}{\partial x_i}\right]-C_{c1}D_t\frac{\varepsilon_{c'}}{\overline{c'^2}}\left(\frac{\partial C}{\partial x_i}\right)^2-C_{c4}\frac{\varepsilon}{k}\varepsilon_{c'} \tag{1.18}$$

(5) **Determination of model constants**

(A) ***Model constants in*** Eq. (1.16)

Principally, since both concentration and temperature are scalar quantity, the analogy between mass transfer and heat transfer can be employed to get the constants in Eq. (1.16). By comparison, the $\varepsilon_{c'}$ Eq. (1.16) is identical with Eq. (A2.10) in Appendix 2 for heat transfer if concentration C is replaced by temperature T and D_t is replaced by α_t. Thus one option is that the model constants for Eq. (A2.10) given by Table (A2.1) in Appendix 2 for heat transfer can be adopted in Eq. (1.16). For instance, according to Sommer model, the model constants are [15]: C_{c1} = 1.8, C_{c2} = 0.72, C_{c3} = 2.2, C_{c4} = 0.8, $\sigma_{\varepsilon_{c'}}$ = 1.0 and C_{c0} = 0.11.

The model constants can be modified to achieve more accurate simulation for an individual process.

(B) ***Model constants in*** Eqs. (1.17) and (1.18)

1. **Model constant C_{c1}**

In view of insufficient research on the determining the model constant C_{c1}, we may take the result by Sun [2] that the value of C_{c1} for the best fitting of experimental data is C_{c1} = 1.8 in using Eq. (1.17) and C_{c1} = 2.0 in using Eq. (1.18).

2. **Model constant C_{c2} and C_{c3}**

By the principle that all anisotropic complicated transport equation should be also valid for isotropic simple case; the model constants can be obtained by reducing the corresponding equation to the simple flow and transport conditions.

For the uniform one dimensional isotropic steady turbulent flow and mass transfer, the equations of k, ε, $\overline{c'^2}$ and $\varepsilon_{c'}$ are reduced to the following forms:

$$\begin{aligned} U\frac{dk}{dx} &= -\varepsilon \\ U\frac{d\varepsilon}{dx} &= -C_{\varepsilon 2}\frac{\varepsilon^2}{k} \\ U\frac{d\overline{c'^2}}{dx} &= -2\varepsilon_{c'} \\ U\frac{d\varepsilon_{c'}}{dx} &= -C_{c3}\frac{\varepsilon_{c'}^2}{\overline{c'^2}} - C_{c4}\frac{\varepsilon\varepsilon_{c'}}{k} \end{aligned} \tag{1.19}$$

Let $r_c = \left(\frac{\overline{c'^2}}{\varepsilon_{c'}}\right)/\left(\frac{k}{\varepsilon}\right)$, the $\varepsilon_{c'}$ can be expressed as follows

$$\varepsilon_{c'} = \frac{\varepsilon\overline{c'^2}}{r_c k} \tag{1.20}$$

Substituting to Eq. (1.19) and rearranging it, we have

$$\begin{aligned} U\frac{d\varepsilon_{c'}}{dx} &= \frac{U}{r_c}\frac{d\left(\varepsilon\overline{c'^2}/k\right)}{dx} \\ &= \frac{U}{r_c}\left[-\frac{\varepsilon\overline{c'^2}}{k^2}\frac{dk}{dx} + \frac{\overline{c'^2}}{k}\frac{d\varepsilon}{dx} + \frac{\varepsilon}{k}\frac{d\overline{c'^2}}{dx}\right] \\ &= \frac{1}{r_c}\left(\frac{\varepsilon^2\overline{c'^2}}{k^2} - C_{\varepsilon 2}\frac{\varepsilon^2\overline{c'^2}}{k^2} - 2\frac{\varepsilon\varepsilon_{c'}}{k}\right) \\ &= -\frac{2}{r_c}\frac{\varepsilon\varepsilon_{c'}}{k} - r_c(C_{\varepsilon 2}-1)\frac{\varepsilon_{c'}^2}{\overline{c'^2}} \end{aligned} \tag{1.21}$$

Comparing Eqs. (1.19) and (1.21), the following relationships are obtained

$$\begin{aligned} C_{c3} &= r_c(C_{\varepsilon 2}-1) \\ C_{c4} &= \frac{2}{r_c} \end{aligned}$$

If r_c is considered approximately constant and set to be 0.9 [1] and $C_{\varepsilon 2} = 1.92$ is taken from standard $k-\varepsilon$ model, we have $C_{c3} = 0.83$, $C_{c4} = 2.22$. Note that C_{c2} and C_{c3} may be changed depending on the value of r_c chosen under different conditions.

3. **Model constant C_{c0}**

Combining the following equations

$$\mu_t = C_\mu \rho \frac{k^2}{\varepsilon}, \quad Sc_t = \frac{\mu_t}{\rho D_t}, \quad r_c = \left(\frac{\overline{c'^2}}{\varepsilon_c}\right) / \left(\frac{k}{\varepsilon}\right), \quad D_t = C_{c0} k \left(\frac{k\overline{c'^2}}{\varepsilon\varepsilon_{c'}}\right)^{\frac{1}{2}},$$

we get the following relationship to calculate C_{c0}

$$C_{c0} = \frac{C_\mu}{Sc_t \sqrt{r_c}}$$

Since Sc_t and r_c are indeterminate, the C_{c0} cannot be obtained. However, if we take the approximate value of $Sc_t = 0.7$ and $r_c = 0.9$ as given by Sherwood et al. [16], and $C_\mu = 0.09$ from standard $k - \varepsilon$ model, we obtain approximately $C_{c0} = 0.14$. On the other hand, if taking $Sc_t = 0.85$, we get $C_{c0} = 0.11$. Thus C_{c0} may be set within the range of 0.11–0.14 to suit different processes.

(C) *Summary*

Model constants in Eq. (1.16), (*modeling form 1*), $C_{c1} = 1.8$, $C_{c2} = 0.72$, $C_{c3} = 2.2$, $C_{c4} = 0.8$, and $C_{c0} = 0.11$.

Model constants in Eq. (1.17), (*modeling form 2*), $C_{c1} = 1.8$, $C_{c3} = 0.83$, $C_{c4} = 2.22$ and $C_{c0} = 0.14$.

Model constants in Eq. (1.18), (*modeling form 3*), $C_{c1} = 2.0$, $C_{c4} = 2.22$ and $C_{c0} = 0.14$.

(6) **Comparison of simulated results by using different modeling form of $\varepsilon_{c'}$ equation**

The use of two-equation model to close mass conservation equation Eq. (1.5) involves four unknowns (C, D_t, $\overline{c'^2}$ $\varepsilon_{c'}$) as the U_i can be calculated by CFD. While the model equations are also four, i.e. Eqs. (1.5) and (1.6), $\overline{c'^2}$ and $\overline{c'^2}$ equations, so that Eq. (1.5) can be closed and solved.

Sun simulated the concentration profile of an industrial scale distillation tray [3] with different modeling form of $\varepsilon_{c'}$ equation [2]. The simulated results are shown in Figs. 1.1 and 1.2.

As seen from Fig. 1.1, the simulated contours of concentration are almost the same in spite of using different form of $\varepsilon_{c'}$ modeling equation. Similar situation is also seen in Fig. 1.2; all the volume average D_t are close to the experimental measurement by Cai [17]. Therefore it is not surprised that the use of different modeling equation and different model constants may give very close result.

Among three $\varepsilon_{c'}$ modeling equations, Eq. (1.17) looks appropriate as it involves only three constants rather than four. However, these constants may be adjusted to suit different processes if necessary.

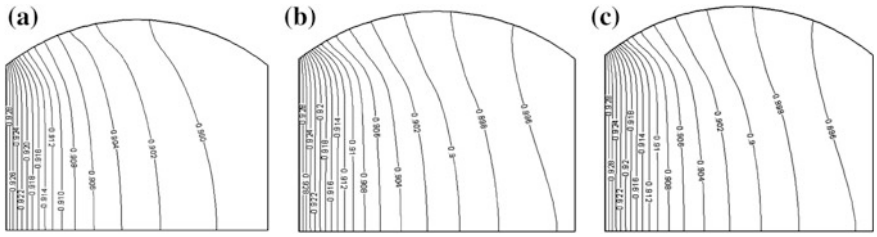

Fig. 1.1 The simulated concentration contours on a column tray by using different $\varepsilon_{c'}$ modeling equations and model constants (I) Operating condition: pressure 165 kPa, liquid rate 30.66 $m^3\ h^{-1}$, vapor rate 5.75 kg s^{-1}, tray No. 2, 20 mm above tray floor, separating system: methylcyclohexane and *n*-heptane **a** by using Eq. (1.16) and $C_{c0} = 0.11$, $C_{c1} = 1.8$, $C_{c2} = 0.72$, $C_{c3} = 2.2$, $C_{c4} = 0.8$, $\sigma_{c'^2} = 1.0$, $\sigma_{\varepsilon_{c'}} = 1.0$, **b** by using Eq. (1.17) and $C_{c0} = 0.14$, $C_{c1} = 1.8$, $C_{c3} = 0.83$, $C_{c4} = 2.22$, $\sigma_{c'^2} = 1.0$, $\sigma_{\varepsilon_{c'}} = 1.0$, **c** by using Eq. (1.18) and $C_{c0} = 0.14$, $C_{c1} = 2.0$, $C_{c4} = 2.22$, $\sigma_{c'^2} = 1.0$, $\sigma_{\varepsilon_{c'}} = 1.0$ (reprinted from ref. [4], Copyright 2007, with permission from Elsevier)

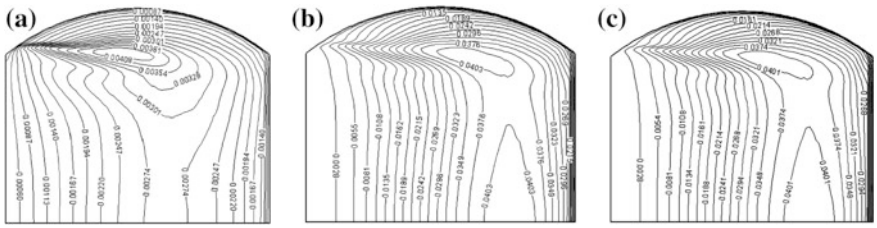

Fig. 1.2 The simulated mass diffusivity D_t contours on a column tray by using different $\varepsilon_{c'}$ modeling equations and model constants (II) The conditions of **a**, **b** and **c** are given in Fig. 1.1 (reprinted from ref. [4], Copyright 2007, with permission from Elsevier)

1.4.2 The $\overline{c'^2} - \varepsilon_{c'}$ Model Equation Sets

If no heat effect is involved in the mass transfer process, the two-equation model consists of two sets of equations, i.e., the CFD equation set for computing velocity U_i distribution and the mass transfer equation set for computing the concentration distribution. Some mass transfer processes are accompanied by heat transfer, and thus the heat transfer equation set is also a part of the model equations.

Several points should be mentioned for the application of model equations

- Since the mass transfer process usually involves two phases, the governing equations should be written for a designated phase, such as liquid phase or gas phase.
- In some cases, the volume and density of each phase are changing due to the mass transferred from one phase to the other.

- In considering the total mass of a fluid phase is not remained constant due to undertaking mass transfer, the continuity equation in CFD is not equal to zero. A source term S_m is added to the continuity equation representing the amount of mass being transferred between phases or generated by chemical reaction; the new equation $\frac{\partial \rho}{\partial t} + \frac{\partial \rho U_i}{\partial x_i} = S_m$ is designated as overall mass conservation equation. Note that, in this case, $\frac{\partial U_i}{\partial x_i} \neq 0$ even at constant ρ; thus Eq. (A1.5) in Appendix 1, in which the assumption of $\frac{\partial U_i}{\partial x_i} = 0$ is applied, is not valid for the fluid flow involving mass transfer.
- Since the mass transfer process involves two or more phases (see Sect. 1.4), the interacted liquid phase model is convenient for the process simulation by computational mass transfer. In applying this model, all parameters are involved, such as $U, u, \rho, k, \varepsilon, \mu, \mu_t, \alpha, \alpha_t, T, T', k_{T'}\varepsilon_{T'}c, C, D, D_t, k_{c'}, \varepsilon_{c'}$ in the model equation are denoted to liquid phase.

The $\overline{c'^2} - \varepsilon_{c'}$ model equation sets are given below. In the following subsections, equations with prefix "A1" and "A2" are given and deduced in Appendixes 1 and 2, respectively.

(I) **Fluid-dynamic equation set ($k - \varepsilon$ model)**

The development of the fluid-dynamic equations for turbulent flow can be found in Appendix 1.

Overall Mass conservation equation

$$\frac{\partial \rho}{\partial t} + \frac{\partial \rho U_i}{\partial x_i} = S_m \tag{1.22}$$

Momentum conservation equation

$$\begin{aligned} \frac{\partial \rho U_i}{\partial t} + \frac{\partial \rho U_i U_j}{\partial x_i} &= -\frac{\partial P}{\partial x_j} + \mu \frac{\partial^2 U_i}{\partial x_i \partial x_i} + \frac{\partial \left(-\rho \overline{u_i' u_j'}\right)}{\partial x_i} + \rho S_i \\ -\rho \overline{u_i' u'}_j &= \mu_t \left(\frac{\partial U_i}{\partial x_j} + \frac{\partial U_j}{\partial x_i}\right) - \frac{1}{3}\rho \delta_{ij} \overline{u_i' u_i'} \end{aligned} \tag{A1.4}$$

k equation

$$\begin{aligned} \frac{\partial (\rho k)}{\partial t} + \frac{\partial (\rho U_i k)}{\partial x_i} &= \frac{\partial}{\partial x_i}\left[\left(\mu + \frac{\mu_t}{\sigma_k}\right)\frac{\partial k}{\partial x_i}\right] + G_k - \rho\varepsilon \\ G_k &= \mu_t \left(\frac{\partial U_j}{\partial x_i} + \frac{\partial U_i}{\partial x_j}\right)\frac{\partial U_j}{\partial x_i} \end{aligned} \tag{A1.11a}$$

ε equation

$$\frac{\partial(\rho\varepsilon)}{\partial t} + \frac{\partial(\rho U_i \varepsilon)}{\partial x_i} = \frac{\partial}{\partial x_i}\left[\left(\mu + \frac{\mu_t}{\sigma_\varepsilon}\right)\frac{\partial \varepsilon}{\partial x_i}\right] + C_{1\varepsilon}\frac{\varepsilon}{k}G_k - C_{2\varepsilon}\rho\frac{\varepsilon^2}{k} \tag{A1.13a}$$

μ_t equation

$$\mu_t = C_\mu \rho \frac{k^2}{\varepsilon} \tag{A1.14}$$

For the model constant, refer to Appendix 1.

(II) **Heat transfer equation set ($\overline{T'^2} - \varepsilon_{T'}$ model)**

The fluid-dynamic equations for turbulent flow can be found in Appendix 2.
Energy conservation equation

$$\frac{\partial \rho T}{\partial t} + U_i \frac{\partial \rho T}{\partial x_i} = \frac{\lambda}{C_p}\frac{\partial^2 T}{\partial x_i \partial x_i} + \frac{\partial\left(-\rho\overline{u_i' T'}\right)}{\partial x_i} + \rho S_T \tag{A2.3}$$

where

$$-\overline{u_i' T'} = \alpha_t \frac{\partial T}{\partial x_i} \tag{A2.4}$$

$\overline{T'^2}$ equation

$$\frac{\partial \rho\overline{T'^2}}{\partial t} + \frac{\partial \rho U_i \overline{T'^2}}{\partial x_i} = \frac{\partial}{\partial x_i}\rho\frac{\partial \overline{T'^2}}{\partial x_i}\left(\frac{\alpha_t}{\sigma_{T'}} + \alpha\right) - 2\rho\alpha_t \frac{\partial T}{\partial x_i}\frac{\partial T}{\partial x_i} - 2\rho\varepsilon_{T'} \tag{A2.7a}$$

$\varepsilon_{T'}$ equation

$$\frac{\partial \rho\varepsilon_{T'}}{\partial t} + \frac{\partial \rho U_i \varepsilon_{T'}}{\partial x_i} = \frac{\partial}{\partial x_i}\left[\rho\left(\frac{\alpha_t}{\sigma_{\varepsilon_{T'}}} + \alpha\right)\frac{\partial \varepsilon_{T'}}{\partial x_i}\right] - C_{T1}\rho\frac{\varepsilon_{T'}}{\overline{T'^2}}\overline{u_i' T'}\frac{\partial T}{\partial x_i} - C_{T2}\rho\frac{\varepsilon_{T'}^2}{\overline{T'^2}} - C_{T3}\rho\frac{\varepsilon\varepsilon_{T'}}{k} \tag{A2.10}$$

α_t equation

$$\alpha_t = C_{T0} k\left(\frac{k}{\varepsilon}\frac{\overline{T'^2}}{\varepsilon_{T'}}\right)^{\frac{1}{2}} \tag{A2.6}$$

For the model constant, refer to Appendix 2.

(III) **Mass transfer equation set ($\overline{c'^2} - \varepsilon_{c'}$ model)**:

Species mass conservation equation

$$\frac{\partial C}{\partial t} + \frac{\partial U_i C}{\partial x_i} = \frac{\partial}{\partial x_i}\left(D\frac{\partial C}{\partial x_i} - \overline{u_i' c'}\right) + S_n \tag{1.3}$$

$$-\overline{u_i' c'} = D_\mathrm{t}\frac{\partial C}{\partial x_i} \tag{1.4}$$

$\overline{c'^2}$ equation

$$\frac{\partial \overline{c'^2}}{\partial t} + \frac{\partial U_i \overline{c'^2}}{\partial x_i} = \frac{\partial}{\partial x_i}\left[\left(\frac{D_\mathrm{t}}{\sigma_{c'^2}} + D\right)\frac{\partial \overline{c'^2}}{\partial x_i}\right] - 2D_\mathrm{t}\left(\frac{\partial C}{\partial x_i}\right)^2 - 2\varepsilon_{c'} \tag{1.10}$$

$\varepsilon_{c'}$ equation

$$\frac{\partial \varepsilon_{c'}}{\partial t} + \frac{\partial U_i \varepsilon_{c'}}{\partial x_i} = \frac{\partial}{\partial x_i}\left[\left(\frac{D_\mathrm{t}}{\sigma_{\varepsilon_{c'}}} + D\right)\frac{\partial \varepsilon_{c'}}{\partial x_i}\right] - C_{c1}\frac{\varepsilon_{c'}}{\overline{c'^2}}\overline{c' u_i'}\frac{\partial C}{\partial x_i} - C_{c2}\frac{\varepsilon}{k}\varepsilon_{c'} - C_{c3}\frac{\varepsilon_{c'}}{\overline{c'^2}}\varepsilon_{c'} \tag{1.17}$$

D_t equation

$$D_\mathrm{t} = C_{c0} k\left(\frac{k\overline{c'^2}}{\varepsilon\varepsilon_{c'}}\right)^{\frac{1}{2}} \tag{1.6}$$

Model constant are: $C_{c0} = 0.11$, $C_{c1} = 1.8$, $C_{c2} = 2.2$, $C_{c3} = 0.8$, $\sigma_{c'^2} = 1.0$, $\sigma_{\varepsilon_{c'}} = 1.0$.

Applying the foregoing equation sets to solve the problem involving flow, heat and mass transfer, there are fifteen unknown quantities, i.e.,

$$U_i, U_j, U_k, p, \mu_\mathrm{t}, k, \varepsilon, T, \alpha_\mathrm{t}, \overline{T'^2}, \varepsilon_{T'}, C, D_\mathrm{t}, \overline{c'^2}, \varepsilon_{c'}$$

The model equations available is also fifteen, namely, seven equations from CFD, four equations from heat transfer, and four equations from mass transfer.

The foregoing equation sets are valid for one phase in the mass transfer process. For a process involving multi-phase, the number of model equations required is duly increased. The solution of the foregoing equation set is tedious and required heavy computer work. Thus the use of solvers provided in commercial software, like FLUENT, STAR CD, CFX, and others are helpful.

In some special cases, if the temperature change in the simulated object is small, such as in a distillation tray, the heat transfer equation set can be omitted to simplify the computation.

1.4.3 Determination of Boundary Conditions

The simulation of a process involving momentum, heat, and mass transfer by numerical method requires not only appropriate mathematic model but also its boundary conditions. The boundary condition of velocity, temperature, concentration, and pressure are depending on the simulated object, while that of $k, \varepsilon, \overline{T'^2}, \varepsilon'_{T'}, \overline{c'^2}, \varepsilon'_{c'}$ should be found by experimental or empirical method.

(A) ***Inlet boundary condition***

The boundary condition of $k - \varepsilon$ model has long been investigated and found that the inlet condition of k is proportional to the average kinetic energy (represented by U^2), that is [18]

$$k_{\text{in}} = (0.003 \sim 0.005)U^2$$

The inlet condition of ε is set to be related to k as follows

$$\varepsilon_{\text{in}} = C_D \frac{k_{\text{in}}^{3/2}}{l}$$

where $0.09 \leq C_D \leq 0.164$ depending on the process to be simulated, l is the characteristic length, it can be the inlet diameter or others to be defined by different authors to suit their simulation. Nevertheless, Patankar et al. [19] pointed out that for the condition of fully developed flow, the choice of different inlet condition did not affect appreciably the simulated result.

For the inlet $\overline{T'^2}$, the investigation by Tavoularis and Corrsin [20] showed that

$$\overline{T_{\text{in}}'^2} = (0.083\Delta T_{\text{in}})^2$$

Recently Ferchichi and Tavoularis [21] reported that

$$\overline{T_{\text{in}}'^2} = (0.08\Delta T_{\text{in}})^2$$

Taking the average, it is

$$\overline{T_{in}'^2} = (0.082\Delta T_{in})^2 = 0.0067\left(\Delta T_{in}^2\right)$$

The report on inlet $\varepsilon_{T'\text{in}}$ is scarce. Liu et al. [6, 7] suggested that

$$\varepsilon_{T'\text{in}} = 0.4\left(\frac{\varepsilon}{k}\right)\overline{T'^2}$$

For the inlet $\overline{c_{\text{in}}'^2}$, Sun considered that it was proportional to C_{in}^2 and proposed [3, 4]

$$\overline{c_{\text{in}}'^2} = (0.082C_{\text{in}})^2 = 0.0067C_{\text{in}}^2$$

Sun also set $\varepsilon_{c'\text{in}}$ for tray column to be [3, 4]

$$\varepsilon_{c'\text{in}} = 0.9\left(\frac{\varepsilon}{k}\right)\overline{c_{\text{in}}'^2}$$

Liu found that better simulated results were obtained in packed column if [6–9]

$$\varepsilon_{c'\text{in}} = 0.4\left(\frac{\varepsilon}{k}\right)\overline{c_{\text{in}}'^2}$$

(B) ***Outlet boundary condition***

The outlet boundary is usually set to the condition where the flow is fully developed to turbulence, so that in the main flow direction x, all physical quantities Φ except pressure are set to be:

$$\frac{\partial \Phi}{\partial x} = 0$$

(C) ***Wall surface boundary condition***

At the wall surface, no-slip condition is applied so that U, k, ε are equal to zero.

(D) ***Near wall computation***

In the near wall region, the standard wall function method can be used to determine the relevant transport quantities.

Referring to section A1.3 in Appendix 1, the near wall region is usually considered to be comprised by lamina sub-layer (includes transition layer) and turbulent layer. The former is dominated by viscous shearing stress and the latter is by Reynolds shearing stress.

(1) In the laminar sub-layer, the dimensionless velocity u^+ is given by Eq. (A1.19) in Appendix 1 as follows:

$$u^+ = \frac{U}{u_\tau} = \frac{Uu_\tau}{u_\tau^2} = \frac{Uu_\tau}{\tau_s/\rho} = \frac{u_\tau}{\tau_s/\rho U} \tag{1.23}$$

The velocity of fluid flow $\frac{\tau_s}{\rho U}$ (m s^{-1}) can be considered analogous to the velocity of flow with mass transfer. Let C_w and C_p respectively be the concentrations at point w on the wall surface and at a point p shortly apart from w, then the average mass velocity (m s^{-1}) under mass transfer condition is equal to the mass flux J_w (kg m^{-2} s^{-1}) divided by the average driving force $\left(C_w - C_p\right)$ (kg m^{-3}). Considering

the ratio of fluid velocity and mass velocity is proportional to the ratio of their diffusivities by analogy, we have

$$\frac{\tau_s}{\rho U} \Big/ \frac{J_w}{(C_w - C_p)} = \sigma \frac{\mu/\rho}{D}$$

or

$$J_w = \sigma \frac{\mu/\rho}{D} (C_w - C_p) \tag{1.24}$$

where $\frac{\mu/\rho}{D}$ is Schmidt number Sc; σ is the proportional constant, in most cases we may let $\sigma = 1$.

Combining Eqs. (1.23) and (1.24), we obtain

$$\frac{1}{Sc} \frac{(C_w - C_p)u_\tau}{J_w} = \frac{yu_\tau}{\mu/\rho} \tag{1.25}$$

Define near wall dimensionless concentration C^+ as

$$C^+ = \frac{(C_w - C_p)u_\tau}{J_w} \tag{1.26}$$

According to Eq. (1.29) and noting the near wall dimensionless distance $y^+ = \frac{yu_\tau}{\nu}$, we have

$$C^+ = y^+ Sc \tag{1.27}$$

In the small region of laminar sub-layer, Sc is substantially a constant; thus C^+ and y^+ are in linear relationship.

(2) In the turbulent region, considering Eq. (1.25) is also valid under the turbulent condition by using turbulent μ_t and Sc_t to replace viscous μ and Sc as follows

$$\frac{1}{Sc_t} \frac{(C_w - C_p)u_\tau}{J_w} = \frac{yu_\tau}{\mu_t/\rho}$$

and referring to Eq. (1.28), $\frac{yu_\tau}{\mu_t/\rho} = \frac{U}{u_\tau}$, we have

$$C^+ = \frac{(C_w - C_p)u_\tau}{J_w} = Sc_t \frac{U}{u_\tau}$$

Differentiate foregoing equation under the condition of constant shearing stress in the near wall region, and note that $\partial\left(\frac{U}{u_\tau}\right) = \frac{1}{\kappa}\frac{\partial y}{y}$ from Eq. (A1.19b) in Appendix 1, we yield

$$\partial C^+ = \partial\left(\frac{U}{u_\tau}\right) = Sc_t \frac{1}{\kappa}\frac{\partial y}{y}$$

After integrating, we obtain

$$C^+ = Sc_t \frac{1}{\kappa}\ln y + A \tag{1.28}$$

where A is integration constant. Let y be the thickness of laminar sub-layer δ_c, the constant A can be evaluated; the following logarithmic equation is obtained after mathematical treatment

$$C^+ = Sc_t \frac{1}{\kappa}\ln(Ey^+)$$

where E is empirical constant, depending on the wall surface condition. For smooth surface, E = 9.8, Karman constant $\kappa = 0.418$.

Substitute Eq. (1.37) to Eq. (1.28) to yield

$$C^+ = \frac{\left(C_w - C_p\right)\rho C_\mu^{1/4} k^{1/2} y}{J_w} \tag{1.29}$$

$$y^+ = \frac{yu_\tau}{v} = \frac{yC_\mu^{1/4}k^{1/2}}{v} \tag{1.30}$$

In the numerical computation of engineering problem, the first grid point is usually located outside of the laminar sub-layer, in other words, only turbulent layer is concerned. Generally, the neglect of laminar sub-layer does not affect substantially the final simulated result.

1.4.4 Experimental Verification of Model Prediction

The simulation by using computational mass transfer $\overline{c'^2} - \varepsilon_{c'}$ model as described in the foregoing sections have been applied and verified by comparing with the experimental data of different kinds of chemical equipment reported in the literature as given in subsequent chapters.

Nevertheless, no published data are available regarding the important aspect, i.e., the inside concentration distribution of an equipment. Thus, experimental work was conducted for the purpose of obtaining the concentration distribution for the comparison with model prediction.

(A) ***Experimental installation***

The experimental installation [22] is shown schematically in Fig. 1.3 for desorption of dissolved oxygen in water by blowing air.

The simulator is a single-pass sieve tray of 1.2 m in diameter with 4.6 mm holes and having 4.6 % opening of the tray area. The length of the outlet weirs is 0.79 m. The clearance under the inlet downcomer is 60 mm. The height of the outlet weir is set separately to be 60, 80 and 100 mm. The air rate, ranging from 2600 to 4000 m^3/h, was fed to the column by a blower and flow through a distributor to ensure uniform inlet condition. The water at the rate of 10–20 m^3 h^{-1} was pumped from the storage tank to the downcomer after saturated with oxygen in the static mixer. The water was circulated back to the storage tank after flowing through the tray. The oxygen was supplied by an oxygen cylinder.

The local concentration of dissolved oxygen in the water was measured by using a measuring probe. The measuring range of the probe is from 0 to 100 mg/L dissolved oxygen with accuracy of 0.1 mg/L. The temperature compensation was automatic. The probe was fixed to a slider, which was attached to a truss with cross guide ways on the top of the tray. The probe, submerged in the liquid, could be moved in three directions. The position of the measuring points is shown in Fig. 1.4. The depth of submergence for the measurement was at 10 and 20 mm above the tray deck. To ensure reliable experimental results, the operation was run until reaching the steady state where the variation of measured concentration was reduced to very small, and the average value was taken as the measuring data. The measurement was point by point with one probe in order to minimize the disturbance to the flow field. Although the concentration distribution over the whole tray was not taken simultaneously, it is the convenient way to provide an experimental basis to verify the predicted concentration at a point on the sieve tray. As the model prediction is three-dimensional, the planar concentration measurement was conducted at the depth of 10 and 20 mm above the tray deck in order to allow the comparison in three dimensions.

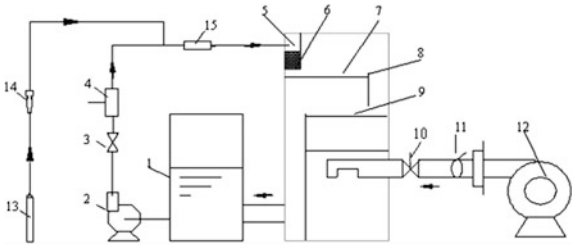

Fig. 1.3 Schematic setup of the experiment for concentration measurement *1* storage tank, *2* water pump, *3* control valve, *4* flow meter, *5* downcomer, *6* packing, *7* sieve tray, *8* outlet weir, *9* gas distributor, *10* control valve, *11* primary control valve, *12* blower, *13* oxygen cylinder, *14* flow meter, *15* static mixer (reprinted from ref. [22], Copyright 2011, with permission from CIESC)

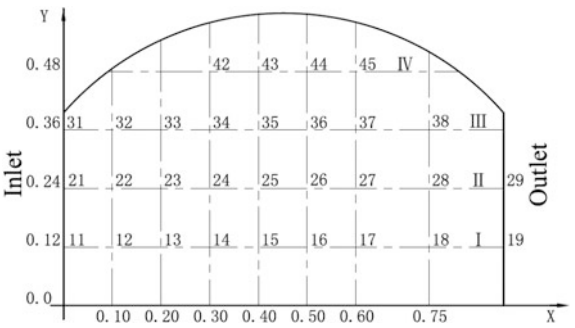

Fig. 1.4 Arrangement of measuring points on the experimental tray (reprinted from ref. [11], Copyright 2011, with permission from Elsevier)

(B) ***Comparison between model simulation and experimental data***

The liquid phase with gas phase interaction model accompanied with $\overline{c'^2} - \varepsilon_{c'}$ model as described in preceding sections were used to predict the concentration distribution and compared with the experimental data as shown in Fig. 1.5.

As seen from Fig. 1.5, the model predictions are reasonably agreed with the experimental measurement in consideration of some inaccuracies involved in both simulation and experiment. The obvious discrepancy between the experimental and simulated results is seen in the middle region of Line II, it may be attributed to the fact that this area is around the border between forward and reversed or vortex flow created in the segmental region, in which the flowing condition is in transition, violent turbulence and appears high fluctuation as observed in our experiment.

1.4.5 Analogy Between Transport Diffusivities

As shown in preceding chapters, on the basis of Boussinesq postulate, the Reynolds stress $-\rho\overline{u_i'u_j'}$, Reynolds heat flux $-\rho\overline{u_i'T'}$ and Reynolds mass flux $-\overline{u_i'c'}$ (or $-\rho\overline{u_i'c'_{\mathrm{mf}}}$) can be expressed respectively as proportional to their gradients of average velocity, temperature, and concentration

$$-\overline{u_i'u_j'} = \frac{\mu_t}{\rho}\left(\frac{\partial U_i}{\partial x_j} + \frac{\partial U_j}{\partial x_i}\right) - \frac{2}{3}\delta_{i,j}\overline{u_i'u_i'} \tag{A1.8}$$

$$-\overline{u_i'T'} = \alpha_t\frac{\partial T}{\partial x_i} \tag{A2.4}$$

$$-\overline{u_i'c'} = D_t\frac{\partial C}{\partial x_i} \tag{1.4}$$

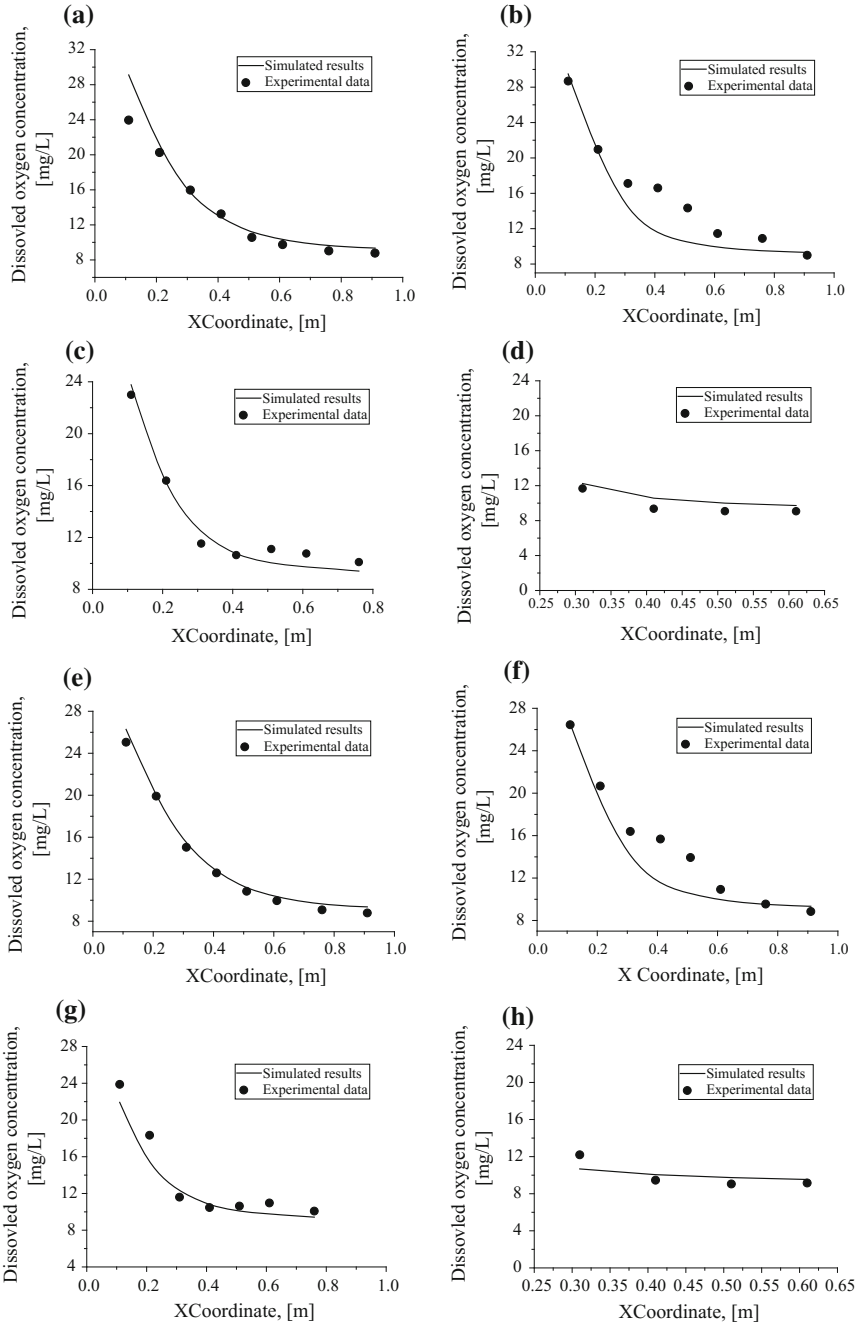

Fig. 1.5 Simulated concentration and experimental measurement, $Q_L = 17.2\ m^{-3}\ h^{-1}$, $G = 4000\ m^{-3}\ h^{-1}$, $h_W = 100$ mm **a** line I for $z = 10$ mm, **b** line II for $z = 10$ mm, **c** line III for $z = 10$ mm, **d** line IV for $z = 10$ mm, **e** line I for $z = 20$ mm, **f** line II for $z = 20$ mm, **g** line III for $z = 20$ mm, **h** line IV for $z = 20$ mm (reprinted from ref. [11], Copyright 2011, with permission from Elsevier)

The correspondent coefficients are designated, respectively, as turbulent diffusivity $\nu_t = \mu_t/\rho$, turbulent thermal diffusivity α_t and turbulent mass diffusivity $D_{t,i}$. The diffusivities equations in $\overline{c'^2} - \varepsilon_{c'}$ model can be written as follows:

$$\nu_t = \frac{\mu_t}{\rho} = C_\mu \frac{k^2}{\varepsilon} = C_\mu k \left(\frac{k}{\varepsilon}\frac{k}{\varepsilon}\right)^{1/2} = C_\mu k \left(\tau_\mu \tau_\mu\right)^{1/2} \tag{A1.14}$$

$$\alpha_t = C_{T0} k \left(\frac{k}{\varepsilon}\frac{\overline{T'^2}}{\varepsilon_{T'}}\right)^{1/2} = C_{T0} k \left(\tau_\mu \tau_T\right)^{1/2} \tag{A2.6}$$

$$D_t = C_{c0} k \left(\frac{k}{\varepsilon}\frac{\overline{c'^2}}{\varepsilon_{c'}}\right)^{1/2} = C_{c0} k \left(\tau_\mu \tau_c\right)^{1/2} \tag{1.6}$$

The following points should be noted.

(1) The analogy between the fluctuating flux and diffusivities is obvious. The similarity of $k - \varepsilon$, $T'^2 - \varepsilon_{T'}$ and $c'^2 - \varepsilon_{c'}$ models demonstrates the "fluctuation variance-dissipation" pattern is the common methodology for closing the transport equation. Starting from this viewpoint, a unified model of computational transport has been suggested by Liu [5] as shown in subsequent section. Notice should be made that in spite of some newer CFD model is emerging, the use of $k - \varepsilon$ model in cooperation of present $T'^2 - \varepsilon_{T'}$ model and $c'^2 - \varepsilon_{c'}$ model is necessary for the methodological consistence.

(2) The coefficients C_μ, C_{T0} and C_{c0} are given differently by different authors; the commonly accepted values are $C_\mu = 0.09$, $C_{T0} = 0.11$, $C_{c0} = 0.11$ or 0.14, although slight change on these values does not give substantial difference in final simulated result.

(3) The turbulent diffusivities ν_t, α_t and D_t as well as their ratio, $\frac{\nu_t}{D_{t,i}}$ (=Sc_t), $\frac{\nu_t}{\alpha_t}$ (=Pr_t) and $\frac{UL}{D_{t,i}}$ (=Pe_t) are varying and not a constant in the process concerned because $k, \varepsilon, \overline{T'^2}, \varepsilon_{T'}, \overline{c'^2}, \varepsilon_{c'}$ are function of position.

(4) Moreover, the turbulent diffusivities, ν_t, α_t and D_t obtained by the two-equation model as given above are applicable to all directions and therefore they are isotropic.

1.4.6 Generalized Equations of Two-Equation Model

As seen from the foregoing sections, the transports of momentum, heat, and mass obey the law of conservation and the model equations are similar in form. The

generalization of the $\overline{c'^2} - \varepsilon_{c'}$ two-equation model as summarized in Appendix 3 may help to broaden the understanding of relevant equations and facilitate the making of computer programming.

1.5 Reynolds Mass Flux Model

Besides applying the postulation similar to the Boussinesq's (or Fick's law) to solve the Reynolds mass flux $-\overline{u_i'c'}$ in terms of isotropic turbulent mass diffusivity D_t as described in preceding Sect. 1.2 by $\overline{c'^2} - \varepsilon_{c'}$ two-equation model, another model has been developed recently to solve the anisotropic Reynolds mass flux $-\overline{u_i'c'}$ directly instead of using D_t to close the turbulent species mass conservation equation. The Reynolds mass flux model discussed in this section could be known as a result following the turbulence closure postulations for the second-order closure turbulence model in the book of Chen and Jaw [23].

1.5.1 Standard Reynolds Mass Flux Model

For the convenience of derivation, the negative Reynolds mass flux $\overline{u_i'c'}$ is considered instead of $-\overline{u_i'c'}$. The exact $\overline{u_i'c'}$ equation can be derived as follows. Subtracting Eq. (1.1) from Eq. (1.3), we have

$$\frac{\partial c'}{\partial t} + \frac{\partial U_i c'}{\partial x_i} + u_i' \frac{\partial c'}{\partial x_i} = D \frac{\partial^2 c'}{\partial x_i \partial x_i} + \frac{\overline{u_i'c'}}{\partial x_i} \tag{1.31}$$

Multiply Eq. (1.31) by u_j' and multiply Eq. (A1.5) by c'; the sum of the two equations is averaged and rearranged to yield the following Reynolds mass flux equation (in the form of fluctuating mass flux $\overline{u_i'c'}$):

$$\begin{aligned} \frac{\partial \overline{u_i'c'}}{\partial t} + \frac{\partial U_j \overline{u_i'c'}}{\partial x_j} &= \frac{\partial}{\partial x_j}\left[-\overline{u_i'u_j'c'} - \delta_{ij}\frac{\overline{p'c'}}{\rho} + D\overline{u_i'\frac{\partial c'}{\partial x_j}} + \frac{\mu}{\rho}\overline{c'\frac{\partial u_i'}{\partial x_j}} \right] + \frac{\overline{p'}}{\rho}\frac{\partial c'}{\partial x_j} \\ &- \left(\overline{u_i'u_j'}\frac{\partial C}{\partial x_j} + \overline{u_j'c'}\frac{\partial U_i}{\partial x_j} \right) - \left(D + \frac{\mu}{\rho} \right) \overline{\frac{\partial c'}{\partial x_j}\frac{\partial u_i'}{\partial x_j}} \end{aligned} \tag{1.32}$$

where $\delta_{ij} = \begin{cases} 1 (i = j) \\ 0 (i \neq j) \end{cases}$.

The left side of the foregoing equation represents the increase of $\overline{u_i'c'}$ with respect to time and coordinate x_i; the bracketed first term on the right side represents the

turbulent and molecular diffusions; the second term represents the influence of fluctuating pressure and concentration on the distribution of Reynolds mass flux; the third term represents the production of $\overline{u_i'c'}$; the fourth term represents the dissipation.

Equation (1.32) should be modeled to suit computation. Applying the modeling rule, the bracketed first term on the right side of Eq. (1.32) can be considered proportional to the gradient of $\overline{u_i'c'}$ and the $\overline{u_i'u_j'}$ for turbulent diffusion, while the molecular diffusion is neglected as it is much smaller than the turbulent diffusion. The modeling form is as follows:

$$-\left[-\overline{u_i'u_j'c'}-\delta_{ij}\overline{\frac{p'c'}{\rho}}+D\overline{u_i'\frac{\partial c'}{\partial x_j}}+\frac{\mu}{\rho}\overline{c'\frac{\partial u_i'}{\partial x_j}}\right]=-\left(C_{c1}\frac{k}{\varepsilon}\overline{u_i'u_j'}+D\right)\frac{\partial\overline{u_i'c'}}{\partial x_k}$$

The addition of $\frac{k}{\varepsilon}$ as coefficient is necessary in order to keep the dimension kg m^{-1} s^{-1} consistent on both sides. It should be stressed that the use of quantity $\frac{k}{\varepsilon}$ is only in accordance with the modeling rule for representing the dimension "time". The use of k and ε equations here as auxiliary parameters in modeling is by no means in connection with the isotropic $k-\varepsilon$ model, and the foregoing modeling term is retained anisotropic.

The modeling of second term is complicated, it can be considered to be related to the fluctuating velocity and the average velocity gradient as follows:

$$\overline{\frac{p'}{\rho}\frac{\partial c'}{\partial x_j}}=-C_{c1}\frac{\varepsilon}{k}\overline{u_i'c'}-C_{c2}'\overline{u_i'c'}\frac{\partial U_i}{\partial x_j}$$

The third term remains unchanged.

For the fourth term since the dissipation rate through molecular diffusion is very small, we let

$$-\left(D+\frac{\mu}{\rho}\right)\overline{\frac{\partial c'}{\partial x_j}\frac{\partial u_i'}{\partial x_j}}=0$$

After modeling, Eq. (1.25) becomes

$$\begin{aligned}\frac{\partial\overline{u_i'c'}}{\partial t}+\frac{\partial U_j\overline{u_i'c'}}{\partial x_j}=&\frac{\partial}{\partial x_j}\left[\left(C_{c1}\frac{k}{\varepsilon}\overline{u_i'u_j'}+D\right)\frac{\partial\overline{u_i'c'}}{\partial x_j}\right]-\left(\overline{u_i'u_j'}\frac{\partial C}{\partial x_j}+\overline{u_j'c'}\frac{\partial U_i}{\partial x_j}\right)\\&-C_{c2}\frac{\varepsilon}{k}\overline{u_i'c'}+C_{c3}'\overline{u_j'c'}\frac{\partial U_i}{\partial x_j}\end{aligned}\tag{1.33}$$

By combining $\overline{u_j'c'}\frac{\partial U_i}{\partial x_j}$ term gives the following form:

$$\frac{\partial \overline{u_i'c'}}{\partial t}+\frac{\partial U_j\overline{u_i'c'}}{\partial x_j}=\frac{\partial}{\partial x_j}\left[\left(C_{c1}\frac{k}{\varepsilon}\overline{u_i'u_j'}+D\right)\frac{\partial \overline{u_i'c'}}{\partial x_j}\right]-\left(\overline{u_i'u_j'}\frac{\partial C}{\partial x_j}\right)$$
$$-C_{c2}\frac{\varepsilon}{k}\overline{u_i'c'}+C_{c3}\overline{u_j'c'}\frac{\partial U_i}{\partial x_j} \tag{1.33a}$$

It was found that the model constants to be $C_{c1}=0.18$, $C_{c2}=3.2$, $C_{c3}=0.55$.

After several examples of computation for mass transfer process, the computed results show that the $C_{c3}\overline{u_j'c'}\frac{\partial U_i}{\partial x_j}$ term is much less than the $C_{c2}\frac{\varepsilon}{k}\overline{u_i'c'}$ term and can be neglected. Hence another form of modeled $\overline{u_ic'}$ equation is

$$\frac{\partial \overline{u_i'c'}}{\partial t}+\frac{\partial U_j\overline{u_i'c'}}{\partial x_j}=\frac{\partial}{\partial x_j}\left[\left(C_{c1}\frac{k}{\varepsilon}\overline{u_i'u_j'}+D\right)\frac{\partial \overline{u_i'c'}}{\partial x_j}\right]-\left(\overline{u_i'u_j'}\frac{\partial C}{\partial x_j}\right)-C_{c2}\frac{\varepsilon}{k}\overline{u_i'c'} \tag{1.33b}$$

where the constants are: $C_{c1}=0.18$, $C_{c2}=3.2$.

1.5.1.1 Model Equation Set

The modeling equations of Reynolds stress model under the condition of having heat effect are given below.

(I) **Fluid-dynamic equation set (Reynolds stress model)**:

Overall Mass conservation equation

$$\frac{\partial \rho}{\partial t}+\frac{\partial \rho U_i}{\partial x_i}=S_m \tag{1.34}$$

Momentum conservation equation

$$\frac{\partial \rho U_i}{\partial t}+\frac{\partial \rho U_iU_j}{\partial x_i}=-\frac{\partial P}{\partial x_j}+\mu\frac{\partial^2 U_i}{\partial x_i\partial x_i}+\frac{\partial\left(-\rho\overline{u_i'u_j'}\right)}{\partial x_i}+\rho S_i \tag{1.35}$$

where $\overline{u_i'u_j'}$ is calculated by

$$\frac{\partial \rho \overline{u_i' u_j'}}{\partial t} + U_k \frac{\partial \rho \overline{u_i' u_j'}}{\partial x_k} = \frac{\partial}{\partial x_k}\left(\rho C_k \frac{k}{\varepsilon}\overline{u_i' u_j'}\frac{\partial \overline{u_i' u_j'}}{\partial x_k} + \mu \frac{\partial \overline{u_i' u_j'}}{\partial x_k}\right) - C_1 \rho \frac{\varepsilon}{k}\left(\overline{u_i' u_j'} - \frac{2}{3}k\delta_{ij}\right) - C_2 \rho\left(\overline{u_i' u_k'}\frac{\partial U_j}{\partial x_k} + \overline{u_j' u_k'}\frac{\partial U_i}{\partial x_k} - \frac{2}{3}\delta_{ij}\overrightarrow{u_i' u_j'}\frac{\partial U_i}{\partial x_j}\right) - \frac{2}{3}\rho\varepsilon\delta_{ij} \tag{A1.23a}$$

where $C_k^* = 0.18$, $C_1 = 2.3$, $C_2 = 0.55$.

(II) **Heat transfer equation set (Reynolds heat flux model)**:

Energy conservation equation

$$\frac{\partial \rho T}{\partial t} + U_i \frac{\partial \rho T}{\partial x_i} = \frac{\lambda}{C_p}\frac{\partial^2 T}{\partial x_i \partial x_i} + \frac{\partial\left(-\rho \overline{u_i' T'}\right)}{\partial x_i} + S_T \tag{A2.3a}$$

where $\overline{u_i' T'}$ is calculated by [23]

$$\frac{\partial \overline{u_j' T'}}{\partial t} + U_i \frac{\partial \overline{u_j' T'}}{\partial x_k} = \frac{\partial}{\partial x_k}\left[\left(C_{T1}\frac{k}{\varepsilon}\overline{u_i' u_j'} + \alpha\right)\frac{\partial \overline{u_j' T'}}{\partial x_k}\right] - \left(\overline{u_i' u_k'}\frac{\partial T}{\partial x_k} + \overline{u_k' T'}\frac{\partial U_j}{\partial x_k}\right) - C_{T2}\frac{\varepsilon}{k}\overline{u_j' T'} + C_{T3}\overline{u_k' T'}\frac{\partial U_j}{\partial x_k} \tag{A2.13}$$

where $C_{T1} = 0.07$, $C_{T2} = 3.2$, $C_{T3} = 0.5$.

(III) **Mass transfer equation set (Reynolds mass flux model)**:

Species mass conservation equation

$$\frac{\partial C}{\partial t} + \frac{\partial U_i C}{\partial x_i} = \frac{\partial}{\partial x_i}\left(D\frac{\partial C}{\partial x_i} - \overline{u_i' c'}\right) + S_n \tag{1.3}$$

where $\overline{u_i' c'}$ is calculated by

$$\frac{\partial \overline{u_i' c'}}{\partial t} + \frac{\partial U_j \overline{u_i' c'}}{\partial x_j} = \frac{\partial}{\partial x_j}\left[\left(C_{c1}\frac{k}{\varepsilon}\overline{u_i' u_j'} + D\right)\frac{\partial \overline{u_i' c'}}{\partial x_j}\right] - \left(\overline{u_i' u_j'}\frac{\partial C}{\partial x_j}\right) - C_{c2}\frac{\varepsilon}{k}\overline{u_i' c'} + C_{c3}\overline{u_j' c'}\frac{\partial U_i}{\partial x_j} \tag{1.33a}$$

where $C_{c1} = 0.09$, $C_{c2} = 3.2$, $C_{c3} = 0.55$.

The auxiliary equations k and ε are calculated by

k equation: Eq. (A1.11)

ε equation; Eq. (A1.13)

Thus Reynolds mass flux model involves Reynolds stress, Reynolds heat flux and Reynolds (fluctuating) mass flux equations, the unknown quantity is increased to twelve to make the total unknown quantities become twenty; they are

$$U_i, U_j, U_k, p, \overline{u_i' u_j'} \text{ (six unknowns)}, T, \overline{u_i' T'} \text{ (three unknowns)}, C, \overline{u_i' c'} \text{ (three unknowns)}, k, \varepsilon$$

The model equations available is also twenty, namely ten equations from CFD, four equations from heat transfer and six equations from mass transfer.

The feature of this model is rigorous and anisotropic, yet more equations are needed to solved which require not only more computer load but also harder to converge.

1.5.1.2 Determination of Boundary Conditions

(I). ***Inlet boundary condition***

At the top of the column, the boundary condition for the liquid phase is set to be [24]

$$\overline{U} = \overline{U_{\text{in}}}, \quad \overline{C} = \overline{C_{\text{in}}}, \quad k = 0.003\overline{U_{\text{in}}}^2, \quad \varepsilon_{in} = 0.09\frac{k_{\text{in}}^{1.5}}{d_{\text{H}}}$$

where d_{H} is the hydraulic diameter of random packing, which can be calculated by [25]:

$$d_{\text{H}} = \frac{4\gamma_\infty}{a(1-\gamma_\infty)}$$

There are no experimental measurements reported or empirical correlations available from the literature for determining the inlet condition of the fluctuating mass flux $\overline{u_i' c'}_{\text{in}}$ and the fluctuating heat flux $\overline{u_i' T'}_{\text{in}}$. In some cases, the following conditions for $\overline{u_i' c'}$ and $\overline{u_i' T'}$ were found to be suitable at the inlet [26]:

$$\left(\overline{u_i' \text{c}'}\right)_{\text{in}} = -0.7(\partial C/\partial x_i)|_{\text{in}} \quad \left(\overline{u_i' \text{T}'}\right)_{\text{in}} = -0.9\frac{\mu_{\text{t}}}{\rho}(\partial T/\partial x_i)|_{\text{in}}$$

where $\mu_{\text{t}} = C_\mu \frac{k_{\text{in}}^2}{\rho \varepsilon_{\text{in}}}$. We found that the foregoing inlet condition is more convenient to use; however, another expression for the inlet condition may be suggested to suit different simulation.

(II) ***Outlet boundary condition***

The flow in the packed column at the outlet is considered as fully developed in turbulent state; the zero normal gradients are applied to all variables except pressure.

(III) ***Wall boundary condition***

The no-slip condition of flow is applied to the wall, and the zero flux condition at the wall is adopted.

1.5.1.3 Influence of Reynolds Mass Flux on Mass Transfer

Many factors in connection with Rayleigh mass flux $-\overline{u_i'c'}$ are influential to the mass transfer. For the convenience of expression, the negative Rayleigh mass flux (also known as fluctuating mass flux) $\overline{u_i'c'}$ (kg m^{-2} s^{-1}), which denotes the rate of fluctuating mass to be transported per unit time (second) per unit cross sectional area (m^2), is mentioned instead of $-\overline{u_i'c'}$ in this section.

In connection with turbulence

The fluctuating mass flux $\overline{u_i'c'}$ is created by both the velocity fluctuation u_i' produced by turbulent fluid flow and the carrying subsequent mass (species) diffusion fluctuation c_i', i.e. it is as a result of combined contributions by turbulent fluctuation flow u_i' and species diffusion fluctuation c'. As the fluctuations originate from fluid turbulence, it may be regarded as *turbulent mass flux*. The value of $\overline{u_i'c'}$ reflects to some extent the combined effect of turbulence and the species concentration. Thus certain $\overline{u_i'c'}$ may produce from thigh turbulence and low species concentration or from low turbulence and high species concentration.

In connection with local mixing

The meaning of mass flux is the transport (flow) of mass per unit area per unit time. Thus the fluctuating mass flux $\overline{u_i'c'}$ (kg m^{-2} s^{-1}) represents the amount of fluctuating mass to be transported per unit cross sectional area (m^2) per unit time (second). It follows that the velocity fluctuation u_i' as well as the concentration fluctuation c' are dissipated subsequently through the mixing of velocity eddies and diffused concentration eddies so as to produce local mixing with neighboring velocity and concentration. The dissipation and generation of eddies are going on unceasingly in the course of mass transfer process. Therefore the transport of $\overline{u_i'c'}$ is accompanied with local (eddies) mixing effect.

In connection with apparent concentration profile

Suppose the fluctuating mass flux $\overline{u_i'c'}$ is transported through a cross sectional plane perpendicular to the fluid flow. According to the Fick's law, the transport of mass flux J_i should be under negative correspondent gradient (for instance, concentration gradient), i.e., $J_i = D\left(\frac{\partial C}{\partial x_i}\right)$ where D is a constant.

With this viewpoint, the profile of $\overline{u_i'c'}$ transport should be under decreasing $\overline{u_i'c'}$ (negative $\overline{u_i'c'}$ gradient) along the flow path. Since c' is the fluctuation of concentration C, it also implies that the $\overline{u_i'c'}$ transport profile follows the concentration decreasing profile (negative concentration gradient). In the case if the concentration profile of the process concerned is in negative gradient, i.e., the fluid (species) concentration is decreasing along the flow path (such as the concentration of reactant in reactor), the profile of $\overline{u_i'c'}$ transport is followed and consistent (coordinated) with the concentration profile of the process; the mass transfer is being enhanced. On the contrary, if the process proceeded under positive concentration gradient, i.e. the fluid (species) concentration is increasing along the flow path (such as the concentration of reaction product in reactor), the profile of $\overline{u_i'c'}$ transport is opposite to the concentration profile of the process. The concentration profile is not in consistent with the $\overline{u_i'c'}$ transport profile, which is unfavorable to the mass transfer process.

Further explanation can be made as follows. The governing equation of mass transfer, Eq. (1.3), can be also written in the following form:

$$\frac{\partial C}{\partial t}+\frac{\partial U_i C}{\partial x_i}=\frac{\partial}{\partial x_i}\left(D\frac{\partial C}{\partial x_i}\right)+\left(-\frac{\partial\left(\overline{u_i'c'}\right)}{\partial x_i}\right)+S_n \tag{1.3a}$$

where the first term on the right side represents the increasing rate of molecular mass flux $D\frac{\partial C}{\partial x_i}$ (molecular diffusion) along coordinate x_i; the second term represents the decreasing rate of $\overline{u_i'c'}$ along coordinate x_i. It is noted that the gradient $\frac{\partial \overline{u_i'c'}}{\partial x_i}$ is also the slope of $\overline{u_i'c'}$ contour in the $\overline{u_i'c'}$ versus x_i plot.

Equation (1.3a) can also be written in the following form:

$$\begin{aligned}\frac{\partial C}{\partial t}+\frac{\partial U_i C}{\partial x_i}&=\frac{\partial}{\partial x_i}\left(D\frac{\partial C}{\partial x_i}\right)+\left(-\frac{\partial\left(\overline{u_i'c'}\right)}{\partial x_i}\right)+S_n\\&=\frac{\partial}{\partial x_i}\left(D\frac{\partial C}{\partial x_i}\right)+S_{\text{comb}}\\S_{\text{comb}}&=\left(-\frac{\partial \overline{u_i'c'}}{\partial x_i}\right)+S_n\end{aligned} \tag{1.3b}$$

where the source term S_{comb} as well as S_n in Eq. (1.3b) retains the meaning of mass exchange between the phase concerned and the surroundings; positive S_{comb} represents mass is transferred to the phase from surroundings, while negative S_{comb} refers mass is depleted from the phase. There are three possible cases for the $\frac{\partial \overline{u_i'c'}}{\partial x_i}$ gradient

- Gradient $\frac{\partial \overline{u_i'c'}}{\partial x_i}$ is negative. It means $\overline{u_i'c'}$ is decreasing along the direction of flow path (coordinate x_i). In this case, the first two terms on the right side of Eq. (1.3a) are added together, i.e., the molecular and turbulent diffusions are

combined to intensify the diffusion effect. This case corresponds to the condition that the $\overline{u_i'c'}$ transport profile is consistent with the process concentration profile. Also it can be seen from Eq. (1.3b) that source term S_{comb} is greater than S_n under positive S_n (like adsorption), i.e. it is equivalent to increasing the amount of mass transfer. On the other hand, if S_n is negative (like desorption), then $S_{\text{comb}} < S_n$, i.e., it is equivalent to decreasing the amount of mass transfer.

- Gradient $\frac{\partial \overline{u_i'c'}}{\partial x_i}$ is zero. It means no $\overline{u_i'c'}$ is transported. In this case, the second term in Eq. (1.3a) is vanished and the turbulent mass flux $\overline{u_i'c'}$ remains constant. The molecular diffusion is still active. Referring to Eq. (1.3b), the amount of mass transfer remains unchanged because $S_{\text{comb}} = S_n$.
- Gradient $\frac{\partial \overline{u_i'c'}}{\partial x_i}$ is positive. It means $\overline{u_i'c'}$ is transported along the reverse direction of the flow path. In this case, the first and second terms on the right side of Eq. (1.3a) offset each other, i.e., the total diffusion is reduced, which is undesirable to the mass transfer. This case corresponds to the condition that the $\overline{u_i'c'}$ transport profile is opposing to the process concentration profile. Referring to Eq. (1.3b), S_{comb} is less than S_n in this case, i.e., the amount of mass transfer is reduced.

The foregoing discussion can be summarized in Table 1.1.

In brief, the transport of turbulent mass flux $\overline{u_i'c'}$ is influential to the process concentration profile; the latter is important as it indicates the effectiveness of a mass transfer process. The analysis of the $\overline{u_i'c'}$ is complicated as it involves the coordination of velocity profile, concentration profile, and $\overline{u_i'c'}$ profiles, yet more information of mass transfer can be obtained.

1.5.1.4 Anisotropic Turbulent Mass Diffusivity

By using the Reynolds mass flux model, the directional $-\overline{u_i'c'}$ can be calculated separately as $-\overline{u_x'c'}$, $-\overline{u_y'c'}$ and $-\overline{u_z'c'}$, so that the anisotropic turbulent mass diffusivity can be obtained based on Eq. (1.4).

Let J_i in the Fick's law equation be the fluctuating mass flux $\overline{u_i'c}$, the following relationship can be written:

$$-\overline{u_i'c'} = \mathbf{D}_{\text{t},i}\frac{\partial C}{\partial x} \tag{1.36}$$

$$-\overline{u_x'c'} = \mathbf{D}_{\text{t},x}\frac{\partial C}{\partial x}, \quad -\overline{u_y'c'} = \mathbf{D}_{\text{t},y}\frac{\partial C}{\partial y}, \quad -\overline{u_z'c'} = \mathbf{D}_{\text{t},z}\frac{\partial C}{\partial z} \tag{1.37}$$

$$\mathbf{D}_{\text{t},x} = \frac{-\overline{u_x'c'}}{\left(\frac{\partial C}{\partial x}\right)}, \quad \mathbf{D}_{\text{t},y} = \frac{-\overline{u_y'c'}}{\left(\frac{\partial C}{\partial y}\right)}, \quad \mathbf{D}_{\text{t},z} = \frac{-\overline{u_z'c'}}{\left(\frac{\partial C}{\partial z}\right)} \tag{1.38}$$

where $\mathbf{D}_{t,x}$, $\mathbf{D}_{t,y}$, $\mathbf{D}_{t,z}$ are the anisotropic turbulent mass diffusivities in x, y, z directions, respectively.

It should be noted that the $\mathbf{D}_{t,i}$ from Reynolds mass flux model and the D_t from two-equation model is entirely different, as $\mathbf{D}_{t,i}$ is calculated from $\overline{u_i c'}$ while D_t is given by the equation $D_t = C_{c0} k \left(\frac{k}{\varepsilon} \frac{\overline{c'^2}}{\varepsilon_{c'}} \right)^{1/2}$. From theoretical viewpoint, the anisotropic $\mathbf{D}_{t,i}$ is more rigorous than the isotropic D_t. The present derivation and discussion of $\mathbf{D}_{t,i}$ are only to demonstrate the anisotropic nature of mass transfer diffusivity and its influence. In the process simulation by using Reynolds mass flux model the $\mathbf{D}_{t,i}$ need not be evaluated.

Strictly speaking, all mass transfer processes are anisotropic. Nevertheless, the flow, heat and mass transfer in most processes are dominant in one direction, such as the axial direction is governing in most packed column. Yet in large diameter packed column the anisotropic nature is magnified and should be concerned and the radial effect cannot be ignored.

To illustrate the difference, the simulation of absorption of CO_2 by MEA solution (see Chap. 3) by using isotropic $\overline{c'^2} - \varepsilon_c$ two-equation model and one dimensional model by Tontiwachwuthikul [18] versus anisotropic Reynolds mass flux model is given in Fig. 1.6a for a packed column of 0.1 m in diameter and Fig. 3.6b for a packed column of 1.9 m in diameter. It is clear seen from the figures that the anisotropic model (the 'present model' in the figure) gives better simulated result than the isotropic models.

1.5.2 *Hybrid Reynolds Mass Flux Model*

In order to reduce the computer load of standard Reynolds mass flux model, the complicated Eq. (A1.23a) for expressing $\overline{u_i' u_j'}$ can be replaced by the simpler

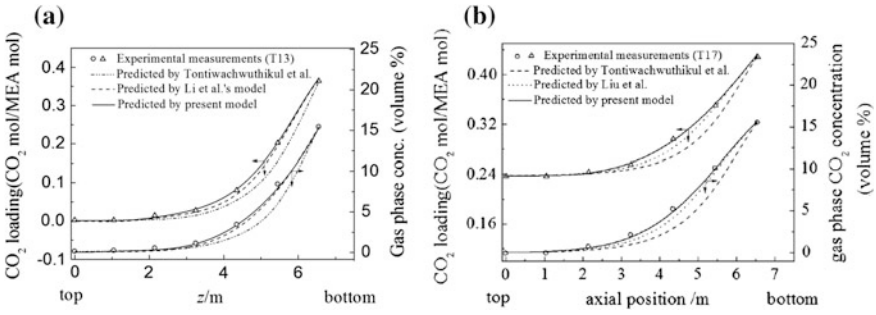

Fig. 1.6 Comparison between isotropic and anisotropic models [27] (*triangle* experimental measurement, *dashed line* two-equation model, *dashed with dotted line* one-dimensional model (isotropic), *line* Rayleigh mass flux model) **a** 0.1 m diameter column, **b** 1.9 m diameter column

Eq. (A1.8). Then the model becomes the combination of Reynolds mass flux and the two-equation model. It is called hereafter as hybrid Reynolds mass flux model. The model equations are given below.

(I) **CFD equation set**:

Overall Mass conservation equation: Eq. (1.34)
Momentum conservation equation: Eq. (A1.4)
$\overline{u_i'u_j'}$ *equation* (*Boussinesq postulate*):

$$-\rho\overline{u_i'u_j'} = \mu_t\left(\frac{\partial U_i}{\partial x_j} + \frac{\partial U_j}{\partial x_i}\right) - \frac{2}{3}\rho\delta_{ij}k \tag{A1.8}$$

$$\mu_t = C_\mu\rho\frac{k^2}{\varepsilon} \tag{A1.14}$$

where the *k equation* is calculated from Eq. (A1.11a) and the involved ε *equation* from Eq. (A1.13a) in Appendix 1.

(II) **Heat transfer equation set (Reynolds heat flux model)**

Energy conservation equation: Eq. (A2.3a)
Fluctuating heat flux equation: Eq. (A2.13)

(III) **Mass transfer equation set**

Species mass conservation equation: Eq. (1.3)
Fluctuating mass flux equation: Eq. (1.33a)

The unknown quantities in this model are: U_i, U_j, U_k, P, k, ε, μ_t, C, $\overline{u_i'c'}$, $\overline{u_j'c'}$, $\overline{u_k'c'}$, totally eleven versus eleven model equations are available. This model can be regarded as a hybrid (mixed) model comprising with $\overline{u_i'c'}$ from Reynolds mass flux model and $\overline{u_i'u_j'}$ from turbulent mass diffusivity model. Hence this model is isotropic.

1.5.3 Algebraic Reynolds Mass Flux Model

The Reynolds mass flux model can also be further simplified by letting the convection terms of $\overline{u_i'c'}$ on the left side of Eq. (1.26) equal to the molecular and turbulent diffusion terms of $\overline{u_i'c'}$ on the right side, then under steady condition, Eq. (1.33a) becomes

$$-\left(\overline{u_i'u_j'}\frac{\partial C}{\partial x_j} + \overline{u_i'c'}\frac{\partial U_i}{\partial x_j}\right) - C_{c2}\frac{\varepsilon}{k}\overline{u_i'c'} + C_{c3}\overline{u_i'c'}\frac{\partial U_i}{\partial x_j} = 0 \tag{1.39}$$

After arranging, the simplified $\overline{u_i'c'}$ expression is as follows:

$$\overline{u_i'c'} = -\frac{k}{C_{c2}\varepsilon}\left(\overline{u_i'u_j'}\frac{\partial C}{\partial x_j} + \overline{u_i'c'}\frac{\partial U_i}{\partial x_j}\right) + \frac{C_{c3}k}{C_{c2}\varepsilon}\overline{u_i'c'}\frac{\partial U_i}{\partial x_j} \tag{1.40}$$

The number of unknown quantities and equations of this model is the same as the Reynolds mass flux model except using Eq. (1.40) to replace Eq. (1.33a) for calculating $\overline{u_i'c'}$ in order to reduce the load of computation.

1.6 Simulation of Gas (Vapor)–Liquid Two-Phase Flow

Most mass transfer equipments consist of gas (vapor) and liquid two-phase flow, for instance, vapor–liquid two-phase crosscurrent flow is undertaken in tray distillation column; gas–liquid two-phase countercurrent flow is taken place in packed absorption column.

For the two phases flow, the modeling equations should be written for the designated phase. While such phase occupies only a fraction of the total volume; and therefore the volume fraction of the designated phase should be involved in the equation for the reason that the fluid velocity of the designated phase is determined by the fractional flow area. Note that, in general, the volume fraction is varying with position.

Let β_θ be the volume fraction of the designated phase θ (for instance, $\theta = \mathrm{L}$ refers to liquid phase $\theta = \mathrm{G}$ refers to gas phase), ρ_θ be the density of the designated phase θ. Both β_θ and ρ_θ need to insert into the CFD equation sets.

The simulated two-phase flow model can be in one of the following three forms:

(I) **Two-fluid modeling form**

There are two kinds of two-fluid models based on different viewpoints:

- *Eularian-Eularian two-fluid model*. In this model, both gas (vapor) and liquid phases are considered as a system to be concerned aiming to obtain the transport information of *each phase*. Model assumptions are made that both phases (the continuous liquid phase and the dispersed gas phase) are considered as two interpenetrating continua so that the Eulerian method (expressed by volume average Navier–Stokes equation) can be applicable to both phases. The model equations for phase θ are as follows:

  Mass conservation equation of phase θ

$$\frac{\partial \rho_\theta}{\partial t} + \frac{\partial \rho U_{\theta i}}{\partial x_i} = S_{\theta m}, \quad \theta = \mathrm{L}, \mathrm{G}$$

Momentum conservation equation of phase θ

$$\frac{\partial \rho U_{\theta i}}{\partial t} + \frac{\partial \rho_\theta U_{\theta i} U_{\theta j}}{\partial x_i} = -\frac{\partial P}{\partial x_j} + \mu_\theta \frac{\partial^2 U_{\theta i}}{\partial x_i \partial x_i} + \frac{\partial \left(-\rho \overline{u_{\theta i} u_{\theta j}}\right)}{\partial x_i} + \rho_\theta S_{\theta i}$$

where θ refers either liquid or gas; $S_{\theta m}$ represents the mass exchange between liquid and gas phases; $S_{\theta i}$ represents the gravitational force, interphase momentum exchange and all interacting forces between two phases. In the closure of momentum equation, the $k - \varepsilon$ model may be used with consideration of the mutual influence between the Reynolds stresses of liquid and gas phases.

The number of equations needed for two-fluid model is more than that of the following interacted liquid phase model and requires more computer capacity with the risk of harder convergence. In practice, for instance, the distillation simulation by some authors [28, 29] neglected the turbulent equations of vapor phase to simplify the simulation.

- *Eulerian-Lagrangian two-fluid model*. In most gas (vapor)-liquid equipments, the liquid exhibit as continuous phase and the gas (vapor) is dispersed phase. Thus Eulerian method (expressed by volume average Navier–Stokes equation) can be applied to the continuous liquid phase for simulating the flow field; while the motion as well as behaviors of dispersed phase is described by Lagrange method, in which the individual dispersed element (bubble) is tracking by an equation of motion, such as Newton's second law, and subjected to the action of all interface forces. However, the bubble motion and interface forces acting to the bubbles are complicated so as the modeling should concern bubble dynamics with all relevant acting forces (gravity, drag, lift, pressure gradient, virtual mass, etc.), as well as, the collision between bubbles and between bubble and the column wall. The coupling between bubble and liquid phases is realized by considering the interphase forces as source terms in the momentum conservation equation of liquid phase.

The feather of this model is the dispersed phase (bubble) can be described in details but at the expense of more computer load.

(II) **Liquid phase under interaction of gas phase (interacted liquid phase) modeling form**

In this modeling form, abbreviated as *interacted liquid phase model*, the liquid phase is considered as the system to be concerned aiming to obtain the transport information of the *liquid phase*. The dispersed phase is considered as the surroundings. The action of the dispersed phase (bubbles) on the liquid phase is treated as the external forces acting on the system (liquid phase). Thus the evaluation of source term S_{Li} in Navier–Stokes equation of liquid phase should cover all the acting forces by the dispersed gas phase. Such model can reduce the number of model equations and computer load. Computation shows that if the interaction source term S_{Li} is properly considered, the final simulated result is substantially equal to that by using two-fluid model.

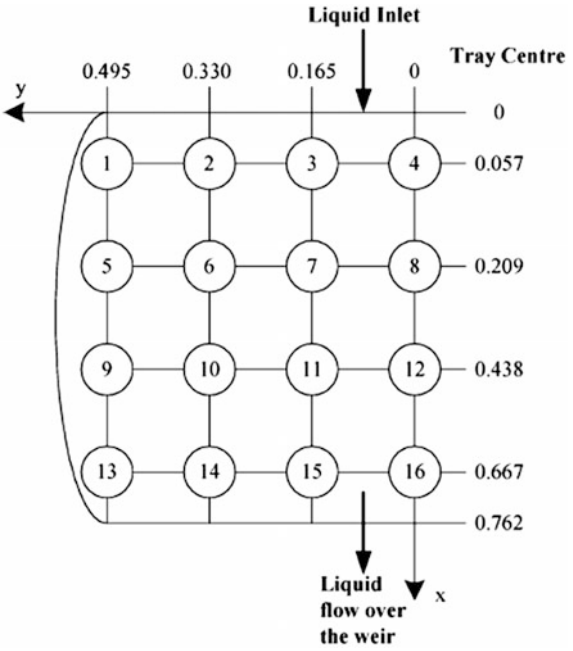

Fig. 1.7 Position of experimental probes (reproduce from Sorari [30])

As an example, the CFD simulations of velocity distribution on a sieve tray of 1.22 m in diameter (Fig. 1.7) reported by Sorari and Bell [30] by using two-fluid model [28] and interacted liquid phase model [31] are shown in Fig. 1.8, in which both simulations are comparable and close to experimental data.

The CFD model in interacted liquid phase form by Wang et al. [31] is given below:

Overall mass conversation

$$\frac{\partial(\rho_{\mathrm{L}}\beta_{\mathrm{L}}U_{\mathrm{L}i})}{\partial x_i} = S_m$$

Momentum conversation

$$\frac{\partial(\rho_{\mathrm{L}}\beta_{\mathrm{L}}U_{\mathrm{L}i}U_{\mathrm{Lj}})}{\partial x_i} = -\beta_{\mathrm{L}}\frac{\partial P}{\partial x_j} + \frac{\partial}{\partial x_i}\left[\beta_{\mathrm{L}}\nu_{\mathrm{e}}\left(\frac{\partial U_{\mathrm{L}j}}{\partial x_i}\right) - \beta_{\mathrm{L}}\rho_{\mathrm{L}}\nu_{\mathrm{e}}\left(\frac{\partial U_i}{\partial x_j} + \frac{\partial U_j}{\partial x_i}\right)\right] + \beta_{\mathrm{L}}\rho_{\mathrm{L}}S_{\mathrm{L}}$$

For the closure of momentum equation, the effective turbulent diffusivity ν_{e} is calculated by using $k-\varepsilon$ model as follows:

$$\nu_{\mathrm{e}} = c_\mu\frac{k^2}{\varepsilon} + \frac{\mu_{\mathrm{L}}}{\rho_{\mathrm{L}}}$$

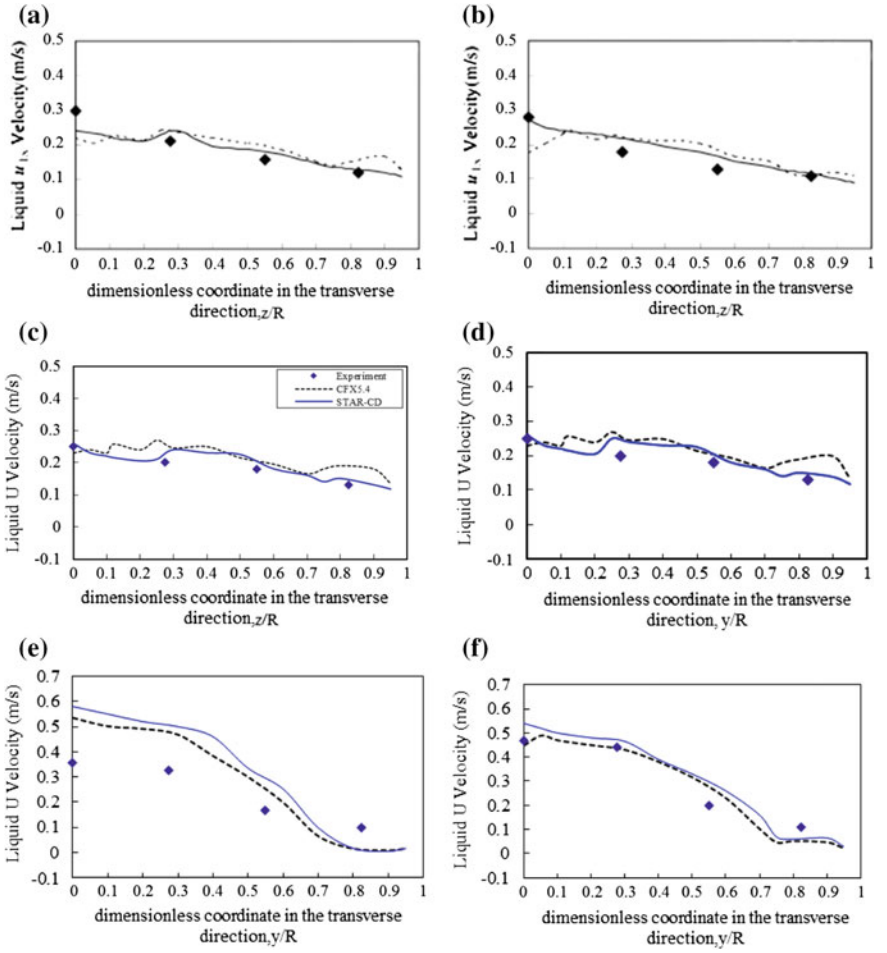

Fig. 1.8 Comparison between simulations by using two-fluid model and interacted liquid phase model for a sieve tray (*filled diamond* experimental data [30], *dashed line* two phases model simulation by Gesit et al. [28], *line* interacted liquid phase model simulation by Wang et al. [31]) **a** upstream profile for $Q_L = 6.94 \times 10^{-3}$ m^3/s and Fs = 1.015, **b** downstream profile for $Q_L = 6.94 \times 10^{-3}$ m^3/s and Fs = 1.015, **c** upstream profile for $Q_L = 6.94 \times 10^{-3}$ m^3/s and Fs = 1.464, **d** $Q_L = 6.94 \times 10^{-3}$ m^3/s and Fs = 1.464, **e** upstream profile for $Q_L = 17.8 \times 10^{-3}$ m^3/s and Fs = 0.801, **f** downstream profile for $Q_L = 17.8 \times 10^{-3}$ m^3/s and Fs = 0.801 (reprinted from ref. [31], Copyright 2004, with permission from American Chemical Society)

where k_L *equation*

$$\frac{\partial \rho_L \beta_L U_i k}{\partial x_i} = \frac{\partial}{\partial x_i}\left[\beta_L\left(\mu + \frac{\mu_t}{\sigma_k}\right)\frac{\partial k}{\partial x_i}\right] - \mu_t \beta_L\left(\frac{\partial U_i}{\partial x_j} + \frac{\partial U_j}{\partial x_i}\right)\frac{\partial U_j}{\partial x_i} + \varepsilon + G_V$$

where G_V is the turbulent energy created by the bubble agitation of the fluid on a tray, $G_V = c_e \frac{\Delta p U_G}{\rho_L h_L}$,

ε_L *equation*

$$\frac{\partial \rho_L \beta_L U_i \varepsilon_L}{\partial x_i} = \frac{\partial}{\partial x_i}\left[\beta_L\left(\mu + \frac{\mu_t}{\sigma_\varepsilon}\right)\frac{\partial \varepsilon}{\partial x_i}\right] - C_{\varepsilon 1}\beta_L \frac{\varepsilon}{k}\mu_t\left(\frac{\partial U_j}{\partial x_i} + \frac{\partial U_i}{\partial x_j}\right)\frac{\partial U_j}{\partial x_i} + [c_1 G_V - c_2 \varepsilon]\frac{\varepsilon}{k}$$

For the detailed expression of the gas–liquid interacting forces in the interacted liquid phase model, the source term S_{Li}, involving gravitational force and interfacial interacting forces as given by Wang, is shown below:

$$S_{Li} = F_g + \begin{bmatrix} F_{Lx} + f_{vmx} + M_{GLx} + f_x \\ F_{Ly} + f_{vmy} + M_{GLy} + f_y \\ F_{Lz} + f_{vmz} + M_{GLz} + f_z \end{bmatrix}$$

The gravity force: $F_g = \beta_L \rho_L g$.

The lift forces (Magnus forces): F_{Lx}, F_{Ly}, and F_{Lz}, which represent the forces of generating a sidewise force on the spinning bubble in the liquid phase by the liquid velocity gradient, are given by Auton et al. [32] as

$$F_{Lx} = 0.25\beta_G \rho_L (U_{Lx} - U_G) \times (\nabla U_{Lx})$$
$$F_{Ly} = 0.25\beta_G \rho_L (U_{Ly} - U_G) \times (\nabla U_{Ly})$$
$$F_{Lz} = 0.25\beta_G \rho_L (U_{Lz} - U_G) \times (\nabla U_{Lz})$$

The virtual mass forces: f_{vmx}, f_{vmy}, f_{vmz}, which account for the additional resistance acting by a bubble undergoing acceleration, are given below by Auton et al. [32]

$$-f_{vmx} = 0.5 \times \beta_G \rho_L (u_{Lx} \cdot \nabla u_{Lx})$$
$$-f_{vmy} = 0.5 \times \beta_G \rho_L (u_{Ly} \cdot \nabla u_{Ly})$$
$$-f_{vmz} = 0.5 \times \beta_G \rho_L (u_{Lz} \cdot \nabla u_{Lz})$$

The interphase drag force: M_{GLx}, M_{GLy}, M_{GLz} are given by Krishna et al. [33]

$$-M_{GLx} = \beta_G \alpha_L (\rho_L - \rho_G) g \frac{1}{(u_s/\beta_G)^2} \frac{1}{\beta_L} \times (u_s - u_{Lx}) |u_s - u_{Lx}|$$

$$-M_{GLy} = \beta_G \alpha_L (\rho_L - \rho_G) g \frac{1}{(u_s/\beta_G)^2} \frac{1}{\beta_L} \times \left(u_s - u_{Ly}\right) \left|u_s - u_{Ly}\right|$$

$$-M_{GLz} = \beta_G \alpha_L (\rho_L - \rho_G) g \frac{1}{(u_s/\beta_G)^2} \frac{1}{\beta_L} \times (u_s - u_{Lz}) |u_s - u_{Lz}|$$

The resistance to the fluid flow: f_x,f_y,f_z, the resistances created by uprising vapor to the fluid flow, is considered to be equivalent to a body force acting vertically and uniformly on the horizontally flowing fluid. This body force, resolved into f_x, f_y, f_z by Yu et al. [34] in the froth regime of fluid flow, can be calculated by means of the froth height h_f as follows:

$$f_x = -\frac{\rho_G u_s}{\rho_L h_f} u_{Lx} \quad f_y = -\frac{\rho_G u_s}{\rho_L h_f} u_{Ly} \quad f_z = -\frac{\rho_G u_s}{\rho_L h_f} u_{Lz}$$

The froth height h_f is evaluated by the Colwell [35] correlation,

$$h_L = \beta_{L,avg} \left[h_w + 0.527 \left(\frac{Q_L}{C_d \beta_{L,avg}} \right)^{0.67} \right]$$

$$C_d = \begin{cases} 0.61 + 0.08 \dfrac{h_{fow}}{h_w}, \dfrac{h_{fow}}{h_w} < 8.315 \\ 1.06 \left(1 + \dfrac{h_w}{h_{fow}} \right)^{1.5}, \dfrac{h_{fow}}{h_w} \geq 8.315 \end{cases}$$

$$h_{fow} = h_f - h_w$$

where $\beta_{L,avg}$ represents the liquid average froth volume fraction,

$$\beta_{L,avg} = \frac{1}{12.6 F_r'^{0.4} (A_B/A_h)^{0.25} + 1}$$

$$F_r' = F_r \left(\frac{\rho_G}{\rho_L - \rho_G} \right)$$

$$F_r = \frac{u_s}{g h_L}$$

It is assumed that the gas and liquid volume fraction β_G, β_L are not varying with position. The β_G can be estimated by

$$\beta_G = 1 - \beta_L$$

where volume fraction of liquid phase β_L is given by [36]

$$\beta_L = \exp\left[-12.55\left(u_s\sqrt{\frac{\rho_G}{\rho_L - \rho_G}}\right)^{0.91}\right]$$

(III) **Mixed phase modeling form**.

In this model, the liquid and vapor are considered to be mixed together as a single mixed continuous phase. The difficulty comes from the evaluation of the liquid–vapor interaction within a phase. This model is not yet well established and still under investigation.

Remarks

In our practice, the application of interacted liquid phase model is successful in simulating liquid–gas (vapor) two-phase processes, such as distillation, absorption, and adsorption, as given in subsequent chapters.

1.7 Model System of CMT Process Computation

Generally speaking, most of the existing mass transfer processes involve fluid flow, heat and mass transfer. Thus the process simulation by using computational mass transfer should comprises momentum, heat and mass transfer model equation sets for coupling computation as given below.

(I) **Computational fluid-dynamics equation set**: It consists of overall mass conservation equation, momentum conservation equation and its closure equations. It aims to find the velocity distribution (velocity profile) and other flow parameters.

(II) **Computational heat transfer equation set**: It consists of energy conservation equation and its closure equations. It aims to find the temperature distribution (temperature profile) and other heat parameters.

(III) **Computational mass transfer equation set**: It consists of species mass conservation equation and its closure equations. It aims to find the concentration distribution (concentration profile) and other mass transfer parameters.

The equations in the foregoing equation set are depending on what model is being used. The corresponding equations for fluid-dynamic model are given in

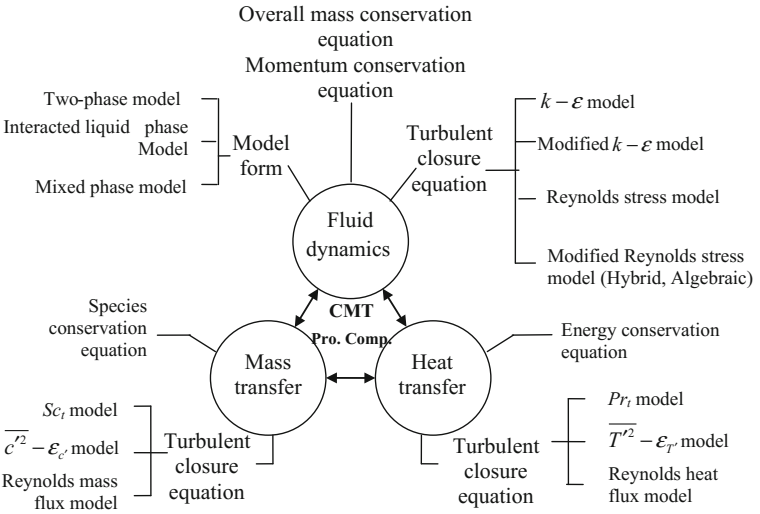

Fig. 1.9 Model system of CMT process computation

Appendix 1; while those for heat and mass transfer model are summarized in Appendix 2 and this chapter, respectively.

The model system of process computation in CMT (computational mass transfer) in this book can be shown schematically in Fig. 1.9.

1.8 Summary

Besides the computation of velocity distribution by CFD and temperature distribution by CHT as presented in previous chapters, the computation of concentration distribution in process equipment so far receives less attention but it is the basis of evaluating the process efficiency and should be much concerned. The challenge of this problem is the closure of the differential species conservation equation. The recently investigated $\overline{c'^2}-\varepsilon_{c'}$ model and Reynolds mass flux model are found to be successful in fulfilling the need.

(1) $\overline{c'^2}-\varepsilon_{c'}$ model, in which the unknown Reynolds mass flux $-\rho\overline{u_i'c'}$ is calculated by Eq. (1.4) involving a new parameter of turbulent mass transfer diffusivity D_t. The D_t can be calculated by Eq. (1.6) where the $\overline{c'^2}$ and $\varepsilon_{c'}$ equations are given by Eqs. (1.1) and (1.17), respectively. Note that the molded $\varepsilon_{c'}$ equation has different forms but they give comparable simulated results each other. Although this model is convenient to be used and give good simulated results in many cases, it is isotropic and its accuracy of simulation is less than that by Reynolds mass flux model.

(2) Reynolds mass flux model, or standard Reynolds mass flux model, in which the unknown $-\rho\overline{u_i'c'}$ is calculated directly by using model equation either Eqs. (1.33) or (1.33a). This model is rigorous and applicable to anisotropic case with mass and heat transfer. The model equations comprise the following equation sets:

- Mass transfer equation set, i.e., Eqs. (1.3) and (1.33);
- Fluid-dynamic (CFD) equation set, i.e. Eqs. (1.34), (1.35), and (A1.23a);
- Heat transfer equation set, i.e., Eqs. (A2.3a) and (A2.13).

The weakness of this model is requiring heavy computer work. For simplifying the computation, the complicated Eq. (A1.23a) can be replaced by Eq. (A1.8), which is called hybrid mass flux model. Another simplification is made by letting Eq. (1.39) to replace Eq. (1.33) for calculating $\overline{u_i'c'}$, called algebraic Reynolds mass flux model. These simplified models are able to give similar simulated results in compared with the standard model.

The Reynolds (turbulent) mass flux $\overline{u_i'c'}$ is the variance of $u_i'c'$ created from the turbulent mass flux uc; the transport of which is by both uc flow and fluctuated concentration diffusion. If both are in the same direction, the process is promoted (enhanced). Inversely, if they are in opposite direction, the counter-action of diffusion causes reduction of uc by mutual mixing. Thus the $\overline{u_i'c'}$ initiated from turbulent effect is influential to the mass transfer.

References

1. Liu BT (2003) Study of a new mass transfer model of CFD and its application on distillation tray. Ph.D. Dissertation, Tianjin University, Tianjin, China (in Chinese)
2. Sun ZM (2005) Study on computational mass transfer in chemical engineering. Ph.D. Dissertation, Tianjin University, Tianjin, China (in Chinese)
3. Sun ZM, Liu BT, Yuan XG, Yu KT (2005) New turbulent model for computational mass transfer and its application to a commercial-scale distillation column. Ind Eng Chem Res 44 (12):4427–4434
4. Sun ZM, Yu KT, Yuan XG, Liu CJ (2007) A modified model of computational mass transfer for distillation column. Chem Eng Sci 62:1839–1850
5. Liu GB (2006) Computational transport and its application to mass transfer and reaction processes in pack-beds. Ph.D. Dissertation, Tianjin University, Tianjin, China (in Chinese)
6. Liu GB, Yu KT, Yuan XG, Liu CJ, Guo QC (2006) Simulations of chemical absorption in pilot-scale and industrial-scale packed columns by computational mass transfer. Chem Eng Sci 61:6511–6529
7. Liu GB, Yu KT, Yuan XG, Liu CJ (2006) New model for turbulent mass transfer and its application to the simulations of a pilot-scale randomly packed column for CO2-NaOH chemical absorption. Ind Eng Chem Res 45:3220–3229

8. Liu GB, Yu KT, Yuan XG, Liu CJ (2008) A computational transport model for wall-cooled catalytic reactor. Ind Eng Chem Res 47:2656–2665
9. Liu GB, Yu KT, Yuan XG, Liu CJ (2009) A numerical method for predicting the performance of a randomly packed distillation column. Int J Heat Mass Transf 52:5330–5338
10. Li WB, Liu BT, Yu KT, Yuan XG (2011) A rigorous model for the simulation of gas adsorption and its verification. Ind Eng Chem Res 50(13):8361–8370
11. Sun ZM, Liu CJ, Yu GC, Yuan XG (2011) Prediction of distillation column performance by computational mass transfer method. Chin J Chem Eng 19(5):833–844
12. Lemoine F, Antoine Y, Wolff M et al (2000) Some experimental investigations on the concentration variance and its dissipation rate in a grid generated turbulent flow. Int J Heat Mass Transf 43(7):1187–1199
13. Spadling DB (1971) Concentration fluctuations in a round turbulent free jet. Chem Eng Sci 26:95
14. Launder BE, Samaraweera SA (1979) Application of a second-moment turbulence closure to heat and mass transport in thin shear flows—two-dimensional transport. Int J Heat Mass Transf 22:1631–1643
15. Sommer TP, So MRC (1995) On the modeling of homogeneous turbulence in a stably stratified flow. Phys Fluids 7:2766–2777
16. Sherwood TK, Pigford RL, Wilke CR (1975) Mass transfer. McGraw Hill, New York
17. Cai TJ, Chen GX (2004) Liquid back-mixing on distillation trays. Ind Eng Chem Res 43 (10):2590–2597
18. Comini G, Del Giudice S (1985) A k-e model of turbulent flow. Numer Heat Transf 8:299–316
19. Patankar SV, Sparrow EM, Ivanovic M (1978) Thermal interactions among the confining walls of a turbulent recirculating flow. Int J Heat Mass Transf 21(3):269–274
20. Tavoularis S, Corrsin S (1981) Experiments in nearly homogenous turbulent shear-flow with a uniform mean temperature-gradient. J Fluid Mech 104 (MAR):311–347
21. Ferchichi M, Tavoularis S (2002) Scalar probability density function and fine structure in uniformly sheared turbulence. J Fluid Mech 461:155–182
22. Sun ZM, Liu CT, Yuan XG, Yu KT (2006) Measurement and numerical simulation of concentration distribution on sieve tray. J Chem Ind Eng (China) 57(8):1878–1883
23. Chen CJ, Jaw SY (1998) Fundamentals of turbulence modeling. Taylor and Francis
24. Jone CJ, Launder BE (1973) The calculation of low-Reynolds-number phenomena with a two-equation model of turbulence. Int J Heat Mass Transf 16:1119–1130
25. Khalil EE, Spalading DB, Whitelaw JH (1975) Calculation of local flow properties in 2-dimensional furnaces. Int J Heat Mass Transf 18:775–791
26. Li WB, Liu BT, Yu KT, Yuan XG (2011) A new model for the simulation of distillation column. Chin J Chem Eng 19(5):717–725
27. Li WB (2012) Theory and application of computational mass transfer for chemical engineering processes. Ph.D. dissertation, Tianjin University, Tianjin
28. Gesit G, Nandakumar K, Chuang KT (2003) CFD modeling of flow patterns and hydraulics of commercial-scale sieve trays. AIChE J 49:910
29. Krishna R, van Baten JM, Ellenberger J (1999) CFD simulations of sieve tray hydrodynamics. Trans IChemE 77 Part A (10):639–646
30. Solari RB, Bell RL (1986) Fluid flow patterns and velocity distribution on commercial-scale sieve trays. AIChE J 32:640
31. Wang XL, Liu CT, Yuan XG, Yu KT (2004) Computational fluid dynamics simulation of three-dimensional liquid flow and mass transfer on distillation column trays. Ind Eng Chem Res 43(10):2556–2567

32. Auton TR, Hunt JCR, Prud'homme M (1988) The force exerted on a body in inviscid unsteady non-uniform rotational flow. J Fluid Mech 197:241
33. Krishna R, Urseanu MI, Van Baten JM et al (1999) Rise velocity of a swarm of large gas bubbles in liquids. Chem Eng Sci 54:171–183
34. Yu KT, Yuan XG, You XY, Liu CJ (1999) Computational fluid-dynamics and experimental verification of two-phase two-dimensional flow on a sieve column tray. Chem Eng Res Des 77A:554
35. Colwell CJ (1979) Clear liquid height and froth density on sieve trays. Ind Eng Chem Proc Des Dev 20:298
36. Bennet DL, Agrawal R, Cook PJ (1983) New pressure drop correlation for sieve tray distillation columns. AIChE J 29:434–442

Chapter 2
Application of Computational Mass Transfer (I) Distillation Process

Abstract In this chapter, the application of computational mass transfer (CMT) method in the forms of two-equation model and Rayleigh mass flux model as developed in previous chapters to the simulation of distillation process is described for tray column and packed column. The simulation of tray column includes the individual tray efficiency and the outlet composition of each tray of an industrial scale column. Methods for estimating various source terms in the model equations are presented and discussed for the implementation of the CMT method. The simulated results are presented and compared with published experimental data. The superiority of using standard Reynolds mass flux model is shown in the detailed prediction of circulating flow contours in the segmental area of the tray. In addition, the capability of using CMT method to predict the tray efficiency with different tray structures for assessment is illustrated. The prediction of tray efficiency for multicomponent system and the bizarre phenomena is also described. For the packed column, both CMT models are used for the simulation of an industrial scale column with success in predicting the axial concentrations and HETP. The influence of fluctuating mass flux is discussed.

Keywords Simulation of distillation · Tray column · Packed column · Concentration profile · Tray efficiency evaluation

Nomenclature

A	Surface area per unit volume of packed column, m^{-1}
c_1, c_2, c_3	Model parameters in transport equation for the turbulent mass flux
C	Concentration, kg m^{-3}
$\overline{C}$	Average concentration, kg m^{-3}
C_μ, $C_{1\varepsilon}$, $C_{2\varepsilon}$, $C_{3\varepsilon}$	Model parameters in k–ε model equations
c'	Fluctuating concentration, kg m^{-3}
$\overline{c'^2}$	Variance of fluctuating concentration, kg^2 m^{-6}
D	Molecular diffusivity, m^2 s^{-1}
D_t	Turbulent mass diffusivity, m^2 s^{-1}

K.-T. Yu and X. Yuan, *Introduction to Computational Mass Transfer*,
Heat and Mass Transfer, DOI 10.1007/978-981-10-2498-6_2

d_e	Equivalent diameter of random packing, m
d_H	Hydraulic diameter of random packing, m
d_p	Nominal diameter of the packed particle, m
E_o	Overall efficiency
E_{MV}	Murphree tray efficiency on gas basis
E_{ML}	Murphree tray efficiency on liquid basis
F	F factor, $U_G\sqrt{\rho_G}$, m s^{-1} (kg m^{-3})$^{0.5}$
g	Acceleration due to gravity, m s^{-2}
G	Production term
H	Height of packed bed measured from column bottom, m
h_f	Height of the liquid layer in tray column, m
h_w	Weir height in tray column, m
K_{OL}	Overall liquid phase mass transfer coefficient in tray column, m s^{-1}
k	Turbulent kinetic energy, m^2 s^{-2}
k_G	Gas phase mass transfer coefficient in packed column, kg m^{-2} s^{-1}
k_L	Liquid phase mass transfer coefficient in packed column, kg m^{-2} s^{-1}
L	Liquid flow rate per unit cross section area, kg m^{-2} s^{-1}
l_w	Weir width, m
m	Distribution coefficient
r	Position in radial direction, m
R	Radius of the column, m
S_C	Source term in species conversation equation, kg m^{-3} s^{-1}
S_m	Source term in momentum equation, N m^{-3}
t	Time, s
U	Superficial velocities, m s^{-1}
U	Interstitial velocity vector, m s^{-1}
u_i'	Fluctuating velocity, m s^{-1}
W	Weir length, m
x	Distance in x direction, m; mole fraction in liquid phase
y	Distance in y direction, m; mole fraction in gas phase
z	Distance in z direction, m
Z	Total height of packed bed, m
β_L, β_V	Volume fraction of liquid phase, vapor phase
α_{re}	Relative volatility
ε	Turbulent dissipation rate, m^2 s^{-3}
$\varepsilon_{c'}$:	Turbulent dissipation rate of concentration fluctuation, kg^2 m^{-6} s^{-1}
γ	Porosity distribution of the random packing bed
μ, μ_G	Liquid and gas phase viscosity, kg m^{-1} s^{-1}
ρ, ρ_G	Liquid and gas phase density, kg m^{-3}
σ	Surface tension of liquid, N m^{-1}

σ_k, σ_ε	Correction factor in k–ε model equations
χ	Characteristic length of packing, m
Φ	Enhancement factor

Subscripts

G Gas
i Coordinates in different direction; component in solution
in Inlet
L Liquid
0 Interface
b Bulk

Distillation is a vapor–liquid separation process widely employed in petrochemical, chemical, and allied industries nowadays. The simulation of distillation has long been investigated since 1930s.

There are two basic types of distillation equipment: column with tray structure (tray column) and column with packing (packed column).

For the tray column, the early approach of simulation is based on the concept of equilibrium tray where the thermodynamic equilibrium between liquid and vapor phases is achieved; and it converts to actual tray by means of empirical tray efficiency. The later advance is to use the rate equation to account for the mass transfer instead of using empirical efficiency and equilibrium relationships. These methods are on the overall basis with the assumption that the flow and concentration are uniform on the column tray.

In the 1990s, the application of CFD to a column tray enables to calculate the velocity distribution (velocity profile), yet the calculation of concentration distribution is still lacking. Nevertheless the concentration distribution is even more important and interested by the chemical engineers as it is the deciding factor for predicting the tray efficiency. The recently developed computational mass transfer enables to overcome this insufficiency and provides a rigorous basis for predicting all transport quantities, including the concentration distribution, of a distillation column.

The status of packed column simulation is similar to that of tray column.

The efficiency of distillation process is very important in optimal design and operation as it is closely related to the column size needed and heat energy consumed. The accurate modeling of distillation process enables to show the nonideal distribution of concentration as well as the fluid flow and the designer and operator can take steps to overcome such nonideality, so as to improve the separation ability of the distillation process.

2.1 Tray Column

The tray column simulation involves mainly the following aspects:

- Velocity distribution to show the deviation from ideal flow: It can be calculated by using CFD as described in Appendix 1;
- Concentration distribution for the calculation of tray efficiency: As stated in Appendix 2, the conventional way of using turbulent Schmidt number Sc_t model for predicting the concentration distribution is not dependable for the reason that the correct Sc_t is not only hard to guess but also it is varying throughout the process. Hence the recently developed $\overline{c'^2} - \varepsilon_{c'}$ two-equation model and the Reynolds mass flux model are recommended to use as described in the subsequent sections.

2.1.1 $\overline{c'^2} - \varepsilon_{c'}$ Two-Equation Model

Interacted liquid phase form (see Appendix 2.6) of two-equation model is employed in this section for process simulation.

2.1.1.1 Model Equations

(I) **The CFD equation set (*k–ε* model, see Appendix 1)**

The detailed development of the CFD equations is given in Appendix 1. The equations with a name prifix "A" refer to those in Appendix 1.

Overall mass conversation

$$\frac{\partial(\rho_L \beta_L U_{Li})}{\partial x_i} = S_m \qquad (A1-3)$$

Momentum conversation

$$\frac{\partial\left(\rho_L \beta_L U_{Li} U_{Lj}\right)}{\partial x_i} = -\beta_L \frac{\partial P}{\partial x_j} + \frac{\partial}{\partial x_i}\left[\beta_L \mu_L \left(\frac{\partial U_{Lj}}{\partial x_i}\right) - \beta_L \rho_L \overline{u_i' u_j'}\right] + \beta_L \rho_L S_{Li} \qquad (A1-4)$$

$$-\rho_L \overline{u'_{Li} u'_{Lj}} = \mu_{Lt}\left(\frac{\partial U_{Li}}{\partial x_j} + \frac{\partial U_{Lj}}{\partial x_i}\right) - \frac{2}{3}\rho_L \delta_{ij} k_L \qquad (A1-8)$$

k_{L} *equation*

$$\frac{\partial \rho_{\mathrm{L}} \beta_{\mathrm{L}} U_{\mathrm{L}i} k_{\mathrm{L}}}{\partial x_i} = \frac{\partial}{\partial x_i}\left[\beta_{\mathrm{L}}\left(\mu_{\mathrm{L}} + \frac{\mu_{\mathrm{Lt}}}{\sigma_k}\right)\frac{\partial k_{\mathrm{L}}}{\partial x_i}\right] - \mu_{\mathrm{Lt}}\beta_{\mathrm{L}}\left(\frac{\partial U_{\mathrm{L}i}}{\partial x_j} + \frac{\partial U_{\mathrm{L}j}}{\partial x_i}\right)\frac{\partial U_j}{\partial x_i} - \rho_{\mathrm{L}}\beta_{\mathrm{L}}\varepsilon_{\mathrm{L}} \tag{A1-11a}$$

ε_{L} *equation*

$$\begin{aligned}\frac{\partial \rho_{\mathrm{L}} \beta_{\mathrm{L}} U_{\mathrm{L}i} \varepsilon_{\mathrm{L}}}{\partial x_i} = {} & \frac{\partial}{\partial x_i}\left[\beta_{\mathrm{L}}\left(\mu_{\mathrm{L}} + \frac{\mu_{\mathrm{Lt}}}{\sigma_\varepsilon}\right)\frac{\partial \varepsilon_{\mathrm{L}}}{\partial x_i}\right] \\ & - C_{\varepsilon 1}\beta_{\mathrm{L}}\frac{\varepsilon_{\mathrm{L}}}{k_{\mathrm{L}}}\mu_{\mathrm{Lt}}\left(\frac{\partial U_{\mathrm{L}j}}{\partial x_i} + \frac{\partial U_{\mathrm{L}i}}{\partial x_j}\right)\frac{\partial U_{\mathrm{L}j}}{\partial x_i} - C_{\varepsilon 2}\beta_{\mathrm{L}}\rho_{\mathrm{L}}\frac{\varepsilon_{\mathrm{L}}^2}{k_{\mathrm{L}}}\end{aligned} \tag{A1-13a}$$

In foregoing equations, the subscript L denotes the liquid phase.

(II) **Heat transfer equation set ($\overline{T'^2} - \varepsilon_{T'}$ model, see** Chap. 2):

The detailed development of the heat transfer equations is given in Appendix 2. The equations with a name prifix "A" refer to those in Appendix 2

Energy conservation equation

$$\frac{\partial \rho \beta_{\mathrm{L}} T}{\partial t} + U_{\mathrm{L}i}\frac{\partial \rho \beta_{\mathrm{L}} T}{\partial x_i} = \frac{\lambda}{C_{\mathrm{p}}}\beta_{\mathrm{L}}\frac{\partial^2 T}{\partial x_i \partial x_i} + \beta_{\mathrm{L}}\frac{\partial\left(-\rho\overline{u'_{\mathrm{L}i}T'}\right)}{\partial x_i} + \rho_{\mathrm{L}}\beta_{\mathrm{L}}S_{\mathrm{T}} \tag{A2-3}$$

or written as:

$$\begin{aligned}\frac{\partial \beta_{\mathrm{L}} T}{\partial t} + U_i\frac{\partial \beta_{\mathrm{L}} T}{\partial x_i} &= \frac{\lambda}{\rho C_{\mathrm{p}}}\beta_{\mathrm{L}}\frac{\partial^2 T}{\partial x_i \partial x_i} + \beta_{\mathrm{L}}\frac{\partial\left(-\overline{u'_{\mathrm{L}i}T'}\right)}{\partial x_i} + \beta_{\mathrm{L}}S_{\mathrm{T}} \\ &= \alpha\beta_{\mathrm{L}}\frac{\partial^2 T}{\partial x_i \partial x_i} + \beta_{\mathrm{L}}\frac{\partial\left(-\overline{u'_{\mathrm{L}i}T'}\right)}{\partial x_i} + \beta_{\mathrm{L}}S_{\mathrm{T}}\end{aligned} \tag{A2-3a}$$

$$-\overline{u'_{\mathrm{L}i}T'} = \alpha_{\mathrm{Lt}}\frac{\partial T}{\partial x_i} \tag{A2-4}$$

$\overline{T'^2}$ *equation*

$$\begin{aligned}\frac{\partial \rho_{\mathrm{L}} \beta_{\mathrm{L}} \overline{T'^2}}{\partial t} + \frac{\partial \rho_{\mathrm{L}} \beta_{\mathrm{L}} U_i \overline{T'^2}}{\partial x_i} = {} & \frac{\partial}{\partial x_i}\beta_{\mathrm{L}}\rho_{\mathrm{L}}\frac{\partial \overline{T'^2}}{\partial x_i}\left(\frac{\alpha_{\mathrm{Lt}}}{\sigma_{T'}} + \alpha\right) - 2\beta_{\mathrm{L}}\rho_{\mathrm{L}}\alpha_{\mathrm{Lt}}\frac{\partial T}{\partial x_i}\frac{\partial T}{\partial x_i} \\ & - 2\beta_{\mathrm{L}}\rho_{\mathrm{L}}\varepsilon_{T'}\end{aligned} \tag{A2-7a}$$

$\varepsilon_{T'}$ *equation*

$$\frac{\partial \rho_{\mathrm{L}} \beta_{\mathrm{L}} \varepsilon_{T'}}{\partial t} + \frac{\partial \rho_{\mathrm{L}} \beta_{\mathrm{L}} U_{\mathrm{L}i} \varepsilon_{T'}}{\partial x_i} = \frac{\partial}{\partial x_i}\left[\rho_{\mathrm{L}} \beta_{\mathrm{L}}\left(\frac{\alpha_t}{\sigma_{\varepsilon_{T'}}} + \alpha\right)\frac{\partial \varepsilon_{T'}}{\partial x_i}\right] - C_{T1}\beta_{\mathrm{L}}\rho_{\mathrm{L}}\frac{\varepsilon_{T'}}{\overline{T'^2}}\overline{u_i' T'}\frac{\partial T}{\partial x_i} - C_{T2}\beta_{\mathrm{L}}\rho_{\mathrm{L}}\frac{\varepsilon_{T'}^2}{\overline{T'^2}} - C_{T3}\beta_{\mathrm{L}}\rho_{\mathrm{L}}\frac{\varepsilon_{\mathrm{L}}\varepsilon_{T'}}{k_{\mathrm{L}}} \tag{A2-10}$$

α_{t} *equation*

$$\alpha_{\mathrm{Lt}} = C_{T0} k_{\mathrm{L}}\left(\frac{k_{\mathrm{L}}}{\varepsilon_{\mathrm{L}}}\frac{\overline{T'^2}}{\varepsilon_{T'}}\right)^{\frac{1}{2}} \tag{A2-6}$$

Model constant are: $C_{T0} = 0.11$, $C_{T1} = 1.8$, $C_{T3} = 2.2$, $C_{T2} = 0.8$, $\sigma_{T'} = 1.0$, $\sigma_{\varepsilon_{T'}} = 1.0$.

If the latent heat of vaporization of the component species in distillation process is approximately equal, the conservation equation of energy (heat) can be omitted and the mathematical model comprises with only CFD and mass transfer equation sets. Otherwise, the heat transfer equation set should be involved.

(III) **Mass transfer equation set (** $\overline{c'^2} - \varepsilon_{c'}$ **model, see** Chap. 3):

Species mass conservation

$$\frac{\partial \beta_{\mathrm{L}} U_{\mathrm{L}j} C}{\partial x_i} = \frac{\partial}{\partial x_i}\beta_{\mathrm{L}}\left(D\frac{\partial C}{\partial x_i} - \overline{u_{\mathrm{L}j}' c'}\right) + \beta_{\mathrm{L}} S_n$$
$$\overline{u_{\mathrm{L}j}' c'} = -D_{\mathrm{Lt}}\frac{\partial C}{\partial x_j} \tag{1.3}$$

$\overline{c_{\mathrm{L}}'^2}$ *equation*

$$\frac{\partial \beta_{\mathrm{L}} U_{\mathrm{L}i}\overline{c_{\mathrm{L}}'^2}}{\partial x_i} = \frac{\partial}{\partial x_i}\left[\beta_{\mathrm{L}}\left(D + \frac{D_{\mathrm{Lt}}}{\sigma_{c'^2}}\right)\frac{\partial \overline{c_{\mathrm{L}}'^2}}{\partial x_i}\right] - 2\beta_{\mathrm{L}} D_{\mathrm{Lt}}\left(\frac{\partial C}{\partial x_i}\right)^2 - 2\beta_{\mathrm{L}}\varepsilon_{c_{\mathrm{L}}'} \tag{1.10}$$

$\varepsilon_{\mathrm{L}c'}$ *equation*

$$U_{\mathrm{L}i}\beta_{\mathrm{L}}\frac{\partial \varepsilon_{\mathrm{L}c'}}{\partial x_i} = \frac{\partial}{\partial x_i}\beta_{\mathrm{L}}\left[\left(D + \frac{D_{\mathrm{Lt}}}{\sigma_{\varepsilon_c}}\right)\frac{\partial \varepsilon_{\mathrm{L}c'}}{\partial x_i}\right] - C_{c1}\beta_{\mathrm{L}} D_t\frac{\varepsilon_{\mathrm{L}c'}}{\overline{c_{\mathrm{L}}^2}}\left(\frac{\partial C}{\partial x_i}\right)^2 - C_{c2}\beta_{\mathrm{L}}\frac{\varepsilon_{\mathrm{L}c'}^2}{\overline{c_{\mathrm{L}}'^2}} - C_{c3}\beta_{\mathrm{L}}\frac{\varepsilon_{\mathrm{L}c'}\varepsilon_{\mathrm{L}c'}}{k_{\mathrm{L}}} \tag{1.17}$$

D_{Lt} equation

$$D_{Lt} = C_{c0} k_L \left(\frac{k_L \overline{c_L'^2}}{\varepsilon_L \varepsilon_{Lc'}} \right)^{\frac{1}{2}} \tag{1.6}$$

Model constants are as follows: $C_{c0} = 0.14$, $C_{c1} = 1.8$, $C_{c2} = 2.2$, $C_{c3} = 0.8$, $\sigma_{c^2} = 1.0$, $\sigma_{\varepsilon_{c'}} = 1.0$

In the foregoing equations, the fraction of liquid β_L in the liquid–vapor mixture for tray column can be calculated by the following correlation [1]:

$$\beta_L = \exp\left[-12.55 \left(U_G \sqrt{\frac{\rho_G}{\rho_L - \rho_G}} \right)^{0.91} \right] \tag{2.1}$$

Usually the net amount of interfacial mass transfer exchange between liquid to vapor and vapor to liquid phases on a tray is small, ρ_L and ρ_G can be considered practically unchanged, so that β_L is substantially constant. It should be noted that in the case of packed column, the β_L is varying because the porosity of the packing is nonuniformly distributed especially in the near wall region as described in Sect. 2.2.

2.1.1.2 Evaluation of Source Terms

The present simulated object is an industrial scale sieve tray column of FRI which is 4 ft. in diameter with six sieve trays for (1) separation of *n*-heptane and methylcyclohexane [2] and (2) stripping of toluene from dilute water solution [3]. They reported the outlet composition and the tray efficiency of each tray under different operating conditions. The details of this column are given in Fig. 2.1 and Table 2.1 [2]. The operating pressure is 165 kPa.

In the numerical computation, the model equations should be first discrete into a large number of small finite elements and solved by algebraic method. Thus, the empirical correlations can be applied to the discrete elements under their local conditions, such as velocity, concentration, and temperature obtained in the course of numerical computation. Note that the local conditions should be within the applicable range of the correlation.

Since the latent heat of vaporization and condensation as well as the density of *n*-heptane and methylcyclohexane are practically equal, the amount of *n*-heptane transferred from liquid phase to the vapor phase is almost equal to the amount of methylcyclohexane transferred from vapor phase to the liquid phase, thus no material is accumulated or depleted on the tray and the liquid density is kept substantially constant. For this separating system, it can be letting the source term $S_m = 0$.

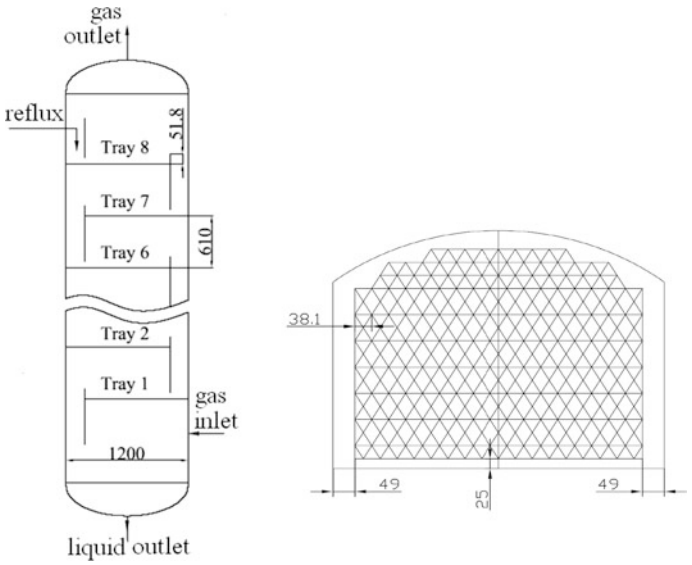

Fig. 2.1 Structure of simulated sieve tray [4]

Table 2.1 Dimension of simulated sieve tray

Item	Value	Item	Value
Column diameter (m)	1.2	Clearance under downcomer (mm)	38
Tray spacing (mm)	610	Downcomer area (m^2)	0.14
Hole diameter and spacing (mm × mm)	12.7 × 38.1	Effective bubbling area (m^2)	0.859
Outlet weir (height × length) (mm × mm)	51 × 940	Hole area (m^2)	0.118

Sun [5–7] and Li [8] simulated this column using interacted liquid phase modeling form with the assumption that the liquid density on a simulated single tray is constant, but for the multi-tray simulation, the density should be changed tray by tray.

The source term S_{Li} in the momentum conservation equation can be calculated by one of the following modes:

(A) Based on superficial vapor velocity: For the *x, y* direction [9]

$$S_{Li} = \frac{\rho_G U_G}{\rho_L h_L} U_{Li}, \quad i = x, y, \tag{2.2}$$

where h_L is given by [10]:

$$h_L = 0.0419 + 0.189h_w - 0.0135F_s + 2.45L/W$$

For the z direction [11]

$$S_{Lz} = \frac{(1-\beta_L)^3}{U_G^2} g(\rho_L - \rho_G)|U_G - U_L|(U_G - U_{Lz})$$

(B) Based on sieve hole vapor velocity

As the vapor velocity leaving the sieve holes is much higher than the superficial and sometimes even forming jet flow; such influential effect can not be ignored, especially under the condition of high F-factor. Referring to Fig. 2.2, the three-dimensional vapor velocities leaving the sieve hole can be expressed as follows [12]:

$$U_{Gz} = 4.0U_h \frac{D_h}{z} \exp\left[\left(\frac{d}{0.1z}\right)^2\right]$$

$$U_{Gx} = U_{Gr}\cos\theta$$

$$U_{Gy} = U_{Gr}\sin\theta$$

$$U_{Gr} = \frac{1}{4}\sqrt{\frac{3}{\pi}}\sqrt{\frac{M_0}{\rho_G}}\frac{1}{z}\frac{\eta - \eta^3/4}{(1+\eta^2/4)^2}$$

$$\eta = \sigma\frac{d}{z},$$

where M_0 is the momentum of the gas phase flowing out the sieve hole.

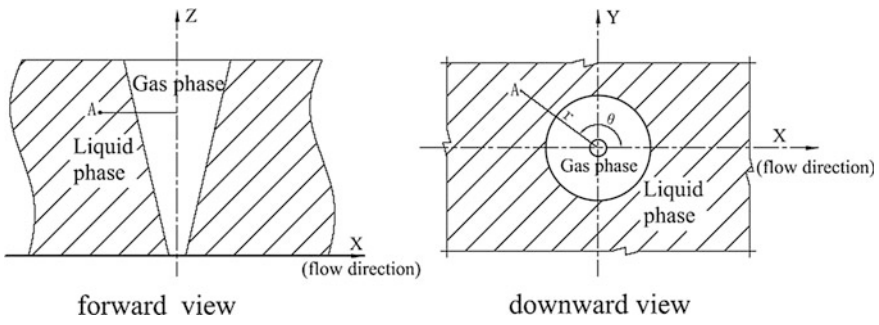

Fig. 2.2 Coordinate of a sieve [4]

The source term S_{Li} in the momentum equation involves the drag force by the jetting vapor F_{drag} and the resistance F_p created by the liquid–vapor cross flow. The F_{drag} is given by [13]

$$F_{drag} = C_T \rho_G (U_{Gi} - U_{Li}) |U_G - U_L| / h_f \quad i = x, y, z$$

The F_p in the x direction is calculated by [12]

$$F_p = -C_p \rho_L U_x^2 / h_f,$$

where $C_p = 0.4$; $h_f = \frac{h_L}{\beta_L}$.

The source term S_{Li} is given as follows:

$$S_x = F_{drag} + F_p$$
$$S_j = F_{drag,j} K \quad (j = y,z)$$

(C) Comparison between two modes

Sun computed the velocity distribution of experimental simulator (Sect. 1.4.4 for details) by using foregoing two modes to show their difference. The result is shown in Fig. 2.3.

As seen from Fig. 2.3, the velocity in mode A is more uniformly distributed than that in mode B except in the region near the column wall. Moreover, the average velocity in the main flow region of mode B is slightly higher than that in mode A but lower locally near the wall. Computation further reveals that, for a large diameter sieve tray with large number of uniformly distributed sieve holes, the simulated results show no substantial difference by using either mode. In subsequent calculation, mode B is used.

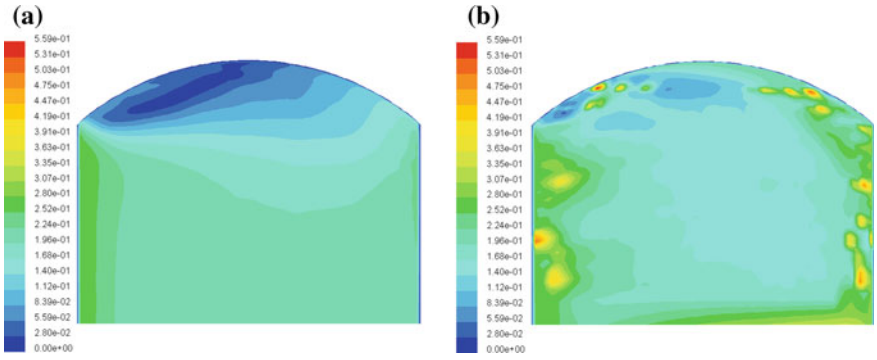

Fig. 2.3 Liquid velocity profiles obtained by using different modes, operation condition: z = 38 mm, F_S = 1.464 m/s $(kg/m^3)^{0.5}$, $L = 6.94 \times 10^{-3}$ m^3/s, **a** based on superficial vapor velocity mode, **b** based on sieve hole vapor velocity [4]

The source term S_n in the species mass conservation equation represents the component species transferred from one phase to the other, which can be calculated by the conventional mass transfer equation

$$S_n = K_{\mathrm{OL}} a \left(C_{\mathrm{L}}^* - C_{\mathrm{L}} \right), \tag{2.3}$$

where K_{OL} ($\mathrm{m^2\ s^{-1}}$) is the overall mass transfer coefficient; a ($\mathrm{m^2\ m^{-3}}$) is the effective interfacial vapor liquid contacting area; C_{L}^* ($\mathrm{kg\ m^{-3}}$) is the average liquid mass concentration in equilibrium with the vapor flowing through the tray; K_{OL} can be given by

$$K_{\mathrm{OL}} = \frac{1}{\frac{1}{k_{\mathrm{L}}} + \frac{1}{m k_{\mathrm{G}}}}, \tag{2.4}$$

where k_{L} and k_{G} are, respectively, the film coefficients of mass transfer on liquid side and gas (vapor) side, respectively, m is the coefficient of distribution between two phases, which is conventionally called Henry's constant. The value of m is dependent on the concentration of the species concerned. If the concentration change on a tray is not large, the value of m might be taken at the average concentration. However, for the simulation of a multi-tray column, where the change of concentration in the column is appreciable, the value of m should be redetermined for each tray. The k_{L}, k_{G}, and a can be calculated by the empirical equation given by Zuiderweg [14] as follows:

$$k_{\mathrm{G}} = \frac{0.13}{\rho_{\mathrm{G}}} - \frac{0.065}{\rho_{\mathrm{G}}^2} \quad \left(1.0 < \rho_{\mathrm{G}} < 80\,\mathrm{kg/m^3}\right) \tag{2.5}$$

$$k_{\mathrm{L}} = \left(\frac{1}{0.37} - 1 \right) m k_{\mathrm{G}} \tag{2.6}$$

The effective vapor–liquid interfacial area a is calculated by $a = \frac{a'}{h_{\mathrm{f}}}$, where h_{f} is the height of liquid level, a' is given by [14]:

$$a' = \frac{43}{F^{0.3}} \left(\frac{F_{\mathrm{bba}}^2 h_{\mathrm{L}} FP}{\sigma} \right)^{0.53},$$

where F_{bba} is the F factor based on the vapor velocity passing through the bubbling area; $h_{\mathrm{L}} = 0.6 h_{\mathrm{w}}^{0.5} p^{0.25} b^{-0.25} (FP)^{0.25}$ ($25\ \mathrm{mm} < h_{\mathrm{w}} < 100\ \mathrm{mm}$), $FP = \frac{U_{\mathrm{L}}}{U_{\mathrm{G}}} \left(\frac{\rho_{\mathrm{L}}}{\rho_{\mathrm{G}}} \right)^{0.5}$, b is the weir length per unit bubbling area.

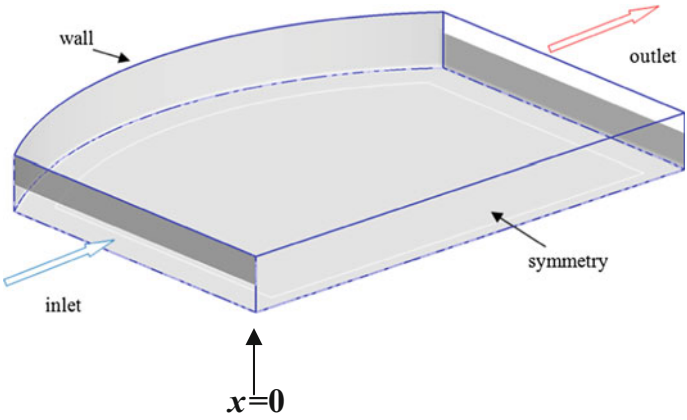

Fig. 2.4 Diagram of boundary conditions [15]

2.1.1.3 Boundary Conditions

Inlet (inlet weir, $x = 0$): the liquid velocity and concentration are considered as uniformly distributed, so that $U_L = U_{L,in}$, $C = C_{in}$ (Fig. 2.4).

For the k–ε equations, the conventional boundary conditions are adopted [16]: $k_{in} = 0.003U_{x,in}^2$ and $\varepsilon_{in} = 0.09k_{in}^{3/2}/\left(0.03 \times \frac{W}{2}\right)$.

The inlet conditions of $\overline{c'^2} - \varepsilon_{c'}$ equations, as presented by Sun [5], are:

$$\overline{c_{L,in}'^2} = [0.082 \cdot (C^* - C_{in})]^2$$

$$\varepsilon_{Lc',in} = 0.9\left(\frac{\varepsilon_{L,in}}{k_{L,in}}\right)\overline{c'^2}_{in}$$

Outlet (outlet weir overflow): we let $\frac{\partial C}{\partial x} = 0$.

Solid border (tray floor, inlet weir wall outlet weir wall and column wall): the boundary conditions for the mass flux are equal to zero. The wall surface is considered to be no-slip of liquid flow.

Interface of the vapor and liquid: we set $\frac{\partial U_x}{\partial z} = 0$, $\frac{\partial U_y}{\partial z} = 0$, and $U_z = 0$.

2.1.1.4 Simulated Results and Verification (I)—Separation of *n*-Heptane and Methylcyclohexane

The model equations were solved numerically by using the commercial software FLUENT 6.2 with finite volume method. The SIMPLEC algorithm was used to solve the pressure–velocity coupling problem in the momentum equations. The

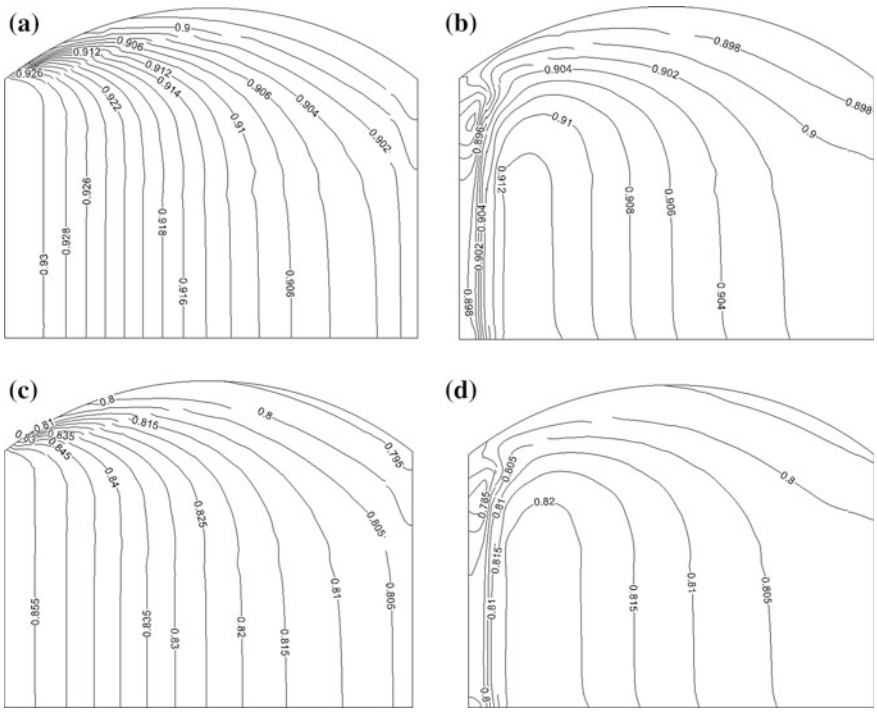

Fig. 2.5 C_6 concentration distribution on trays [4] **a** at 20 mm above the floor of tray number 8, **b** 70 mm above the floor of tray number 8, **c** at 20 mm above the floor of tray number 6, **d** 70 mm above the floor of tray number 6

second-order upwind spatial discretization scheme was employed for all differential equations.

Samples of the computed results, Fig. 2.5a, b show, respectively, the computed concentration distribution on tray 8 and tray 6. Unfortunately, no experimental data on the concentration field of the tray is available in the literature for the comparison. However, we may compare indirectly by means of the outlet concentration of each tray.

From the concentration distribution on a tray as shown in Fig. 2.5a, b, the outlet composition of each tray can be obtained as shown in Fig. 2.6a and compared with the experimental data.

As seen from Fig. 2.6a, the computed outlet concentration of each tray is in good agreement with the experimental measurement except for the tray 4. As we understand, for the total reflux operation, the outlet concentration should form a smooth curve on the plot. The deviation on tray 4 is obvious and likely to be due to experimental error or some other unknown reasons. The average deviation of the outlet composition is 3.77 %.

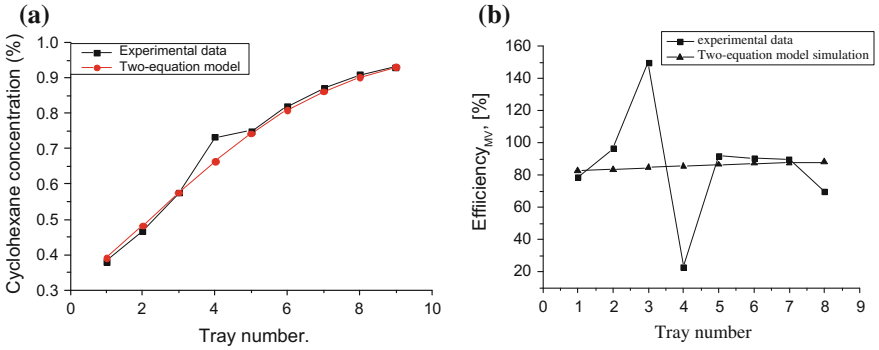

Fig. 2.6 Simulation results and experimental data **a** outlet concentration, **b** Murphree tray efficiency (reprinted from Ref. [5], Copyright 2005, with permission from American Chemical Society)

Another way of comparison is by means of individual tray efficiency. The common expression of tray efficiency is the gas phase Murphree efficiency which is defined by

$$E_{\mathrm{MV}} = \frac{y_n - y_{n+1}}{y_n^* - y_{n+1}} \tag{2.7}$$

where y_n^* is the species concentration (mole fraction) of gas phase in equilibrium with the liquid phase concentration x_n (mole fraction); y_n and y_{n+1} are, respectively, the gas concentration in mole fraction leaving and entering the tray. The comparison between simulated results and experimental data is showed in Fig. 2.6b, in which disagreement in tray number 3 and 4 reveals the experimental error in the outlet concentration from tray 4 because the tray efficiency can not be as high as 150 % for tray 3 and as low as 20 % for tray 4.

The overall tray efficiency of all trays in the column is commonly used for distillation column evaluation in order to reduce the error of individual tray efficiency. Figure 2.7 shows the simulated overall tray efficiency versus experiment measurement under different vapor rate expressed as F factor $\left(F = U_{\mathrm{G}}\sqrt{\rho_{\mathrm{G}}}\right)$. The simulation is seen to be confirmed.

A feature of computational mass transfer is able to predict the liquid turbulent mass diffusivity D_{t} which is commonly regarded as representing the extent of backmixing (nonideal flow) and thus it is an influential factor to the tray efficiency. Figure 2.8 display the distribution of D_{Lt} on tray number 8 at the depth z of 50 and 100 mm, respectively, apart from tray floor. As seen from the figure, the D_{Lt} is nonuniformly distributed, which reflexes the effectiveness or efficiency of mass transfer is varying with position on a tray.

The volume average of D_{Lt} calculated is compared with experimental data reported by Cai and Chen [17] for the same tray column under different vapor rate (F factor) as shown in Fig. 2.9. Although the experimental measurement is

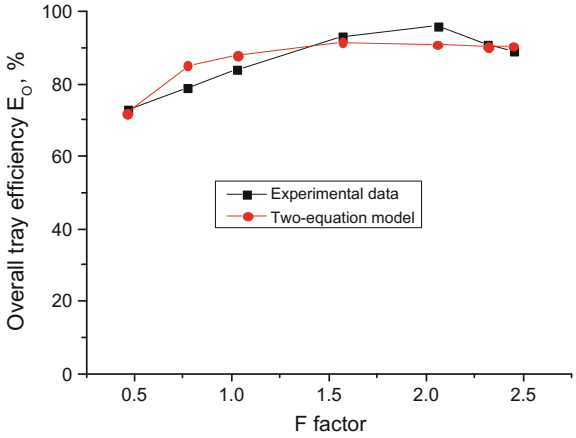

Fig. 2.7 Simulated overall tray efficiency and experimental data (reprinted from Ref. [5], Copyright 2005, with permission from American Chemical Society)

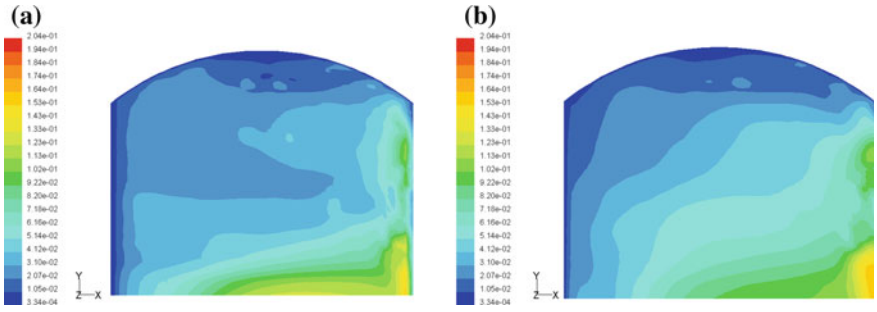

Fig. 2.8 Distribution of liquid turbulent mass diffusivity on tray number 8, **a** Tray No. 8, 50 mm above tray floor, p = 165 kPa, L = 30.66 m^3/h, **b** Tray No. 8, 100 mm above tray floor p = 165 kPa, L = 30.66 m^3/h [4]

performed by using inert tracer technique and the comparison is only approximate, yet it demonstrates that the prediction of D_{Lt} is feasible by using the method of computational mass transfer without doing tedious experimental work.

2.1.1.5 Simulated Results and Verification (II)—Stripping of Toluene from Dilute Water Solution

Kunesh [3] reported the experimental data for the column as shown in Fig. 2.1 for the stripping of toluene from dilute water solution. They gave the outlet composition and the tray efficiency of each tray under different operating conditions.

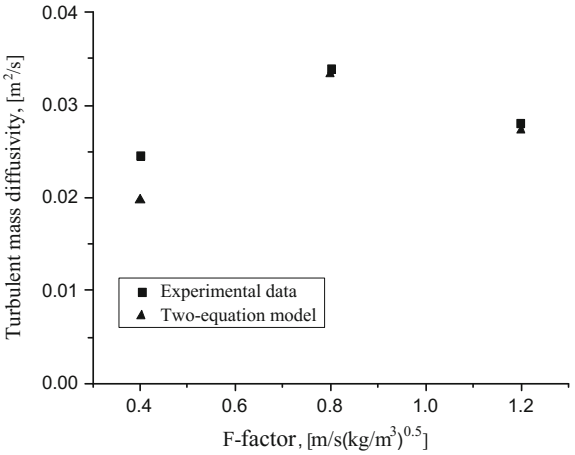

Fig. 2.9 Simulated turbulent mass diffusivity and experimental data [4]

Sun [7] simulated the outlet concentration of each tray, expressed in area-weighted average, versus tray number for a typical run 16552 is shown in Fig. 2.10 and compare with the experimental data. According to the Fenske-Underwood equation under constant relative volatility and low concentration, a plot of logarithmic concentration versus tray number should yields a straight line. In Fig. 2.10, both simulated and experimental points are shown closely to a line with agreement each other. The conventional method of assuming constant turbulent Schmidt number, Sc_t, for instance equal to 0.7, is also shown in Fig. 2.10, and the deviation of arbitrary assuming a constant Sc_t can be clearly seen.

The simulated concentration distribution on a sieve tray is given in Fig. 2.11, in which the stripping action on the tray is seen to be unevenly progressed.

Based on the simulated concentration distribution as shown in Fig, 2.11, the local tray efficiencies can be obtained. The simulated tray efficiency by area average

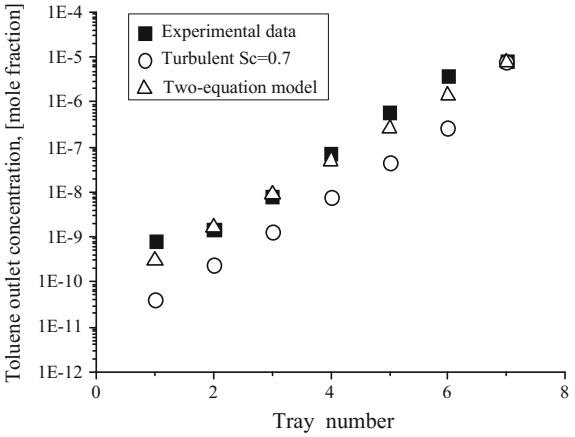

Fig. 2.10 Simulated outlet concentration and experimental measurement, Run 16552 Q_L = 76.3 m^3/h, Fs = 1.8 (m/s)$(kg/m^3)^{0.5}$ (reprinted from Ref. [7], Copyright 2011, with permission from Elsevier)

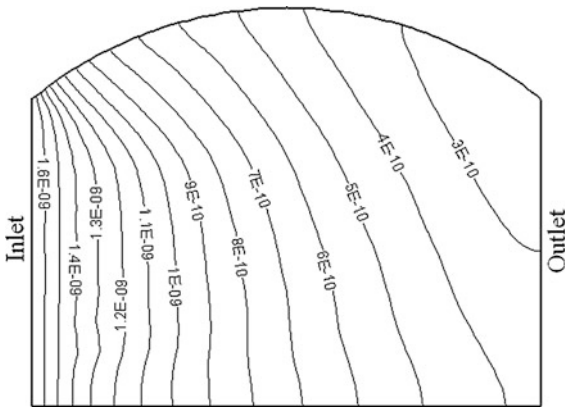

Fig. 2.11 Simulated concentration distribution, tray 6, Run 16552 Q_L = 76.3 m^3/h, Fs = 1.8 (m/s) $(kg/m^3)^{0.5}$ 20 mm above tray floor (reprinted from Ref. [7], Copyright 2011, with permission from Elsevier)

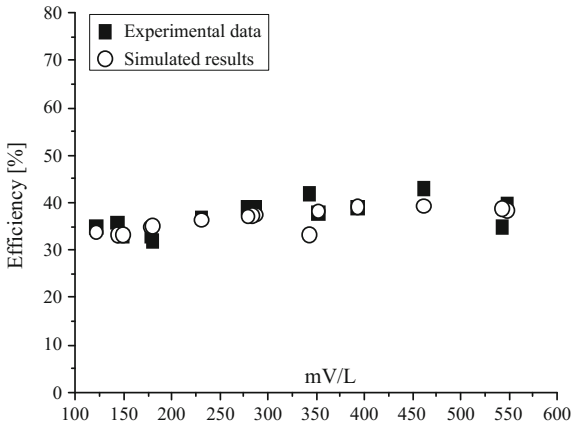

Fig. 2.12 Simulated and experimental tray efficiency under different $m\frac{V}{L}$ Q_L = 76.3 m^3/h, Fs = 1.8 (m/s) $(kg/m^3)^{0.5}$ (reprinted from Ref. [7], Copyright 2011, with permission from Elsevier)

for run 16552 is 33.4 % in comparison with the experimental value of 36 %. More simulated tray efficiencies at different *mV/L* are compared with the experimental measurements as shown in Fig. 2.12, in which reasonable agreement is seen between them.

As another example of illustration, the simulated distribution of D_{Lt} across the tray for run 16552 is shown in Fig. 2.13. The diverse distribution of D_{Lt} is chiefly due to the complicated non-uniform flow and concentration distributions on the tray. In practice, the mass transfer diffusivity is expressed macroscopically by the volume average. For instance, the predicted volume average values of D_{Lt} for three runs under different operations are 0.035, 0.030 and 0.021 m^2/s, respectively, which are within the reasonable range reported by Cai and Chen [17].

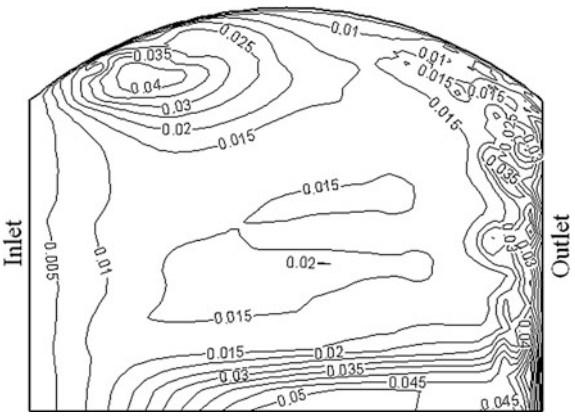

Fig. 2.13 Distribution of turbulent mass transfer diffusivity, tray 6, Run 16552 Q_L = 76.3 m^3/h, Fs = 1.8 (m/s) $(kg/m^3)^{0.5}$ 20 mm above tray floor (reprinted from Ref. [7], Copyright 2011, with permission from Elsevier)

2.1.1.6 Prediction of Tray Efficiency for Different Tray Structures

By means of the simulated concentration distribution on a tray, the influence of tray structure on the tray efficiency can be calculated. Sun [7] simulated foregoing sieve tray distillation column as shown in Sect. 2.1.1.3 for separating cyclohexane (C_6) and *n*-heptane (*n*-C_7) mixture with different tray structures, including sieve hole arrangement, heights of inlet weir, and outlet weir. As an example of illustration, the tray efficiency with different height of outlet weirs is predicted and compared each other. The simulated concentration distributions on the same sieve tray with different outlet weir height h_w are shown in Fig. 2.14.

The inlet concentration of C_6 to both trays was 0.482 in mole fraction; the simulated outlet concentrations for outlet weir height h_w equal to 20 and 100 mm were found to be 0.393 and 0.383, respectively. Higher outlet concentration of C_6 on the h_w = 100 tray may be due to deeper liquid layer resulting more interacting area and time between vapor and liquid and therefore enhance the mass transfer.

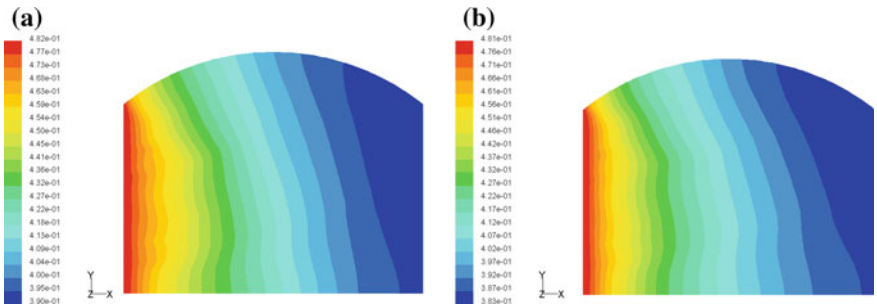

Fig. 2.14 Simulated concentration profile of a sieve trays number 1 at different outlet weir height $h_w x_{in}$ = 0.482 Q_L = 30.66 m^3h^{-1}, G = 5.75 Kg s^{-1} P = 165 kPa total reflux 20 mm above tray floor **a** h_w = 20 mm, **b** h_w = 100 mm (reprinted from Ref. [7], Copyright 2011, with permission from Elsevier)

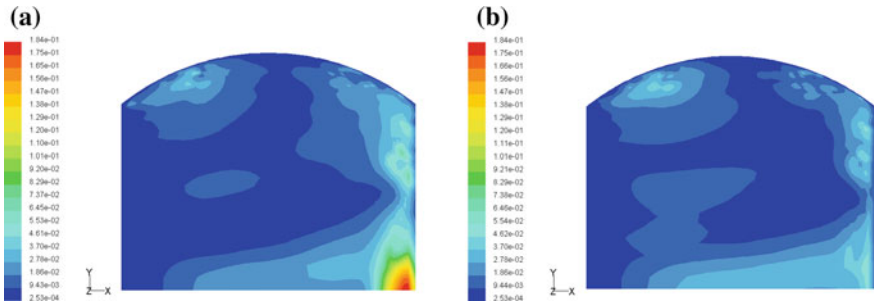

Fig. 2.15 Simulated turbulent mass transfer diffusivity profile of sieve trays number 1 x_{in} = 0.482, Q = 30.66 m^3h^{-1}, P = 165 kPa, total reflux, 20 mm above tray floor **a** h_w = 20 mm, **b** h_w = 100 mm (reprinted from Ref. [7], Copyright 2011, with permission from Elsevier)

The corresponding Murphree tray efficiencies obtained were 86.7 and 89.5 % for h_w equal to 20 and 100 mm, respectively. The simulated D_{Lt} for both cases are shown in Fig. 2.15, in which different profiles are clearly seen. However, such simulated results do not mean that higher outlet weir is a good choice, as the higher tray efficiency achieved is on the expense of higher pressure drop which means to require more energy of operation. However, it demonstrates that the application of computational mass transfer to evaluate the mass transfer efficiency of different tray structures is feasible, which is helpful in designing new column and assessing existing column.

2.1.2 Reynolds Mass Flux Model

The interacted liquid phase modeling form is employed for present simulation. The simplified assumptions of constant liquid fraction β_L and density ρ_L on a tray are applied.

2.1.2.1 Standard Reynolds Mass Flux Model

Model equations

(I) The CFD equation set (k–ε model)

Overall mass conversation

$$\frac{\partial(\rho_L \beta_L U_{Li})}{\partial x_i} = S_m \qquad (A1-3)$$

Momentum conversation

$$\frac{\partial\left(\rho_{\mathrm{L}}\beta_{\mathrm{L}}U_{\mathrm{L}i}U_{\mathrm{L}j}\right)}{\partial x_i}=-\beta_{\mathrm{L}}\frac{\partial P}{\partial x_j}+\frac{\partial}{\partial x_i}\left[\beta_{\mathrm{L}}\mu_{\mathrm{L}}\left(\frac{\partial U_{\mathrm{L}j}}{\partial x_i}\right)-\beta_{\mathrm{L}}\rho_{\mathrm{L}}\overline{u'_{\mathrm{L}i}u'_{\mathrm{L}j}}\right]+S_{\mathrm{L}i}\quad(\mathrm{A1}-4)$$

where $\overline{u'_{\mathrm{L}i}u'_{\mathrm{L}j}}$ is given by:

$$\begin{aligned}&\frac{\partial\rho\beta_{\mathrm{L}}\overline{u'_{\mathrm{L}i}u'_{\mathrm{L}j}}}{\partial t}+U_{\mathrm{L}k}\frac{\partial\rho_{\mathrm{L}}\overline{\beta_{\mathrm{L}}u'_{\mathrm{L}i}u'_{\mathrm{L}j}}}{\partial x_k}=\frac{\partial}{\partial x_k}\left(\rho\beta_{\mathrm{L}}C_k\frac{k_{\mathrm{L}}^2}{\varepsilon}\frac{\partial\overline{u'_{\mathrm{L}i}u'_{\mathrm{L}j}}}{\partial x_k}+\mu_{\mathrm{L}}\frac{\partial\overline{u'_{\mathrm{L}i}u'_{\mathrm{L}j}}}{\partial x_k}\right)\\&-\rho_{\mathrm{L}}\beta_{\mathrm{L}}\left(\overline{u'_{\mathrm{L}i}u'_{\mathrm{L}k}}\frac{\partial U_{\mathrm{L}j}}{\partial x_k}+\overline{u'_{\mathrm{L}j}u'_{\mathrm{L}k}}\frac{\partial U_{\mathrm{L}i}}{\partial x_k}\right)\\&-C_1\rho_{\mathrm{L}}\beta_{\mathrm{L}}\frac{\varepsilon_{\mathrm{L}}}{k_{\mathrm{L}}}\left(\overline{u'_{\mathrm{L}i}u'_{\mathrm{L}j}}-\frac{2}{3}k_{\mathrm{L}}\delta_{ij}\right)\\&-C'_2\rho_{\mathrm{L}}\beta_{\mathrm{L}}\left(\overline{u'_{\mathrm{L}i}u'_{\mathrm{L}k}}\frac{\partial U_{\mathrm{L}j}}{\partial x_k}+\overline{u'_{\mathrm{L}j}u'_{\mathrm{L}k}}\frac{\partial U_{\mathrm{L}i}}{\partial x_k}-\frac{2}{3}\delta_{ij}\overrightarrow{u'_{\mathrm{L}i}u'_{\mathrm{L}j}}\frac{\partial U_{\mathrm{L}i}}{\partial x_j}\right)-\frac{2}{3}\rho_{\mathrm{L}}\beta_{\mathrm{L}}\varepsilon_{\mathrm{L}}\delta_{ij}\end{aligned}\quad(\mathrm{A1}-23)$$

where the constants are: C_k = 0.09, C_1 = 2.3, C'_2 = 0.4 [11].

(II) The mass transfer equation set (Reynolds mass flux model)

Species mass conservation

$$\frac{\partial\beta_{\mathrm{L}}U_{\mathrm{L}j}C}{\partial x_i}=\frac{\partial}{\partial x_i}\beta_{\mathrm{L}}\left(D_{\mathrm{L}}\frac{\partial C}{\partial x_i}-\overline{u'_{\mathrm{L}j}c'}\right)+S_n\quad(1.3)$$

Fluctuating mass flux $\overline{u'_ic'}$

$$\begin{aligned}\frac{\partial\overline{\beta_{\mathrm{L}}u'_{\mathrm{L}i}c'}}{\partial t}+\frac{\partial\beta_{\mathrm{L}}U_j\overline{u'_{\mathrm{L}i}c'}}{\partial x_j}&=\frac{\partial}{\partial x_j}\left[\left(C_{c1}\rho_{\mathrm{L}}\beta_{\mathrm{L}}\frac{k_{\mathrm{L}}^2}{\varepsilon_{\mathrm{L}}}+\frac{\mu_{\mathrm{L}}}{\rho_{\mathrm{L}}}\right)\frac{\partial\overline{u'_{\mathrm{L}i}c'}}{\partial x_j}\right]\\&-\left(\overline{u'_iu'_j}\frac{\partial C}{\partial x_j}\right)-C_{c2}\beta_{\mathrm{L}}\frac{\varepsilon}{k}\overline{u'_{\mathrm{L}i}c'}+C_{c3}\beta_{\mathrm{L}}\overline{u'_{\mathrm{L}j}c'}\frac{\partial U_{\mathrm{L}i}}{\partial x_j}\end{aligned}\quad(1.26\mathrm{a})$$

where the constants are: $C_{c1}=0.09$, $C_{c2}=3.2$, $C_{c3}=0.55$.

Auxiliary equations

k_{L} equation

$$\begin{aligned}\frac{\partial\rho\beta_{\mathrm{L}}U_{\mathrm{L}i}k_{\mathrm{L}}}{\partial x_i}&=\frac{\partial}{\partial x_i}\left[\beta_{\mathrm{L}}\left(\mu_{\mathrm{L}}+\frac{\mu_{\mathrm{L}t}}{\sigma_k}\right)\frac{\partial k_{\mathrm{L}}}{\partial x_i}\right]\\&-\mu_{\mathrm{L}t}\beta_{\mathrm{L}}\left(\frac{\partial U_{\mathrm{L}i}}{\partial x_j}+\frac{\partial U_{\mathrm{L}j}}{\partial x_i}\right)\frac{\partial U_{\mathrm{L}j}}{\partial x_i}-\rho_{\mathrm{L}}\beta_{\mathrm{L}}\varepsilon_{\mathrm{L}}\end{aligned}\quad(\mathrm{A1}-11\mathrm{a})$$

ε_L *equation*

$$\frac{\partial \rho_L \beta_L U_{Li} \varepsilon_L}{\partial x_i} = \frac{\partial}{\partial x_i}\left[\beta_L\left(\mu_L + \frac{\mu_{Lt}}{\sigma_{L\varepsilon}}\right)\frac{\partial \varepsilon_L}{\partial x_i}\right] - C_{\varepsilon 1}\beta_L \frac{\varepsilon}{k}\mu_{Lt}\left(\frac{\partial U_{Lj}}{\partial x_i} + \frac{\partial U_{Li}}{\partial x_j}\right)\frac{\partial U_{Lj}}{\partial x_i} - C_{\varepsilon 2}\beta_L \rho_L \frac{\varepsilon_L^2}{k_L} \quad \text{(A1 – 13a)}$$

The boundary conditions are the same as given in Sect. 2.1.1.3.

Verification of simulated result and comparison

The simulated column tray is shown in Sect. 2.1.1.1 for separating *n*-heptane and methylcyclohexane. Li et al. [8] and Li [15] simulated the concentration profiles for all trays at different levels from the tray floor, among which the tray number 8 and 6 are shown in Fig. 2.16a, b, respectively.

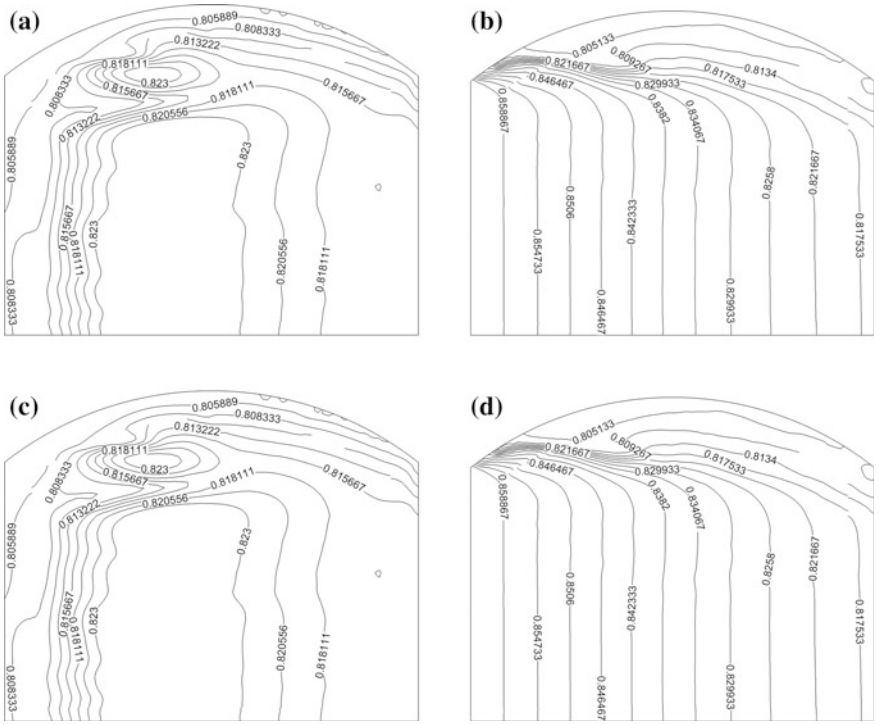

Fig. 2.16 Concentration contour of *x*–*y* plan on trays by Standard Reynolds mass flux model **a** 20 mm above tray floor of tray number 8, **b** 70 mm above tray floor of tray number 8 **c** 20 mm above tray floor of tray number 6, **d** 70 mm above tray floor of tray number 6 [15]

2.1.2.2 Hybrid Reynolds Mass Flux Model

The model equations are the same as the Standard Reynolds mass flux model except that the $\overline{u'_{\mathrm{L}i}u'_{\mathrm{L}j}}$ term is simplified by using Eq. (A1-8) as follows:

$$-\rho\overline{u'_{\mathrm{L}i}u'_{\mathrm{L}j}} = \mu_{\mathrm{Lt}}\left(\frac{\partial U_{\mathrm{L}i}}{\partial x_j} + \frac{\partial U_{\mathrm{L}j}}{\partial x_i}\right) - \frac{2}{3}\rho_{\mathrm{L}}\delta_{ij}k_{\mathrm{L}} \qquad (\mathrm{A1}-8)$$

The hybrid Reynolds mass flux model and algebraic Reynolds mass flux model, which only need to solve simpler Eq. (A1-8) instead of complicated Eq. (A1-23), may be a proper choice for multiple tray computation if their simulated results are very close to the standard Reynolds mass flux model. For comparison, the simulated column trays in Sect. 2.1.1.1 for separating *n*-heptane and methylcyclohexane are used. Li [4] simulated concentration profiles of all trays at different levels above the tray floor, among which the tray number 8 and tray number 6 are shown in Fig. 2.17a, b.

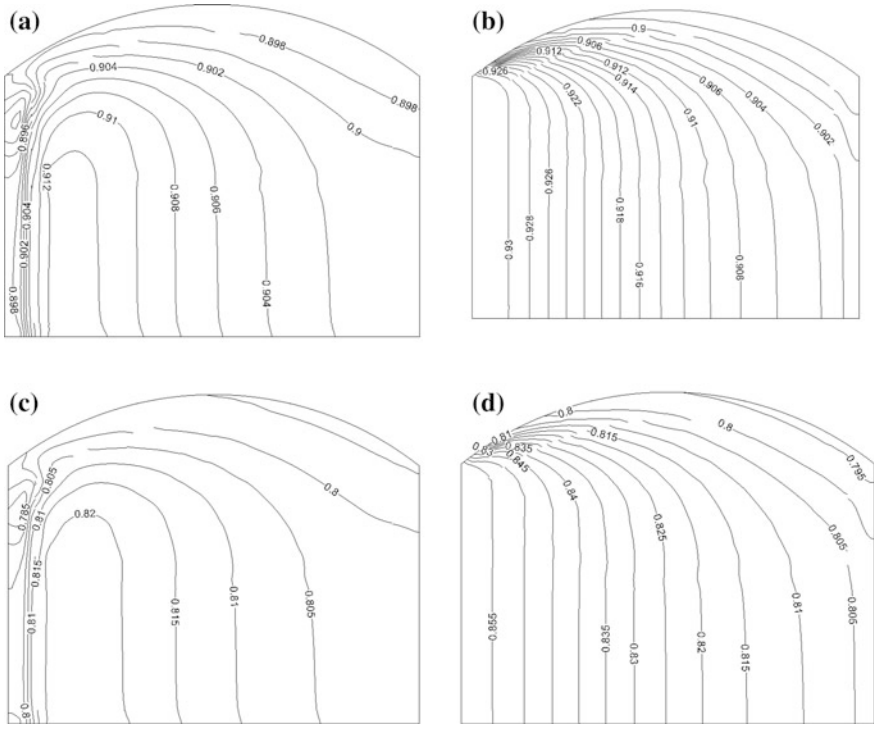

Fig. 2.17 Concentration contour of *x*–*y* plan on trays by Hybrid Reynolds mass flux model, **a** 20 mm above tray floor of tray number 8, **b** 70 mm above tray floor of tray number 8, **c** 20 mm above tray floor of tray number 6, **d** 70 mm above tray floor of tray number 6 [15]

It is found that by comparing Fig. 2.16a versus Fig. 2.17a and Fig. 2.6b versus Fig. 2.17b, the simulated results between standard and hybrid Reynolds mass flux models is practically the same except at the very small region near the end of the inlet weir and the neighboring segmental wall. Such difference is coming from the fact that the standard mass flux model is anisotropic enabling to give more precised three-dimensional flow and mass transfer simulation, while the hybrid Reynolds mass flux model is isotropic and cannot show the detailed three dimensional behaviors in that region. However, if overlooking the difference in this small region, it indicates that the hybrid Reynolds mass flux model can be used for overall simulation instead of using the complicated standard Reynolds mass flux model for the simulation of all trays in a multi-tray column with less computer work.

The simulated result by using hybrid Reynolds mass flux model can also compared with that obtained by using two-equation model as shown in Fig. 2.17, in which the agreement between them is seen except in the region near inlet weir and column wall, where the hybrid Reynolds mass flux model gives more detailed concentration distribution than the two-equation model.

The verification of hybrid Reynolds mass flux model can also be made by comparing with the experimental outlet concentration of each tray as shown in Figs. 2.18 and 2.19, in which the result by using two-equation model is also presented. It can be seen that the hybrid Reynolds mass flux model gives closer outlet concentration to the experimental measurement than the two-equation model, although both of them are considered to be verified by experiment. The verifications of simulated Murphree tray efficiencies by using hybrid Reynolds mass flux models and two-equation model can also be checked by comparing with experimental data as shown in Figs. 2.19a. The comparison of outlet C_6 from each tray between Standard and hybrid Reynolds mass flux model is given in Fig. 2.19b, in which the agreement between them is seen.

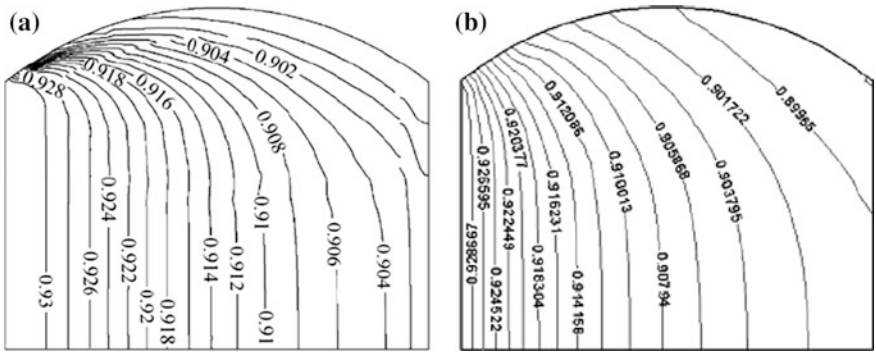

Fig. 2.18 Comparison between hybrid Reynolds mass flux model and two-equation model by simulated concentration contours of 20 mm above tray floor on tray number 8 **a** Hybrid Reynolds mass flux model (reprinted from Ref. [8], Copyright 2011, with permission from Elsevier), **b** $\overline{c'^2} - \varepsilon_{c'}$ Two-equation model (reprinted from Ref. [5], Copyright 2005, with permission from American Chemical Society)

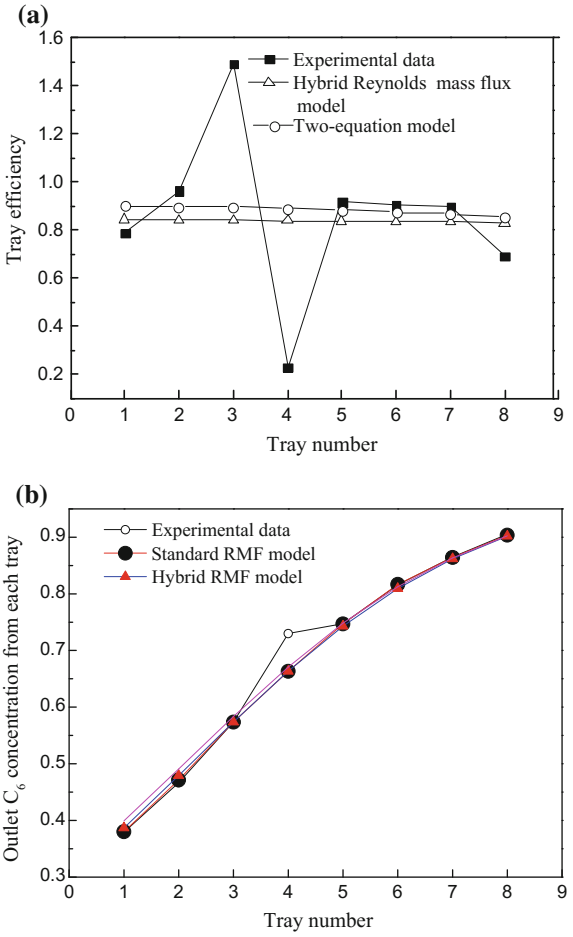

Fig. 2.19 Comparisons of simulated results by different models with experimental data [15] **a** tray efficiency, **b** outlet C_6 concentration. **b** Comparisons of the outlet C_6 concentration between standard and hybrid Reynolds mass flux model simulations and experimental data [15]

Generally speaking, the overall simulated result of a distillation tray column by using two-equation model and different Reynolds mass flux model is very close each other and checked with experimental measurements, but if detailed mass transfer and flow information's on the trays are needed, the standard Reynolds mass flux model is the better choice.

Reynolds mass flux

In this section for convenience, the fluctuating mass flux $\overline{u'_{\mathrm{Li}}c'}$, which is the negative Reynolds mass flux $-\overline{u'_{\mathrm{Li}}c'}$, is used for illustration instead of using Reynolds mass flux.

In the course of solving the model equation, the fluctuating mass flux $\overline{u'_x c'}$, $\overline{u'_y c'}$, $\overline{u'_z c'}$ can be obtained simultaneously [15]. The radial distributions of them at different axial position of tray 8 are given in Fig. 2.20a. The sum of fluctuating mass flux in all directions, $\overline{u'_{\mathrm{Li}}c'} = \overline{u'_x c'} + \overline{u'_y c'} + \overline{u'_z c'}$, is shown in Fig. 2.20b.

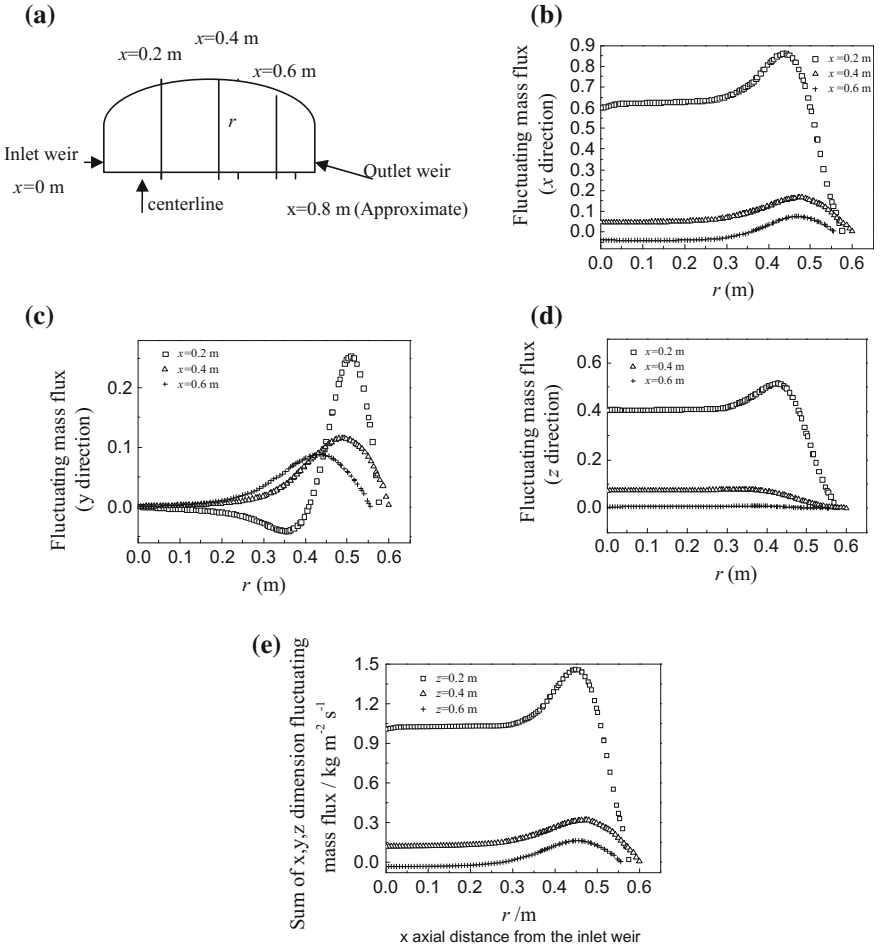

Fig. 2.20 Simulation results of fluctuating mass flux on tray number 8 by Standard Rayleigh mass flux model [15] **a** the tray for simulation, **b** *x* direction (*main flow*), **c** *r* direction (*perpendicular to main flow*), **d** z direction (*depth*), **e** profiles of $\overline{u'_{Li}c'} = \overline{u'_x c'} + \overline{u'_y c'} + \overline{u'_z c'}$ at different axial distance of tray

As seen in Fig. 2.20b, the fluctuating mass flux $\overline{u'_x c'}$ is greater near the inlet weir region (x = 0.2) than that around the outlet weir region (x = 0.6) because c as well as is c' is decreased with x (main flow) direction in distillation process. In the r direction, which is perpendicular to the main flow, all the $\overline{u'_x c'}$, $\overline{u'_y c'}$ and $\overline{u'_z c'}$ contours are almost unchanged up to about 0.3r, then slightly increasing until about r = 0.45r reaching the maximum. This tendency is seen both in Figs. 2.20b–d.

Such maximum point indicates the appearance of greatest mass flux transport as well as turbulent diffusion and vortical mixing there due to the impact with the reversed flow (large scale vortex) created in the segmental region of the column. Such simulated result is consistent with many experimental works that the reversed flow was observed around this region. In Figs. 2.19b and 2.20 the $\overline{u_i'c'}$ and $\overline{u_x'c'}$ contours along r (radial) direction showing almost zero gradient from $r = 0$ to about 0.3 indicates that the turbulent (fluctuating) mass flux flow remains constant, i.e., the turbulent effect is kept steady in this region (see Sect. 1.6.1.3). However, the foregoing mentioned variation of concentration is very small and cannot be found clearly in the profile of concentration contour.

2.1.2.3 Algebraic Reynolds Mass Flux Model

The hybrid Reynolds mass flux model can be further reducing the complexity of model equations by setting the convection term on the left side of Eq. (1.26) equal to the turbulent and molecular diffusions term on the right side under steady condition to obtain Eq. (1.27) as shown below.

$$\overline{u_i'c'} = -\frac{k}{C_{c2}\gamma\beta_L\varepsilon}\left(\overline{u_i'u_j'}\frac{\partial C}{\partial x_j} + \overline{u_i'c'}\frac{\partial U_i}{\partial x_j}\right) + \frac{C_{c3}k}{C_{c2}\varepsilon}\overline{u_i'c'}\frac{\partial U_i}{\partial x_j} \tag{1.27}$$

The algebraic Reynolds mass flux model is using Eq. (1.277) to replace Eq. (1.26); all other model equations are the same as the hybrid Reynolds mass flux model.

To testify this model, Li [4] simulated the sieve tray column as mentioned in Sect. 2.1.1.1. The concentration profile on tray No. 8 are simulated and compared with the simulated results by using different Reynolds mass flux models as shown in Fig. 2.21, from which it is seen that the standard give more detailed information than the other two simplified models although generally speaking their simulated profiles are similar.

The comparison can also be made by the outlet concentration and Murphree efficiency of each tray as shown in Figs. 2.22 and 2.23. The simulated outlet concentrations by using algebraic Reynolds mass flux model are slightly higher than that by the hybrid model; while in Fig. 2.23 the simulated Murphree tray efficiencies by using algebraic Reynolds mass flux mode are slightly lower; although both of them are seen to be sufficiently confirmed by experimental data except tray 4, where experimental error is obvious.

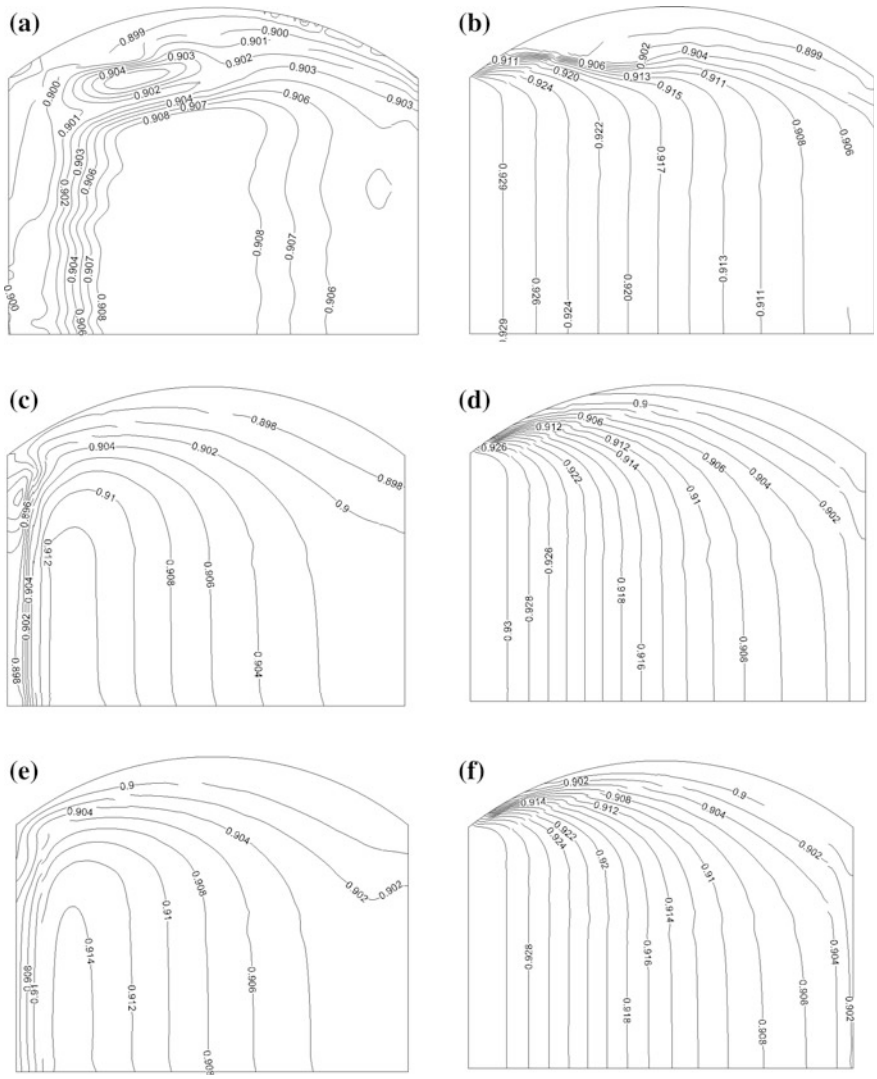

Fig. 2.21 Simulated results of the C_6 concentration profiles of the x–y plane on tray number 8 simulated by different Reynolds flux models for $F = 2.44$ m s^{-1} (kg m^3)$^{0.5}$ [15] **a** Standard Reynolds mass flux model at 70 mm above the tray floor, **b** Standard Reynolds mass flux model at 20 mm above the tray floor, **c** Hybrid Reynolds mass flux model at 70 mm above the tray floor, **d** Hybrid Reynolds mass flux model at 20 mm above the tray floor, **e** Algebraic Reynolds mass flux model at 70 mm above the tray floor, **f** Algebraic Reynolds mass flux model at 20 mm above the tray floor

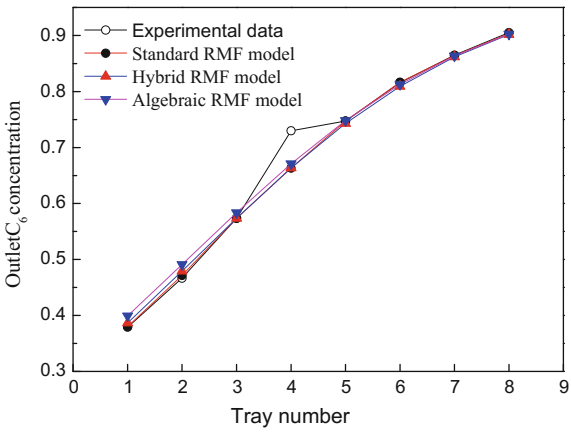

Fig. 2.22 Comparison of simulated results for outlet concentrations of each tray by different models with experimental data [15]

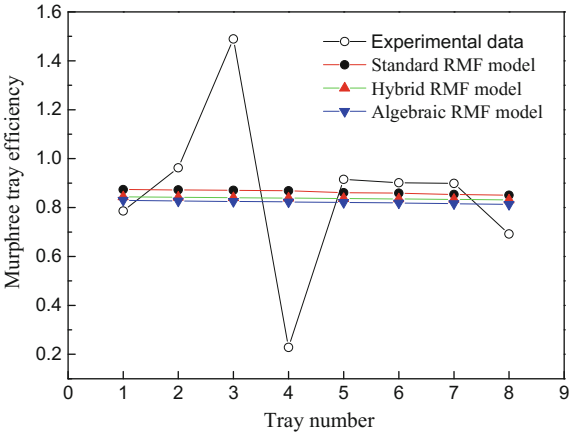

Fig. 2.23 Comparison of simulated results for tray efficiencies by different models with experimental data [15]

2.1.3 Prediction of Multicomponent Point Efficiency

2.1.3.1 Difference Between Binary and Multicomponent Point Efficiency

The separation efficiency in multicomponent distillation is quite different with that in binary (two components) distillation in the following aspects:

(1) In binary system, the diffusion flux between liquid and vapor phases is proportional to the negative concentration gradient; while it is not true in multicomponent system.
(2) In binary system, the diffusion coefficient for component *i* and *j* is equal; while in multicomponent it is not equal.

(3) In binary system, the range of point efficiency is from 0 to 1; while it is ranging from $-\infty$ to $+\infty$ for multicomponent system.

The complication appeared in multicomponent system is chiefly due to the complex nature of molecular interaction to form nonideal solution and may appear bizarre behaviors (see Sect. 2.1.3.6).

The point efficiency is an essential information in distillation design and operation. The tray efficiency can be calculated by the CMT models presented in this chapter, it shows that the tray efficiency is in connection with the tray structure, flow pattern and operating conditions and thus it is only referred to a specific distillation column under specific condition. On the other hand, the point efficiency which depends on only the local condition of vapor–liquid contact and the physical properties of the system is the better way to evaluate the feasibility of using distillation tray column for the separation.

The research on point efficiency has been undertaken over many decades and developed different expressions under the name of the author, like Murphree [18], Hanson [19], Standart [20] and Holland [21]. Among them, the Murohree point efficiency E_{MV} is commonly used, which is defined for tray column as the ratio of the concentration decrease of vapor between entering and leaving the tray and that if the leaving vapor is in thermodynamic equilibrium with the liquid on the tray. Mathematically it can be expressed as follows:

$$E_{\mathrm{MV}} = \frac{y_{i,n} - y_{i,n+1}}{y^*_{i,n} - y_{i,n+1}}, \tag{2.8}$$

where subscript n denotes the tray number; y_{n+1} and y_n are, respectively, the concentration (component *i)* of vapor entering and leaving the tray; $y^*_{i,n}$ is the vapor concentration in equilibrium with the liquid at this local point. Note that the subscript i and j in this section refer to the component i and j, respectively, but not the coordinate direction of flow. The nomenclature can be seen clearly from Fig. 2.24.

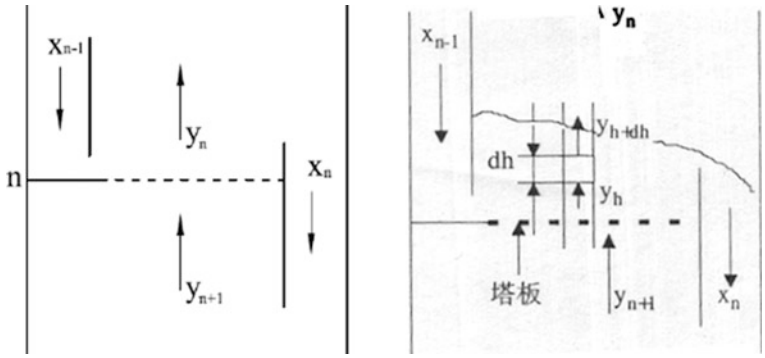

Fig. 2.24 Micro-element (cell) taken on sieve tray

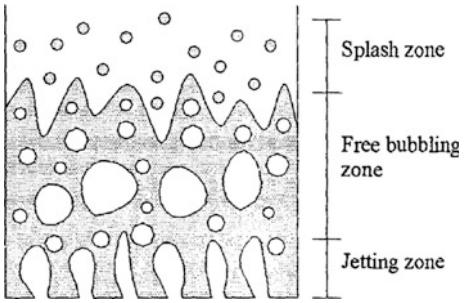

Fig. 2.25 Formation of vapor bubbles from sieve holes in different zones

Murphree point efficiency can be also expressed in terms of liquid concentration as follows:

$$E_{\mathrm{ML}} = \frac{x_{i,n-1} - x_{i,n}}{x_{i,n-1} - x_{i,n}^{*}} \tag{2.9}$$

The vapor phase Murphree point efficient E_{MV} is frequently used especially in distillation, while the liquid phase point efficient E_{ML} is suitable for the liquid phase control processes, such as absorption and desorption processes.

Precisely, the mass transfer undertaken in the vertical direction above the tray deck is complicated as shown typically in Fig. 2.25, involving jetting, dispersed bubbles, splashing as well as the generation of liquid drops as entrainment in the tray spacing. Usually it is divided into three zones, i.e.,

- *froth zone* (jetting),
- *bubble dispersing zone* (free bubbling),
- *bubble breaking zone* (liquid drops splashing as entrainment in tray space).

Since the bubble breaking (splash) zone has very small contribution to the mass transfer, the first two zones, in which the liquid as continuous phase and the vapor as dispersed phase, are dominant and have been established as two-zone model in the literature.

2.1.3.2 The Oldershaw Sieve Tray

The sieve tray developed by Oldershaw [22, 23] is recognized as the common distillation tray to be used for representing the point efficiency. The construction parameters are given in Table 2.2 and the column is shown in Fig. 2.26. The simulation of which is the convenient way to find the point efficiency of the corresponding separating system.

Wang [24] simulated the Oldershaw sieve tray [24] with consideration of using two zones model for the liquid on the tray. The distillation is three components nonideal solution (ethanol, isopropanol, water) for the purpose of investigating the bizarre phenomenon of multicomponent distillation.

Table 2.2 Main construction parameters of Oldershaw sieve tray

Parameter	Value
Tray diameter (mm)	38
Diameter of tray spacing (mm)	64
Sieve hole diameter (mm)	1.25
Thickness of tray floor (mm)	1.2
Perforation (%)	6.38
Height of outlet weir (mm)	15–38

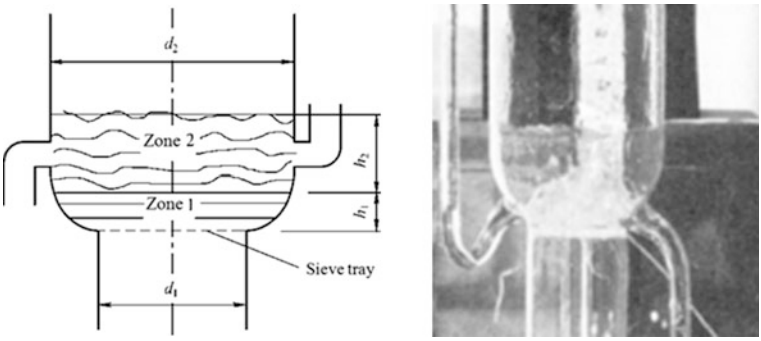

Fig. 2.26 Construction and operation of Oldershaw sieve tray (reprinted from Ref. [23], Copyright 1987, with permission from American Chemical Society)

For the nonideal multicomponent vapor–liquid system, the Maxwell–Stefan equation is usually employed to evaluate the mass transfer behaviors. The fundamentals of Maxwell–Stefan equation is briefly introduced in Sect. 1.4.2.

2.1.3.3 Experimental Work on Multicomponent Tray Efficiency

Wang [24] performed the following experimental works to verify the simulation. Experiment was conducted in Oldershaw sieve tray as shown in Fig. 2.27. Two multicomponent systems are used for testing the point efficiency, i.e., three-component system (ethanol, isopropanol, water) and four-component system (ethanol, isopropanol, tert-butyl alcohol, water). The initial composition of three component system in sequence is as follows:

$$(\boldsymbol{x}_{\mathrm{b}}) = (0.447 \quad 7{,}0.220 \quad 9{,}0.331 \quad 4)^{\mathrm{T}}$$

The composition of entering vapor is

$$(\boldsymbol{y}_{\mathrm{F}}) = (0.444 \quad 7{,}0.221 \quad 4{,}0.333 \quad 9)^{\mathrm{T}}$$

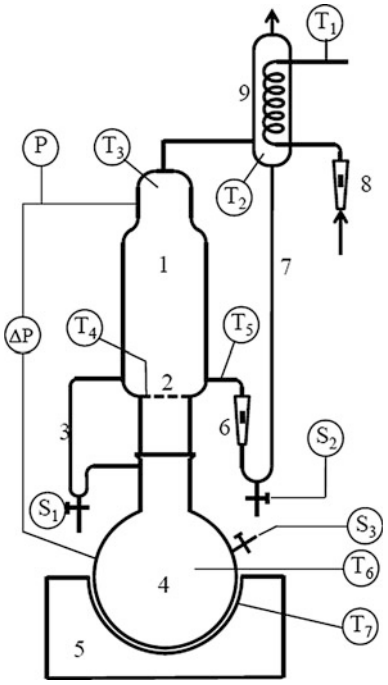

Fig. 2.27 Experimental setup (*1* column, *2* Oldershaw tray, *3* downcomer, *4* Reboiler, *5* heating pot, *6* flow meter, *7* reflux tube, *8* cooling water meter, *9* condenser, *P* pressure measuring point, *T* temperature measuring point, *S* sampling point)

The operating conditions are: temperature $T = 351.4$ K, $Q_V = 1.652 \times 10^{-4}$ $m^3\ s^{-1}$, $h_L = 11.28$ mm. The experimental setup is shown schematically in Fig. 2.27.

2.1.3.4 Simulation Model for Point Efficiency

For calculating Murphree tray efficiency, we need to know the composition of vapor leaving the tray y_{out} which can be obtained as follows. Since the range of composition change on a tray is small, we may assume the vapor–liquid equilibrium relationship to be linear, i.e.,

$$(y^*) = [\boldsymbol{K}^{eq}][\boldsymbol{\Gamma}](x_b), \tag{2.10}$$

where $[\boldsymbol{K}^{eq}]$ is $(n - 1)$ rank diagonal matrix, representing the equilibrium constant of the binary pairs. Also at the interface,

$$(y_0) = [\boldsymbol{K}^{eq}][\boldsymbol{\Gamma}](x_0), \tag{2.11}$$

where y_0 is the vapor concentration at interface. Then we have

$$(y^* - y_0) = [\boldsymbol{K}^{\mathrm{eq}}][\boldsymbol{\Gamma}](x_\mathrm{b} - x_0)$$

The mass flux transferred can be calculated by (see Sect. 3.7.2 of Chap. 3)

$$N_i^\mathrm{L} = -c_\mathrm{t}\left[\beta^\mathrm{L}\right]\left[R^\mathrm{L}\right]^{-1}\left[\boldsymbol{\Gamma}^\mathrm{L}\right](x_\mathrm{b} - x_0) \tag{1.47}$$

$$N_i^\mathrm{V} = -c_\mathrm{t}\left[\beta^\mathrm{V}\right]\left[R^\mathrm{V}\right]^{-1}\left[\boldsymbol{\Gamma}^\mathrm{V}\right](x_b - x_0) \tag{1.48}$$

In the calculation, the liquid bulk concentration x_b is known. Equation set (1.47) and (1.48) can be solved by stepwise iteration as given below to obtain the mass flux being transferred between liquid and vapor phases N_i $\left(N_i = N_i^\mathrm{L} = N_i^\mathrm{V}\right)$.

For the vapor passing through the liquid on the tray, the vapor concentration is changing from y_in to y_out, and should be calculated by differential method. Take a differential element Δh on the sieve tray as shown in Fig. 2.28, we have

$$\mathrm{d}G_i = N_i \alpha A \mathrm{d}h$$

and

$$\mathrm{d}G_i = c_\mathrm{t}^\mathrm{V} u_\mathrm{s} \alpha A \mathrm{d}y,$$

where G_i is the vapor flow rate; A is the area of the bubbling zone on the tray; α is the surface area of the bubbles. Combine foregoing equations to yield

$$\mathrm{d}y_i = \left(\frac{N_i a}{c_\mathrm{t}^\mathrm{V} \alpha u_\mathrm{s}}\right)\mathrm{d}h$$

Integrating consecutively above equation from $h = 0$ at the tray deck to $h = h_1$ for the bubble formation zone and from h_1 to h_2 for the dispersed bubble zone, the y_out can be found for calculating the point efficiency. The trial and error method for

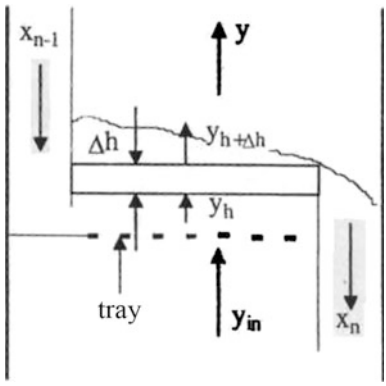

Fig. 2.28 Differential element on the tray

stepwise calculation is employed to obtain the solution. The equations needed for computation of each zone are given below.

Bubble formation zone

Experimental work shows that the main form of vapor in this layer is jetting. The diameter of the vapor jet d_j which is related to the liquid height h_L and the diameter of sieve hole d_h, was correlated by Hai [25]:

$$d_j = 1.1d_h + 0.25h_L$$

Thus the surface area of the jet column is as follows:

$$\alpha = \frac{4\varphi d_j}{(d_h)^2},$$

where φ is the fraction of hole area. As the vapor flow through the jet column is similar to its flow through the falling film column, the mass transfer coefficient k^V can be calculated by the following relationship for two-component system [26]:

$$k^V = 2.0\sqrt{\frac{D^V}{\pi t_V}} = 0.046\left(\frac{D^V}{d_j}\right)(Re)^{0.96}(Sc)^{0.44}$$

$$Re = \frac{d_j u_j \rho_V}{\mu_V}, \quad Sc = \frac{\mu_V}{\rho_V D^V}$$

$$u_j = \frac{Q_V}{[(\pi/4)(d)^2]\varphi} \cdot \left(\frac{d_h}{d_j}\right)^2 = u_h\left(\frac{d_h}{d_j}\right)^2, \quad t_V = \frac{h_j}{u_j},$$

where d_j is the diameter of the vapor jet; u_j and u_h are, respectively, the vapor velocity based on jet diameter and sieve hole diameter.

Bubble dispersion zone

The vapor column reaching to this zone is broken into bubbles of different size and distributed diversely. The average diameter of the bubble can be estimated by the following equation [27]:

$$d_{max} = (0.5We_c)^{0.6}\left(\frac{\sigma}{\rho_L}\right)^{0.6}(u_s g)^{-0.4}\left(\frac{\rho_V}{\rho_L}\right)^{-0.2}$$

$$We_c = \left(\frac{\tau d_{max}}{\sigma}\right)\left(\frac{\rho_V}{\rho_L}\right)^{1/3},$$

where We_c is Weber group; σ is the surface tension; τ is the residence time which is given by [27]

$$\tau = 2\rho_L(u_s g d_{max})^{4/3}$$

It was reported [28, 29] that the ratio of average and maximum bubble diameters is a constant, i.e.,

$$\frac{d_{\mathrm{av}}}{d_{\max}} = 0.62$$

The reliability of foregoing estimation is seen to be confirmed by some experimental data from literature as shown in Table 2.3.

The vapor fraction β_{V} in this layer for sieve hole smaller than 2 mm can be estimated by equation below

$$\frac{\beta_{\mathrm{V}}}{1-\beta_{\mathrm{V}}} = 8.5Fr^{0.5}, \quad Fr \leq 4.68 \times 10^{-4}\varphi^{-0.56}$$

$$\frac{\beta_{\mathrm{V}}}{1-\beta_{\mathrm{V}}} = 1.25\varphi^{-0.14}Fr^{0.25}, \quad Fr > 4.68 \times 10^{-4}\varphi^{-0.56}$$

$$Fr = \frac{(u_{\mathrm{s}})^2}{gh_{\mathrm{L}}},$$

where φ is the fraction of sieve perforation on the tray. By the iteration of foregoing equations, the d_{av} can be obtained as well as the surface area of the bubble by

$$\mathrm{a} = \frac{6}{d_{\mathrm{av}}} \cdot \beta_{\mathrm{V}}$$

The mass transfer coefficient between bubble and the liquid on the tray was measured for binary system by Zaritzky [31] and correlated by Prado and Fair [32] as follows:

$$k^{\mathrm{V}} = Sh\frac{D^{\mathrm{V}}}{d_{\mathrm{av}}}$$

$$Sh = -11.878 + 25.879(\lg Pe) - 5.640(\lg Pe)^2$$

$$Pe = \frac{d_{\mathrm{av}}u_{\mathrm{b}}}{D^{\mathrm{V}}}, \quad u_{\mathrm{b}} = \frac{Q_{\mathrm{V}}}{\frac{\pi}{4}(d)^2\beta_{\mathrm{V}}\rho_{\mathrm{V}}},$$

Table 2.3 Calculated bubble diameter compared with experimental measurements

Sieve hole (m/s)	Calculated d_{av} (mm)	Experimental value by Sharma [29] (mm)	Experimental value by Raper [30] (mm)	Experimental value by Geary [27] (mm)
1.70	3.35	4.0	2.0–5.0	2.0–4.0
1.94	3.60			
2.01	3.60			
2.24	3.55			
2.26	4.05			

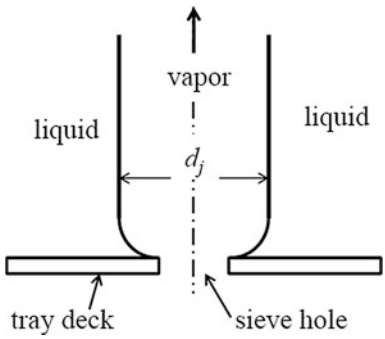

Fig. 2.29 Vapor column from sieve hole

where D^{V} is the molecular diffusivity of component i in the vapor phase.

Steps of calculation

As seen in Fig. 2.29, let the height of the two liquid zones on the tray be h $(h = h_1 + h_2)$, take a differential element Δh on the tray where $y_{in} = y_h$ and $y_{out} = y_{h+\Sigma\Delta h}$. The mass flux of component i in the element can be calculated as follows:

1. Let $y_{in} = y_{bh}$ and assume $y_{out} = y^0_{bh+\Delta h}$, the average concentration of component i is $y_{av} = \frac{1}{2}\left(y_{bh} + y_{bh+\Delta h}\right)$
2. Calculate the mass flux to be transferred by aforementioned method so as to obtain the concentration of vapor leaving from the differential element. If it is close enough to the assumed value, then proceed to the next differential element above until reaching to the top of the liquid zone to obtain the outlet vapor concentration from the tray.

As an example, Wang [24] give the calculated result along liquid height h as shown in Table 2.4

As seen, the mass transfer is high at low liquid level and decrease as the vapor goes up to the top of the froth. It indicates the bubble formation zone is dominant in the mass transfer process.

2.1.3.5 Simulated Results and Comparison with Experimental Data

The comparisons between simulated and experimental Murphree point efficiencies of three-component and four-components systems are given, respectively, in Tables 2.5 and 2.6. The error in most cases is less than few percent which is acceptable for estimation purpose.

Table 2.4 Calculated result of mass flux transferred along liquid height

Liquid height h from tray deck (mm)	Vapor concentration, mole fraction			Mass flux transferred N (mol m^{-2} s^{-1})		
	Ethanol	Isopropanol	Water	Ethanol	Isopropanol	Water
1.30	0.4461	0.2216	0.3323	12.36×10^{-6}	1.663×10^{-5}	-11.68×10^{-5}
2.60	0.4474	0.2218	0.3308	11.95×10^{-6}	1.566×10^{-5}	-11.27×10^{-5}
3.89	0.4488	0.2219	0.3293	11.56×10^{-6}	1.473×10^{-5}	-10.86×10^{-5}
5.19	0.4500	0.2221	0.3279	11.18×10^{-6}	1.384×10^{-5}	-10.48×10^{-5}
6.49	0.4513	0.2222	0.3265	10.81×10^{-6}	1.300×10^{-5}	-10.10×10^{-5}
7.79	0.4524	0.2224	0.3252	10.46×10^{-6}	1.220×10^{-5}	-9.743×10^{-5}
9.09	0.4536	0.2225	0.3239	10.12×10^{-6}	1.143×10^{-5}	-9.396×10^{-5}
10.38	0.4547	0.2226	0.3227	9.876×10^{-6}	1.070×10^{-5}	-9.061×10^{-5}
11.68	0.4558	0.2228	0.3215	9.466×10^{-6}	1.001×10^{-5}	-8.739×10^{-5}
12.98	0.4568	0.2229	0.3203	9.158×10^{-6}	0.935×10^{-5}	-8.428×10^{-5}
14.18	0.4621	0.2234	0.3145	8.625×10^{-6}	0.815×10^{-5}	-7.887×10^{-5}
15.38	0.4665	0.2237	0.3098	7.144×10^{-6}	0.517×10^{-5}	-6.410×10^{-5}
16.59	0.4702	0.2239	0.3060	5.926×10^{-6}	0.296×10^{-5}	-5.214×10^{-5}
17.79	0.4732	0.2239	0.3029	4.924×10^{-6}	0.135×10^{-5}	-4.246×10^{-5}
18.99	0.4757	0.2239	0.3003	4.096×10^{-6}	0.020×10^{-5}	-3.460×10^{-5}
20.19	0.4778	0.2239	0.2983	3.413×10^{-6}	-0.062×10^{-5}	-2.822×10^{-5}
21.39	0.4796	0.2238	0.2966	2.847×10^{-6}	-0.116×10^{-5}	-2.304×10^{-5}
22.60	0.4810	0.2237	0.2952	2.378×10^{-6}	-0.152×10^{-5}	-1.882×10^{-5}
23.80	0.4823	0.2236	0.2941	1.989×10^{-6}	-0.172×10^{-5}	-1.539×10^{-5}
25.00	0.4833	0.2235	0.2932	1.666×10^{-6}	-0.183×10^{-5}	-1.259×10^{-5}

Table 2.5 Comparison of simulated point efficiency with experimental data (I) [system: ethanol (1), isopropanol (2), water (3)]

Expt. No.	Component	Liquid concentration on tray, mole fraction	Experimental point efficiency	Simulated point effIciency	Error = Sim. − Exp.
1	1	0.1247	0.9888	0.8155	−0.1733
	2	0.6434	0.9924	0.9430	−0.0494
	3	0.2319	0.9932	0.9709	−0.0223
2	1	0.0859	0.8529	0.8280	−0.0249
	2	0.7434	0.9710	0.9494	−0.0216
	3	0.1707	0.9903	0.9695	−0.0208
3	1	0.4477	0.8679	0.8745	−0.0066
	2	0.2209	2.8615	2.8842	0.0227
	3	0.3314	0.8558	0.9072	0.0514
4	1	0.2589	0.6976	0.6771	−0.205
	2	0.4210	0.0846	0.1044	0.198
	3	0.3201	0.7732	0.7526	−0.0027
5	1	0.2115	0.7807	0.8338	0.0531
	2	0.4510	1.1921	1.1591	−0.0330
	3	0.3375	0.8625	0.8984	0.0359

Table 2.6 Comparison of simulated point efficiency with experimental data (II) [system: ethanol (1), isopropanol (2), tert-butyl alcohol (3), water(4)]

Expt. No.	Component	Liquid concentration on tray, mole fraction	Point efficiency		Error
			Experimental	Simulated	
1	1	0.3436	0.9035	0.8225	−0.0343
	2	0.2679	0.8087	0.8238	0.0186
	3	0.0640	0.7242	0.7801	0.0773
	4	0.3245	0.9706	0.9070	−0.0655
2	1	0.2313	0.9625	0.8154	−0.1528
	2	0.4694	0.9977	0.9279	−0.0699
	3	0.1231	0.7667	0.9163	0.1951
	4	0.1763	0.9292	0.9682	0.0419
3	1	0.4866	0.9108	0.9341	0.0256
	2	0.0781	1.2949	0.8274	−0.3611
	3	0.0788	1.5687	1.6066	0.0241
	4	0.3566	0.8928	0.9507	0.0648
4	1	0.0507	0.9027	0.8939	−0.0097
	2	0.0465	0.9100	0.8466	−0.0697
	3	0.3963	0.8686	0.8968	0.0324
	4	0.5065	0.8659	0.9092	0.0500
5	1	0.3488	0.8741	0.8282	−0.0525
	2	0.3534	0.8702	0.9133	0.0496
	3	0.0809	0.9261	0.9019	−0.0262
	4	0.2170	0.9384	0.9972	0.0627
6	1	0.3717	0.9891	0.9444	−0.0452
	2	0.1339	5.2322	7.3893	0.4123
	3	0.0669	0.8891	0.9618	0.0818
	4	0.4275	0.9882	0.9620	−0.026
7	1	0.8658	0.7967	0.7867	−0.0125
	2	0.0145	0.8643	0.9694	0.1216
	3	0.0396	0.9631	0.9190	−0.0458
	4	0.0801	1.0429	1.0323	−0.0102
8	1	0.1360	0.9437	0.9491	0.0057
	2	0.1102	0.7173	0.5346	−0.2547
	3	0.2214	0.8633	0.8590	−0.0050
	4	0.5344	0.8813	0.9165	0.0400

2.1.3.6 The Bizarre Phenomena of Multicomponent System

The bizarre phenomena of multicomponent system can be illustrated by the case of three component system as calculated by Wang given in preceding section. The simulated diffusion flux of isopropanol is plotted versus driving force of mass transfer $(y_0 - y)$ as shown in Fig. 2.30.

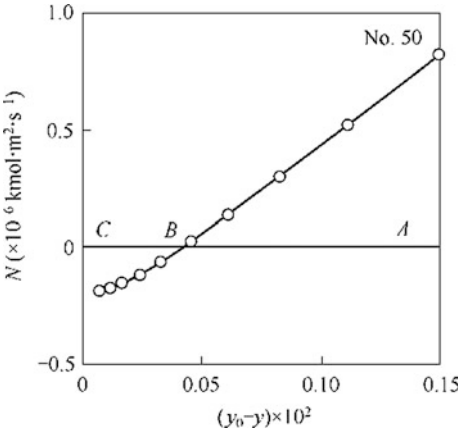

Fig. 2.30 The diffusion mass flux of isopropanol in three components system versus driving force of mass transfer

As seen in the figure that the driving force $(y_0 - y)$ is positive between A and B, the direction of mass transfer is from y_0 (vapor) to y (liquid). At point B, although the driving force is positive, but the mass flux of isopropanol transferred is zero; such phenomenon is regarded as *diffusion barrier* which is not happened in binary system. From point B to C, the driving force is still positive, yet the isopropanol transferred is negative, i.e., the direction of mass transfer is reversed and such phenomenon is regarded as *reversed diffusion*. Moreover, as seen in Fig. 2.31, at the liquid height about $h = 25$, the driving force is approaching zero, but the isopropanol still able to undertake mass transfer between phases; such phenomenon is regarded as *osmotic diffusion*. It should be mentioned that such *bizarre phenomena* is only happened for isopropanol in the three component system but not for ethanol and water. Thus, the complication of nonideal multicomponent system depends on many factors and still under investigation. The plot of simulated results is also given in Fig. 2.31.

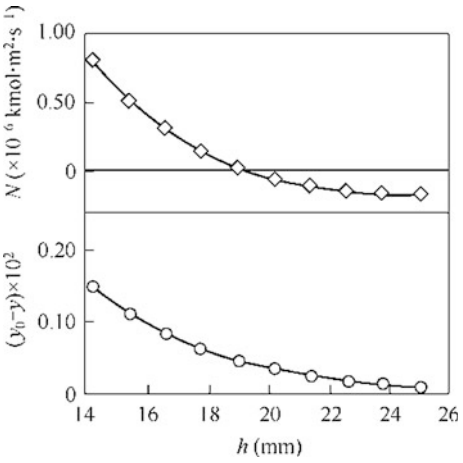

Fig. 2.31 Mass transfer flux and driving force of isopropanol in three components system versus liquid height

2.2 Packed Column

The simulation of packed column by computational mass transfer methodology have been made by Liu [33] and Li [8] as given in following sections:.

The model assumptions are the same as the tray column except that axially symmetrical condition is applied for the packed column.

The packed column to be simulated are that reported by Sakata [2], it is 1.22 m in diameter packed with 50.8 mm carbon steel Pall ring of 3.66 m height for separating *n*-heptane and methylcyclohexane under 165.5 kPa and total reflux operation.

2.2.1 $\overline{c'^2} - \varepsilon_c$ Two-Equation Model

2.2.1.1 Modeling Equations

The model equation for packed column, comprised CFD equation set and mass transfer equation set. Unlike the tray column, the porosity of packed column is nonuniformly distributed and the liquid fraction β_L should be retained in the model equations. The interacted liquid phase model equations are.

Overall mass conservation

$$\frac{\partial(\rho_L \gamma \beta_L U_{Li})}{\partial x_i} = S_m, \tag{2.12}$$

where γ is the porosity of the packed bed.

Momentum conservation

$$\frac{\partial \rho_L \gamma \beta_L U_{Li} U_{Lj}}{\partial x_i} = -\gamma \beta_L \frac{\partial P}{\partial x_j} + \gamma \beta_L \frac{\partial}{\partial x_i}\left[\mu_L \frac{\partial U_{Li}}{\partial x_i} - \rho_L \overline{u'_{Li} u'_{Lj}}\right] + \gamma \beta_L S_{Li} \tag{2.13}$$

where $\overline{u'_{Li} u'_{Lj}}$ by

$$-\rho_L \overline{u'_{Li} u'_{Lj}} = \mu_{Lt}\left(\frac{\partial U_{Li}}{\partial x_j} + \frac{\partial U_{Lj}}{\partial x_i}\right) - \frac{2}{3}\rho_L \delta_{ij} k_L \tag{A1.8}$$

k_L equation

$$\frac{\partial \rho_L \gamma \beta_L U_{Li} k_L}{\partial x_i} = \frac{\partial}{\partial x_i}\left[\gamma \beta_L \left(\mu_L + \frac{\mu_{Lt}}{\sigma_{k_L}}\right)_L \frac{\partial k_L}{\partial x_j}\right] + \gamma \beta_L (G_{Lk} - \varepsilon_L) \tag{2.14}$$

ε_{L} *equation*

$$\frac{\partial \rho_{\mathrm{L}} \gamma \beta_{\mathrm{L}} U_{\mathrm{L}i} \varepsilon_{\mathrm{L}}}{\partial x_i} = \frac{\partial}{\partial x_i}\left[\gamma \beta_{\mathrm{L}}\left(\mu_{\mathrm{L}} + \frac{\mu_{\mathrm{Lt}}}{\sigma_{\varepsilon_{\mathrm{L}}}}\right)\frac{\partial \varepsilon_{\mathrm{L}}}{\partial x_i}\right] + \gamma \beta_{\mathrm{L}}\left(C_{1\varepsilon} G_{\mathrm{L}k} - C_{2\varepsilon}\rho_{\mathrm{L}}\varepsilon_{\mathrm{L}}\right)\frac{\varepsilon_{\mathrm{L}}}{k_{\mathrm{L}}} \quad (2.15)$$

The model constants are $c_\mu = 0.09$, $\sigma_k = 1.0$, $\sigma_\varepsilon = 1.3$, $C_{1\varepsilon} = 1.44$, $C_{2\varepsilon} = 1.92$.

Species mass conservation equation

$$\frac{\partial \gamma \beta_{\mathrm{L}} U_{\mathrm{L}i} C}{\partial x_i} = \frac{\partial}{\partial x_i}\gamma \beta_{\mathrm{L}}\left(D_{\mathrm{Lt}}\frac{\partial C}{\partial x_i} - \overline{u'_{\mathrm{L}i} c'}\right) + S_n \quad (2.16)$$

$\overline{c'^2}$ *equation*

$$\frac{\partial \gamma \beta_{\mathrm{L}} U_{\mathrm{L}i} \overline{c'^2}}{\partial x_i} = \frac{\partial}{\partial x_i}\left[\gamma \beta_{\mathrm{L}}\left(D_{\mathrm{L}} + \frac{D_{\mathrm{L}i}}{\sigma_{c'^2}}\right)\frac{\partial \overline{c'^2}}{\partial x_i}\right] - 2\gamma \beta_{\mathrm{L}} D_{\mathrm{Lt}}\left(\frac{\partial C}{\partial x_i}\right)^2 - 2\gamma \beta_{\mathrm{L}}\varepsilon_{c'} \quad (1.10)$$

$\varepsilon_{c'}$ *equation*

$$\begin{aligned} U_i \gamma \beta_{\mathrm{L}} \frac{\partial \varepsilon_{c'}}{\partial x_i} &= \frac{\partial}{\partial x_i}\left[\gamma \beta_{\mathrm{L}}\left(D_{\mathrm{L}} + \frac{D_{\mathrm{Lt}}}{\sigma_{\varepsilon_c}}\right)\frac{\partial \varepsilon_{c'}}{\partial x_i}\right] \\ &\quad - C_{c1}\gamma \beta_{\mathrm{L}} D_{\mathrm{Lt}}\frac{\varepsilon_{c'}}{\overline{c'^2}}\left(\frac{\partial C}{\partial x_i}\right)^2 - C_{c2}\frac{\varepsilon_{c'}^2}{\overline{c'^2}} - C_{c3}\gamma \beta_{\mathrm{L}}\frac{\varepsilon_{c'}\varepsilon_{c'}}{k_{\mathrm{L}}} \end{aligned} \quad (1.17)$$

D_{t} *equation*

$$D_{\mathrm{Lt}} = C_{c0} k_{\mathrm{L}}\left(\frac{k_{\mathrm{L}}\overline{c'^2}}{\varepsilon_{\mathrm{L}}\varepsilon_{c'}}\right)^{\frac{1}{2}} \quad (1.6)$$

Model constants are: $C_{c0} = 0.14$, $C_{c1} = 1.8$, $C_{c2} = 2.2$, $C_{c3} = 0.8$, $\sigma_{c^2} = 1.0$.

2.2.1.2 Boundary Conditions

Inlet (reflux at column top $x = 0$): $U_{\mathrm{L}} = U_{\mathrm{in}}$, $V_{\mathrm{L}} = 0$, $C_i = C_{i,\mathrm{in}}$. For the other parameters, we may set to be [1, 34]:

$$\begin{aligned} k_{\mathrm{L,in}} &= 0.003 U_{\mathrm{L,in}}^2 \\ \varepsilon_{\mathrm{L,in}} &= 0.09\frac{k_{\mathrm{L,in}}^{1.5}}{d_{\mathrm{H}}} \\ \overline{c'^2} &= \left(0.082 C_{\mathrm{in}}\right)^2 = 0.0067 C_{\mathrm{in}}^2 \\ \varepsilon_{c'} &= 0.4\left(\frac{\varepsilon_{\mathrm{in}}}{k_{\mathrm{in}}}\right)\overline{c'^2_{\mathrm{in}}} \end{aligned}$$

Outlet (column bottom): fully developed turbulent condition is assumed so that the gradients of all parameters Φ except pressure are set to be zero

$$\frac{\partial \Phi}{\partial x} = 0$$

Column symmetrical axis ($r = 0$): the radial gradients of all parameters Φ except pressure are equal to zero.

$$\frac{\partial \Phi}{\partial r} = 0$$

Column wall ($r = R$): the relevant flux is equal to zero.
Near column wall region: standard wall function is employed.

2.2.1.3 Evaluation of Source Term

As stated in Sect. 2.1, considering the latent heat of both species is almost equal, so that $S_n = 0$.

The source term $S_{\mathrm{L}i}$ is expressed by

$$S_{\mathrm{L}i} = \rho_{\mathrm{L}} g + F_{\mathrm{LS},i} + F_{\mathrm{LG}},$$

where F_{LS} is the flow resistance created by random packing, F_{LG} is the interface drag force between liquid and vapor phases. The F_{LS} can be evaluated by using following correlation [35]:

$$F_{\mathrm{LS}} = -\left[A\mu_{\mathrm{L}} \frac{(1-\gamma)^2}{\gamma^2 d_{\mathrm{e}}^2} + B\rho_L \frac{(1-\gamma)}{\gamma d_{\mathrm{e}}} |\boldsymbol{U}_{\mathrm{L}}|\right] \boldsymbol{U}_{\mathrm{L}},$$

where $\boldsymbol{U}$ is interstitial velocity vector; γ is the porosity; d_{e} is the equivalent diameter of the packing; constants $A = 150$, $B = 1.75$.

The F_{LG} is calculated by

$$F_{\mathrm{LG}} = \frac{\Delta p_{\mathrm{L}}}{|\boldsymbol{U}_{\mathrm{slip}}|} \boldsymbol{U}_{\mathrm{slip}},$$

where Δp_{L} is the wet-bed pressure drop; $\boldsymbol{U}_{\mathrm{slip}}$ is slip velocity vector between vapor and liquid and equal to

$$\boldsymbol{U}_{\mathrm{slip}} = \boldsymbol{U}_{\mathrm{G}} - \boldsymbol{U}_{\mathrm{L}}$$

The S_n in species equation, similar to the tray column, can be calculated by:

$$S_n = K_{\mathrm{OL}} a \left(C_{\mathrm{G}}^{*} - C_{\mathrm{L}} \right)$$

$$K_{\mathrm{OL}} = \frac{1}{\frac{1}{k_{\mathrm{L}}} + \frac{1}{m k_{\mathrm{G}}}}$$

The gas and liquid film coefficients k_{L}, k_{G} and the volumetric effective surface area a are obtained from the correlation by Wagner et al. [34] as follows:

$$k_{\mathrm{L}} = \left(\frac{4 \Phi_{\mathrm{L}} D_{\mathrm{L}} U_{\mathrm{L}}}{\pi h \gamma \chi} \right)^{0.5}$$

$$k_G = \left(\frac{4 \Phi_{\mathrm{G}} D_{\mathrm{G}} U_{\mathrm{G}}}{\pi (\gamma - h\,\gamma) \chi} \right)^{0.5},$$

where the enhancement factor Φ_{L} and Φ_{G} is set equal to 1 under experimental condition; χ is characteristic length depending on bed height Z:

$$\chi = C_{\mathrm{p}k}^2 Z$$

The coefficient $C_{\mathrm{p}k}$ for 50.8 mm pall ring packing is equal to 0.031.

The vapor liquid contacting area a is calculated by [34]

$$\frac{a}{a_{\mathrm{T}}} = \frac{h\gamma}{1.0 - \gamma},$$

where a_{T} is the specific area of the packing; γ is the porosity; h is the total liquid holdup of the packing which comprises static holdup h_{s} and dynamic holdup h_{d}. For 50.8 mm Pall ring packing, h_{s} is calculated by [36]

$$h_{\mathrm{s}} = 0.033 \exp\left(-0.22 \frac{g \rho_{\mathrm{L}}}{\sigma_{\mathrm{L}} a_{\mathrm{T}}^2} \right)$$

and h_{d} by [37]

$$h_{\mathrm{d}} = 0.555 \left(\frac{a_{\mathrm{T}} U_{\mathrm{L}}^2}{g \gamma^{4.65}} \right)^{1/3}$$

2.2.1.4 Simulated Result and Verification—Separation of Methylcyclohexane and *n*-Heptane

Average axial concentration along column height and verification

The simulated radial averaged axial concentration along radial direction at different column height as shown in Fig. 2.32. The plot is made by $\ln\left(\frac{x}{1-x}\right)$ versus column height z (z is the height of the packed bed measured from the column

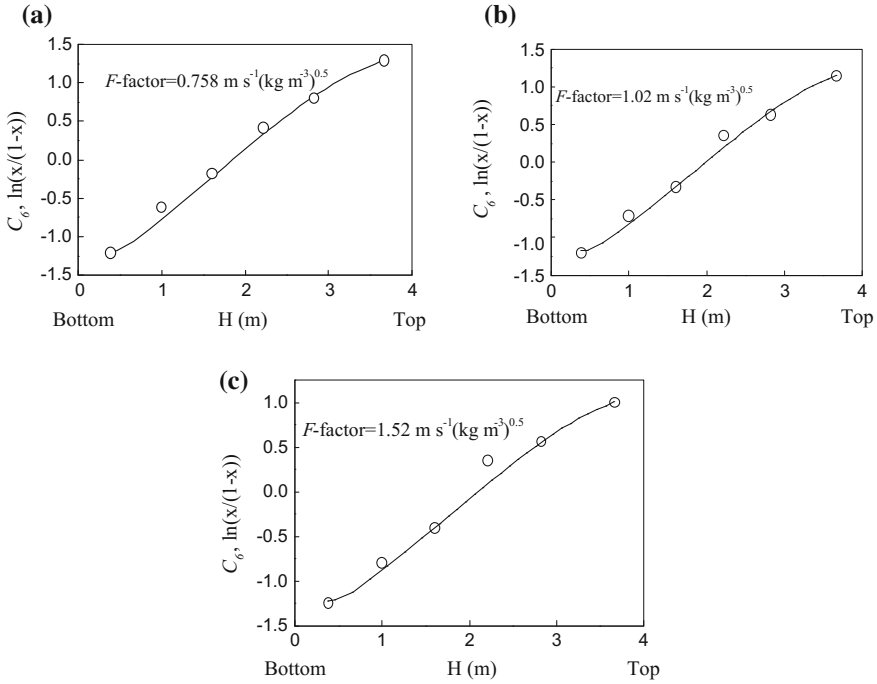

Fig. 2.32 Comparisons of the concentration profiles in liquid phase between two-equation model predictions (*solid lines*) and experimental data (*circles*) (*H is height of packed*) **a** *F*-factor = 0.758 m s^{-1} (kg m^{-3})$^{0.5}$, **b** *F*-factor = 1.02 m s^{-1} (kg m^{-3})$^{0.5}$, **c** *F*-factor = 1.52 m s^{-1} (kg m^{-3})$^{0.5}$ (reprinted from Ref. [33], Copyright 2009, with permission from Elsevier)

bottom) because according to the Fenske equation such plot should be in a straight line at constant relative volatility which is applicable to the present case. The simulated curve is nearly a straight line and in good agreement with the experimental data.

HETP and verification

The separation efficiency of packed column is usually expressed in terms of HETP (Height Equivalent of Theoretical Plate). According to the Fenske equation, the slope of $\ln\left(\frac{x}{1-x}\right)$ versus Z plot is equal to $\frac{\ln \alpha_{re}}{\mathrm{HETP}}$ where α_{re} is the relative volatility of the separating system. The simulated HETP can be obtained from Fig. 2.32 by smoothing the computed curve to a straight line and find the slop. As shown in Fig. 2.33, the simulated HETP is confirmed by the experimental data.

Turbulent mass diffusivity distribution

The volume average turbulent mass diffusivity D_{Lt} computed by the two-equation model is shown in Fig. 2.34 at different F factor, and more detailed distribution is given in Fig. 2.35. These figures show that the turbulent mass diffusivity is higher in the upper part of the column and lower in the near wall region. The reason is due to higher concentration around the upper column in distillation

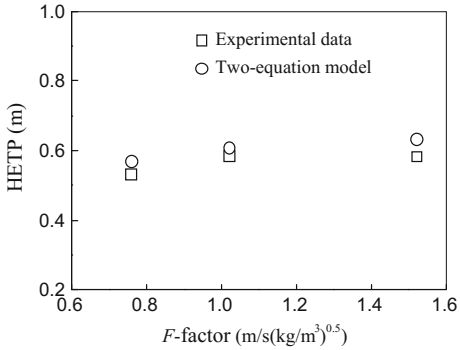

Fig. 2.33 HETP comparison between predictions and measurements (reprinted from Ref. [33], Copyright 2009, with permission from Elsevier)

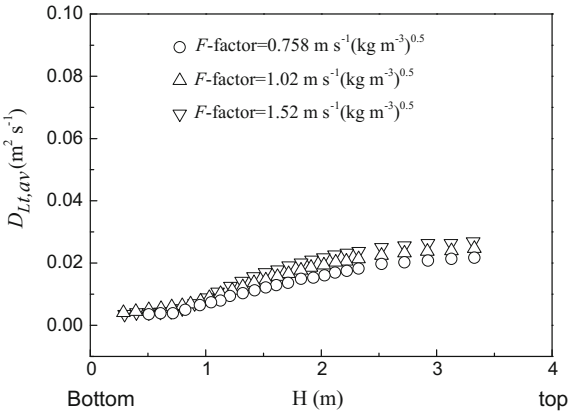

Fig. 2.34 Average turbulent mass diffusivity along the column height at different F factor (reprinted from Ref. [33], Copyright 2009, with permission from Elsevier)

process so as to undertaking more quantity of mass transfer. At the same time the wall effect accounts for the mass transfer lower down in the near wall region.

2.2.2 Reynolds Mass Flux Model

Li [8] simulated the packed column as described in Sect. 4.2.1 by using Reynolds mass flux model instead of two-equation model and compare their difference. The simulated results for three forms of Reynolds mass flux model (standard, hybrid and algebraic) are given in subsequent sections.

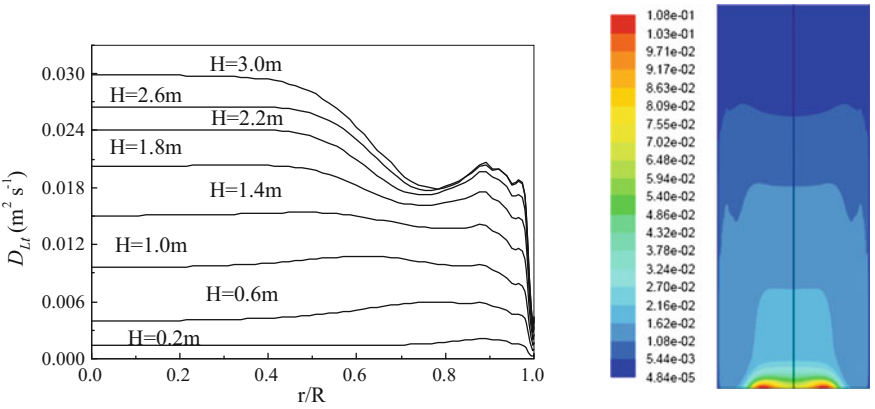

Fig. 2.35 Distribution of turbulent mass diffusivity in the column F = 1.02 m s^{-1} (kg m^{-3})$^{0.5}$, H Height of packed bed (*H = 0 at the column bottom*) (reprinted from Ref. [33], Copyright 2009, with permission from Elsevier)

2.2.2.1 Standard Reynolds Mass Flux Model

Interacted liquid phase model with constant fluid density ρ and constant liquid fraction β is employed for simulation. The model equations are.

Overall mass conservation

$$\frac{\partial \rho \gamma \beta_{\mathrm{L}} U_{\mathrm{L}i}}{\partial x_i} = S_{\mathrm{m}} \tag{2.17}$$

Momentum conservation

$$\frac{\partial \rho \gamma \beta_{\mathrm{L}} U_{\mathrm{L}i} U_{\mathrm{L}j}}{\partial x_i} = -\gamma \beta_{\mathrm{L}} \frac{\partial P}{\partial x_j} + \frac{\partial}{\partial x_i} \gamma \beta_{\mathrm{L}} \left[\mu_{\mathrm{L}} \frac{\partial U_{\mathrm{L}i}}{\partial x_i} - \rho \overline{u'_{\mathrm{L}i} u'_{\mathrm{L}j}} \right] + \gamma \beta_{\mathrm{L}} S_{\mathrm{L}i} \tag{2.18}$$

where $\overline{u'_{\mathrm{L}i} u'_{\mathrm{L}j}}$ is calculated by

$$\begin{aligned} \frac{\partial \overline{u'_{\mathrm{L}i} u'_{\mathrm{L}j}}}{\partial t} + U_k \frac{\partial \overline{u'_{\mathrm{L}i} u'_{\mathrm{L}j}}}{\partial x_k} = {} & \frac{\partial}{\partial x_k} \left(C_k \frac{k}{\varepsilon} \overline{u'_i u'_j} \frac{\partial \overline{u'_{\mathrm{L}i} u'_{\mathrm{L}j}}}{\partial x_k} + \frac{\mu}{\rho} \frac{\partial \overline{u'_{\mathrm{L}i} u'_{\mathrm{L}j}}}{\partial x_k} \right) \\ & - \left(\overline{u'_{\mathrm{L}i} u'_{\mathrm{L}k}} \frac{\partial U_{\mathrm{L}j}}{\partial x_k} + \overline{u'_{\mathrm{L}j} u'_{\mathrm{L}k}} \frac{\partial U_{\mathrm{L}i}}{\partial x_k} \right) - C_1 \frac{\varepsilon}{k} \left(\overline{u'_{\mathrm{L}i} u'_{\mathrm{L}j}} - \frac{2}{3} k_{\mathrm{L}} \delta_{ij} \right) \\ & - C_2 \left(\overline{u'_{\mathrm{L}i} u'_{\mathrm{L}k}} \frac{\partial U_j}{\partial x_k} + \overline{u'_{\mathrm{L}j} u'_{\mathrm{L}k}} \frac{\partial U_{\mathrm{L}i}}{\partial x_k} - \frac{2}{3} \delta_{ij} \overrightarrow{u'_{\mathrm{L}i} u'_{\mathrm{L}k}} \frac{\partial U_{\mathrm{L}i}}{\partial x_k} \right) - \frac{2}{3} \varepsilon_{\mathrm{L}} \delta_{ij} \end{aligned} \tag{1.23}$$

where the constants are: C_k = 0.09, C_1 = 2.3, C_2 = 0.4.

Species mass conservation equation

$$\frac{\partial \gamma \beta_{\mathrm{L}} U_{\mathrm{L}i} C}{\partial x_i} = \frac{\partial}{\partial x_i} \lambda \beta_{\mathrm{L}} \left(D_{\mathrm{L}} \frac{\partial C}{\partial x_i} - \overline{u'_{\mathrm{L}i} c'} \right) + \gamma \beta_{\mathrm{L}} S_{\mathrm{L}n} \tag{1.3}$$

Fluctuating mass flux equation

$$\begin{aligned} \frac{\partial \overline{u'_{\mathrm{L}i} c'}}{\partial t} + \frac{\partial U_{\mathrm{L}j} \overline{u'_{\mathrm{L}i} c'}}{\partial x_j} = \frac{\partial}{\partial x_j} \left[\left(C_{c1} \frac{k_{\mathrm{L}}}{\varepsilon_{\mathrm{L}}} \overline{u'_{\mathrm{L}i} u'_{\mathrm{L}j}} + \frac{\mu}{\rho} \right) \frac{\partial \overline{u'_{\mathrm{L}i} c'}}{\partial x_j} \right] \\ - \left(\overline{u'_{\mathrm{L}i} u'_{\mathrm{L}j}} \frac{\partial C}{\partial x_j} \right) - C_{c2} \frac{\varepsilon}{k} \overline{u'_{\mathrm{L}i} c'} + C_{c3} \overline{u'_{\mathrm{L}j} c'} \frac{\partial U_{\mathrm{L}i}}{\partial x_j} \end{aligned} \tag{1.26a}$$

where $C_{c1} = 0.09$, $C_{c2} = 3.2$, $C_{c3} = 0.55$.

Auxiliary equations

k_{L} equation

$$\begin{aligned} \frac{\partial \rho \gamma \beta_{\mathrm{L}} U_{\mathrm{L}i} k_{\mathrm{L}}}{\partial x_i} = \frac{\partial}{\partial x_i} \left[\gamma \beta_{\mathrm{L}} \left(\mu_{\mathrm{L}} + \frac{\mu_{\mathrm{Lt}}}{\sigma_k} \right) \frac{\partial k_{\mathrm{L}}}{\partial x_i} \right] \\ - \mu_{\mathrm{t}} \gamma \beta_{\mathrm{L}} \left(\frac{\partial U_{\mathrm{L}i}}{\partial x_j} + \frac{\partial U_{\mathrm{L}j}}{\partial x_i} \right) \frac{\partial U_{\mathrm{L}j}}{\partial x_i} - \rho_{\mathrm{L}} \gamma \beta_{\mathrm{L}} \varepsilon_{\mathrm{L}} \end{aligned} \tag{A1.11a}$$

ε_{L} equation

$$\begin{aligned} \frac{\partial \rho_{\mathrm{L}} \gamma \beta_{\mathrm{L}} U_{\mathrm{L}i} \varepsilon_{\mathrm{L}}}{\partial x_i} = \frac{\partial}{\partial x_i} \left[\gamma \beta_{\mathrm{L}} \left(\mu_{\mathrm{L}} + \frac{\mu_{\mathrm{Lt}}}{\sigma_\varepsilon} \right) \frac{\partial \varepsilon_{\mathrm{L}}}{\partial x_i} \right] \\ - C_{\varepsilon 1} \gamma \beta_{\mathrm{L}} \frac{\varepsilon_{\mathrm{L}}}{k_{\mathrm{L}}} \mu_{\mathrm{Lt}} \left(\frac{\partial U_{\mathrm{L}j}}{\partial x_i} + \frac{\partial U_{\mathrm{L}i}}{\partial x_j} \right) \frac{\partial U_{\mathrm{L}j}}{\partial x_i} - C_{\varepsilon 2} \gamma \beta_{\mathrm{L}} \rho_{\mathrm{L}} \frac{\varepsilon_{\mathrm{L}}^2}{k_{\mathrm{L}}} \end{aligned} \tag{A1.13a}$$

The model constants are $c_\mu = 0.09$, $\sigma_k = 1.0$, $\sigma_\varepsilon = 1.3$, $C_{1\varepsilon} = 1.44$, $C_{2\varepsilon} = 1.92$.

The boundary conditions and the evaluation of source terms are the same as given in Sects. 2.1.2.2 and 2.1.2.3.

Simulated result and verification

The simulated C_6 concentrations profile of the whole column at different F factor is shown in Fig. 2.36. In comparison with Fig. 2.22 simulated by using two-equation model, the concentration in the main flow area is almost the same but in the near wall region is somewhat difference. The volume average axial concentration distribution is given in Fig. 2.37, in which the simulated curve is seen to be in agreement with the experimental data.

Reynolds mass flux

The fluctuating mass flux (negative Reynolds mass flux) in axial and radial directions and their sum are given in Figs. 2.38 and 2.39.

In the distillation column tray, the species concentration is decreasing from inlet to the outlet weir, i.e., under negative gradient. The positive $\overline{u'_x c'}$ means that the diffusion of turbulent mass flux $\overline{u'_x c'}$ is consistent with the bulk mass flow and promotes the mass transfer in x direction.

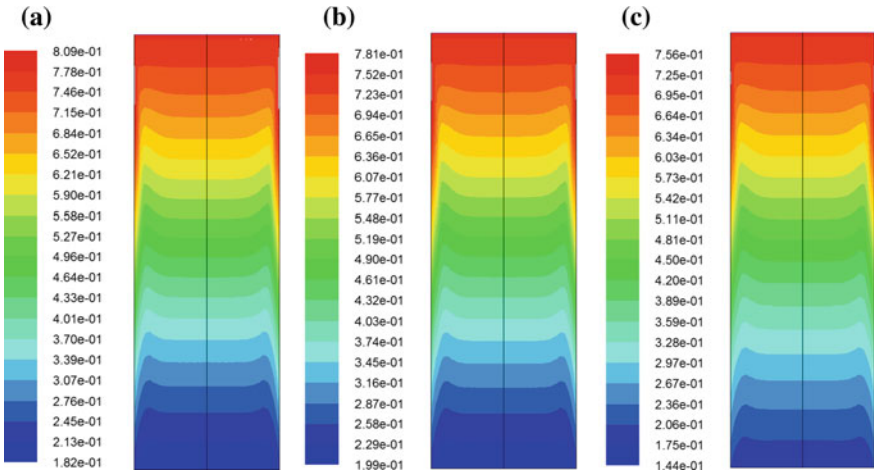

Fig. 2.36 Concentration profile of C_6 by standard Reynolds mass flux model, **a** F = 0.758 m s^{-1} (kg m^3)$^{0.5}$, **b** F = 1.02 m s^{-1} (kg m^3)$^{0.5}$, **c** F = 1.52 m s^{-1} (kg m^3)$^{0.5}$ [15]

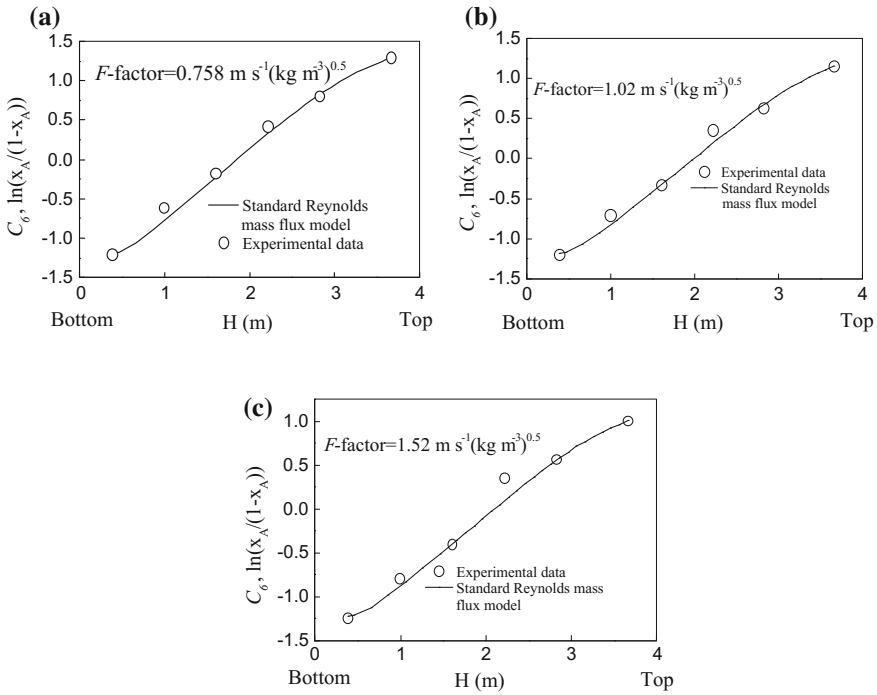

Fig. 2.37 Average C_6 concentration along column height at different F factors [15]

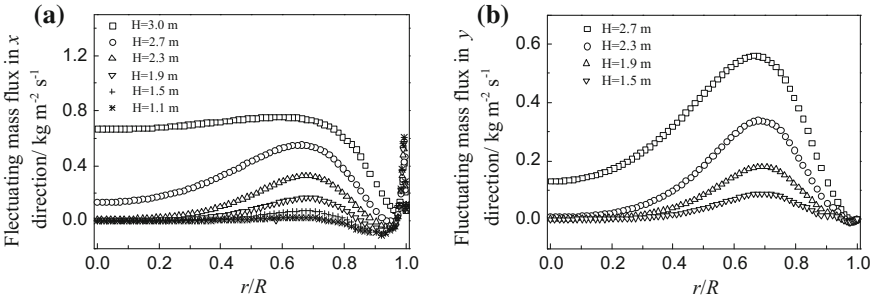

Fig. 2.38 Simulated fluctuating mass flux in Axial (x) and radial (y) directions at different bed height H **a** $\overline{u'_x c'}$, **b** $\overline{u'_y c'}$ [15]

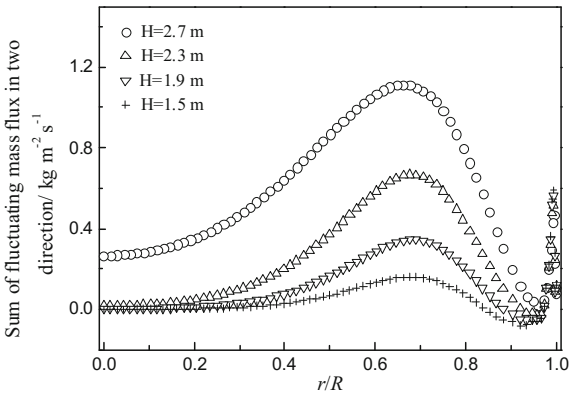

Fig. 2.39 Profiles of $\overline{u'_x c'} + \overline{u'_y c'}$ at different packed height H (*H is measured from column bottom*) [15]

As seen in Fig. 2.38a, most of the $\overline{u'_{Li} c'}$ gradient in y (radial) directions is almost zero around the column centerline ($r/R = 0$) of the lower part of the column ($H < 1.9$ m) indicating only molecular diffusion is existed. At the upper part of the column ($H > 2.3$ m), $\overline{u'_x c'}$ contour is increasing from $r/R = 0$ to about $r/R = 0.7$, indicating the turbulent diffusion $\overline{u'_x c'}$ is promoted with increasing rate (see Sect. 3.5.2.4). Afterward, from $r/R = 0.7$, the slope is turning to negative, which means the diffusion rate is decreasing until about $r/R = 0.95$. Thus, the diffusion of $\overline{u'_x c'}$ in radial direction displies wavy changes and follows the pattern of decreasing → increasing → decreasing → increasing sharply → decreasing sharply near the column wall.

In Fig. 2.38b, the $\overline{u'_y c'}$ contours behave similar to the $\overline{u'_x c'}$ indicating the radial $\overline{u'_y c'}$ diffusion is variating with the pattern of decreasing → increasing → decreasing sharply to the column wall.

As seen in Fig. 2.39, the overall tendency of $\overline{u'_{Li} c'}$ (equal to $\overline{u'_x c'} + \overline{u'_y c'}$) is similar to both $\overline{u'_x c'}$ and $\overline{u'_y c'}$. It is noted that $\overline{u'_x c'}$ is much greater than $\overline{u'_y c'}$ in this case, that means the $\overline{u'_{Li} c'}$ diffusion is dominated by $\overline{u'_x c'}$.

It should be noted that the radial variation in concentration is small and may not be seen clearly in the concentration profile of the whole column. However, the detailed information about the mass transfer, which can be obtained by using Rayleigh mass flux model, is helpful to the column design and the evaluation of process efficiency.

2.2.2.2 Hybrid Reynolds Mass Flux Model

The model equations are the same as the standard Reynolds mass flux model except that the calculation of $\overline{u'_{\mathrm{L},i}u'_{\mathrm{L},j}}$ is by Eq. (A1.8) instead of Eq. (A1.23).

Simulated result and verification

The simulated C_6 concentration profile of whole column is shown in Fig. 2.40, which is almost identical with Fig. 2.36.

The simulated radial averaged axial concentration distribution is compared with experimental data and the simulated result by using standard Reynolds mass flux model as shown in Fig. 2.41. These figures display no substantial different between hybrid and standard Reynolds mass flux models.

The comparison of simulated result on radial averaged axial concentration between hybrid Reynolds mass flux model and two-equation model is given in Fig. 2.42. As seen from the figures, both show close to the experimental data and the one better than the other only in upper or lower part of the column.

The simulated HETP by hybrid Reynolds model is compared with that by two-equation model as shown in Fig. 2.43. The prediction by hybrid Reynolds model is better than two-equation model for low and high F factors but not in the intermediate range.

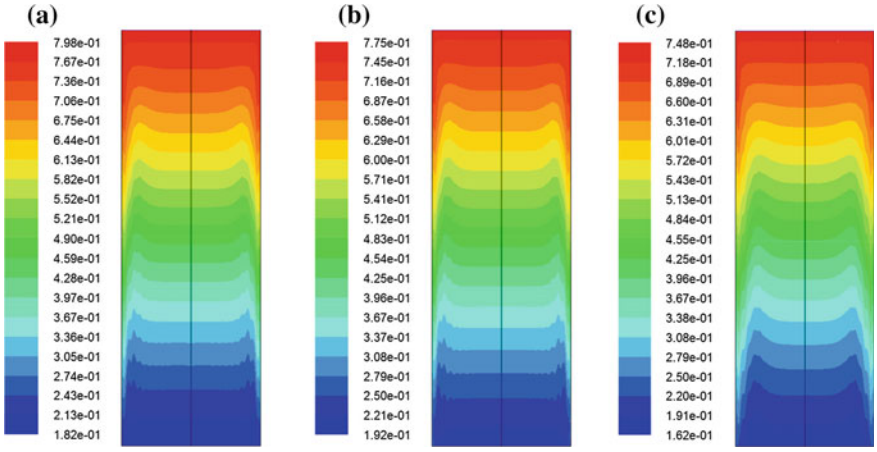

Fig. 2.40 Concentration profiles by hybrid Reynolds mass flux model **a** $F = 0.758$ m s^{-1} (kg m^{-3})$^{0.5}$, **b** $F = 1.02$ m s^{-1} (kg m^{-3})$^{0.5}$, **c** $F = 1.52$ m s^{-1} (kg m^{-3})$^{0.5}$ (reprinted from Ref. [8], Copyright 2011, with permission from Elsevier)

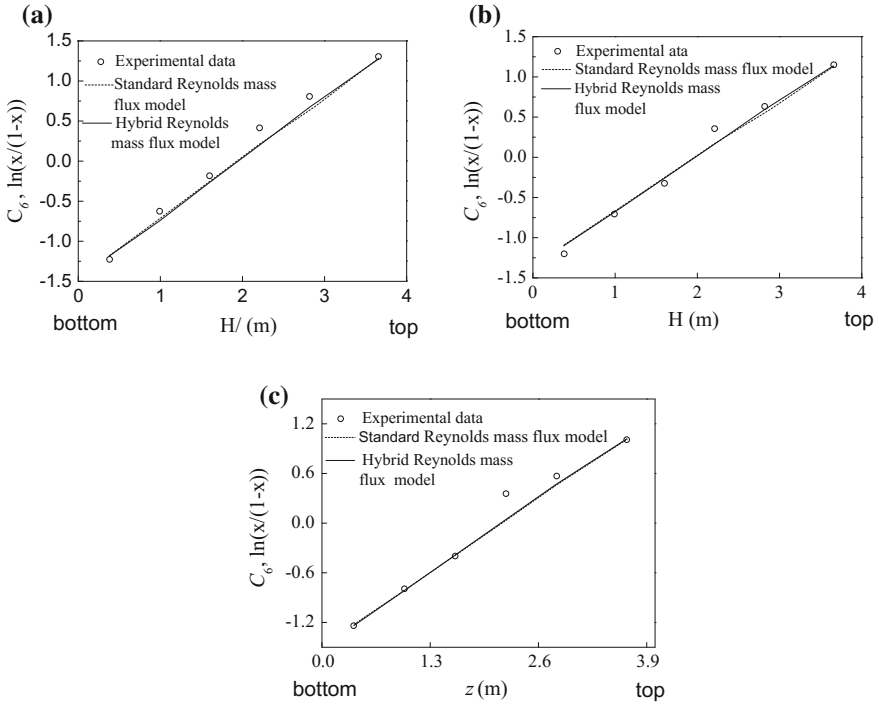

Fig. 2.41 Comparison between standard and hybrid Reynolds mass flux models with experimental data [15] **a** F = 0.758 m s^{-1} (kg m^3)$^{0.5}$, **b** F = 1.02 m s^{-1} (kg m^3)$^{0.5}$, **c** F = 1.52 m s^{-1} (kg m^3)$^{0.5}$

2.2.2.3 Algebraic Reynolds Mass Flux Model

The model equations are the same as the standard Reynolds mass flux except $\overline{u'_{\mathrm{L}i}u'_{\mathrm{L}j}}$ and $\overline{u'_{\mathrm{L}i}c'}$ equations are changed to the following algebraic form:

$$\overline{u'_{\mathrm{L}i}u'_{\mathrm{L}j}} = -\frac{k}{C_1\varepsilon}\left(\overline{u'_{\mathrm{L}j}u'_{\mathrm{L}k}}\frac{\partial U_{\mathrm{L}j}}{\partial x_k}+\overline{u'_{\mathrm{L}j}u'_{\mathrm{L}k}}\frac{\partial U_{\mathrm{L}i}}{\partial x_k}\right) - \frac{k_{\mathrm{L}}C_2}{C_1\varepsilon_{\mathrm{L}}}\left(\overline{u'_{\mathrm{L}i}u'_{\mathrm{L}k}}\frac{\partial U_{\mathrm{L}j}}{\partial x_k}+\overline{u'_{\mathrm{L}j}u'_{\mathrm{L}k}}\frac{\partial U_i}{\partial x_k}-\frac{2}{3}\overline{u'_{\mathrm{L}i}u'_{\mathrm{L}k}}\frac{\partial U_{\mathrm{L}i}}{\partial x_k}\delta_{ij}\right)+\frac{2}{3}\frac{1}{C_1}k_{\mathrm{L}}\delta_{ij} \tag{A1.24}$$

where C_k = 0.09, C_1 = 2.3, C_2 = 0.4

$$\overline{u'_{\mathrm{L}i}c'} = -\frac{k}{C_{c2}\varepsilon}\left(\overline{u'_{\mathrm{L}i}u'_{\mathrm{L}j}}\frac{\partial C}{\partial x_j}+\overline{u'_{\mathrm{L}i}c'}\frac{\partial U_{\mathrm{L}i}}{\partial x_j}\right)+\frac{C_{c3}k_{\mathrm{L}}}{C_{c2}\varepsilon_{\mathrm{L}}}\overline{u'_{\mathrm{L}i}c'}\frac{\partial U_{\mathrm{L}i}}{\partial x_j} \tag{1.27}$$

where C_2 = 3.2, C_3 = 0.55.

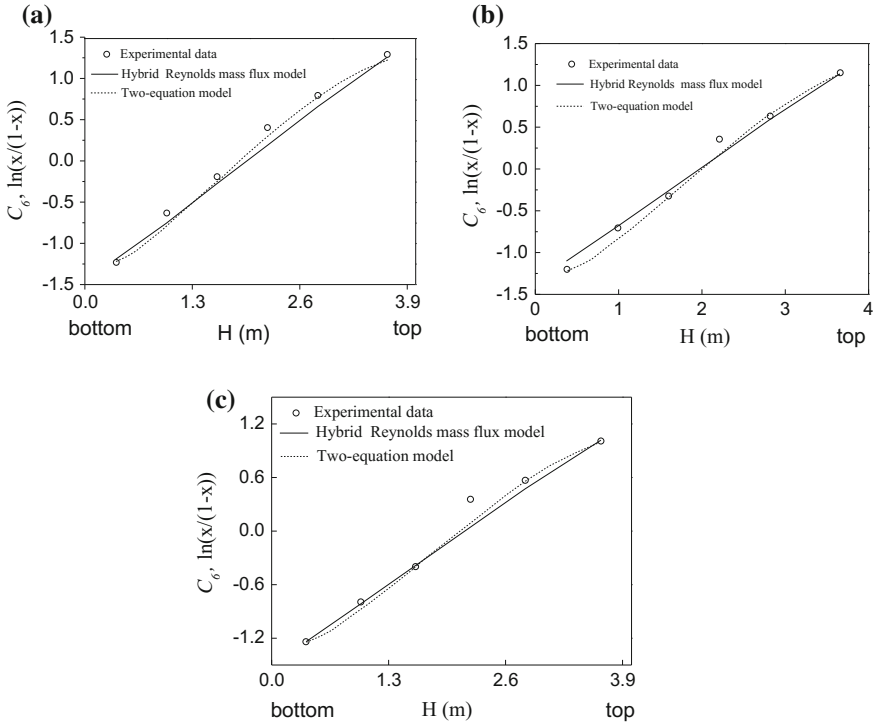

Fig. 2.42 Comparison of hybrid Reynolds model and two-equation model with experimental data **a** $F = 0.758$ m s^{-1} (kg m^{-3}), **b** $F = 1.02$ m s^{-1} (kg m^{-3}), **c** $F = 1.52$ m s^{-1} (kg m^{-3}) (reprinted from Ref. [8], Copyright 2011, with permission from Elsevier)

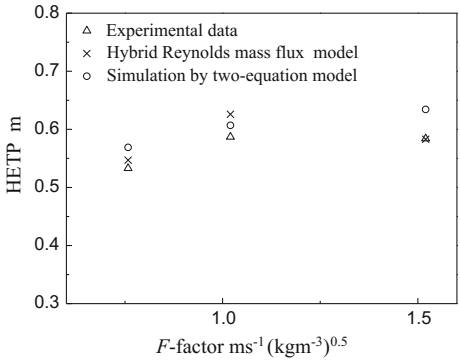

Fig. 2.43 HETP by hybrid Reynolds mass flux model and two-equation model (reprinted from Ref. [8], Copyright 2011, with permission from Elsevier)

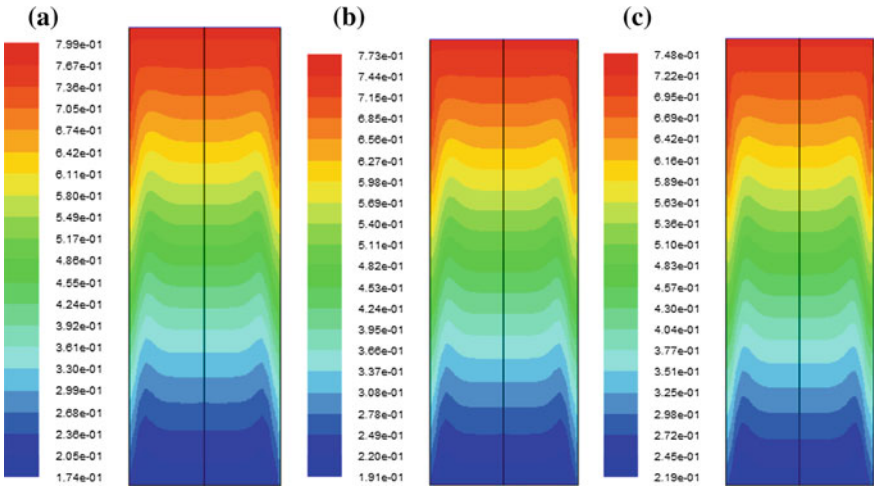

Fig. 2.44 Concentration profiles by using algebraic Reynolds mass flux model **a** $F = 0.758$ m s^{-1} (kg m^3)$^{0.5}$, **b** $F = 1.02$ m s^{-1} (kg m^3)$^{0.5}$, **c** $F = 1.52$ m s^{-1} (kg m^3)$^{0.5}$ [15]

The simulated C_6 concentration profiles of the whole column are shown in Fig. 2.44, which is substantially identical with Fig. 2.40 by hybrid Reynolds mass flux model simulation.

The verification of algebraic Reynolds mass flux model as well as the comparison with hybrid model is shown in Fig. 2.45. At low F factor, these two models are in agreement with experiment, but at high F factor the algebraic Reynolds mass flux model shows greater deviation from the experimental data.

2.3 Separation of Benzene and Thiophene by Extractive Distillation

Extractive distillation is frequently employed for the separation of mixture with close boiling point. It features by adding an extractive agent to increase the relative volatility of the mixture concerned so as to make the separation easier with less number of theoretical plates or transfer unit required. Liu et al. [38] employed this process for the separation of benzene (boiling point 80.09 °C) and thiophene (boiling point 84.16 °C) in a packed column with *N*-methyl-2pyrrolidone (NMP) as the extractive agent. The flow sheet is shown schematically in Fig. 2.46.

The extractive column was 0.19 m in diameter, packed with 2 × 2 mm stainless θ rings packing. The column consisted four sections of 700, 600, 1000, 4000 mm packing, respectively, in sequence from the column top. The operating pressure was 101.325 kPa. The extractive agent, *N*-methyl-2pyrrolidone (NMP) was introduced at the column top at 2.4 ml per min. and the feed containing 90 % benzene and 10 % NMP was entered between Sects. 2.2 and 2.3 at 0.4 ml per min.

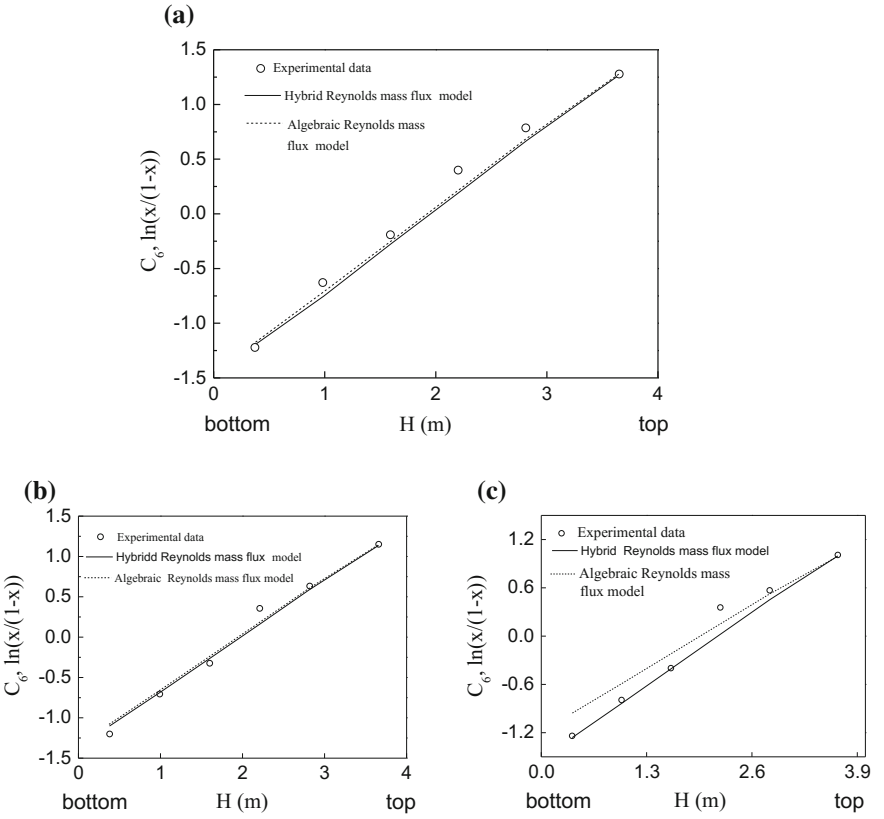

Fig. 2.45 Comparison of algebraic and hybrid Reynolds mass flux models with experimental data, **a** F-factor = 0.758 m s^{-1} (kg m^{-3})$^{0.5}$, **b** F-factor = 1.02 m s^{-1} (kg m^{-3})$^{0.5}$, **c** F-factor = 1.52 m s^{-1} (kg m^{-3})$^{0.5}$ [15]

The operating reflux ratio was 20:1 where about 99 % benzene was drawn as top product at 0.4 ml per min. and the bottom product was about 5 % thiophene.

Model equations

The model equations and boundary conditions are the same as given in Sect. 2.1.1.1 except the source terms should be revaluated.

(1) The source term S_m

Since the molecular weight of benzene (78) is close to that of thiophene (84), the mass transfer in distillation do not change substantially the amount of liquid phase in the process, we may let

$$S_m = 0$$

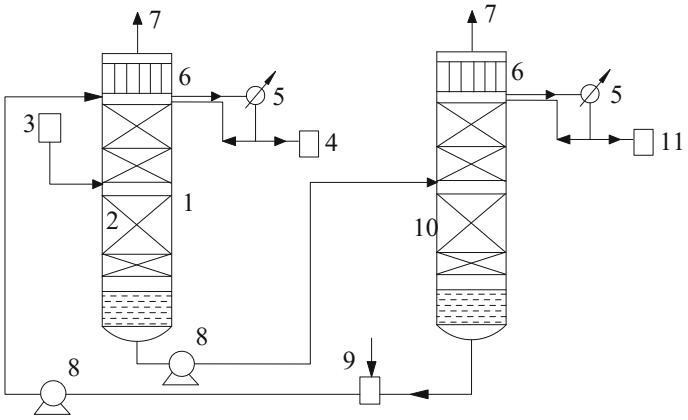

Fig. 2.46 Experimental installation of extractive distillation (*1* extractive distillation column, *2* packing, *3* feed tank, *4* product tank, *5* condenser, *6* partial condenser, *7* vent, *8* pump, *9* extractive agent tank, *10* extractive agent recovery column, *11* recovered extractive agent tank) (reprinted from Ref. [15], Copyright 2011, with permission from CIESC)

(2) Source term S_n

The rate of mass transfer for benzene can be calculated by the following equations:

$$S_{n,\mathrm{B}} = k_{\mathrm{L}} a_{\mathrm{eff}} M_{\mathrm{B}} X\left(x_{\mathrm{B}} - x_{\mathrm{B},i}\right)$$
$$S_{n,\mathrm{B}} = k_{\mathrm{G}} a_{\mathrm{eff}} M_{\mathrm{B}} Y\left(y_{\mathrm{B},i} - y_{\mathrm{B}}\right),$$

where subscripts B refers to benzene and i refers to interface; M_{B} is kg per mole of benzene; X and Y is the total moles of mixture in liquid and vapor phase, respectively; x and y are the mole fractions; the interfacial $x_{\mathrm{B},i}$ and $y_{\mathrm{B},i}$ are in equilibrium obeying the relationship at constant relative volatility α_{re}:

$$y_{\mathrm{B},i} = \frac{\alpha_{\mathrm{re}} x_{\mathrm{B},i}}{1 + (\alpha_{\mathrm{re}} - 1) x_{\mathrm{B},i}}$$

Since the system concerned is nonideal, the α_{re} is calculated by thermodynamics as follows:

$$\alpha_{\mathrm{re}} = \frac{y_{\mathrm{B}}/x_{\mathrm{B}}}{y_{\mathrm{T}}/x_{\mathrm{T}}} = \frac{\gamma_{\mathrm{B}} p_{\mathrm{B}}^0}{\gamma_{\mathrm{T}} p_{\mathrm{T}}^0},$$

where γ and p^0 are, respectively, the activity coefficients and vapor pressures; subscripts B and T refer to benzene and thiophene, respectively. The vapor pressure p^0 is calculated by Antoine equation [39] as follows

$$\log_{10} p^0 = a_1 + a_2/T + a_3 \log_{10} T + a_4 T + a_5$$

The constants are given in Table 2.7.

The activity coefficients γ_A and γ_B are calculated using Wilson model [40]

$$\ln \gamma_i = 1 - \ln\left(\sum_j A_{ij} x_j\right) - \sum_j \frac{A_{ij} x_j}{\sum_k A_{jk} x_k},$$
$$\ln A_{ij} = a_{ij} + b_{ij}/T$$

where a_{ij} and b_{ij} are given in Table 2.8.

After combining foregoing equations, we yield the equation for S_n as follows:

$$m_0 S_{n,\mathrm{B}}^2 + m_1 S_{n,\mathrm{B}} + m_2 = 0, \tag{A}$$

where m_0, m_1 and m_2 are:

$$m_0 = \frac{\alpha_{\mathrm{re}} - 1}{k_{\mathrm{L}} k_{\mathrm{G}} M_{\mathrm{B}}^2 a_{\mathrm{eff}}^2 XY}$$
$$m_1 = \frac{(\alpha_{\mathrm{re}} - 1) y_{\mathrm{B}} - \alpha_{\mathrm{re}}}{k_{\mathrm{L}} a_{\mathrm{eff}} M_{\mathrm{B}} X} - \frac{(\alpha_{\mathrm{re}} - 1) x_{\mathrm{B}} + 1}{k_{\mathrm{G}} a_{\mathrm{eff}} M_{\mathrm{B}} Y}$$
$$m_2 = \alpha_{\mathrm{re}} x_{\mathrm{B}} - ((\alpha_{\mathrm{re}} - 1) x_{\mathrm{B}} + 1) y_{\mathrm{B}},$$

where the mass transfer coefficients k_{L}, k_{G} can be calculated by the correlations by Wagner et al. [34] as shown in Sect. 2.2.1.3; the effective interfacial area a_{eff} is obtained by using Onda correlation given in Sect. 2.1.1.1.

Table 2.7 Antoine constants

Material	Const.				
	a_1	a_2	a_3	a_4	a_5
Benzene	31.772	−2725.4	−8.4443	-5.3534×10^{-09}	2.7187×10^{-06}
Thiophene	36.602	−2979.4	−10.104	1.1445×10^{-09}	3.2472×10^{-06}

Table 2.8 Wilson parameters

Term	Value		
Component i	Benzene	Benzene	Thiophene
Component j	Thiophene	NMP	NMP
a_{ij}	7.0499	2.5723	0
a_{ji}	−4.6713	−2.7964	0
b_{ij}	−2452.1033	−1041.9158	−290.8908
b_{ji}	1610.3286	1002.4481	146.9923

In finding k_L and k_G, the molecular diffusivity of benzene in gas and liquid phase are calculated by the correlations given by Fuller and Perkins, respectively [41]. The viscosities of benzene and thiophene are obtained from Perry Handbook [42].

Then the source term S_n ($S_{n\mathrm{B}}$) can be calculated by solving the aforementioned equation (A).

Interacting force F_{LG} between two phases

The vapor liquid interacting force can be measured by the pressure drop Δp of the vapor through the packing. For the 2 × 2 stainless θ rings, Chang et al. [43] proposed a correlation for the Δp_w of gas flowing through wetted packing as follows

$$\frac{\Delta p_w}{Z} = 300 \times 10^{90U_{L,s}} \left(\frac{a_T}{\gamma^3}\right)^{0.3} \left(\sqrt{\rho_G U_{G,s}^2}\right)^{1.5}$$

Under the condition of no liquid flow, the Δp of gas flowing through dry packing Δp_d are

$$\frac{\Delta p_d}{Z} = 300 \left(\frac{a_T}{\gamma^3}\right)^{0.3} \left(\sqrt{\rho_G U_{G,s}^2}\right)^{1.5}$$

Thus the Δp_L due to the vapor liquid interaction can be

$$\frac{\Delta p_L}{Z} = 300 \times \left(10^{90U_{L,s}} - 1.0\right) \left(\frac{a_T}{\gamma^3}\right)^{0.3} \left(\sqrt{\rho_G U_{G,s}^2}\right)^{1.5}$$

Consequently the vapor liquid interacting force can be expressed as

$$\mathbf{F}_{LG} = \frac{\Delta p_L}{|\mathbf{U}_{slip}|} \mathbf{U}_{slip},$$

where the slip velocity $\mathbf{U}_{slip}$ is equal to the different between the average gas velocity $\mathbf{U}_G$ and liquid velocity $\mathbf{U}$:

$$\mathbf{U}_{slip} = \mathbf{U}_G - \mathbf{U}$$

Simulation results and verification

Under the reflux ratio of 20:1, the simulated concentration distribution of benzene at x = 0.2 m (measured from column top) is given in Fig. 2.47. As seen in these figures, the concentrations of benzene are gradually lowering toward the column wall due to the velocity is decreased and the boundary condition is set zero mass flux at the wall, while the concentration of NMP is increasing.

The radial concentrations of benzene were averaged at each x to obtain the average benzene concentrations along the column height as shown in Fig. 2.48.

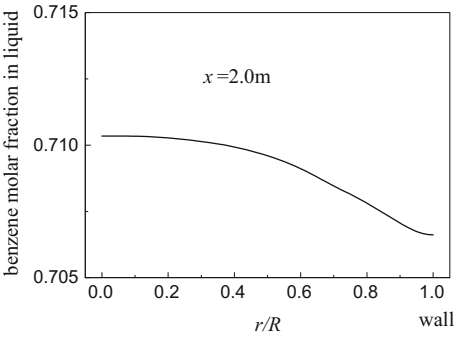

Fig. 2.47 Molar fraction of benzene in liquid phase along radial direction at x = 2.0 m (measured from column top) (reprinted from Ref. [38], Copyright 2011, with permission from CIESC)

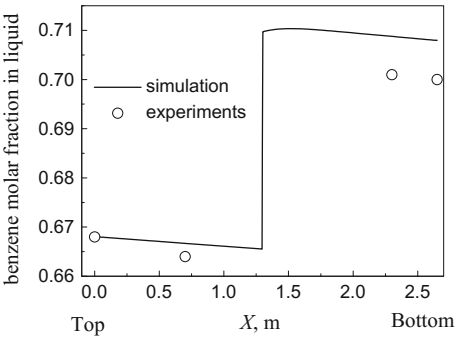

Fig. 2.48 Molar fraction of benzene in liquid phase along radial direction at x = 2.0 m (measured from column top) (reprinted from Ref. [38], Copyright 2011, with permission from CIESC)

In Fig. 2.48 the benzene concentration is suddenly increased at about x = 1.3 m due to adding the feed at this point with 90 % benzene. The simulated result is roughly in agreement with the experimental data although the former shows about half percent higher than the latter. Such discrepancy is probably due to the inaccuracy of α_{re} predicted by thermodynamic model.

2.4 Summary

The simulation of distillation process is described for tray column and packed column by using CMT models. The simulated results are presented and compared with published experimental data.

(1) Tray column. Both $\overline{c'^2} - \varepsilon_{c'}$ model and Reynolds mass flux model are used for simulating an industrial scale tray distillation column to obtain the outlet concentration of each tray and the individual tray efficiency. Both simulated results are in agreement with the experimental measurement. Precisely, only the standard Reynolds mass flux model can give the details of circulating flow contours in the segmental area of the tray. It indicates the superiority of the

anisotropic standard Reynolds mass flux model over the others. Furthermore, the prediction of tray efficiency with different tray structures by CMT model as illustrated in this chapter is helpful for selecting the optimal one by the designer. The prediction of tray efficiency for multicomponent system and the bizarre phenomena is also described.

(2) Packed column. The simulated packed column is 1.22 m in diameter and 3.66 m height packed with Pall ring. Both $\overline{c'^2} - \varepsilon_{c'}$ model and Reynolds mass flux model (including standard, hybrid and algebraic model form) give satisfactory results in comparison with published experimental data in axial concentration distribution and HETP.

References

1. Bennet DL, Agrawal R, Cook PJ (1983) New pressure drop correlation for sieve tray distillation columns. AIChE J 29:434–442
2. Sakata M, Yanagi T (1979) Performance of a commercial scale sieve tray. Inst Chem Eng Symp Ser 3(2):21–34
3. Kunesh JG, Ognisty TP, Sakata M, Chen GX (1996) Sieve tray performances for steam stripping toluene from water in a 4-ft diameter column. Ind Eng Chem Res 35:2660–2671
4. Sun ZM (2005) Study on computational mass transfer in chemical engineering. PhD dissertation, Tianjin University
5. Sun ZM, Liu BT, Yuan XG, Yu KT (2005) New turbulent model for computational mass transfer and its application to a commercial-scale distillation column. Ind Eng Chem Res 44 (12):4427–4434
6. Sun ZM, Yu KT, Yuan XG, Liu CJ (2007) A modified model of computational mass transfer for distillation column. Chem Eng Sci 62:1839–1850
7. Sun ZM, Liu CJ, Yu GC, Yuan XG (2011) Prediction of distillation column performance by computational mass transfer method. Chinese J Chem Eng 19(5):833–844
8. Li WB, Liu BT, Yu KT, Yuan XG (2011) A new model for the simulation of distillation column. Chin J Chem Eng 19(5):717–725
9. Zhang MQ, Yu KT (1994) Simulation of two dimensional liquid phase flow on a distillation tray. Chin J Chem Eng 2(1):63–71
10. AIChE Research Committee (1958) Bubble tray design manual. AIChE, New York
11. Krishna R, van Baten JM, Ellenberger J, Higler AP, Taylor R (1999) CFD simulations of sieve tray hydrodynamics. Chem Eng Res Des, Trans Inst Chem Eng Part A 77:639–646
12. Dai GC, Chen MH (1988) Fluid dynamics in chemical engineering. Chemical Industry Press, Beijing
13. Leboeuf F, Huang GP, Kulisa P et al (1991) Model and computation of discrete jets in crossflow. Eur J Mech B-fluid 10(6):629–650
14. Zuiderweg FJ (1982) Sieve tray—a view on the state of the art. Chem Eng Sci 37:1441–1464
15. Li WB (2012) Theory and application of computational mass transfer for chemical engineering processes. PhD dissertation, Tianjin University
16. Nallasamy M (1987) Turbulence models and their applications to the prediction of internal flows: a review. Comput Fluids 15(2):151–194
17. Cai TJ, Chen GX (2004) Liquid back-mixing on distillation trays. Ind Eng Chem Res 43 (10):2590–2597
18. Murphree EV (1925) Rectifying column calculations. Ind Eng Chem 17(7):747–750

19. Hausen H (1953) A definition of exchange efficiency of rectifying plates for binary and ternary mixtures. Chem Ind Tech 25:595
20. Standard G (1965) Studies on distillation-V: generalized definition of a theoretical plate or stage of contacting equipment. Chem Eng Sci 20(6):611–622
21. Holland CD, McMahon KS (1970) Comparison of vaporization efficiencies with Murphree-type efficiencies in distillation-I. Chem Eng Sci 25(3):431–436
22. Oldershaw C (1941) Perforated plate columns for analytical batch distillations. Ind Eng Chem Anal Ed 13(4):65–268
23. Kalbassi MA, Biddulph MW (1987) A modified oldershaw column for distillation efficiency measurements. Ind Eng Chem Res 26(6):1127–1132
24. Wang ZC (1997) Non-ideal multi-component mass transfer and point efficiency on a sieve tray. PhD dissertation, Tianjin University
25. Hai NT (1980) PhD dissertation, The University of New South Wales, Australia
26. Calderbank PH, Moo-Young M (1960) The mass transfer efficiency of distillation and gas absorption plate columns. Part 2. Inst Chem Eng Symp Ser 6:59
27. Geary NW, Rice RG (1991) Bubble size prediction for rigid and flexible spargers. AIChE J 37 (2):161–168
28. Hesketh RP, Fraser Russell TW, Etchells AW (1987) Bubble size in horizontal pipelines. AIChE J 33(4):663–667
29. Sharma MM, Gupta RK (1967) Mass transfer characteristics of plate columns without downcomer. Trans Inst Chem Engrs 45(1):T169–T175
30. Raper JA, Kearney MS, Burgess JM et al (1982) The structure of industrial sieve tray froths. Chem Eng Sci 37(4):501–506
31. Zaritsky NE, Calvelo A (1979) Internal mass transfer coefficient within single bubbles. Theory and experiment. Can J Chem Eng 57:58–64
32. Prado M, Fair JR (1990) Fundamental model for the prediction of sieve tray efficiency. Ind Eng Chem Res 29(6):1031–1042
33. Liu GB, Yu KT, Yuan XG, Liu CJ (2009) A numerical method for predicting the performance of a randomly packed distillation column. Int J Heat Mass Tran 52:5330–5338
34. Wagner I, Stichlmair J, Fair JR (1997) Mass transfer in beds of modern, high-efficiency random packings. Ind Eng Chem Res 36:227–237
35. Ergun S (1952) Fluid flow through packed columns. Chem Eng Prog 48:89–94
36. Engel V, Stichmair J, Geipel W (1997) A new model to predict liquid holdup in packed columns-using data based on capacitance measurement techniques. Inst Chem Eng Symp Ser 939–947
37. Stichlmair J, Bravo JL, Fair JR (1989) General model for prediction of pressure drop and capacity of countercurrent gas/liquid packed columns. Gas Separ Purif 3(3):19–28
38. Liu GB, Liu BT, Yuan XG, Zeng AW, Yu KT (2010) Computational mass transfer simulation of extractive distillation and its experimental confirmation. CIESC J 61(7):1809–1814
39. Zhang SQ (1986) Chemical engineering handbook. Shandong Science and Technology Press
40. Wilson GM (1964) Vapor-Liquid Equilibrium. XI. A new expression for the excess free energy of mixing. J Am Chem Soc 86(2):127–130
41. Poling BE, Prausnitz JM, Connell JT (2001) The properties of gases and liquids. McGraw Hill, New York
42. Perry RH, Green DW (2001) Perry's Chemical Engineers Handbook. McGraw Hill, New York
43. Chang YL, Feng QH, Kun Z (2004) Hydromechanics performance measurement and comparison of four species of mini type packings. Chin J Process Eng 4(6):496–501

Chapter 3
Application of Computational Mass Transfer (II) Chemical Absorption Process

Abstract In this chapter, the two CMT models, i.e., $\overline{c'^2}$ - $\varepsilon_{c'}$ model and Reynolds mass flux model (in standard, hybrid, and algebraic forms) are used for simulating the chemical absorption of CO_2 in packed column by using MEA, AMP, and NaOH separately and their simulated results are closely checked with the experimental data. It is noted that the radial distribution of D_t is similar to α_t but quite different from μ_t. It means that the conventional assumption on the analogy between the momentum transfer and the mass transfer in turbulent fluids is unjustified and thus the use of CMT method for simulation is necessary. In the analysis of the simulation results, some transport phenomena are interpreted in terms of the co-action or counter-action of the turbulent mass flux diffusion.

Keywords Simulation of absorption · CO_2 absorption · Turbulent mass transfer diffusivity · Concentration profile

Nomenclature

a	Surface area per unit volume of packed bed, m^{-1}
a_{eff}	Effective area for mass transfer between the gas phase and liquid phase, 1/m
a_w	Wetted surface area, m^{-1}
$\overline{c^2}$	Concentration variance, $kg^2\ m^{-6}$
$\overline{C}$	Average concentration of mass fraction, kg m^{-3}
C_μ,c_1, c_2	Model parameters in k-ε model equations, dimensionless
C_{c0},C_{c1}, C_{c2}, C_{c3}	Model parameters in $\overline{c^2}$-ε_c model equations, dimensionless
C_p	Liquid phase specific heat, J/kg/K
C_{t0},C_{t1}, C_{t2}, C_{t3}	Model parameters in $\overline{t^2}$-ε_t model equations, dimensionless
D	Molecular diffusivity, $m^2\ s^{-1}$
D_{eff}	Effective diffusivity, $m^2\ s^{-1}$
D_G	Molecular diffusivity of CO_2 in gas phase, $m^2\ s^{-1}$
D_t	Turbulent diffusivity for mass transfer, $m^2\ s^{-1}$
d_e	Equivalent diameter of random packing, m
d_H	Hydraulic diameter of random packing, m

K.-T. Yu and X. Yuan, *Introduction to Computational Mass Transfer*,
Heat and Mass Transfer, DOI 10.1007/978-981-10-2498-6_3

d_p	Nominal diameter of the packed particle, m
E	Enhancement factor, dimensionless
G	Gas phase flow rate per unit cross-section area, kg m^2 s^{-1}
H_A	Physical absorption heat of mol CO_2 absorbed, J $kmol^{-1}$
H_R	Chemical reaction heat of mol CO_2 absorbed, J $kmol^{-1}$
H_s	Static holdup, dimensionless
H_t	Total liquid holdup, dimensionless
k	Turbulent kinetic energy, m^2/s^2
k_2	Second-order reaction rate constant, m^3 kmol.s^{-1}
k_G	Gas phase mass transfer coefficient, kmol.m.s.kPa^{-1}
k_L	Liquid phase mass transfer coefficient without chemical reaction, m s^{-1}
$k_{R,L}$	liquid phase mass transfer coefficient with chemical reaction, m s^{-1}
L	Liquid flow rate per unit cross-section area, kg.m^2 s^{-1}
R	Position in radial direction, m
R_c	The rate of reaction, kmol m^3 s^{-1}
r	Radius of the column, m
$\overline{t^2}$	Temperature variance, dimensionless
T	Liquid temperature, K
U	Liquid superficial velocity, m s^{-1}
X	Molar concentration in the liquid bulk, kmol m^{-3}
X_i	Molar concentration at interface, kmol m^{-3}
x	Distance measured from column top (x = 0 at the column top), m
α,α_{eff}, α_t	Molecular, turbulent and effective thermal diffusivities, respectively, m^2 s^{-1}
β	Volume fraction of liquid phase based on pore space, dimensionless
ε	Turbulent dissipation rate, m^2 s^{-3}
ε_c	Turbulent dissipation rate of concentration fluctuation, kg^2 m^{-6} s^{-1}
ε_t	Turbulent dissipation rate of temperature fluctuation, s^{-1}
Φ	Variable, dimensionless
v_t	Turbulent diffusivity, m^2 s^{-1}
ρ	Liquid density, kg/m^3
ρ_G	Gas phase density, kg/m^3
σ	Surface tension of aqueous solutions, dynes/cm, or N/m
σ_c, σ_{ε_c}	Model parameters in $\overline{c^2}$-ε_c model equations, dimensionless
σ_t, σ_{ε_t}	Model parameters in $\overline{t^2}$-ε_t model equations, dimensionless
σ_k,σ_ε	Model parameters in k–ε model equations, dimensionless

Gas absorption is an important separation process commonly employed in chemical production. The processing gas usually is a mixture containing absorbate (component species) which is being absorbed by a liquid absorbent. If the absorbent and the absorbate undergoing chemical reaction, it is chemical absorption; otherwise it is physical absorption.

The absorption of CO_2 from flue gas is a typical chemical absorption, which has been becoming the focus of research nowadays by scientists and chemical engineers due to the environmental consideration. Many absorbents can be used for CO_2 absorption, among them the derivatives of amine are commonly used in the industries, such as monoethanolamine (MEA), 2-amino-2-methyl-1-propanol (AMP), diethanolamine (DEA), and methyldiethanolamine (MDEA). The reaction between CO_2 and the amine is reversible, and the CO_2 absorbed by amine can be easily desorbed by heating or other means to make the amine easy to be reused in a recycling process.

The operation of gas absorption is mostly counter-current that is the gas entering to the bottom of the column and the liquid flowing down from the top. There are two usual kinds of equipment for absorption: packed column and tray column. The former is most frequently used in industries and thus it will be the object of simulation in this chapter.

Chemical reaction is accompanied with heat effect and the model equation sets should involve the heat transfer besides the mass transfer and fluid flow.

Over the last decades, the application of computational fluid dynamics (CFD) to study the velocity and temperature profiles in packed column have been frequently reported [1–5]. However, for the prediction of concentration profile, the method commonly employed is by guessing an empirical turbulent Schmidt number Sc_t or using experimentally determined turbulent mass diffusivity D_t obtained using the inert tracer technique under the condition of no mass transfer [6, 7]. Nevertheless, the use of such empirical methods of computation, as pointed out in Chap. 3, is unreliable and not always possible. To overcoming these drawbacks, the development of rigorous mathematical model is the best choice.

In this chapter, the work by Liu [8, 9] and by Li [10] on the absorption of CO_2 by the aqueous solution of MEA, AMP, and NaOH is used as an example to show the prediction of absorption behaviors using computational mass transfer model, and also the model predictions are tested by comparing with the published experimental data.

3.1 $\overline{c'^2} - \varepsilon_c$ Two-Equation Model

The interacted liquid phase $\overline{c'^2} - \varepsilon_c$ two-equation model (abbreviated as two-equation model hereafter) under steady operating condition is employed for the simulation of CO_2 absorption by aqueous absorbent with the following assumptions:

(1) Only the CO_2 component in the gas phase is absorbed by the aqueous solution, and the water in aqueous absorbent does not vaporize to gas phase.
(2) The heat of absorption and heat of reaction are all absorbed instantaneously by liquid phase. The heat conduction by the packing is negligible.
(3) The heat loss to the environment is neglected.
(4) The packed column for absorption is axially symmetrical.

The model equations involve fluid dynamics, heat transfer, and mass transfer equation sets as given below.

(I) The CFD equation set

Overall mass conversation

$$\frac{\partial(\rho_{\mathrm{L}}\gamma\beta_{\mathrm{L}}U_{\mathrm{L}i})}{\partial x_i} = S_m \tag{2.1}$$

where γ is the porosity of the packed bed, β_{L} is the volume fraction of liquid in the porous space. Note that in absorption process, the mass of absorbent is changed due to the absorption of absorbate (species), therefore $S_m \neq 0$ and ρ is not a constant. The liquid faction β_{L} is considered constant in the column.

Momentum conversation

$$\frac{\partial\left(\rho_{\mathrm{L}}\gamma\beta_{\mathrm{L}}U_{\mathrm{L}i}U_{\mathrm{L}j}\right)}{\partial x_i} = -\gamma\beta_{\mathrm{L}}\frac{\partial P}{\partial x_j} + \frac{\partial}{\partial x_i}\left[\gamma\beta_{\mathrm{L}}\mu_{\mathrm{L}}\left(\frac{\partial U_{\mathrm{L}j}}{\partial x_i}\right) - \gamma\beta_{\mathrm{L}}\rho_{\mathrm{L}}\overline{u_i'u_j'}\right] + S_{\mathrm{L}i}$$

$$-\rho_{\mathrm{L}}\overline{u_i'u_j'} = \mu_t\left(\frac{\partial U_{\mathrm{L}i}}{\partial x_j} + \frac{\partial U_{\mathrm{L}j}}{\partial x_i}\right) - \frac{2}{3}\rho\delta_{ij}k_{\mathrm{L}} \tag{A1.8}$$

$$\mu_t = \rho c_\mu \frac{k_{\mathrm{L}}^2}{\varepsilon_{\mathrm{L}}}$$

k_{L} *equation*

$$\frac{\partial(\rho_{\mathrm{L}}\gamma\beta_{\mathrm{L}}U_{\mathrm{L}i}k_{\mathrm{L}})}{\partial x_i} = \frac{\partial}{\partial x_i}\left(\gamma\beta_{\mathrm{L}}\left(\mu_{\mathrm{L}} + \frac{\mu_t}{\sigma_k}\right)\frac{\partial k_{\mathrm{L}}}{\partial x_i}\right) + \rho_{\mathrm{L}}\gamma\beta_{\mathrm{L}}G_k - \rho_{\mathrm{L}}\gamma\beta_{\mathrm{L}}\varepsilon_{\mathrm{L}}$$

$$G_k = \mu_t\left(\frac{\partial U_{\mathrm{L}j}}{\partial x_i} + \frac{\partial U_{\mathrm{L}i}}{\partial x_j}\right)\frac{\partial U_{\mathrm{L}i}}{\partial x_k}$$

ε_{L} *equation*

$$\frac{\partial\rho_{\mathrm{L}}\gamma\beta_{\mathrm{L}}U_i\varepsilon_{\mathrm{L}}}{\partial x_i} = \frac{\partial}{\partial x_i}\left[\gamma\beta_{\mathrm{L}}\left(\mu + \frac{\mu_t}{\sigma_\varepsilon}\right)_{\mathrm{L}}\frac{\partial\varepsilon_{\mathrm{L}}}{\partial x_i}\right] + \gamma\beta_{\mathrm{L}}(C_{1\varepsilon}G_{\mathrm{L}k} - C_{2\varepsilon}\rho_{\mathrm{L}}\varepsilon_{\mathrm{L}})\frac{\varepsilon_{\mathrm{L}}}{k_{\mathrm{L}}}$$

Model constants are [11]: $c_\mu = 0.09$, $\sigma_k = 1.0$, $\sigma_\varepsilon = 1.3$, $C_1 = 1.44$, $C_2 = 1.92$.

(II) The heat transfer equation set

Energy conservation

$$\frac{\partial\left(\rho_{\mathrm{L}}\gamma\beta_{\mathrm{L}}C_pU_{\mathrm{L}i}T\right)}{\partial x_i} = \frac{\partial}{\partial x_i}\left(\rho_{\mathrm{L}}\gamma\beta_{\mathrm{L}}C_p(\alpha+\alpha_t)\frac{\partial T}{\partial x_i}\right) + S_T$$

where C_p is the specific heat of the fluid; S_T is the source term; α and α_t are respectively the molecular diffusivity and turbulent thermal diffusivity. The source term S_T represents heat of solution and reaction as well as other thermal effects. The unknown α_t is obtained using $\overline{T'^2} - \varepsilon_{T'}$ model, in which

$$\alpha_t = C_{T0}k\left[\frac{k}{\varepsilon}\frac{\overline{T'^2}}{\varepsilon_{T'}}\right]^{1/2}$$

$\overline{T'^2}$ equation

$$\frac{\partial\left(\rho_{\mathrm{L}}\gamma\beta_{\mathrm{L}}U_{\mathrm{L}i}\overline{T'^2}\right)}{\partial x_i} = \frac{\partial}{\partial x_i}\left[\rho_{\mathrm{L}}\gamma\beta_{\mathrm{L}}\left(\alpha+\frac{\alpha_t}{\sigma_{T'}}\right)\frac{\partial\overline{T'^2}}{\partial x}\right] - 2\rho_{\mathrm{L}}\alpha_t\left(\frac{\partial T}{\partial x_i}\right)^2 - 2\rho_{\mathrm{L}}\gamma\beta_{\mathrm{L}}\varepsilon_{T'}$$

$\varepsilon_{T'}$ equation

$$\frac{\partial(\rho_{\mathrm{L}}\gamma\beta_{\mathrm{L}}U_{\mathrm{L}i}\varepsilon_{T'})}{\partial x_i} = \frac{\partial}{\partial x_i}\left[\rho_{\mathrm{L}}\gamma\beta_{\mathrm{L}}\left(\alpha+\frac{\alpha_t}{\sigma_{\varepsilon_{T'}}}\right)\frac{\partial\varepsilon_{T'}}{\partial x_i}\right] - C_{T1}\rho_{\mathrm{L}}\alpha_t\left(\frac{\partial T}{\partial x_i}\right)^2\frac{\varepsilon_{T'}}{\overline{T'^2}} - C_{T2}\gamma\beta_{\mathrm{L}}\frac{\varepsilon_{T'}^2}{\overline{T'^2}} - C_{T3}\gamma\beta_{\mathrm{L}}\frac{\varepsilon\varepsilon_{T'}}{k}$$

Model constants are: C_{T0} = 0.10, C_{T1} = 1.8, C_{T2} = 2.2, C_{T3} = 0.8, σ_t = 1.0。

(III) The mass transfer equation set

Species mass conservation

$$\frac{\partial(\rho_{\mathrm{L}}\gamma\beta_{\mathrm{L}}U_{\mathrm{L}i}C)}{\partial x_i} = \frac{\partial}{\partial x_i}\left(\rho_{\mathrm{L}}\gamma\beta_{\mathrm{L}}(D_{\mathrm{L}}+D_t)\frac{\partial C}{\partial x_i}\right) + S_n$$

For finding turbulent mass diffusivity D_t, the $\overline{c'^2} - \varepsilon_{c'}$ two-equation model is employed.

$$D_t = c_{c0}k\left(\frac{k}{\varepsilon}\frac{\overline{c'^2}}{\varepsilon_{c'}}\right)$$

$\overline{c'^2}$ *equation*

$$\frac{\partial\left(\rho_{\mathrm{L}}\gamma\beta_{\mathrm{L}}U_{\mathrm{L}i}\overline{c'^2}\right)}{\partial x_i}=\frac{\partial}{\partial x_i}\left[\rho_{\mathrm{L}}\gamma\beta_{\mathrm{L}}\left(D_{\mathrm{L}}+\frac{D_t}{\sigma_c}\right)\frac{\partial\overline{c'^2}}{\partial x_i}\right]-2\rho_{\mathrm{L}}\gamma\beta_{\mathrm{L}}D_t\left(\frac{\partial C}{\partial x_i}\right)^2-2\rho_{\mathrm{L}}\gamma\beta_{\mathrm{L}}\varepsilon_{c'}$$

$\varepsilon_{c'}$ *equation*

$$\frac{\partial\rho_{\mathrm{L}}\gamma\beta_{\mathrm{L}}U_{\mathrm{L}i}\varepsilon_{c'}}{\partial x_i}=\frac{\partial}{\partial x_i}\left[\rho_{\mathrm{L}}\gamma\beta_{\mathrm{L}}\left(D_{\mathrm{L}}+\frac{D_t}{\sigma_{\varepsilon_{c'}}}\right)\frac{\partial\varepsilon_{c'}}{\partial x_i}\right]-C_{c1}\rho_{\mathrm{L}}\gamma\beta_{\mathrm{L}}D_t\left(\frac{\partial C}{\partial x_i}\right)^2\frac{\varepsilon_{c'}}{\overline{c'^2}}-C_{c2}\gamma\beta_{\mathrm{L}}\frac{\varepsilon_{c'}^2}{\overline{c'^2}}-C_{c3}\gamma\beta_{\mathrm{L}}\frac{\varepsilon\varepsilon_{c'}}{k}$$

Model constants are: C_{c0} = 0.11, C_{c1} = 1.8, C_{c2} = 2.2, C_{c3} = 0.8, σ_c = 1.0,

The volume fraction β_{L} of the liquid phase is based on porous space, which can be expressed by $\beta_{\mathrm{L}}=H_t/\gamma$ from the total liquid holdup H_t and the unevenly distributed porosity γ under the operating condition concerned. The total liquid holdup H_t is defined as the sum of the static holdup H_s and the operating holdup H_{op}, i.e., $H_t = H_s + H_{\mathrm{op}}$. The correlations for estimating H_s, and H_{op} for metal Pall rings are [12, 13].

$$H_s=0.033\exp\left(-0.22\frac{g\rho}{\sigma a^2}\right)$$

$$H_{\mathrm{op}}=0.555\left(\frac{a\mu^2}{g\gamma^{4.55}}\right)^{1/3}$$

The porosity γ of randomly packed bed is a constant around the center and increase to a maximum in the neighborhood of the wall region, which had been observed by many experimental investigations [14–16]. Thus the uneven porosity distribution is being considered and calculated by the following correlation reported by Liu [2]:

$$\gamma=\gamma_\infty+\frac{(1-\gamma_\infty)}{2}Er\{(1-0.3p_d)\times\cos\left(\frac{2\pi}{c_\gamma+1.6Er^2}\frac{R-r}{p_d d_p}\right)+0.3p_d\}$$

where γ_∞ is the porosity of an unbounded packing, R is the radius of the column, r is the position in radial direction, Er is the exponential decaying function as given by Wellek [17]

$$Er=\exp\left[-1.2p_d\left(\frac{R-r}{d_p}\right)^{3/4}\right]$$

where p_d is the period of oscillation normalized by the nominal particle size and $p_d = 0.94\times(2 + 1.414)/3$ for Pall rings; c_γ is a constant depending on the ratio of the particle size to column size as follows:

$$c_\gamma = \frac{2R}{n_\gamma p_d d_p} - 1.6\ \exp\left[-2.4 p_d \left(\frac{R}{d_p}\right)^{3/4}\right]$$

where

$$n_\gamma = \text{int}\left\{\frac{2}{1 + 1.6\exp\left[-2.4 p_d \left(R/d_p\right)^{3/4}\right]} \frac{R}{p_d d_p}\right\}$$

Boundary condition

Inlet (column top, $x = 0$):For fluid flow, $U = U_{\text{in}}$, $V = 0$, $T = T_{\text{in}}$, $C_i = C_{i,\text{in}}$,

$$k_{\text{in}} = 0.003 U_{\text{in}}^2$$

$$\varepsilon_{\text{in}} = 0.09 \frac{k_{\text{in}}^{1.5}}{d_H}$$

For $\overline{T'^2}$, the work by Ferchichi and Tavoularis [18] is adopted:

$$\overline{T_{\text{in}}'^2} = (0.082\Delta T)^2 = 0.0067(\Delta T)^2$$

where $\Delta T = 0.1\ K$ is set as initial value.

For $\overline{c'^2}$, the analogy to heat transfer is applied:

$$\overline{c'^2} = \left(0.082 C_{i,\text{in}}\right)^2 = 0.0067 C_{i,\text{in}}^2$$

For $\varepsilon_{c'}$ and $\varepsilon_{T'}$, it is set to be:

$$\varepsilon_{c'} = 0.4\left(\frac{\varepsilon_{\text{in}}}{k_{\text{in}}}\right)\overline{c_{\text{in}}'^2}$$

$$\varepsilon_{T'} = 0.4\left(\frac{\varepsilon_{\text{in}}}{k_{\text{in}}}\right)\overline{T_{\text{in}}'^2}$$

Outlet (column bottom): Assuming the fluid is fully developed to the turbulent state, the gradients of all parameters Φ along x direction is equal to zero except pressure:

$$\frac{\partial \Phi}{\partial x} = 0$$

Axial symmetry: At the center of the column (y = 0), symmetrical condition is set

$$\frac{\partial \Phi}{\partial y} = 0$$

Column wall(*r=R*): no-slip condition is set and all parameters equal to zero except pressure.

Near wall region: The standard wall function is applied.

3.1.1 Absorption of CO_2 by Aqueous MEA in Packed Column

3.1.1.1 Chemical Reaction Between CO_2 and Aqueous MEA

When CO_2 is being absorbed and reacts with aqueous MEA solutions, the following reactions are taking place:

$$CO_{2,g} \longrightarrow CO_{2,L} + H_A \tag{R1}$$

$$CO_{2,L} + 2BNH_2 \xrightarrow{k_2} BNHCOO^- + BNH_3^+ + H_R \tag{R2}$$

$$CO_{2,L} + BNHCOO^- + 2H_2O \xrightarrow{k_2} BNH_3^+ + 2HCO_3^- \tag{R3}$$

Letter B denotes the group $HOCH_2$–CH_2^-, step (R1) represents the physical absorption of CO_2 by water, accompanied by the heat of solution H_A. At very short time of exposure in industrial practice, the effect of reaction (R3) can be neglected, and only reaction (R2) affects the absorption rate of CO_2. Reaction (R2) can be resolved to two steps

$$CO_{2,L} + BNH_2^- \longrightarrow BNHCOO^- + H^+ \tag{R4}$$

$$BNH_2 + H^+ \longrightarrow BNH_3^+ \tag{R5}$$

Reaction (R4) can be considered as second order, which is the rate controlling step, because reaction (R5) is a proton transfer reaction and virtually instantaneous. Therefore, the absorption of CO_2 in MEA solutions can be regarded as gas absorption accompanied by a second-order reaction, and the overall reaction is

represented by reaction (R2). The rate of reaction R_c can be expressed by the following equation:

$$R_c = k_2 \, [\mathrm{CO_2}] \, [\mathrm{MEA}]$$

where k_2 is the second-order reaction rate constant, which is given by Hikita et al. [19]

$$\log k_2 = 10.99 - \frac{2152}{T}$$

3.1.1.2 Evaluation of Source Terms

The source term F_{LS} and F_{LG} in S_{Li} as well as β_L has been given in Sect. 2.2.1.

The source term S_m (Kg m^{-3} s^{-1}) represents the rate of CO_2 absorbed by the liquid phase, which can be calculated by the following mass transfer equation:

$$S_m = k_L a_e E \left(C^*_{CO_2} - C_{CO_2} \right)$$

where k_L is the liquid phase mass transfer film coefficient (m^2 s^{-1}); a_e is the effective mass transfer area per unit volume (m^2 m^{-3}); E is the enhancement factor due to accompany with chemical reaction; $C^*_{CO_2}$ and C_{CO_2} are respectively the concentration of CO_2 in the interface and bulk liquid (kg m^{-3}). Enhancement factor E can be calculated by the correlation [17]

$$E = 1 + \left[\frac{1}{(E_i - 1)^{-1.35} + (E_1 - 1)^{-1.35}} \right]^{1/1.35}$$

$$E_i = 1 + \frac{D_{MEA,L} X_{MEA}}{2 D_{CO_2,L} X_{i,CO_2}}$$

$$Ha = \frac{D_{CO_2,L} k_2 X_{MEA}}{(k_L)^2}$$

$$E_1 = \frac{\sqrt{Ha}}{\tanh \sqrt{Ha}}$$

where X_{MEA} is the mole fraction of MEA in liquid phase (kmol m^{-3}); $D_{MEA,L}$ is the molecular diffusivity of MEA; k_2 is the second-order reaction rate constant; k_L is the liquid phase mass transfer coefficient without chemical reaction (m^2 s^{-1}).

The k_L and a_e can be obtained by the following correlation [20]:

$$k_L = 0.0051\left(\frac{\mu g}{\rho}\right)^{1/3}\left(\frac{L}{a_w\mu_L}\right)^{2/3}\left(\frac{\mu_L}{\rho D_{CO_2,L}}\right)^{-1/2}(ad_p)^{0.4}$$

$$\frac{a_w}{a} = 1 - \exp\left\{-1.45\left(\frac{\sigma_{ct}}{\sigma}\right)^{0.75}\left(\frac{L}{a\mu_L}\right)^{0.1}\left(\frac{L^2a}{\rho^2 g}\right)^{-0.05}\left(\frac{L^2}{\rho a\sigma}\right)^{0.2}\right\}$$

where a and a_w are respectively the dry and wet surface area of packing per unit bed volume (m^2/m^3); and a_e is considered equal to a_w. The calculation of the parameters in foregoing equations is given in Ref. [8].

The source term S_n represents the rate of MEA consumed due to reacting with CO_2, which can be obtained from the rate of CO_2 absorbed S_m and reaction (2) by stoichiometric calculation as follows:

$$S_n = -\frac{S_m}{44} \times 61 \times 2$$

The source term S_T represents the heat generated by absorption H_A and by reaction H_R, which can be calculated by

$$S_T = \frac{S_m}{M_{CO_2}}(H_A + H_R)$$

where M_{CO_2} (kg mol^{-1}) is the molar mass of CO_2; H_A is the heat of physical absorption, H_A = 1.9924×10^7 (J $kmol^{-1}$ CO_2 absorbed) [21], and H_R is the heat of chemical reaction, H_R = 8.4443×10^7 (J $kmol^{-1}$ CO_2 reacted) [22].

3.1.1.3 Simulated Results and Verification

(I) Industrial column

The object of simulation is an industrial absorber of 1.9 m in diameter packed with 2″ Pall rings and 14.1 m in packing height for removing CO_2 from natural gas using aqueous MEA solutions. Fifteen runs of experimental data of the absorption column reported by Pintola [23] are the concentration and temperature at the top and bottom of the column.

Axial and radial concentration and temperature distributions along the column

Liu employed two-equation model for simulating [8] the axial and radial concentration as well as the temperature profiles as shown in Fig. 3.1 including gas phase CO_2 concentration, CO_2 absorbed (CO_2 loading) in MEA, liquid phase temperature, and free MEA concentration. As seen in this figure, the absorption is taken place mainly at the bottom of the tower.

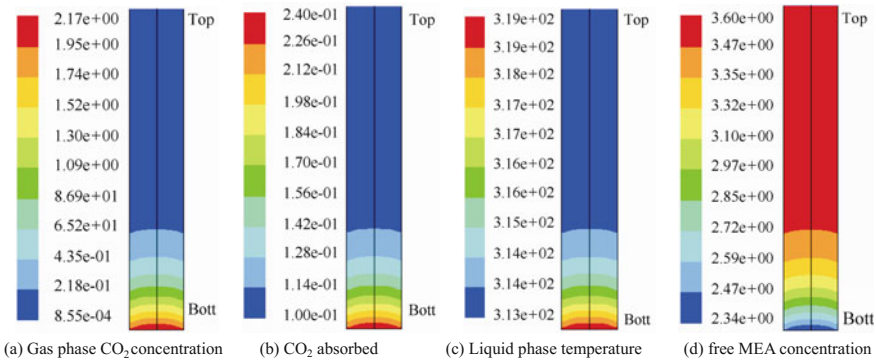

Fig. 3.1 Simulated profiles for Run 115 by two-equation model **a** gas phase CO_2 concentration, **b** CO_2 absorbed, **c** liquid phase temperature, **d** free MEA concentration (reprinted from ref [8], Copyright 2006, with permission from Elsevier)

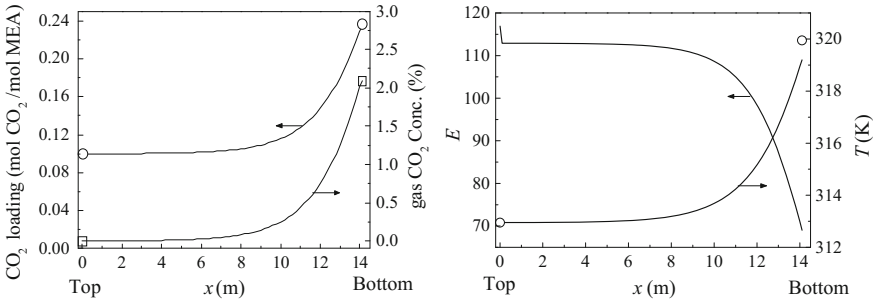

Fig. 3.2 Simulation by two-equation model (*solid curve*) and experimental data (*circle and square*) for Run T115 by two-equation model (*x is measured from column top*) (reprinted from ref [8], Copyright 2006, with permission from Elsevier)

The distribution of simulated average axial MEA concentration along the column is shown in Fig. 3.2. As seen in the figure, the simulated top and bottom concentrations

using two-equation model are closely checked by the experimental measurement.

Axial distribution of turbulent diffusivities D_t, α_t ***and*** v_t

The use of present two-equation model enables to find the distribution of diffusivities D_t, α_t and v_t in the whole column as shown in Fig. 3.3 and their average at different height of the column is given in Fig. 3.4.

As shown in the figure, both D_t and α_t are found to be almost constant around the center region of the packed bed until about $r/R = 0.8$, and suddenly increased to a maximum, then decreased sharply toward the wall surface. Such simulated phenomenon is consistent with the experimental results using inert tracer technique.

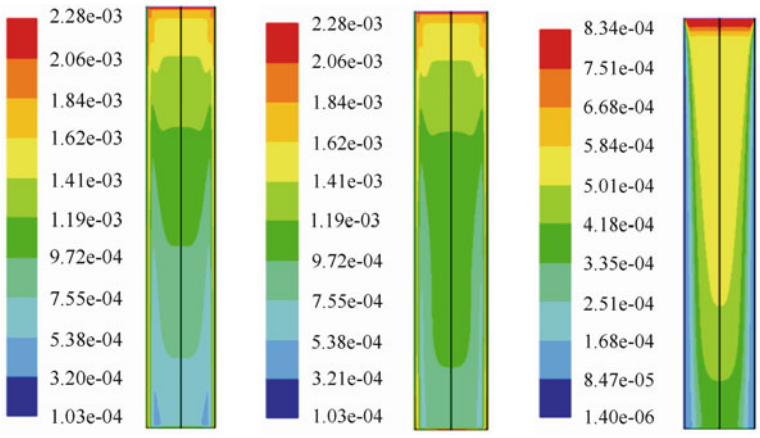

(a) D_t (b) α_t (c) v_t

Fig. 3.3 Simulated diffusivities distributions for Run T115 by two-equation model [10] **a** D_t, **b** α_t, **c** v_t, (**a**) D_t, (**b**) α_t, (**c**) v_t

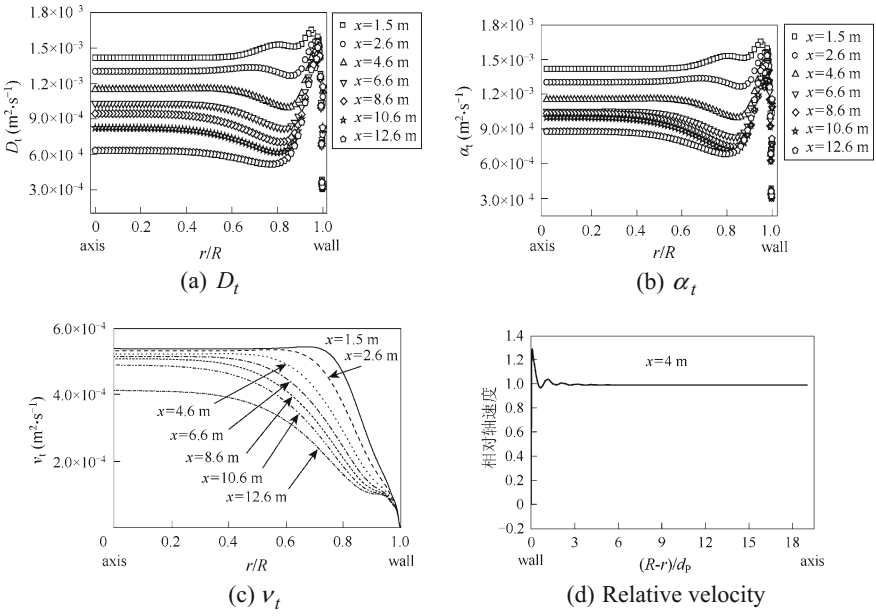

x – distance measured from column top

Fig. 3.4 Simulated diffusivities and relative radial liquid velocity at different column height for Run T115 by two-equation model (*x is measured from column top*) **a** D_t, **b** α_t, **c** v_t, **d** relative velocity (reprinted from ref [8]. Copyright 2006, with permission from Elsevier), (**a**) D_t, (**b**) α_t, (**c**) v_t, (**d**) relative velocity. x—distance measured from column top

It is also clearly seen that the shape of the v_t curve is not similar to that of D_t and α_t throughout the column, that means the similarity between D_t or α_t and v_t is not justified, thus the Schmidt number $\left(Sc = \frac{v}{D_t}\right)$ and Prandtl number $\left(\Pr = \frac{v_t}{\alpha_t}\right)$ cannot be a constant and are varying locally with the position.

(II) **Pilot scale column**

The object of simulation is a pilot scale column reported by Tontiwachwuthikul [24] for the absorption of CO_2 from air mixture by aqueous MEA solution. The column is 0.1 m in diameter and packed with 1/2″ ceramic Berl saddles with a total packing height of 6.55 m. The column consisted of six equal height sections, and the samples were taken at the inlet and outlet of each section for analyzing the concentration. Ten sets of experimental data were reported including the variation of radial averaged carbonation reaction (CO_2 loading or CO_2 absorbed), the temperature in the liquid phase and the radial averaged CO_2 concentration in the gas phase along the column height.

The simulated average axial gas phase CO_2 concentrations and CO_2 absorbed (CO_2 loading) are compared with the experimental data as shown in Fig. 3.5, in which agreement between them is seen. The simulated distribution of diffusivities D_t, α_t and v_t are given in Figs. 3.6.

Again from Fig. 3.6, the similarity between D_t and α_t and dissimilarity with v_t are also clearly seen. The sharp decrease of all diffusivities at about r/R = 0.6 is related with the velocity decreasing due to wall effect.

Axial distribution of average concentration and temperature

Take Run T 17 as an example, the simulated gas CO_2 concentration, CO_2 loading, liquid phase temperature, and the enhancement factor are shown in Fig. 3.7.

In Fig. 3.7a, it is interested to note the difference of simulated results between using the two-equation model without knowing the diffusivity in advance and using the conventional one-dimensional model with published experimental diffusivity

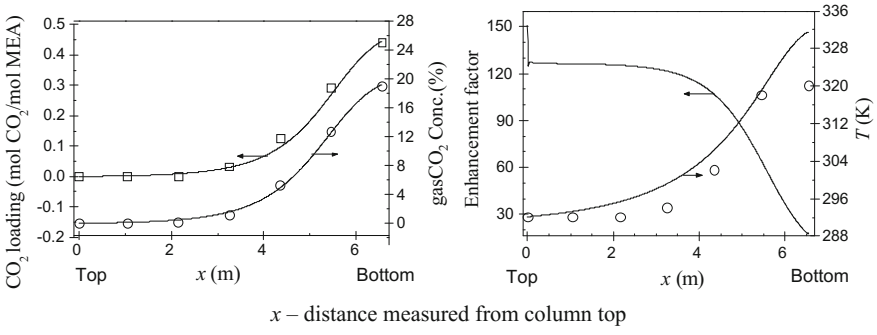

Fig. 3.5 Comparison between Simulation by two-equation model (*solid curve*) and experimental data (*circle and square*) for Run T22 (*x is measured from column top*). (reprinted from ref [8]., Copyright 2006, with permission from Elsevier). *x*—distance measured from column top

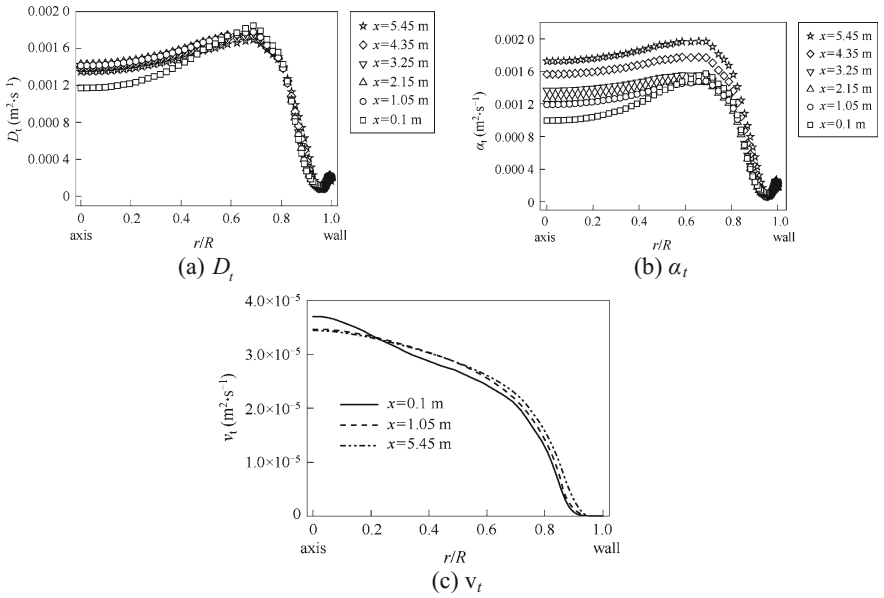

Fig. 3.6 Simulated diffusivities at different height of column by two-equation model for Run T22 (*x is measured from column top*) **a** D_t, **b** α_t, **c** v_t (reprinted from ref [8]. Copyright 2006, with permission from Elsevier). *x*—distance measured from column top

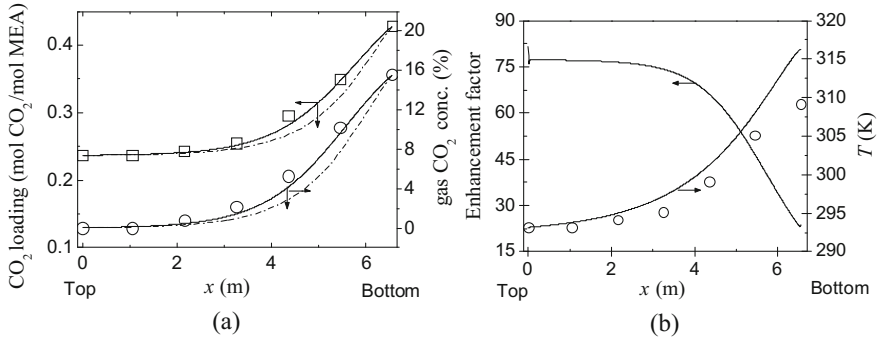

Fig. 3.7 Comparisons of experimental data, the simulation by two-equation model and by conventional model for Run T17 (*dash dot lines–one-dimensional model with mass diffusivity obtained by inert tracer technique, solid curve–Two-equation model, circle and square–experimental data*) **a** CO_2 loading, **b** enhancement factor (reprinted from ref [8]. Copyright 2006, with permission from Elsevier)

obtained by employing the inert tracer technique [12]. The simulated results by the conventional model on gas CO_2 concentration and liquid CO_2 loading profiles along the axial direction are shown in Fig. 3.7a by the dash dot lines. It should be pointed out that the column is taller than it is needed as seen in Fig. 3.1, thus the liquid phase concentration in the upper part of the column is very small and hardly distinguished the difference in the figure regardless what model is being used for simulation. However, the difference is clearly seen at the lower part of the column, in which the simulation using the two-equation model is better than the conventional.

In Fig. 3.7b, the simulated radial averaged axial temperature is somewhat higher than the experimental temperature, and deviate obviously at the bottom of the column. The error may come from (1) The cooling of outlet liquid by the incoming gas at the column bottom is neglected; (2) The heat consumed by the evaporation of water in the liquid phase is ignored; (3) The heat loss to the environment is not considered.

3.1.2 Absorption of CO_2 by Aqueous AMP in Packed Column

The advantage of using AMP as absorbent for the absorption of CO_2 is the high rate of absorption, less corrosion and low energy of recovery, also low stability of the absorbed amino product which is easy to hydrolysis to liberate free AMP.

3.1.2.1 Chemical Reaction Between AMP and CO_2

The reaction between AMP and CO_2 can be represented by the following steps with liberation of heat of solution and reaction:

$$CO_{2,G} \longrightarrow CO_{2,L} + H_A \tag{R1}$$

$$CO_{2,L} + RR'NH \longrightarrow RR'NH^+COO^- + H_R \tag{R2}$$

$$RR'NH^+COO^- + RR'NH \longrightarrow RR'NCOO^- + RR'NH_2^+ \tag{R3}$$

$$RR'NCOO^- + H_2O \longrightarrow RR'NH + HCO_3^- \tag{R4}$$

$$RR'NH + CO_2 + H_2O \longrightarrow RR'NH_2^+ + HCO_3^- \tag{R5}$$

where R and R′ denote respectively $HOCH_2C(CH_3)_2^-$ and H. The step (R3) is unstable and easily turn to step (R4) for hydrolysis. From the overall step (R5), one

mole of AMP can absorb one mole of CO_2, and the reaction can be considered as second order. The rate of chemical absorption R_c can be expressed as

$$R_c = k_2 \, [CO_2] \, [AMP]$$

where the coefficient k_2 is given by [25]

$$\ln k_2 = 23.69 - 5\ 176.49/T$$

3.1.2.2 Simulated Results and Verification

The object of simulation, a pilot scale packed column, is the same as given in Sect. 3.1.1.3 (II). Ten sets of experimental data for absorption of CO_2 by AMP aqueous solution was reported by Tontiwachwuthikul [24], in which three sets are taken as examples for comparison with present simulation.

The determination of source terms in the modeling equations is similar to Sect. 3.1.1.2 except the physical parameters should be reevaluated. Refer to Ref. [26] for details.

Distribution of average radial concentration and temperature along column height

The simulated radial averaged axial concentration and temperature of the aqueous AMP are shown by the curves in Fig. 3.8 for Run T27 and Fig. 3.9 for Run T29. In these figures the experimental points are also given for comparison. Agreement is seen between simulation and experimental measurement.

The influence of inlet boundary condition of $\overline{c'^2_{in}}$ and $\overline{T'^2_{in}}$ on the simulated result

In previous simulation the inlet boundary conditions of $\overline{c'^2_{in}}$ and $\overline{T'^2_{in}}$ are set as $\overline{c'^2} = \left(0.082 C_{i,in}\right)^2$ and $\overline{T'^2_{in}} = (0.082\Delta T)^2$. The influence of boundary condition

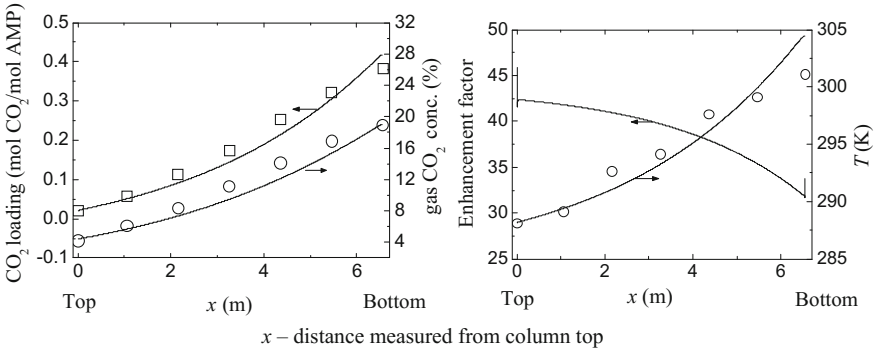

Fig. 3.8 Comparison between simulation by two-equation model (*curve*) and experimental data (*circle and square*) for Run T27 (*x is measured from column top*). *x*—distance measured from column top [26]

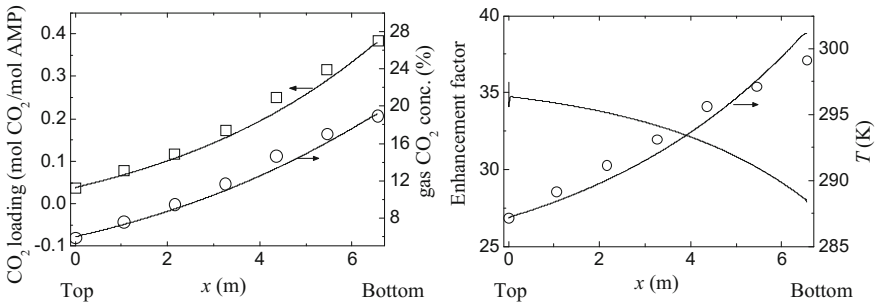

Fig. 3.9 Comparison between simulation by two-equation model (*solid line*) and experimental data (*circle and square*) for Run T29 [26]

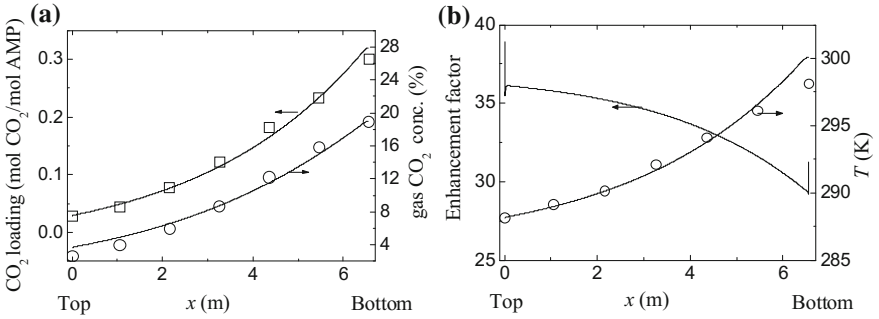

Fig. 3.10 Simulation by two-equation model (*curve*) and experimental data (*circle*) for Run T30 [26]

was investigated by changing the condition to $\overline{T_{\text{in}}'^2} = 0.003(\Delta T)^2$ and $\overline{c'^2} = 0.003C_{\text{in}}^2$. As given in Figs. 3.7, 3.8, 3.9 and 3.10, the simulated results for T30 using these two boundary settings are substantially the same and can only be represented by a unique curve. However, it is true for the example T30, the influence of boundary condition in general is yet to be further investigated.

Variation of D_t and α_t in radial directions

The turbulent mass diffusivity D_t and turbulent thermal diffusivity α_t can be obtained by present model computations as shown in Fig. 3.11. Once again it demonstrates that the choice of different boundary conditions of $\overline{c_{\text{in}}'^2}$ and $\overline{T_{\text{in}}'^2}$ do not affect substantially the simulated result in this case. Compare Fig. 3.11 with Fig. 3.6, the shape of D_t and α_t along radial direction for T30 and T22 is highly similar, even their values are very close each other.

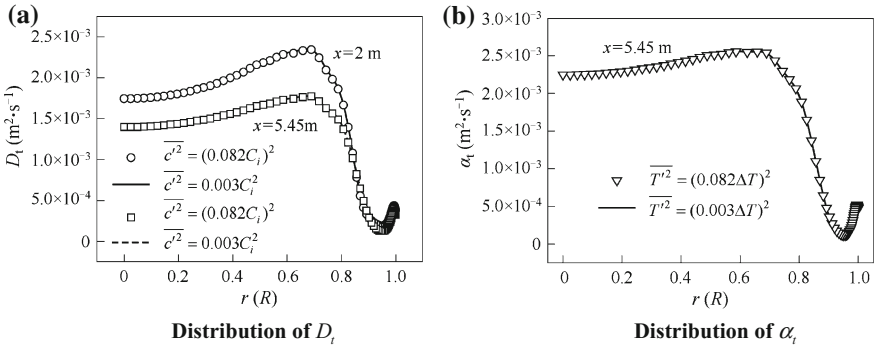

Fig. 3.11 Distribution of D_t and α_t in radial direction for Run T 30 by two-equation model at different inlet boundary conditions (*x is measured from column top*) **a** distribution of D_t, **b** distribution of α_t. *X*—distance measured from column top [26]

3.1.3 Absorption of CO_2 by Aqueous NaOH in Packed Column

3.1.3.1 Chemical Reaction Between NaOH and CO_2

The absorption of CO_2 and the reaction between CO_2 and NaOH in the aqueous solution are undertaken the following steps:

$$CO_{2,g} \xrightarrow{H_A} CO_{2,L} \tag{R1}$$

$$CO_{2,L} + OH^- \xrightarrow{H_R, k_2} HCO_3^- \tag{R2}$$

$$HCO_3^- + OH^- \longrightarrow CO_3^{2-} + H_2O \tag{R3}$$

$$CO_{2,L} + 2OH^- \longrightarrow CO_3^{2-} + H_2O \tag{R4}$$

Reaction (R1) expresses the physical absorption of CO_2 by water, accompanied with the evolution of heat of solution H_A. Reaction (R2) is known as the rate controlling step because reaction (R3) is a proton transfer reaction and is very faster than reaction (R2). Thus the absorption of CO_2 by aqueous NaOH solution can be regarded as a gas absorption accompanied with second-order reaction (R2), and the overall reaction is represented by (R4).

The second-order reaction rate constant k_2 for CO_2—NaOH reaction was correlated by Pohorecki [27] as a function of temperature and ionic strengths I_c of aqueous electrolyte solutions as follows:

$$\log k_2 = 11.895 - \frac{2382}{T} + 0.221 I_c - 0.016 I_c^2$$

The model equations are given in Sect. 3.1, the determination of source terms in the modeling equations is similar to Sect. 3.1.2 except the physical parameters should be reevaluated as given in reference [9].

3.1.3.2 Simulated Results and Verification

The object of simulation and verification is a randomly packed column reported by Tontiwachwuthikul [24]; the structure of this pilot scale column has been described in Sect. 3.1.1.3 (II). Twelve sets of experimental data for the absorption of CO_2 by NaOH were presented by the authors, among which six sets are taken to check the validity of the present simulated results.

Distributions of radial averaged concentration and temperature in the Liquid Phase along the column height

The simulated distributions of average radial OH^- concentration in liquid phase, C_{OH}^- and CO_2 concentration in gas phase as well as the temperature along the column height are shown in Figs. 3.11, 3.12, 3.13, 3.14, 3.15, 3.16 and 3.17 with experimental data for comparison.

As seen in these figures, the agreement between the simulations and experimental results for OH^- concentration in liquid phase and CO_2 concentration in gas phase is satisfactory. However, the predicted temperature profiles along the column by simulation show somewhat lower than the experimental measurement, especially near the bottom of the column. As stated in previous section, there are several

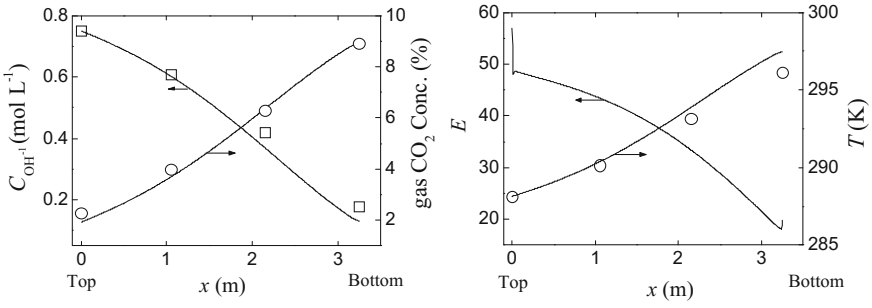

Fig. 3.12 Comparison of simulated results by two-equation model (*solid line*) with experimental data (*circle and square*) for RunT1 (reprinted from ref [9]. Copyright 2006, with permission from American Chemical Society)

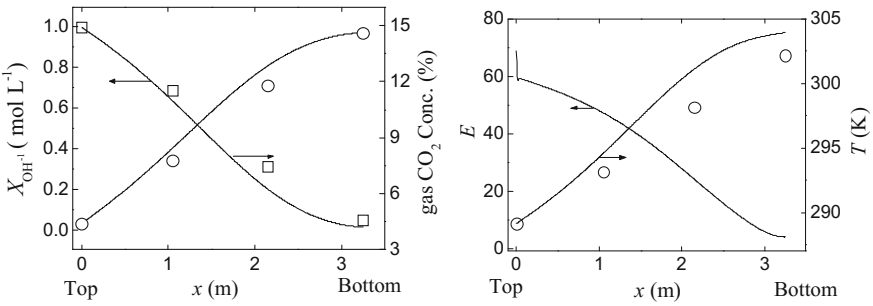

Fig. 3.13 Comparison of simulated results by two-equation model (*solid line*) with experimental data (*circle and square*) for RunT2 (reprinted from ref [9]. Copyright 2006, with permission from American Chemical Society)

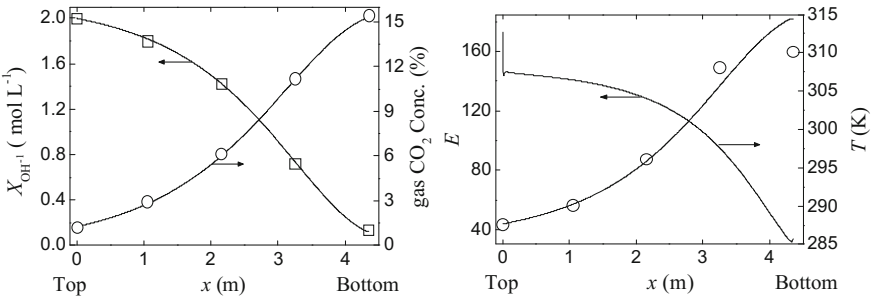

Fig. 3.14 Comparison of simulated results by two-equation model (*solid line*) with experimental data (*circle and square*) for RunT7. (reprinted from ref [9]. Copyright 2006, with permission from American Chemical Society.)

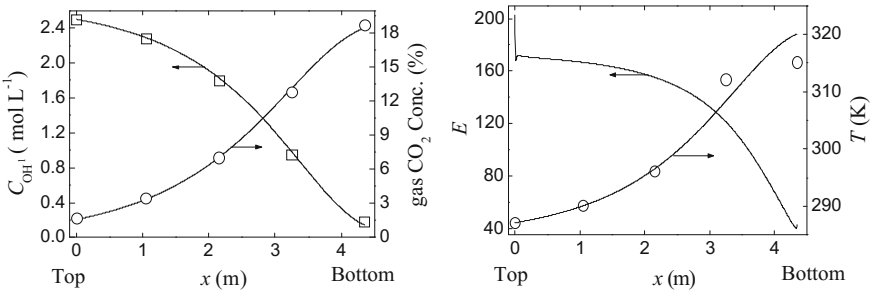

Fig. 3.15 Comparison of simulated results by two-equation model (*solid line*) with experimental data (*circle and square*) for RunT8 (reprinted from ref [9]. Copyright 2006, with permission from American Chemical Society)

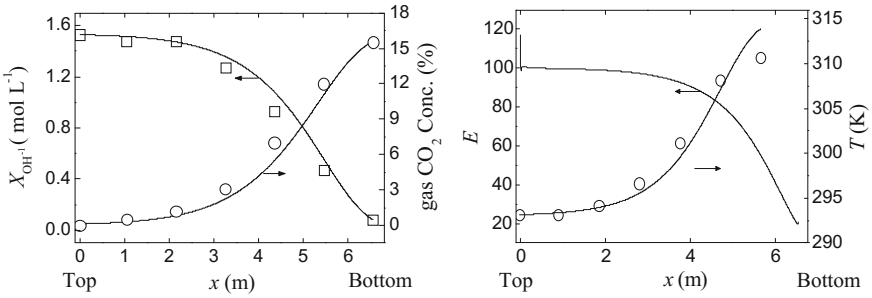

Fig. 3.16 Comparison of simulated results by two-equation model (*solid line*) with experimental data (*circle and square*) for RunT11 (reprinted from ref [9]. Copyright 2006, with permission from American Chemical Society)

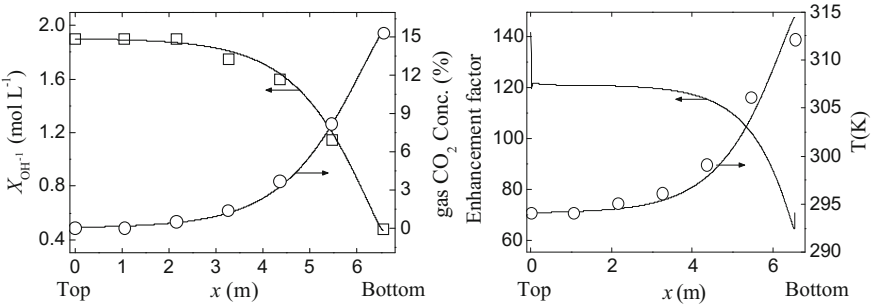

Fig. 3.17 Comparison of simulated results by two-equation model (*solid line*) with experimental data (*circle and square*) for RunT12 (reprinted from ref [9]. Copyright 2006, with permission from American Chemical Society)

reasons for such deviation: first, in the assumption, the cooling of descending liquid by the entering gas is ignored; second the evaporation of solvent water in liquid phase is neglected, leading to overestimate the liquid temperature; third, the assumption of adiabatic operation means the neglect of heat exchange between the column and environment.

Also as seen in these figures, the enhancement factor, E, increases from column bottom to the top. Take T11 as an example shown in Fig. 3.16, the enhancement factor E increases from about 20 at the column bottom to about 100 at the column top, which means the rate of chemical absorption is about 20–100 times higher than that of physical absorption.

Liquid Velocity Profile along the Radial Direction

Due to the nonuniformly distributed porosity, especially higher porosity near the wall region, the fluid flow seriously deviates from the plug flow. As seen from Fig. 3.18a and b, serious "wall flow" is appeared, and the flow becomes relatively uniform only about $2d_p$ apart from the wall. Similar result has been observed by many investigators.

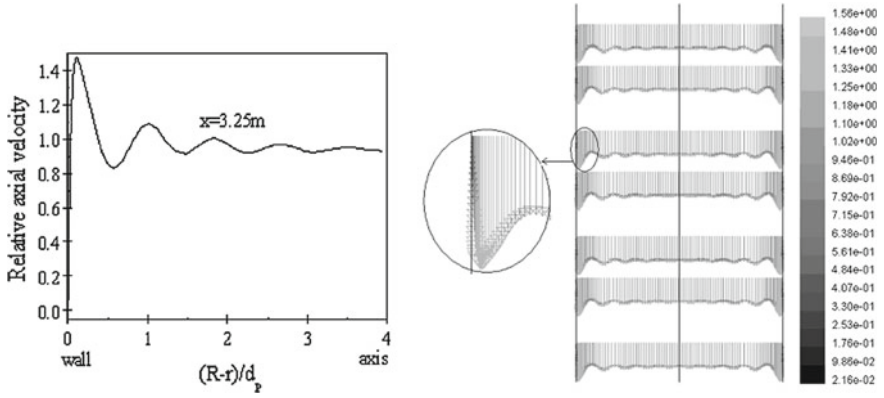

(a) Axial velocity profile **(b) Schematic distribution**

Fig. 3.18 Relative axial velocity profile two-equation model for T12 **a** axial velocity profile**, b** schematic distribution (reprinted from ref [9]. Copyright 2006, with permission from American Chemical Society)

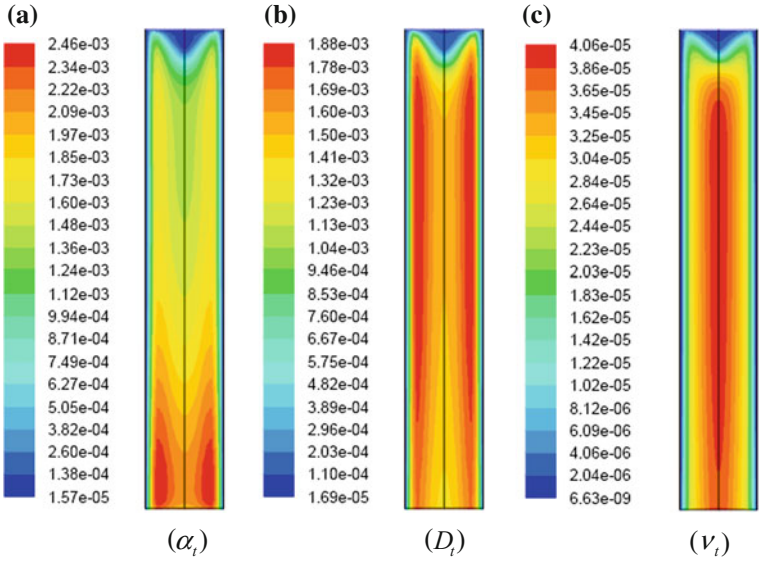

Fig. 3.19 Simulated diffusivities ($m^2.s^{-1}$) by two-equation model **a** α_t**, b** D_t**, c** v_t [26]

Distributions of D_t, α_t ***and*** v_t ***along column height***

The simulated profiles of D_t, α_t and v_t obtained along the whole column are displayed in Fig. 3.19.

The radial distributions of D_t, α_t and v_t at different height of the column are displayed in Figs. 3.20, 3.21, and 3.22. These figures show the nonuniform

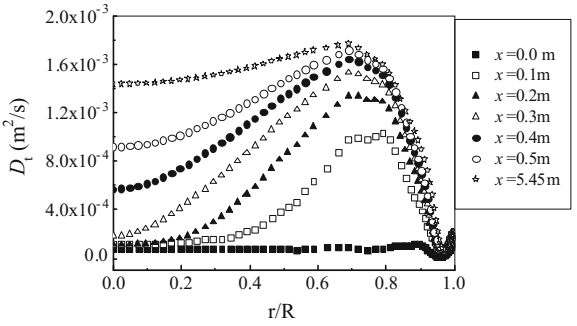

Fig. 3.20 Radial distribution of D_t at different column height for T12 (*x is measured from column top*) (reprinted from ref [9]. Copyright 2006, with permission from American Chemical Society). *x*—distance measured from column top

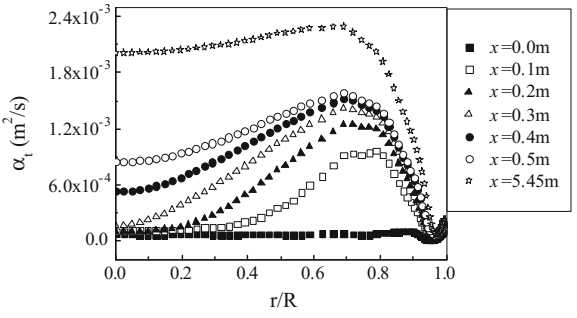

Fig. 3.21 Radial distribution of α_t at different column height for T12 (*x is measured from column top*) [21]. *x*—distance measured from column top

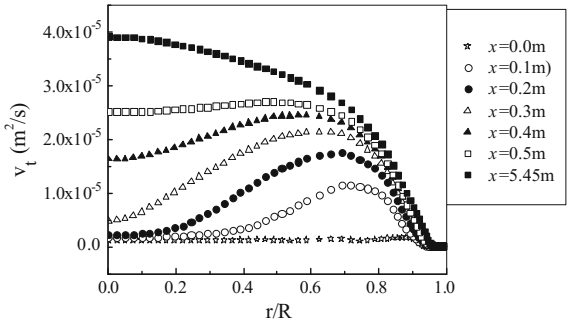

Fig. 3.22 Radial distribution of v_t at different column height for T12 (*x is measured from column top*) [26]. *x*—distance measured from column top

distribution of diffusivity and the similarity between the shape of D_t and α_t. The dissimilarity of v_t with D_t and α_t is seen obviously, which indicates once again that the Schmidt number and Prandtl number are not a constant throughout the column.

3.2 Reynolds Mass Flux Model

In this section, the standard Reynolds mass flux model (abbreviated as RMF model) is employed for simulation.

The assumptions of Reynolds mass flux model as applied to the chemical absorption column are the same as the $c'^2 - \varepsilon_{c'}$ two-equation model in 3.1.

The mathematical model in interacted liquid phase form is given below.

(I) The Mass Transfer Equation Set

Species mass conservation equation

$$\frac{\partial}{\partial x_i}(\gamma\beta_L U_{Li} C) = \frac{\partial}{\partial x_i}\left[\gamma\beta_L\left(D\frac{\partial C}{\partial x_i} - \overline{u_i'c'}\right)\right] + S_n$$

where γ is the porosity of the packed bed; β_L is the volume fraction of liquid in the vapor-liquid mixture based on pore space; $\overline{C}$ and c' are respectively the average and the fluctuated mass concentration (kg m^{-3}); D is the molecular diffusivity of absorbent in the liquid phase.

Fluctuating mass flux $\overline{u_i'c'}$ equation

$$\frac{\partial\overline{u_i'c'}}{\partial t} + \frac{\partial U_j\overline{u_i'c'}}{\partial x_j} = \frac{\partial}{\partial x_j}\left[\left(C_{c1}\frac{k}{\varepsilon}\overline{u_i'u_j'} + \frac{\mu}{\rho}\right)\frac{\partial\overline{u_i'c'}}{\partial x_j}\right] - \left(\overline{u_i'u_j'}\frac{\partial C}{\partial x_j}\right) - C_{c2}\frac{\varepsilon}{k}\overline{u_i'c'} + C_{c3}\overline{u_j'c'}\frac{\partial U_{Li}}{\partial x_j} \tag{1.26a}$$

where $C_{c1} = 0.09$, $C_{c2} = 3.2$, $C_{c3} = 0.55$; k and ε equations are given by Eq. (A1.11a) and Eq. (A1.13a), respectively.

(II) Accompanied CFD Equation Set

Overall mass conservation

$$\frac{\partial(\rho\gamma\beta_{\mathrm{L}} U_{\mathrm{L}i})}{\partial x_i} = S_m$$

Momentum conservation

$$\frac{\partial\left(\rho\gamma\beta_{\mathrm{L}} U_{\mathrm{L}i} U_{\mathrm{L}j}\right)}{\partial x_j} = -\gamma\beta_{\mathrm{L}}\frac{\partial p}{\partial x_i} + \frac{\partial}{\partial x_j}\gamma\beta_{\mathrm{L}}\left(\frac{\mu}{\rho}\frac{\partial(\rho U_{\mathrm{L}i})}{\partial x_j} - \rho\overline{u_i'u_j'}\right) + S_{\mathrm{L}F}$$

where S_F is the source term of the liquid flow, $\overline{u_i'u_j'}$ is calculated according to Eq. (1.23) as follows:

$$\frac{\partial \overline{u_i'u_j'}}{\partial t} + U_k \frac{\partial \overline{u_i'u_j'}}{\partial x_k} = \frac{\partial}{\partial x_k}\left(C_k \frac{k}{\varepsilon} \overline{u_i'u_j'} \frac{\partial \overline{u_i'u_j'}}{\partial x_k} + \frac{\mu}{\rho} \frac{\partial \overline{u_i'u_j'}}{\partial x_k} \right) - \left(\overline{u_i'u_k'} \frac{\partial U_{\mathrm{L}j}}{\partial x_k} + \overline{u_j'u_k'} \frac{\partial U_{\mathrm{L}i}}{\partial x_k} \right)$$

$$-C_1 \frac{\varepsilon}{k}\left(\overline{u_i'u_j'} - \frac{2}{3}k\delta_{ij} \right) - C_2 \left(\overline{u_i'u_k'} \frac{\partial U_{\mathrm{L}j}}{\partial x_k} + \overline{u_j'u_k'} \frac{\partial U_{\mathrm{L}i}}{\partial x_k} - \frac{2}{3}\delta_{ij} \overline{u_i'u_k'} \frac{\partial U_{\mathrm{L}i}}{\partial x_k} \right) - \frac{2}{3}\varepsilon\delta_{ij} \tag{1.23}$$

k_{L} equation

$$\frac{\partial \rho\gamma\beta_{\mathrm{L}} U_{\mathrm{L}i} k_{\mathrm{L}}}{\partial x_i} = \frac{\partial}{\partial x_i}\left[\gamma\beta_{\mathrm{L}} \left(\mu + \frac{\mu_t}{\sigma_k} \right) \frac{\partial k}{\partial x_i} \right] - \mu_t \gamma\beta_{\mathrm{L}} \left(\frac{\partial U_{\mathrm{L}i}}{\partial x_j} + \frac{\partial U_{\mathrm{L}j}}{\partial x_i} \right) \frac{\partial U_{\mathrm{L}j}}{\partial x_i} - \rho\gamma\beta_{\mathrm{L}}\varepsilon_{\mathrm{L}} \tag{1.11a}$$

ε_{L} equation

$$\frac{\partial \rho\gamma\beta_{\mathrm{L}} U_{\mathrm{L}i} \varepsilon_{\mathrm{L}}}{\partial x_i} = \frac{\partial}{\partial x_i}\left[\gamma\beta_{\mathrm{L}} \left(\mu + \frac{\mu_t}{\sigma_\varepsilon} \right) \frac{\partial \varepsilon_{\mathrm{L}}}{\partial x_i} \right] - C_{\varepsilon 1} \gamma\beta_{\mathrm{L}} \frac{\varepsilon_{\mathrm{L}}}{k} \mu_t \left(\frac{\partial U_{\mathrm{L}j}}{\partial x_i} + \frac{\partial U_{\mathrm{L}i}}{\partial x_j} \right) \frac{\partial U_{\mathrm{L}j}}{\partial x_i} - C_{\varepsilon 2} \gamma\beta_{\mathrm{L}} \rho_{\mathrm{L}} \frac{\varepsilon_{\mathrm{L}}^2}{k} \tag{A1.13a}$$

(III) Accompanied CHT Equation Set

Energy conservation

$$\frac{\partial (\rho\gamma\beta_{\mathrm{L}} c_p U_{\mathrm{L}i} T)}{\partial x_i} = \frac{\partial}{\partial x_i}\left[\rho\gamma\beta_{\mathrm{L}} c_p \left(\alpha \frac{\partial C}{\partial x_i} - \overline{u_i'T'} \right) \right] + S_T$$

where T is the average temperature of liquid phase, c_p is the specific heat of liquid phase, S_T is the thermal source term including the heat of solution, heat of reaction and others; α is the molecular thermal diffusivity.

Fluctuating heat flux $\overline{u_i'T'}$

$$\frac{\partial \overline{u_i'T'}}{\partial t} + U_i \frac{\partial \overline{u_i'T'}}{\partial x_k} = \frac{\partial}{\partial x_k}\left[\left(C_{T1}\frac{k}{\varepsilon}\overline{u_i'u_j'} + \alpha\right)\frac{\partial \overline{u_i'T'}}{\partial x_k}\right] - \left(\overline{u_i'u_k'}\frac{\partial T}{\partial x_k} + \overline{u_k'T'}\frac{\partial U_j}{\partial x_k}\right) - C_{T2}\frac{\varepsilon}{k}\overline{u_i'T'} + C_{T3}\overline{u_k'T'}\frac{\partial U_i}{\partial x_k} \tag{A2.13}$$

where $C_{T1} = 0.07$, $C_{T2} = 3.2$, $C_{T3} = 0.5$.

The auxiliary k and ε equations are given in (II) CFD equation set.

Boundary Conditions

(1) **Inlet Condition (column top, x = 0)**

At the top of the column, the boundary condition for the liquid phase is set to be [28]

$$U = U_{\text{in}}, C = C_{in}, k = 0.003\,U_{\text{ln}}^2, \varepsilon_{\text{in}} = 0.09\frac{k_{\text{in}}^{1.5}}{d_{\text{H}}}$$

where d_{H} is the hydraulic diameter of random packing, which can be calculated by

$$d_{\text{H}} = \frac{4\gamma_\infty}{a(1-\gamma_\infty)}$$

Since no experimental measurements are reported or empirical correlations are available from the literature for determining the inlet condition of the fluctuating mass flux $\overline{u_i'c_{\text{in}}'}$ and fluctuating heat flux $\overline{u_i'T_{\text{in}}'}$, the following conditions for $\overline{u_i'c'}$ and $\overline{u_i'T'}$ are adopted based on the best fitting of experimental data [24, 26]

$$\left(\overline{u_i'c'}\right)_{\text{in}} = -0.7(\partial C/\partial x_i)|_{\text{in}} \quad \left(\overline{u_i'T'}\right)_{\text{in}} = -0.9(\partial T/\partial x_i)|_{\text{in}}$$

It is found that the foregoing inlet condition is applicable to many other simulations with satisfactory results.

Outlet Condition (column bottom)

The flow in the packed column at the outlet is considered as fully developed in turbulent state; the zero normal gradients are applied for all variables Φ except pressure.

(2) **Axis Condition**

Under the assumption that all variables Φ in the packed column are axially symmetrical, we have $\partial\Phi/\partial x = 0$ at y = 0 of the column central axis.

(3) **Wall Conditions**

The no-slip condition of flow is applied to the wall, and the zero flux condition at the wall is adopted.

Evaluation of Source Terms

The object of simulation and the evaluation of source terms S_m, S_F, S_T, S_n are the same as in Sect. 3.1.

3.2.1 Absorption of CO_2 by Aqueous MEA in Packed Column

3.2.1.1 Simulated Results and Verification

The liquid phase temperature profile

The simulated profile of liquid phase temperature in the packed column is given in Fig. 3.23a. The axial distribution of liquid phase temperature after radial average is shown in Fig. 3.23b.

Since the reported experimental measurements are only inlet and outlet temperature of liquid phase, the validity of the present model can only be checked by comparing with such limited data. As seen from Fig. 3.23b, the simulated outlet temperature is a little higher than the experimental measurement (about 0.3 K). This

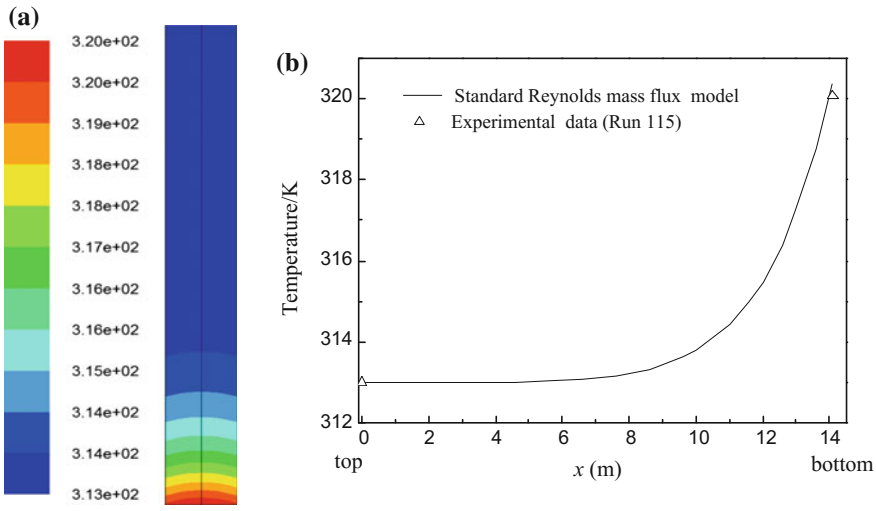

Fig. 3.23 Simulated temperature profiles of liquid phase in the column of absorption of CO_2 into aqueous MEA (Run 115) by RMF model [10] **a** profile of liquid phase temperature in the column, **b** comparison of axial distribution of radial average temperature in the column with experimental data

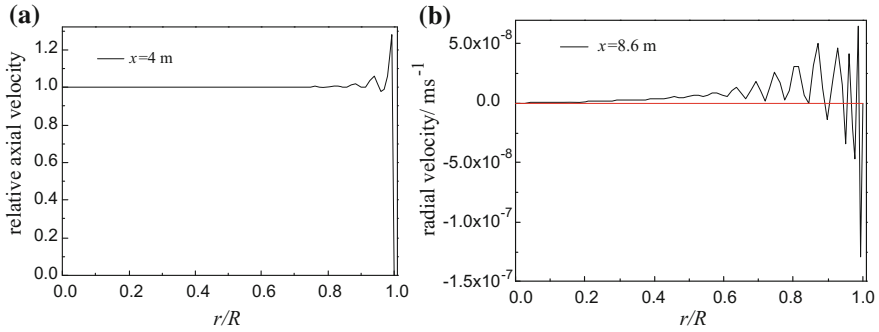

Fig. 3.24 Simulated velocity profiles of the liquid in the column of absorption of CO_2 into aqueous MEA (Run 115) by RMF model [10] **a** axial velocity profile of the liquid along radial direction, **b** radial velocity profiles of the liquid along radial direction

error may be due to the neglect of heat loss to the environment in the assumption, which results somewhat increase of the fluid temperature, other sources of error are similar to the absorption by MEA and AMP as given in previous sections.

The axial and radial liquid phase velocity distributions

The simulated axial velocity distribution along radial direction is shown in Fig. 3.24a. As seen, the axial liquid velocity is almost constant from column center to about $r/R = 0.8$ due to relatively uniform porosity in this region of the column. The obvious up and down variation of velocity near the wall region is mainly due to the nonuniform porosity. The simulated radial velocity along radial direction is shown in Fig. 3.24b, in which the radial velocity increases slowly from $r/R = 0$ to about 0.4. From 0.4 to the column wall, the wavy variation of the radial velocity is intensified sharply, especially around $r/R = 0.9$. It shows that the influence of nonuniform porosity is appreciable especially near the wall.

The profile of CO_2 loading

Figure 3.25a gives the distribution of CO_2 loading in the packed column. It can be seen from this figure that most absorptions are taken place at the bottom part of the column, while at the top part only trace of CO_2 is removed. As shown in Fig. 3.25b, the simulated CO_2 loading at the bottom of the column is closely checked by the published outlet data.

The Profile of CO_2 concentration in gas phase is given in Fig. 3.26a. The average radial concentration along axial direction is given in Fig. 3.26b. As seen in the figure, the prediction on outlet concentration is confirmed by experimental data.

The MEA concentration profile

As shown in Fig. 3.27a and b, the free MEA molar concentration in the liquid phase increases from column center to the wall at different height of the column. It can be explained that the liquid velocity is slow, down near the wall in the randomly packed column (see Figs 3.24), resulting worse contact with the gas phase, and consequently less CO_2 to be absorbed. This is also the reason why the CO_2

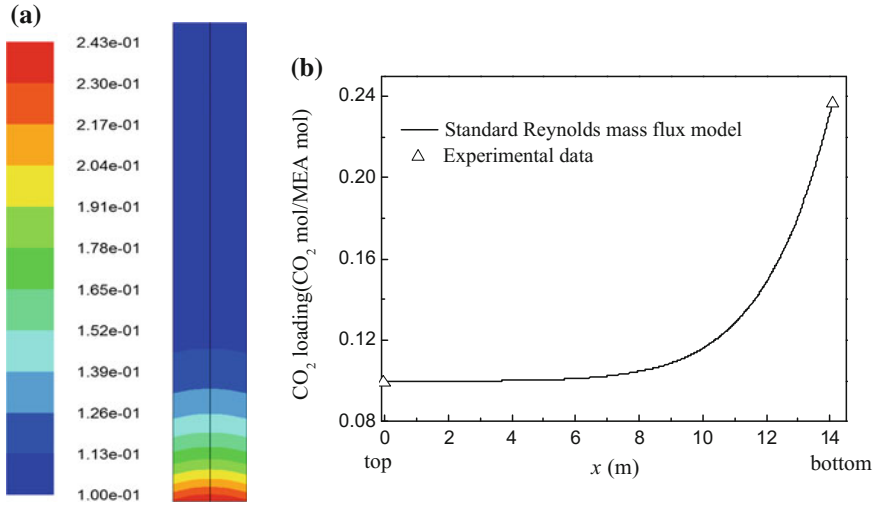

Fig. 3.25 Simulated profiles of CO_2 loading in the packed column of absorption of CO_2 into aqueous MEA (Run 115) by RMF model [10] **a** profile of CO_2 loading in the packed column, **b** comparison of axial profile of average CO_2 loading with experimental data

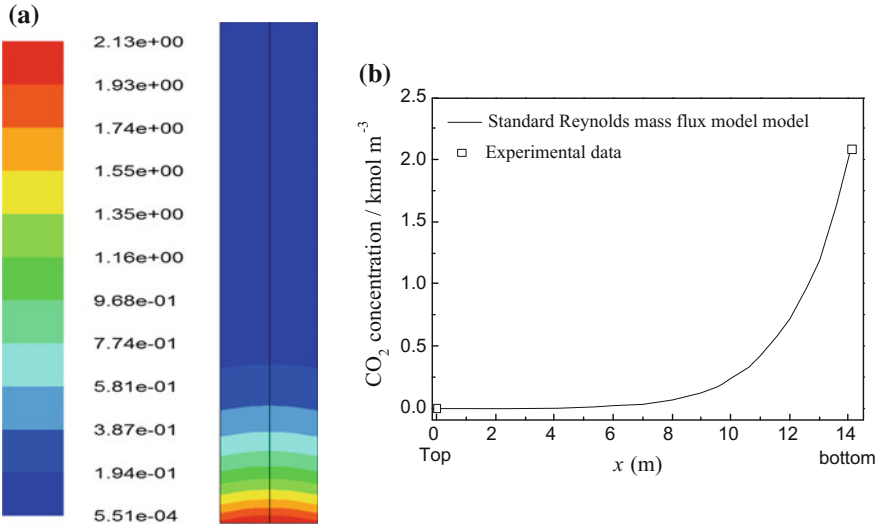

Fig. 3.26 Simulated profiles of CO_2 concentration in gas phase in the packed column of absorption of CO_2 into aqueous MEA (Run115) by RMF model [10] **a** profile of CO_2 concentration in gas phase, **b** profile of average CO_2 concentration along radial direction

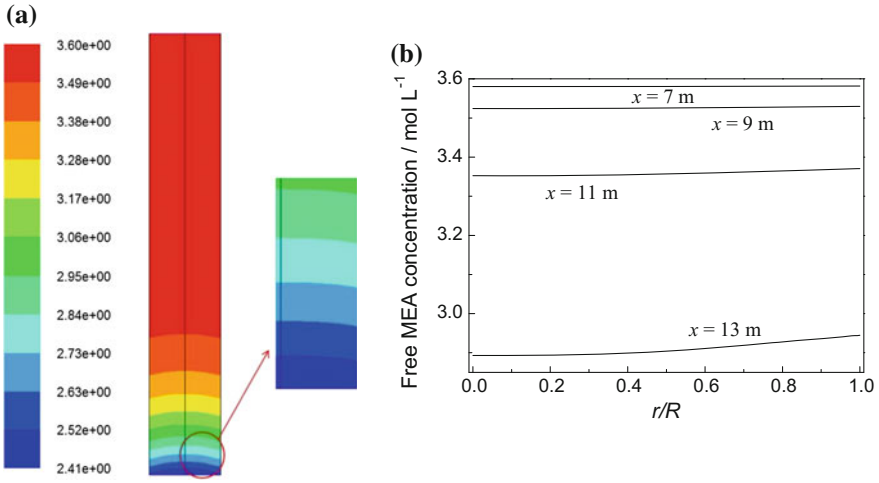

Fig. 3.27 Simulated Profile of MEA concentration in the column for absorption of CO_2 into aqueous MEA (Run 115) by RMF model [10] **a** profile of MEA concentration in the column, **b** distribution of MEA concentration in radial direction

loading in liquid phase decreases with the distance away from the column center at a given height near the column bottom, as shown in Fig. 3.25a.

3.2.1.2 Anisotropic Mass Diffusivity

Since the Reynolds mass flux model can be solved for the anisotropic fluctuating mass flux $\overline{u_i'c'}$ directly, it is possible to estimate the mass transfer by means of eddy diffusion in any directions. Such estimation can be made by defining an anisotropic turbulent mass diffusivity $\mathbf{D_{t,i}}$. Similar to Eq. (1.36), let us consider $\overline{u_i'c'}$ to be proportional to the concentration gradient, i.e.,

$$-\overline{u_i'c'} = \mathbf{D}_{t,i}\frac{\partial C}{\partial x_i}, \text{or } \mathbf{D}_{t,i} = -\overline{u_i'c'}\Big/\frac{\partial C}{\partial x_i} \tag{1.37}$$

It should be noted that the $\mathbf{D_{t,i}}$ such defined is different from the D_t for the Boussinesq postulation as given in Eq. (1.4), which is an isotropic parameter characterizing the ability of mass transfer by the flactuation of the fluid velocity.

The axial turbulent (fluctuating) mass flux $\overline{u_x'c'}$

As seen from Fig. 2.8b, the $\overline{u_x'c'}$ is increasing rapidly at the lower part of the column ($x > 8$ m), it indicates the $\overline{u_x'c'}$ increasing profile is in counteraction with the decreasing average MEA concentration profile as seen in Fig. 3.27b, so that the mass transfer in x_i direction is enhanced. Also the positive slop of $\overline{u_x'c'}$ in the plot implies that the rate of enhancement is much greater at the bottom than at the top. In

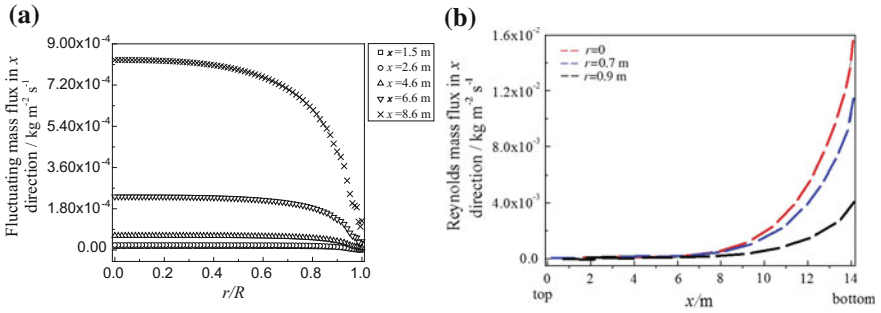

Fig. 3.28 Simulated profiles of $\overline{u'_x c'}$ of MEA in the absorption of CO_2 into aqueous MEA (Run115) [10] **a** profiles of $\overline{u'_x c'}$ along radial direction, **b** profiles of $\overline{u'_x c'}$ along axial direction

Fig. 2.8b, $\overline{u'_x c'}$ is almost constant at the upper part of the column ($x < 6$), and increase rapidly toward the column bottom; it means that the turbulent effect in axial direction is kept unchanged at the column top and advance intensely along the lower part of the bottom.

In the radial direction as shown in Fig. 3.28a, $\overline{u'_x c'}$ also remained unchanged from column center to about $r/R = 0.6$ From $r/R = 0.6$ to the column wall, although the positive $\overline{u'_x c'}$ is gradually lower down with low rate (negative slope), it counteracts with the axial MEA concentration increasing profile (see $x = 11$ and 13 in Fig. 3.27b), so that the axial MEA concentration is being suppressed to some extent in this region.

The axial mass transfer diffusivity $\mathbf{D_{t,x}}$

Figure 3.29 gives the concentration gradient of MEA along the x direction. From Eq. (1.37) and Figs. 3.28a and 3.29, the axial turbulent mass diffusivity $\mathbf{D}_{t,x}$ can be

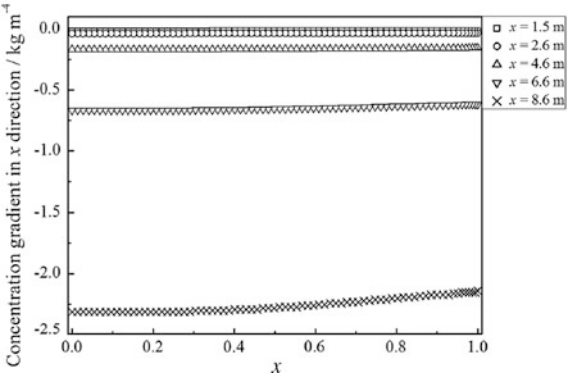

Fig. 3.29 Simulated profile of average MEA concentration gradient along axial direction in the absorption of CO_2 into aqueous MEA (Run 115) [10]

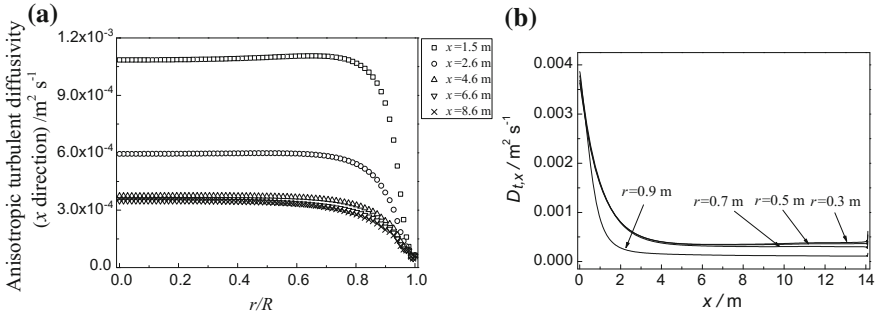

Fig. 3.30 Simulated profiles of $\mathbf{D}_{t,\mathbf{x}}$ for MEA in the absorption of CO_2 into aqueous MEA (Run 115), (*x is measured from column top*) [10] **a** $\mathbf{D}_{t,\mathbf{x}}$ along radial direction, **b** $\mathbf{D}_{t,\mathbf{x}}$ along axial directions

obtained as given in Fig. 3.30. As seen in Fig. 3.30b, the $\mathbf{D}_{\mathbf{t},\mathbf{x}}$ is decreasing along the upper part of the column ($x < 4$), it means the mass transfer is not active in this region. In the radial direction, the $\mathbf{D}_{\mathbf{t},\mathbf{x}}$ is almost constant from column center to about $r/R = 0.8$ and gradually down to zero with negative slope; which implies the $\overline{u_x'c'}$ diffusion remains steady until $r/R = 0.8$ and falls to zero at the wall with slow rate. It is also noted that although $\mathbf{D}_{\mathbf{t},\mathbf{x}}$ is high at the column top ($x = 1.5$ m), yet the MEA concentration gradient there is very low (see Fig. 3.29) to make the fluctuating mass flux $\overline{u_x'c'}$ is very small.

At the lower part of the column (e.g., $x = 8.6$), although $\mathbf{D}_{\mathbf{t},\mathbf{x}}$ is low, the concentration gradient (absolute value) is high, and so the product $\overline{u_x'c'}$ becomes higher toward the bottom as seen in Fig. 3.28b.

The radial mass transfer diffusivity $\mathbf{D}_{\mathbf{t},\mathbf{y}}$

The profile of $\overline{u_y'c'}$ is given in Fig. 3.31. The negative $\overline{u_y'c'}$ means its diffusion is under negative gradient of C (see Sect. 3.6.1.3), which suppresses the increasing MEA concentration in radial direction. In Fig. 3.33 the $\mathbf{D}_{\mathbf{t},\mathbf{y}}$ contour displays a

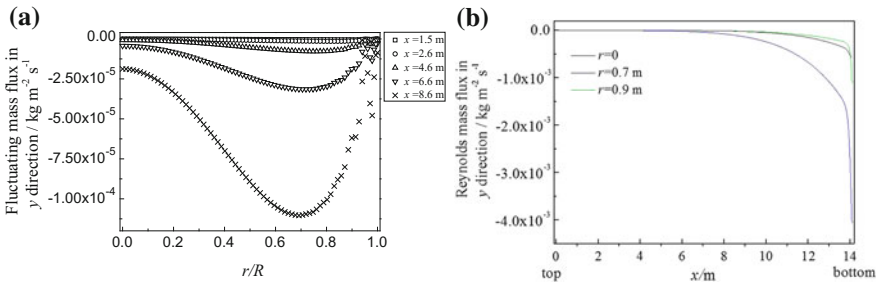

Fig. 3.31 Simulated profiles of $\overline{u_y'c'}$ for MEA in the absorption of CO_2 into aqueous MEA (Run 115) [10] **a** $\overline{u_y'c'}$ along radial direction**, b** $\overline{u_y'c'}$ along axial direction

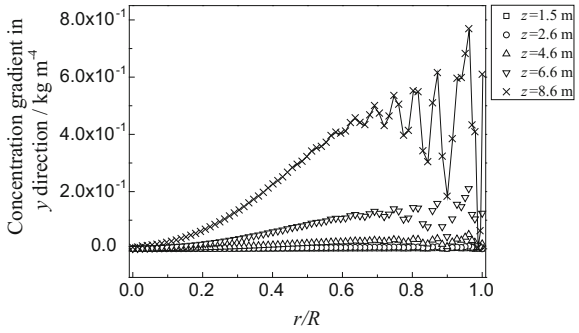

Fig. 3.32 Simulated profiles of MEA concentration gradient along radial direction (Run 115)

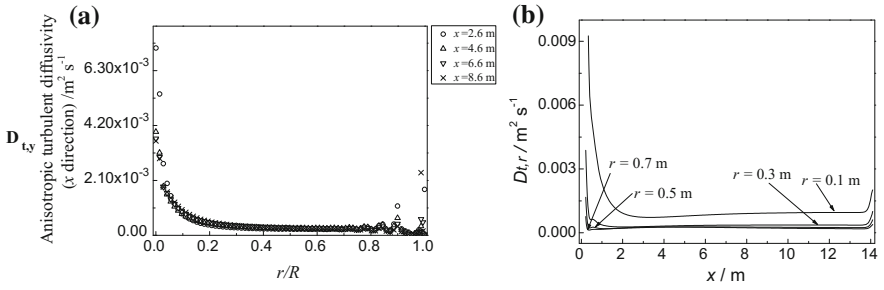

Fig. 3.33 Simulated profiles of $\mathbf{D}_{t,y}$(*x is measured from column top*)for MEA in the absorption of CO_2 into aqueous MEA (Run 115) [10] **a** $\mathbf{D}_{t,y}$ along radial direction, **b** $\mathbf{D}_{t,y}$ along axial direction

sudden increase to very high value near the column center. But the radial concentration gradient around the column center is nearly zero according to the axial symmetrical assumption, as shown in Fig. 3.32, so that very small value of denominator in $\mathbf{D_{t,y}} = -\overline{u'_y c'} \Big/ \frac{\partial C}{\partial y}$ makes high. $\mathbf{D_{t,\,y}}$

As stated in Sect. 1.5.1.4, the anisotropic diffusivities $\mathbf{D_{t,x}}$ and $\mathbf{D_{t,y}}$ obtained by Reynolds mass flux model are not comparable with the D_t from two-equation model, but it is interesting to see the difference between anisotropic $\mathbf{D_{t,\,x}}$ as shown in Fig. 3.30 and the isotropic D_t as shown in Fig. 3.7a. Both $\mathbf{D_{t,\,x}}$ and D_t are in the same order of magnitude, although $\mathbf{D_{t,\,x}}$ is somewhat lower than D_t. Their tendency is similar as their values are high at the column top and low at the column bottom.

It is also noted that the dissimilarity between $\mathbf{D_{t,x}}$ and $\mathbf{D_{t,y}}$ demonstrates the anisotropy of the absorption packed column.

The total fluctuating mass flux

The total fluctuating mass fluxes $\overline{u'_x c'} + \overline{u'_y c'}$ along the radial direction at different bed height for Run 115 are shown in Fig. 3.4. It is also noted that the profile of $\overline{u'_x c'} + \overline{u'_y c'}$ in this simulation is practically equal to that of $\overline{u'_x c'}$ in Fig. 3.28a because

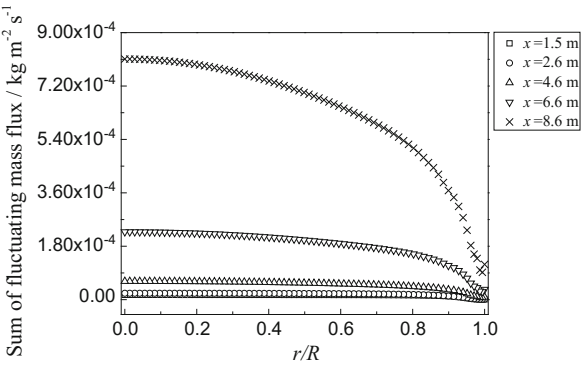

Fig. 3.34 Simulated profile of $\overline{u'_x c'} + \overline{u'_y c'}$ at different packed height (*Run 115*), (*x is measured from column top*) [10]

in the present case the $\overline{u'_x c'}$ is much greater than the $\overline{u'_y c'}$, as seen by comparing Fig. 3.28a and Fig. 3.31a. Thus $\overline{u'_x c'}$ diffusion is the main contribution to the turbulent effect (Fig. 3.34).

3.2.2 The Absorption of CO_2 by Aqueous NaOH in Packed Column

The simulation is using standard Reynolds mass flux model, the model equation sets, the boundary conditions, and the evaluation of source terms are the same as given in Sect. 3.1.3. The simulated results are given in the following sections.

3.2.2.1 The Simulated Results and Verification

The liquid phase temperature profile

The simulated profile of liquid phase temperature for experiment T11 is shown in Fig. 3.35 and compare with experimental data. The simulated temperature at the column bottom is somewhat higher than the experimental measurement due to the same reason for the case of MEA absorption as stated in Sect. 3.2.1.1.

The NaOH concentration profile

The simulated profile of OH^- for T11 is given in Fig. 3.36. The simulated radial averaged axial concentration is seen to be confirmed by the experimental data.

3.2.2.2 The Anisotropic Mass Diffusivity

The radial distribution of axial liquid phase velocity

The radial averaged axial liquid phase velocity is shown in Fig. 3.37. As seen in the figure, wavy fluctuating of axial velocity in this case may be due to the uneven

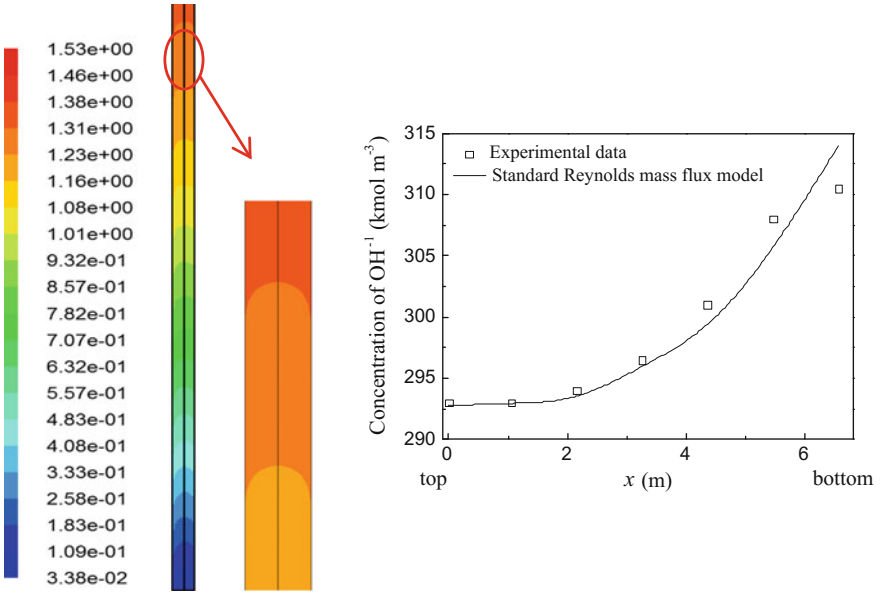

Fig. 3.35 Simulated profile of liquid phase temperature in the column for CO_2 absorption into aqueous NaOH (T11) [10]

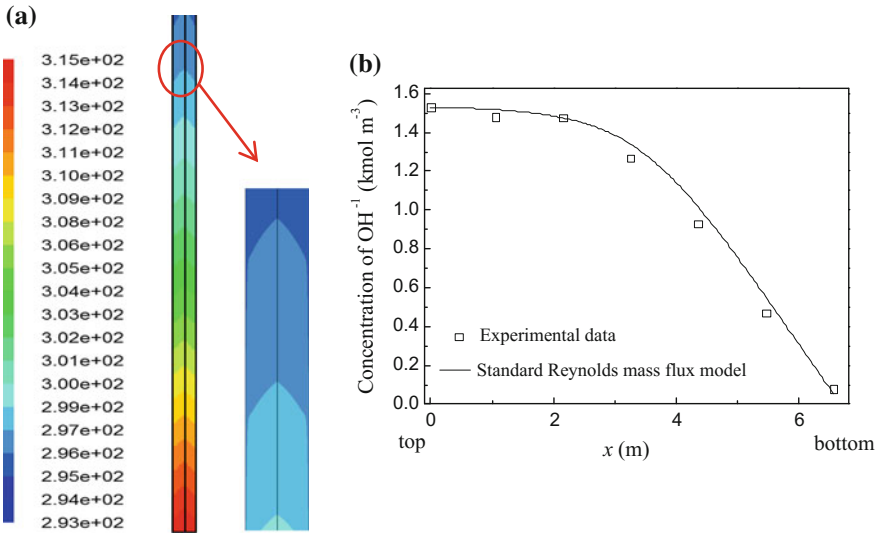

Fig. 3.36 Simulated profile of average OH^- concentration in the column for CO_2 absorption into aqueous NaOH (*T11*) [10] **a** profile of average OH^- concentration, **b** average OH^- along axial direction

porosity of the packing and the ratio of column diameter to packing size is only about eight. Such wavy velocity affects significantly the shape of the anisotropic Reynolds mass flux and the mass diffusivities as seen in Figs. 3.38 and 3.39.

The anisotropic mass diffusivity

(1) ***The axial mass diffusivity***

The anisotropic mass diffusivity $\mathbf{D_{t,\,x}}$ is calculated using Eq. (1.37), the axial fluctuating mass flux, the concentration gradient, and the axial mass diffusivity are given in Fig. 3.38. Note that the wavy shape of $\overline{u_x'c'}$ and $\mathbf{D_{t,\,x}}$ contours are as the result of existing intense wavy axial velocity distribution along radial direction as seen in Fig. 3.37.

The distributions of $\overline{u_x'c'}$ and $\mathbf{D_{t,\,x}}$ along the axial direction are also shown in Fig. 3.39. Similar to the absorption by MEA, the $\overline{u_x'c'}$ diffusion (turbulent effect) is small along the upper part of the column and becomes intense along the lower part of the column as shown in Fig. 3.38a. Again, the difference between the radial and axial diffusivities can be clearly seen from Fig. 3.38c and Fig. 3.39b.

(2) ***The radial mass diffusivity***

As seen in Fig. 3.40, the negative $\overline{u_y'c'}$ suppresses the NaOH radial decreasing concentration profile with decreasing rate toward the column bottom. The wavy shape of radial velocity and $\overline{u_y'c'}$ also affects the $\mathbf{D_{t,y}}$ to be waving.

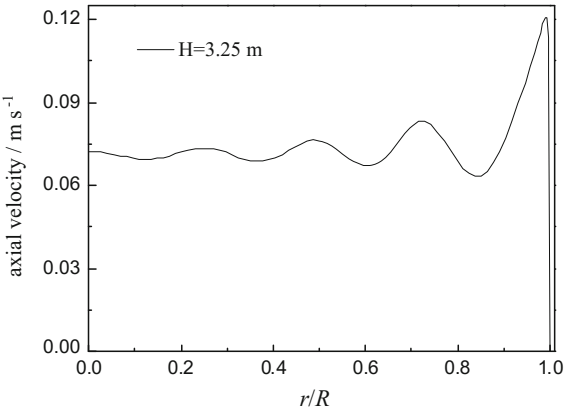

Fig. 3.37 Simulated radial profile of axial velocity at z = 3.25 m in the column for CO_2 absorption into aqueous NaOH (*T11*) [10]

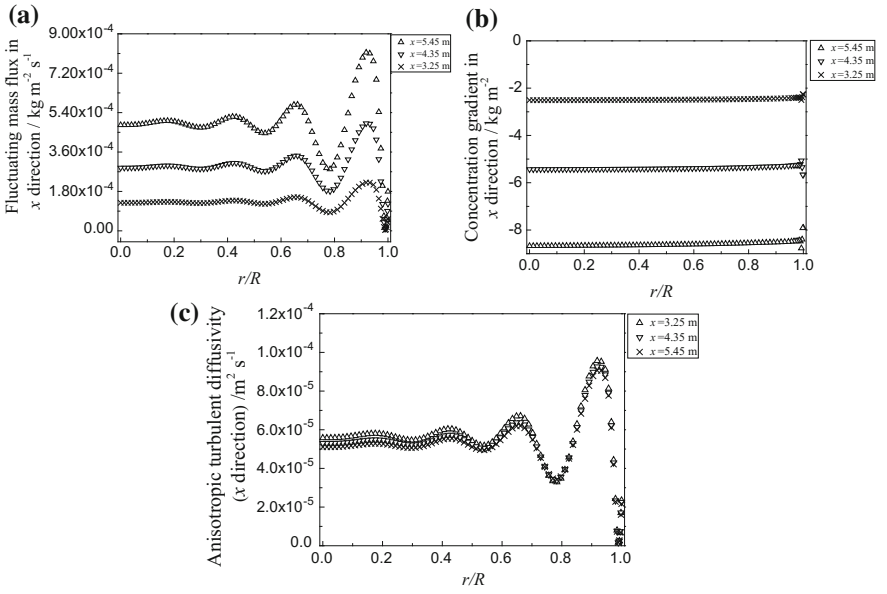

Fig. 3.38 Simulated axial fluctuating mass flux, concentration gradient, and axial mass diffusivity of OH^- in the column for CO_2 absorption into aqueous NaOH (*T11*), *x*—distance measured from column top (*x is measured from column top*) [10] **a** $\overline{u'_x c'}$ in radial direction**, b** the concentration gradient $\frac{\partial C}{\partial x}$ in radial direction**, c** $\mathbf{D_{t,x}}$ in radial direction

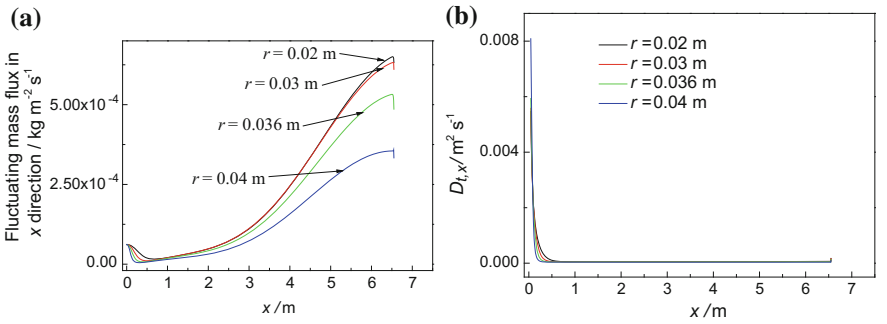

Fig. 3.39 Simulated axial fluctuating mass flux and axial diffusivity of OH^- in the column for CO_2 absorption into aqueous NaOH (*T11*), x –distance measured from column top (*x is measured from column top*) [10] **a** $\overline{u'_x c'}$ in axial direction**, b** $\mathbf{D_{t,x}}$ in axial direction

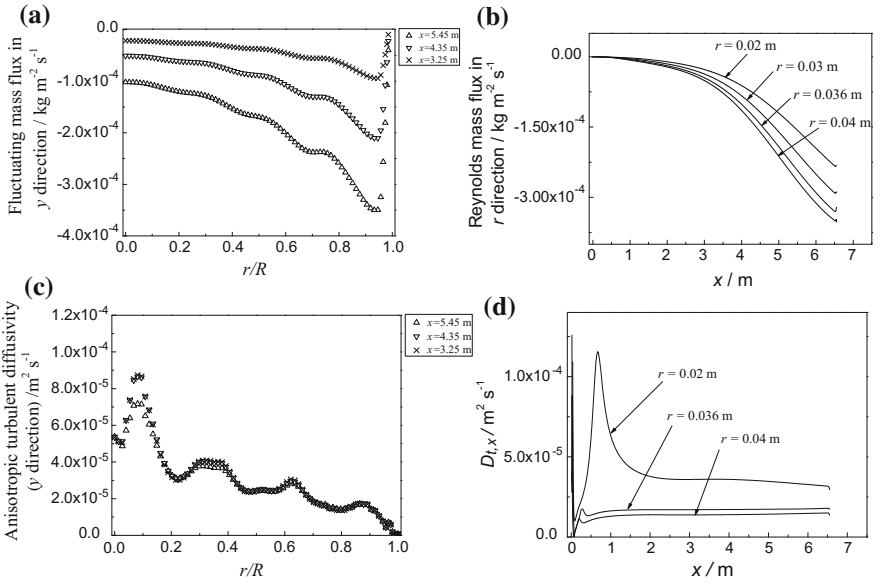

Fig. 3.40 Simulated fluctuating mass flux and mass diffusivity of OH^- in the column for CO_2 absorption into aqueous NaOH (*T11*), *x*—distance measured from column top (*x is measured from column top*) [10] **a** $\overline{u'_y c'}$ in radial direction**, b** $\overline{u'_y c'}$ in axial direction**, c** $D_{t,y}$ in radial direction**, d** $D_{t,y}$ in axial direction

3.3 Summary

In this chapter, the two CMT models, i.e., $\overline{c'^2} - \varepsilon_{c'}$ model and Reynolds mass flux model (standard, hybrid, and algebraic forms) are used for simulating the chemical absorption of CO_2 in packed column by MEA, AMP, and NaOH separately and their simulated results are closely checked with the experimental data. It is noted that the radial distribution of D_t is similar to α_t but quite different from μ_t. It means the conventional assumption that $Sc_t \left(= \frac{\mu_t}{\rho D_t}\right)$ and $\mathrm{Pr}_t \left(= \frac{\mu_t}{\rho \alpha_t}\right)$ are constant throughout the column is unjustified. Also the appearance of negative $\overline{u'_y c'}$ in MEA and NaOH absorption indicates that the increasing tendency of their radial concentrations due to lower absorption is promoted by the coaction of the turbulent mass flux diffusion.

References

1. Yin FH, Sun CG, Afacan A, Nandakumar K, Chuang KT (2000) CFD modeling of masstransfer processes in randomly packed distillation columns. Ind Eng Chem Res 39 (5):1369–1380
2. Liu SJ (2001) A continuum model for gas-liquid flow in packed towers. Chem Eng Sci 56:5945–5953

3. Hjertager LK, Hjertager BH, Solberg T (2002) CFD modelling of fast chemical reactions in turbulent liquid flows. Com Chem Eng 26(4–5):507–515
4. Jiang Y, Khadilkar MR, Al-Dahhan MH, Dudukovic AP (2002) CFD of multiphase flow inpacked-bed reactors: I. k-fluid modeling issues. AIChE J 48(4):701–715
5. Jiang Y, Khadilkar MR, Al-Dahhan MH, Dudukovic MP (2002) CFD of multiphase flow in packed-bed reactors: II. Results and applications. AIChE J 48(4):716–730
6. Yin FH, Afacan A, Nandakumar K, Chuang KT (2002) Liquid holdup distribution in packed columns: gamma ray tomography and CFD simulation. Chem Eng Process 41(5):473–483
7. de Lemos MJS, Mesquita MS (2003) Turbulent mass transport in saturated rigid porous media. Int J Heat Mass Transfer 30(1):105–113
8. Liu GB, Yu KT, Yuan XG, Liu CJ (2006) Simulations of chemical absorption in pilot-scale and industrial-scale packed columns by computational mass transfer. Chem Eng Sci 61 (19):6511–6529
9. Liu GB, Yu KT, Yuan XG, Liu CJ (2006) New model for turbulent mass transfer and its application to the simulations of a pilot-scale randomly packed column for CO_2-NaOH chemical absorption. Ind Eng Chem Res 45(9):3220–3229
10. Li WB (2012) Theory and applications of computational mass transfer, Ph.D. dissertation, Tianjin University, Tianjin, China
11. Chen CJ, Jaw SY (1998) Fundamentals of turbulence modeling. Taylor and Francis, Washington, DC
12. Sater VE, Levenspiel O (1966) Two-phase flow in packed beds. Ind Eng Chem Fundam 5:86–92
13. Engel V, Stichmair J, Geipel W (1997) A new model to predict liquid holdup in packed columns—using data based on capacitance measurement techniques. Institute Chemical Engineering Symposium Series, Part 2:939–947
14. Giese M, Rottschafer K, Vortmeyer D (1998) Measured and modeled superficial flow profiles in packed beds with liquid flow. AIChE J 44:484–490
15. Roblee LHS, Baird RM, Tierney JW (1958) Radial porosity variations in packed beds. AIChE J 4:460–464
16. de Klerk A (2003) Voidage variation in packed beds at small column to particle diameter ratio. AIChE J 49:022–2029
17. Wellek RM, Brunson RJ, Law FH (1978) Enhancement factors for gas absorption with 2nd order irreversible chemical-reaction. Can J Chem Eng 56:181–186
18. Ferchichi M, Tavoularis S (2002) Scalar probability density function and fine structure in uniformly sheared turbulence. J Fluid Mech 461:155–182
19. Hikita H, Asai S, Katsu Y, Ikuno S (1979) Absorption of carbon-dioxide into aqueous monoethanolamine solutions. AIChE J 25:793–800
20. Onda K, Takeuchi H, Okumoto Y (1968) Mass transfer coefficients between gas and liquid phases in packed columns. J Chem Eng Japan 1:56–62
21. Danckwerts PV (1979) Reaction of CO_2 with ethanolamines. Chem Eng Sci 34(4):443–446
22. Kohl AL, Nielsen RB (1997) Gas purification. Gulf Publishing Company, Houston
23. Pintola T, Tontiwachwuthikul P, Meisen A (1993) Simulation of pilot plant and industrial CO_2-MEA absorbers. Gas Sep Purif 7:47–52
24. Tontiwachwuthikul P, Meisen A, Lim CJ (1992) CO_2 absorption by NaOH, monoethanolamine and 2-Amino-2-Methyl-1-Propanol Solutions in a packed-column. Chem Eng Sci 47 (2):381–390
25. Saha AK, Bandyopadhyay SS, Biswas AK (1995) Kinetics of absorption of CO_2 into aqueous-solutions of 2-Amino-2-Methyl-1-Propanol. Chem Eng Sci 50(22):3587–3598
26. Liu GB (2006) Computational transport and its application to mass transfer and reaction processes in packed beds. Ph.D. dissertation, Tianjin University, Tianjin, China
27. Pohorecki R, Moniuk W (1988) Kinetics of reaction between carbon-dioxide and hydroxyl ions in aqueous-electrolyte solutions. Chem Eng Sci 43(7):1677–1684
28. Jones WP, Launder BE (1973) The calculation of low-Reynolds-number phenomena with a two-equation model of turbulence. Int J Heat Mass Transfer 16:1119–1130

Chapter 4
Application of Computational Mass Transfer (III)—Adsorption Process

Abstract In this chapter, adsorption process is simulated using computational mass transfer (CMT) models as presented in Chap. 3. As the adsorption process is unsteady and accompanied with heat effect, the time parameter and the energy equation as presented in Chap. 2 are involved in the model equations. The simulated concentration profile of the column at different times enables to show the progress of adsorption along the column as an indication of the process dynamics. The simulated breakthrough curve and regeneration curve for adsorption and desorption by the two CMT models, i.e., the $\overline{c'^2} - \varepsilon_{c'}$ model and the Reynolds mass flux model, are well checked with the experimental data. Some issues that may cause discrepancies are discussed.

Keywords Simulation of adsorption · Concentration profile · Breakthrough curve · Regeneration curve

Nomenclature

a_p	Surface area per unit volume of packed column, m^{-1}
c	Mass concentration, $kg.m^{-3}$
c_{pg}, c_{ps}	Specific heat of gas phase and solid phase, respectively, J kg^{-1} K^{-1}
C_μ, $C_{1\varepsilon}$, $C_{1\varepsilon}$	Turbulence model constants for the velocity field
C_{c0}, C_{c1}, C_{c2}, C_{c3}	Turbulence model constants for the concentration field
C_{t0}, C_{t1}, C_{t2}, C_{t3}	Turbulence model constants for the temperature field
$\overline{c^2}$	Concentration variance, kg^2 m^{-6}
D	Molecular diffusivity, m^2 s^{-1}
D_t	Turbulent mass diffusivity, m^2 s^{-1}
d_H	Hydraulic diameter of packing, m
d_p	Nominal packing diameter, m
Er	Exponential decaying function
F	Flow rate, L min^{-1}
g	Gravity acceleration, m s^{-2}
Gr	Grashof number ($Gr = \rho^2 g\beta\ (T_g - T_0)\ d_{col}^3/\mu^2$)

K.-T. Yu and X. Yuan, *Introduction to Computational Mass Transfer*,
Heat and Mass Transfer, DOI 10.1007/978-981-10-2498-6_4

H	Packing height measured from column bottom, ($H = 0$ at column bottom), m
h	Heat transfer coefficient from gas phase to packing, W m^{-2} K^{-1}
h_w	Heat transfer coefficient from gas phase to ambient, W m^{-2} K^{-1}
h_{w1}	Heat transfer coefficient from gas phase to column wall, W m^{-2} K^{-1}
h_{w2}	Heat transfer coefficient from column to ambient, W m^{-2} K^{-1}
ΔH	Heat of adsorption of adsorbate, J mol^{-1}
k	Turbulent kinetic energy, m^2 s^{-2}
K_G	Mass transfer coefficient of gas phase and intraparticle, m s^{-1}
k_G	Mass transfer coefficient of gas phase, m s^{-1}
k_g	Thermal conductivity of gas, W m^{-1} K^{-1}
k_p	Intraparticle mass transfer coefficient, m s^{-1}
k_s	Thermal conductivity of adsorbent particle, W m^{-1} K^{-1}
M	Molecular weight of adsorbate, kg mol^{-1}
Nu	Nusselt number ($Nu = hR_p/k_g$)
P	Total pressure of gas phase in the column, atm
Pr	Prandtl number ($Pr = C_{pg}\mu/k_g$)
q	Adsorbate concentration in solid phase, respectively, mol kg^{-1}
r	Radial distance from the axis of the column, m
R	Inner radius of the column, m
R_τ	Velocity to concentration timescale ratio
R_p	Packing radius, m
Re_p, Re_{col}	Reynolds number base on packing and column diameter, respectively ($Re_p = \rho\|u\|d_p/\mu$, $Re_{col} = \rho\|u\|d_{col}/\mu$)
Sc, Sc_t	Schmidt number base on molecular and turbulent diffusivity, respectively ($Sc = \mu/\rho D$, $Sc_t = \mu/\rho D_t$)
S_c	Source term of mass transfer, kg m^{-3} s^{-1}
S_m	Source term of momentum transfer, N m^{-3}
S_{Tg}	Thermal source term of the gas phase, J m^{-3} s^{-1}
S_{Ts}	Thermal source term of the solid phase, J m^{-3} s^{-1}
t	Time, mina
T_g	Gas phase temperature, K
$T_{g,in}$	Inlet temperature of the gas phase, K
T_s	Solid phase temperature, KT_{w1}, T_{w2} temperature of the inner and outer walls, K
T_0	Ambient temperature and initial temperature of the solid phase, K
$\overline{T'^2}$	Temperature variance, t^2

u	Gas interstitial velocity vector, m s^{-1}
u'	Gas fluctuating velocity, m s^{-1}
x	Axial distance from column top ($x = 0$ at column top), m
y_w	Distance from the column wall, m
z	Height of packing measured from the gas phase inlet of the column, m
Z	Total packing height of the column, m
α, α_t	Molecular, turbulent thermal diffusivity, respectively, m^2 s^{-1}
ε	Turbulent dissipation, m^2 s^{-3}
ε_c	Turbulent dissipation of the concentration fluctuation, kg^2 m^{-6} s^{-1}
ε_t	Turbulent dissipation rate of temperature fluctuation, s^{-1}
γ	Local column porosity
γ_∞	Porosity in an unbounded packing
γ_p	Particle porosity
δ_{ij}	Kronecker delta
ρ	Gas density, kg m^{-3}
ρ_g	Total gas concentration, mol m^{-3}
ρ_s	Apparent density of the solid adsorbent, kg m^{-3}
μ, μ_t	Gas molecular, turbulent viscosity, respectively, kg m^{-1} s^{-1}
σ_k, σ_ε, σ_c, $\sigma_{\varepsilon c}$, σ_t, $\sigma_{\varepsilon t}$	Turbulence model constants for diffusion of k, ε, $\overline{c^2}$, ε_c, $\overline{t^2}$, ε_t

Adsorption process has been widely used in many chemical and related industries, such as the separation of hydrocarbon mixtures, the desulfurization of natural gas, and the removal of trace impurities in fine chemical production. Most of the adsorption researches in the past are focused on the experimental measurement of the breakthrough curve for studying the dynamics. The conventional model used for the adsorption process is based on one-dimensional or two-dimensional dispersion, in which the adsorbate flow is either simplified or computed using computational fluid dynamics (CFD), and the distribution of adsorbate concentration is obtained by adding dispersion term to the adsorption equation with unknown turbulent mass diffusivity D_t. Nevertheless, the usual way to find the D_t is either by employing empirical correlation obtained from inert tracer experiment or by guessing a Schmidt number applied to the whole process. As stated in Chap. 3, such empirical method is unreliable and lacking theoretical basis.

Theoretically, the unknown diffusivity can be obtained directly by the closure of the mass transfer differential equation by a proper method in order to solve at once all unknown parameters in the equation. In the following sections, the two-equation $\overline{c'^2} - \varepsilon_{c'}$ model and Rayleigh mass flux model are used for this purpose as presented by Li [1].

4.1 $\overline{c'^2} - \varepsilon_c$ Two-Equation Model for Gas Adsorption

Assumptions

(1) The gas flow in the randomly packed adsorption column is axially symmetrical and in turbulent state;
(2) The concentration of adsorbate in the gas phase is very low;
(3) The driving force of adsorption is the concentration difference between gas phase and outer surface of the solid adsorbent, and thus the mass transfer calculation is based on the surface area and the surface concentration of the solid adsorbent;
(4) The column has no insulation, and the heat is lost from the column outer surface to the environment.

4.1.1 $\overline{c'^2} - \varepsilon_{c'}$ Model Equations

The $\overline{c'^2} - \varepsilon_{c'}$ two-equation model equations for adsorption are similar to those of absorption except that adsorption is an unstable process and the time parameter should be involved. On the other hand, the gas adsorption process consists of gas and solid phases, and the corresponding equations should established for each phase

(I) The CFD equation set

Mass conversation for gas phase

$$\frac{\partial(\rho_G\gamma)}{\partial t} + \frac{\partial(\rho_G\gamma U_i)}{\partial x_i} = S_{mG}$$

Momentum conversation for gas phase

$$\frac{\partial(\rho_G\gamma U_i)}{\partial t} + \frac{\partial\left(\rho_G\gamma U_i U_j\right)}{\partial x_i} = -\gamma\frac{\partial P}{\partial x_j} + \frac{\partial}{\partial x_i}\left(\gamma\mu\frac{\partial U_j}{\partial x_i} - \gamma\rho_G\overline{u_i'u_j'}\right) + S_{FG}$$

$$-\rho_G\overline{u_i'u_j'} = \mu_t\left(\frac{\partial U_i}{\partial x_j} + \frac{\partial U_j}{\partial x_i}\right) - \frac{2}{3}\delta_{ij}\rho_G k$$

$$\mu_t = C_\mu\rho_G\frac{k^2}{\varepsilon}$$

k equation

$$\frac{\partial(\rho_G\gamma k)}{\partial t} + \frac{\partial(\rho_G\gamma U_i k)}{\partial x_i} = \frac{\partial}{\partial x_i}\left[\gamma\left(\mu + \frac{\mu_t}{\sigma_k}\right)\frac{\partial k}{\partial x_i}\right] + \gamma G_k - \rho_G\gamma\varepsilon$$

ε equation

$$\frac{\partial(\rho_G\gamma\varepsilon)}{\partial t}+\frac{\partial(\rho_G\gamma U_i\varepsilon)}{\partial x_i}=\frac{\partial}{\partial x_i}\left[\gamma\left(\mu+\frac{\mu_t}{\sigma_\varepsilon}\right)\frac{\partial\varepsilon}{\partial x_i}\right]+C_{1\varepsilon}\gamma\frac{\varepsilon}{k}G_k-C_{2\varepsilon}\gamma\rho_G\frac{\varepsilon^2}{k}$$
$$G_k=\mu_t\left(\frac{\partial U_i}{\partial x_j}+\frac{\partial U_j}{\partial x_i}\right)\frac{\partial U_j}{\partial x_i},\tag{A1.15c}$$

where γ is the porosity of the packed bed; model constants are [2]: $C_\mu = 0.09,\ C_{1\varepsilon} = 1.44,\ C_{2\varepsilon} = 1.92,\ \sigma_k = 1.0,\ \sigma_\varepsilon = 1.3$.

(II) The heat transfer equation set

Energy conservation for adsorbate in gas phase

$$\frac{\partial(\rho_G\gamma C_{pG}T_G)}{\partial t}+\frac{\partial(\rho_G\gamma C_{pG}U_iT_G)}{\partial x_i}=\frac{\partial}{\partial x_i}\left[\rho_G\gamma C_{pG}(\alpha+\alpha_t)\frac{\partial T_G}{\partial x_i}\right]+S_{TG},$$

where T_G is the temperature of the gas phase; C_{pG} is the specific heat of the gas phase. *Energy conservation for solid adsorbent*

$$\frac{\partial\left[\rho_s(1-\gamma)C_{ps}T_s\right]}{\partial t}=\frac{\partial}{\partial x_i}\left[(1-\gamma)\lambda_s\frac{\partial T_s}{\partial x_i}\right]+S_{TS},$$

where C_{ps} is specific heat of the solid adsorbent.

Energy conservation for the column wall

$$\frac{\partial\left(\rho_w C_{pw}T_w\right)}{\partial t}=\frac{\partial}{\partial x_i}\left(\lambda_w\frac{\partial T_w}{\partial x_i}\right)+S_{TW},$$

where C_{pw} is the specific heat of the wall material;

$\overline{T'^2}$ *equation*

$$\frac{\partial\left(\rho_G\gamma\overline{T'^2}\right)}{\partial t}+\frac{\partial\left(\rho_G\gamma U_i\overline{T'^2}\right)}{\partial x_i}=\frac{\partial}{\partial x_i}\left[\rho_G\gamma\left(\frac{\alpha_t}{\sigma_T}+\alpha\right)\frac{\partial\overline{T'^2}}{\partial x_i}\right]+2\rho_G\gamma\alpha_t\frac{\partial T_G}{\partial x_j}\frac{\partial T_G}{\partial x_j}-2\rho_G\gamma\varepsilon_{T'}$$

$\varepsilon_{T'}$ *equation*

$$\frac{\partial(\rho_G\gamma\varepsilon_{T'})}{\partial t}+\frac{\partial(\rho_G\gamma U_i\varepsilon_{T'})}{\partial x_i}=\frac{\partial}{\partial x_i}\left[\rho_G\gamma\left(\frac{\alpha_t}{\sigma_{\varepsilon_{T''}}}+\alpha\right)\frac{\partial\varepsilon_{T'}}{\partial x_i}\right]+C_{T1}\rho_G\gamma\alpha_t\frac{\varepsilon_{T'}}{\overline{T'^2}}\left(\frac{\partial T_G}{\partial x_i}\right)^2-C_{T2}\gamma\rho_G\frac{\varepsilon_{T'}^2}{\overline{T'^2}}-C_{T3}\rho_G\gamma\frac{\varepsilon\varepsilon_{T'}}{k}$$

α_t *equation*

$$\alpha_t = C_{T0} k \left(\frac{k\overline{T'^2}}{\varepsilon \varepsilon_{T'}} \right)^{\frac{1}{2}}$$

Model constants are [3]: $C_{T0} = 0.11,\ C_{T1} = 1.8,\ \ C_{T2} = 2.2,\ C_{T3} = 0.8,\ \sigma_{T'} = 1.0,\ \sigma_{\varepsilon_{T'}} = 1.0.$

(III) The mass transfer equation set

Species mass conservation for gas phase

$$\frac{\partial(\gamma C)}{\partial t} + \frac{\partial(\gamma U_i C)}{\partial x_i} = \frac{\partial}{\partial x_i}\left[\gamma D \frac{\partial C}{\partial x_i} - \overline{u_i' c'} \right] + S_{CG}$$

$$\overline{u_i' c'} = D_t \frac{\partial C}{\partial x_i},$$

where C is the mass concentration (kg m^{-3}) of adsorbate in the gas phase.

$\overline{c'^2}$ *equation*

$$\frac{\partial\left(\overline{\gamma c'^2}\right)}{\partial t} + \frac{\partial\left(\gamma U_i \overline{c'^2}\right)}{\partial x_i} = \frac{\partial}{\partial x_i}\left[\gamma \left(\frac{D_t}{\sigma_c} + D \right) \frac{\partial \overrightarrow{c'^2}}{\partial x_i} \right] + 2\gamma D_t \left(\frac{\partial C}{\partial x_i} \right)^2 - 2\gamma \varepsilon_{c'}$$

$\varepsilon_{c'}$ *equation*

$$\frac{\partial(\gamma \varepsilon_{c'})}{\partial t} + \frac{\partial(\gamma U_i \varepsilon_{c'})}{\partial x_i} = \frac{\partial}{\partial x_i}\left[\gamma \left(\frac{D_t}{\sigma_{\varepsilon_{c'}}} + D \right) \frac{\partial \varepsilon_{c'}}{\partial x_i} \right] + C_{c1} \rho_G \gamma D_t \frac{\varepsilon_{c'}}{\overline{c'^2}} \left(\frac{\partial C}{\partial x_i} \right)^2 - C_{c2} \gamma \frac{\varepsilon_{c'}^2}{\overline{c'^2}} - C_{c3} \gamma \frac{\varepsilon \varepsilon_{c'}}{k}$$

D_t *equation*

$$D_t = C_{c0} k \left(\frac{k\overline{c'^2}}{\varepsilon \varepsilon_{c'}} \right)^{\frac{1}{2}}$$

Model constants are [4]: $C_{c0} = 0.11,\ C_{c1} = 1.8,\ \ C_{c2} = 2.2,\ C_{c3} = 0.8,\ \sigma_{c'} = 1.0,\ \sigma_{\varepsilon_{c'}} = 1.3.$

4.1.2 Boundary Conditions

Inlet (column bottom, x = 0): Similar to the absorption column in Chap. 5:

$$u = u_{\text{in}},\ C = C_{\text{in}},\ T = T_{\text{in}}$$
$$k_{\text{in}} = 0.003u_{\text{in}}^2,\ \varepsilon_{\text{in}} = 0.09\frac{k_{\text{in}}^{1.5}}{d_{\text{H}}},$$
$$\overline{c_{\text{in}}'^2} = (0.082C_{\text{in}})^2,\ \varepsilon_{c',\text{in}} = R_\tau\left(\frac{\varepsilon_{\text{in}}}{k_{\text{in}}}\right)\overline{c_{\text{in}}'^2}$$
$$\overline{T_{\text{in}}'^2} = (0.082\Delta T)^2,\ \varepsilon_{t',\text{in}} = R_{\tau,t}\left(\frac{\varepsilon_{\text{in}}}{k_{\text{in}}}\right)\overline{T_{\text{in}}'^2},$$

where d_{H} is the hydraulic diameter of the particle, which is calculated by

$$d_{\text{H}} = \frac{4\gamma_\infty}{a_{\text{p}}(1-\gamma_\infty)},$$

where γ_∞ is the average porosity of the unbounded packed bed; a_{p} is the volumetric packing surface, which is given by

$$a_{\text{p}} = \frac{6(1-\gamma_\infty)}{d_{\text{p}}},$$

where R_τ represents the timescale, $R_\tau = \left(C_{\text{c0}}\frac{k_{\text{in}}^2}{\varepsilon_{\text{in}}}\frac{1}{D_t}\right)^2$.

Outlet (column top): Consider as fully developed turbulence.

Column wall: No slip condition is adopted. Zero flux condition is not satisfied for the present model and the boundary conditions of $\overline{c_{\text{w}}'^2}$ and $\overline{T_{\text{w}}'^2}$ are set as follows:

$$\overline{c_{\text{w}}'^2} = \left(0.082\overline{C_{\text{in}}}\right)^2,\ \varepsilon_{c',\text{w}} = R_{\tau,w}\frac{\varepsilon_{\text{w}}}{k_{\text{w}}}\overline{c'^2}$$
$$\overline{T_{\text{w}}'^2} = (0.082\Delta T)^2,\ \varepsilon_{T',\text{w}} = R_{\tau,t,w}\frac{\varepsilon_{\text{w}}}{k_{\text{w}}}\overline{T_{\text{w}}'^2},$$

where $R_{\tau,\text{w}} = \left(C_{\text{c0}}\frac{k_{\text{w}}^2}{\varepsilon_{\text{w}}}\frac{1}{D_{\text{t}}}\right)^2$, which should be calculated by the method of trial and error as the D_{t} is known only after the simulation. However, if D_{t} is greater than 10^{-3}, the $R_{\tau,\text{w}}$ is substantially equal to one. The k_{w} and ε_{w} can be obtained from the standard wall function of k-ε model.

4.1.3 Evaluation of Source Terms

Determination of S_{FG}

The source term S_{FG} in the momentum equation represents the resistance of gas flow by the solid adsorbent (packing particles), which can be calculated by [5]:

$$S_{FG} = \gamma(F_{GS} + \rho g)$$
$$F_{GS} = \frac{150\mu_G}{d_p^2}\frac{(1-\gamma)^2}{\gamma^3}U + \frac{1.75\rho_G}{d_p}\frac{(1-\gamma)}{\gamma^3}U^2,$$

where γ is calculated by [6]:

$$\gamma = \gamma_\infty + \frac{1-\gamma_\infty}{2}Er\left[(1-0.3P_d)\times\cos\left(\frac{2\pi}{a_\gamma + 1.6Er^2}\frac{R-r}{P_d d_p}\right) + 0.3P_d\right],$$

where γ_∞ is the porosity in an unbounded packed bed; R is the radius of the packed bed; r is the radial position concerned; a_γ is a constant depending on the ratio of the particle size to the column size:

$$a_\gamma = \frac{2R}{n_\gamma P_d d_p} - 1.6\exp\left[-2.4P_d\left(\frac{R}{d_p}\right)^{3/4}\right]$$
$$n_\gamma = \text{int}\left\{\frac{2}{1+1.6\exp\left[-2.4P_d(R/d_p)3/4\right]}\frac{R}{P_d d_p}\right\}$$

The Er is the exponential decaying function, which is given by

$$Er = \exp\left[-1.2P_d\left(\frac{R-r}{d_p}\right)^{3/4}\right],$$

where P_d is the period of oscillation normalized by the nominal particle size and $P_d = 0.94$ for sphere particle.

Determination of S_{TG}

The source term S_{TG} in the adsorbate conservation equation for gas phase can be expressed by

$$S_{TG} = h_s(1-\gamma)a_p(T_s - T_G) - h_w a_{w1}(T_G - T_{w1})$$

The first term on the right-hand side of foregoing equation represents the transfer of heat of adsorption from the outer surface of solid adsorbent particle to the gas phase; the second term represents the heat transfer from the gas phase to the column wall. In the equation, h_s is heat transfer film coefficient between solid adsorbent surface and the gas phase; a_p is the outer surface of the solid adsorbent; T_s is the

outer temperature of the solid adsorbent; T_G is the temperature of the gas phase; h_w is the heat transfer film coefficient between gas phase and the inner wall of the column; a_{w1} is the inner area of the column wall; T_{w1} is the temperature of the inner wall.

Determination of S_{TS}

The source term S_{TS} in the equation of energy conservation for solid adsorbent can be written as

$$S_{TS} = \Delta H \rho_s (1-\gamma)\frac{\partial q}{\partial t} - h_s(1-\gamma)a_p(T_s - T_G),$$

where ΔH is the heat of adsorption; q is the concentration of adsorbate in the solid surface; $\frac{\partial q}{\partial t}$ is the rate of adsorption, equal to S_{mG}; h_s is the film coefficient of heat transfer. h_s can be calculated by [7]:

$$h_s = \frac{h_G}{R_p}Nu, \quad Nu = \frac{0.357}{2\gamma}Re_p^{0.641}Pr^{1/3},$$

where Re_p is the Reynolds number based on particle diameter.

Determination of S_{TW}

The source term S_{TW} in the energy conservation equation for the column wall is given by

$$S_{TW} = h_{w1}a_{w1}(T_G - T_{w1}) - h_{w2}a_{w2}(T_{w2} - T_0)$$

The first term on the right side of the equation represents the heat transfer from gas phase to the inner wall of the column; the second term represents the heat transfer from outer wall of the column to the environment. The T_{w1} and T_{w2} are, respectively, the temperature of the inner and outer walls of the column; T_0 is environmental temperature; h_{w1} is the film coefficient of heat transfer between gas and inner column wall; h_{w2} is the film coefficient of heat transfer between outer column wall and the environment; a_{w1} and a_{w2} are, respectively, the inner and outer area of the column wall. Considering the high thermal conductivity of the column wall, T_{w1} and T_{w2} are practically equal, and the difference between a_{w1} and a_{w2} is very small, the foregoing equation can be written as

$$h_{w1}a_{w1}(T_G - T_{w1}) = h_{w2}a_{w2}(T_{w2} - T_0) = h_w a_w (T_G - T_0) = Q_w,$$

where Q_w is the heat loss from outer surface of the adsorption column to the environment; h_w is the film coefficient of heat transfer, which is equal to

$$h_w = \frac{h_{w1}h_{w2}}{h_{w1} + h_{w2}},$$

where h_{w1} and h_{w2} can be calculated by [8]:

$$h_{w1} = 0.023 \frac{k_G}{d_{col}} (Re_{col})^{0.8} (\mathrm{Pr})^{0.3}$$
$$h_{w2} = b_h \frac{k_G}{Z} (Gr\ Pr)^n,$$

where k_G is the thermal conductivity of the gas phase, d_{col} is the column inner diameter, Re_{col} is the Reynolds number based on the column diameter, Pr is the Prandtl number, Z is the height of the packed bed, Gr is the Grashof number, and b_h and n are heat convection parameters.

Determination of S_{mG}

Source term S_{mG} (kg m^{-3} s^{-1}) in the species conservation equation represents the rate of mass adsorbed, which can be expressed by

$$S_{mG} = K_G a_p \left(c_A - c_A^*\right),$$

where c_A is the mass concentration of adsorbate in the gas phase (kg m^{-3}), c_A^* is the c_A in equilibrium with the solid adsorbent surface; K_G is the mass transfer coefficient (m^2 s^{-1}) based on the gas-phase driving force $(c_A - c_A^*)$ and includes the intraparticle mass transfer; a_p is the volumetric surface area of the packing particle (m^2 m^{-3}). K_G is given by [9]:

$$\frac{1}{K_G} = \frac{1}{k_G} + \frac{1}{\gamma_p k_p},$$

where γ_p is the porosity of the particle; k_G is the film coefficient of mass transfer between gas phase and the outer surface of the particle; k_p is the intraparticle mass transfer coefficient of the particle, which can be calculated by [10]:

$$k_p = \frac{5D_p}{R_p},$$

where R_p is the particle radius; D_p is the pore diffusivity as given by Yang [11]. The k_G can be calculated by the following correlation [12]:

$$\frac{k_G d_p}{D} = 2.0 + 1.1\ Re_p^{0.6} Sc^{0.33},$$

where Re_p is the Reynolds number based on particle diameter.

4.1.4 Simulated Results and Verification

The object of simulation is the adsorption of methylene chloride vapor in air on an activated carbon column, and the simulated results were compared with published

Table 4.1 Properties of the adsorption column and the adsorbent particles

Term (unit)	Value
Inside diameter R (m)	0.41
Packed column height Z (m)	0.20
Average particle size d_p (m)	0.002
Bulk density ρ_s (kg m^{-3})	420
Particle porosity γ_p	0.67
Average column porosity γ_∞	0.42
Specific heat of gas C_{pg} (J kg^{-1} K^{-1})	970
Specific heat of adsorbent C_{ps} (J kg^{-1} K^{-1})	836
Ambient temperature T_0 (K)	298
Thermal conductivity of adsorbent k_s (W m^{-1} K^{-1})	0.3
Heat of adsorption of adsorbate ΔH (J mol^{-1})	28,020

experimental data [13]. The details of adsorption column and adsorbent particle properties are given in Table 4.1.

Since the adsorption process is unsteady, a convenient method of solution is dividing the process time into a large number of time intervals Δt for stepwise computation. The Δt in present case is set to be 1 min which is about 1/140 of the total adsorption time.

The simulated results and comparison with experimental data are given below.

Concentration profile along the column at different times

The simulated profiles of adsorbate, methylene chloride, at different times are given in Fig. 4.1, in which the development of the concentration profiles in the column with time is seen. The concentration profiles enable to provide detailed inside information of the breakthrough curve. For instance, although Y_{out}/Y_{in} almost approaches to zero at 15 and 45 min., large amounts of methylene chloride have been adsorbed in the column as shown in the concentration profile. From 105 to 135 min., the adsorption in the column is substantially being saturated,but Y_{out}/Y_{in} is still less than 1.0. As also seen in the figure, the methylene chloride

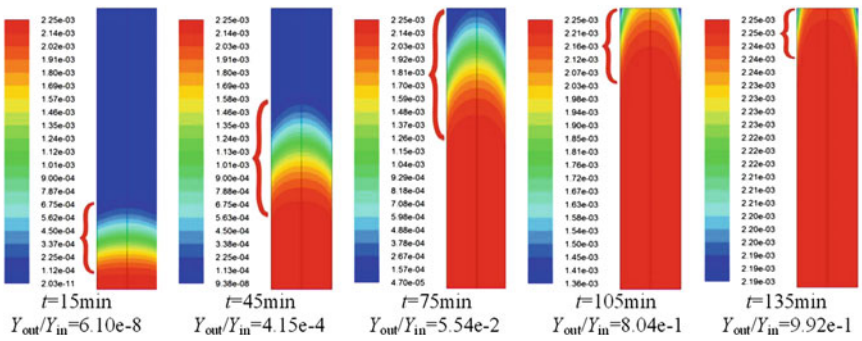

Fig. 4.1 Sequences of concentration profiles along the column at different times. (two-equation model). Reproduced from Li et al. [1]

concentration distributions along radial direction are unevenly parabolic shape. It is due to the existence of flow dispersion, nonuniform porosity, and the wall effect; these influential factors have been considered and modeled in the present simulation. Besides, Fig. 4.1 also shows more details of the progress of the adsorption in the column at different times. The rate of adsorption in the column from 15 to 45 min is seen much faster than from 105 to 135 min. This result is helpful to understand the process dynamics and the optimization of the adsorption process.

In the adsorption column, the adsorption is taken place only in certain part of column height as represented by the red bracket shown in Fig. 4.1. The parabolic form of concentration distribution is obvious due to the wall effect.

Breakthrough curve

From the radial average of Y_{out} and Y_{in} at different times as given in Fig. 4.1, the simulated breakthrough curve can be obtained as shown in Fig. 4.2. The simulated curve matches closely the experimental data. In this figure the simulation by Hwang et al. [13] is also given. Their simulation was based on assuming the turbulent mass diffusivity D_t to be separately 1.5×10^{-2}, 1.5×10^{-3}, and 1.5×10^{-4}, and the best fitting to the experimental data was found to be 1.5×10^{-3}; such simulation is shown in Fig. 4.1. The advantage of present model is avoiding the use of any empirical or guessing means to estimate the D_t.

Distribution of the turbulent diffusivities

Figure 4.3 shows the profile of turbulent mass diffusivity D_t in the adsorption column at $t = 75$ min. It is clearly seen that the distribution of D_t is complicated and cannot be much simplified as a constant as usually done. Moreover, D_t is determined by many factors, such as the type and the shape of solid adsorbent, operating condition, adsorption system, thus only the simulated profile can show the distribution of D_t so that the inside picture of mass transfer can be further understood. More details on the radial variation at different heights of the column for D_t and μ_t are given in Figs. 4.3 and 4.4. The turbulent Schmidt number Sc_t can be calculated by $Sc_t = \mu_t/D_t$ as shown in Fig. 4.5, in which Sc_t is seen changing sharply in axial

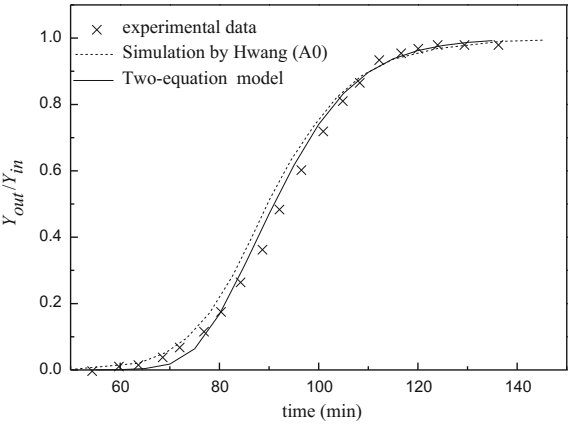

Y is the mole fraction of adaorbate in gas phase

Fig. 4.2 Comparison between simulated breakthrough curve and experimental data. Reprinted with permission from A rigorous model for the simulation of gas adsorption and its verification. *Ind. Eng. Chem. Res.*, 2011, 50(13): 8361–8370. Copyright (2011) American Chemical Society

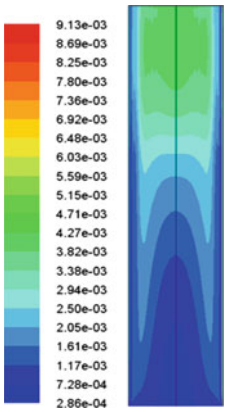

(a) Distribution along column

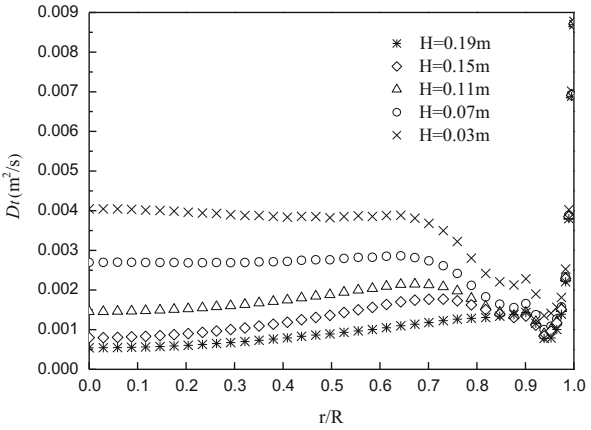

(b) Radial distribution

H 羊 Height of the packed bed measured from column bottom (H=0 at column bottom)

Fig. 4.3 Profiles of D_t at 75 min. Reprinted with permission from A rigorous model for the simulation of gas adsorption and its verification. *Ind. Eng. Chem. Res.*, 2011, 50(13): 8361–8370. Copyright (2011) American Chemical Society

and radial directions. The value of Sc_t in the main flow region is changing significantly from 0.035 to 0.01.

Similarly, the radial distribution of turbulent Peclet number Pe_t can be calculated as shown in Fig. 4.6a, in which its variation throughout the column is seen. It is interested to compare Figs. 4.5 and 4.6 with the radial distribution of velocity as shown in Fig. 4.6b. The velocity drops sharply near the column wall is the main cause of making Sc_t and Pe_t approach zero toward the wall.

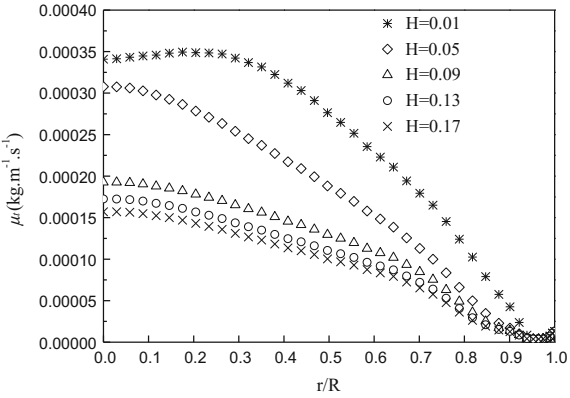

H 羊 Height of the packed bed measured from column bottom (H=0 at column bottom)

Fig. 4.4 Radial distribution of μ_t at 75 min. Reprinted with permission from A rigorous model for the simulation of gas adsorption and its verification. *Ind. Eng. Chem. Res.*, 2011, 50(13): 8361–8370. Copyright (2011) American Chemical Society

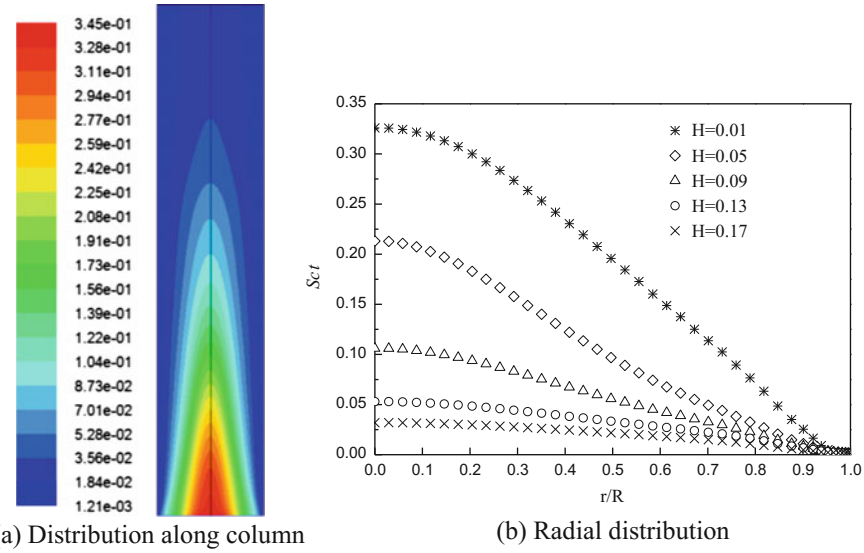

Fig. 4.5 Profiles of Sc_t at 75 min. Reprinted with permission from A rigorous model for the simulation of gas adsorption and its verification. *Ind. Eng. Chem. Res.*, 2011, 50(13): 8361–8370. Copyright (2011) American Chemical Society

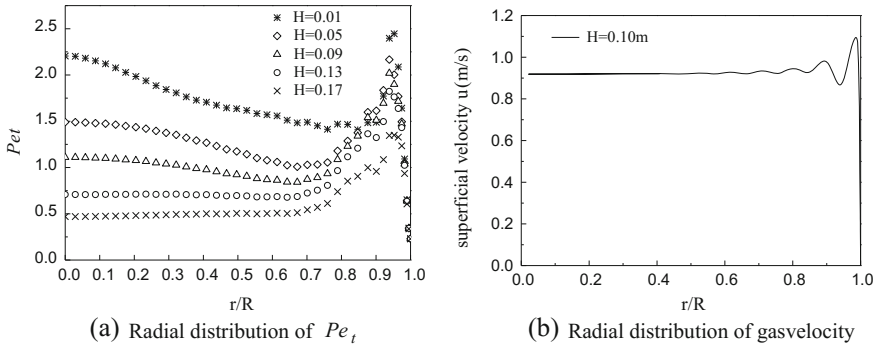

Fig. 4.6 Radial distribution of Pe_t and gas velocity at 75 min. Reprinted with permission from A rigorous model for the simulation of gas adsorption and its verification. *Ind. Eng. Chem. Res.*, 2011, 50(13): 8361–8370. Copyright (2011) American Chemical Society

4.1.5 Simulation for Desorption (Regeneration) and Verification

The model equations for desorption are the same as in Sect. 4.1. The object of simulation is also the experimental desorption of methylene chloride by Hwang [13] in the same column as adsorption. The purge gas is nitrogen at the inlet temperature of 298 K.

Concentration profiles of the purge gas along the column

The serial concentration profiles of the purge gas at different times are given in Fig. 4.7, which shows the details of the progress of the regeneration in the column.

Regeneration curve

The simulated regeneration curve can be obtained by the radial average of Y_{out} and Y_{in} of the purge gas at different times (Fig. 4.7) as plotted in Fig. 4.8, in which comparison is made with experimental data. It shows that the ratio Y_{in}/Y_{out} of methylene chloride increases rapidly at the initial stage, reach maximum about 4.1 at 16 min, then decrease to 1.0 at 35 min, and gradually drop to zero. The simulated curve is in agreement with the experimental measurement. In Fig. 4.8, the simulation curve by Hwang [13] is also given; it was done by preassuming different values of D_t and found the best fitted curve. The serial concentration profiles of the purge gas along the column are given in Fig. 4.7, which shows the details of the behaviors of the regeneration in the column.

Temperature distribution of the purge gas

The simulated profiles of the purge gas temperature along the column at different times are given in Fig. 4.9 showing the uneven axial and radial temperature distribution.

In order to compare the simulated result with experimental data, the radial average of purge gas temperatures at different times and at different heights (z = 0 m, 0.1 m, 0.2 m of the column) are calculated as shown in Fig. 4.10.

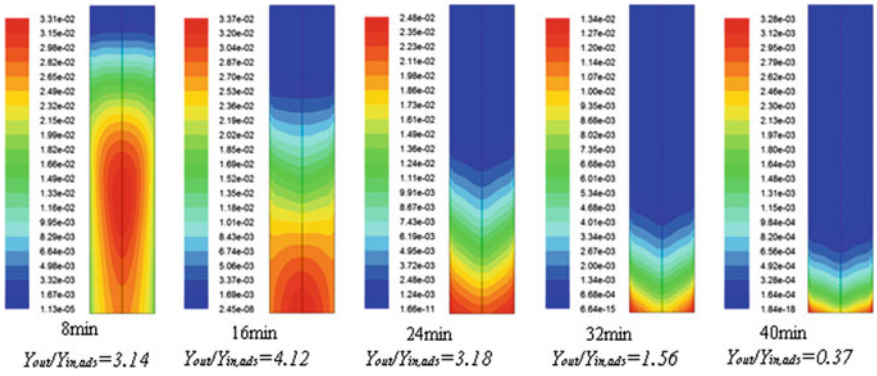

Fig. 4.7 Concentration profiles of the purge gas at different times. (two-equation model). Reprinted with permission from A rigorous model for the simulation of gas adsorption and its verification. *Ind. Eng. Chem. Res.*, 2011, 50(13): 8361–8370. Copyright (2011) American Chemical Society

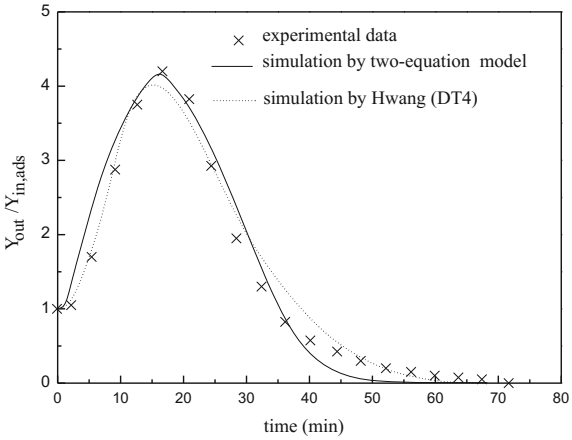

Fig. 4.8 Comparison between simulated regeneration curve with experimental data. Reprinted with permission from A rigorous model for the simulation of gas adsorption and its verification. *Ind. Eng. Chem. Res.*, 2011, 50(13): 8361–8370. Copyright (2011) American Chemical Society

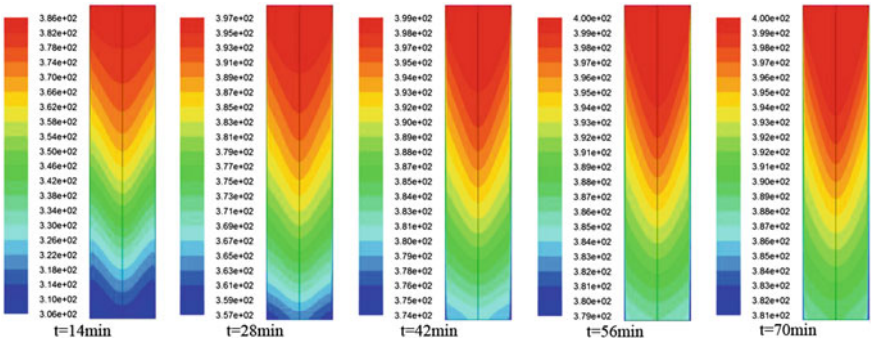

Fig. 4.9 Temperature profiles of purge gas along column at different times (two-equation model). Reprinted with permission from A rigorous model for the simulation of gas adsorption and its verification. *Ind. Eng. Chem. Res.*, 2011, 50(13): 8361-8370. Copyright (2011) American Chemical Society

As seen from Fig. 4.10, each temperature curve consists of an ascending part and a relatively steady part. The initial entering purge gas temperature is 299 K and it is gradually heated up to 399 K by a preheater. Following the progress of regeneration, the heat supply by incoming hot purge gas is greater than the heat needed for desorption and environmental loss; therefore, the gas temperatures at different column heights are raised sharply forming the ascending part of the temperature curve. When most of the methylene chloride have been desorbed and only a smaller part of the sensible heat of the purge gas is sufficient to balance the heat needed for remaining desorption and the heat loss, so that the purge gas

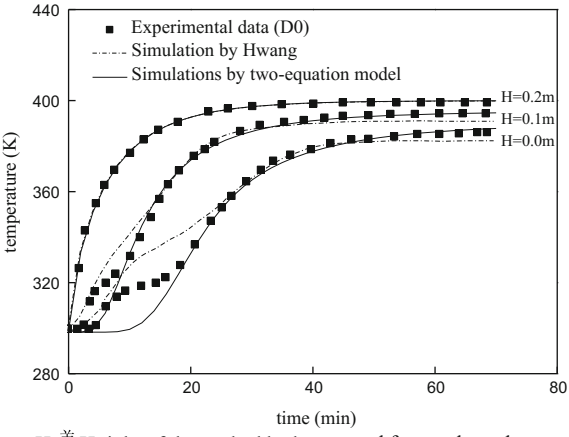

Fig. 4.10 Comparison of purge gas temperature and experimental data. Reprinted with permission from A rigorous model for the simulation of gas adsorption and its verification. *Ind. Eng. Chem. Res.*, 2011, 50(13): 8361–8370. Copyright (2011) American Chemical Society

temperature is maintained almost constant, forming the relatively steady part of the temperature curve. In Fig. 4.10, some deviations could be seen in the region of the ascending part profiles for the z = 0.1 and 0.2 m the curves; it may be due to the assumption that the heat of desorption is equal to the heat of adsorption in magnitude but opposite in sign in the ascending part is overestimated, so that the measured temperatures of purge gas are higher than the simulated temperatures at H = 0.1 m before 10 min and H = 0.2 m before 20 min. After those times, the regeneration approaching to the end and the heat needed for desorption gradually drop to zero; thus, the simulated temperatures are closely checked by the measurements. As mentioned previously, the simulated curve by Hwang is obtained by setting three values of D_t and to find the best one to fit the experimental data.

4.2 Reynolds Mass Flux Model

In this section, the standard Reynolds mass flux model (abbreviated as standard RMF model) is employed. The assumptions are the same as in Sect. 4.1.

4.2.1 Model Equations

(I) The CFD equation set

Mass conversation for gas phase

$$\frac{\partial(\rho_{\mathrm{G}}\gamma)}{\partial t}+\frac{\partial(\rho_{\mathrm{G}}\gamma U_i)}{\partial x_i}=S_{\mathrm{mG}}$$

Momentum conversation for gas phase

$$\frac{\partial(\rho_{\mathrm{G}}\gamma U_i)}{\partial t}+\frac{\partial\left(\rho_{\mathrm{G}}\gamma U_iU_j\right)}{\partial x_i}=-\gamma\frac{\partial P}{\partial x_j}+\frac{\partial}{\partial x_i}\left(\gamma\mu\frac{\partial U_j}{\partial x_i}-\gamma\rho_{\mathrm{G}}\overline{u_i'u_j'}\right)+S_{\mathrm{FG}},$$

where $\overline{u_i'u_j'}$ is given by

$$\begin{aligned}\frac{\partial\overline{u_i'u_j'}}{\partial t}+U_k\frac{\partial\overline{u_i'u_j'}}{\partial x_k}=&\frac{\partial}{\partial x_k}\left(C_0\frac{k}{\varepsilon}\overline{u_i'u_j'}\frac{\partial\overline{u_i'u_j'}}{\partial x_k}+\frac{\mu}{\rho}\frac{\partial\overline{u_i'u_j'}}{\partial x_k}\right)-\left(\overline{u_i'u_k'}\frac{\partial U_j}{\partial x_k}+\overline{u_i'u_k'}\frac{\partial U_i}{\partial x_k}\right)\\&-C_1\frac{\varepsilon}{k}\left(\overline{u_i'u_j'}-\frac{2}{3}k\delta_{ij}\right)-C_2\left(\overline{u_i'u_k'}\frac{\partial U_j}{\partial x_k}+\overline{u_i'u_k'}\frac{\partial U_i}{\partial x_k}-\frac{2}{3}\delta_{ij}\overrightarrow{u_i'u_k'}\frac{\partial U_i}{\partial x_k}\right)-\frac{2}{3}\varepsilon\delta_{ij}\end{aligned}\tag{1.23}$$

The constants are as follows: $C_0 = 0.09$, $C_1 = 2.3$, $C_2 = 0.4$. The k and ε in foregoing equation are given by

$$\begin{aligned}\frac{\partial(\rho_{\mathrm{G}}\gamma k)}{\partial t}+\frac{\partial(\rho_{\mathrm{G}}\gamma U_ik)}{\partial x_i}&=\frac{\partial}{\partial x_i}\left[\gamma\left(\mu+\frac{\mu_t}{\sigma_k}\right)\frac{\partial k}{\partial x_i}\right]+\gamma G_k-\rho_{\mathrm{G}}\gamma\varepsilon\\\frac{\partial(\rho_{\mathrm{G}}\gamma\varepsilon)}{\partial t}+\frac{\partial(\rho_{\mathrm{G}}\gamma U_i\varepsilon)}{\partial x_i}&=\frac{\partial}{\partial x_i}\left[\gamma\left(\mu+\frac{\mu_t}{\sigma_\varepsilon}\right)\frac{\partial\varepsilon}{\partial x_i}\right]+C_{1\varepsilon}\gamma\frac{\varepsilon}{k}G_k-C_{2\varepsilon}\rho_{\mathrm{G}}\gamma\frac{\varepsilon^2}{k}\\G_k&=\mu_t\left(\frac{\partial U_i}{\partial x_j}+\frac{\partial U_j}{\partial x_i}\right)\frac{\partial U_i}{\partial x_k},\end{aligned}$$

where γ is the porosity of the packed bed; model constants are as follows [2]: $C_{1\varepsilon} = 1.44$, $C_{2\varepsilon} = 1.92$, $\sigma_k = 1.0$, $\sigma_\varepsilon = 1.3$.

(II) The heat transfer equation set

Energy conservation for adsorbate in gas phase

$$\frac{\partial(\rho_{\mathrm{G}}\gamma C_{\mathrm{pG}}T_{\mathrm{G}})}{\partial t}+\frac{\partial(\rho_{\mathrm{G}}\gamma C_{\mathrm{pG}}U_iT_{\mathrm{G}})}{\partial x_i}=\frac{\partial}{\partial x_i}\left[\rho_{\mathrm{G}}\gamma C_{\mathrm{pG}}\alpha\frac{\partial T_{\mathrm{G}}}{\partial x_i}-\overline{u'T'}\right]+S_{\mathrm{TG}},$$

where $\overline{u_i'T'}$ is given by

$$\begin{aligned}\frac{\partial\overline{u_i'T'}}{\partial t}+U_i\frac{\partial\overline{u_i'T'}}{\partial x_k}=&\frac{\partial}{\partial x_k}\left[\left(C_{T1}\frac{k}{\varepsilon}\overline{u_i'u_j'}+\alpha\right)\frac{\partial\overline{u_i'T'}}{\partial x_k}\right]\\&-\left(\overline{u_i'u_k'}\frac{\partial T}{\partial x_k}+\overline{u_k'T'}\frac{\partial U_j}{\partial x_k}\right)-C_{\mathrm{T2}}\frac{\varepsilon}{k}\overline{u_i'T'}+C_{\mathrm{T3}}\overline{u_k'T'}\frac{\partial U_i}{\partial x_k}\end{aligned}$$

The constants are: $C_{t1} = 0.07$, $C_{t2} = 3.2$, $C_{T3} = 0.5$.

Energy conservation for solid adsorbent

$$\frac{\partial\left[\rho_s(1-\gamma)C_{ps}T_s\right]}{\partial t} = \frac{\partial}{\partial x_i}\left[(1-\gamma)\lambda_s\frac{\partial T_s}{\partial x_i}\right] + S_{TS}$$

Energy conservation for the column wall

$$\frac{\partial\left(\rho_w C_{pw}T_w\right)}{\partial t} = \frac{\partial}{\partial x_i}\left(\lambda_w\frac{\partial T_w}{\partial x_i}\right) + S_{TW}$$

(III) **The mass transfer equation set**

Species mass conservation for gas phase

$$\frac{\partial(\gamma C)}{\partial t} + \frac{\partial(\gamma U_i C)}{\partial x_i} = \frac{\partial}{\partial x_i}\left[\gamma D\frac{\partial C}{\partial x_i} - \overline{u_i'c'}\right] + S_{CG},$$

where $\overline{u_i'c'}$ is calculated by

$$\begin{aligned}\frac{\partial\overline{u_i'c'}}{\partial t} + U_j\frac{\partial\overline{u_i'c'}}{\partial x_i} = \frac{\partial}{\partial x_i}\left[\left(C_{c1}\frac{\varepsilon}{k}\overline{u_i'u_j'} + \frac{\mu}{\rho}\right)\frac{\partial\overline{u_i'c'}}{\partial x_j}\right] \\ - \left(\overline{u_i'u_j'}\frac{\partial C}{\partial x_j} + \overline{u_j'c'}\frac{\partial U_i}{\partial x_j}\right) - C_{c2}\frac{\varepsilon}{k}\overline{u_i'c'} + C_{c3}\overline{u_j'c'}\frac{\partial U_i}{\partial x_j}\end{aligned} \tag{1.26}$$

The model constants are: $c_1 = 0.09$, $c_2 = 1.8$, $c_3 = 0.6$

Boundary condition and evaluation of source terms

Inlet ($x = 0$): Similar to the absorption column in Chap. 3:

$$u = u_{in},\ C = C_{in},\ T = T_{in}$$

Outlet ($x = Z$): Consider as fully developed turbulence.

Column wall: No slip condition is adopted.

Evaluation of source terms: The evaluation is the same as in Sect. 4.1.

4.2.2 Simulated Results and Verification

The object of simulation is the adsorption of methylene chloride vapor in air on an activated carbon column as described in Sect. 4.1.2.

Concentration profile along the column at different times

The simulated profiles of adsorbate, methylene chloride, at different times are given in Fig. 4.11, in which the development of the concentration profiles in the

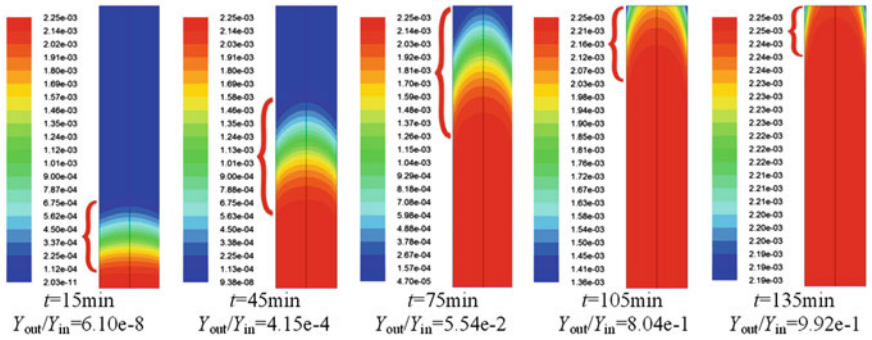

Fig. 4.11 Sequences of concentration distribution along adsorption column in mole fraction at different times (standard Reynolds mass flux model) [14]

column with time is seen. In comparison with Fig. 4.1, it is found that the simulation is closely similar. Yet after careful comparison, the shape of concentration distribution in the adsorption section (represented by the red brackets) is somewhat different. The parabolic shape of purge gas concentration distribution is more obvious using standard Reynolds mass flux model due to better simulation near the column wall.

Breakthrough curve

The simulated breakthrough curve and experimental data are shown in Fig. 4.12, in which the simulation is in agreement with experimental data.

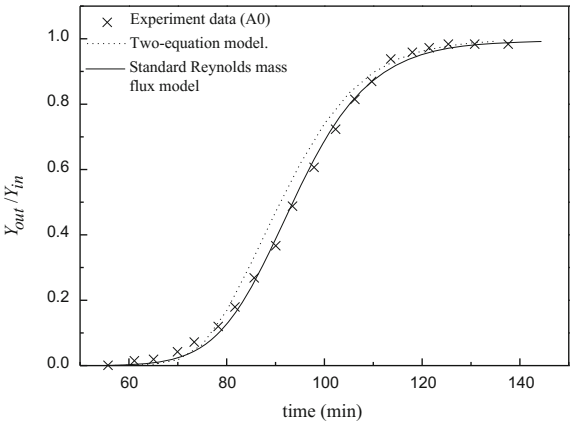

Fig. 4.12 Comparison of simulated breakthrough curve with experimental data [14]

Y is the mole fraction of adaorbate in gas phase

4.2.3 Simulation for Desorption (Regeneration) and Verification

The model equations for desorption are the same as in Sect. 4.1 and the object of simulation is the same as in Sect. 4.1.5, i.e., experimental desorption of methylene chloride from solid adsorbent by Hwang [13].

Concentration profiles of the purge gas along the column

The simulated concentration profiles of the regeneration (desorption) column is shown in Fig. 4.13.

Regeneration curve

The simulated regeneration curve using standard Reynolds mass flux model is shown in Fig. 4.14.

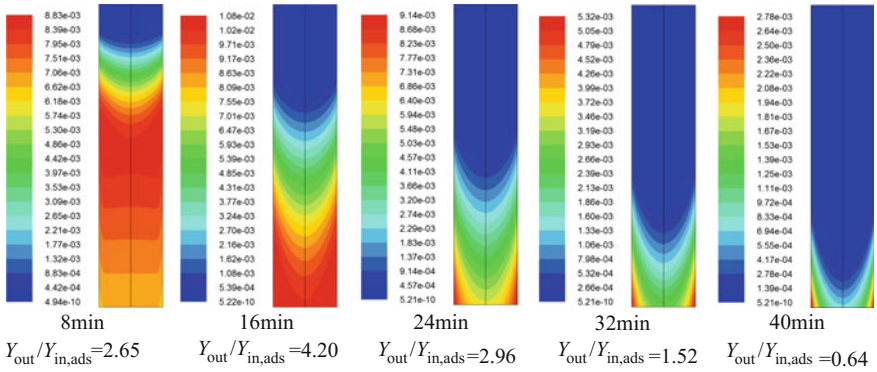

Fig. 4.13 Sequences of concentration distribution along regeneration column in mole fraction at different times (standard Reynolds mass flux model)

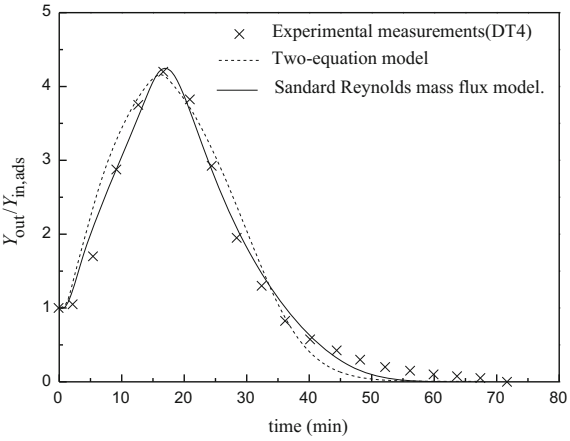

Fig. 4.14 Comparison between different simulated regeneration curves with experimental data

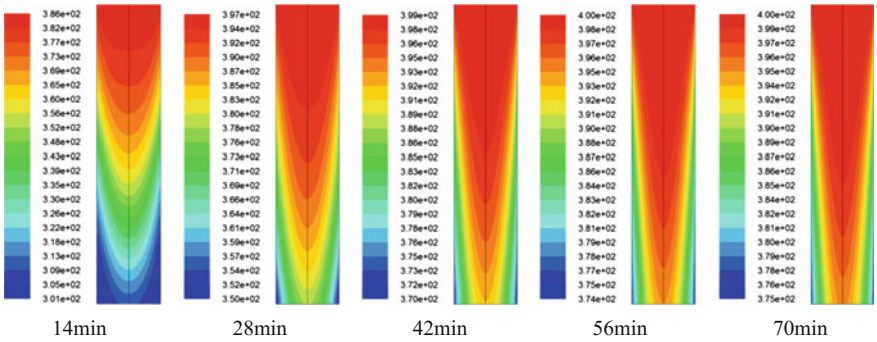

Fig. 4.15 Temperature profiles of purge gas along column at different times (Standard Reynolds mass flux model)

As seen in Fig. 4.14, the simulated curve using standard Reynolds mass flux model is better than that by two-equation model.

Temperature distribution of the purge gas

The simulated profiles of the purge gas temperature along the column at different times are given in Fig. 4.15.

The radial average of purge gas temperatures at different times and at different heights (H = 0 m, 0.1 m, 0.2 m of the column) are calculated as shown in Fig. 4.16.

As seen in Fig. 4.16, the deviation of experimental data is obvious in H = 0.1 and 0.2 and the simulations are in agreement with other experimental data.

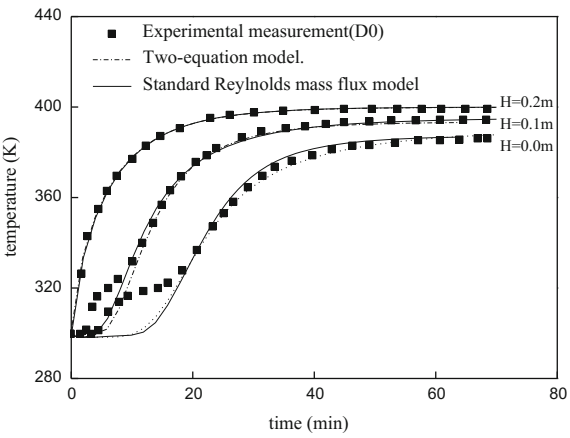

Fig. 4.16 Comparison of simulated purge gas temperature with experimental data

4.3 Summary

As the adsorption process is unsteady and accompanied with heat effect, the time parameter is involved in the model equations. The simulated concentration profile of the column at different times enables to show the progress of adsorption along the column as an indication of the process dynamics. The simulated breakthrough curve for adsorption and regeneration curve for desorption by the two CMT models are well checked with the experimental data except some deviation on the regeneration curve at the inlet of purge gas. This discrepancy may be due to incorrect assumption on the heat of desorption.

References

1. Li WB, Liu BT, Yu KT, Yuan XG (2011) A rigorous model for the simulation of gas adsorption and its verification. Ind Eng Chem Res 50(13):8361–8370
2. Launder BE, Spalding DB (1972) Lectures in mathematical models of turbulence. Academic Press, London
3. Jone WP, Launder BE (1973) The calculation of low-reynolds-number phenomena with a two-equation model of turbulence. Int J Heat Mass Transf 16:1119–1130
4. Elghobashi SE, LaRue JG (1983) The effect of mechanical stream on the dissipation rate of a scalar variance. In: 4th Symposium on turbulent shear flows, Karlsruhe, Germany, pp 1–5
5. Ergun S (1952) Fluid flow through packed columns. Chem Eng Prog 48(2):89–94
6. Liu S, Long J (2000) Gas-liquid countercurrent flows through packed towers. J Porous Media 3(2):99–113
7. Butt JB (1980) Reaction kinetics and reactor design. Prentice-Hall, NJ
8. Levenspiel O (1993) Engineering flow and heat exchange. Plenum Press, New York
9. Silva JAC, Rodrigues AE (1997) Fixed-bed adsorption of n-pentane/isopentane mixtures in pellets of 5A zeolite. Ind Eng Chem Res 36:3769–3777
10. Glueckauf E (1955) Formulae for diffusion into spheres and their application to chromatography. J Chem Soc 51:1540
11. Yang RT (1987) Gas separation. Adsorption process, Butterworth, Stoneham
12. Wakao N (1978) Particle-to-fluid transfer coefficients and fluid diffusivities at low flow rate in packed beds. Chem Eng Sci 31:1115
13. Hwang KS (1997) Adsorption and thermal regeneration of methylene chloride vapor on an activated carbon bed. Chem Eng Sci 52(7):1111–1123
14. Li WB (2012) Theory and application of computational mass transfer for chemical engineering processes. Ph.D. dissertation, Tianjin University, Tianjin

Chapter 5
Application of Computational Mass Transfer (IV) Fixed-Bed Catalytic Reaction

Abstract In this chapter, an exothermic catalytic reaction process is simulated using computational mass transfer (CMT) models as presented in Chap. 1. The difference between the simulation in this chapter from those in Chaps. 2–4 is that chemical reaction is involved. The source term S_n in the species conservation equation represents not only the mass transferred from one phase to the other, but also the mass created or depleted by a chemical reaction. Thus the application of the CMT model is extended to simulating the chemical reactor. The simulation is carried out on a wall-cooled catalytic reactor for the synthesis of vinyl acetate from acetic acid and acetylene using both $\overline{c'^2} - \varepsilon_{c'}$ model and Reynolds mass flux model. The simulated axial concentration and temperature distributions are in agreement with the experimental measurement. As the distribution of μ_t shows dissimilarity with D_t and α_t, the Sc_t or Pr_t are thus varying throughout the reactor. The anisotropic axial and radial turbulent mass transfer diffusivity are predicted where the wavy shape of axial diffusivity $\boldsymbol{D}_{\mathbf{t,x}}$ along the radial direction indicates the important influence of catalysis porosity distribution on the performance of a reactor.

Keywords Simulation of chemical reactors · Exothermic catalytic reaction · Concentration profile · Turbulent mass transfer diffusivity profile

Nomenclature

a	Surface area, m
C	Mass concentration, kg m^{-3}
$\overline{c^2}$	Concentration variance, kg^2 m^{-6}
C_μ, c_1, c_2	Model parameters in k-ε model equations
C_{c0}, C_{c1}, C_{c2}, C_{c3}	Model parameters in $\overline{c^2}$-ε_c model equations
C_{D0}, C_{D1}, C_{D2}, C_{D3}, C_{D4}	Model parameters in $\overline{t^2}$-ε_t model equations
C_p	Specific heat, J kg^{-1} K^{-1}
C_{si}^s	Mass concentration of reactive species at the surface of catalyst

K.-T. Yu and X. Yuan, *Introduction to Computational Mass Transfer*,
Heat and Mass Transfer, DOI 10.1007/978-981-10-2498-6_5

d_e	Effective diameter of catalyst particle, m
D_e	Effective turbulent mass diffusivity, $m^2\ s^{-1}$
D_s	Intradiffusivity of the catalyst, $m^2\ s^{-1}$
D_t	Turbulent mass diffusivity, $m^2\ s^{-1}$
G	Gas phase flow rate per unit cross-section area, $kg\ m^{-2}\ s^{-1}$
h	Film coefficient of mass transfer, $m\ s^{-1}$
H	Axial distance measured from column bottom ($H = 0$ at column bottom), m
ΔH_r	Heat of reaction, $kJ\ mol^{-1}$
k	Turbulent kinetic energy, $m^2\ s^{-2}$
M	Molar mass, $kg\ mol^{-1}$
Pe_t	Turbulent Peclet number
r	Position in radial direction, m
R	Radius of the column, m; molar reaction rate, mol/kg catalyst.s; apparent reaction rate $mol{\cdot}kg^{-1}\ s^{-1}$
R_0	The resistant coefficient of porous media
R_s	Apparent reaction rate, $kmol\ kg^{-1}$ (cat) s^{-1}
Sc	Turbulent Schmidt number
t_0	Fluid inlet temperature, °C
$\overline{t^2}$	Temperature variance, K^2
T	Temperature, K
U	Fluid superficial velocity, $m\ s^{-1}$
x	Axial position, m
z	Dimensionless distance, $z = (R-r)/d_e$
α, α_t	Molecular and turbulent thermal diffusivities, respectively, $m^2\ s^{-1}$
ε	Turbulent dissipation rate, $m^2\ s^{-3}$
ε_c	Turbulent dissipation rate of concentration fluctuation, $kg^2\ m^{-6}\ s^{-1}$
ε_t	Turbulent dissipation rate of temperature fluctuation, $K^2\ s^{-1}$
Φ	Variable
γ	Porosity distribution of the random packing bed
$\gamma\infty$	Porosity in an unbounded packing
λ	Thermal conductivity, $KJ\ m^{-1}\ K^{-1}\ s^{-1}$
μ_t	Turbulent viscosity, $kg\ m^{-1}\ s^{-1}$
ρ	Density, $kg\ m^{-3}$
ρ_b	Bulk density of catalyst, kg/m^3
ν_t	Turbulent kinetic viscosity, $m^2\ s^{-1}$
σ_c, σ_{ε_c}	Model parameters in $\overline{c^2}$–ε_c model equations
σ_t	Model parameter in $\overline{t^2}$–ε_t model equations
σ_k, σ_ε	Model parameters in k–ε model equations

Subscripts

c Coolant
G Gas phase
i Interface
s Catalyst; reactive species
w Reactor wall
1 Inner
2 Outer

Superscripts

s Surface

The methodology of computational mass transfer is not only applicable to the process involving mass, heat and momentum transfer accompanied with chemical reaction as presented in previous chapters but also to the catalytic reaction process. In this chapter, a fixed-bed catalytic reactor with cooling jacket is used as an example for illustration.

The fixed-bed reactors are most commonly used for undertaking industrial heterogeneous catalytic reactions in the basic chemical, petrochemical, and allied industries, such as the carbon monoxide conversion and ammonia synthesis, the ethylene oxide and vinyl acetate synthesis, and many other reactive processes. The design and performances of such kind of reactors have been extensively reported.

The one-dimensional plug flow model is used early for reactor design and analysis, where the concentration and temperature gradients were assumed only to occur in the axial direction. Later, the flow model with axial mixing is introduced to take into account the mixing effect, which is influential to the temperature and concentration gradients as well as the reactor performances. Afterward the uneven radial concentration distribution was considered using empirical correlations. At the same time, some researchers used the two-dimensional pseudohomogeneous model with the consideration of the radial velocity distribution. The advancement of applying pseudohomogeneous CFD model to reactor design enabled to calculate the velocity profile, whereas the temperature and concentration distributions were obtained using either the turbulent Prandtl number (Pr_t) and turbulent Schmidt number (Sc_t) or the empirical correlations obtained using inert tracer technique for predicting the unknown diffusivities of heat and mass transfer [1]. In fact, such empirical correlations, even available, are unreliable as stated in Chap. 1. The use of computational mass transfer model can overcome such drawback as the turbulent mass and thermal diffusivities need not to be known in advance. In this chapter, the two-equation model and Reynolds mass flux model of computational mass transfer are used for illustrative simulation.

5.1 $\overline{c'^2} - \varepsilon_c$ Two-Equation Model for Catalytic Reactor

Liu [2] used the computational mass transfer $\overline{c'^2} - \varepsilon_c$ two-equation model (abbreviated as two-equation model) for simulating a catalytic reactor with cooling jacket for producing vinyl acetate from acetic acid and acetylene as described below.

5.1.1 Model Equation

Assumptions

(1) Both the reactant and product are in homogeneous fluid phase and the operation is steady;
(2) The fluid phase flow is axially symmetrical in the catalytic reactor (packed column) and in turbulent state;
(3) The temperature of outer catalyst surface is equal to the fluid temperature;
(4) The temperature at the outer wall of the cooling jacket is constant;
(5) The heat created by the friction between catalysis and the fluid is neglected;
(6) The activity of the catalyst remains unchanged.

The mass and volume of the fluid phase are changing in the course of chemical reaction, the source term S_m in the overall mass conservation equation is not equal to zero and the fluid density is not a constant.

In the model equations, the variables $U_i, k, \varepsilon, \rho$, etc., are referred to the gaseous fluid phase (reactant and product) without subscript. Subscripts s and w refer the conditions at the solid phase (catalyst) and reactor wall, respectively.

(I) **CFD equation set**

(A) *Overall mass conservation*

$$\frac{\partial(\rho\gamma U_i)}{\partial x_i} = S_m$$

(B) *Momentum conservation*

$$\frac{\partial\left(\rho\gamma U_i U_j\right)}{\partial x_i} = -\gamma\frac{\partial P}{\partial x_j} + \frac{\partial}{\partial x_i}\left[\gamma\mu\left(\frac{\partial U_j}{\partial x_i}\right) - \gamma\rho\overline{u_i' u_j'}\right] + \gamma(\rho g + R_0 U_i)$$

$$-\rho\overline{u_i' u_j'} = \mu_t\left(\frac{\partial U_i}{\partial x_j} + \frac{\partial U_j}{\partial x_i}\right) - \frac{2}{3}\delta_{ij}\rho k$$

$$\mu_t = \rho C_\mu \frac{k^2}{\varepsilon}$$

(C) *k equation*

$$\frac{\partial(\rho\gamma U_i k)}{\partial x_i} = \frac{\partial}{\partial x_i}\left(\gamma\left(\mu + \frac{\mu_t}{\sigma_k}\right)\frac{\partial k}{\partial x_i}\right) + \gamma G_k - \rho\gamma\varepsilon$$

$$G_k = \mu_t\left(\frac{\partial U_i}{\partial x_j} + \frac{\partial U_j}{\partial x_i}\right)\frac{\partial U_j}{\partial x_i}$$

(D) *ε equation*

$$\frac{\partial(\rho\gamma U_i \varepsilon)}{\partial x_i} = \frac{\partial}{\partial x_i}\left(\gamma\left(\mu + \frac{\mu_t}{\sigma_\varepsilon}\right)\frac{\partial \varepsilon}{\partial x_i}\right) + C_1\gamma G_k\frac{\varepsilon}{k} - C_2\gamma\rho\frac{\varepsilon^2}{k},$$

where γ is the porosity of the catalytic bed; R_0 is the coefficient of resistance created by the fluid flow through the catalyst; μ_t is the turbulent diffusivity of the fluid. The model constants are [3]: C_μ = 0.09, σ_k = 1.0, σ_ε = 1.3, C_1 = 1.44,C_2 = 1.92.

(II) **Heat transfer equation set**

Energy conservation equations:

(A) *Energy conservation of gas phase*

$$\begin{aligned}\frac{\partial\left(\gamma\rho C_p U_i T\right)}{\partial x_i} &= \frac{\partial}{\partial x_i}\left(\gamma\rho C_p(\alpha + \alpha_t)\frac{\partial T}{\partial x_i}\right) + Q_1 - Q_2 \\ &= \frac{\partial}{\partial x_i}\left(\gamma\rho C_p\alpha_e\frac{\partial T}{\partial x_i}\right) + h_s a_s\left(T_s^s - T\right) - h_w a_{w1}(T - T_{w1}),\end{aligned}$$

where T is the temperature of the gas phase; α_t is the thermal diffusivity; α_e is the effective thermal diffusivity $(= \alpha + \alpha_t)$; a_s is the outer surface area of the catalyst ($m^2\ m^{-3}$), T_s^s is the outer temperature of the catalyst; h_s is the gas film mass transfer coefficient between catalyst and the gas phase (kJ $m^{-2}\ K^{-1}$); a_{w1} is the inner surface area of the reactor wall ($m^2 \cdot m^{-3}$); T_{w1} is the temperature at the inner wall of the reactor; h_{w1} is the gas film mass transfer coefficient between gas phase and inner wall of the reactor. The terms on the right side of the equation $Q_1 = h_s a_s\left(T_s^s - T\right)$ represents the heat transfer from the catalyst to the gas phase and $Q_2 = h_{w1}a_{w1}(T - T_{w2})$ represents the heat transfer from the gas phase to the inner wall of the reactor.

(B) *Energy conservation of catalyst*

$$\frac{\partial}{\partial x_i}\left((1-\gamma)\lambda_s\frac{\partial T_s}{\partial x_i}\right)+(1-\gamma)\rho_s(\Delta HR)-h_s a_s\left(T_s^s-T\right)=0,$$

where T_s, ρ_s, λ_s are, respectively, the inner temperature of the catalyst, density of catalyst, thermal conductivity of the catalyst (kJ m^{-1} K^{-1} s^{-1}); R is the apparent reaction rate (mol kg^{-1} s^{-1}); ΔH is the molar heat of reaction (kJ mol^{-1}); h_s is the film coefficient of mass transfer between catalyst and fluid.

(C) *Energy conservation of reactor wall*

$$\frac{\partial}{\partial x_i}\left(\lambda_w\frac{\partial T_w}{\partial x_i}\right)+h_{w1}a_{w1}(T-T_{w1})-h_{w2}a_{w2}(T_{W2}-T_c)=0,$$

where T_w,λ_w is, respectively, the temperature and the thermal conductivity of the reactor wall; h_{w1} is the gas film coefficient of mass transfer coefficient between gas phase and the inner wall surface of the reactor; h_{w2} is the liquid film coefficient of mass transfer coefficient between the outer wall surface of the reactor and the liquid coolant; a_{w1},a_{w2} are, respectively, the inner and outer surfaces of the reactor wall; T_{w1},T_{w2} are, respectively, the temperature of the inner wall surface and the temperature of liquid coolant at the outer wall surface of the reactor; T_c is the average temperature of the coolant.

The turbulent thermal diffusivity

The turbulent thermal diffusivity α_t is calculated using the $\overline{T'^2}-\varepsilon_{T'}$ two-equation model:

$$\alpha_t=C_{T0}k\left(\frac{k}{\varepsilon}\frac{\overline{T'^2}}{\varepsilon_{T'}}\right)$$

$\overline{T'^2}$ *equation*

$$\frac{\partial}{\partial x_i}\left(\rho\gamma U_i\overline{T'^2}\right)=\frac{\partial}{\partial x_i}\left(\rho\gamma\left(\alpha+\frac{\alpha_t}{\sigma_T}\right)\frac{\partial\overline{T'^2}}{\partial x_i}\right)+2\rho\gamma\alpha_t\left(\frac{\partial T}{\partial x_i}\right)^2-2\gamma\varepsilon_{T'}$$

$\varepsilon_{T'}$ *equation*

$$\frac{\partial\rho\gamma U_i\varepsilon_{T'}}{\partial x_i}=\frac{\partial}{\partial x_i}\left[\rho\gamma\left(\alpha+\frac{\alpha_t}{\sigma_{T'}}\right)\frac{\partial\varepsilon_{T'}}{\partial x_i}\right]+C_{T1}\frac{\varepsilon_{T'}}{\overline{T'^2}}\rho\gamma\alpha_t\left(\frac{\partial T}{\partial x_i}\right)^2-C_{T2}\rho\frac{\varepsilon_{T'}}{\overline{T'^2}}\varepsilon_{T'}-C_{T3}\rho\gamma\frac{\varepsilon}{k}\varepsilon_{T'}$$

The model constants are [4]: $C_{T0} = 0.10$, $C_{T1} = 1.8$,$C_{T2} = 2.2$, $C_{T3} = 0.8$, $\sigma_t = 1.0$.

(III) **Mass transfer equation set**

(A) *Mass conservation of reactive species (gas phase)*

$$\frac{\partial(\gamma U_i C)}{\partial x_i} = \frac{\partial}{\partial x_i}\left(\gamma D_e \frac{\partial C}{\partial x_i}\right) + ha_s\left(C_{si}^s - C\right),$$

where C is the mass concentration of the gaseous reactive species (kg m^{-3}), D_e is the effective thermal diffusivity $D_e = D + D_t$; h is the film coefficient of mass transfer between gas phase and the surface of the catalyst; C_{si}^s is the mass concentration of reactive species at the surface of catalyst; a_s is the outer surface area of the catalyst.

(B) *Mass conservation of the solid phase*

$$\frac{\partial}{\partial x_i}\left(D_s \frac{\partial T_s}{\partial x_i}\right) + (1-\gamma)\rho_s(MR) - ha_s\left(C_s^s - C\right) = 0,$$

where D_s is the intradiffusivity of the catalyst; M is the molar mass of the reactive species (kg mol^{-1}); R is the molar reaction rate (mol/kg catalyst. s); ρ_s is the density of the catalyst. If the resistance of intradiffusion is neglected, the foregoing equation can be simplified to

$$k_G a_s\left(C_{si}^s - C\right) = \rho_s(1-\gamma)MR$$

The turbulent mass diffusivity

The turbulent mass diffusivity of the reactive species D_t can be obtained according to $\overline{c'^2} - \varepsilon_{c'}$ model as follows:

$$D_t = C_{T0} k \left(\frac{k}{\varepsilon}\frac{\overline{c'^2}}{\varepsilon_{c'}}\right)^{1/2}$$

$\overline{c'^2}$ *equation*

$$\frac{\partial(U_i\overline{\gamma c'^2})}{\partial x_i} = \frac{\partial}{\partial x_i}\left(\gamma\left(D_L + \frac{D_t}{\sigma_{c'}}\right)\frac{\partial(\overline{c'^2})}{\partial x_i}\right) + 2D_t\gamma\left(\frac{\partial C}{\partial x_i}\right)^2 - 2\gamma\varepsilon_{c'}$$

$\varepsilon_{c'}$ equation

$$\frac{\partial(\gamma U_i \varepsilon_{c'})}{\partial x_i} = \frac{\partial}{\partial x_i}\left(\gamma\left(D_L + \frac{D_t}{\sigma_{\varepsilon_{c'}}}\right)\frac{\partial(\varepsilon_{c'})}{\partial x_i}\right) + C_{c1}\gamma D_t\left(\frac{\partial C}{\partial x_i}\right)^2 \frac{\varepsilon_{c'}}{\overline{c'^2}} - C_{c2}\gamma\frac{\varepsilon_{c'}^2}{\overline{c'^2}} - C_{c3}\gamma\frac{\varepsilon_{c'}\varepsilon}{k}$$

The model constants are [5]: $C_{c0} = 0.11$, $C_{c1} = 1.8$, $C_{c2} = 2.2$, $C_{c3} = 0.8$, $\sigma_c = 1.0$, $\sigma_{\varepsilon_c} = 1.0$.

5.1.2 Boundary Conditions

Inlet (column bottom, $x = 0$): $U = U_{in}$, $V = 0$, $k = 0.003U_{in}^2$, $\varepsilon = 0.09k^{3/2}/d_e$

$$T = T_{in} = T_w, \quad \overline{T'^2} = (0.082\Delta T)^2, \quad \varepsilon_{T'} = 0.4\frac{\varepsilon}{k}\overline{t^2}$$

$$C_{AC} = C_{AC,in}, \quad C_{HAc} = C_{HAc,in}, \quad \overline{c_i^2} = (0.082C_{i,in})^2, \quad \varepsilon_{c_i} = 0.4\frac{\varepsilon}{k}\overline{c_i^2}$$

Outlet (column top, $x = Z$): The fluid flow is considered as fully developed, the gradient of all parameters Φ except pressure is equal to zero.

Axis: all of the variables Φ have a zero gradient due to the assumption of axial symmetry.

Wall: no slip condition is applied; all parameters related to flow are equal to zero.

$$U = V = k = \varepsilon = \overline{T'^2} = \varepsilon_t = \overline{c'^2} = \varepsilon_{c'} = 0$$

Near wall region: the method of standard wall function is employed and the mass flux $\frac{\partial C}{\partial r} = 0$.

5.1.3 Determination of the Source Terms

Porosity of the catalyst bed

For the reactor filled with catalyst of small cylindrical particle, the porosity γ can be represented by the following correlations [5]:

$$\gamma = 2.14z^2 - 2.53z + 1, \quad z \le 0.637$$

$$\gamma = \gamma_\infty + 0.29\exp(-0.6z)\cos(2.3\pi(z - 0.16)) + 0.15\exp(-0.9z), \quad z > 0.637,$$

where γ_∞ is the porosity with unbounded boundary; z is the dimensionless distance from the wall, defined as

$$z = (R - r)/d_e,$$

where d_e is the equivalent diameter of the catalyst.

Coefficient of flow resistance R_0

When fluid phase flowing through the catalyst, the frictional resistance is created. The coefficient of the frictional force R_o can be calculated by the modified Ergun equation [6]:

$$R_0 = 150\mu_L \frac{(1-\gamma)^2}{\gamma^2 d_e^2} + 1.75\rho_G \frac{(1-\gamma)}{\gamma^2 d_e} |\mathbf{U}|$$

Source term S_i

The source term S_i representing the mass of component i is generated by the chemical reaction and can be calculated from the reaction rate,

$$S_i = \pm M_i R_s F_b,$$

where M_i is the molar weight of component i; R_s is the apparent reaction rate, which will be given in the subsequent section; F_b is the bulk density of catalyst. In the equation, negative and positive signs refer to the reactant and product components, respectively.

5.1.4 The Simulated Wall-Cooled Catalytic Reactor

Simulation is made for a wall-cooled fixed-bed catalytic reactor reported by Valstar [7], in which the synthesis of vinyl acetate from acetic acid and acetylene is untaken with zinc acetate on activated carbon as catalyst. The internal and external diameters of the tubular reactor are, respectively, 0.041 and 0.0449 m and the reactor length is 1 m. The gaseous mixture is flowing upward from the bottom of the reactor. The reactor tube is surrounded by a jacketed tube with an internal diameter of 0.0725 m. Cooling oil is pumped through the annular space between the reactor and the cooling tube. The oil temperature is controlled to within ±0.5°C. The radial average conversions and the temperature profiles along the radial direction at different axial positions are measured. The properties of reaction mixture are listed in Table 5.1, and the catalyst specification is listed in Table 5.2.

Table 5.1 Reaction mixture specifications [7]

Case no	t_0 (°C)	Molar ratio	Aver. mol. weight (kg/kmol)	G (kg/m^2 s)	μ 10^{-5} (Ns/m^2)	Re_p	c_p (J/kg K)	k_L (J/m K s)
1	176.1	1.5	39.6	0.242	1.372	58	1680	0.0333
2	176.0	1.5	39.6	0.186	1.369	45	1680	0.0333
3	186.4	1.5	39.6	0.242	1.376	58	1710	0.0344
4	176.1	4.0	32.8	0.200	1.375	48	1800	0.0380

Table 5.2 Catalyst specification [7]

Term (unit)	Value
Average length (mm)	5.4
Average diameter (mm)	2.8
Effective diameter d_e (mm)	3.3
Specific external surface (m^2/g)	0.00217
Specific external surface (m^2/g)	350
Bed porosity	0.36
Bulk density (kg/m^3)	570–600
Particle density (kg/m^3)	910
Thermal conductivity (J/m K s)	0.184

The overall chemical reaction of vinyl acetate synthesis is as follows:

$$CH_3COOH + CH \equiv CH \xrightarrow{Zn(Ac)_2} CH_3COOCH = CH_2 + \Delta H_r$$

The apparent reaction rate of foregoing reaction is given below [7]:

$$R_s = \frac{k_\infty \exp(-E/R_gT)p_{AC}}{1 + \exp(-\Delta H_1/R_gT)\exp(-\Delta S_1/R_g)p_{HAc} + C_r p_{VA}},$$

where k_∞ = 5100 (kmol kg(cat)$^{-1}$ s^{-1} atm^{-1}), E = 85,000 (kJ kmol^{-1}), ΔH_1 = (31,500 kJ·kmol^{-1}), ΔS_1 = −71,000 (kJ kmol^{-1} K^{-1}); C_r = 2.6 (atm^{-1}) for molar ratio of acetylene to acetic acid equal to 1.5; $C_r = \exp\left(-\frac{70000}{R_gT}\right)\exp\left(\frac{170}{R_g}\right)$ (atm^{-1}) for a molar ratio of acetylene to acetic acid equal to 4. The heat of reaction, ΔH_r is function of temperature:

$$\Delta H_r = \Delta_f H_{VA,m} - \Delta_f H_{HAc,m} - \Delta_f H_{AC,m}$$

$$\Delta_f H_{i,m} = A + BT + CT^2,$$

where subscripts VA, HAc, and AC denote, respectively, vinyl acetate, acetic acid, and acetylene; their coefficients *A, B,* and *C* are listed in Table 5.3.

Table 5.3 Coefficients for heat of reaction [8]

Component	A	B	C
Vinyl acetate	−298.36	−6.9870E−02	3.9316E−05
Acetic acid	−417.91	−5.8243E−02	3.3466E−05
Acetylene	228.04	1.5754E−03	−3.5319E−06

5.1.5 Simulated Result and Verification

The species concentration distribution along the whole reactor

Following the progress of the reaction from the bottom ($H = 0$) to the top ($H = 1$) of the reactor, the concentration of acetic acid is gradually decreasing and the product, vinyl acetate, is increasing; that means the conversion is consequently increasing along the reactor from bottom to top. From the simulated concentration profile of acetic acid in the whole column, its concentration in radial direction is averaged at different heights and at different operating conditions of the reactor in order to obtain the average acetic acid conversion along the axial direction. The simulated conversion curve is shown in Fig. 5.1 and compared with the experimental data [8]; satisfactory agreement between them is seen.

The radial temperature profile.

As an example, one of the temperature profiles along the whole reactor is shown in Fig. 5.2. The radial temperatures are averaged at different reactor heights and under different operating conditions as shown in Fig. 5.3, in which the experimental measurements by Valstar et al. and their prediction [8] are also given for comparison. It is seen that the simulated temperature profiles by the present model are closer to the experimental measurements than that by Valstar [8].

The distribution of turbulent mass diffusivity D_t

Using present two-equation model, both the diffusivity profiles of acetylene and acetic acid along the reactor can be obtained as shown in Fig. 5.4. As seen in the figure, the turbulent mass diffusivity of acetylene $D_{t,AC}$ in axial direction becomes steady after traveling from inlet to a distance about 20-fold of effective catalyst diameter d_e (d_e in present case is 3.3 mm). As seen in Fig. 5.4b, the distribution of $D_{t,AC}$ in radial direction in the main flow region increases gradually to a maximum until to about r/R = 0.8 and then decreases sharply toward the column wall. Such tendency is in consistent with the experimental measurement. It is the result of the uneven distribution of porosity, velocity, temperature, and concentration near the wall region.

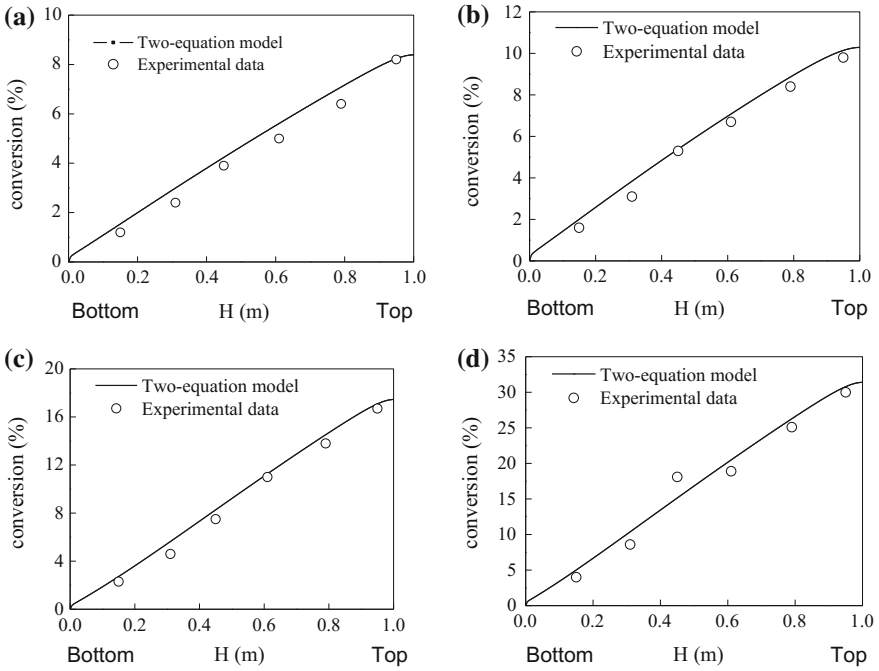

Fig. 5.1 Simulated and measured conversion profiles along reactor axis **a** Case 1, molar ratio = 1.5, t_0 = 176.1 °C, G = 0.242 kg m^{-2} s^{-1}, **b** Case 2, molar ratio = 1.5, t_0 = 176.0 °C, G = 0.186 kg m^{-2} s^{-1}, **c** Case 3, molar ratio = 1.5, t_0 = 186.4 °C, G = 0.242 kg m^{-2} s^{-1}, **d** Case 4, molar ratio = 4.0, t_0 = 176.1 °C, G = 0.200 kg m^{-2} s^{-1} (Reprinted from ref. [2], Copyright 2008, with permission from American Chemical Society)

The turbulent mass diffusivity of acetic acid $D_{t,HAc}$ is also given in Fig. 5.4c, the tendency of its axial and radial distribution is similar to those of acetylene because both of them are in the same temperature and velocity fields although the concentration field is different.

The distribution of turbulent thermal diffusivity α_t

The turbulent thermal diffusivity α_t can also be calculated using two-equation model as shown in Fig. 5.5, in which, similar to the turbulent mass diffusivity D_t, the α_t reaches almost steady condition after traveling a distance about 50-fold of the effective catalyst diameter from the entrance, and decreases sharply afterward.

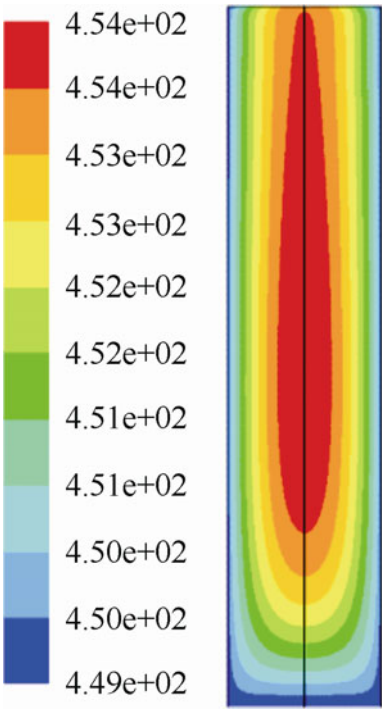

Fig. 5.2 Simulated temperature profile along the reactor for Case 1, molar ratio = 1.5, t_0 = 176.1 °C, G = 0.242 kg m^{-2} s^{-1} (Reprinted from ref. [2], Copyright 2008, with permission from American Chemical Society)

The distribution of turbulent diffusivity v_t

For the comparison purpose, the simulated turbulent diffusivity (kinematic viscosity) v_t is also given in Fig. 5.6. On careful study, the tendency of axial and radial distribution of v_t is similar to that of D_t, and α_t only appears not far from the entrance ($H \leq 0.1$ in the figure), although they are all drop down almost to zero at the wall. The comparison again displays that the $\frac{v_t}{D_t}$ ratio (Sc_t) and $\frac{v_t}{\alpha_t}$ ratio (Pr_t) are complicated, and cannot be simply considered as a constant.

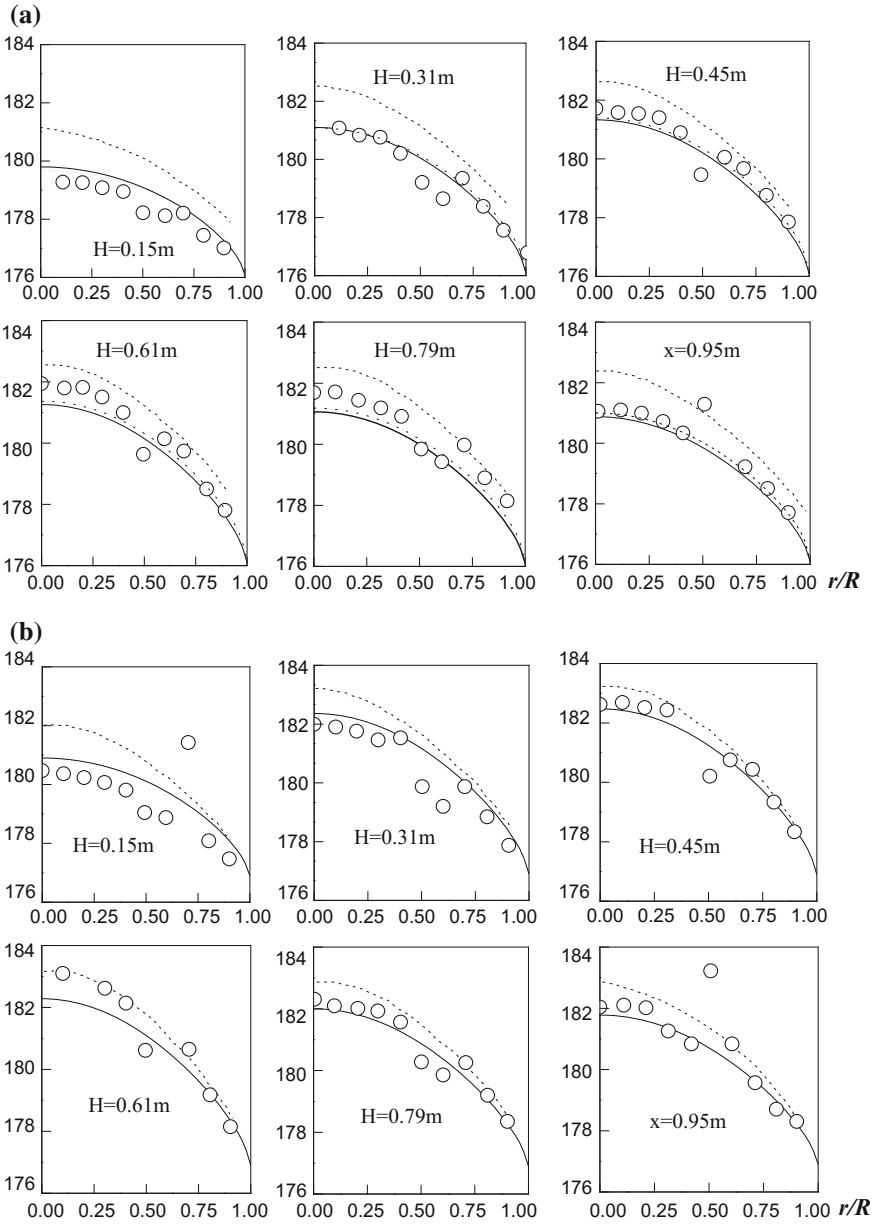

Fig. 5.3 Radial temperature distribution along reactor (*dashed lines* Simulated by two-equation model, *dotted lines* Simulated by Valstar, *open circle* experimental data, *H* bed height measured from bottom, $H = 0$ at the reactor bottom) **a** Case 1, molar ratio = 1.5, t_0 = 176.1 °C, G = 0.242 kg m^{-2} s^{-1}, **b** Case 2, molar ratio = 1.5, t_0 = 176.0 °C, G = 0.186 kg m^{-2} s^{-1}, **c** Case 3, molar ratio = 1.5, t_0 = 186.4 °C, G = 0.242 kg m^{-2} s^{-1}, **d** Case 4, molar ratio = 4.0, t_0 = 176.1 °C, G = 0.200 kg m^{-2} s^{-1} (Reprinted from ref. [2], Copyright 2008, with permission from American Chemical Society)

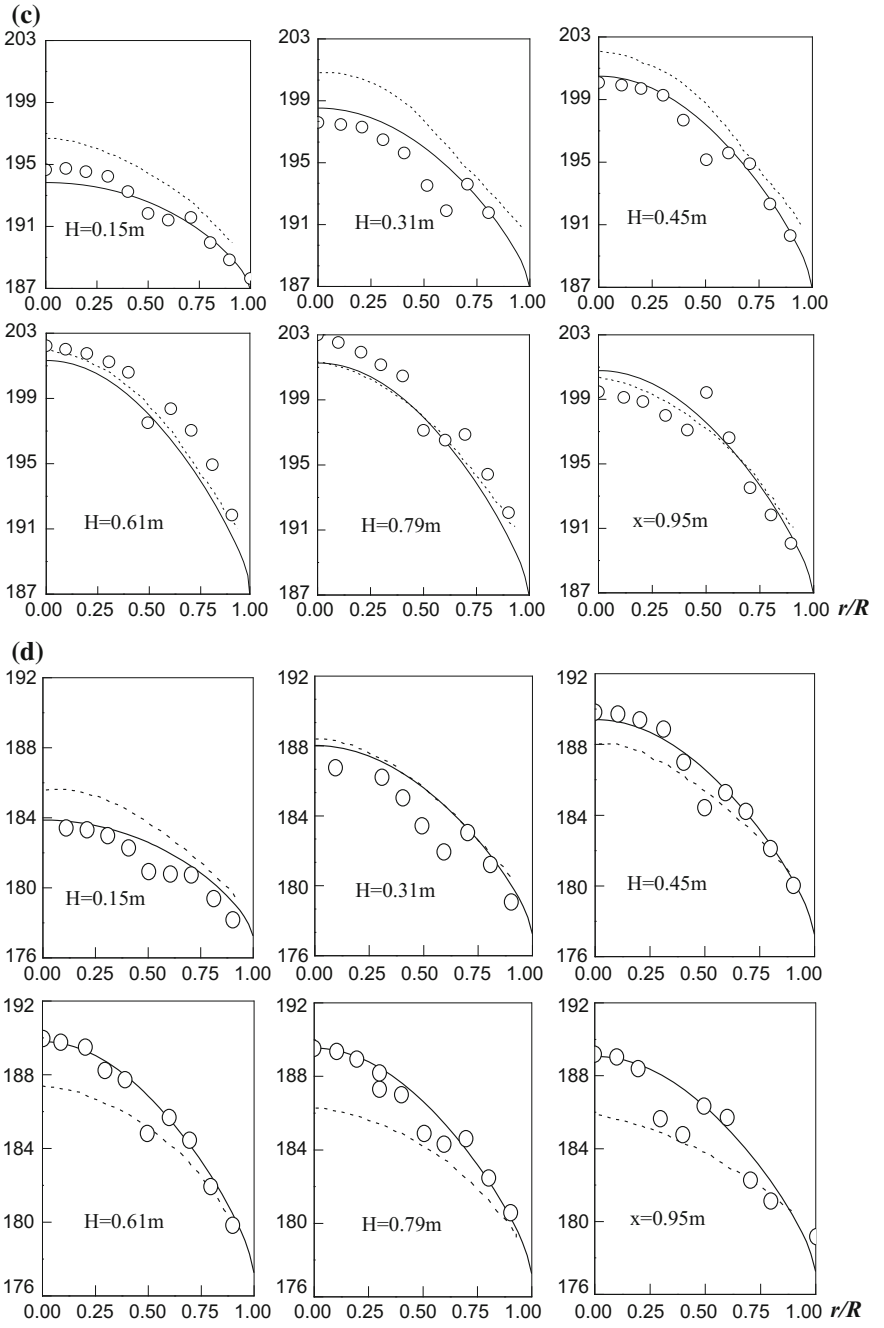

Fig. 5.3 (continued)

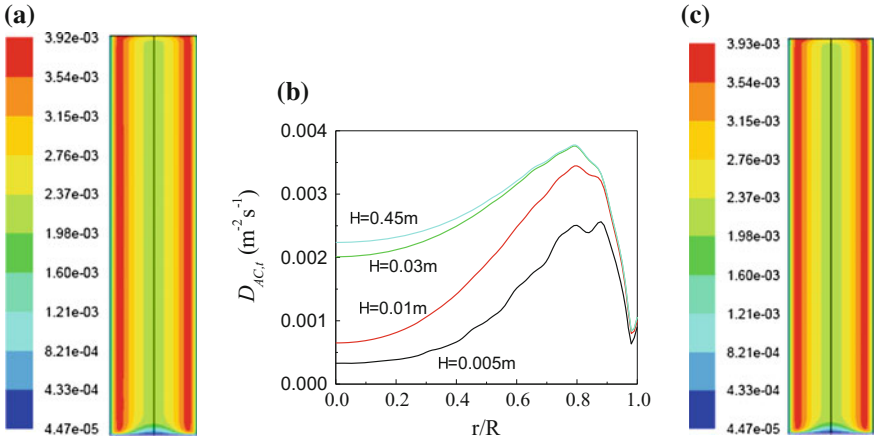

Fig. 5.4 Simulated axial and radial distribution of turbulent mass diffusivity **for** Case 1 **a** acetylene, **b** acetylene, **c** acetic acid (Reprinted from ref. [2], Copyright 2008, with permission from American Chemical Society)

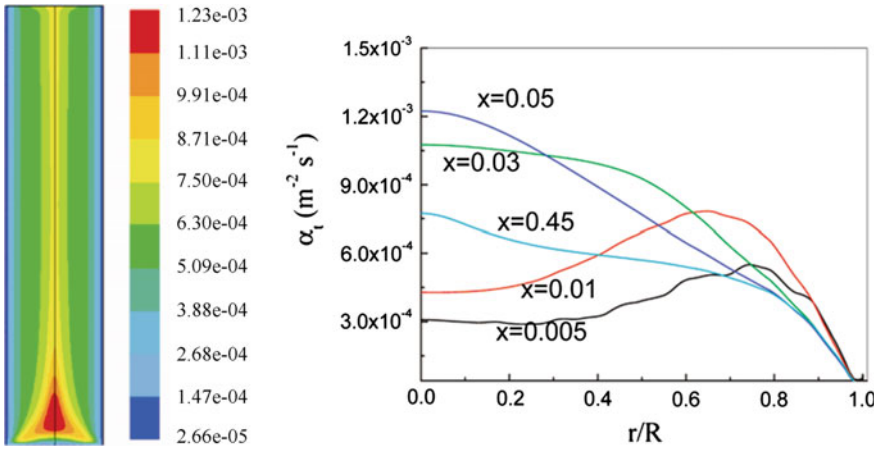

Fig. 5.5 Simulated axial and radial distribution of turbulent thermal diffusivity for Case 1 (Reprinted from ref. [2], Copyright 2008, with permission from American Chemical Society)

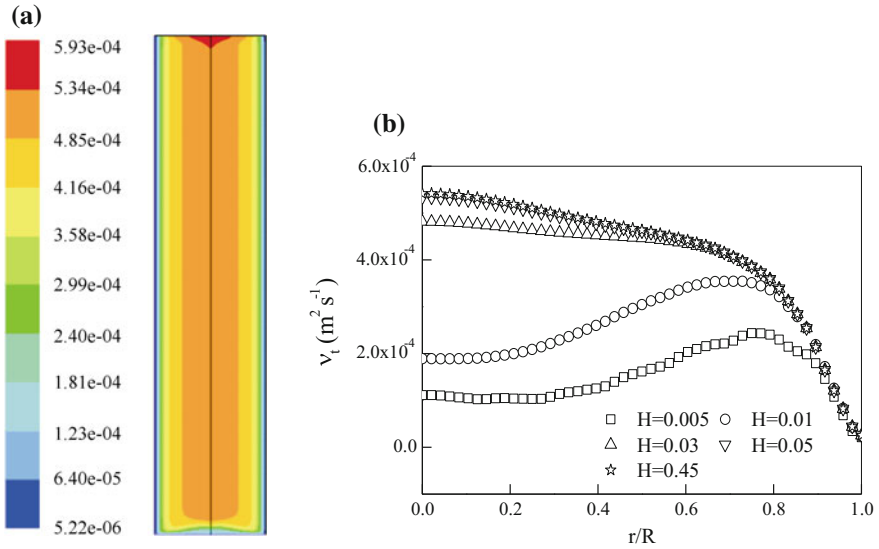

Fig. 5.6 Simulated axial and radial distribution of turbulent diffusivity for Case 1 (Reprinted from ref. [2], Copyright 2008, with permission from American Chemical Society)

5.2 Reynolds Mass Flux Model for Catalytic Reactor

Li [9] employed standard Reynolds mass flux model to simulate the water-cooled reactor as described in Sect. 5.1.3.

5.2.1 Model Equations

The model equations are similar to the $\overline{c'^2} - \varepsilon_c$ two-equation except that the parameters, $\overline{u_i' u_j'}$, $\overline{u_i' T'}$, and $\overline{u_i' c'}$, are not solved by diffusivity method but are calculated directly using Reynolds stress, Reynolds heat flux, and Reynolds mass flux equations.

(I) **CFD equation set**

Overall mass conservation

$$\frac{\partial(\rho\gamma U_i)}{\partial x_i} = S_m$$

Momentum conservation

$$\frac{\partial(\rho_G \gamma U_i U_j)}{\partial x_i} = -\gamma \frac{\partial P}{\partial x_j} + \frac{\partial}{\partial x_i}\left[\gamma\mu\left(\frac{\partial U_j}{\partial x_i}\right) - \gamma\rho_G \overline{u_i' u_j'}\right] + \gamma(\rho_G g + R_0 U_i),$$

where $\overline{u_i' u_j'}$ is calculated by

$$\frac{\partial \overline{u_i' u_j'}}{\partial t} + U_k \frac{\partial \overline{u_i' u_j'}}{\partial x_k} = \frac{\partial}{\partial x_k}\left(C_0 \frac{k}{\varepsilon}\overline{u_i' u_j'}\frac{\partial \overline{u_i' u_j'}}{\partial x_k} + \frac{\mu}{\rho}\frac{\partial \overline{u_i' u_j'}}{\partial x_k}\right) - \left(\overline{u_i' u_k'}\frac{\partial U_j}{\partial x_k} + \overline{u_j' u_k'}\frac{\partial U_i}{\partial x_k}\right)$$

$$-C_1 \frac{\varepsilon}{k}\left(\overline{u_i' u_j'} - \frac{2}{3}k\delta_{ij}\right) - C_2\left(\overline{u_i' u_k'}\frac{\partial U_j}{\partial x_k} + \overline{u_j' u_k'}\frac{\partial U_i}{\partial x_k} - \frac{2}{3}\delta_{ij}\overrightarrow{u_i' u_k'}\frac{\partial U_i}{\partial x_k}\right) - \frac{2}{3}\varepsilon\delta_{ij} \tag{A1.23}$$

The constants are: $C_0 = 0.09$, $C_1 = 2.3$, $C_2 = 0.4$. The k and ε in foregoing equation are given by

$$\frac{\partial \rho U_i k}{\partial x_i} = \frac{\partial}{\partial x_i}\left[\left(\mu + \frac{\mu_t}{\sigma_k}\right)_L \frac{\partial k}{\partial x_j}\right] + (G_k - \varepsilon) \tag{2.3}$$

$$\frac{\partial \rho U_i \varepsilon}{\partial x_i} = \frac{\partial}{\partial x_i}\left[\left(\mu + \frac{\mu_t}{\sigma_\varepsilon}\right)_L \frac{\partial \varepsilon}{\partial x_i}\right] + \rho(C_{1\varepsilon} G_{Lk} - C_{2\varepsilon}\varepsilon)\frac{\varepsilon}{k} \tag{2.4}$$

The model constants are: $c_\mu = 0.09$, $\sigma_k = 1.0$, $\sigma_\varepsilon = 1.3$, $C_{1\varepsilon} = 1.44$, $C_{2\varepsilon} = 1.92$.

(II) **Heat transfer equation set**

(A) *Energy conservation of gas phase*

$$\frac{\partial(\gamma\rho C_p U_i T)}{\partial x_i} = \frac{\partial}{\partial x_i}\left[\gamma\rho C_p\left(\alpha\frac{\partial \overline{C}}{\partial x_i} - \overline{u_i' T'}\right)\right] + S_T$$

$$S_T = Q_1 - Q_2 = h_s a_s\left(T_s^s - T\right) - h_w a_{w1}(T - T_{w1}),$$

where $Q_1 = h_s a_s\left(T_s^s - T\right)$ represents the heat transfer from the catalyst to the gas phase; $Q_2 = h_{w1} a_{w1}(T - T_{w2})$ represents the heat transfer from the gas phase to the inner wall of the reactor. The $\overline{u_i T'}$ is calculated by Reynolds heat flux equation as follows:

$$\frac{\partial \overline{u_i' T'}}{\partial t} + U_i \frac{\partial \overline{u_i' T'}}{\partial x_k} = \frac{\partial}{\partial x_k}\left[\left(C_{\mathrm{T1}} \frac{k}{\varepsilon} \overline{u_1' u_j'} + \alpha\right) \frac{\partial \overline{u_i' T'}}{\partial x_k}\right] - \left(\overline{u_i' u_k'} \frac{\partial T}{\partial x_k} + \overline{u_k' T'} \frac{\partial U_j}{\partial x_k}\right) - C_{\mathrm{T2}} \frac{\varepsilon}{k} \overline{u_i' T'} + C_{\mathrm{T3}} \overline{u_k' T'} \frac{\partial U_i}{\partial x_k}, \tag{A2.18}$$

where the constants are: $C_{\mathrm{t1}} = 0.07$, $C_{\mathrm{t2}} = 3.2$, $C_{\mathrm{t1}} = 0.5$.

(B) *Energy conservation of catalyst*

$$\frac{\partial}{\partial x_i}\left((1-\gamma)\lambda_{\mathrm{s}} \frac{\partial T_{\mathrm{s}}}{\partial x_i}\right) + (1-\gamma)\rho_{\mathrm{s}}(\Delta HR) - h_{\mathrm{s}} a_{\mathrm{s}}\left(T_{\mathrm{s}}^{\mathrm{s}} - T\right) = 0$$

(C) *Energy conservation of reactor wall*

$$\frac{\partial}{\partial x_i}\left(\lambda_{\mathrm{w}} \frac{\partial T_{\mathrm{w}}}{\partial x_i}\right) + h_{\mathrm{w1}} a_{\mathrm{w1}}(T - T_{\mathrm{w1}}) - h_{\mathrm{w2}} a_{\mathrm{w2}}(T_{\mathrm{W2}} - T_{\mathrm{c}}) = 0$$

(III) **Mass transfer equation set**

(A) *Mass conservation of reactive species (gas phase)*

$$\frac{\partial \beta_{\mathrm{L}} U_i C}{\partial x_i} = \frac{\partial}{\partial x_i} \beta_{\mathrm{L}} (D \frac{\partial C}{\partial x_i} - \overline{u_i' c'}) + \beta_{\mathrm{L}} S_n \tag{1.3}$$

$$S_n = h a_{\mathrm{s}}\left(C_{\mathrm{si}}^{\mathrm{s}} - C\right),$$

where $\overline{u_i' c'}$ is given by Reynolds mass flux equation as follows:

$$\frac{\partial \overline{u_i' c'}}{\partial t} + \frac{\partial U_j \overline{u_i' c'}}{\partial x_j} = \frac{\partial}{\partial x_j}\left[\left(C_{\mathrm{c1}} \frac{k}{\varepsilon} \overline{u_i' u_j'} + \frac{\mu}{\rho}\right) \frac{\partial \overline{u_i' c'}}{\partial x_j}\right] - \left(\overline{u_i' u_j'} \frac{\partial C}{\partial x_j}\right) - C_{\mathrm{c2}} \frac{\varepsilon}{k} \overline{u_i' c'} + C_{\mathrm{c3}} \overline{u_j' c'} \frac{\partial U_i}{\partial x_j} \tag{1.33a}$$

The constants are: $C_{\mathrm{c1}} = 0.09$, $C_{\mathrm{c2}} = 3.2$, $C_{\mathrm{c3}} = 0.55$.

(B) *Mass conservation of the solid phase*

$$\frac{\partial}{\partial x_i}\left(D_s\frac{\partial T_s}{\partial x_i}\right)+(1-\gamma)\rho_s(MR)-k_G a_s\left(C_s^s-C\right)=0$$

If the resistance of intradiffusion is neglected, the foregoing equation can be simplified to

$$k_G a_s\left(C_{si}^s-C\right)=\rho_s(1-\gamma)MR$$

Boundary conditions and determination of source terms

The boundary conditions and determination of source terms are the same as in Sect. 5.1.1 and 5.1.2.

5.2.2 Simulated Result and Verification

The reactor simulated is a wall-cooled fixed-bed catalytic reactor reported by Valstar [7] for the synthesis of vinyl acetate from acetic acid and acetylene with zinc acetate on activated carbon as catalyst as given in Sect. 5.1.2.

Simulated concentration profiles of the species in the reactor

As an example, the profiles of acetic acid, acetylene, and vinyl acetate along the whole column are shown in Fig. 5.7, in which the radial concentration distribution is clearly seen.

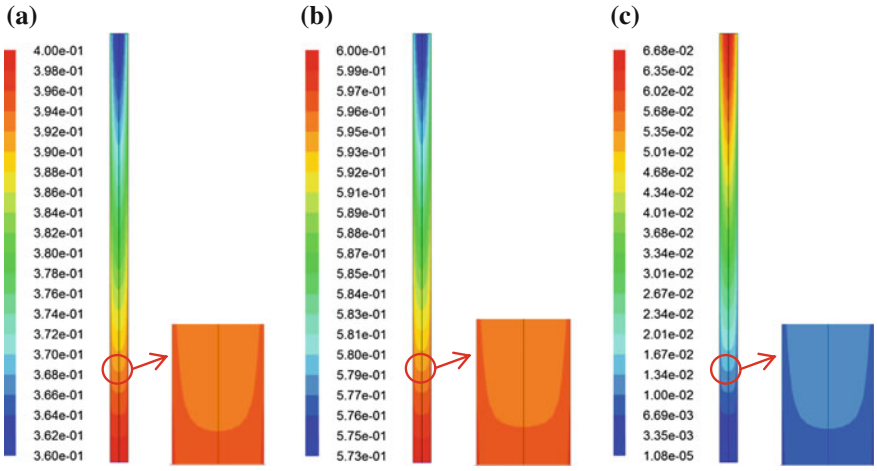

Fig. 5.7 Simulated profiles of molar fraction **a** acetic acid, **b** acetylene and **c** vinyl acetate [9]

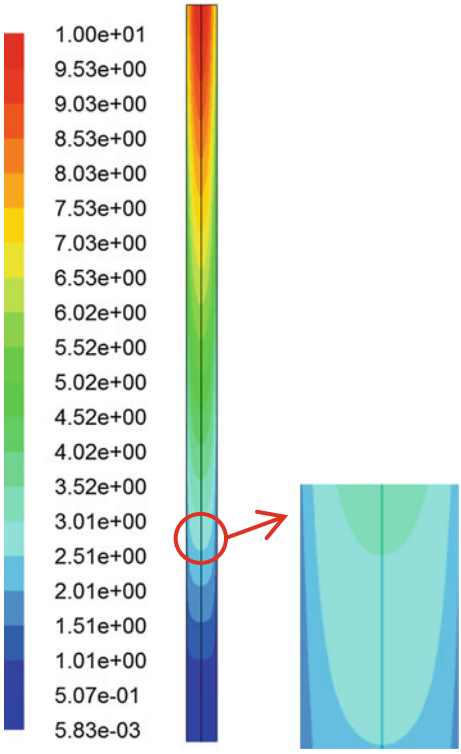

Fig. 5.8 Simulated profiles of acetic acid conversion (%) in the fixed bed [9]

Simulated acetic acid conversion

From the simulated radial concentration distribution along the column, the conversion of acetic acid can be found as shown in Fig. 5.8. The simulated radial conversion is averaged at different heights of reactor to find the average conversion along the axial direction under different operating conditions as given in Fig. 5.9. The simulated curve is confirmed by the measured data reported by Valstar [7]. In this figure, the simulation using two-equation model is also plotted for comparison; it can be seen that the simulation is better using Reynolds mass flux model than by two-equation model.

Simulated temperature profiles of the gas phase

An example of the simulated temperature profile of gas phase in the reactor is shown in Fig. 5.10.

Comparison with experimental data and two-equation model

The radial temperature averaged at different heights along the axial direction is given in Fig. 5.11 and is compared with the experimental data and the simulation using two-equation model. As seen in the figure, the simulation using Reynolds mass flux model is better than that by two-equation model although both of them are considered in agreement with the experimental data.

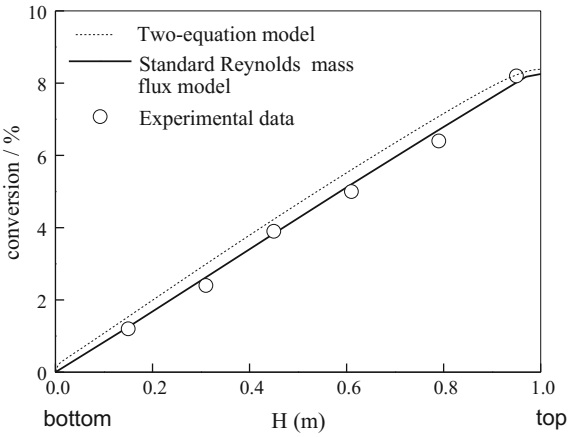

Fig. 5.9 Simulated comparison of acetic acid conversion along axial direction between simulation and experimental data for Case 1 [9]

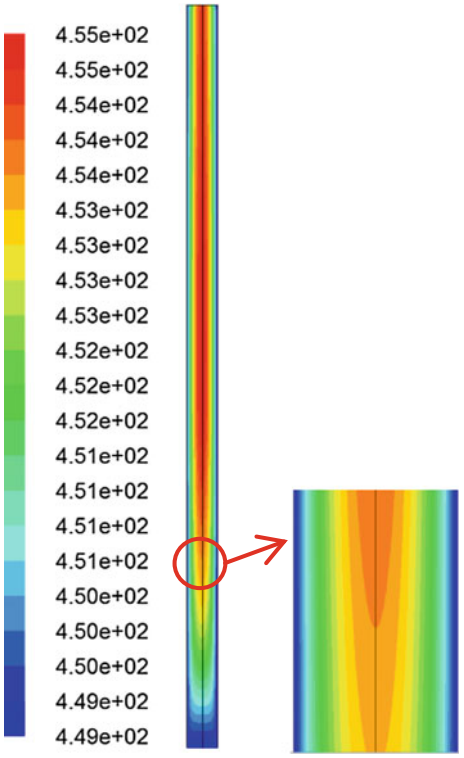

Fig. 5.10 Simulated profiles of temperature (K) in the reactor [9]

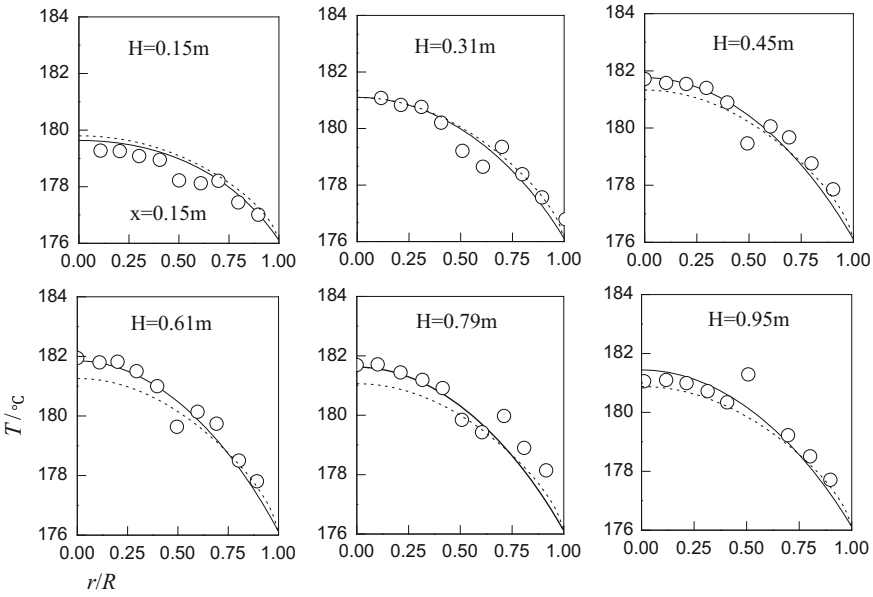

Fig. 5.11 Comparison of radial temperature profiles at different packed heights between simulation obtained by the standard Reynolds mass flux model (*line*), two-equation model (*dash*), and experimental data (*circle*) for Case 1 (*H* distance of bed height measured from column bottom) [9]

5.2.3 *The Anisotropic Mass Diffusivity*

(1) *The axial mass diffusivity*

Figure 5.12a shows the wavy shape profile of $\overline{u_x'c'}$ in radial direction with alternating positive and negative slope, but its tendency is likely to be gradually increasing, which is consistent with the increasing profile of vinyl acetate as shown in Fig. 5.7 so as to enhance the reaction in axial direction. Also in Fig. 5.12b, the positive $\overline{u_x'c'}$ is seen decreasing around the column top ($x < 1$), while it turns to increasing rapidly over the remaining part of the column. It indicates that the $\overline{u_x'c'}$ diffusion is in coaction with the axial increasing profile of vinyl acetate (Fig. 5.7) so that the reaction in axial direction is enhanced by turbulent diffusion.

From Eq. (1.37) and Figs. 5.12a and 5.13a, the axial turbulent mass diffusivity $\mathbf{D_{t,x}}$ can be obtained as given in Fig. 5.14. As seen in the figure, $\mathbf{D_{t,x}}$ is in the wavy shape and fluctuated strongly beyond $r/R = 0.6$. It is mainly due to the high fluctuation of gas phase velocity in both axial and radial directions as shown in Fig. 5.15. However, the tendency of turbulent effect looks increasing toward the column bottom.

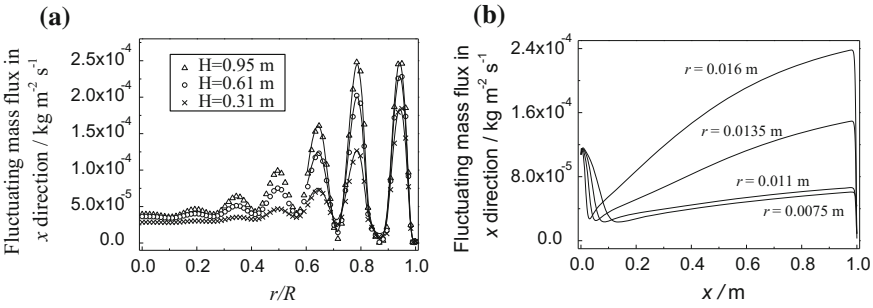

Fig. 5.12 Simulated $\overline{u'_x c'}$ profiles [9] **a** $\overline{u'_x c'}$ in radial direction, **b** $\overline{u'_x c'}$ in axial direction

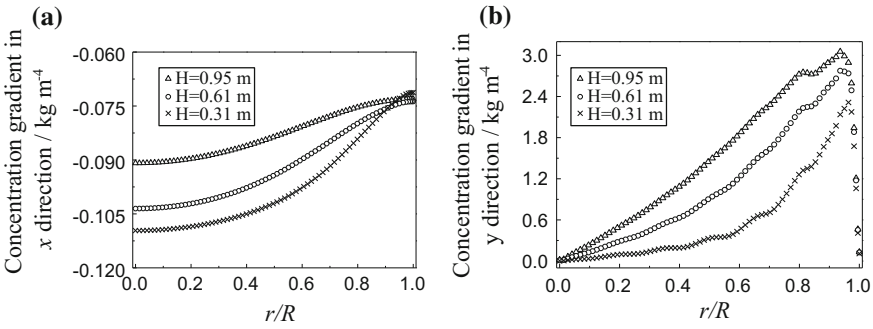

Fig. 5.13 Simulated concentration gradients of vinyl acetate [9] **a** axial $\frac{\partial C}{\partial x}$ gradient of vinyl acetae, **b** radial $\frac{\partial C}{\partial y}$ gradient

(2) *The radial mass diffusivity*

The profile of $\overline{u'_y c'}$ is given in Fig. 5.16, in which all $\overline{u'_y c'}$ is negative. It indicates that the negative gradient of $\overline{u'_y c'}$ diffusion is in contradiction with the positive process gradient $(\partial C/\partial y)$ of vinyl acetate as shown in Fig. 5.7, so that the reaction in radial direction is suppressed.

From Eq. (1.37) and Figs. 5.16 and 5.13, the radial turbulent mass diffusivity $\mathbf{D_{t,y}}$ can be obtained as given in Fig. 5.17. As seen in the figure, $\mathbf{D_{t,y}}$ is very high near the column center; it is due to very low $(\partial C/\partial y)$ gradient there as the concentration is assumed to be symmetrical to the centerline.

The profile of $\overline{u'_i c'}$(sum of $\overline{u'_x c'}$ and $\overline{u'_y c'}$) is given in Fig. 5.16. The wavy shape and negative $\overline{u'_i c'}$ are noted. The negative $\overline{u'_i c'}$ indicates that the axial turbulent diffusion is overwhelmed by the radial diffusion.

The radial turbulent mass diffusivity $\mathbf{D_{t,y}}$ is shown in Fig. 5.17, and the sum of the fluctuating mass flux is given in Fig. 5.18.

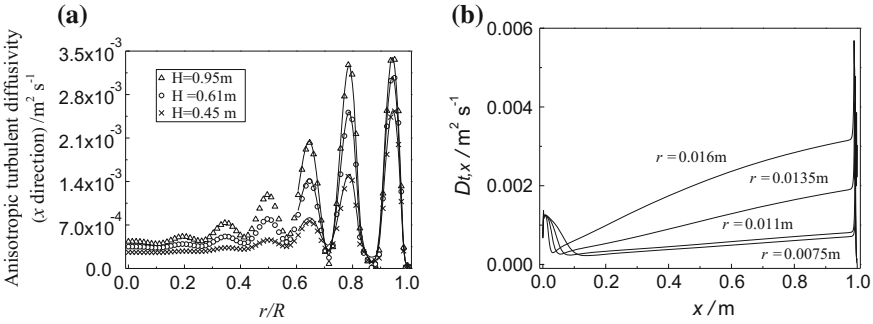

Fig. 5.14 Simulated $\mathbf{D_{t,x}}$[9] **a** $\mathbf{D_{t,x}}$ in radial direction, **b** $\mathbf{D_{t,x}}$ in axial direction

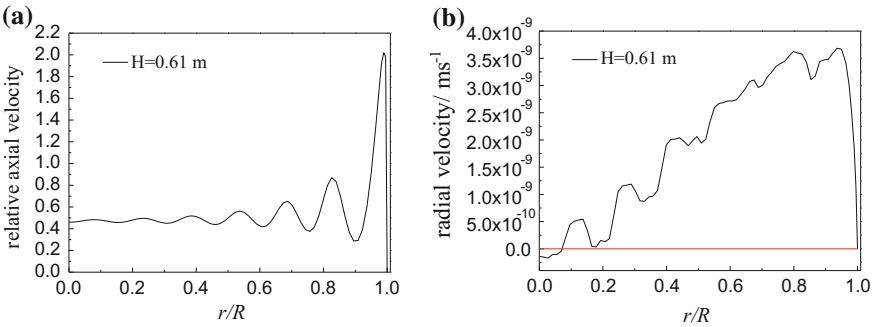

Fig. 5.15 Simulated profiles of axial and radial velocities along radial direction at H = 0.61 m [9] **a** axial velocity, **b** radial velocity

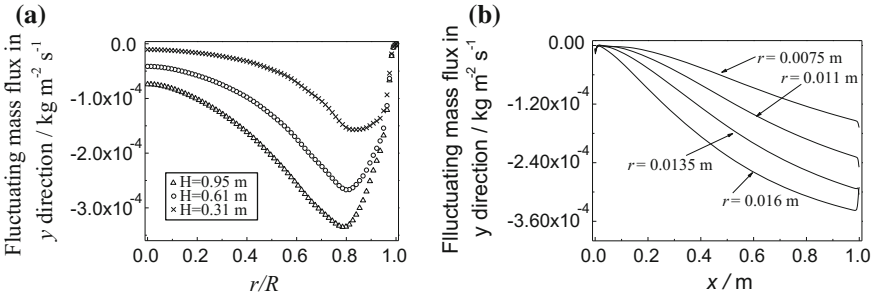

Fig. 5.16 Simulated $\overline{u'_y c'}$ [9] **a** $\overline{u'_y c'}$ in radial direction, **b** $\overline{u'_y c'}$ in axial direction

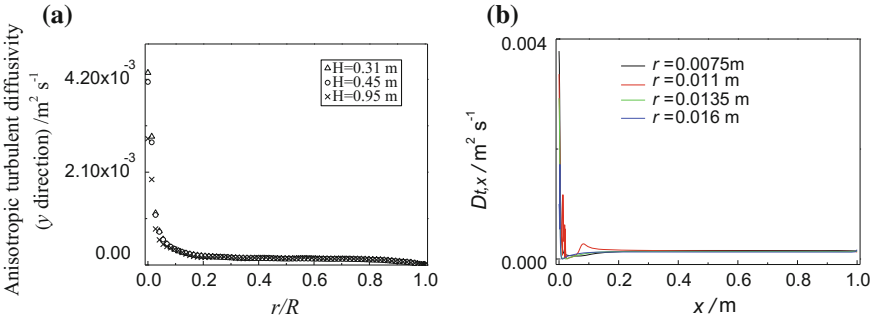

Fig. 5.17 Simulated profiles of $\mathbf{D_{t,y}}$[9] **a** $\mathbf{D_{t,x}}$ in radial direction, **b** $\mathbf{D_{t,x}}$ in axial direction

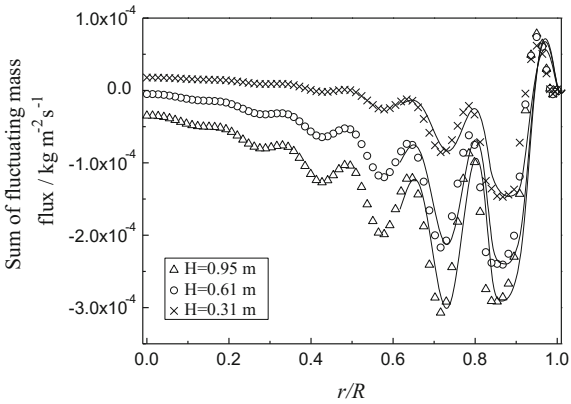

Fig. 5.18 Simulated profile of $\overline{u_i'c'}$(sum of $\overline{u_x'c'}$ and $\overline{u_y'c'}$) [9]

5.3 Summary

The source term S_n in the species conservation equation Eq. (1.1) can represent the mass created or depleted by a chemical reaction besides the mass transferred from one phase to the other. Thus CMT model can be used for simulating the chemical reactor. A catalytic reactor with water-cooled jacket is chosen as typical example for illustration. The CMT model equations regularly comprise mass transfer equation set and the accompanied fluid dynamic equation set and heat transfer equation set. Note that the source term S_n is calculated in terms of reaction rate. The simulated results of a wall-cooled catalytic reactor for the synthesis of vinyl acetate from acetic acid and acetylene by both $\overline{c'^2} - \varepsilon_{c'}$ model and Reynolds mass flux model for simulating the axial concentration and temperature distributions are in agreement with the experimental measurement. As the distribution of μ_t shows dissimilarity with D_t and α_t, the Sc_t or Pr_t are varying throughout the reactor. The wavy shape of axial diffusivity $\mathbf{D_{t,x}}$ along the radial direction indicates the important influence of porosity distribution on the performance of a reactor.

References

1. Froment GF, Bischoff KB (1990) Chemical reactor analysis and design. Wiley, New York
2. Liu GB, Yu KT, Yuan XG, Liu CJ (2008) A computational transport model for wall-cooled catalytic reactor. Ind Eng Chem Res 47:2656–2665
3. Launder BE, Spalding DB (1972) Lectures in mathematical models of turbulence. Academic Press, London
4. Elghobashi SE, Launder BE (1983) Turbulent time scales and the dissipation rate of temperature variance in the thermal mixing layer. Phys Fluids 26(9):2415–2419
5. de Klerk A (2003) Voidage variation in packed beds at small column to particle diameter ratio. AIChE J 49(8):2022–2029
6. Ergun S (1952) Fluid flow through packed columns. Chem Eng Prog 48:89–94
7. Valstar JM, van den Berg PJ, Oyserman J (1975) Comparison between twodimensional fixed bed reactor calculations and measurements. Chem Eng Sci 30(7):723–728
8. Yaws CL (2003) Yaws' handbook of thermodynamic and physical properties of chemical compounds, Knovel
9. Li WB (2012) Theory and application of computational mass transfer, PhD dissertation, Tianjin University, Tianjin, China

Chapter 6
Application of Computational Mass Transfer (V) Fluidized Chemical Process

Abstract In this chapter, the CMT models developed in Chap. 1 are implemented for the simulation of concentration, velocity, and temperature distributions in gas-solid particle fluidized processes. A $c'^2 - \varepsilon_{c'}$ two-equation model is developed and applied to the removal of CO_2 in flue gas by K_2CO_3 particle in a bubbling fluidized bed; while a Reynolds mass flux model is used for the process of decomposition of ozone in riser and downer of a circulating fluidized bed (CFB). The simulation results are validated with experimental data. Anisotropic feature of the eddy diffusivity in the fluidized process is discussed.

Keywords Concentration profile in fluidized process · Bubbling fluidized bed · Circulating fluidized bed (CFB) · Anisotropic eddy diffusivity

Nomenclature

a, b, c	EMMS-based drag model parameters
C_i	Mass fraction of species i in gas phase
C_μ, $C_{\varepsilon 1}$, $C_{\varepsilon 2}$, $C_{\varepsilon 3}$	Turbulence model constants for the velocity field
C_{c0}, C_{c1}, C_{c2}, C_{c3}, C_{c4}	Turbulence model constants for the concentration field
C_D	Drag coefficient
$\overline{c^2}$	Concentration variance
d_p	Mean particle diameter, m
D_g	Molecular diffusivity of ozone in gas phase, $m^2\ s^{-1}$
$D_{t,g}$	Turbulent mass diffusivity of ozone in gas phase, $m^2\ s^{-1}$
e_{ss}	Restitution coefficient
g	Gravity acceleration, $m\ s^{-2}$
$g_{0,ss}$	Radial distribution function
G_s	Particle circulation rate, $kg\ m^{-2}\ s^{-1}$
$\overline{\overline{I}}$	Identity matrix
k_g, k_p	Turbulent kinetic energy of gas and particle, respectively, $m^2\ s^{-2}$
k_r	Apparent reaction rate constant, s^{-1}
p_s	Particulate phase pressure, Pa

K.-T. Yu and X. Yuan, *Introduction to Computational Mass Transfer*,
Heat and Mass Transfer, DOI 10.1007/978-981-10-2498-6_6

P_g	Gas phase pressure, kPa
r	Radial distance from the axis of the riser, m
R	Universal gas constant, kJ kmol^{-1} K^{-1}
Re	Reynolds number
R_{O_3}	Source term of turbulent mass transfer equation for ozone, kg m^{-3} s^{-1}
Sc_t	Turbulent Schmidt number ($Sc_t = v_{g,t}/D_{g,t}$)
t	Time, s
T_g	Gas phase operation temperature, K
X_{O_3}	Mole concentration of O_3 in gas phase, kmol m^{-3}
u	Gas interstitial velocity vector, m s^{-1}
$\vec{u}_g, \vec{u}_s$	Gas and particle velocity vector, m s^{-1}
U_g	Superficial velocity of the gas phase, m s^{-1}
X	Total height of the CFB riser, m
x	Height of the CFB riser from the bottom inlet, m
α_g, α_s	Gas and solid volume fraction, respectively
β_{gs}	Interphase exchange coefficient, kg m^3 s^{-1}
ε_g, ε_s	Dissipation rate of turbulent kinetic energy, m^2 s^{-3}
ε_c	Dissipation rate of the concentration variance, s^{-1}
γ	Collisional dissipation of energy, J m^{-3} s^{-1}
ξ_s	Solid bulk viscosity, kg m^{-1} s^{-1}
ρ_g, ρ_s	Gas and particle density, respectively, kg m^{-3}
$\bar{\bar{\tau}}$	Stress tensor, Pa
Γ_Θ	Diffusion coefficient for granular energy, Pa s
Θ_s	Granular temperature, m^2 s^{-2}
μ_g, $\mu_{g,t}$	Gas molecular and turbulent viscosity, respectively, kg m^{-1} s^{-1}
μ_s, $\mu_{s,col}$, $\mu_{s,kin}$	Solid shear viscosity, collisional viscosity and kinetic viscosity, respectively, kg m^{-1} s^{-1}
σ_k, σ_ε, σ_c, $\sigma_{\varepsilon c}$, σ_m	Turbulence model constants for diffusion of k, ε, $\overline{c^2}$, ε_c
ϕ_{gs}	Exchange of fluctuation energy, kg m^{-1} s^{-3}

Subscripts

g	Gas phase
in	Inlet of the riser
out	Outlet of the riser
s	Particle phase
t	Turbulence

Fluidization has been commonly recognized as an unit operation dealing with particle-fluid processes in chemical engineering since last century. As the particle-fluid flow is complicated, the research has so far focused on the CFD simulation, while the mass transfer as well as the concentration aspects was seldom

concerned. Nevertheless, the latter is the basis of chemical process and cannot be overlooked. Recently, attempt has been made to fill this gap by using CMT methodology.

In this chapter, the CMT models are employed to simulate the following fluidized chemical processes:

(1) The removal of CO_2 in flue gas by K_2CO_3 particle in a bubbling fluidized bed by using $c'^2 - \varepsilon_{c'}$ two-equation model;
(2) The decomposition of ozone in riser and downer of a circulating fluidized bed (CFB) by using both two-equation model and Reynolds mass flux model.

The simulated results are found to be satisfactorily confirmed with the experimental data, indicating that the CMT models are suitable to be used for simulating fluidized chemical processes.

6.1 Flow Characteristics of Fluidized Bed

Fluidization is an emerging technology since last century and has been applied to chemical, metallurgical, pharmaceutical, food processing, and allied industries. Broadly speaking, fluidization is a process that the solid particles are carrying by a flowing fluid (gas or liquid) undertaking mass (and/or heat) transfer or chemical reaction for the purpose of enhancing process efficiency due their intimates phase contact. A number of typical patterns during the development of the fluidization of particle-fluid two phases flow in a circular tube under different operating conditions can be identified and are shown in Fig. 6.1.

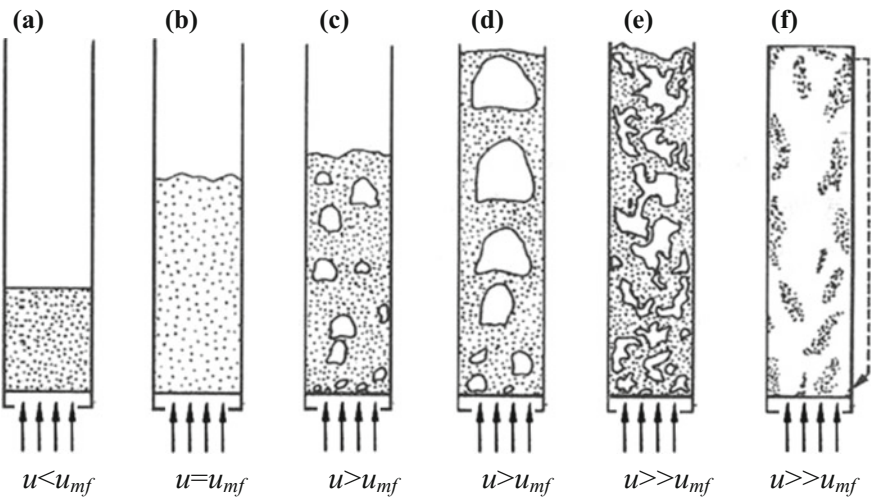

Fig. 6.1 Flow patterns of fluidization at different fluid velocity

When the fluid velocity u in the particle-fluid flow is less than the *critical fluidization velocity* (denoted by u_{mf}), the particle bed is stationary, like a fixed packed bed as shown in Fig. 6.1a. When $u = u_{mf}$, the particle bed begins slightly expended with small fluctuation and even forms some small bubble occasionally (Fig. 6.1b, c). At higher u, more bubbles of larger size are appeared and they are breakup and coalescence at the same time, such fluid-bubble flow pattern is regarded as bubble fluidization (Fig. 6.1d, e). Further increase of fluid velocity promotes the turbulence of the bubble bed and the solid particles begin to cluster forming a dense solid phase and a dilute fluid phase (Fig. 6.1f). If the fluid velocity is high enough to carry out the particles leaving the fluidized bed, the fluid velocity is called *carry out velocity*, u_{out}. In this case, a particle capture device is provided and the escaping particles are being collected and fed back to the bottom of the fluidized tube for recycling.

Thus fluidization process can be undertaken in two operating conditions:

- Fixed fluidized bed operation (FFB, Fig. 6.2a) where $u \leq u_{mf}$
- Circulating fluidized bed operation (CFB, Fig. 6.2b) where $u \geq u_{out}$. The CFB is often used for the advantage of continuous fluidization operation with

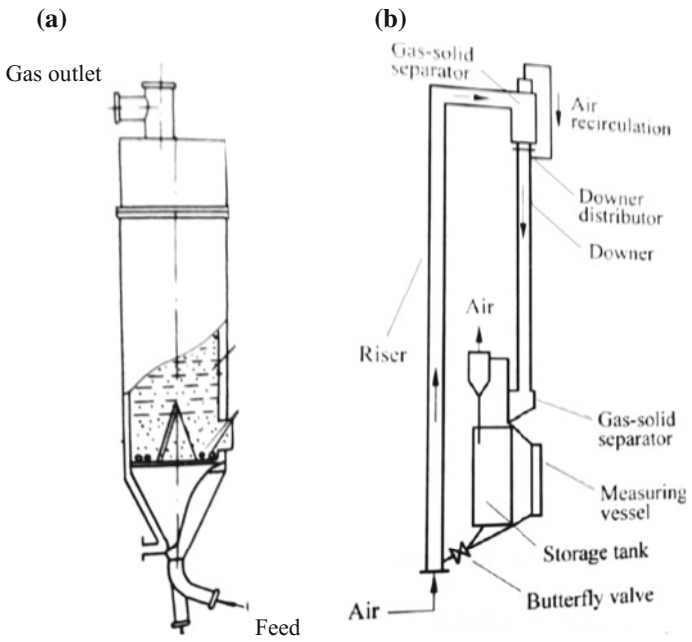

Fig. 6.2 Fixed and fluidized bed (CFB) reactor **a** catalytic fixed bed fluidized reactor, **b** circulating fluidized bed reactor

gas-particle separation devices capturing the escaping particles and returning them to the bottom of the reactor as shown schematically in Fig. 6.2b.

General speaking, the flow in the fluidized bed consist of two phases: the fluid phase and particle phase. Nevertheless, gas-particle flow in the fluidized bed is quite complicated because of the presence of turbulent flow of both gas and particles with mutual interaction between fluid-particle and particle-particle, and consequently causes difficulties in evaluation their interaction. Considerable cold-flow and hot-flow model experiments for fluidized bed have been made in the past 20 years, and some important phenomena involving fluid-dynamics, mass, and heat transfer were reported such as the nonuniform radial distribution of particles (or called core-annulus structure of particles) [1, 2] as well as the uneven distribution of species concentration [2, 3]. Since such kind of experimental study is laborious, many researchers focused on developing engineering models for rigorous simulation.

During the past decades, many theoretical works have been undertaken on modeling and simulating fluid-dynamics in fluidized bed using CFD approach. To tackle the gas-solid flow, generally, there are two methodologies:

- Eulerian–Lagrangian approach, and
- Eulerian–Eulerian approach or two-fluid model (TFM).

The TFM have been so far widely employed in modeling the gas-solid flow. The idea of TFM method is that both gas and solid phases are treated as interpenetrating continua based on the Eulerian method. The success of TFM depends on proper description of the phase interacting forces and the solid stress. The interacting forces are used to describe the momentum transfer between the two phases; while the solid stress represents the solid phase force due to particle–particle interactions. Many investigators [4, 5] have found that anisotropy of the gas-solid turbulent flows is essential for successful description of CFB fluid-dynamics. In addition, the structure and interaction of particles in the solid phase is multi-fashioned, such as the formation of different clusters with different behaviors of the solid phase.

The CMT model, as applied in preceding chapters, consists of the following two sets of modeling equations

- The turbulent mass transfer (and heat transfer if necessary) equation set for describing the mass transfer (and/or heat transfer) behaviors of the process. It includes the mass transfer (and/or heat transfer) differential equation of the reactive species and the method of its closure, such as the use of $c'^2 - \varepsilon_{c'}$ two-equation model and the Reynolds mass flux model in CMT methodology.
- The fluid-dynamic model for describing the flow behaviors. Two-fluid model (TFM) is used in this chapter, which contains a fluid phase and a solid phase. Each phase possess the continuity equation and momentum conservation equation. In the solid phase, the interaction between dense solid (particle clusters and aggregation, etc.) and the fluid should be taking account.

6.2 $\overline{c'^2} - \varepsilon_c$ Two-Equation Model for Simulating Fluidized Process [6, 7]

The simulation objects in this chapter are:

(1) The removal of CO_2 in flue gas by K_2CO_3 particles in a fixed fluidized bed (FFB) reactor [8].
(2) The decomposition of ozone in CFB reactor.

6.2.1 The Removal of CO_2 in Flue Gas in FFB Reactor

Model Equation

(1) **The turbulent mass transfer equation set**

1. **Mass transfer equation**

Mass conservation equation of component species i in gas phase:

$$\frac{\partial(\rho_g \alpha_g y_{g,i})}{\partial t} + \frac{\partial(\rho_g \alpha_g u_{g,i} y_{g,i})}{\partial x_i} = \frac{\partial}{\partial x_i}\left[(D + D_t)\frac{\partial(\rho_g \alpha_g y_{g,i})}{\partial x_i}\right] + S_{g,i},$$

where D and D_t are the molecular and turbulent diffusivity, respectively.

Mass conservation equation of component species i in solid phase:

$$\frac{\partial(\rho_s \alpha_s y_{s,i})}{\partial t} + \frac{\partial(\rho_s \alpha_s u_{s,i} y_{s,i})}{\partial x_i} = \frac{\partial}{\partial x_i}\left[D_{\text{eff}}\frac{\partial(\rho_s \alpha_s y_{s,i})}{\partial x_i}\right] + S_{s,i},$$

where D_{eff} is the effective diffusivity of the solid phase. This parameter is hardly to be evaluated and usually is taken from experimental data. In the CMT two-equation model, the D_{eff} can be calculated by the following equation:

$$D_{\text{gn,t}} = C_{c0} k_g \left(\frac{k_g}{\varepsilon_g}\frac{\overline{c_n^2}}{\varepsilon_c}\right)^{1/2},$$

where $\overline{c^2}$ equation:

$$\frac{\partial}{\partial t}\left(\alpha_g \rho_g \overline{c_n^2}\right) + \nabla \times \left(\alpha_g \rho_g \bar{u}_g \overline{c_n^2}\right) = \nabla \times \left[\left(D_{\text{gn}} + \frac{D_{\text{gn,t}}}{\sigma_c}\right)\alpha_g \nabla \overline{c_n^2}\right] + 2\rho_g \alpha_g \nabla \overline{C_n} \nabla \overline{C_n} - 2\rho_g \alpha_g \varepsilon_c,$$

ε_c equation

$$\frac{\partial}{\partial t}\left(\alpha_g \rho_g \varepsilon_c\right) + \nabla \times \left(\alpha_g \rho_g \vec{u}_g \varepsilon_c\right) = \nabla \times \left[\left(D_{gn} + \frac{D_{gn,t}}{\sigma_c}\right)\rho_g \alpha_g \nabla \varepsilon_c\right] + C_{c1}\rho_g \alpha_g \nabla \overline{C_n} \nabla \overline{C_n} \frac{\varepsilon_c}{\overline{c_n^2}} - C_{c2}\rho_g \alpha_g \frac{\varepsilon_c^2}{\overline{c_n^2}} - C_{c3}\rho_g \alpha_g \frac{\varepsilon_g \varepsilon_c}{k_g}$$

Model constant are [9] $C_{c0} = 0.11,\ C_{c1} = 1.8,\quad C_{c2} = 2.2,\ C_{c3} = 0.8,$ $\sigma_c = 1.0,\ \sigma_\varepsilon = 1.0.$

The boundary conditions for $\overline{c^2} - \varepsilon_c$ model are as follows:

Inlet condition $\overline{c_{in}^2} = \left(0.082\overline{C_{gn,in}}\right)^2$

$$\varepsilon_{c,in} = R_\tau \left(\frac{\varepsilon_{g,in}}{k_{g,in}}\right)\overline{c_{in}^2},$$

where R_τ is the time scale, $R_\tau = \frac{k/\varepsilon}{\overline{c^2}/\varepsilon_c}$. According to the method of estimation by Liu [10], we get $R_\tau = 3 \times 10^{-3}$.

Outlet condition fully developed turbulent flow.

2. **Heat transfer equation**

Heat energy conservation equation of component species i in gas phase:

$$\frac{\partial\left(\rho_g \alpha_g c_{pg} T_g\right)}{\partial t} + \frac{\partial\left(\rho_g \alpha_g u_{g,i} c_{pg} T_g\right)}{\partial x_i} = \frac{\partial}{\partial x_i}\left[\alpha_{g,eff}\frac{\partial\left(\rho_g \alpha_g c_{pg} T_g\right)}{\partial x_i}\right] + S_{tg},$$

where C_p is the specific heat.

Heat energy conservation equation of component species i in solid phase:

$$\frac{\partial\left(\rho_s \alpha_s c_{ps} T_s\right)}{\partial t} + \frac{\partial\left(\rho_s \alpha_s u_{s,i} c_{ps} T_s\right)}{\partial x_i} = \frac{\partial}{\partial x_i}\left[\alpha_{s,eff}\frac{\partial\left(\rho_s \alpha_s c_{ps} T_s\right)}{\partial x_i}\right] + S_{ts},$$

where the effective thermal diffusivity a_{eff} is calculated from $\overline{T'^2} - \varepsilon_{T'}$ model.

(2) **The fluid-dynamic equation set**

1. **Continuity equations**

For gas phase $\frac{\partial\left(\rho_g \alpha_g\right)}{\partial t} + \frac{\partial\left(\rho_g \alpha_g u_{g,i}\right)}{\partial x_i} = S_{m,g}$

For solid phase

$$\frac{\partial\left(\rho_s \alpha_s\right)}{\partial t} + \frac{\partial\left(\rho_s \alpha_s u_{s,i}\right)}{\partial x_i} = S_{m,s}$$

2. **Momentum equations**

In TFM, the fluid and solid phases are interpenetrated and interacted, the source term S_i in the momentum Eq. (1.1–1.4) of Chap. 1 is extended and included the following terms:

$$\begin{aligned} S_i &= (\text{interfacial drag force}) + (\text{body force}) + (\text{amount of mass being transferred}) \\ &= \beta_{\mathrm{gs}}\left(u_{\mathrm{g},i} - u_{\mathrm{s},i}\right) + \rho_{\mathrm{g}}\alpha_{\mathrm{g}}g + \tau_{\mathrm{g}} + u_{\mathrm{g},i}R_{m,\mathrm{g}} \end{aligned}$$

In addition, to follow most expression in fluidization literatures, the stress term $\frac{\partial\left(-\rho\overline{u'_i u'_j}\right)}{\partial x_j}$ in momentum Eq. (1.4) is replaced by the stress symbol τ. Thus, the momentum equation for gas phase is

$$\frac{\partial\left(\rho_{\mathrm{g}}\alpha_{\mathrm{g}}u_{\mathrm{g},j}\right)}{\partial x_j} + \frac{\partial\left(\rho_{\mathrm{g}}\alpha_{\mathrm{g}}u_{\mathrm{g},i}u_{\mathrm{g},j}\right)}{\partial x_j} = -\alpha_{\mathrm{g}}\frac{\partial p_{\mathrm{g}}}{\partial x_i} + \tau_{\mathrm{g}} + \beta_{\mathrm{gs}}\left(u_{\mathrm{g},i} - u_{\mathrm{s},i}\right) + \rho_{\mathrm{g}}\alpha_{\mathrm{g}}g + u_{\mathrm{g},i}R_{m,\mathrm{g}}$$

For solid phase

$$\frac{\partial\left(\rho_{\mathrm{s}}\alpha_{\mathrm{s}}u_{\mathrm{s},j}\right)}{\partial x_j} + \frac{\partial\left(\rho_{\mathrm{s}}\alpha_{\mathrm{s}}u_{\mathrm{s},i}u_{\mathrm{s},j}\right)}{\partial x_j} = -\alpha_{\mathrm{s}}\frac{\partial p_{\mathrm{s}}}{\partial x_i} + \tau_{\mathrm{s}} + \beta_{\mathrm{gs}}\left(u_{\mathrm{s},i} - u_{\mathrm{g},i}\right) + \rho_{\mathrm{s}}\alpha_{\mathrm{s}}g + + u_{\mathrm{s},i}S_{m,\mathrm{s}}$$

In foregoing equations, α is the volume fraction, subscripts g and s refers to gas and solid phase, respectively, τ_{s} is the stress tensor of the solid phase which is expressed by:,

$$\tau_{\mathrm{s}} = \alpha_{\mathrm{s}}\mu_{\mathrm{s}}\left(\frac{\partial u_{\mathrm{s},i}}{\partial x_j} + \frac{\partial u_{\mathrm{s},j}}{\partial x_i}\right) + \alpha_{\mathrm{s}}\left(\lambda_{\mathrm{s}} - \frac{2}{3}\mu_{\mathrm{s}}\right)\frac{\partial u_{\mathrm{s},i}}{\partial x_i}$$

μ_{s} is the shear viscosity of solid phase, β is the drag coefficient, λ is the bulk volume viscosity, R is the amount of mass transfer which can be calculated by

$$R_{\mathrm{mg}} = -r(M_{\mathrm{CO_2}} + M_{\mathrm{H_2O}}),$$

where r is the reaction rate, M is the molar mass of corresponding species.

The μ_{s} is calculated by

$$\begin{aligned} \mu_{\mathrm{se}} &= \alpha_{\mathrm{s}}\mu_{\mathrm{s}} + \mu_{\mathrm{s,t}} \\ \mu_{\mathrm{s,t}} &= C_\mu\alpha_{\mathrm{s}}\rho_{\mathrm{s}}f_\mu k_{\mathrm{s}}^2/\varepsilon_{\mathrm{s}}, \end{aligned}$$

where k_{s} equation $\frac{\partial}{\partial t}\left(\alpha_{\mathrm{q}}\rho_{\mathrm{q}}k_{\mathrm{q}}\right) + \nabla\times\left(\alpha_{\mathrm{q}}\rho_{\mathrm{q}}\bar{u}_{\mathrm{q}}k_{\mathrm{q}}\right) = \nabla\times\left(\frac{\mu_{\mathrm{qe}}}{\sigma_k}\alpha_{\mathrm{q}}\nabla k_{\mathrm{q}}\right) + G_{\mathrm{qp}} - \alpha_{\mathrm{q}}\rho_{\mathrm{q}}\varepsilon_{\mathrm{q}}$

ε_s equation $\frac{\partial}{\partial t}\left(\alpha_q \rho_q \varepsilon_q\right) + \nabla \times \left(\alpha_q \rho_q \vec{u}_q \varepsilon_q\right) = \nabla \times \left(\frac{\mu_{qe}}{\sigma_\varepsilon} \alpha_q \nabla \varepsilon_q\right) + \frac{\varepsilon_q}{k_q}\left(C_1 G_{qp} - C_2 \alpha_q \rho_q \varepsilon_q\right)$

The subscript q refers to the gas and solid phase correspondingly, i.e., q = g, s. The model constants are C_μ=0.09, C_1=1.44, C_2=1.92, $\sigma_k = 1.0$, $\sigma_\varepsilon = 1.3$.

The drag coefficient β is taken from the Yang model [11]

$$\beta_{gs} = 150\frac{\alpha_s^2 \mu_g}{\alpha_g d_p^2} + 1.75\frac{\alpha_s \rho_g}{d_p}\left|\vec{u_s} - \vec{u_g}\right|, \quad \alpha_g \le 0.74,$$

$$\beta_{gs} = \frac{3}{4} C_D \frac{\alpha_s \alpha_g \rho_g}{d_p}\left|\vec{u_s} - \vec{u_g}\right| f_{\alpha_g}, \quad \alpha_g > 0.74,$$

where $C_D = \begin{cases} \frac{24}{\alpha_g Re(1+0.15Re^{0.687})} & Re \le 1000 \\ 0.44 & Re > 1000 \end{cases}$; $Re = \frac{\rho_g \alpha_g \left|\vec{u_s} - \vec{u_g}\right| d_p}{\mu_g}$.

The correction factor f_{α_g} is given by:

$$f_{\alpha_g} = -0.5760 + \frac{0.0214}{4\left(\alpha_g - 0.7463\right)^2 + 0.0044} \quad 0.74 \le \alpha_g \le 0.82$$

$$f_{\alpha_g} = -0.0101 + \frac{0.0038}{4\left(\alpha_g - 0.7789\right)^2 + 0.004} \quad 0.82 < \alpha_g \le 0.97$$

$$f_{\alpha_g} = -31.8295 + 32.8295\alpha_g \quad \alpha_g > 0.97$$

For the bubbling fluidized bed, Ayobi suggest a correction factor C as follows [2],

$$\beta_{gs,new} = C\beta_{gs},$$

where $C = 0.2$.

The solid pressure p_s can be found by the kinetic theory of granular flow as follows:

$$p_s = \alpha_s \rho_s \Theta_s + 2\rho_s(1+e_{ss})\,\alpha_s^2 g_{0,ss}\Theta_s$$

$$g_{0,ss} = \left[1 - \left(\frac{\alpha_s}{\alpha_{s,max}}\right)^{1/3}\right]^{-1}$$

$$\frac{3}{2}\left[\frac{\partial}{\partial t}(\alpha_s \rho_s \Theta_s) + \nabla \times \left(\alpha_s \rho_s \vec{u_s} \Theta_s\right)\right] = \nabla \times \left[\left(\frac{2}{3}\Gamma_\Theta + \frac{\mu_s}{\sigma_\Theta}\right)\nabla \Theta_s\right] + \phi_{gs} - \gamma$$

$$\Gamma_\Theta = \frac{15 d_p \rho_s \alpha_s \sqrt{\Theta_s \pi}}{4(41-33\eta)}\left[1 + \frac{12}{5}\eta^2(4\eta-3)\alpha_s g_{0,ss} + \frac{16}{5\pi}(41-33\eta)\eta\alpha_s g_{0,ss}\right]$$

$$\eta = \frac{1}{2}(1+e_{ss})$$

where Θ is terminologically called as granular temperature, representing the fluctuation of average particle mean velocity which effects the energy of the particle just like that of temperature. The viscosity of solid μ_s is calculated by

$$\mu_s = \mu_{s,col} + \mu_{s,kin} + \mu_{s,fr}$$

$$\mu_{s,col} = \frac{4}{5}\alpha_s \rho_s d_s g_{0,ss}(1+e_{ss})\left(\frac{\Theta_s}{\pi}\right)^{1/2}$$

$$\mu_{s,kin} = \frac{\alpha_s \rho_s d_s \sqrt{\Theta_s \pi}}{6(3-e_{ss})}\left[1+\frac{2}{5}(1+e_{ss})(3e_{ss}-1)\alpha_s g_{0,ss}\right]$$

$$\mu_{s,fr} = \frac{p_s \sin\phi}{2\sqrt{I_{2D}}}$$

Simulation of CO_2 removal in fluidized bed

The object of simulation is the removal of CO_2 from flue gas by K_2CO_3 particles in bubbling fluidized bed as reported by Ayobi et al. [8]. The experimental setup is shown in Fig. 6.3.

The chemical reaction is as follows;

$$K_2CO_3(s) + CO_2(g) + H_2O(g) \rightarrow 2KHCO_3(s)$$

The reaction rate is given by [8]

$$r_n = -k_{reac} X_{CO_2} X_{H_2O} \alpha_s M_n,$$

where $k_{reac} = 50,000\ m^3\ kmol^{-1}\ s^{-1}$, X_{CO_2}, X_{H_2O} are the mole fraction of CO_2 and H_2O in gas phase., respectively.

Two inlet conditions of flue gas concentration corresponding to the experimental work are simulated:

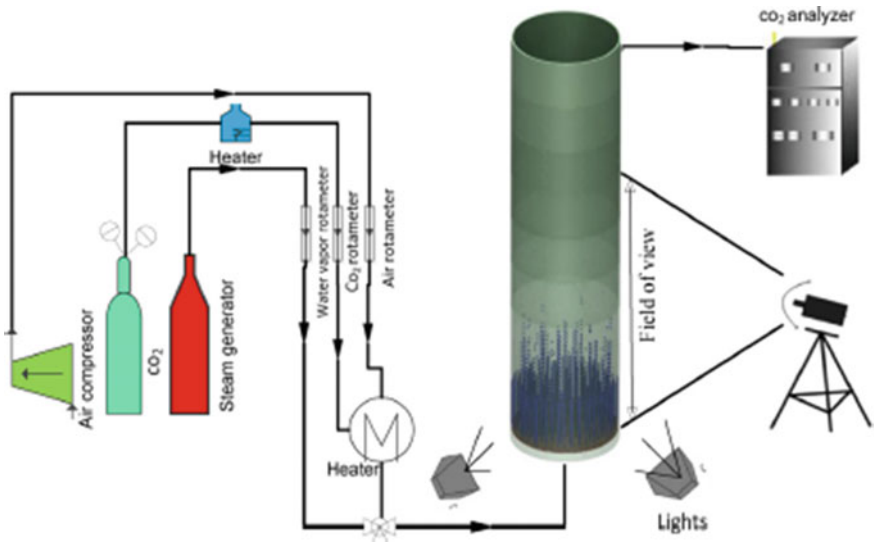

Fig. 6.3 Experimental setup for CO_2 removal by K_2CO_3 in fluidized bed (reprinted from Ref. [8], Copyright 2014, with permission from Elsevier)

Case 1: $y_{CO_2} = 0.10, y_{H_2O} = 0.05, y_{air} = 0.85$
Case 2: $y_{CO_2} = 0.05, y_{H_2O} = 0.10, y_{air} = 0.85$.

Simulated results and verification

The simulated results of outlet CO_2 concentration at different time are shown in Fig. 6.4.

As seen from Fig. 6.4, the simulated result by $\overline{c'^2} - \varepsilon_c$ two-equation model of CMT is better than that by Ayobi, indicating the CMT model is suitable to the fluidized process.

The simulated radial averaged CO_2 concentration along the fluidized bed is given in Figs. 6.5 and 6.6.

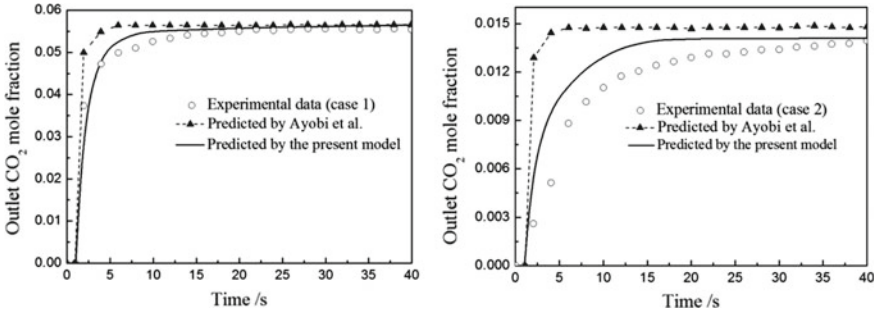

(a) Case 1 (b) Case 2

Fig. 6.4 Outlet concentration of CO_2 at different time. **a** Case 1, **b** Case 2

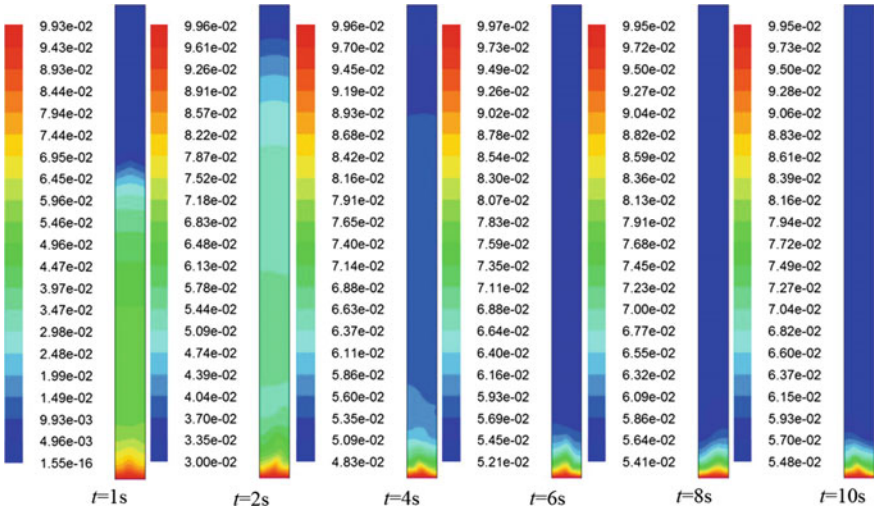

Fig. 6.5 CO_2 concentration in the fluidized bed at different time

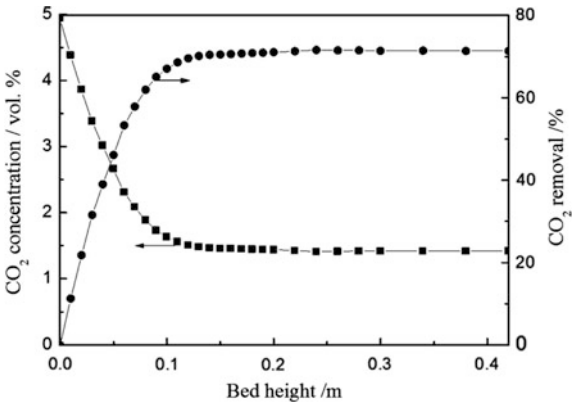

Fig. 6.6 Radial averaged CO_2 concentration along the fluidized bed (case 1)

Figure 6.5 indicates that (1) The radial distribution of CO_2 concentration is nonuniform. (2) The CO_2 concentration is high at the central region of the bed and descends gradually toward the wall. The reason of such character may be due to the solid fraction is higher near the wall as seen in Figs. 6.7 and 6.8 so that the reaction of CO_2 is faster there and thus CO_2 concentration becomes lower. In addition, it maybe also due to the uneven distribution of gas velocity as shown in Fig. 6.9.

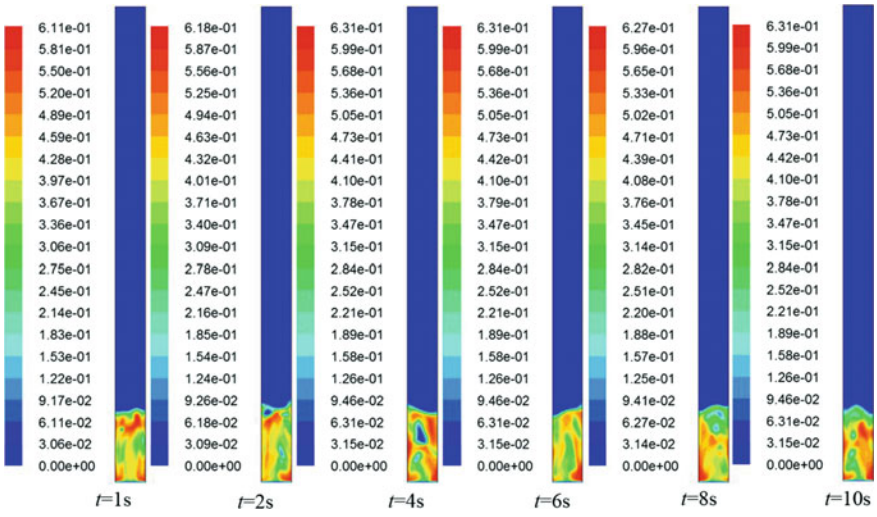

Fig. 6.7 Volume fraction of solid along fluidized bed at different time

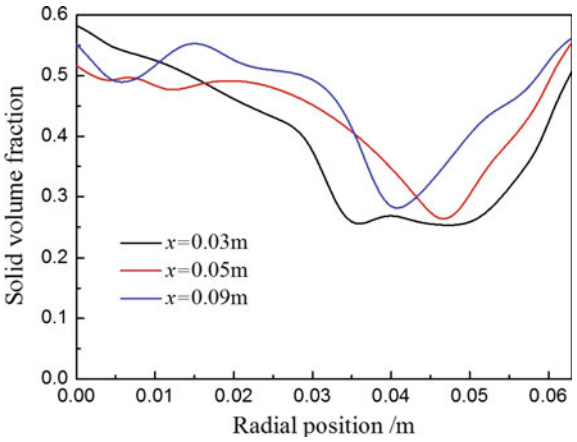

Fig. 6.8 Radial distribution of solid volume fraction at different bed height

x -- bed height measured from the bottom of the fluidized bed

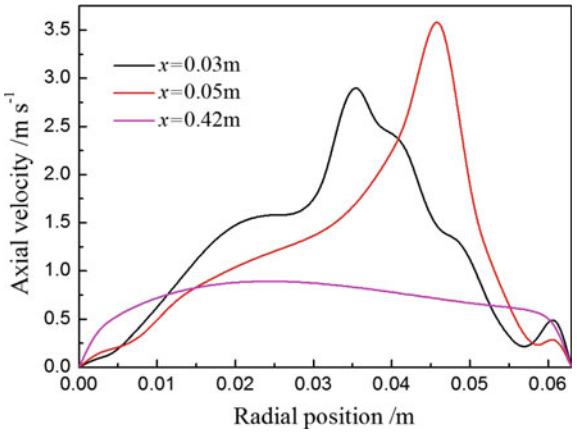

Fig. 6.9 Radial distribution of axial gas velocity at t = 10 s (case 1)

The gas phase mass diffusivity D_t is of great concern in studying fluidization. Conventionally, it is assumed to be a constant but present simulation indicates it is varying with position and time as seen from Figs. 6.10 and 6.11. In the central region, D_t shows wavy variation and then lower down toward the wall. Such pattern may be related with the turbulence of gas phase flow which is more violence in the center region. The D_t is high near the inlet (x = 0.03 m) owning to sudden increase turbulence from uniform inlet flow, then D_t behaves relatively steady at further beyond the inlet as the gas phase flow there is becoming steady.

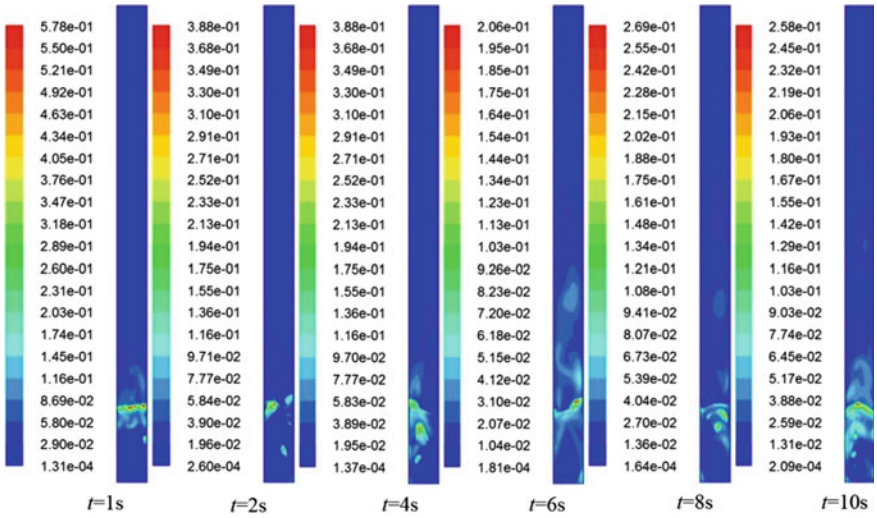

Fig. 6.10 Distribution of turbulent mass diffusivity along bed height at different time (case 1)

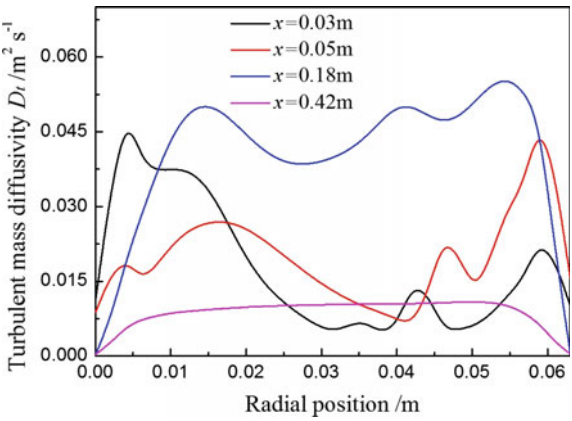

Fig. 6.11 Radial distribution of gas phase turbulent mass diffusivity (case 1)

Simulation of Ozone Decomposition in the Riser of CFB Reactor

The model equations are the same as given in Sect. 6.2.1 except that the inlet ozone concentration is very low (20 ppm) and the heat transfer equation can be omitted.

The simulated radial profiles of ozone concentration at different CFB riser heights and experimental data are shown in Fig. 6.12.

As seen from Fig. 6.12, the simulated results are in reasonable agreement with the experimental data, indicating once again the two-equation model of CMT can

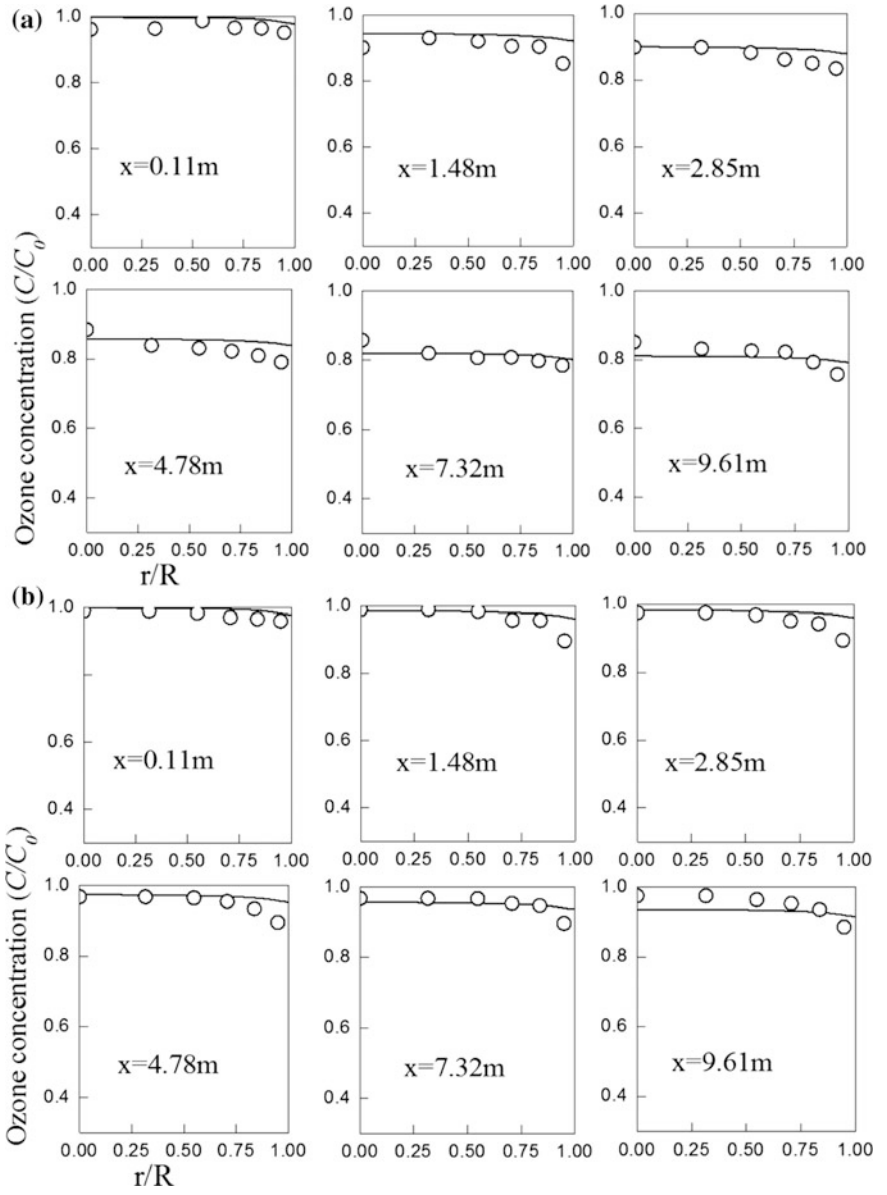

Fig. 6.12 Radial profiles of ozone concentration at different CFB riser heights (Ug3-Gs100)

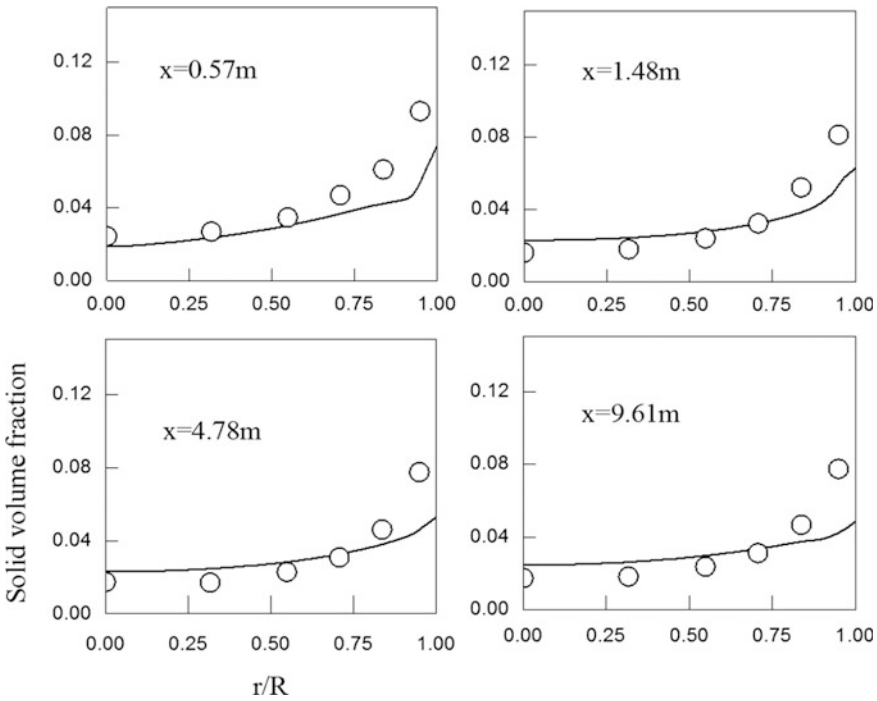

Fig. 6.13 Radial profiles of solid volume fraction at different CFB riser heights (Ug3-Gs100)

be used for simulating fluidization process. Note that the ozone concentrations are lower near the wall, it may be due to the particle density is high at the wall region so as to decompose more ozone there. The distribution of particle density is given in Fig. 6.13.

It should be mentioned that discrepancy between simulations and experimental data are obviously seen in Figs. 6.11and 6.12. The error of simulation may come from model assumptions: first, the radial symmetry (two-dimensional model) and second, unique particle diameter. Actually, the radial direction is unsymmetrical and the particle diameters are in varying size.

The radial profiles of gas and solid phase velocities at different CFB riser heights are displayed in Fig. 6.14.

As seen in Fig. 6.14, the velocities of gas and solid phases in the central region are higher than those near the wall, especially at the lower part of the riser $x = 0.57$ m. This may be as a result of low solid density in the central part and high-solid density near the wall as given in Fig. 6.13.

From the two-equation model of CMT, the isotropic turbulent diffusivity $D_{g,t}$ can be obtained as given in Fig. 6.15 where the tendency of $D_{g,t}$ is decreasing from center to the wall. It can be explained that higher central velocity causes more

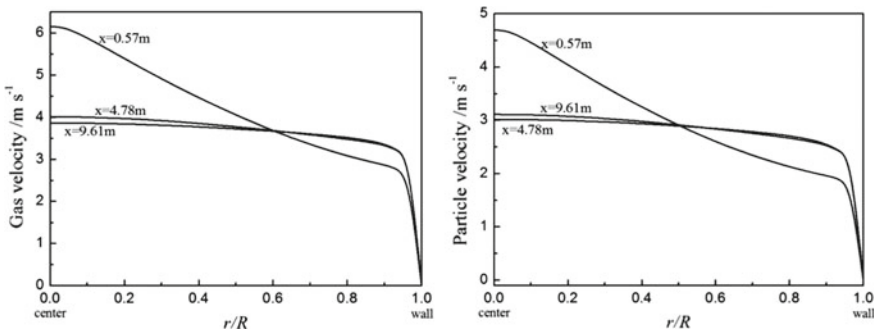

(a)Velocity of gas phase; (b) Velocity of solid phase

Fig. 6.14 Radial profiles of gas and solid phase velocities at different CFB riser heights (Ug3-Gs100). **a** Velocity of gas phase; **b** velocity of solid phase

turbulence so as higher turbulent diffusivity. The average volumetric isotropic turbulent diffusivity $D_{g,t}$ is found to be 2.07×10^{-2} m/s.

6.2.2 *Simulation of Ozone Decomposition in the Downer of CFB Reactor*

The model equations are similar to that of precedent Sect. 6.2.1 except that the boundary conditions are as follows:

$$\textit{Inlet condition } \overline{U} = \overline{U_{\text{in}}},\ k_{\text{in}} = 0.003\overline{U_{\text{in}}}^2,\ \varepsilon_{\text{in}} = 0.09\frac{k_{\text{in}}^{1.5}}{d_{\text{H}}},$$

$$\overline{C} = \overline{C_{\text{in}}},\ \overline{c_{\text{in}}'^2} = \left(0.082\overline{C_{\text{in}}}\right)^2,\ \varepsilon_{c',\text{in}} = R_\tau\left(\frac{\varepsilon_{\text{in}}}{k_{\text{in}}}\right)\overline{c_{\text{in}}'^2},$$

$$R_\tau = \left(C_{T0}\frac{k_{\text{in}}^2}{\varepsilon_{\text{in}}}\frac{1}{D_{\text{t}}}\right),^2$$

where R_τ represents the time scale, the negative, and plus signs of R_τ refer respectively to the reactant (ozone) and product (oxygen), the D_{t} in present case is in the order of 10, so that R_τ is approximate equal to 0.1, d_{H} is hydraulic diameter, calculated by

$$d_{\text{H}} = \frac{4\gamma_\infty}{a(1-\gamma_\infty)}$$

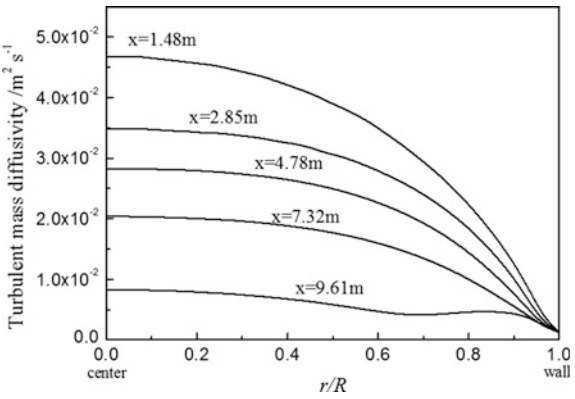

Fig. 6.15 Radial profiles of gas phase isotropic turbulent mass diffusivity $D_{g,t}$ (Ug5-Gs100)

γ_∞ is the average voidage, α is the volumetric surface area, given below

$$a = \frac{6(1-\gamma_\infty)}{d_p}$$

Outlet condition Fully developed turbulence.
Wall condition No slip and mass flux of species is zero.

The drag force in the model equation is taken from the following model:

$$\beta_{gs} = 0.006475 C_D \frac{\alpha_s \alpha_g \rho_g}{d_p} \left|\vec{u}_s - \vec{u}_g\right| \left(\frac{\rho_g}{\rho_{mix}}\right) \alpha_s^{-\chi} \quad \text{for} \quad \left(0.0003 < \alpha_s < \alpha_{s,choking}\right)$$

$$C_D = \begin{cases} \frac{24}{Re(1+0.15Re^{0.687})}, & Re \le 1000 \\ 0.44, & Re > 1000 \end{cases} \qquad Re = \frac{\rho_g \alpha_g \left|\vec{u}_s - \vec{u}_g\right| d_p}{\mu_g}$$

Simulated results

The simulated radial profiles of ozone concentration at different CFB downer heights and experimental data are shown in Fig. 6.15. In Figs. 6.15 and 6.16, where the ○ point is experimental data, the black line is the simulated result.

Figure 6.16a display the ozone concentration is lower in the wall region; it can be explain that the particle volume fraction is high near the wall as seen in Fig. 6.17 so that more ozone is decomposed there.

Comparison between Figs. 6.11 and 6.15, also Figs. 6.12 and 6.16 shows similarity, indicating the behaviors of riser and downer is similar in tendency. The simulated results are in reasonable agreement with the experimental although some errors are seen. The discrepancy may come from the assumptions of axial symmetry and unique particle diameter which deviate from actual case.

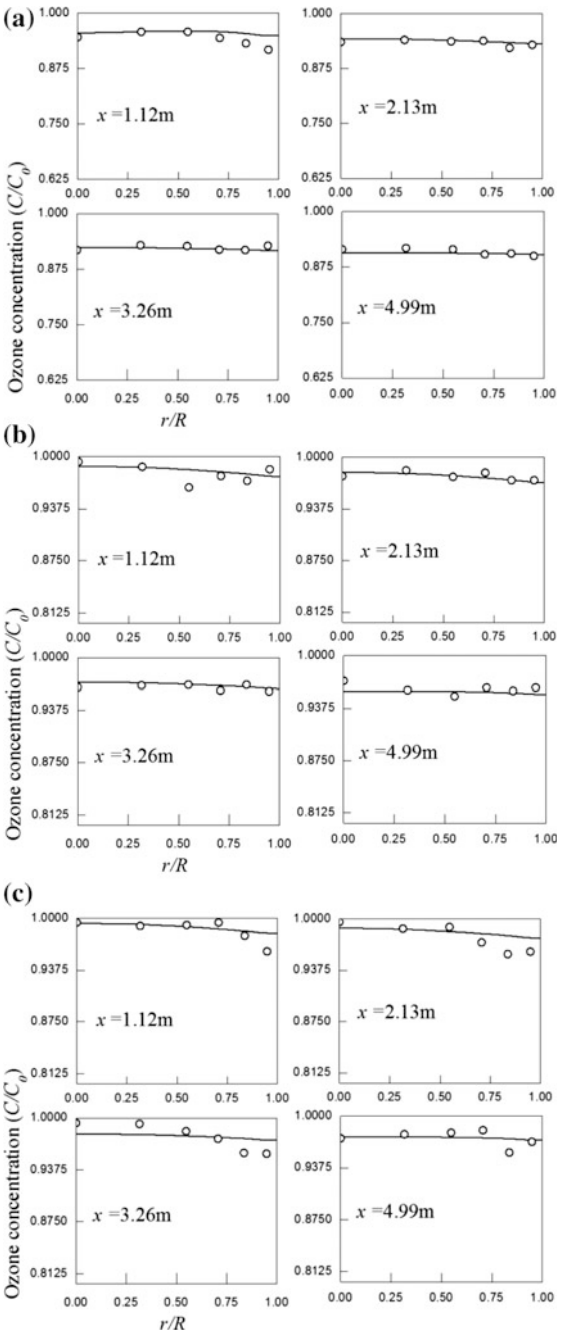

Fig. 6.16 Simulated and experimental measurement of downer ozone concentration profiles along radial direction at different axial positions for three cases of experiment: **a** Ug2-Gs100; **b** Ug5-Gs100; **c** Ug5-Gs50 (reprinted from Ref. [7], Copyright 2015, with permission from Elsevier)

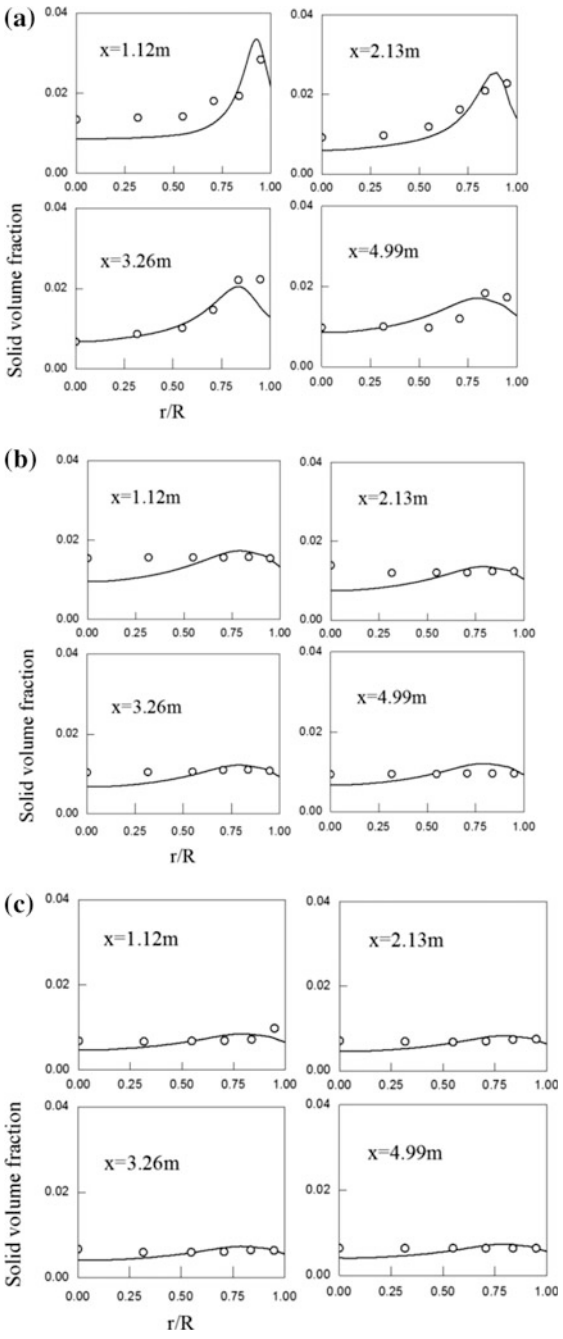

Fig. 6.17 Solid volume fraction profiles along radial direction at different axial positions for experiment **a** Ug2-Gs100; **b** Ug5-Gs100; **c** Ug5-Gs50 (reprinted from Ref. [7], Copyright 2015, with permission from Elsevier)

6.3 Reynolds Mass Flux Model for Simulating Fluidized Process

6.3.1 Model Equations

(1) **Turbulent mass transfer part of model equation and its closure**

Mass conservation equation for species in gas phase:

$$\frac{\partial}{\partial t}\left(\rho_{\mathrm{g}}\alpha_{\mathrm{g}}\overline{C_n}\right)+\frac{\partial}{\partial x_i}\left(\rho_{\mathrm{g}}\alpha_{\mathrm{g}}\overline{u_{\mathrm{g}i}}\,\overline{C_n}\right)=\frac{\partial}{\partial x_i}\left[\rho_{\mathrm{g}}\alpha_{\mathrm{g}}\left(D_{\mathrm{gn}}\frac{\partial\overline{C_n}}{\partial x_i}-\overline{u'_{\mathrm{g}i}c'_n}\right)\right]+R_i,$$
$$n=\mathrm{O}_2,\mathrm{O}_3$$

where $\overline{C}$ is the species mass fraction in gas phase, i.e. $\overline{C_{\mathrm{O}_3}}+\overline{C_{\mathrm{O}_2}}+\overline{C_{\boldsymbol{air}}}=1$; the subscript n denotes the species of ozone and oxygen; $D_{\boldsymbol{gn}}$ is the molecular diffusivity of species in gas phase; $-\rho_{\boldsymbol{g}}\alpha_{\mathrm{g}}\overline{u'_{\boldsymbol{g}i}c'_n}$ is the Reynolds mass flux (kg m^{-2} s^{-1}), which is an unknown term to be determined. In conventional model, the Reynolds mass flux $-\rho_{\boldsymbol{g}}\alpha_{\boldsymbol{g}}\overline{u'_{\boldsymbol{g}i}c'_n}$ is often solved by applying the generalized Boussinesq's postulation $-\rho_{\boldsymbol{g}}\alpha_{\mathrm{g}}\overline{u'_{\boldsymbol{g}i}c'_n}=D_{\boldsymbol{gn,t}}\left(\partial\overline{C_n}/\partial x_i\right)$, where the coefficient $D_{\boldsymbol{gn,t}}$, commonly called the turbulent mass diffusivity, is isotropic and determined either by using empirical correlations from inert tracer experiments or by guessing a constant turbulent Schmidt number Sc_{t} [12, 13]. Such approach is convenient to be used; nevertheless, the right choice of turbulent Schmidt numbers Sc_{t} or its empirical correlations is relying on experience. Moreover, the Schmidt number $Sc_{\mathrm{t}}=\frac{\mu}{\rho D_{\mathrm{gn}}}$ implies that the D_{gn} and μ are in simple proportion, that means the concentration distribution is proportional to that of velocity, which is obviously unjustified. As stated in foregoing section, many investigators have found that the turbulent mass diffusion in CFB is anisotropic [14] which indicates that the use of isotropic Sc_{t} and $D_{\boldsymbol{gn,t}}$ is unacceptable. Therefore, the newly developed anisotropic Reynolds mass flux model [15] seems a reasonable attempt to tackle this problem by using the following anisotropic Reynolds mass flux model expression for closing the turbulent mass transfer equation:

$$\frac{\partial\left(\rho_{\mathrm{g}}\alpha_{\mathrm{g}}\overline{u'_{\mathrm{g}i}c'_n}\right)}{\partial t}+\frac{\partial\left(\rho_{\mathrm{g}}\alpha_{\mathrm{g}}\overline{u_{\mathrm{g}i}}\,\overline{u'_{\mathrm{g}i}c'_n}\right)}{\partial x_j}=\frac{\partial}{\partial x_j}\left(C_{C1}\frac{k_{\mathrm{g}}}{\varepsilon_{\mathrm{g}}}\overline{u'_{\mathrm{g}l}u'_{\mathrm{g}m}}\frac{\partial\left(\rho_{\mathrm{g}}\alpha_{\mathrm{g}}\overline{u'_{\mathrm{g}i}c'_n}\right)}{\partial x_k}+D\frac{\partial\left(\rho_{\mathrm{g}}\alpha_{\mathrm{g}}\overline{u'_{\mathrm{g}i}c'_n}\right)}{\partial x_j}\right)$$
$$-\rho_{\mathrm{g}}\alpha_{\mathrm{g}}\overline{u'_{\mathrm{g}i}u'_{\mathrm{g}j}}\frac{\partial\overline{C_n}}{\partial x_j}-C_{c2}\rho_{\mathrm{g}}\alpha_{\mathrm{g}}\frac{\varepsilon_{\mathrm{g}}}{k_{\mathrm{g}}}\overline{u'_{\mathrm{g}i}c'_n}-C_{c3}\rho_{\mathrm{g}}\alpha_{\mathrm{g}}\overline{u'_{\mathrm{g}j}c'_n}\frac{\partial\overline{u_{\mathrm{g}i}}}{\partial x_j},$$

where the constants were found to be [15]: $C_{\mathrm{C1}}=0.09$, $C_{\mathrm{C2}}=3.2$, $C_{\mathrm{C3}}=0.55$; For computing the foregoing equation, it should be modeled according to the modeling rules as follows:

$$\frac{\partial\left(\rho_g\alpha_g\overline{u'_{gi}u'_{gj}}\right)}{\partial t}+\frac{\partial\left(\rho_g\alpha_g\overline{u_{gj}u'_{gi}u'_{gj}}\right)}{\partial x_j}=\frac{\partial}{\partial x_j}\left[C_{u1}\frac{k}{\varepsilon}\overline{u'_{gl}u'_{gm}}\delta\frac{\partial\left(\rho_g\alpha_g\overline{u'_{gi}u'_{gj}}\right)}{\partial x_k}+\frac{\mu_g}{\rho_g}\frac{\partial\left(\rho_g\alpha_g\overline{u'_{gi}u'_{gj}}\right)}{\partial x_j}\right]+\rho_g\alpha_g P_{ij}$$
$$-\frac{2}{3}\delta_{ij}\rho_g\alpha_g\varepsilon_g-C_{u2}\rho_g\alpha_g\frac{\varepsilon_g}{k_g}\left(\overline{u'_{gi}u'_{gj}}-\frac{2}{3}\delta_{ij}k_g\right)+C_{u3}\rho_g\alpha_g\left(P_{ij}-\frac{1}{3}P_{ii}\right)+\Omega_{gs},$$

where Ω_{gs} represents the interaction of the gas-particle phases; $P_{ij}=-\left(\overline{u'_iu'_m}\frac{\partial\overline{U_j}}{\partial x_m}+\overline{u'_ju'_m}\frac{\partial\overline{U_i}}{\partial x_m}\right)$; and the model constants are: $C_{u1}=0.09,\ C_{u1}=2.3,\ C_{u1}=0.4$.

The auxiliary k_g and ε_g equations are listed below:

k_g equation:

$$k_g=\frac{1}{2}\overline{u'_{gi}u'_{gi}}$$

ε_g equation:

$$\frac{\partial\left(\rho_g\alpha_g\varepsilon_g\right)}{\partial t}+\frac{\partial\left(\rho_g\alpha_g\varepsilon_g\overline{u_{gi}}\right)}{\partial x_j}=\frac{\partial}{\partial x_j}\left[C_\varepsilon\frac{k}{\varepsilon}\overline{u'_{gl}u'_{gm}}\delta\frac{\partial\left(\rho_g\alpha_g\varepsilon_g\right)}{\partial x_k}+\frac{\mu_g}{\rho_g}\frac{\partial\left(\rho_g\alpha_g\varepsilon_g\right)}{\partial x_j}\right]$$
$$+C_{1\varepsilon}\rho_g\alpha_g\frac{\varepsilon_g}{k_g}\overline{u'_{gi}u'_{gj}}\frac{\partial\overline{u_{gi}}}{\partial x_j}-C_{2\varepsilon}\rho_g\alpha_g\frac{\varepsilon_g^2}{k_g},$$

where the constants are: $C_\varepsilon=0.07,\ C_{1\varepsilon}=1.45,\ C_{2\varepsilon}=1.92$.

The rate of the ozone decomposition, r, is [16]:

$$r=k_rX_{O_3}\alpha_s \tag{1}$$

where k_r is the reaction rate constant and is determined experimentally [16] by Li et al. X_{O_3} is the mole concentration of the ozone in gas phase.

Thus, the source term R_i is determined by:

$$R_i=\pm r\frac{P_g}{RT_g}M_i, \tag{2}$$

where the negative and plus signs refer respectively to the reactant (ozone) and product (oxygen); P_g, T_g are the pressure and operating temperature of the gas phase; M_i is the molar mass of species.

(2) **The CFD part of model equation**

For the simulation of the gas-particle two-phase flow, the Reynolds stress model derived from solid kinetic theory and the drag model based on energy minimization multi-scale (EMMS) principal [9, 10] are used in the present simulation. The governing equations and constitutive relations for this part are summarized in Table 6.1.

Table 6.1 Main equations and constitutive relations for the two-fluid model of gas-particle flows

(1). Continuity equations of gas and particle phases

$$\frac{\partial}{\partial t}\left(\alpha_{\mathrm{g}}\rho_{\mathrm{g}}\right)+\nabla\times\left(\alpha_{\mathrm{g}}\rho_{\mathrm{g}}\overrightarrow{u_{\mathrm{g}}}\right)=0$$

$$\frac{\partial}{\partial t}\left(\alpha_{\mathrm{s}}\rho_{\mathrm{s}}\right)+\nabla\times\left(\alpha_{\mathrm{s}}\rho_{\mathrm{s}}\overrightarrow{u_{\mathrm{s}}}\right)=0$$

$$\alpha_{\mathrm{g}}+\alpha_{\mathrm{s}}=1$$

(2). Momentum equations for gas and particle phases

$$\frac{\partial}{\partial t}\left(\alpha_{\mathrm{g}}\rho_{\mathrm{g}}\overrightarrow{u_{\mathrm{g}}}\right)+\nabla\times\left(\alpha_{\mathrm{g}}\rho_{\mathrm{g}}\overrightarrow{u_{\mathrm{g}}}\overrightarrow{u_{\mathrm{g}}}\right)=\nabla\times\left(\overline{\overline{\tau_{\mathrm{g,e}}}}\right)+\alpha_{\mathrm{g}}\left(\rho_{\mathrm{g}}\overrightarrow{\mathrm{g}}-\nabla P_{\mathrm{g}}\right)+\beta_{\mathrm{gs}}\left(\overrightarrow{u_{\mathrm{s}}}-\overrightarrow{u_{\mathrm{g}}}\right)$$

$$\frac{\partial}{\partial t}\left(\alpha_{\mathrm{s}}\rho_{\mathrm{s}}\overrightarrow{u_{\mathrm{s}}}\right)+\nabla\times\left(\alpha_{\mathrm{s}}\rho_{\mathrm{s}}\overrightarrow{u_{\mathrm{s}}}\overrightarrow{u_{\mathrm{s}}}\right)=\nabla\times\left(\alpha_{\mathrm{s}}\overline{\overline{\tau_{\mathrm{s,e}}}}\right)+\alpha_{\mathrm{s}}\left(\rho_{\mathrm{s}}\overrightarrow{\mathrm{g}}-\nabla P_{\mathrm{s}}\right)+\beta_{\mathrm{gs}}\left(\overrightarrow{u_{\mathrm{g}}}-\overrightarrow{u_{\mathrm{s}}}\right)$$

where

$$\overline{\overline{\tau_{\mathrm{g,e}}}}=\overline{\overline{\tau_{\mathrm{g}}}}+\overline{\overline{\tau_{\mathrm{g,t}}}}$$

$$\overline{\overline{\tau_{\mathrm{g}}}}=\mu_{\mathrm{g}}\alpha_{\mathrm{g}}\left(\nabla\overrightarrow{u_{\mathrm{g}}}+\nabla\overrightarrow{u_{\mathrm{g}}}^{\mathrm{T}}\right)-\frac{2}{3}\mu_{\mathrm{g}}\alpha_{\mathrm{g}}\nabla\overrightarrow{u_{\mathrm{g}}}\overline{\overline{I}}$$

$$\overline{\overline{\tau_{\mathrm{g,t}}}}=-\rho_{\mathrm{g}}\alpha_{\mathrm{g}}\overline{u'_{\mathrm{g}i}u'_{\mathrm{g}j}}$$

$$\overline{\overline{\tau_{\mathrm{s,e}}}}=\overline{\overline{\tau_{\mathrm{s}}}}+\overline{\overline{\tau_{\mathrm{s,t}}}}$$

$$\overline{\overline{\tau_{\mathrm{s}}}}=\mu_{\mathrm{s}}\alpha_{\mathrm{s}}\left(\nabla\overrightarrow{u_{\mathrm{s}}}+\nabla\overrightarrow{u_{\mathrm{s}}}^{\mathrm{T}}\right)+\left(\xi_{\mathrm{s}}-\frac{2}{3}\mu_{\mathrm{s}}\right)\alpha_{\mathrm{s}}\nabla\overrightarrow{u_{\mathrm{s}}}\overline{\overline{I}}$$

$$\overline{\overline{\tau_{\mathrm{s,t}}}}=-\rho_{\mathrm{s}}\alpha_{\mathrm{s}}\overline{u'_{\mathrm{s}i}u'_{\mathrm{s}j}}$$

The Reynolds stress equation for particle phase is given as follow

$$\frac{\partial\left(\rho_{\mathrm{s}}\alpha_{\mathrm{s}}\overline{u'_{\mathrm{s}i}u'_{\mathrm{s}j}}\right)}{\partial t}+\frac{\partial\left(\rho_{\mathrm{s}}\alpha_{\mathrm{s}}\overline{u_{\mathrm{s}j}}\overline{u'_{\mathrm{s}i}u'_{\mathrm{s}j}}\right)}{\partial x_j}=\frac{\partial}{\partial x_j}\left[C_{u1}\frac{k_{\mathrm{s}}}{\varepsilon_{\mathrm{s}}}\overline{u'_l u'_m}\delta\frac{\partial\left(\rho_{\mathrm{s}}\alpha_{\mathrm{s}}\overline{u'_{\mathrm{s}i}u'_{\mathrm{s}j}}\right)}{\partial x_k}+\frac{\mu_{\mathrm{s}}}{\rho_{\mathrm{s}}}\frac{\partial\left(\rho_{\mathrm{s}}\alpha_{\mathrm{s}}\overline{u'_{\mathrm{s}i}u'_{\mathrm{s}j}}\right)}{\partial x_j}\right]+\rho_{\mathrm{s}}\alpha_{\mathrm{s}}P_{ij}$$
$$-\frac{2}{3}\delta_{ij}\rho_{\mathrm{s}}\alpha_{\mathrm{s}}\varepsilon_{\mathrm{s}}-C_{u2}\rho_{\mathrm{s}}\alpha_{\mathrm{s}}\frac{\varepsilon_{\mathrm{s}}}{k_{\mathrm{s}}}\left(\overline{u'_{\mathrm{s}i}u'_{\mathrm{s}j}}-\frac{2}{3}\delta_{ij}k_{\mathrm{s}}\right)+C_{u3}\rho_{\mathrm{s}}\alpha_{\mathrm{s}}\left(P_{ij}-\frac{1}{3}P_{ii}\right)+\Omega_{\mathrm{sg}}$$

The model constants are (Zheng et al. 2001): $C_{u1}=0.09,\ C_{u1}=2.3,\ C_{u1}=0.4$

The auxiliary k_{s} and ε_{s} equations are:

$$k_{\mathrm{s}}=\frac{1}{2}\overline{u'_{\mathrm{s}i}u'_{\mathrm{s}i}}$$

$$\frac{\partial(\rho_{\mathrm{s}}\alpha_{\mathrm{s}}\varepsilon_{\mathrm{s}})}{\partial t}+\frac{\partial(\rho_{\mathrm{s}}\alpha_{\mathrm{s}}\varepsilon_{\mathrm{s}}\overline{u_{\mathrm{s}i}})}{\partial x_j}=\frac{\partial}{\partial x_j}\left[C_{\varepsilon}\frac{k}{\varepsilon}\overline{u'_{\mathrm{s}l}u'_{\mathrm{s}m}}\delta\frac{\partial(\rho_{\mathrm{s}}\alpha_{\mathrm{s}}\varepsilon_{\mathrm{s}})}{\partial x_k}+\frac{\mu_{\mathrm{s}}}{\rho_{\mathrm{s}}}\frac{\partial(\rho_{\mathrm{s}}\alpha_{\mathrm{s}}\varepsilon_{\mathrm{s}})}{\partial x_j}\right]$$
$$+C_{1\varepsilon}\rho_{\mathrm{s}}\alpha_{\mathrm{s}}\frac{\varepsilon_{\mathrm{s}}}{k_{\mathrm{s}}}\overline{u'_{\mathrm{s}i}u'_{\mathrm{s}j}}\frac{\partial\overline{u_{\mathrm{s}i}}}{\partial x_j}-C_{2\varepsilon}\rho_{\mathrm{s}}\alpha_{\mathrm{s}}\frac{\varepsilon_{\mathrm{s}}^2}{k_{\mathrm{s}}}$$

where the constants are: $C_{\varepsilon}=0.07,\ C_{1\varepsilon}=1.45,\ C_{2\varepsilon}=1.92$

(3). Equations for relevant parameters

The drag model equations [9, 10]

Here the modified drag model [9, 10] obtained from the energy minimization multi-scale (EMMS) approach. The EMMS drag model has proved to be an effective way for modeling a system of FCC particles, which is the case of the present simulation.

$$\beta_{\mathrm{gs}}=\frac{3}{4}C_{\mathrm{D}}\frac{\alpha_{\mathrm{s}}\alpha_{\mathrm{g}}\rho_{\mathrm{g}}}{d_{\mathrm{p}}}\left|\overrightarrow{u_{\mathrm{s}}}-\overrightarrow{u_{\mathrm{g}}}\right|\alpha_{\mathrm{g}}^{-2.65}f_{z_{\mathrm{g}}}$$

$$f_{z_{\mathrm{g}}}=a(Re+b)^{c}$$

(continued)

Table 6.1 (continued)

$$\begin{cases} a = 0.8526 - \frac{0.5846}{1+\left(\alpha_g/0.4325\right)^{22.6279}} & 0.4 \le \alpha_g \le 0.46 \\ c = 0 \end{cases}$$

$$\begin{cases} a = 0.0320 - \frac{0.7399}{1+\left(\alpha_g/0.4912\right)^{54.4265}} & 0.4 \le \alpha_g \le 0.545 \\ b = 0.00225 + \frac{772.0074}{1+10^{66.3224\left(\alpha_g-0.3987\right)}} + \frac{0.02404}{1+10^{53.8948\left(0.5257-\alpha_g\right)}} \\ c = 0.1705 - \frac{0.1731}{1+\left(\alpha_g/0.5020\right)^{37.7091}} \end{cases}$$

$$\begin{cases} a = \left(2124.956 - 2142.3\alpha_g\right)^{-0.4896} & 0.545 \le \alpha_g \le 0.99 \\ b = \left(0.8223 - 0.1293\alpha_g\right)^{13.0310} \\ c = \frac{\left(\alpha_g - 1.0013\right)}{-0.06633 + 9.1391\left(\alpha_g - 1.0013\right) + 6.9231\left(\alpha_g - 1.0013\right)^2} \end{cases}$$

$$\begin{cases} a = 0.4243 + \frac{0.8800}{1+\exp\left(-\left(\alpha_g - 0.9942\right)/0.00218\right)}\left(1 - \frac{1}{1+\exp\left(-\left(\alpha_g - 0.9989\right)/0.00003\right)}\right) & 0.99 \le \alpha_g \le 0.9997 \\ b = 0.01661 + 0.2436\exp\left(-0.5\left(\frac{\alpha_g - 0.9985}{0.00191}\right)^2\right) \\ c = 0.0825 - 0.0574\exp\left(-0.5\left(\frac{\alpha_g - 0.9979}{0.00703}\right)^2\right) \end{cases}$$

$$\begin{cases} a = 1 & 0.9997 \le \alpha_g \le 1 \\ c = 0 \end{cases}$$

$$C_D = \begin{cases} \frac{24}{\alpha_g Re\left(1+0.15Re^{0.687}\right)}, & Re \le 1000 \\ 0.44, & Re > 1000 \end{cases}$$

$$Re = \frac{\rho_g \alpha_g \left|\overrightarrow{u_s} - \overrightarrow{u_g}\right| d_p}{\mu_g}$$

Particulate phase pressure equation [17]

$p_s = \alpha_s \rho_s \Theta_s + 2\rho_s(1+e_{ss})\alpha_s^2 g_{0,ss}\Theta_s$

where the radial distribution function is [18]:

$$g_{0,ss} = \left[1 - \left(\frac{\alpha_s}{\alpha_{s,max}}\right)^{1/3}\right]^{-1}$$

Granular temperature equation [19]:

$$\frac{3}{2}\left[\frac{\partial}{\partial t}\left(\alpha_s \rho_s \Theta_s\right) + \nabla \times \left(\alpha_s \rho_s \overrightarrow{u_s} \Theta_s\right)\right] = \nabla \times \left(\Gamma_\Theta \nabla \Theta_s\right) + \overline{\overline{\tau_{s,e}}} \nabla \overrightarrow{u_s} - p_s \nabla \overrightarrow{u_s} + \phi_{gs} - \gamma$$

where the diffusion coefficient for particle phase energy fluctuation is [17]:

$$\Gamma_\Theta = \frac{15 d_p \rho_s \alpha_s \sqrt{\Theta_s \pi}}{4(41-33\eta)}\left[1 + \frac{12}{5}\eta^2(4\eta - 3)\alpha_s g_{0,ss} + \frac{16}{5\pi}(41 - 33\eta)\eta\alpha_s g_{0,ss}\right], \quad \eta = \frac{1}{2}(1+e_{ss})$$

The exchange of fluctuation energy is [20]:

$\phi_{gs} = -3\beta_{gs}\Theta_s$

The collisional dissipation of energy fluctuation is [21]:

$$\gamma = 3\left(1 - e_{ss}^2\right)\alpha_s^2 g_{0,ss}\rho_s \Theta_s \left[\frac{4}{d_p}\sqrt{\frac{\Theta_s}{\pi}} - \nabla \overrightarrow{u_s}\right]$$

Particulate phase shear stresses equation

$\mu_s = \mu_{s,col} + \mu_{s,kin} + \mu_{s,fr}$ where the frictional viscosity $\mu_{s,fr}$ in present simulation is set to be zero; the collisional viscosity and kinetic viscosity are [20, 22]

$$\mu_{s,col} = \frac{4}{5}\alpha_s \rho_s d_s g_{0,ss}(1+e_{ss})\left(\frac{\Theta_s}{\pi}\right)^{1/2}$$

$$\mu_{s,kin} = \frac{\alpha_s \rho_s d_s \sqrt{\Theta_s \pi}}{6(3-e_{ss})}\left[1 + \frac{2}{5}(1+e_{ss})(3e_{ss}-1)\alpha_s g_{0,ss}\right]$$

Particulate bulk viscosity [21]

$$\xi_s = \frac{4}{3}\alpha_s \rho_s d_s g_{0,ss}(1+e_{ss})\left(\frac{\Theta_s}{\pi}\right)^{1/2}$$

Table 6.2 The feedstock properties and main operating conditions [16]

Feedstock properties	
Gas density (kg m^{-3})	1.225
Gas viscosity (kg m^{-1} s^{-1})	1.7894×10^{-5}
Particle density (kg m^{-3})	1370
Particle mean diameter (μm)	60
Operating conditions	
Inlet ozone concentration (ppm)	10–25
Gas superficial velocities (m s^{-1})	2–5
Particle circulation rates (kg m^{-2} s^{-1})	50, 100
Gas temperature (K)	295.15
Reaction rate constants (s^{-1})	3.76.4.07

6.3.2 *Simulation of the Riser in CFB Ozone Decomposition*

The object of the simulation is an experimental CFB riser for the catalytic ozone decomposition. The riser has an inner radius of 0.0381 m and a height of 10.2 m. The geometry of the CFB riser is shown in Fig. 6.18. The feedstock properties and main operating conditions are listed in Table 6.2. More information about the simulated CFB riser is available in the literature reported by Li et al. [16].

Appropriate boundary conditions are necessary for solving the model equations. In order to make the solution possible, some simplified boundary conditions are adopted. The bottom inlet of the CFB riser is set to be "velocity inlet" condition and the velocities, volume fractions, and mass content of ozone are specified according to the desired operating conditions. The turbulent energies and dissipation rates of the two phases are specified as these proposed by Zheng et al. [23]; while the inlet condition for the Reynolds stress is set to be [24]:

$$\overline{u_i' u_j'} = \begin{cases} \frac{2}{3} k_{\text{in}}, & i = j \\ 0, & i \neq j \end{cases}$$

The generalized Boussinesq's postulation is adopted for $\overline{u_{gi}' c_n'}$ inlet:

$$\left(-\overline{u_{gi}' c_n'}\right)_{\text{in}} = D_{\text{t}} \left(\partial \overline{C_n} / \partial x_i\right),$$

where D_{t} and α_{t} are recommended to be $D_{\text{t}}=\nu_{\text{t}}/0.7$ and $\alpha_{\text{t}}=\nu_{\text{t}}/0.9$, thus:

$$\left(-\overline{u_{gi}' c_n'}\right)_{\text{in}} = \frac{\nu_{\text{t,in}}}{0.7} \left(\partial \overline{C_n} / \partial x_i\right)\Big|_{\text{in}}$$

and the inlet turbulent viscosity $\nu_{t,in} = C_\mu \frac{k_{in}^2}{\varepsilon_{in}}$ with constant $C_\mu = 0.09$.

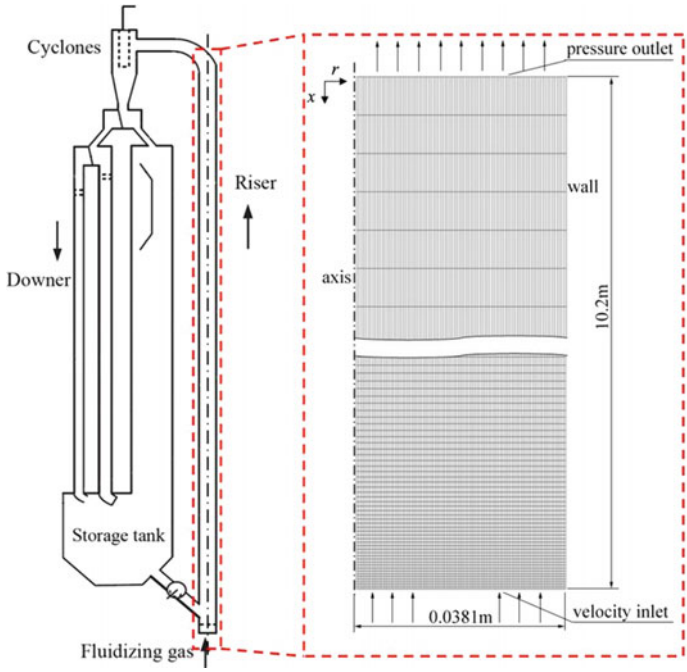

Fig. 6.18 Geometry of the computational domain and the mesh scheme (reprinted from Ref. [6], Copyright 2015, with permission from Elsevier)

The outlet at the top of the riser is set as the "pressure outlet" boundary. At the axis of the riser, the condition of $\partial \Phi / \partial r = 0$ is set for all variables. As for the wall, no-slip boundary condition is applied for the gas phase, and the partial-slip boundary condition is adopted for the particle phase.

Grid-size and time-step-size analysis

The computation domain (0.038 m × 10.2 m) and the grid arrangement of the CFB riser are shown in Fig. 6.18, which comprise totally 139050 quadrilateral cells.

To ensure that the simulated results presented in this paper are independent of mesh density, the CFB riser was meshed with different radial and axial grid points of 45 × 775, 90 × 1545, and 135 × 2318. The simulated results on axial profiles of solid volume fraction under different mesh densities (with time-step-size of 0.00001 s) are shown in Fig. 6.19. It is seen that grid points of 45 × 775 would result in significant deviation. It is better to refine the mesh scheme so as to improve the computation-stability. Since satisfactory computation-stability can be got with the mesh scheme of 90 × 1545 and no substantial difference of the simulated result is found with increasing number of grids beyond 139050, the mesh scheme of 90 × 1545 is chosen for the present simulation.

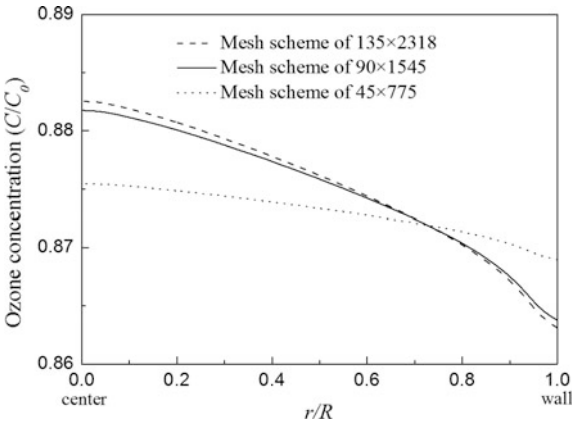

Fig. 6.19 Comparison of the predicted axial profiles of ozone concentration with different mesh schemes (reprinted from Ref. [6], Copyright 2015, with permission from Elsevier)

To further optimize the time-step-size, simulations are run for different time-step-sizes: 0.00001, 0.00005, 0.0001, and 0.0002 s. And it is found that time-step-size larger than 0.0002 s would result in divergences of the Reynolds mass flux equation. Although convergent results can be obtained by using the time-step-size of 0.0002 s, the computation-stability is worse in the course of simulation. Further on, as seen in Fig. 6.20 that the time-step-size less than 0.0001 s provide no substantially different results but needs much more computation-time. Therefore, the 0.0001 s time-step-size and 90×1545 mesh scheme are used as the based computation settings for every case.

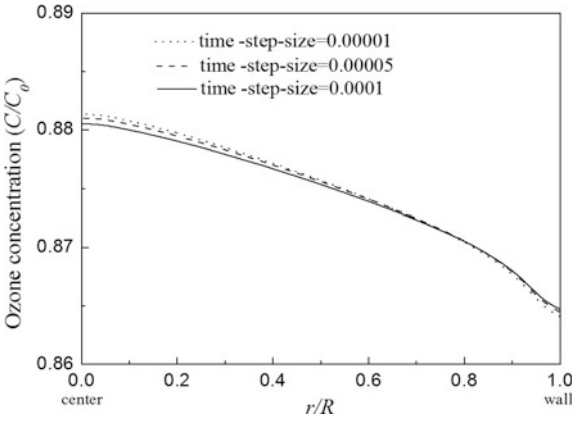

Fig. 6.20 Comparison of the simulated radial profiles of ozone concentration with different time-step-sizes (reprinted from Ref. [6], Copyright 2015, with permission from Elsevier)

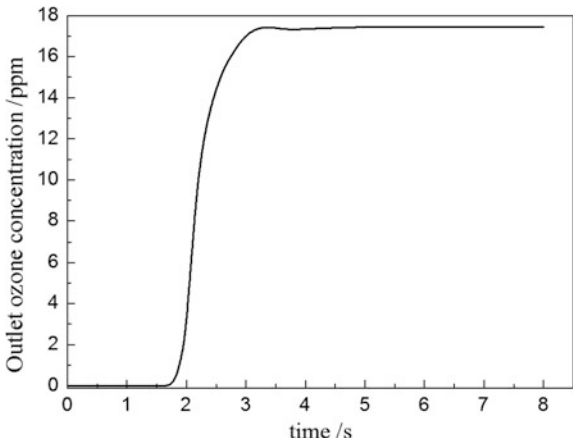

Fig. 6.21 Outlet ozone concentration versus flow time (Ug4-Gs100) (reprinted from Ref. [6], Copyright 2015, with permission from Elsevier)

It should be noted that the solutions will reach "steady condition" after a certain flow time of unsteady state simulation. In the course of simulation, the outlet ozone concentration (after radial averaged) is plotted versus the flow time as shown in Fig. 6.21. When the outlet concentration is substantially constant, it is assumed that all solutions have reached the steady condition.

Simulated results and verification

Six sets of experimental data on ozone decomposition in CFB riser were reported by Li et al. [16]. only experiments Ug4-Gs100, Ug5-Gs50, Ug5-Gs100, are taken as examples for comparison.

(1) **Outlet ozone concentration**

Figure 6.21 gives the outlet ozone concentration (after radial averaged) versus the flow time. It is demonstrated that the outlet concentration remains nearly unchanged with time after 4 s. Therefore, the solutions after $t = 4$ s are considered as the steady solutions. All of the following simulated results are referring to those of steady conditions.

(2) **Radial and axial profiles of ozone concentration and solid volume fraction**

Figure 6.22 shows the radial profiles of the dimensionless ozone concentration (ratio of the local ozone concentration to the inlet ozone concentration) versus *r/R*. Satisfactory agreement is found between the simulations and the experimental data [16], which confirms the validity of the present CMT model for the ozone decomposition in CFB risers. At a fixed axial position, the ozone concentration is decreased slightly near the wall region, due to the higher solid volume fraction in

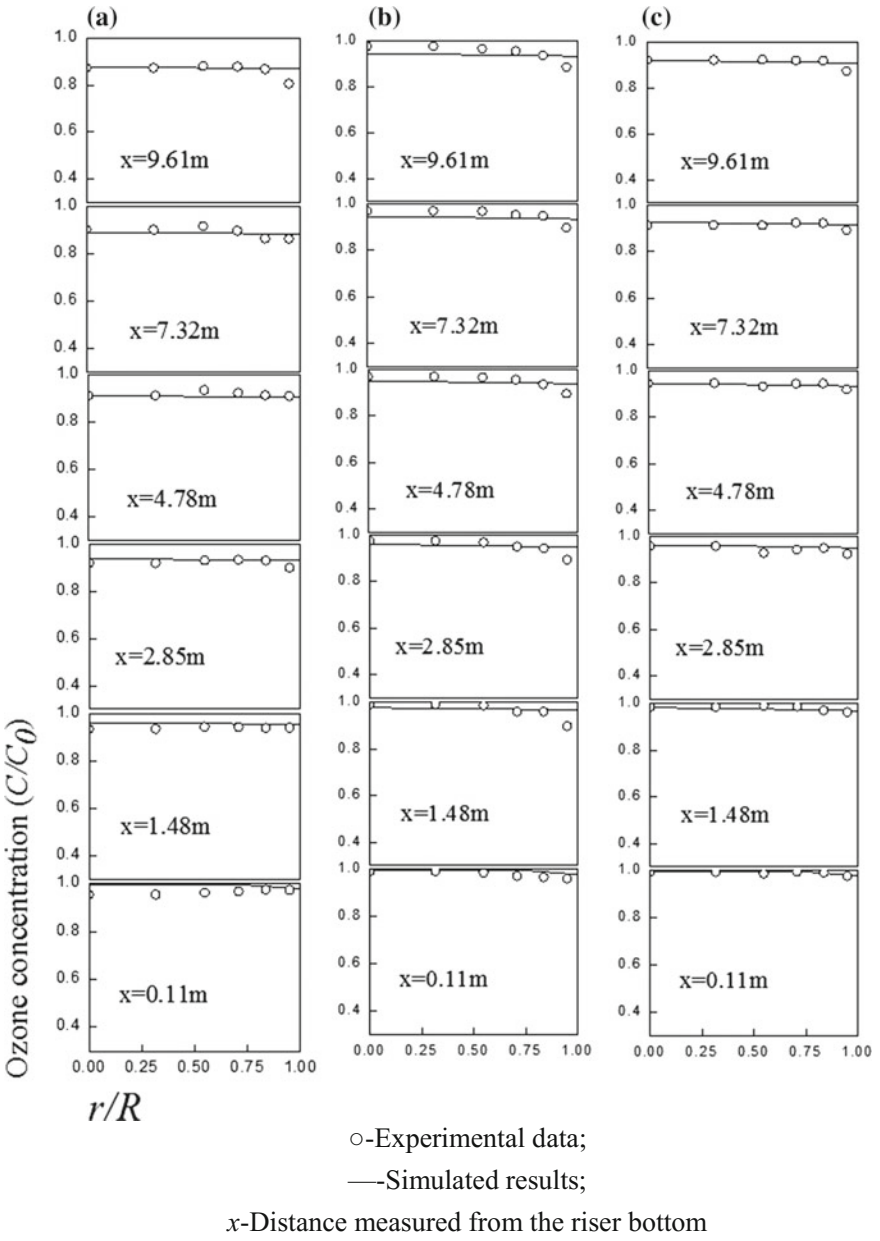

Fig. 6.22 Simulated and experimental measurement of ozone concentration profiles along radial direction at different axial positions for three cases of experiment. **a** Ug4-Gs100; **b** Ug-Gs50; **c** Ug5-Gs100

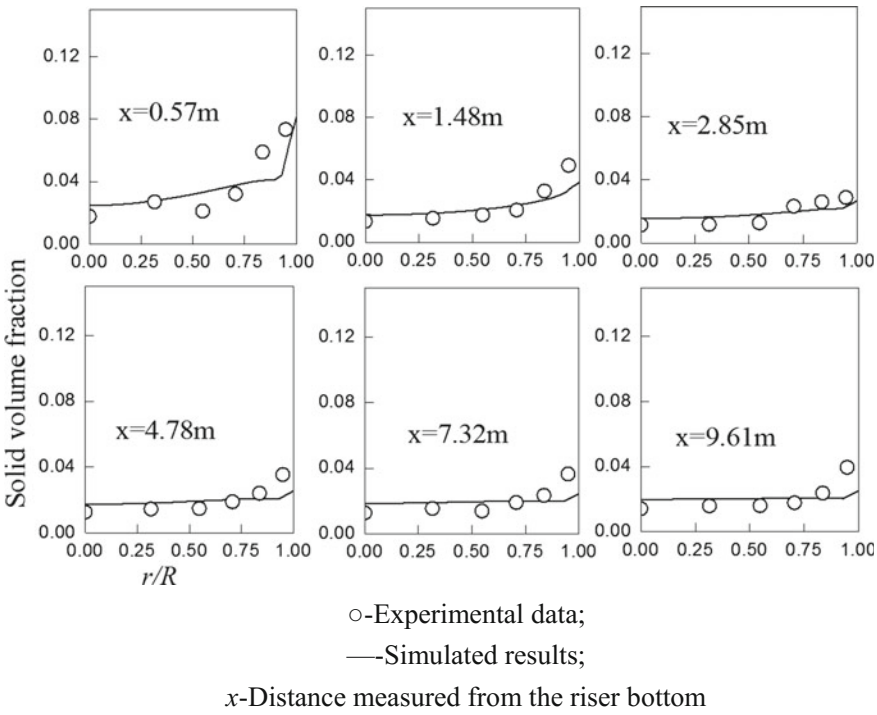

Fig. 6.23 Solid volume fraction profiles along radial direction at different axial positions for experiment Ug5-Gs100 (reprinted from Ref. [6], Copyright 2015, with permission from Elsevier)

this region than in the center as shown in Fig. 6.23. That means the higher solid concentration promotes the ozone decomposition to make the ozone concentration lower down which leads the C/C_o becoming lower near the wall. This is so called core-annulus structure of particles, and have been observed by many investigators [1–3, 20]. It is also seen from Figs. 6.22 and 6.23 that some deviations are seen between the simulation and experimental measurements. This may be due to the following reasons: first, the particles used for the experiment are in different sizes. Yet in the simulation a mean particle size is used for convenience. Second, the present model is based on the assumption of axis-symmetry, which deviates from the actual flowing condition.

The axial profiles of ozone concentration and solid volume fraction are given in Figs. 6.24 and 6.25, which indicates that the simulated axial profile of ozone concentration and solid volume fraction by using the present CMT model (solid lines) agree satisfactorily with the experimental data reported by Li et al. [16].

Figure 6.24 demonstrates that the simulation by Reynolds mass flux model gives better result than the two-equation model indicating that the fluidized flow is

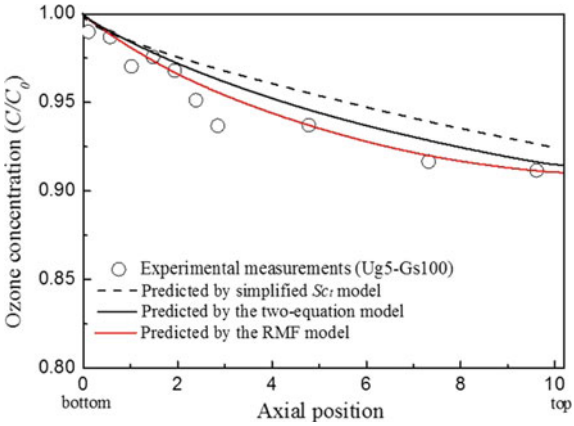

Fig. 6.24 Axial profiles of radial averaged ozone concentration (Ug5-Gs100)

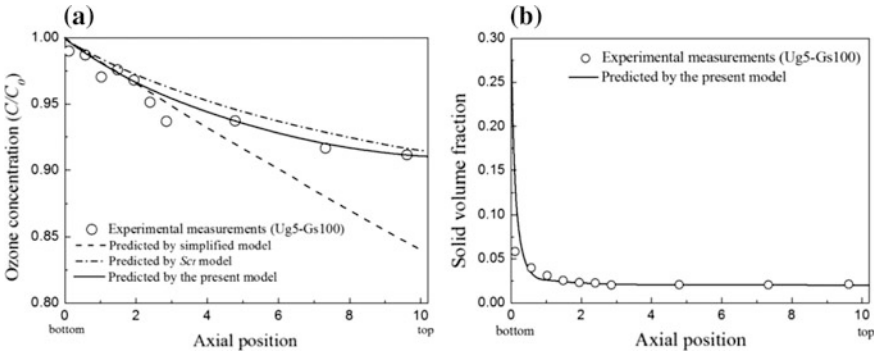

Fig. 6.25 Comparison between simulated and experimental axial profiles of **a** ozone concentration and **b** solid volume fraction (Ug5-Gs100) (reprinted from Ref. [6], Copyright 2015, with permission from Elsevier)

anisotropic rather than isotropic. Figure 6.25a also gives the predicted concentration profiles by using the simplified plug-flow reactor (PFR) model and the turbulent Schmidt number (Sc_t) model. The PFR model is based on plug flow in the reactor, which neglects the effect of turbulent mass diffusion and takes the values of radial average velocities and phase volume fractions from experiments. The simulated results by the PFR model for experiment Ug5-Gs100 on ozone concentration profile are shown in Fig. 6.25a by dot line and seen with considerable error. As mentioned in the foregoing section, there are many attempts on modeling and simulating concentration profiles by using Sc_t model. As seen in Fig. 6.25a, the

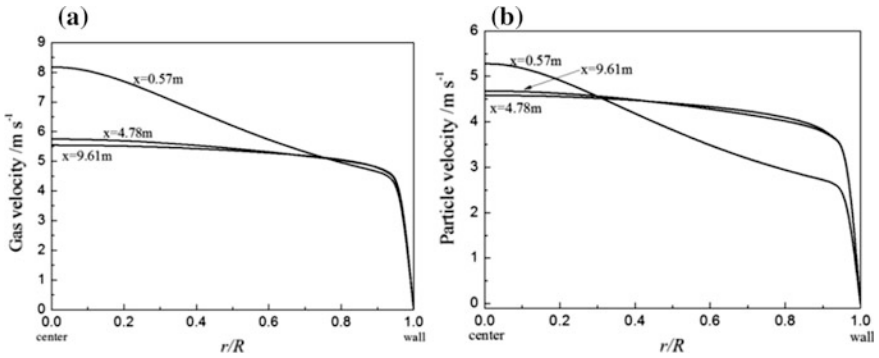

Fig. 6.26 Radial profiles of gas and particle velocities: **a** gas velocity; **b** particle velocity (Ug5-Gs100) (*x*-distance measured from the riser bottom) (reprinted from Ref. [6], Copyright 2015, with permission from Elsevier)

axial profiles of ozone concentration is clearly shown that the present CMT model give better simulation than the Sc_t model (dash line). It indicates that the use of Sc_t model or the use of isotropic turbulent mass diffusivity would produce appreciable error in simulating the concentration profiles of CFB riser.

(3) **Velocity profiles**

Figure 6.26a, b shows the profiles of gas and particle axial velocities along radial direction. It is found that the gas and solid velocities in the core region are showing convex shape of velocity profile with much higher axial velocity than that in the annulus region. This could be attributed to the core-annulus structure of particles as shown in Fig. 6.23. As a result of higher particle density in the annulus region, the resistance of gas-particle flow is increased so as to reduce the gas velocity. Moreover, the application of nonslip and partial-slip wall conditions will further result in decreasing of velocity when approaching to the wall. The convex shape of velocity profile is more clearly seen in the lower part of the riser, due to the more significant core-annulus structure of particles in this region (see Fig. 6.23).

Figure 6.27 shows the axial velocity profiles of particle along axial direction of the bed. The comparison of the CMT model predictions and experimental measurements shows that the particle velocity is accelerated rapidly in the lower part of the riser, reaches a maximum value, and then keeps almost unchanged. This phenomenon is cause by the dramatically gas-particle interaction near the riser inlet, where the particle velocity is much lower than the gas velocity. When the particle velocity is accelerated to a certain value and the drag force between gas and particle phases is balanced with the gravitational force, then, the particle velocity is maintained almost constant.

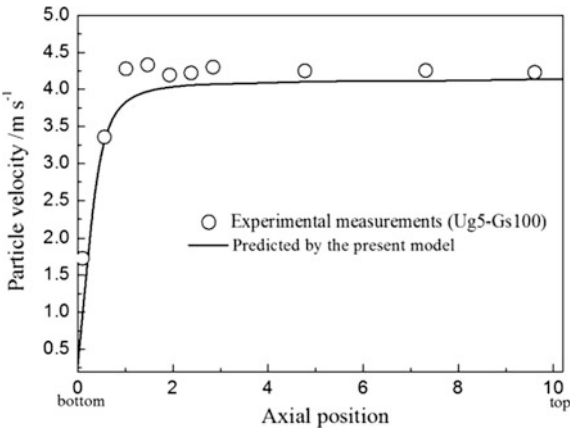

Fig. 6.27 Comparison between simulated and experimental axial profiles of particle velocity (Ug5-Gs100) (reprinted from Ref. [6], Copyright 2015, with permission from Elsevier)

(4) **Profiles of anisotropic turbulent mass diffusivity**

Figures 6.28 and 6.29 show the anisotropic Reynolds mass flux and the concentration gradient of the ozone in gas phase obtained by using the present CMT model. According to the generalized Boussinesq's postulation, the anisotropic turbulent mass diffusivity can be represented by the following equations:

$$D_{t,x} = \overline{u_x' c'} \Big/ -\frac{\partial \overline{C}}{\partial x} \quad \text{and} \quad D_{t,r} = \overline{u_r' c'} \Big/ -\frac{\partial \overline{C}}{\partial r}$$

It is noted that the evaluation of $D_{t,x}$ and D_{tr} here is severed to show that the turbulent diffusivity is anisotropic and not isotropic as usually considered. It is not necessary to evaluate them in the course of simulation of concentration distribution by using the present CMT model.

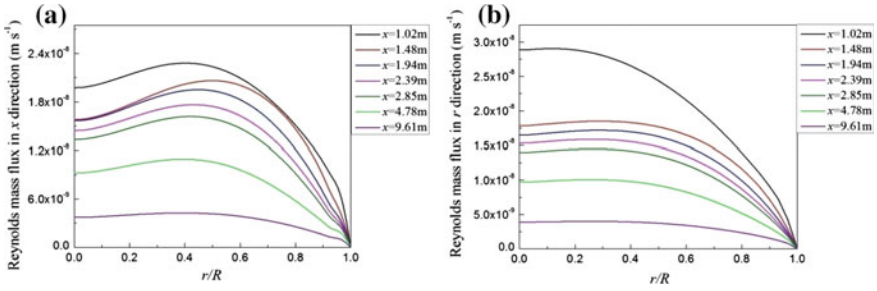

Fig. 6.28 Simulated profiles of Reynolds mass flux in axial and radial directions: **a** profiles of $\overline{u_x' c'}$; **b** profiles of $\overline{u_r' c'}$ for experiment (Ug5-Gs100)

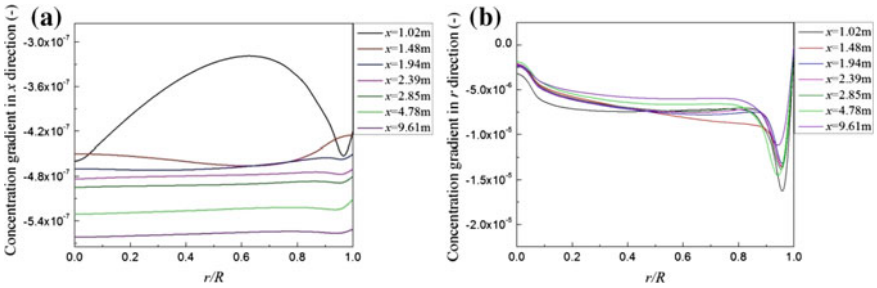

Fig. 6.29 Simulated profiles of ozone concentration gradient in axial and radial directions: **a** profiles of $\partial\overline{C} / \partial x$; **b** profiles of $\partial\overline{C} / \partial r$ for experiment (Ug5-Gs100)

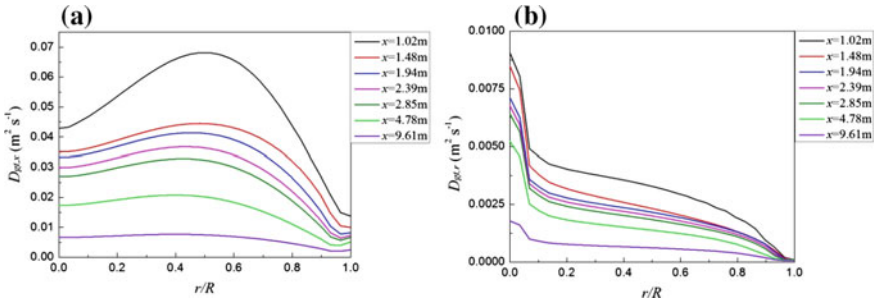

Fig. 6.30 Simulated profiles of turbulent mass diffusivity: **a** profiles of $D_{t,x}$; **b** profiles of $D_{t,r}$ for experiment (Ug5-Gs100) (reprinted from Ref. [6], Copyright 2015, with permission from Elsevier)

For illustration, the turbulent mass diffusivities $D_{t,x}$ and $D_{t,r}$ are calculated and shown in Fig. 6.30. It is seen that there is no analogy between the diffusivities in the two directions.

From Fig. 6.29a, the axial turbulent mass diffusivity is found to be decreased with riser height. It also can be found from this figure that the value of $D_{gt,x}$ is decreased when approaching to the riser wall. It can be understood that the velocity is reduced in the near wall region and the turbulence of gas phase is constrained due to the nonslip condition applied at the wall. As for the distributions of radial turbulent mass diffusivity $D_{gt,r}$, a general tendency of descending is found from the column center to the column wall and from the bottom inlet of the riser to the top outlet.

Figure 6.31 shows the comparisons of volume averaged axial and radial gas turbulent mass diffusivities (for experiment Ug5-Gs100) with those reported in the literatures [25–29] surveyed by [14]. The results from literatures appear quite different, due to the fact that the experimental turbulent mass diffusivity is obtained from different experimental facilities under different operating conditions. The

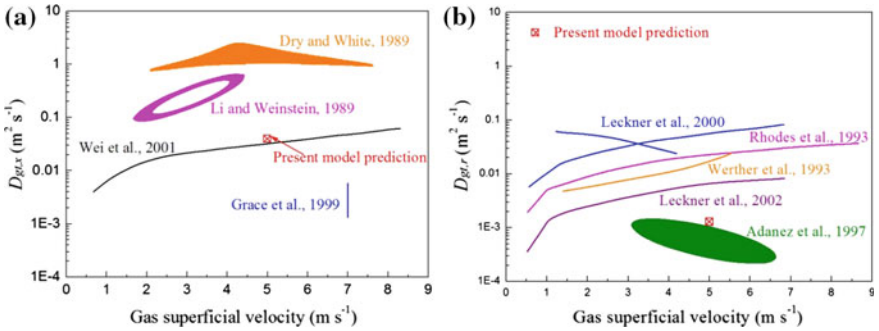

Fig. 6.31 Effect of gas superficial velocity on gas turbulent mass diffusivity: **a** axial gas turbulent mass diffusivity $D_{gt,x}$; **b** radial gas turbulent mass diffusivity $D_{gt,y}$ (reprinted from Ref. [6], Copyright 2015, with permission from Elsevier)

simulated turbulent mass diffusivities using present CMT model are found to be in reasonable agreement with the average experimental data. As seen in the figures, the values of axial turbulent mass diffusivity are found to be greater than the radial one, which is consistent with the finding by [30]. This explains why using the unique isotropic turbulent mass diffusivity would produce error in simulation, as shown in Fig. 6.25a.

6.3.3 *Simulation of the Downer in CFB Ozone Decomposition*

The model equations and boundary conditions are the same as in Sect. 6.3.2.

The simulated results are given below:

Simulation of ozone concentration radial profile at different bed height

The radial profiles of ozone concentration along different axial position are shown in Figs. 6.32 and 6.33 is the comparison with experimental data.

As seen in Fig. 6.33 the simulation by Reynolds mass flux model is confirmed by the experimental data. It demonstrates that the behaviors of mass transfer and flow in downer are also anisotropic so that the anisotropic Reynolds model gives close simulation. For more understanding, the simulated radial profiles of anisotropic turbulent mass diffusivity are shown in Fig. 6.34.

Figure 6.34 displays the difference of simulated axial and radial diffusivities to support the anisotropic characters of riser and downer in fluidized bed.

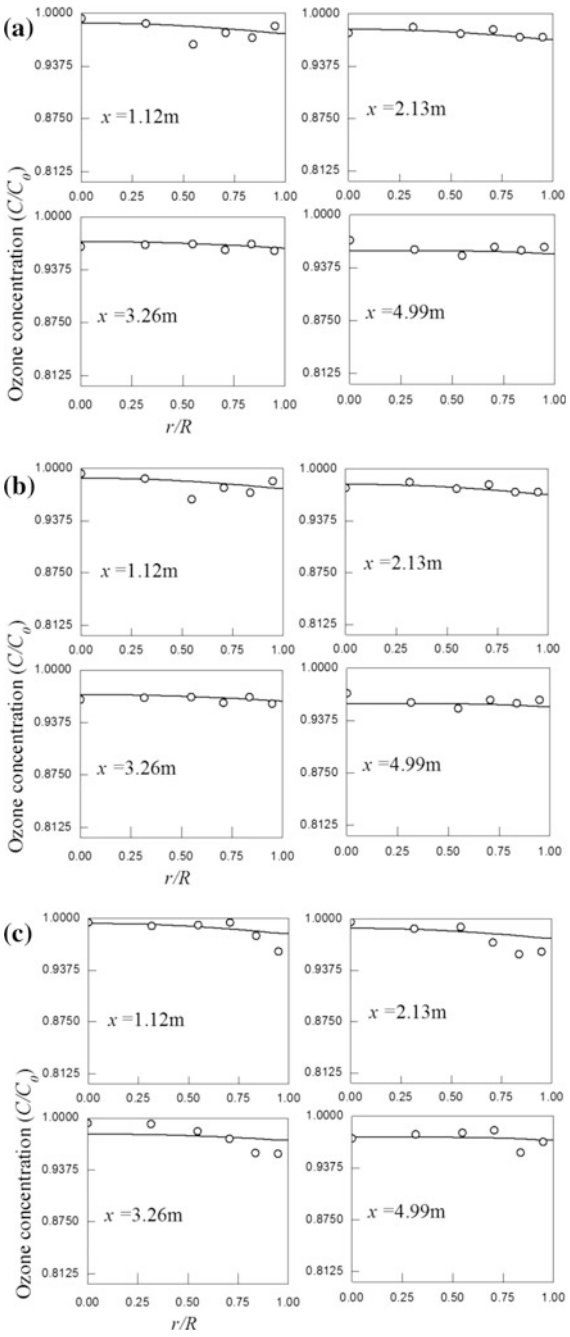

Fig. 6.32 Simulated and experimental measurement of ozone concentration profiles along radial direction at different axial positions for three cases of experiment: **a** Ug4-Gs100; **b** Ug-Gs50; **c** Ug5-Gs10

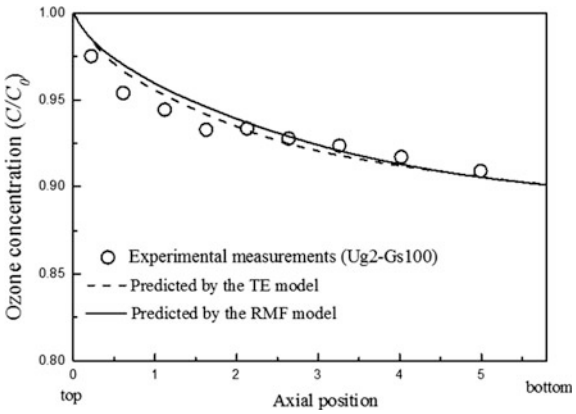

Fig. 6.33 Axial profile of ozone concentration at different axial position

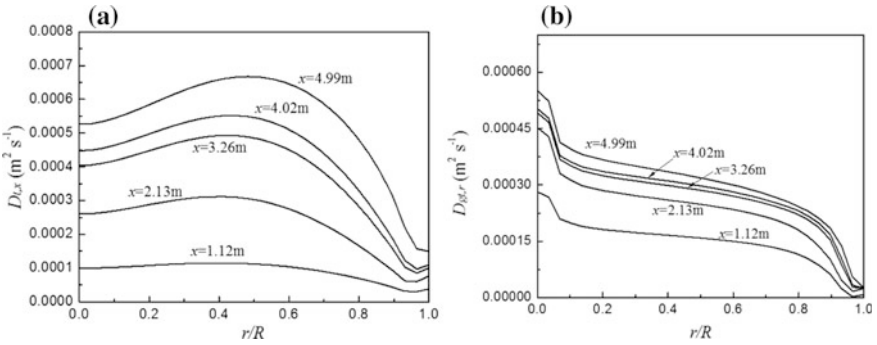

Fig. 6.34 Radial profiles of anisotropic turbulent mass diffusivity (Ug2-Gs100). **a** Axial turbulent mass diffusivity; **b** radial turbulent mass diffusivity

6.4 Summary

In this chapter, CMT model is applied to simulating the reaction process in the fixed fluidized bed (FFB) and in the CFB. To validate the CMT application, simulation is made for the CO_2 removal and ozone decomposition in CFB and compare with experimental results.

The following major remarks can be made:

(1) The validity of CMT model is confirmed by the satisfactory agreement between the simulated results and the experimental data in the profiles of concentration, solid volume fraction, and fluid velocity of fluidized bed.
(2) The concentration distribution as well as the mass transfer behaviors in fluidized bed is anisotropic as shown by both experimental work and CMT simulation.

(3) The turbulent mass diffusion in a fluidized reactor is found to be anisotropic as shown by the CMT simulation which is consistent with the reported experimental study in the literature.
(4) Comparison of simulated results with experimental data shows that the CMT model behaviors better than the PFR model without considering turbulent mass diffusivity and the empirical Sc_t model based on isotropic turbulent mass diffusivity.
(5) The simulation by using Reynolds mass flux model of CMT is shown better than that by using two-equation model due to the reason that the fluidized flow is anisotropic rather than isotropic.
(6) Accurate simulation can be achieved for fluidized bed only if all the anisotropic behavior is taken into account.

References

1. Helland E, Bournot H, Occelli R, Tadrist L (2007) Drag reduction and cluster formation in a circulating fluidized bed. Chem Eng Sci 62:148–158
2. Yan A, Zhu J (2004) Scale-up effect of riser reactors (1): axial and radial solids concentration distribution and flow development. Ind Eng Chem Res 43:5810–5819
3. Bolland O, Nicolai R (2001) Describing mass transfer in circulating fluidized bed by ozone decomposition. Chem Eng Commun 187:1–21
4. Kallio S, Airaksinen J, Guldén M, Hermanson A, Peltola J, Ritvanen J, Seppälä M, Shah S, Taivasssalo V (2009) Experimental and numerical study of hydrodynamics in a circulating fluidized bed. In: Proceedings of Finnish-Swedish Flame Days, Naantali
5. M'Bouana NLP, Zhao FX, Zhang QH, Lu HL (2014) Numerical simulation of gas-solid flow in square cyclone separators with downward exit. J Harbin Inst Technol 21:83–90
6. Li WB, Yu KT, Yuan XG, Zhu J, Liu BT, Shao YY (2015) An isotropic Reynolds mass flux model for the simulation of chemical reaction in gas particle CFB riser. Chem Eng Sci 135:117–127
7. Li WB, Yu KT, Liu BT, Yuan XG (2015) Computational fluid dynamics simulation of hydrodynamics and chemical reaction in a CFB downer. Powder Technol 269:425–436
8. Ayobi M, Shahhosseini S, Behjat Y (2014) Computational and experimental investigation of CO_2 capture in gas–solid bubbling fluidized bed. J Taiwan Inst Chem Eng 45:421–430
9. Lu B, Wang W, Li J (2011) Eulerian simulation of gas–solid flows with particles of Geldart groups A, B and D using EMMS-based meso-scale model. Chem Eng Sci 66:4624–4635
10. Lu B, Wang W, Li J (2009) Searching for a mesh-independent sib-grid model for CFD simulation of gas-solid riser flow. Chem Eng Sci 64:3437–3447
11. Yang N, Wang W, Ge W, Li J (2004) Simulation of heterogeneous structure in a circulating fluidized bed riser by combining the two fluid model with the EMMS approach. Ind Eng Chem Res 43:5548–5561
12. Bruchmüller J, van Wachem BGM, Gu S, Luo KH, Brown RC (2012) Modeling the thermochemical degradation of biomass inside a fast pyrolysis fluidized bed reactor. AIChE J 58:3030–3042
13. Chang J, Zhang K, Chen H, Yang Y, Zhang L (2013) CFD modelling of the hydrodynamics and kinetic reactions in a fluidised-bed MTO reactor. Chem Eng Res Des 91:2355–2368
14. Breault RW (2006) A review of gas–solid dispersion and mass transfer coefficient correlations in circulating fluidized beds. Powder Technol 163:9–17

15. Li WB, Liu BT, Yu KT, Yuan XG (2011) A new model for the simulation of distillation column. Chin J Chem Eng 19:717–725
16. Li D, Ray AK, Ray MB, Zhu J (2013) Catalytic reaction in a circulating fluidized bed riser: ozone decomposition. Powder Technol 242:65–73
17. Syamlal M, O'Brien TJ (1989) Computer simulation of bubbles in a fluidized bed. AIChE Symp Ser 85:22–31
18. Ogawa S, Umemura A, Oshima N (1980) On the equations of fully fluidized granular materials. Zeitschrift für angewandte Mathematik und Physik ZAMP 31:483–493
19. Ding J, Gidaspow D (1990) A bubbling fluidization model using kinetic theory of granular flow. AIChE J 36:523–538
20. Gidaspow D, Bezburuah R, Din J (1991) Hydrodynamics of circulating fluidized beds: kinetic theory approach
21. Lun CKK, Savage SB, Jeffrey DJ, Chepurniy N (1984) Kinetic theories for granular flow: inelastic particles in Couette flow and slightly inelastic particles in a general flowfield. J Fluid Mech 140:223–256
22. Syamlal M, Rogers W, O'Brien TJ (1993) MFIX documentation: volume 1, theory guide. National Technical Information Service, Springfield, VA
23. Zheng Y, Wan X, Qian Z, Wei F, Jin Y (2001) Numerical simulation of the gas–particle turbulent flow in riser reactor based on k–ε–kp–εp–Θ two-fluid model. Chem Eng Sci 56:6813–6822
24. Nishimura M, Tokuhiro A, Kimura N, Kamide H (2000) Numerical study on mixing of oscillating quasi-planar jets with low Reynolds number turbulent stress and heat flux equation models. Nucl Eng Des 202:77–95
25. Amos G, Rhodes MJ, Mineo H (1993) Gas mixing in gas–solids risers. Chem Eng Sci 48:943–949
26. Dry RJ, White CC (1989) Gas residence-time characteristics in a high-velocity circulating fluidised bed of FCC catalyst. Powder Technol 58:17–23
27. Gayán P, de Diego LF, Adánez J (1997) Radial gas mixing in a fast fluidized bed. Powder Technol 94:163–171
28. Li J, Weinstein H (1989) An experimental comparison of gas backmixing in fluidized beds across the regime spectrum. Chem Eng Sci 44:1697–1705
29. Sternéus J, Johnsson F, Leckner B (2002) Characteristics of gas mixing in a circulating fluidised bed. Powder Technol 126:28–41
30. Wei F, Du B, Fan LS (2001) Gas mixing in a turbulent fluidized bed with fines addition at high temperatures and pressures, fluidization X. United Engineering Foundation, Beijing

Chapter 7
Mass Transfer in Multicomponent Systems

Abstract Theoretical basis and empirical correlations applicable in the computational mass transfer model for binary and multicomponent mass transfer are discussed in this chapter. The description of multicomponent mass transfer is best by applying the Maxwell–Stefan equation is shown to be the best way of description of multicomponent mass transfer. Generalized Fick's law for multicomponent mass transfer, related parameters' estimation models, and thermodynamic models are also discussed in this chapter.

Keywords Mass transfer across gas–liquid interface · Multicomponent mass transfer · Maxwell–Stefan equation · Fick's law · Empirical correlation

Nomenclature

$[B]$	Matrix of inverted Maxwell–Stefan Diffusivities, m^{-2} s
D	Maxwell–Stefan diffusivity, m^2 s^{-1};
D	Molecular diffusivity, m^2 s^{-1}
D_{AB}^{F}	Fick's law diffusivity, m^2 s^{-1}
E_{MV}	Murphree tray efficiency on gas basis
E_{ML}	Murphree tray efficiency on liquid basis
F	F factor, $U_G\sqrt{\rho_G}$, m s^{-1}(kg m^{-3})$^{0.5}$
F^E	Excess free energy (in thermodynamic)
g	Excess free energy (in group contribution)
h	Weir height in tray column, m
J	Mass transfer flux, mol m^{-2} s^{-1}
k_G	Gas phase mass transfer coefficient in packed column, kg m^{-2} s^{-1}
k_L	Liquid phase mass transfer coefficient in packed column, kg m^{-2} s^{-1}
$[k]$	Matrix of mass transfer coefficients, m s^{-1}
L	Liquid flow rate per unit cross-sectional area, kg m^{-2} s^{-1}
l	Characteristic length, m;
$[N_i]$	Molar mass flux of diffusing species i, mol^{-2} s^{-1}
$[N_t]$	Molar mass flux of multicomponent solution, mol^{-2} s^{-1}
r	Position in radial direction, m
$[R]$	Matrix of inverted mass transfer coefficients, m^{-1} s

K.-T. Yu and X. Yuan, *Introduction to Computational Mass Transfer*,
Heat and Mass Transfer, DOI 10.1007/978-981-10-2498-6_7

Sc	Schmidt number
Sc_t	Turbulent Schmidt number
t	Time, s
U	Superficial velocities, m s^{-1}
x	Mole fraction in liquid phase
$[X]$	Matrix of correction factor
y	Mole fraction in gas phase
ϕ_L, ϕ_V	Volume fraction of liquid phase, vapor phase
$[\beta]$	Matrix of molar exchange of mass transfer in counterdiffusion due to the difference of latent hear of vaporization between component i and j, dimensionless
$[\Gamma]$	Matrix of nonideality factor (in terms of activity coefficient γ), dimensionless
δ	Kronecker sign thickness of fluid film, m
ε	Turbulent dissipation rate, m^2 s^{-3}
μ, μ_G	Liquid and gas phase viscosity, kg m^{-1} s^{-1}
ρ, ρ	Liquid and gas phase density, kg m^{-3}
σ	Surface tension of liquid, N m^{-1}
τ_μ, τ_c, τ_m	Characteristic time scale, s

Subscripts

G	Gas
in	Inlet
L	Liquid
0	Interface
b	Bulk

In solving the mass transfer Eq. (1.1) in Chap. 1, the evaluation of the source term S_n, which is the mass rate (mass flux) transferred from adjacent phase (outside of the phase concerned) or generated by chemical reaction (inside of the phase), is very important as it highly affects the final result. For the gas–liquid two phases mass transfer process under steady state condition and assuming the driving force of mass transfer is the linear concentration difference, we can write the conventional formula for calculating the mass transfer rate of species i (dimension kg m^{-2} s^{-1}), denoted by S_n or N_i, as follows:

$$S_n = N_i = k_L\left(C_{iL}^* - C_{iL}\right) = k_G\left(C_{iG} - C_{iG}^*\right) \tag{7.1}$$

Note that in this section the subscript i and j denotes species i and j, not the directions i, j; k_L and k_G are respectively the film mass transfer coefficient of liquid and gas (m s^{-1}); C_{iL} and C_{iG} are respectively the bulk concentration of component i (kg m^{-3}) in liquid phase and gas phase; C_{iL}^* and C_{iG}^* are respectively the concentration of component i at the interface in thermodynamic equilibrium with the C_{iL} and C_{iG} (kg m^{-3}). The importance of evaluation of mass transfer coefficient k_L or

k_G is clearly seen from the foregoing equation. Nevertheless, the prediction of the coefficient is difficult and so far only relies on experimental measurement. There are two different cases:

- For the two-component mass transfer, some empirical correlations based on experimental data are available in literature.
- For the multicomponent mass transfer, the mass transfer rate is closely related to the composition due to the complicated molecular interaction between components and exhibit different characters with two-component system. For instance, for the two-component system, the mass flux is transferred from high to low concentration, yet in multicomponent system some components can be transferred from low to high concentration. This is what we called "bizarre phenomena" (see Sect. 2.1.3.6). Thus the mass transfer coefficient in multicomponent system is complicated and can be calculated only under the individual condition based on the coefficients of relevant two-component pairs (see Sect. 7.2.2). For this reason, no general correlation for multicomponent mass transfer has been proposed.

7.1 Mass Transfer Rate in Two-Component (Binary) System

The mass transfer coefficient of two-component system is the basic information necessary for the prediction of mass transfer rate in the process. The calculation of mass transfer for multicomponent system is also based on the mass transfer coefficients of the correspondent binary pairs (see Sect. 2.1.3).

One of the traditional models for predicting the binary mass transfer coefficient is based on the penetration theory by Higbie [1]. It is used as our starting point.

Let us consider the case of a wetted wall (falling film) column undergoing gas absorption with the following assumptions:

1. The component i in gas phase is absorbed by binary liquid absorbent containing components i and j.
2. The velocity of falling absorbent is very low and mass is transferred by molecular diffusion. The absorption rate is low so as to keep the density of absorbent remains unchanged.
3. Penetration theory is applied, thus a fluid element (cluster of fluid particle) may stochastically move to the interface and stay there from $t = 0$ to $t = t_{Hx}$, during that time interval component i is diffused from gas to liquid phase under unsteady condition.

With the foregoing assumptions, Eq. (1.1) is simplified to the following form:

$$\frac{\partial C_i}{\partial t} = D\frac{\partial^2 C_i}{\partial z^2} \tag{7.2}$$

where D is the molecular diffusivity of component i in the fluid; z is the direction perpendicular to the interface; C_i is the concentration of component i in the fluid element; C_{iz} is the concentration of i at distance z from interface; C_i^* is the concentration of i at interface in equilibrium with C_i.

The boundary conditions are:

At $t = 0$, $z = 0$, $C_i = C_i$ (fluid element just arrive interface and still remains at the bulk concentration C_i).
At $t > 0$, $z = 0$, $C_i = C_i^*$ (interfacial gas–liquid equilibrium of component i has been established).
At $t > 0$, $z = z$, $C_i = C_{iz}$ (bulk concentration of component i).

The solution of Eq. (7.2) at constant D is found to be

$$\frac{C_i^* - C_i}{C_i^* - C_{iz}} = \operatorname{erf}\frac{z}{2\sqrt{Dt}} \tag{7.3}$$

Thus the relationship of C_i along z at different t can be obtained. Let the mass flux of component i diffused from interface to the bulk be J_i, then from the potential concept (or Fick's law) we have $J_i = D\left(-\frac{\partial C_i}{\partial z}\right)_{z=0}$. Combining with foregoing equations and after mathematical treatment, the relationship between J_i and t can be obtained as follows:

$$J_i = \left(C_i^* - C_{iz}\right)\sqrt{\frac{D}{\pi t}}$$

Integrate foregoing equation from $t = 0$ to $t = t_H$, the average rate of mass flux being transferred N_i is obtained:

$$N_i = \frac{\int_0^{t_H} J_i \mathrm{d}t}{t_H} = 2\left(C_i^* - C_{iz}\right)\sqrt{\frac{D}{\pi t_H}}$$

By the definition of mass transfer coefficient k_L, i.e., $N_i = k_L\left(C_{iL}^* - C_{iL}\right)$, we obtain k_L by employing penetration theory as follows:

$$k_L = 2\sqrt{\frac{D}{\pi t_H}} \tag{7.4}$$

According to the penetration theory, the t_H is the residence time of a fluid element at the interface undergoing the gas–liquid contact. Thus $t_H = \frac{l}{u}$ where u is the velocity of the fluid element at the interface (equal to the velocity of falling

absorbent), l is the length of the fluid element traveled with velocity u at the time interface. The k_L equation becomes

$$k_L = 2\sqrt{\frac{Du}{\pi l}}$$

The l here may be regarded as characteristic length. Expressing the k_L in the form of dimensionless Sherwood number Sh_L, we have

$$Sh_L = \frac{k_L l}{D} = 2\frac{l}{D}\sqrt{\frac{D_t u}{\pi l}} = \sqrt{\frac{4lu}{\pi D}} = \sqrt{\frac{4}{\pi}\left(\frac{lu\rho}{\mu}\right)\left(\frac{\mu}{\rho D}\right)} = 1.128(Re)^{0.5}(Sc)^{0.5}$$

In using the foregoing *Sh-Re-Sc* form for the regression of the experimental data, the exponent 0.5 should be corrected and adjusted. The *Sh-Re-Sc* form of empirical equation is employed by some authors to fit the experimental data covering both lamina and turbulent flow as shown in Table 6.1.1:

$$Sh_L = C_0 Re^a Sc^b \tag{7.5}$$

where C_0, a, b are constants to be determined based on experimental data.

As seen from Table 7.1, the exponent in empirical Eq. (1.43) may change greatly by fitting the experimental data.

Equation (7.5), i.e., the *Sh-Re-Sc* form, is usually be modified to suit different equipment and condition of mass transfer by adding extra geometric term or dimensionless group. Table 7.2 is given some examples.

As indicated in Table 7.3, the mass transfer coefficient k_L in the Sherwood group *Sh* is not only affected by the geometry of equipment and internal construction, such as the *d/l* ratio or the ratio of packing size and column diameter, but also the fluid properties such as ρ, μ, σ in the dimensionless group.

Besides *Sh-Re-Sc* form, the k_L or k_G correlations are usually expressed according to the authors' data analysis. Some empirical correlations are given in Table 7.3 as examples.

In case that the interfacial effects, such as Marangoni interfacial convection, are occurred in the mass transfer process, the influence by the surface tension gradient $\Delta\sigma$ on k_L should also be concerned in the empirical expression (see Chap. 9) so that k_L is generally affected by the following variables:

$$k_L = f(D_t, u, \rho, \mu_t, l, \Delta\sigma)$$

or expressed as an exponential equation

$$k_L = (\text{constant}) D_t^a u^b \rho^c \mu_t^d l^e \Delta\sigma^f$$

Table 7.1 Some published empirical correlations for binary system with *Sh-Re-Sc* form

Equation	Application	Reference
$Sh = 0.015Re^{0.89}Sc^{0.5}$	Packed column absorption	[2]
	Packing: ceramic saddle	
$Sh = 4.1Re^{0.39}Sc^{0.33}$	Packed column absorption	[3]
	Packing: stainless Pall ring	
$Sh = 0.01099Re^{0.3955}Sc^{0.5}$	Wetted wall column absorption	[4]
	$Re < 75$	
$Sh = 2.3Re^{0.43}Sc^{0.33}$	Packed column	[4]
	Packing: copper Raschig ring	
$Sh = 2.995 \times 10^{-2}Re^{0.2134}Sc^{0.5}$	Falling film column	[5]
	Gas absorption	
$Sh = 3.725 \times 10^{-2}Re^{0.2715}Sc^{0.5}$	Gas absorption	[6]
	Absorbent: $CaCl_2$ solution	
	$100 < Re < 700$	
$Sh = 2.326 \times 10^{-3}Re^{0.6938}Sc^{0.5}$	Gas absorption	[6]
	Absorbent:	
	$700 < Re < 1600$	
$Sh_g = 0.0279Re^{0.791}Sc^{0.44}$	Wetted wall tower	[7]
	System: isopropanol–water–air	
	isopropanol-water-N_2	
$Sh = 4.22Re^{1/3}Sc^{1/2}$	Gas absorption	[8]
	System: glucose solution-CO_2	
$Sh = (0.012 \pm 0.001)Re^{0.89\pm0.05}Sc^{0.33}$	Gas absorption	[9]
	System: sediment water-O_2	
$Sh = 1.15Sc^{1/3}Re^{1/2}$	Fluid-particle ion exchange, $Re < 1000$	[10]
$Sh_G = 0.00031Re_G^{1.05}Re_L^{0.207}Sc_G^{0.5}$	Concurrent wetted wall column	[11]
$Sh = 1.38Re^{0.34}Sc^{0.33}$	Hollow fiber contactor	[12]
$Sh = 0.648Re^{0.379}Sc^{0.33}$	Spiral wound pervaporation	[13]
$Sh = 0.048Re^{0.6}Sc^{1/3}$	Hollow fiber reverse osmosis	[14]

By dimensional analysis, the following dimensionless equation is obtained:

$$\frac{k_L l}{D_t} = (constant)\left(\frac{l\rho u}{\mu_t}\right)^{\alpha}\left(\frac{\mu_t}{\rho D_t}\right)^{\beta}\left(\frac{\Delta\sigma l}{\mu_t D_t}\right)^{\gamma}$$

or

$$Sh_L = (\text{constant})Re^{\alpha}Sc_t^{\beta}Ma^{\gamma} \tag{7.6}$$

where Ma is Marangoni number (see Chap. 8); α, β, γ are constants.

Table 7.2 Some published empirical correlations with modification of *Sh-Re–Sc* form

Equation	Application	Reference
$Sh_g = 0.0044 Re_g Sc_g^{0.5} We_l^{0.111}$	Falling film tower. CO_2 absorption	[15]
$Sh = 1.62 Re^{0.33} Sc^{0.33} \left(\frac{d}{l}\right)^{0.33}$	Falling film tower. CO_2 absorption by ethanol, water	[16]
$Sh = 2 Re^{1/2} Sc^{1/2} (d/l)^{1/2}$	Tube reactor, lamina flow,	[17]
$Sh = 0.85 Re^{0.54} Sc^{0.33} \left(\frac{d_p}{d}\right)^{-0.75} \left(\frac{d_p}{L}\right)^{0.43}$	Fluidized bed	[18]
$Sh = 8.748 \times 10^2 Re^{0.024} Sc^{-0.133} Eu^{-0.012}$	Bubble column reactor, CO/kerosene system	[19]
$Sh = 2.136 \times 10^{-4} Re_f^{0.4} Sc^{0.65} Ga_f^{0.52}$	Falling film tower. CO_2 absorption by ethanol, water	[20]

where $We = \rho \alpha u^2/\sigma$, $Ga = l^3 \rho^2 g/\mu^2$, $Bo = q/\gamma \rho_v u_v$, $Fr = u/gl$, $Eu = p/\rho u^2$
α is the diameter of liquid drop, d is the column diameter, l is the characteristic length

Table 7.3 Some empirical mass transfer coefficient equations from experimental data

Equation	Application	Reference
$k_G = 1.195 u_G \left[\frac{d_p \rho_G u_G}{\mu_G (1-\varepsilon)}\right]^{-0.36} Sc_G^{-2/3}$	Random packing	[21]
$k_L = 25.1 \frac{D_L}{d_p} \left(\frac{d_p \rho_L u_L}{\mu_L}\right)^{0.45} Sc_L^{0.5}$		
$k_L = \frac{0.0051}{(a_p d_p)^{-0.4}} \left(\frac{\mu_L g}{\rho_L}\right)^{1/3} \left(\frac{\rho_L u_L}{a_e \mu_L}\right)^{2/3} Sc_L^{-0.5}$	Random packing	[22]
$k_G = c \left(\frac{D_G}{a_p d_p^2}\right) \left(\frac{\rho_G u_G}{a_p \mu_G}\right)^{0.7} Sc_G^{1/3}$		
$k_L = C_L \left(\frac{\rho_L g}{\mu_L}\right)^{1/6} \left(\frac{D_L}{d_h}\right)^{0.5} \left(\frac{u_L}{a_p}\right)^{1/3}$	Random packing	[23]
$k_G = C_G \frac{a_p^{0.5} D_G}{\sqrt{d_h (\varepsilon - h_L)}} \left(\frac{\rho_G u_G}{a_p \mu_G}\right)^{3/4} Sc_G^{1/3}$		
$k_G = 0.0338 \frac{D_G}{d_{eq}} \left[\frac{\rho_G d_{eq} (u_{Le} + u_{Ge})}{\mu_G}\right]^{0.8} Sc_G^{0.33}$ $k_L = 2\sqrt{\frac{D_L}{\pi 8} \left(\frac{9\Gamma^2 g}{8\rho_L \mu_L}\right)^{1/3}}$ where $u_{Ge} = \frac{u_G}{\in \sin \alpha}, u_{Le} = \left(\frac{9\Gamma^2 g}{8\rho_L \mu_L}\right)^{1/3}$	Structured packing	[24]
$k_G = \sqrt{\left(\frac{Sh_{G,lam} D_G}{d_{hG}}\right) + \left(\frac{Sh_{G,turb} D_G}{d_{hG}}\right)^{-2}}$ where $Sh_{G,lam} = 0.664 Sc_G^{1/3} \sqrt{Re_{Grv} \frac{d_{hG}}{l_{G,pe}}}$ $Sh_{G,turb} = \frac{(Re_{Grv} Sc_G \xi_{GL} \varphi/8)\left[1 + (d_{hG}/l_{G,pe})^{2/3}\right]}{1 + 12.7\sqrt{\xi_{GL} \varphi/8}\left(Sc_G^{2/3} - 1\right)}$ $k_L = 2\sqrt{\frac{D_L u_{Le}}{0.9\pi d_{hG}}}$	Structured packing	[25]
$k_L = 2.6 \times 10^{-5} \mu_L^{0.25}$	Sieve tray column	[26]
$k_G = \frac{0.13}{\rho_v} - \frac{0.065}{\rho_V^2}$		

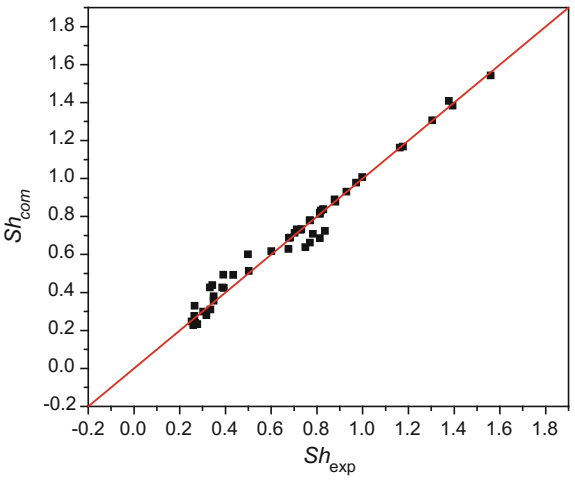

Fig. 7.1 Predicted *Sh* versus experimental data

The importance of considering the interfacial effect on mass transfer coefficient can be seen by the following example. The Sh_L model for binary system containing phosphoric acid and ethyl hexanol was reported below by Akita and Yoshida [27] with average error of 14.49 %:

$$Sh = 1.263Re^{0.662}Sc^{0.0761}$$

Zhou [28] employed Eq. (7.6) for the regression of the published data of the same system and obtained the following equation with average error 9.62 % as shown in Fig. 7.1.

$$Sh = 0.0245Re^{0.5229}Sc^{0.0761}Ma^{0.3427}$$

Thus the consideration of interfacial effect, such as Marangoni convection, if occurred, is necessary to achieve better regressive empirical k_L equation.

Similar situation can be extended to the interfacial effect by Rayleigh convection, which is represented by the Rayleigh number Ra ($Ra = \frac{g\Delta\rho l^3}{D\mu}$ where $\Delta\rho$ is the density difference between interface and the bulk liquid), and Eq. (7.6) can be extended to the following form if necessary.

$$Sh = (\text{constant})Re^aSc^bMa^cRa^d$$

The constructional characteristics of the equipment cannot be ignored, thus a constructional dimensionless group, denoted as Ψ, is usually added to the k_L equation:

$$Sh = C_0Re^aSc^bMa^dRe^e\Psi^f$$

where exponents a to f are constants.

Similar expressions can also be obtained for the gas phase mass transfer coefficient k_G.

In short, the determination of mass transfer coefficient of two-component system is still relied on experimental measurement although the use of dimensionless group in the data regression can be helpful and reasonable. The collection of published correlations of mass transfer coefficient by Wang [29] and Zhou [28] can be used as reference.

7.2 Mass Transfer in Multicomponent System

In multicomponent distillation calculation, it is usually taking two main separating materials as key component and considers it as a binary system. However, when a mixture containing considerable amount multiple substances is to be separated, the use of key component method may lead to serious error in evaluating point efficiency as seen from Table 7.4.

The complication appeared in multicomponent system is chiefly due to the complex nonideal nature of component molecular interaction in a mass transfer process which may results:

- Osmotic diffusion, i.e., diffusion of component *i* may occur when the driving force, the concentration difference between the interface and the bulk, is equal to zero;
- Diffusion barrier, i.e., diffusion of component *i* does not occur even at the presence of its concentration difference;
- Reversed diffusion, i.e., diffusion of component *i* opposite to the direction of its driving force.

The three bizarre behaviors mentioned above are the peculiar characters of multicomponent distillation which can be predicted by simulation. Also the Murphree point efficiency of a component can be greater than 1, which is impossible in binary distillation as shown in subsequent section.

There are two basic equations for the calculation of multicomponent mass transfer, namely

- Generalized equation of Fick's law;
- Maxwell–Stefan equation of diffusion transport.

Table 7.4 Comparison binary and multicomponent point efficiencies

Items	Binary	Multicomponent
Component equilibrium constant	Equal	Unequal
Component diffusivity	Equal	Unequal
Component mass transfer coefficient	Equal	Unequal
Component point efficiency	Equal	Unequal
Range of point efficiency	0–1	$-\infty$ to $+\infty$

7.2.1 Generalized Fick's Law

The Fick's law [30] states that the diffusion flux J_A of component A is proportional to the concentration gradient; or mathematically,

$$J_A = -c_t D_{AB}^F \frac{dx_A}{dz} \tag{7.7}$$

where c_t is the total molar concentration of the solution (kmol m^{-3}); x_A is the mole fraction of component A; D_{AB}^F is the diffusion coefficient of Kick's law (m^2 s^{-1}); z is the direction of diffusion. For the binary system, D_{AB}^F is equal to the coefficient of molecular diffusion.

If Fick's law is applied to the multicomponent system, it is called generalized Fick's law expressed as follows:

$$J_i = -c_t \sum_{j=1}^{n} D_{ij}^F \frac{dx_j}{dz}, \quad i = 1,2,\ldots,n-1 \tag{7.8}$$

where D_{ij}^F is the diffusion coefficient of "component pair ij", terminated as mutual diffusion coefficient expressing the effect of concentration gradient of component j on the diffusion flux of component i, and regarded as coupling effect. Since $\sum_{i=1}^{n} J_i = 0$, only $n - 1$ independent can be written. The generalized Fick's law becomes

$$(J) = -c_t \left[D^F\right] \frac{d(x)}{dz} \tag{7.9}$$

where $|D^F|$ is the matrix of the D_{ij}^F.

Obviously, the diffusion coefficient D_{ij}^F of generalized Fick's law cannot reflect the nonideal character of multicomponent mass transfer, which is very important in multicomponent distillation. Thus the generalized Fick's law is seldom to be used.

7.2.2 Maxwell–Stefan Equation

In order to represent the nonideal character of multicomponent system, the irreversible thermodynamics has been employed as the theoretical basis.

The basic viewpoint of irreversible thermodynamics is that when two molecules of different component moving with different velocities, frictional force between them is produced due to the mutual molecular calescence or mutual molecular interacting force. The diffusion of component i is restricted by such frictional force, the extent of which can be considered to be proportional to the molecular density of component j and the relative velocity of component i with other molecules.

For the evaluation of frictional force, the following example may be used as illustration. A binary solution containing solute i and solvent j is undertaking one dimensional diffusion. Taking a differential element at constant temperature and total pressure, if component i is diffused from one side of the element to the other side, then the concentration as well as thermodynamic properties (such as activity coefficient and enthalpy etc.,) will be changed, if the small change of temperature and enthalpy can be neglected, the activity of component i ($i = \gamma x$ in which γ is the activity coefficient, x is the mole fraction of component i) in both sides of the element is not equal so as to make the chemical potential μ is also not equal. In thermodynamics, the chemical potential of component i at constant T and P, $\mu_{i,T,P}$, is represented by $\mu_{i,T,P} = \mu^0_{i,T,P} + RT \ln \gamma_i x_i$ where $\mu^0_{i,T,P}$ is the chemical potential at standard state. Thus chemical potential gradient $\frac{d\Delta_{T,P}\mu_i}{\mathrm{d}z}$ is established between two sides of the differential element. It is understood that the true driving force of mass transfer is the chemical potential gradient.

The most convenient method to express the relationship of chemical potential gradient is considered that the gradient is proportional to the relative velocity different between component molecule i and j, $\left(u_i - u_j\right)$ and activity of j, that is

$$\frac{d\Delta_{T,P}\mu_i}{\mathrm{d}z} = \varphi\left[\gamma_j x_j\left(u_i - u_j\right)\right]$$

where φ is the proportional constant which is related to the diffusion coefficient between i and j, D_{ij}, and can be expressed as $\frac{RT}{D_{ij}}$; then we can write the generalized chemical potential to be:

$$\nabla_{T,P}\mu_i = RT\frac{\gamma_j x_j\left(u_i - u_j\right)}{D_{ij}}, \quad i = 1, 2, \ldots, n-1$$

If the influence of all component j to component i is additive, we may obtain the expression of chemical potential of component i in multicomponent solution. That is the generalized Maxwell–Stefan diffusion equation as follows [31, 32]:

$$\frac{1}{RT}\nabla_{\mathrm{T,P}}\mu_i = \sum_{\substack{j=1 \\ j\neq i}}^{n}\frac{\gamma_j x_j(u_j - u_i)}{D_{ij}}, \quad i = 1, 2\ldots, n-1 \tag{7.10a}$$

For the ideal solution, γ_j = 1, Eq. (7.10a) can be simplified to:

$$\frac{1}{RT}\nabla_{\mathrm{T,P}}\mu_i = \sum_{\substack{j=1 \\ j\neq i}}^{n}\frac{x_j(u_j - u_i)}{D_{ij}}, \quad i = 1, 2, \ldots, n-1 \tag{7.10b}$$

where, D_{ij} is called Maxwell–Stefan diffusion coefficient, it represents the mutual influence of component pair i, j molecules in the diffusion process.

Multiplying x_i on both sides of Eq. (7.10a), and combine $N_i = c_t x_i u_i = J_i + x_i N_t$, where N_i is the molar flux of component i, c_t is the total molar concentration, J_i为 is the molecular diffusion flux of component i, N_t is the total molar flux, Eq. (7.10b) can be written as:

$$\frac{x_i}{RT}\nabla_{T,P}\mu_i = \sum_{\substack{j=1 \\ j\neq 1}}^{n} \frac{x_i N_j - x_j N_i}{c_t D_{ij}} = \sum_{\substack{j=1 \\ j\neq 1}}^{n} \frac{x_i J_j - x_j J_i}{c_t D_{ij}}, \quad i = 1, 2, \ldots, n-1 \tag{7.11}$$

Since Maxwell–Stefan diffusion equation is based on the theory of irreversible thermodynamics, thus the diffusion coefficient should obey Onsager reciprocal relationship, i.e. [31].

$$D_{ij} = D_{ji}, \quad i, j = 1, 2, \ldots, n \tag{7.12}$$

For the component diffusion in nonideal solution, the x_i in Eq. (7.8) should be $\gamma_i x_i$. Combine with the mass conservation $\sum_{i=1}^{n} N_i = 0$ and energy conservation in mass transfer $\sum_{i=1}^{n} \lambda_i N_i = 0$ (neglect the small difference of component enthalpy, where λ_i is the latent heat of vaporization of component i), the Maxwell–Stefane Eq. (7.11) becomes the following matrix equation:

$$N_i = -c_t[\boldsymbol{\beta}][\boldsymbol{R}]^{-1}[\boldsymbol{\Gamma}]\frac{\mathrm{d}(x)}{\mathrm{d}z} \tag{7.13}$$

where $[\boldsymbol{\beta}]$ is the matrix of molar exchange of mass transfer in counterdiffusion due to the difference of latent heat of vaporization between component i and j. The elements of which are:

$$\beta_{ij} = \delta_{ij} - x_i\left(\frac{\lambda_j - \lambda_n}{\sum_{k=1}^{n} x_k \lambda_k}\right), \quad i, j = 1, 2, \ldots, n-1 \tag{7.14}$$

where δ_{ij} is Kronecker symbol, when $i = j$, $\delta_{ij} = 1$, when $i \neq j$, $\delta_{ij} = 0$.

$[R]$ is the matrix of inverted diffusivity with the following elements:

$$R_{ii} = \frac{x_i}{D_{in}} + \sum_{\substack{k=1 \\ k\neq i}}^{n} \frac{x_k}{D_{ik}}, \quad i = 1, 2\ldots, n-1 \tag{7.15}$$

$[\Gamma]$ is the matrix of thermodynamic factor with the following elements:

$$\Gamma_{ij} = \delta_{ij} + \frac{x_i}{x_j}\frac{\partial \ln \gamma_i}{\partial \ln \gamma_j}, \quad i,j = 1,2,\ldots,n-1 \tag{7.16}$$

Both Fick's law and Maxwell–Stefan diffusion equation are the basic equations for describing the multicomponent mass transfer, the relationship between them is as follows:

$$\left[\boldsymbol{D}^{\mathrm{F}}\right] = [\boldsymbol{\beta}][R]^{-1}[\boldsymbol{\Gamma}] \tag{7.17}$$

As seen the Maxwell–Stefan equation reflects more parameters in multicomponent mass transfer and thus widely be used.

The boundary conditions of Eq. (7.13) are

$$\begin{aligned} t > 0, \quad z = 0, \quad (x) = (x_0) \\ t > 0, \quad z = \Delta h, \quad (x) = (x_b) \end{aligned}$$

where x_b is the concentration of the bulk liquid entering the element; x_0 is the liquid concentration at the vapor-liquid interface. Letting $\sum_{i=1}^{n} \lambda_i N_i = 0$ by assuming the latent heat of vaporization λ_i of the components is mostly almost equal and solve Eq. (7.10a) with the following assumptions:

- The diffusivity D_{ij} is constant in the mass transfer process;
- The concentration gradient $\frac{\mathrm{d}(x)}{\mathrm{d}z}$ is constant (linear) and equal to $\frac{x_0 - x_b}{\delta}$, where δ is the thickness of the film.

Equation (7.11) can then be transformed approximately to the following form as given by Krishna [32] and Song [33]

$$N_i = -c_t[\beta][R]^{-1}[\Gamma](x_0 - x_b) \tag{7.18}$$

For liquid phase, we can write

$$N_i^L = -c_1\left[\beta^{\mathrm{L}}\right]\left[R^{\mathrm{L}}\right]^{-1}\left[\Gamma^{\mathrm{L}}\right](x_0 - x_b) \tag{7.18a}$$

Similar, we have

$$N_i^{\mathrm{V}} = -c_1\left[\beta^{\mathrm{V}}\right]\left[R^{\mathrm{V}}\right]^{-1}\left[\Gamma^{\mathrm{V}}\right](y_0 - y_b) \tag{7.18b}$$

As the overall mass transfer flux N_{T} is equal to N_i^{L} or N_i^{V} under steady condition, Eq. (7.18a) or Eq. (7.18b) is more convenient for the calculation. Nevertheless, all the parameters in the equation is based on average composition, i.e., $(x_0 - x_b)/2$, thus stepwise iteration should be used.

7.3 Application of Multicomponent Mass Transfer Equation

7.3.1 Prediction of Point Efficiency of Tray Column

The Maxwell–Stefan equation is an effective tool to calculate the mass transfer flux of multicomponent distillation.

The point efficiency is an important basic information of distillation which demonstrates the effectiveness of local vapor–liquid mass transfer in a specific point. Several definition point efficiency have been proposed in literature, among which the Murphree point efficiency has been widely used, which can be expressed by the following two forms:

- Murphree tray efficiency expressed in vapor phase concentration, which is defined as follows

$$E_{\mathrm{OG}}(i,k) = \frac{y_{i,k}^{\mathrm{O}} - y_{i,k}^{\mathrm{I}}}{y_{i,k}^{*} - y_{i,k}^{\mathrm{I}}} \tag{7.19}$$

where subscript (i, k) denotes the value of component i at the local point k, $y_{i,k}^{\mathrm{O}}$ is the vapor concentration (in mole fraction) leaving the local point k, $y_{i,k}^{\mathrm{I}}$ is the vapor concentration entering the local point k, $y_{i,k}^{*}$ is the vapor concentration in equilibrium with the liquid concentration at local point k.

- Murphree tray efficiency expressed by liquid phase concentration, which is defined below

$$E_{\mathrm{OL}}(i,k) = \frac{x_{i,k}^{\mathrm{O}} - x_{i,k}^{\mathrm{I}}}{x_{i,k}^{*} - x_{i,k}^{\mathrm{I}}} \tag{7.20}$$

where $x_{i,k}^{\mathrm{O}}$ and $x_{i,k}^{\mathrm{I}}$ is respectively the liquid concentration of component i entering and leaving the local point k, $x_{i,k}^{*}$ is the liquid concentration in equilibrium with the vapor.

Although point efficiency is basic information of distillation, yet it is difficult to simulate and verify experimentally. One way to solve such difficulty is to reduce the size of a tray to such an extent that it is equivalent to a local point. Thr Oldshaw sieve tray [34, 35] can meet such requirement, the construction of which is shown in Fig. 7.2.

As given in previous section, the mass transfer undertaken in the vertical column of an element involves the following regimes in the tray spacing:

- *froth regime* (jetting),
- *bubble dispersing regime* (free bubbling),
- *bubble breaking regime* (liquid drops splashing as entrainment in tray space).

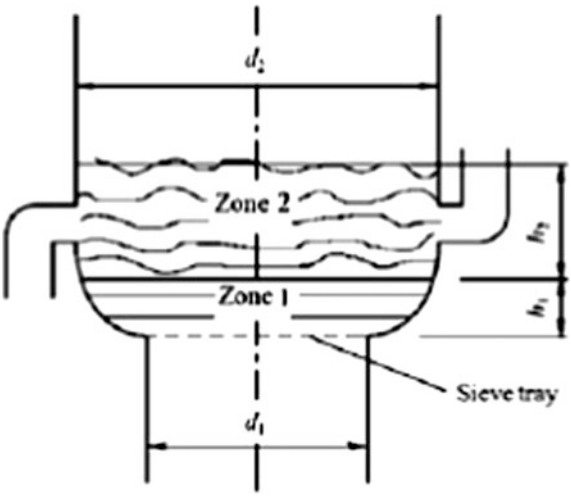

Fig. 7.2 Construction of Oldershaw sieve tray

Since the bubble breaking regime has very small contribution to the mass transfer, the first two regimes, in which the liquid as continuous phase and the vapor as dispersed phase, are dominant and have been established as two-regime model in the literature.

7.3.2 Two-Regime Model for Point Efficiency Simulation

The main parameters in this model are described as follows [36].

1. ***Jetting regime***

   (i) Mass transfer area

The diameter of vapor jet d_j is related to the clear liquid height h_L and the diameter of sieve hole d_h, it was correlated by Hai [37]: as follows:

$$d_j = 1.1d_h + 0.25h_L$$

From d_j, the specific mass transfer area in this regime can be calculated by:

$$\alpha = \frac{4\varphi d_j}{(d_h)^2}$$

where φ is the fraction of hole area.

(ii) Mass transfer coefficient

As the vapor flow through the jetting regime is similar to its flow through the falling film column, the mass transfer coefficient k^V can be calculated by the following relationship for two-component system [38]:

$$k^{\mathrm{V}} = 2.0\sqrt{\frac{D^{\mathrm{V}}}{\pi t_{\mathrm{V}}}} = 0.046\left(\frac{D^{\mathrm{V}}}{d_j}\right)(Re)^{0.96}(Sc)^{0.44}$$

$$Re = \frac{d_j u_j \rho_{\mathrm{V}}}{\mu_{\mathrm{V}}}, \quad Sc = \frac{\mu_{\mathrm{V}}}{\rho_{\mathrm{V}} D^{\mathrm{V}}}$$

$$\mathrm{u_j} = \frac{\mathrm{Q_V}}{\left[(\pi/4)(\mathrm{d})^2\right]\varphi} \cdot \left(\frac{d_{\mathrm{h}}}{d_{\mathrm{j}}}\right)^2 = \mathrm{u_h}\left(\frac{d_{\mathrm{h}}}{d_{\mathrm{j}}}\right)^2, \quad t_{\mathrm{V}} = \frac{h_j}{u_j}$$

where d_j is the diameter of the vapor jet; u_j and u_h are respectively the vapor velocity based on jet diameter and sieve hole diameter. h_j is the height of the jet column. The residence time of vapor t_{V} is equal to

$$t_{\mathrm{V}} = \frac{h_j}{u_j}$$

For the multicomponent system, the mass transfer coefficient can be written as follows:

$$\left[\mathbf{k}^{\mathrm{V}}\right] = \frac{2}{\sqrt{\pi t_{\mathrm{V}}}}\left\{\left[\mathbf{B}^{\mathrm{V}}\right]^{-1}\right\}^{1/2} = \left\{\left[\mathbf{B}^{\mathrm{V}}\right]^{-1}\right\}^{1/2}$$

where $[\mathrm{B}^{\mathrm{V}}] = \frac{\pi t_{\mathrm{V}}}{4}[\boldsymbol{B}^{\mathrm{V}}]$ with the following elements;

$$[\mathbf{B}_{ii}^{\mathrm{V}}] = \frac{y_i}{\left(k_{\mathrm{in}}^{\mathrm{V}}\right)^2} + \sum_{\substack{k=1 \\ k\neq i}}^{n} \frac{y_k}{\left(k_{ik}^{V}\right)^2}, \quad i = 1, 2, \ldots, n-1, i \neq j$$

$$[\mathbf{B}_{ij}^{\mathrm{V}}] = -x_i\left[\frac{1}{\left(k_{ij}^{\mathrm{V}}\right)^2} + \frac{1}{(k_{in}^{\mathrm{V}})^2}\right], \quad i = 1, 2, \ldots, n-1, i \neq j$$

2. ***Bubble dispersion regime***

In many chemical processes where gas is a dispersing phase, in a distillation tray for example, vapor is in the form of small bubble of different size and distributed diversely. In such a case, the average diameter of the bubble can be estimated by the following equation [39]:

$$d_{\max} = (0.5We_{\mathrm{c}})^{0.6}\left(\frac{\sigma}{\rho_{\mathrm{L}}}\right)^{0.6}(u_{\mathrm{s}}g)^{-0.4}\left(\frac{\rho_{\mathrm{V}}}{\rho_{\mathrm{L}}}\right)^{-0.2}$$

$$We_{\mathrm{c}} = \left(\frac{\tau \mathrm{d}_{\max}}{\sigma}\right)\left(\frac{\rho_{\mathrm{V}}}{\rho_{\mathrm{L}}}\right)^{1/3}$$

where We_c is critical Weber group; σ is the surface tension; τ is the residence time which is given by [38]

$$\tau = 2\rho_L(u_s g d_{max})^{4/3}$$

It was reported [40] that the ratio of average and maximum bubble diameters is an constant, i.e.,

$$\frac{d_{av}}{d_{max}} = 0.62$$

The reliability of foregoing estimation is seen to be roughly confirmed by some experimental data from literature as shown in Table 7.5.

The vapor fraction β_V in this regime for sieve hole smaller than 2 mm can be estimated by equation below

$$\frac{\beta_V}{1-\beta_V} = 8.5Fr^{0.5}, \quad Fr \leq 4.68 \times 10^{-4}\varphi^{-0.56}$$

$$\frac{\beta_V}{1-\beta_V} = 1.25\varphi^{-0.14}Fr^{0.25}, \quad Fr > 4.68 \times 10^{-4}\varphi^{-0.56}$$

$$Fr = \frac{(u_s)^2}{gh_L}$$

where φ is the fraction of sieve perforation on the tray. By the iteration of foregoing equations, the d_{av} can be obtained as well as the surface area of the bubble by

$$a = \frac{6}{d_{av}} \cdot \beta_V$$

The mass transfer coefficient between bubble and the liquid on the tray was measured for binary system by Zaritzky [43] and correlated by Prado [44] as follows

Table 7.5 Calculated bubble diameter compared with experimental measurements

Sieve hole (m/s)	Calculated d_{av} (mm)	Experimental value by Sharma [41] (mm)	Experimental value by Raper [42] (mm)	Experimental value by Geary [39] (mm)
1.70	3.35	4.0	2.0–5.0	2.0–4.0
1.94	3.60			
2.01	3.60			
2.24	3.55			
2.26	4.05			

$$k^{\mathrm{V}} = Sh\frac{D^{\mathrm{V}}}{d_{\mathrm{av}}}$$

$$Sh = -11.878 + 25.879(\lg Pe) - 5.640(\lg Pe)^2$$

$$Pe = \frac{d_{\mathrm{av}}u_{\mathrm{b}}}{D^{\mathrm{V}}}, \quad u_{\mathrm{b}} = \frac{Q_{\mathrm{V}}}{\frac{\pi}{4}(d)^2\beta_V\rho_{\mathrm{V}}}$$

where D^{V} is the molecular diffusivity of component i in the vapor phase.

3. ***Steps of calculation***

Take a local vertical element on a sieve tray as shown in Fig. 7.3.

The vertical element on Fig. 7.3 is considered equivalent to the Oldershaw sieve tray column. Referring to Fig. 7.2, let the total height of the two liquid regime lyers on the tray be h ($h = h_1 + h_2$), take a differential element Δh on the tray where $y_{\mathrm{in}} = y_h$ and $y_{\mathrm{out}} = y_{h+\Sigma\Delta h}$. The mass flux of component i in the element can be calculated as follows.

1. At first, let $y_{\mathrm{in}} = y_{bh}$ and assume $y_{\mathrm{out}} = y^0_{bh+\Delta h}$, the average concentration of component i is $y_{av} = \frac{1}{2}\left(\mathrm{y_{bh}} + \mathrm{y_{bh+\Delta h}}\right)$
2. Calculate the mass flux to be transferred by aforementioned method so as to obtain the concentration of vapor leaving from the differential element. If it is close enough to the assumed value, then proceed to the next differential element above until reaching to the top of the liquid regime to obtain the outlet vapor concentration from the tray.

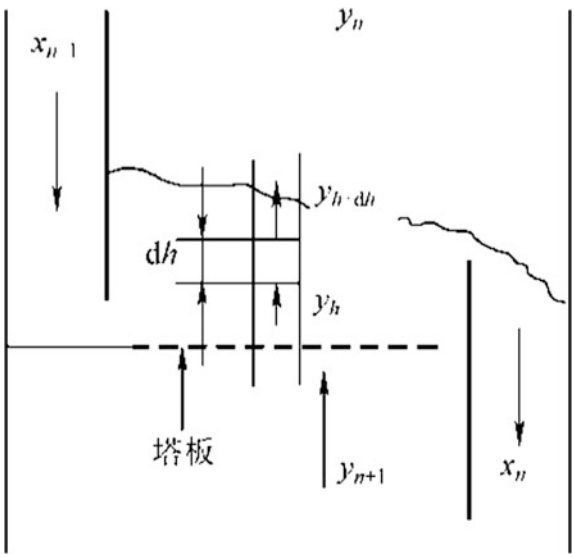

Fig. 7.3 A local vertical element (perpendicular to the tray deck)

7.3.3 Example of Simulation

As an example, Wang [36] calculate a three-component system (ethanol, isopropanol, water) under the following conditions:

The liquid concentrations on the tray are:

$$(\boldsymbol{x}_{\mathrm{b}}) = (0.447\ 7, 0.220\ 9, 0.331\ 4)^{\mathrm{T}}$$

where concentration x_{b} in mole fraction are in the sequence of ethanol, isopropanol and water.

The vapor concentrations on the tray are:

$$(\boldsymbol{y}_{\mathrm{F}}) = (0.444\ 7, 0.221\ 4, 0.333\ 9)^{\mathrm{T}}$$

The operating temperature is 351.4 K; volumetric vapor flow rate $Q_{\mathrm{V}} = 1.652 \times 10^{-4}\mathrm{m}^3\ \mathrm{s}^{-1}$; clear liquid height $h_{\mathrm{L}} = 11.28$ mm, perforation of the sieve tray is 6.38 % with 1.25 mm hole diameter.

Wang [36] give the calculated result along liquid height h as shown in Table 7.6.

Table 7.6 Calculated result of mass flux transferred along liquid height

Liquid height h From tray deck (mm)	Vapor concentration, mole fraction			Mass flux transferred N (mol $\mathrm{m}^{-2}\ \mathrm{s}^{-1}$)		
	Ethanol	Isopropanol	Water	Ethanol	Isopranol	Water
1.30	0.446 1	0.221 6	0.332 3	12.36×10^{-6}	1.663×10^{-5}	-11.68×10^{-5}
2.60	0.447 4	0.221 8	0.330 8	11.95×10^{-6}	1.566×10^{-5}	-11.27×10^{-5}
3.89	0.448 8	0.221 9	0.329 3	11.56×10^{-6}	1.473×10^{-5}	-10.86×10^{-5}
5.19	0.450 0	0.222 1	0.327 9	11.18×10^{-6}	1.384×10^{-5}	-10.48×10^{-5}
6.49	0.451 3	0.222 2	0.326 5	10.81×10^{-6}	1.300×10^{-5}	-10.10×10^{-5}
7.79	0.452 4	0.222 4	0.325 2	10.46×10^{-6}	1.220×10^{-5}	-9.743×10^{-5}
9.09	0.453 6	0.222 5	0.323 9	10.12×10^{-6}	1.143×10^{-5}	-9.396×10^{-5}
10.38	0.454 7	0.222 6	0.322 7	9.876×10^{-6}	1.070×10^{-5}	-9.061×10^{-5}
11.68	0.455 8	0.222 8	0.321 5	9.466×10^{-6}	1.001×10^{-5}	-8.739×10^{-5}
12.98	0.456 8	0.222 9	0.320 3	9.158×10^{-6}	0.935×10^{-5}	-8.428×10^{-5}
14.18	0.462 1	0.223 4	0.314 5	8.625×10^{-6}	0.815×10^{-5}	-7.887×10^{-5}
15.38	0.466 5	0.223 7	0.309 8	7.144×10^{-6}	0.517×10^{-5}	-6.410×10^{-5}
16.59	0.470 2	0.223 9	0.306 0	5.926×10^{-6}	0.296×10^{-5}	-5.214×10^{-5}
17.79	0.473 2	0.223 9	0.302 9	4.924×10^{-6}	0.135×10^{-5}	-4.246×10^{-5}
18.99	0.475 7	0.223 9	0.300 3	4.096×10^{-6}	0.020×10^{-5}	-3.460×10^{-5}
20.19	0.477 8	0.223 9	0.298 3	3.413×10^{-6}	-0.062×10^{-5}	-2.822×10^{-5}
21.39	0.479 6	0.223 8	0.296 6	2.847×10^{-6}	-0.116×10^{-5}	-2.304×10^{-5}
22.60	0.481 0	0.223 7	0.295 2	2.378×10^{-6}	-0.152×10^{-5}	-1.882×10^{-5}
23.80	0.482 3	0.223 6	0.294 1	1.989×10^{-6}	-0.172×10^{-5}	-1.539×10^{-5}
25.00	0.483 3	0.223 5	0.293 2	1.666×10^{-6}	-0.183×10^{-5}	-1.259×10^{-5}

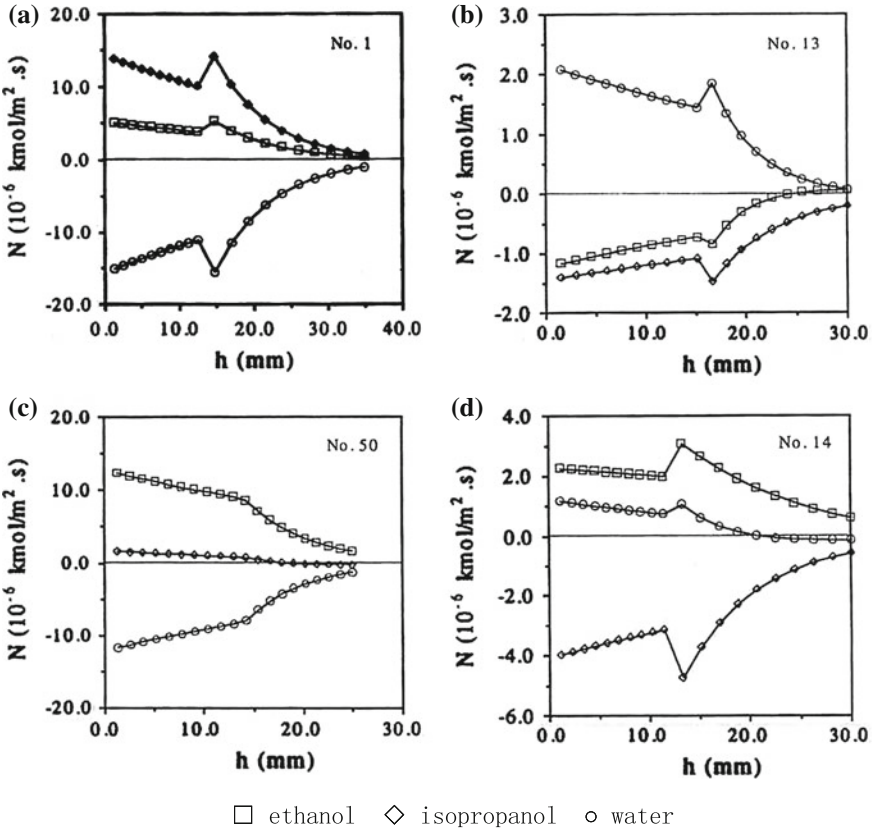

Fig. 7.4 Mass transfer flux N along the liquid height h. *Rectangle* ethanol, *triangle* isopropanol, *circle* water

As seen, the mass transfer is higher at low liquid level and decrease as the vapor goes up to the top of the froth. It indicates the jetting regime where the vapor bubble is formed and dispersed is dominant in the mass transfer process.

The simulated results are also plotted in Fig. 7.4, in which the results of four different experiments No. 1, 13. 14, 50 are displayed. The condition of these experiments are given in Table 7.8.

In Fig. 7.4, the mass transfer flux is decreased with the liquid height for all four experiment runs. The "turning point" on the curves represents the bounder of jetting and bubble dispersed regimes.

As seen experiment No. 1 in Table 7.7, all point efficiencies are within normal condition, i.e., less than i, and no bizarre phenomena are found. But in Experiment No. 13, 14 and 50, the bizarre phenomena are appeared in component ethanol and isopropanol, i.e., the point efficiencies are greater than 1. It demonstrates the biazrre phenomena are happened only under certain specific condition.

Table 7.7 Simulated point efficiency of four experimental runs

Run number	Component	Tray liquid concentration	Point efficiency
1	1	0.1359	0.9465
	2	0.4429	0.9733
	3	0.4192	0.9655
13	1	0.8991	1.1835
	2	0.0370	0.9225
	3	0.0739	0.9826
14	1	0.7256	0.8827
	2	0.2159	0.9290
	3	0.0595	1.1217
50	1	0.4477	0.8475
	2	0.2209	2.8842
	3	0.3314	0.9072

1 Ethanol, *2* isopropanol, *3* water

7.4 Verification of Simulated Result

7.4.1 Experimental Work

Wang [36] constructed a Oldershaw sieve tray column for the experimental study of multicomponent mass transfer, the main dimension of which is given in Table 7.8.

The experimental installation is shown in Fig. 7.5. Two multicomponent systems are used for testing the point efficiency, i.e., a three component system (ethanol, isopropanol and water) and a four component system (ethanol, isopropanol, tert-butyl alcohol, water). The initial composition of three component system in sequence is as follows:

$$(\boldsymbol{x}_{\mathrm{b}}) = (0.447\ 7, 0.220\ 9, 0.331\ 4)^{\mathrm{T}}$$

The composition of entering vapor is

$$(\boldsymbol{y}_{\mathrm{F}}) = (0.444\ 7, 0.221\ 4, 0.333\ 9)^{\mathrm{T}}$$

Table 7.8 Main dimension of experimental Oldershaw sieve tray

Parameters	Dimension
Diameter of tray spacing (mm)	64
Sieve hole diameter (mm)	1.25
Thickness of tray floor (mm)	1.2
Perforation (%)	6.38
Height of outlet weir (mm)	15–38

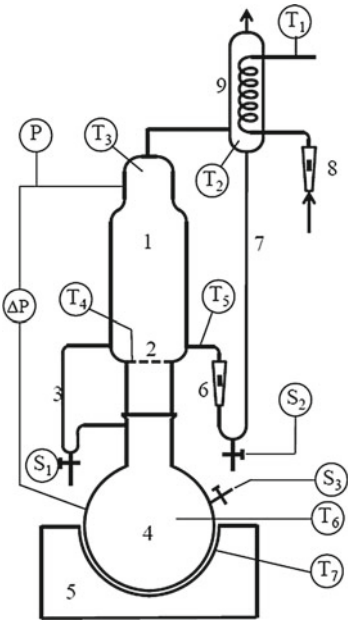

1-column
2-Oldershaw tray
3-downcomer
4-Reboiler
5-heating pot
6-flow meter
7- reflux tube
8-cooling water meter
9-condenser
P-pressure measuring point
T-temperature measuring point
S-sampling point

Fig. 7.5 Experimental setup of Oldershaw column

The operating conditions are: temperature $T = 351.4$ K, $Q_V = 1.652 \times 10^{-4}$ m^3 s^{-1}, $h_L = 11.28$ mm. The experimental setup is shown schematically in Fig. 7.5.

The experimental Oldershaw column was improved in the following aspects:

- Only one sieve tray was installed instead of multiple trays for the convenience of comparison with simulated result with an accurate concentration measurements;
- An outside downcomer construction was used to facilitate the sampling;
- The space above the tray was enlarged to reduce the influences of entrainment and wall effect.

The parameters for the main dimension of the experimental Oldershaw column are given in Table 7.9.

Table 7.9 Main construction parameters of Oldershaw sieve tray

Parameter	Dimension
Tray diameter (mm)	38
Diameter of tray spacing (mm)	64
Sieve hole diameter (mm)	1.25
Thickness of tray floor (mm)	1.2
Perforation (%)	6.38
Height of outlet weir (mm)	15–38

Table 7.10 Comparison of simulated point efficiency with experimental data (I) (system: ethanol (1), isopropanol (2), water (3))

Expt. No.	Component	Liquid concentration on tray, mole fraction	Experimental point efficiency	Simulated point efficiency	Error = Sim. − Exp.
1	1	0.124 7	0.988 8	0.815 5	−0.1733
	2	0.643 4	0.992 4	0.943 0	−0.0494
	3	0.231 9	0.993 2	0.970 9	−0.0223
2	1	0.085 9	0.852 9	0.828 0	−0.0249
	2	0.743 4	0.971 0	0.949 4	−0.0216
	3	0.170 7	0.990 3	0.969 5	−0.0208
3	1	0.447 7	0.867 9	0.874 5	−0.0066
	2	0.220 9	2.861 5	2.884 2	0.0227
	3	0.331 4	0.855 8	0.907 2	0.0514
4	1	0.258 9	0.697 6	0.677 1	−0.205
	2	0.421 0	0.084 6	0.104 4	0.198
	3	0.320 1	0.773 2	0.752 6	−0.0027
5	1	0.211 5	0.780 7	0.833 8	0.0531
	2	0.451 0	1.192 1	1.159 1	−0.0330
	3	0.337 5	0.862 5	0.898 4	0.0359

7.4.2 Comparison of Simulation with Experimental

Wang conducted experimental measurement in a Oldershaw sieve tray column for validating the aforementioned simulation. The comparison of experimental data and simulated results are given in Table 7.10. And comparison was also made for a four components system (ethanol, isopropanol, tetra-butyl alcohol and water) as shown in Table 7.11.

As seen in Tables 7.10 and 7.11 the simulated results are fairly confirmed by the experimental data. It is indicated that the method of simulation of multicomponent mass transfer presented in this chapter is reliable.

7.4.3 The Bizarre Phenomena of Multicomponent System

The bizarre phenomena can be illustrated by the foregoing case of three-component system as calculated by Wang given in preceding section. The simulated diffusion flux of isopropanol is plotted versus the driving force of mass transfer $(y_0 - y)$ as shown in Fig. 7.6.

Table 7.11 Comparison of simulated point efficiency with experimental data (II) [System: ethanol (1), isopropanol (2), tert-butyl alcohol (3), water(4)]

Expt. No.	Component	Liquid concentration on tray, mole fraction	Point efficiency		Error
			Experimental	Simulated	
1	1	0.343 6	0.903 5	0.822 5	−0.034 3
	2	0.267 9	0.808 7	0.823 8	0.018 6
	3	0.064 0	0.724 2	0.780 1	0.077 3
	4	0.324 5	0.970 6	0.907 0	−0.065 5
2	1	0.231 3	0.962 5	0.815 4	−0.152 8
	2	0.469 4	0.997 7	0.927 9	−0.069 9
	3	0.123 1	0.766 7	0.916 3	0.195 1
	4	0.176 3	0.929 2	0.968 2	0.041 9
3	1	0.486 6	0.910 8	0.934 1	0.025 6
	2	0.078 1	1.294 9	0.827 4	−0.361 1
	3	0.078 8	1.568 7	1.606 6	0.024 1
	4	0.356 6	0.892 8	0.950 7	0.064 8
4	1	0.050 7	0.902 7	0.893 9	−0.009 7
	2	0.046 5	0.910 0	0.846 6	−0.069 7
	3	0.396 3	0.868 6	0.896 8	0.032 4
	4	0.506 5	0.865 9	0.909 2	0.050 0
5	1	0.348 8	0.874 1	0.828 2	−0.052 5
	2	0.353 4	0.870 2	0.913 3	0.049 6
	3	0.080 9	0.926 1	0.901 9	−0.026 2
	4	0.217 0	0.938 4	0.997 2	0.062 7
6	1	0.371 7	0.989 1	0.944 4	−0.045 2
	2	0.133 9	5.232 2	7.389 3	0.412 3
	3	0.066 9	0.889 1	0.961 8	0.081 8
	4	0.427 5	0.988 2	0.962 0	−0.026 5
7	1	0.865 8	0.796 7	0.786 7	−0.012 5
	2	0.014 5	0.864 3	0.969 4	0.121 6
	3	0.039 6	0.963 1	0.919 0	−0.045 8
	4	0.080 1	1.042 9	1.032 3	−0.010 2
8	1	0.136 0	0.943 7	0.949 1	0.005 7
	2	0.110 2	0.717 3	0.534 6	−0.254 7
	3	0.221 4	0.863 3	0.859 0	−0.005 0
	4	0.534 4	0.881 3	0.916 5	0.040 0

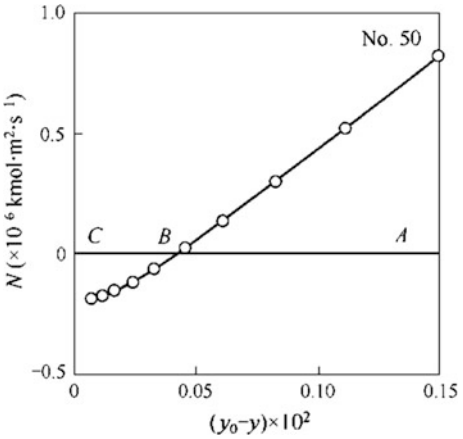

Fig. 7.6 The diffusion mass flux of isopropanol in three-component system versus driving force of mass transfer

In Fig. 7.6, the following phenomena can be noticed:

- At point B, although the driving force is positive, the mass flux of isopropanol transferred is zero; such phenomenon is usually regarded as *diffusion barrier* which cannot be happened in binary system.
- From point B to C, the driving force is still positive, yet the isopropanol transferred is negative, i.e., the direction of mass transfer is against the driving force and such phenomenon is usually regarded as *reversed diffusion*.
- As seen in Fig. 7.7 at the liquid height about $h = 25$, the driving force is approaching zero, but the isopropanol still undertakes mass transfer between phases; such phenomenon is usually regarded as *osmotic diffusion*.

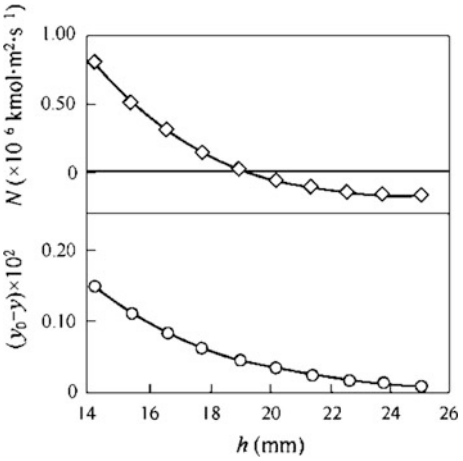

Fig. 7.7 Mass transfer flux and driving force of isopropanol in three components system versus liquid height

It should be mentioned that such *bizarre phenomena* is only happened for isopropanol in this special case of three component system but it does not appeared for ethanol and water. And thus the cause of bizarre phenomena of nonideal multicomponent system is complex and still needs investigations.

7.5 Determination of Vapor–Liquid Equilibrium Composition

In using Eq. (7.1) to find the rate of mass transfer, the value of equilibrium composition c^* can be either taken from the literature, or estimated by one of the following methods:

- Semi-empirical equation method;
- Group contribution method;
- Experimental measurement.

These methods are discussed in the subsequent sections.

7.5.1 Thermodynamic Relationship of Nonideal Solution

For an ordinary distillation column that is operated at atmospheric pressure, the partial pressure of component i in liquid phase for a multicomponent system, can be defined by modified Raoult's law as follows:

$$p_i = \gamma_i p_i^* x_i \tag{7.21}$$

where p_i is the partial pressure of component i in the system; γ_i is the activity coefficient of component i in liquid phase; p_i^* is the saturate vapor pressure of pure component i.

Similarly in the vapor phase at low pressure, the modified Dalton's law can be applied in the following form

$$p_{i\mathrm{G}} = \gamma_{i\mathrm{G}} P y_i \tag{7.22}$$

where p_i is the partial pressure of component i in vapor phase at the temperature and total pressure under consideration; P is the total pressure of the system

When Raoult's law is applied to a saturated solution in equilibrium with its vapor at constant temperature the isobaric condition cannot be maintained for all variation in composition. Thus the value of p_i should be corrected for changes in total pressure. The effect of total pressure P on p_i in thermodynamic is written as

$$\ln \frac{p_1^0}{p_1^*} = \frac{V_{1L}}{RT}\left(P - P_1^*\right) \tag{7.23}$$

where V_{1L} is the average volume of pure liquid component 1. Combining Eqs. (7.21) and (7.23), we obtain:

$$p_1 = p_1^* x_1 \exp\left[-\frac{V_{1L}}{RT}\left(p - p_1^*\right)\right] \tag{7.24}$$

Comparing Eqs. (7.21) and (7.24), we have

$$\gamma_1 = \exp\left[-\frac{V_{1L}}{RT}\left(p - p_1^*\right)\right]$$

Excess free energy

The relationship between the free energy and the activity coefficient of liquid may be derived from a gaseous solution composed by component 1 and 2, both at the pressure P. As the gaseous mixture is at total pressure P, the pressure of component 1 and 2 should be changed from P to its partial pressure. The change of free energy accompanied with the change of pressure at constant temperature of gaseous 1 F_1^* is given by

$$\Delta F_1^* = RT \ln \frac{p_1}{P} = RT \log y_1$$

Similarly for gas 2, we have

$$\Delta F_2^* = RT \ln \frac{p_2}{P} = RT \log y_2$$

The total change of free energy for the isothermal and isobaric mixing of ideal gases, therefore, is as follows

$$\begin{aligned} \Delta F_{\mathrm{T,P}}^* &= y_1 \Delta F_1^* + y_2 \Delta F_2^* \\ &= y_1 RT \ln y_1 + y_2 RT \ln y_2 \end{aligned} \tag{7.25a}$$

The free energy of the gaseous solution F_{m} can be written as:

$$F_{\mathrm{m}} = \left(F_{\mathrm{m}}^*\right)_{\mathrm{ideal}} + F_{\mathrm{T,P}}^E$$

where $\left(F_{\mathrm{m}}^*\right)_{\mathrm{ideal}}$ is the change of free energy for the isothermal and isobaric mixing of ideal gas; $F_{\mathrm{T,P}}^{\mathrm{E}}$ is the excess part of free energy due to isothermal and isobaric mixing.

If n_1 moles of gas 1 is mixed with n_2 moles of gas 2, the F^{E} of gaseous solution can be written as

$$(n_1+n_2)F_{\mathrm{m}} = n_1F_1 + n_2F_2 + n_1RT\ln x_1 + n_2RT\ln x_2 + (n_1+n_2)F^{\mathrm{E}} \quad (7.25b)$$

Applying Eqs. (7.25a) and (7.25b) to the liquid solution, in which n_1 moles of component 1 is mixed with n_2 moles of component 2, and both at their own partial pressure, the free energy of formation of a liquid solution at pressure P will be

$$(n_1+n_2)F_{\mathrm{m}} = n_1F_1 + n_2F_2 + n_1RT\ln x_1 + n_2RT\ln x_2 + (n_1+n_2)\int_{p_i^0}^{P} V_{\mathrm{m}}\mathrm{d}p \quad (7.26)$$

The foregoing equation can be also written in the form of

$$F_{\mathrm{m}} = \left(F_{\mathrm{m}}^{*}\right)_{\mathrm{ideal}} + F^{\mathrm{E}}$$

where F^{E} is the excess free energy of the liquid mixture and also expressed as.

$$\Delta F^{\mathrm{E}} = (n_1+n_2)\int_{p_i^0}^{P} V_{\mathrm{m}}\mathrm{d}P \quad (7.27a)$$

Differentiating Eq. (7.26) with respect to n_1, holding n_2 constant, the partial free energy of gas 1 is obtained as follows

$$\overline{F_1} = \left[\frac{\partial(n_1+n_2)F_{\mathrm{m}}}{\partial n_1}\right]_{n_2} = F_1 + RT\ln x$$

From definition of activity for nonideal solution, $a = \gamma x$, we have,

$$\overline{F_1} = F_1 + RT\ln a_1 = F_1 + RT\ln\gamma_1 x_1$$

It follows that

$$\ln\gamma_1 = \left[\frac{\partial(n_1+n_2)F^{\mathrm{E}}}{\partial n_1}\right]_{n_2} \quad (7.27b)$$

Similarly, we have

$$\ln\gamma_2 = \left[\frac{\partial(n_1+n_2)F^{\mathrm{E}}}{\partial n_2}\right]_{n_1}$$

7.5.2 Prediction of Activity Coefficient: (1) Semi-empirical Equation

As seen from Eqs. (7.27a) and (7.27b), the finding of γ_1 is possible if F^E is known. In the literature, there are many equations of state available for semi-empirical calculation, for example, the simple van der Waals equation which has the following form;

$$P = \frac{RT}{V-b} - \frac{a}{V^2}$$

where a and b are constants. The Peng-Robinson equation takes the form of

$$P = \frac{RT}{V-b} - \frac{a}{V(V+b)+b(V-b)}$$

The Beattie-Bridgeman equation was arranges to the following form by Beattie [45]

$$P = \frac{RT}{V} + \frac{\beta}{V^2} + \frac{\gamma}{V^3} + \frac{\delta}{V^4}$$

where $\beta = RTB_0 - A_0 - \frac{Rc}{T^2}$

$$\gamma = -RTB_0 b + aA_0 - \frac{RB_0 c}{T^2}$$

$$\delta = \frac{RB_0 bc}{T^2}$$

Generally speaking, most of the equation of state can be arranged into the following form:

$$PV = RT + \beta P$$

where β is the coefficient of individual equation of state. The above equation can be expanded to a series as follows

$$P = \frac{RT}{V-\beta} = \frac{RT}{V}\left[1 + \left(\frac{\beta}{V}\right) + \left(\frac{\beta}{V}\right)^2 + \cdots\right]$$

Applying the following simple mixing rule to the gaseous mixture, $\beta_m = \sum \beta_i y_i$

Thus $\beta_m = \beta_1 y_1 + \beta_2 y_2$ is for a binary mixture. Substituting Eq. (7.28) to (7.27a), we have

$$F^{\mathrm{E}} = (n_1 + n_2)\left[-\frac{3RT}{2V^2}\left(\beta_1 - \beta_2^2\right)^2\right] y_1 y_2 + \cdots \tag{7.28}$$

The higher exponent terms of above equation are $y_1^2 y_2, y_1 y_2^2, \ldots$.

Applying the foregoing equation to the liquid solution (mixture), the following mixing rule can be used for the van der Waals equation of state:

$$\sqrt{a_{\mathrm{m}}} = \Sigma(\sqrt{a_i})x_i$$
$$b_{\mathrm{m}} = \Sigma b_i x_i$$

where a_{m} and b_{m} are the constants of the liquid solution (mixture). And Eq. (7.28) becomes

$$F^{\mathrm{E}}_{\mathrm{p,T}} = (RT + \varphi)\frac{\Sigma_{ij} m_{ij} x_i x_j}{\Sigma V_i x_i} + R^2 T^2 \frac{\Sigma_{ijk} m_{ijk} x_i x_j x_k}{\Sigma V_i x_i} + \cdots \tag{7.29}$$

where m is a constant depending on P and T; φ is a constant, V is considered as an empirical constant. Due to van der Waals equation is not accurate enough, the theoretical prediction by using Eq. (7.29) may produce serious error. However, we may use Eq. (7.29) as a semi-empirical equation and consider V an empirical constant denoted by q, then Eq. (7.29) becomes

$$F^{\mathrm{E}}_{\mathrm{p,T}} = (RT + \varphi)\frac{\Sigma_{ij} m_{ij} x_i x_j}{\Sigma q_i x_i} + R^2 T^2 \frac{\Sigma_{ijk} m_{ijk} x_i x_j x_k}{\Sigma q_i x_i} + \cdots \tag{7.30}$$

According to different values of q and φ, Eq. (7.30) can be converted into different models for F^{E}. For instance [46],

Let $(q_i/q_j) = 1$ $\varphi = 0$: the model of Margules
Let $(q_i/q_j) = (A_{ij}/B_{ij})$ $\varphi = 0$: the model of van Laar
Let $(q_i/q_j) = (V_{ij}/V_{ij})$ $\varphi = 0$: the model of Scatchard

Based on Eq. (7.30), some semi-empirical equations were used for evaluating F^{E}, such as:

1. **Margules equation** [47]. The simplest form of Eq. (7.30) is as follows

$$F^{\mathrm{E}} = m_{12} y_1 y_2$$

It was given by Margules that F^{E} could be represent by a power series Similar Eq. (7.28) as follows

$$F^{\mathrm{E}} = a_{12} x_1 x_2 + a_{112} x_1^2 x_2 + a_{122} x_1 x_2^2 + \cdots \tag{7.31}$$

where a_{12}, a_{112}, a_{122} etc. are empirically determined coefficients. The reason of using terms $x^n x^m$ is due to the fact that when $x_1 = 0$ or $x_2 = 0$, the F^E is zero. As the simplest application of this series, only the first term is used, i.e.,$F^E = a_{12}x_1x_2$, it is called two-suffix equation. Combing with Eq. (7.27a) yields

$$\ln \gamma_1 = \left(\frac{a_{12}}{RT}\right)x_2^2 = A_{12}x_2^2$$

where A_{12} is a constant. It is noted that when $x_2 = 1$, $\ln \gamma_1 = A_{12}$; thus it can be obtained by:

- The extrapolation of $\ln \gamma_1$ versus x_2 plot, A_{12} is obtained at $x_2 = 1$.
- With the data of $\ln \gamma_1$ at various x_1, A_{12} can be obtained at various x_1 and take the average.

The weakness of this method of predicting activity coefficient is that at least one value of γ_1 at x_2 should be known from literature or experimental measurement.

Similarly, we have

$$\ln \gamma_2 = \left(\frac{a_{12}}{RT}\right)x_1^2 = A_{12}x_1^2$$

For a ternary solution with composition x_1, x_2, x_3, the two suffix F^E becomes

$$F^E = a_{12}x_1x_2 + a_{13}x_1x_3 + a_{23}x_2x_3$$

And then, the Margules two suffix equation for ternary solution can by given by

$$\begin{aligned}
\ln \gamma_1 &= A_{12}x_2^2 + A_{13}x_3^2 + x_2x_3(A_{12} + A_{13} - A_{23}) \\
\ln \gamma_2 &= A_{12}x_1^2 + A_{23}x_3^2 + x_1x_3(A_{12} + A_{23} - A_{13}) \\
\ln \gamma_3 &= A_{13}x_1^2 + A_{23}x_2^2 + x_1x_3(A_{13} + A_{23} - A_{12})
\end{aligned}$$

2. **van Laar equation** [48]

Van Laar found on semi-empirical basis that F^E could be expressed by the following equation

$$F^E = \frac{a_{12}x_1x_2}{a_1x_1 + a_2x_2}$$

If this equation is substituted into Eq. (7.27b), we obtain for a binary system,

$$\ln \gamma_1 = \frac{A_{12}}{\left[1 + \left(\frac{A_{12}x_2}{B_{12}x_2}\right)\right]^2}$$

where constants are defined as follows

$$A_{12} = \left(\frac{a_{12}}{a_2}\right)\frac{1}{RT}$$
$$B_{12} = \left(\frac{a_{12}}{a_1}\right)\frac{1}{RT}$$

For the ternary solution, the F^{E} is given as bellow

$$F^{\mathrm{E}} = \frac{a_{12}x_1x_2 + a_{13}x_1x_3 + a_{23}x_2x_3}{a_1x_1 + a_2x_2 + a_3x_3}$$

One can get

$$\ln\gamma_1 = Z_2^2A_{12} + Z_3^2A_{13} + Z_{23}A_{23}$$

The $\ln\gamma$ equations are

$$\ln\,\gamma_1 = A_{12}Z_2^2 + A_{13}Z_3^2 + Z_2Z_3\left[A_{12} + A_{13} - B_{23}\left(\frac{A_{13}}{B_{13}}\right)\right]$$
$$\ln\,\gamma_2 = B_{12}Z_2^2 + A_{23}Z_3^2 + Z_1Z_3\left[B_{12} + B_{13} - A_{13}\left(\frac{A_{12}}{B_{12}}\right)\right]$$
$$\ln\,\gamma_3 = B_{13}Z_2^2 + B_{23}Z_2^2 + Z_1Z_2\left[A_{13} + B_{23} - B_{13}\left(\frac{B_{23}}{A_{23}}\right)\right]$$

where the term Z is defined as

$$Z_1 = \frac{x_1}{x_1 + x_2\left(\frac{B_{12}}{A_{12}}\right) + x_3\left(\frac{B_{13}}{A_{13}}\right)}$$
$$Z_2 = \frac{x_2}{x_2 + x_3\left(\frac{B_{23}}{A_{23}}\right) + x_1\left(\frac{A_{12}}{B_{12}}\right)}$$
$$Z_3 = \frac{x_3}{x_3 + x_1\left(\frac{A_{13}}{B_{13}}\right) + x_2\left(\frac{A_{23}}{B_{23}}\right)}$$

As seen from foregoing equations, the prediction of ternary vapor–liquid equilibrium composition can be achieved from binary data.

The precedent examples demonstrate the prediction of γ of multicomponent solution is possible by using corresponding binary data.

7.5.3 Prediction of Activity Coefficient (2) Group Contribution Method

The principle of group contribution method is based on the prostitution that the property of a chemical compound is the sum of the contributions (property) by the corresponding constituent group. For example, ethanol C_2H_5OH or CH_3CH_2OH is considered to be composed by CH_3, CH_2 and OH groups. The property of ethanol is the sum of that of the three groups. Thus the properties of thousands of chemical compound in the world can be considered as the combinatory sum of that given by about 50 groups.

By this method, the property of a compound Q is the sum of the property by the constituent groups Q_i, i.e., $Q = \Sigma Q_i$. Nevertheless, the property of each group is always affected by the interaction of other groups. Therefore Q should be

$$Q = \Sigma Q_i + Q_m$$

where Q_i and Q_m are respectively the contribution (property) by the constituent group and contribution by group interaction, and in literature it is called respectively the combinatorial term and the residual term. Likewise, considering the thermodynamic property $\ln \gamma$, we can write

$$\ln \gamma = \ln \gamma_0 + \ln \gamma_m \tag{7.32}$$

1. **UNIFAC** (Universal Quasi-chemical Functional Group Activity Coefficient)

As shown in foregoing section, the $\ln \gamma$ is considered as the sum of combinatorial part and residual part. According to Flory-Higgins, $\ln \gamma_0$ is calculated by

$$\ln \gamma_0 = \ln\left(\frac{\phi_i}{x_i}\right) + 1 + \frac{\phi_i}{x_i} \tag{7.33}$$

$$\phi_i = \frac{x_i r_i}{\Sigma x_j r_j}$$

where ϕ_i is the volume fraction of component i in solution; r_i and r_j are the volume parameter of component i and j respectively.

The residual part $\ln \gamma_m$ is calculated by

$$\ln \gamma_m = \Sigma x_i \frac{z}{a} q_i \ln \frac{\theta_{ii}}{\theta_i} \tag{7.34}$$

where z is the lattice coordination number; a is the interaction parameter; q_i is the molecular surface area parameter for component i; θ_{ii} is the surface area fraction; θ_i is the local area fraction. The tables for finding these parameters are provided in literature, such as Lassen et al. [49, 50].

The procedure of finding $\ln\gamma$ is firstly to find $\ln\gamma_0$ and $\ln\gamma_m$ according to Eqs. (7.33) and (7.34) from the corresponding tables, and secondly substitute to Eq. (7.32).

2. **NRTL** (Nonrandom Two Liquid) [51]

A relationship between local mol fraction x_{11} of molecule 1 and mole fraction x_{21} of molecule 2 in the neighborhood of molecule 1 was proposed by Wilson as follows [52]:

$$\frac{x_{21}}{x_{11}} = \frac{x_2}{x_1}\frac{\exp\left(-g_{21}/RT\right)}{\exp\left(-g_{11}/RT\right)}$$

where x_1 and x_2 are the overall mole fracture of the mixture; g_{21} and g_{11} are the energy of interaction between 12 and 11 pairs of molecules as shown in Fig. 7.8. Wilson [52] also gave the F^E expression as follows

$$\frac{F^E}{RT} = x_1 \ln\left(\frac{\xi_{11}}{x_1}\right) + x_2 \ln\left(\frac{\xi_{22}}{x_2}\right)$$

where ξ_{11} and ξ_{22} are the local volume fractions which is given by

$$\xi_{11} = \frac{x_1}{x_1 + x_2(v_2/v_1)\exp(-(-g_{21} - g_{11})/RT)}$$
$$\xi_{22} = \frac{x_2}{x_2 + x_1(v_1/v_2)\exp(-(-g_{12} - g_{22})/RT)}$$

where v is the molar volume.

Renon and Prausnitz proposed a Nonrandom Two Liquid model (NRTL) [51] by considering the nonrandomness of mixing. To take into this account, they assume the local mole fraction x_{21} and x_{11} are given by

$$\frac{x_{21}}{x_{11}} = \frac{x_2}{x_1}\frac{\exp\left(-\alpha_{12}g_{21}/RT\right)}{\exp\left(-\alpha_{12}g_{11}/RT\right)} \tag{7.35}$$

where α_{12} is a constant characteristic of the nonrandomness of the mixture; g is the excess free energy per mole; g_{ij} is the energy of interaction between i-j pair of molecules.

After interchange the subscript, we have

$$\frac{x_{12}}{x_{22}} = \frac{x_1}{x_2}\frac{\exp\left(-\alpha_{12}g_{12}/RT\right)}{\exp\left(-\alpha_{12}g_{22}/RT\right)}$$
$$x_{21} + x_{11} = 1, \quad x_{12} + x_{22} = 1$$

Based on Eq. (7.35), one yields

$$x_{21} = \frac{x_2 \exp(-\alpha_{12}(g_{21} - g_{11})/RT)}{x_1 + x_2 \exp(-\alpha_{12}(g_{21} - g_{11})/RT)} \tag{7.36}$$

and

$$x_{12} = \frac{x_1 \exp(-\alpha_{12}(g_{12} - g_{22})/RT)}{x_2 + x_1 \exp(-\alpha_{12}(g_{12} - g_{22})/RT)} \tag{7.37}$$

The NRTL model assumed that there are two kinds of molecule cell in a binary mixture: one for molecule 1 and the other for molecule 2 as shown in Fig. 7.8. The residual free energy is the sum of all residual energy for two body interactions experienced by the center molecule 1. The residual free energy for a cell containing molecule1 at the center is $g^{(1)}$ which is given by

$$g^{(1)}_{\text{pure}} = g_{11}$$

Similarly, for a cell containing molecule 2 to be

$$g^{(2)} = x_{12}g_{12} + x_{22}g_{22} \quad \text{and} \quad g^{(2)}_{\text{pure}} = g_{22}$$

As seen from foregoing equations, the excess free energy is the sum of two parts: (1) Trqnsfer x_1 from a cell of pure liquid 1 into the cell 1 of the solution pure; (2) Transfer molecule 2 from a cell of liquid x_2 into cell 2 of the solution $\left(g^{(2)} - g^{(2)}_{\text{pure}}\right)x_2$. Therefore

$$F^{\text{E}} = x_1\left(g^{(1)} - g^{(1)}_{\text{pure}}\right) + x_2\left(g^{(2)} - g^{(2)}_{\text{pure}}\right)$$

The foregoing equations also can be written to the following form

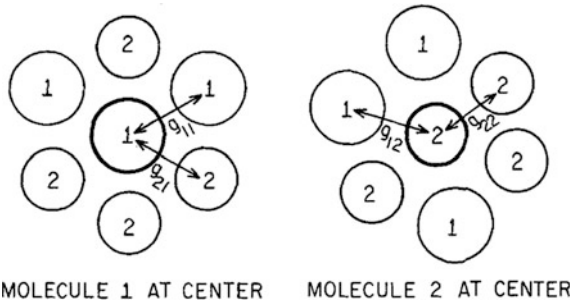

Fig. 7.8 Two types of molecule cell. Reproduced from AIChE Journal 1968, 14, 135

$$F^{\mathrm{E}} = x_1 x_{21}(g_{21} - g_{11}) + x_2 x_{12}(g_{12} - g_{22}) \tag{7.38}$$

where g_{12} and g_{22} are given by Eqs. (7.36) and (7.37) as well as Eq. (7.38) together is called "NRTL equation". From F^{E} we can find the activity coefficient γ for a binary solution to be

$$\ln \gamma_1 = x_2^2 \left(\tau_{21} \frac{\exp(-2\alpha_{12}\tau_{21})}{[x_1 + x_2 \exp(-\alpha_{12}\tau_{21})]^2} + \tau_{21} \frac{\exp(-\alpha_{12}\tau_{12})}{[x_2 + x_1 \exp(-\alpha_{12}\tau_{12})]^2} \right)$$

$$\ln \gamma_2 = x_1^2 \left(\tau_{12} \frac{\exp(-2\alpha_{12}\tau_{12})}{[x_2 + x_1 \exp(-\alpha_{12}\tau_{12})]^2} + \tau_{21} \frac{\exp(-\alpha_{12}\tau_{21})}{[x_1 + x_2 \exp(-\alpha_{12}\tau_{21})]^2} \right)$$

were τ is normalized parameter for symmetric system; τ_{ji} is a coefficient defined by

$$\begin{aligned} \tau_{12} &= (g_{12} - g_{22})/RT \\ \tau_{21} &= (g_{21} - g_{11})/RT. \end{aligned} \tag{7.39}$$

The binary interaction parameters and the nonrandomness parameter (a_{12}) can be found from literature. As an example, the parameters for the methanol (1) + methyl acetate (2) system were obtained from the database and the other binary interaction parameters as well as the nonrandomness parameters (a_{13}, a_{23}) were correlated from experimental vapor–liquid equilibrium data by minimization of the objective function as given in subsequent section.

7.5.4 *Experimental Measurement of Activity Coefficient [53]*

The liquid and vapor equilibrium composition in distillation calculation can be evaluated by the method described in precedent sections. However, the prediction is always in some degree of deviation and cannot be guaranteed as reliable. Thus the experimental measurement is necessary in some cases.

The experimental measurement of a three components vapor liquid equilibrium composition is described below as an example.

Apparatus and Procedure

The VLE for the ternary mixture methanol (1) + methyl acetate (2) + 1-octyl-3-methylimidazolium hexafluorophosphate ([OMIM][PF_6]) (3) was measured by a circulation vapor–liquid equilibrium still (a modified Othmer still) as shown in Fig. 7.9.

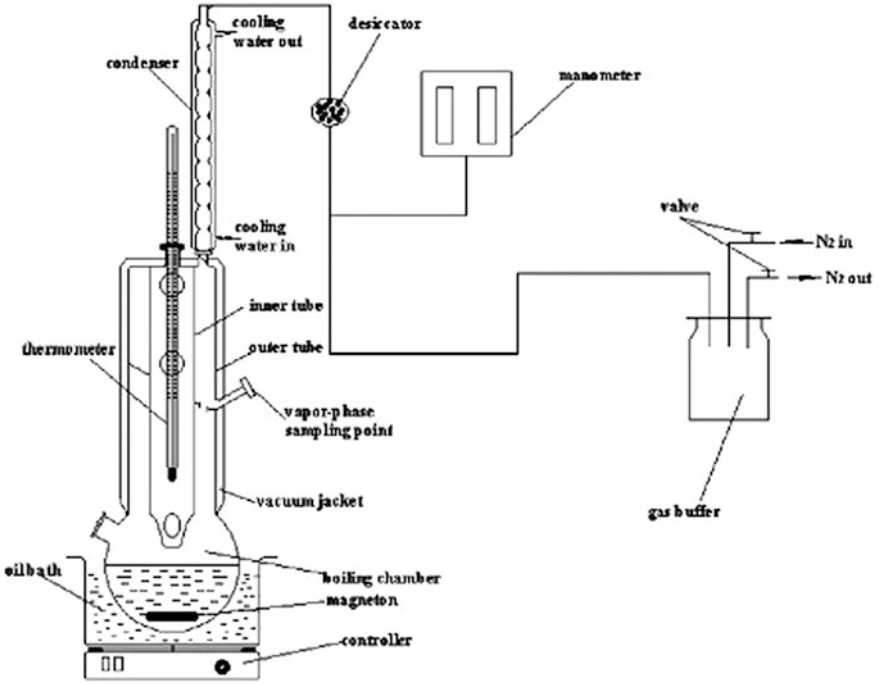

Fig. 7.9 Apparatus for vapor–liquid equilibrium concentration measurement

After the mixture in the equilibrium still was maintained in the constant boiling temperature for about 30 min; then samples were taken every 20 min, from the vapor and liquid phase of the system, respectively. To verify the equilibrium state, samples were taken until the standard deviation of the last five samples was less than 0.0015 for both vapor and liquid phase. The total sampling process lasted for about 2 h, so that the sampling process could ensure the vapor and liquid phases are in equilibrium state. In each VLE experiment, the pressure was kept at 101.3 ± 0.05 kPa. The solutions for VLE measurement were prepared gravimetrically using an electronic balance (Acculab Alc 210.4) with a standard uncertainty of 0.0001 g.

Sample Analysis

Gas chromatography (GC) was used to analyze the compositions of the condensed vapor and the concentrations of methanol and methyl acetate in liquid phase. The GC (SP-1000) was equipped with a FID detector and the column was SE-30 ($50\ \text{m} \times 0.32\ \text{mm} \times 0.5\ \mu\text{m}$).

7.6 Results and Discussion

Experimental Data

The reliability of our experimental method has been verified by the VLE data of methanol (1) + methyl acetate (2) in our previous work. [22]Measurement for the ternary system of methanol (1) + methyl acetate (2) + [OMIM][PF_6] (3) was conducted at 101.3 kPa and the concentrations of ionic liquid added to the system were kept at x_3 = 0.2, 0.4 and 0.6 mol fraction respectively. The isobaric VLE data for the methanol (1) + methyl acetate (2) + ion liquid (3) are listed in Table 7.12.

In the table, x_3 represents the mole fraction of ionic liquid in the liquid phase and x_1' represents the mole fraction of methanol in the liquid phase excluding ionic liquid, y_1 is mole fraction of methanol in the vapor phase, T is the equilibrium temperature, α_{12} is relative volatility of methanol and methyl acetate. Since the vapor pressure of IL can be neglected, there are only methanol and methyl acetate in the vapor phase.

7.6.1 Correlation of the Phase Equilibrium

The NRTL model is commonly used to correlate the vapor–liquid equilibrium data, In this work, we also used the NRTL model to correlate the VLE data. The NRTL model is given in Eq. (7.35) in which the parameters a_{13}, a_{23}, were correlated from ternary experimental vapor–liquid equilibrium data by minimization of the objective function F [34]:

$$F = \sum_{j=1}^{N}\left(\sum_{i=1}^{C}\left(\frac{y_{j,i}^{\mathrm{cal}} - y_{j,i}^{\mathrm{exp}}}{\sigma_y}\right)^2 + \left(\frac{T_j^{\mathrm{cal}} - T_j^{\mathrm{exp}}}{\sigma_{\mathrm{T}}}\right)^2 + \left(\frac{P_j^{\mathrm{cal}} - P_j^{\mathrm{exp}}}{\sigma_p}\right)^2 + \sum_{i=1}^{C}\left(\frac{x_{j,i}^{\mathrm{cal}} - x_{j,i}^{\mathrm{exp}}}{\sigma_x}\right)^2\right)$$

where N is the number of data points; C is the number of components; y is the mole fraction in vapor phase; x is the mole fraction in vapor phase; T is the equilibrium temperature; P is the equilibrium pressure; σ_y, σ_T, σ_P, σ_x are estimated standard deviations for y, T, P and x, respectively (σ_y = 0.002, σ_T = 0.07 K, σ_P = 0.05 kPa, σ_x = 0.002); the superscript exp and cal denote the experimental and calculated values, respectively. The six binary interaction parameters as well as the nonrandomness parameters ($a_{12} = a_{21}$, $a_{13} = a_{31}$ and $a_{23} = a_{32}$) are all given in Table 7.13.

Table 7.12 Vapor–liquid equilibrium data for the ternary system methanol (1) + methyl acetate (2) + [OMIM][PF_6] (3) at P = 101.3 kPa

x_3	T/K	x_1'	y_1	α_{12}
0.200	337.62	0.000	0.000	
0.201	335.02	0.102	0.175	1.867
0.199	333.56	0.192	0.285	1.677
0.198	333.25	0.301	0.380	1.423
0.202	333.32	0.412	0.481	1.323
0.200	333.55	0.523	0.565	1.185
0.201	334.36	0.601	0.612	1.047
0.200	335.32	0.698	0.683	0.932
0.203	336.62	0.792	0.771	0.884
0.201	338.52	0.903	0.872	0.732
0.202	341.68	1.000	1.000	
0.400	349.88	0.000	0.000	
0.401	345.52	0.090	0.192	2.403
0.401	343.21	0.199	0.355	2.215
0.400	342.05	0.290	0.439	1.916
0.397	341.52	0.391	0.540	1.828
0.402	341.51	0.502	0.635	1.726
0.400	341.53	0.620	0.730	1.657
0.399	341.88	0.713	0.792	1.533
0.401	342.52	0.788	0.841	1.423
0.400	343.42	0.901	0.920	1.264
0.403	345.21	1.000	1.000	
0.601	368.38	0.000	0.000	
0.598	361.14	0.100	0.241	2.858
0.603	357.26	0.208	0.422	2.780
0.599	354.47	0.311	0.542	2.622
0.600	353.52	0.399	0.634	2.609
0.602	351.95	0.500	0.711	2.460
0.602	351.23	0.601	0.783	2.396
0.601	350.45	0.701	0.849	2.398
0.601	350.87	0.792	0.902	2.417
0.600	351.23	0.900	0.956	2.414
0.599	350.28	1.000	1.000	

The experimental results and the calculated results by NTRL model are given in Figs. 7.10 and 7.11.

As shown in these figures, the calculated results agree well with the experimental results. The maximum absolute deviation Δy, mean absolute deviation σy and root mean square deviation δy between the experimental and calculated values of vapor

Table 7.13 Values of binary parameters in the NRTL model

i component	*j* component	a_{ij}	ϕ_{ij}	ϕ_{kj}
Methanol (1)	Methyl acetate (2)	0.296	223.376	146.111
Methanol (1)	[OMIM][PF_6] (3)	0.381	508.857	29.956
Methyl acetate (2)	[OMIM][PF_6] (3)	0.156	1333.943	−991.742

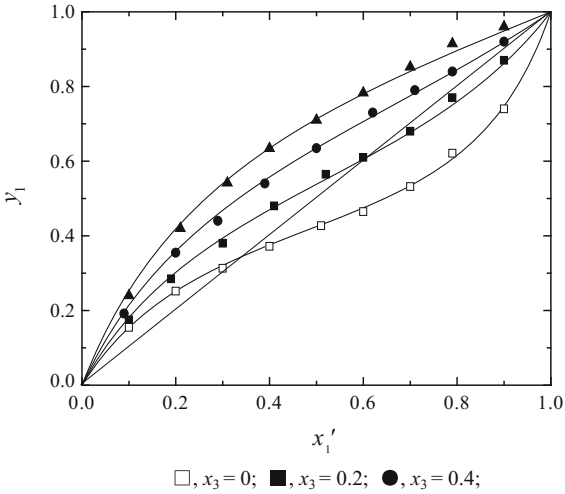

Fig. 7.10 Isobaric VLE diagram for methanol (1) + methyl acetate (2) + [OMIM][PF_6] (3) system at 101.3 kPa: *open rectangle*, $x_3 = 0$; *filled rectangle*, $x_3 = 0.2$; *filled circle*, $x_3 = 0.4$; *filled triangle*, $x_3 = 0.6$; *solid lines*, calculated by the NRTL model

phase mole fractions ($\Delta y = \max \left| y^{\exp} - y^{\text{cal}} \right|$; $\sigma y = (1/N)\sum \left| y^{\exp} - y^{\text{cal}} \right|$; $\delta y = [(1/N)\sum (y^{\exp} - y^{\text{cal}})^2]^{1/2}$) are 0.014, 0.007 and 0.008, respectively. The maximum absolute deviation ΔT, mean absolute deviation σ_T and root mean square deviation δT between the experimental and calculated values of equilibrium temperatures ($\Delta T = \max \left| T^{\exp} - T^{\text{cal}} \right|$; $\sigma_T = (1/N)\sum \left| T^{\exp} - T^{\text{cal}} \right|$; $\delta_T = [(1/N)\sum (T^{\exp} - T^{\text{cal}})^2]^{1/2}$) are 0.65 K, 0.157 K and 0.226 K, respectively.

For methanol + methyl acetate system, the boiling points of methanol and methyl acetate are 337.8 K and 330.9 K, respectively. In common sense, methyl acetate is the volatile component. The investigation of the VLE of methanol + methyl acetate + 1-ethyl-3-methylimidazolium acetate in previous work, [22]and found that 1-ethyl-3-methylimidazolium acetate ([EMIM][Ac]) can eliminate the azeotropic point of methanol + methyl acetate with methyl acetate as volatile component. In this work, [OMIM][PF_6] was chosen as entrainer and [OMIM][PF_6] also can eliminate the azeotropic point of methanol + methyl acetate, but methanol becomes the volatile component (see Figs. 7.10 and 7.11).

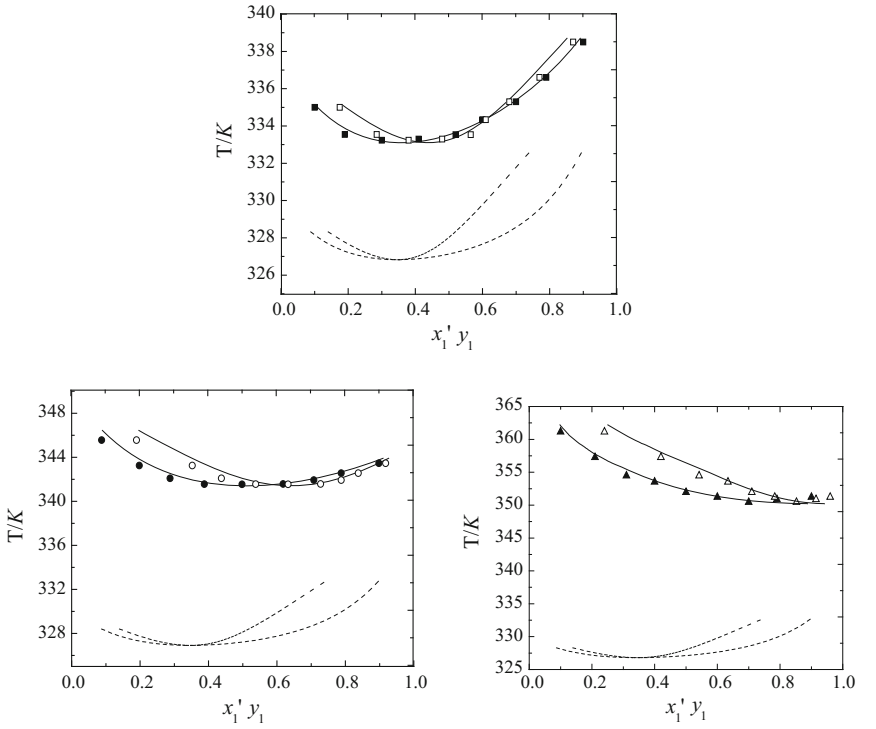

Fig. 7.11 *T*, *x*, *y* diagram for the ternary system of methanol (1) + methyl acetate (2) containing [OMIM][PF_6] (3) at different contents of ionic liquid. *Filled rectangle*, x_1' (x_3 = 0.2); *open rectangle*, y_1 (x_3 = 0.2); *filled circle*, x_1' (x_3 = 0.4); *open circle*, y_1 (x_3 = 0.4); *filled rectangle*, x_1' (x_3 = 0.6); *open rectangle*, y_1 (x_3 = 0.6); *solid lines*, calculated by the NRTL model; dashed lines, calculated by the NRTL model for IL-free system

Figure 7.12 show that the ionic liquid [OMIM][PF_6] produces a notable salting out effect on methanol for methanol + methyl acetate system and the salting out effect of ionic liquid increases with its mole fraction in liquid phase. This phenomena may be attributed to the interaction between methanol and [OMIM][PF_6] is less than that between methyl acetate and [OMIM][PF_6], so the relative volatility of methanol to methyl acetate can be increased by [OMIM][PF_6]. The minimum mole fraction of [OMIM][PF_6] to eliminate the azeotropic point calculated by NRTL equation is 0.28 at 101.3 kPa.

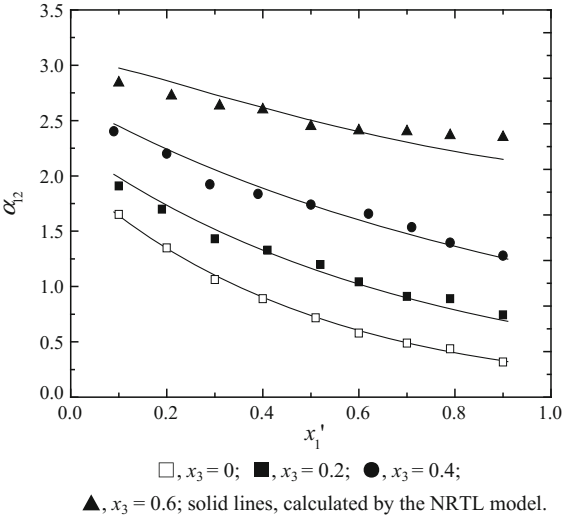

Fig. 7.12 Relative volatility of methanol (1) to methyl acetate (2) at 101.3 kPa: *open rectangle*, $x_3 = 0$; *filled rectangle*, $x_3 = 0.2$; *filled circle*, $x_3 = 0.4$; *filled triangle*, $x_3 = 0.6$; *solid lines*, calculated by the NRTL model

7.7 Summary

1. The description of multicomponent mass transfer is best by applying the Maxwell–Stefan equation. The derivation and steps of calculation of this equation as well as the verification with experimental data are presented in this chapter.
2. Most of the multicomponent mixtures are nonideal solution, The characteristics of multicomponent distillation is different from the binary distillation not only in the nonideal vapor–liquid equilibrium relationship but also the appearance of peculiar bizarre phenomena, such as diffusion barrier, reversed diffusion and osmotic diffusion.
3. The prediction of point efficiency by using two-regime model is presented and the calculated result is verified by the experimental data in both a ternary and ternary system.
4. The determination of equilibrium composition of nonideal solution in vapor liquid system is given by using the methods of semi-empirical correlation of Margules and van Laar, group contribution of UNIFAC and NRTL as well as experimental measurement.

References

1. Higbie R (1935) The rate of absorption of a pure gas into a still liquid during short periods of exposure. Trans Am Inst Chem Eng 35:360–365
2. Doan HD, Fayed ME (2000) Entrance effect and gas-film mass-transfer coefficient in at large diameter packed column. Ind Eng Chem Res 39:1039–1047

3. Gostick J, Doan HD, Lohi A, Pritzkev MD (2003) Investigation of local mass transfer in a packed bed of pall rings using a limiting current technique. Ind Eng Res 42:3626–3634
4. Yih SM, Chen KY (1982) Gas absorption into wavy and turbulent falling liquid films in a wetted-wall. Chem Eng Commun 17(1–6):123–136
5. Gostick J, Doan HD, Lohi A, Pritzkev MD (2003) Investigation of local mass transfer in a packed bed of pall rings using a limiting current technique. Ind Eng Chem Res 42:3626–3634
6. Chen YM, Sun CY (1997) Experimental study on the heat and mass transfer of a combined absorber evaporator exchanger. Int J Heat Mass Transf 40:961–971
7. Krupiczka R, Rotkegel A (1997) An experimental study of diffusional cross-effect in multicomponent mass transfer. Chem Eng Sci 52(6):1007–1017
8. Vasquez G, Antorrena G, Navaza JM, Santos V, Rodriguez T (1993) Adsorption of CO_2 in aqueous solutions of various viscosities in the presence of induced turbulence. Int Chem Eng 33(4):649–655
9. Sterinberger N, Hondzo M (1999) Diffusional mass transfer at sediment water interface. J Environ Eng 125(2):192–200
10. Carberry JJ (1960) A boundary-layer model of fluid-particle mass transfer in mixed beds. AIChE J 4:460
11. Nielsen CHE, Kiil S, Thomsen HW, Dam-Johansen K (1998) Mass transfer in wetted-wall columns: correlations at high Reynolds numbers. Chem Eng Sci 53(3):495–503
12. Yang MC, Cussler EL (1986) Designing hollow-fiber contactors. AIChE J 32 (11)
13. Hichey PJ, Gooding CH (1994) Mass transfer in spiral wound pervaporation modules. J Membrane Sci 92(1):59–74
14. Sekino M (1995) Study of an analytical model for hollow fiber reverse osmosis module systems. Desalination 100(1):85–97
15. Erasmus AB, Nieuwoudt I (2001) Mass transfer in structured packing: a wetted-wall study. Ind Eng Chem Res 40:2310–2321
16. Cussler EL (1989) Diffusion. Cambridge University Press, New York
17. Baerns M, Hofmann H, Renken A (1987) Chemische Reaktionstechnik Stuttgart: G. Thieme
18. Jordan U, Schumpe A (2001) The gas density effect on mass transfer in bubble columns with organic liquids. Chem Eng Sci 56(21):6267–6272
19. Yang W, Wang J, Jin Y (2001) Mass transfer characteristics of syngas components in slurry system at industrial conditions. Chem Eng Technol 24(6):651–657
20. Hameed MS, Saleh Muhammed M (2003) Mass transfer into liquid falling film in straight and helically coiled tubes. Int J Heat Mass Transf 46(10):1715–1724
21. Shulman HL, Ullrich CF, Proulx AZ et al (1955) Performance of packed columns. 2. Wetted and effective interfacial areas, gas- and liquid-phase mass transfer rates. AIChE J 1(2):253–258
22. Onda K, Takeuchi H, Okumoto Y (1968) Mass transfer coefficients between gas and liquid phases in packed columns. J Chem Eng Jpn 1(1):56–62
23. Billet R, Schultes M (1992) Advantage in correlating packing column performance. Inst Chem Eng Symp Ser 128(2):B129–B136
24. Bravo JL, Rocha JA, Fair JR (1985) Mass transfer in gauze packings. Hydrocarb Process 64 (1):91–95
25. Olujic Z, Kamerbeek AB, De Graauw J (1999) A corrugation geometry based model for efficiency of structured distillation packing. Chem Eng Process 38(4–6):683–695
26. Zuiderweg FJ (1892) Sieve teay: a view on starte of art. Chem Eng Sci 37:1441–1464
27. Akita K, Yoshida F (1973) Gas holdup and volumetric mass transfer coefficient in bubble column. Ind Eng Chem Process Des Dev 12(1):76–80
28. Zhou CF (2005) Study on the influence of Marangoni effect and other factor on the mass transfer coefficients. M.S. dissertation, Tianjin University, Tianjin, China (in Chinese)
29. Wang GQ, Yuan XG, Yu KT (2005) Review of mass-transfer correlations for packed columns. Ind Eng Chem Res 44:8715–8729
30. Bird RB, Steward WE, Lightfoot EN (1960) Tansport phenomena. Wiley, New York

31. Lightfoot EN, Cussler FL, Rettic RL (1962) Applicability of the Stefan-Maxwell equations to multicomponent diffusion in liquids. AIChE J 8(5):708–710
32. Krishna R (1985) Model for prediction of point efficiencies for multicomponent distillation. Chem Eng Res Des 63(5):312–322
33. Song HW, Wang SY, Han JC, Wu JW (1996) A new model for predicting distillation point efficiencies of non-ideal multicomponent mixture. CIESC J 47(5):571
34. Oldershaw C (1941) Perforated plate columns for analytical batch distillations. Ind Eng Chem Anal Ed 13(4):265–268
35. Kalbassi MA, Biddulph MW (1987) A modified Oldershaw column for distillation efficiency measurements. Ind Eng Chem Res 26(6):1 127–1 132
36. Wang ZC (1997) Non-ideal multicomponent mass transfer and point efficiencies on a sieve tray. PhD dissertation, Tianjin University, Tianjin, China (in Chinese)
37. Hai NT (1980) Ph.D. Thesis, The University of New South Wales, Australia
38. Raper JA (1979) Ph.D. Thesis, The University of New South Wales, Australia
39. Geary NW, Rice RG (1991) Bubble size prediction for rigid and flexible spargers. AIChE J 37 (2):161–168
40. Hesketh RP, Russell TWF, Etchells AW (1987) Bubble size in horizontal pipelines. AIChE J 33(4):663–667
41. Sharma MM, Gupta RK (1967) Trans Inst Chem Eng 45:T169
42. Raper JA, Kearney MS, Fell CJD (1982) The structure of industrial sieve tray froths. Chem Eng Sci 37:501–506
43. Zaritsky NE, Calvelo A (1979) Can J Chem Eng 57:58–64
44. Prado JA, Fair RJ (1990) Fundamental model for the prediction of sieve tray efficiency. Ind Eng Chem Res 29(6):1031–1042
45. Beattie JA (1930) Proc Nat Acad Sci 16:14
46. Yu KT (1952) Distillation (Chap. 2). Lecture note of graduate course “Advanced Unit Operation”. Tianjin University
47. Margules M (1895) Sitzber Akad Wiss Math Naturw Klesse It104, 1243
48. van Laar JJ (1910) Z Physik Chem 72:723
49. Fredenslund A, Jones RL, Prausnitz JM (1975) Group-contribution estimation of activity coefficients in nonideal liquid mixtures. AIChE J 21(6):1086–1099
50. Larsen RL, Rasmussen P, Fredenslund A (1987) A modified UNIFAC group-contribution model for prediction of phase equilibria and heats of mixing. Ind Eng Chem Res 26 (11):2274–2286
51. Renon H, Prausnitz JM (1968) Local compositions in thermodynamic excess functions for liquid mixtures. AIChE J 14:135–144
52. Wilson GM (1964) JACS 86:127–131
53. Cai JL, Cui XB, Zhang Y, Li R, Feng TY (2011) Isobaric vapor–liquid equilibrium for methanol + methyl acetate + 1-octyl-3-methylimidazolium hexafluorophosphate at 101.3 kPa. J Chem Eng Data 56:2884–2888

Chapter 8
Micro Behaviors Around Rising Bubbles

Abstract Velocity and concentration distribution near the interface of moving bubble in liquid are investigated experimentally and numerically. The tangential and nominal velocity distributions of liquid in the vicinity of the interface are measured by a Laser Doppler anemometer. Then a numerical model for predicting the liquid velocity distribution around a bubble is developed and the results are compared with some other models by checking with the experimental data from a Particle Imaging Velocimeter (PIV). The species concentration distribution of liquid near the interface is measured by using holographic interferometer. It is shown in the experiment that the concentration at distance about 10^{-2} mm from the interface is far from the thermodynamic equilibrium value, and some insight in understanding the interfacial mass transfer is discussed.

Keywords Gas–liquid interface · Moving bubble · Interfacial mass transfer phenomenon · Concentration near interface · Velocity distribution near interface

Nomenclature

P	Pressure, Pa
R	Axial length from bubble center, $(R = R_B + y)$
$r(x)$	Radius normal to flow direction, m
r^*	Radial distance $[r^* = r(x)/R_B]$
R_B	Radius of rising bubble, m
S	Cross-correlation coefficient
t	Contact time of fluid and bubble, s
T	Temperature
u	Liquid flow velocity, cm s^{-1}
U	Velocity of external fluid, m s^{-1}
U_B	Velocity of rising bubble, m s^{-1}
u	Tangential velocity, m s^{-1}
v	Radial velocity, m s^{-1}
X	Coordination in X direction
x	Length from the front stagnation point, radian, n
Y	Coordination in Y direction

K.-T. Yu and X. Yuan, *Introduction to Computational Mass Transfer*,
Heat and Mass Transfer, DOI 10.1007/978-981-10-2498-6_8

y Normal distance to the surface of bubble, m
η Dimensionless variable
v Dynamical viscosity ($v = \rho/\mu$), $m^2\ s^{-1}$
θ Center angle from the front stagnation point ($\theta = r/R$)
μ Viscosity of the fluid, kg $s^{-1}\ m^{-1}$
ξ Function of η
ρ Density of the fluid, kg m^{-3}
ψ Stream function

In the gas (vapor)–liquid contacting process, the mass transfer from one phase (for instance, liquid phase) to the other (vapor phase) is conventionally considered to be composed of the following three steps.

First, the mass from liquid phase diffuse from the bulk to the bubble interface; Secondly, the liquid and gas phases in the bubble interface are coexisted and supposed they are in thermodynamic equilibrium; Thirdly, the mass diffuse from interface to the bulk vapor phase.

Based on the concept of phase equilibrium at the interface, many mass transfer models were developed, among which the film model [1], penetration theory [2], and surface renewal model [3] are three well-known classical theories and have been extensively used in vapor–liquid processes.

In the late 1980s, Gibbs gave up the traditional proposition of maintaining phase equilibrium at the interface and proposed the theory of "Gibbs adsorption layer" in the interface, in which the quantity of mass transferred from bulk liquid to the bulk gas, undergoes the following steps in sequence:

- Solute diffuse to the interface from bulk liquid;
- Accumulation of solute in the "adsorption layer";
- Diffusion of solute in the adsorption layer;
- Diffusion of solute from the interface (adsorption layer) to the gas phase.

However, the mechanism of mass transfer through the interface is still a problem to be investigated. Due to the rapid development and extensive application of the laser Doppler, holographic interference, and computer online measurement techniques, much attention has been paid to study experimentally the interfacial process.

The liquid phase in separation process is usually considered as continuum and the vapor phase is dispersed in the form of different size bubbles.

8.1 Fluid Velocity Near the Bubble Interface [4, 5]

It is commonly recognized that fluid velocity near the interface has considerable significance in the understanding of mass transfer mechanism between vapor and liquid. In this section, two-dimensional Laser Doppler anemometer technique was employed to investigate the hydrodynamic and turbulent structure near the interface

of a bubble. In order to measure the velocity as well as concentration field near the bubble interface, it is necessary to trace exactly the surface of a moving bubble by the laser beams. Such measurement, however, is technically very difficult. An alternative approach is to keep the bubble stationary in a downward stream current of liquid, i.e., against a countercurrent liquid stream, so as to make the measurement possible. The experimental setup is shown in Fig. 8.1.

In this section, a velocity model for estimating the contact time of fluid elements near the front part of a bubble is given under the unsteady flow condition and solved mathematically. The small influence by the Karman vortex shedding from the rear part of the bubble is neglected. For the verification of the present model, an experimental setup of Particle Image Velocimetry (PIV) accompanied with digital image processing was established as described in Sect. 8.1.2.

The experimental systems are air–water and air–ethanol, the diameters of bubbles are adjusted to be 0.67 and 0.42 mm, respectively. It was found that the velocity near the interface of a bubble is highly fluctuated and stochastic as shown in Fig. 8.2 for the instantaneous tangential velocity of the rear bubble wake. Thus, time average velocity is employed in the measurement.

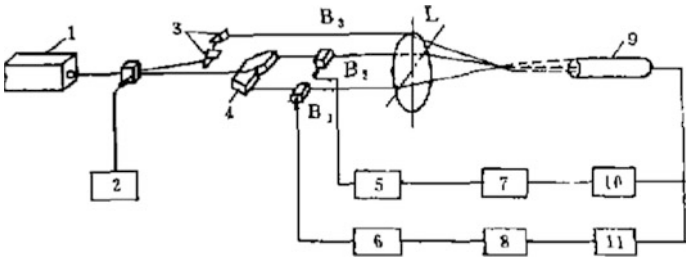

Fig. 8.1 Schematic diagram of two-dimensional laser Doppler anemometer (*1* He–Ne laser source, *2* accelerator, *3* refractive lens, *4* splitter, *5* VCD2, *6* VCD1, *7* frequency identifier 2, *8* frequency identifier 1, *9* optical detector, *10* filter amplifier 2, *11* filter amplifier 1, and B_1, B_2, B_3 frequency shift drivers) (reprinted from Ref. [4], Copyright 1992, with permission from CIESC) B1, B2, B3—frequency shift driver

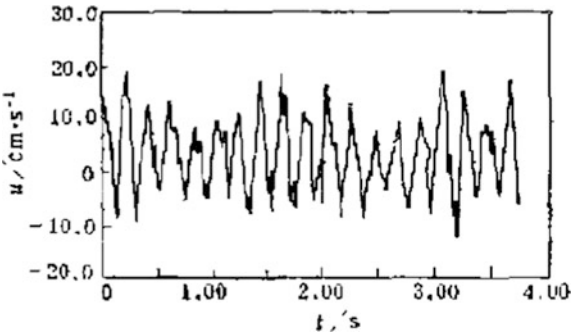

Fig. 8.2 Recorded tangential velocity of the rear bubble wake (d_e = 0.67 mm) (reprinted from Ref. [4], Copyright 1992, with permission from CIESC)

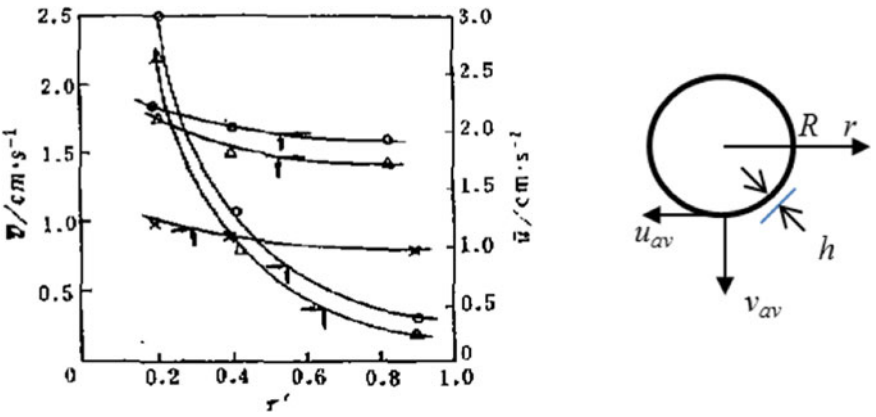

Fig. 8.3 Velocity distribution near the bubble surface (u_{av} tangential velocity, v_{av} normal velocity, and r' radius of the bubble) (reprinted from Ref. [4], Copyright 1992, with permission from CIESC)

Considering the complicated situation of flow near the bubble interface, the measurement was undertaken separately for the front track and rear wake. Figure 8.3 shows the time average tangential velocity u_{av} and normal velocity v_{av} at different time and bulk fluid velocity u_0. The measured distance from the bubble surface h is 0.08 mm. As seen in the figure, the $\bar{u}$ is decreased greatly with the radius of the bubble r', while the $\bar{v}$ is also in the same tendency but with less decreasing rate.

As seen in the figure, the time average normal velocity $\bar{v}$ near rear interface diminished from center to the edge of the wake, while the tangential velocity $\bar{u}$ show only a little change.

8.1.1 *Model Equation of Velocity Distribution Near a Rising Bubble [6]*

Derivation of basic equations

The flowing fluid is in relative motion with respect to a rising bubble. For the cross-current and countercurrent flow between the bubble and fluid, the mathematical methods are identical except on the direction of the flow. For simplicity, we choose a coordinate system that is linked with the external flow around the bubble. The position of a fluid element is specified by the radius $r(x)$ perpendicular to the direction of the bubble motion, i.e., $r(x) = R\sin(x/R)$ and $R = R_B + y$, where x is the distance measured along a meridian from the front stagnation point, y is the coordinate normal to the bubble wall (Fig. 8.4). The tangential and normal velocity components to the wall are represented, respectively, by u and v, and the velocity of main flow is $U(x.t)$. Furthermore, as far as incompressible fluid is concerned, the

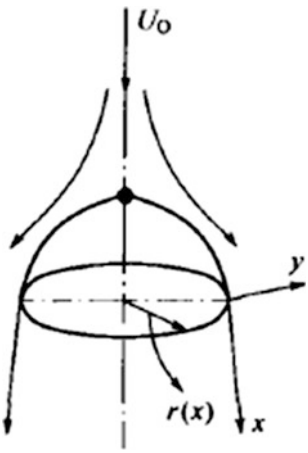

Fig. 8.4 Schematic diagram of coordinates

present coordinate system is equivalent to the conventional one. The advantage of such choices is that the boundary layer separation occurs at the point where $\partial u/\partial y|_y = 0$.

Assumptions are made as follows:

(1) The bubble is spherical with constant radius R_B.
(2) The bubble accelerates very rapidly and reaches its full velocity soon after it is formed.

In this case, the conventional governing equations of the boundary layer, i.e., the continuity equation and the momentum equation, are as follows

$$\frac{\partial(ur)}{\partial x} + \frac{\partial(vr)}{\partial y} = 0 \tag{8.1}$$

$$\rho\left(\frac{\partial u}{\partial t} + u\frac{\partial u}{\partial x} + v\frac{\partial u}{\partial y}\right) = -\frac{\partial p}{\partial x} + \mu\frac{\partial^2 u}{\partial y^2} + \mu\frac{\partial^2 u}{\partial x^2} \tag{8.2}$$

with the boundary conditions:

$$\begin{array}{ll} y = 0 & u = 0, v = 0 \\ y = \infty & u = U(x,t) \end{array}$$

where $U(x,t)$ is the velocity of main fluid. The viscous term $\mu\partial^2 u/\partial x^2$ can be neglected since it is much smaller than the term $\mu\partial^2 u/\partial y^2$, and Eq. (8.2) becomes

$$\rho\left(\frac{\partial u}{\partial t} + u\frac{\partial u}{\partial x} + v\frac{\partial u}{\partial y}\right) = -\frac{\partial p}{\partial x} + \mu\frac{\partial^2 u}{\partial y^2} \tag{8.3}$$

For the fluid motion outside the boundary layer, the acceleration term and the viscous term can be ignored, then the relationship between $U(x,t)$ and the pressure becomes

$$\rho\left(\frac{\partial U}{\partial t}+U\frac{\partial U}{\partial x}\right)=-\frac{\partial p}{\partial x} \tag{8.4}$$

The governing equations can be solved by means of successive approximation, in which the fluid velocity around the rising bubble can be expressed as a sum of the first approximation u_0 and the second approximation u_1.

$$u(x,y,t)=u_0(x,y,t)+u_1(x,y,t) \tag{8.5}$$

where u_0 denote the velocity of fluid in boundary layer after the bubble starts impulsively from rest, and u_1 represents the increment of u_0 during the development of boundary layer. For simplicity, a stream function ψ and a dimensionless variable $\eta=y/2\sqrt{vt}$ are introduced

$$u=\frac{1}{r}\frac{\partial\psi}{\partial y},\quad v=-\frac{1}{r}\frac{\partial\psi}{\partial x} \tag{8.6}$$

According to Eq. (8.5), the stream function can be represented by the Blasius series

$$\psi(x,y,t)=2\sqrt{vt}\left\{rU\xi_0(\eta)+t\left[rU\xi_{1a}(\eta)\frac{\partial U}{\partial x}+U^2\xi_{1b}(\eta)\frac{dr}{dx}\right]+\ldots\right\} \tag{8.7}$$

where $\xi_0(\eta)$, $\xi_{1a}(\eta)$, and $\xi_{1b}(\eta)$ are dimensionless functions of η, and U is the velocity of fluid outside the boundary layer. Substituting Eq. (8.7) into Eq. (8.5), the expressions of u and v are obtained

$$u=U\left\{\xi_0'+t\left[\frac{\partial U}{\partial x}\xi_{1a}'(\eta)+\frac{U}{r}\frac{\mathrm{d}r}{\mathrm{d}x}\xi_{1b}'\right]\right\} \tag{8.8}$$

$$-v=\frac{2\sqrt{vt}}{r}\left\{\left(U\frac{\mathrm{d}r}{\mathrm{d}x}+r\frac{\mathrm{d}U}{\mathrm{d}x}\right)\xi_0+t\left[\begin{array}{r}\left\langle U\frac{\mathrm{d}r}{\mathrm{d}x}\frac{\mathrm{d}U}{\mathrm{d}x}+r\left(\frac{\mathrm{d}U}{\mathrm{d}x}\right)^2+rU\frac{\mathrm{d}^2U}{\mathrm{d}x^2}\right\rangle\xi_{1a}\\+\left\langle 2U\frac{\mathrm{d}r}{\mathrm{d}x}\frac{\mathrm{d}U}{\mathrm{d}x}+U^2\frac{\mathrm{d}^2r}{\mathrm{d}x^2}\right\rangle\xi_{1b}\end{array}\right]+\ldots\right\} \tag{8.9}$$

Combining Eqs. (8.3) and (8.4), and neglecting u_1 since u_0 is dominant, we have

$$\rho\left(\frac{\partial u_0}{\partial t}+u_0\frac{\partial u_0}{\partial x}+v_0\frac{\partial u_0}{\partial y}\right)=\rho\left(U\frac{\partial U}{\partial x}+\frac{\partial U}{\partial t}\right)+\mu\frac{\partial^2 u_0}{\partial y^2} \tag{8.10}$$

The convective terms are much smaller than the acceleration terms $\partial u_0/\partial t$ and $\partial U/\partial t$ due to the fact that fluid around the bubble is at rest before the bubble starts to move. Under these conditions, Eq. (8.10) is rewritten as

$$\frac{\partial u_0}{\partial t}-\frac{\mu}{\rho}\frac{\partial^2 u_0}{\partial y^2}=\frac{\partial U}{\partial t} \tag{8.11}$$

Substituting Eq. (8.5) into Eq. (8.2), and considering Eq. (8.11), Eq. (8.2) is rewritten as

$$\frac{\partial u_1}{\partial t}+u\frac{\partial u}{\partial x}+v\frac{\partial u}{\partial y}=U\frac{\partial U}{\partial x}+\frac{\mu}{\rho}\frac{\partial^2 u_1}{\partial y^2} \tag{8.12}$$

For a distillation process, the distance that a rising bubble is dragged through is the height of the liquid bed on a tray, so it is impossible that the boundary layer is fully developed, and then the first approximation, u_0, is that dominant term. Based on the above analysis, the convective term can be expressed by u_0 and v_0, and Eq. (8.12) is reduced as

$$U\frac{\partial U}{\partial x}-u_0\frac{\partial u_0}{\partial x}-v_0\frac{\partial u_0}{\partial y}=\frac{\partial u_1}{\partial t}-v\frac{\partial^2 u_1}{\partial y^2} \tag{8.13}$$

The boundary conditions with regard to Eqs. (8.12) and (8.14) are: $u_0=u_1=0$ at $y=0$; $u_0=U(x,t)$, $u_1=0$ at $y=\infty$.

In the coordinate system linked with the bubble, the potential flow is defined by the conditions $t\le 0$, $U(x,t)=0$, and $t>0$, $U(x,t)=U(x)$. In this particular case we have $\partial U/\partial t=0$. The differential equation of the first approximation becomes

$$\frac{\partial u_0}{\partial t}-v\frac{\partial^2 u_0}{\partial y^2}=0 \tag{8.14}$$

As the first approximation of Eq. (8.14), letting $u_0=U\xi_0'$ and inserting it into Eq. (8.5), we obtain the following ordinary differential equation for $\xi_0(\eta)$

$$\xi_0^{(3)}+2\eta\xi_0^{(2)}=0 \tag{8.15}$$

with the boundary conditions $\xi_0=\xi_0'=0$ at $\eta=0$, and $\xi_0'=1$ at $\eta=\infty$. The solution is

$$\xi_0'(\eta) = \mathrm{erfc}(\eta) = \frac{2}{\sqrt{\pi}} \int_{\eta}^{\infty} \mathrm{e}^{-\eta^2} \mathrm{d}\eta = 1 - \frac{2}{\sqrt{\pi}} \int_{0}^{\eta} \mathrm{e}^{-\eta^2} \mathrm{d}\eta \tag{8.16}$$

Substituting the approximations of u_0, u_1, v_0, v_1 in Eqs. (8.8) and (8.9) into Eq. (8.13), we obtain the following differential equations for ξ_{1a} and ξ_{1b}

$$\begin{aligned} &\frac{\partial U}{\partial x}\left\{\left[1-(\xi_0)^2\right] + \xi_0\xi_0^{(2)} - \xi_{1a}' + \frac{\eta}{2}\xi_{1a}^{(2)} + \frac{1}{4}\xi_{1a}^{(3)}\right\} \\ &\quad + \frac{U}{r}\frac{\partial r}{\partial x}\left\{\xi_0\xi_0^{(2)} - \xi_{1b}' + \frac{\eta}{2}\xi_{1b}^{(2)} + \frac{1}{4}\xi_{1b}^{(3)}\right\} = 0 \end{aligned} \tag{8.17}$$

According to the system of coordinate selected, the following relationships for the outer flow hold.

$$U(x,t) = \frac{3}{2}U_{\mathrm{B}} \sin\frac{x}{R}, \quad r(x) = R\sin\frac{x}{R} \tag{8.18}$$

Hence, the terms $\partial U/\partial x$ and $(U/t)\partial r/\partial x$ in Eq. (8.17) have the same sign and are nonzero when $x/R \in [0, \pi/2)$ and $x/R \in (\pi/2, \pi]$. The only condition which satisfies Eq. (8.17) is that the terms in two brackets equal to zero. Then we obtain the differential equations for ξ_{1a} and ξ_{1b} as follows:

$$\xi_{1a}^{(3)} + 2\eta\xi_{1a}^{(2)} - 4\xi_{1a}' = 4(\xi_0'^2 - 1 - \xi_0\xi_0^{(2)}) \tag{8.19}$$

$$\xi_{1b}^{(3)} + 2\eta\xi_{1b}^{(2)} - 4\xi_{1b}' = -4\xi_0\xi_0^{(2)} \tag{8.20}$$

with boundary conditions

$$\begin{aligned} &\eta = 0 \quad \xi_{1a} = \xi_{1a}' = 0, \ \xi_{1b} = \xi_{1b}' = 0 \\ &\eta = \infty \quad \xi_{1a}' = 0, \ \xi_{1b}' = 0 \end{aligned}$$

Substituting Eq. (8.18) into Eqs. (8.8) and (8.9), u and v can be expressed as

$$u = \frac{3}{2}U_{\mathrm{B}} \sin\theta \left[\xi_0' + \frac{3}{2}\frac{U_{\mathrm{B}}}{R}t(\xi_{1a}' + \xi_{1b}')\cos\theta\right] \tag{8.21}$$

$$-v = \frac{2\sqrt{vt}}{R}U_{\mathrm{B}}\left[3\xi_0\cos\theta + \frac{9}{4}\frac{U_{\mathrm{B}}}{R}t(2-3\sin^2\theta)(\xi_{1a}+\xi_{1b})\right] \tag{8.22}$$

The contact time t between a bubble and a fluid element at a given position (x, y) terminates when separation of boundary layer occurs. Since the condition of boundary layer separation is $\partial u/\partial y|_y = 0$, we differentiate Eq. (8.21) with respect to y, and obtain the following relationship:

$$\xi_0^{(2)} + \frac{3}{2}\frac{U_B}{R}\cos\theta\left[\xi_{1a}^{(2)} + \xi_{1b}^{(2)}\right]t = 0 \tag{8.23}$$

The equations for ξ_{1a} and ξ_{1b} now can be solved simultaneously with Eqs. (8.16) and (8.23), and then the velocity components u and v near the bubble rising can be computed. For the calculation of the tangential and radial velocities near a bubble from the above equations, the following steps are used.

(1) For a given y and θ, assume a contact time t_c, then calculate η, $\xi_0^{(2)}\eta$, $\xi_{1a}^{(2)}\eta$ and $\xi_{1b}^{(2)}\eta$ numerically from Eqs. (8.16), (8.19), and (8.20). Substitute these values into Eq. (8.23) to calculate t_c. Repeat the procedure for calculating t_c and its true value can be obtained by trial and error or by the method of iteration.
(2) Based on y, θ and t_c obtained from Step (1), $\xi_0(\eta)$ and $\xi_0'(\eta)$ are calculated from Eq. (8.16), $\xi_{1a}(\eta)$ and $\xi_{1a}'(\eta)$ from Eq. (8.19), $\xi_{1b}(\eta)$ and $\xi_{1b}'(\eta)$ from Eq. (8.20). Substituting these values into Eqs. (8.21) and (8.22), two velocity components u and v can be obtained.
(3) The time averages of two velocity components are computed by the following relationships:

$$\bar{u} = \int_0^{t_c} u\mathrm{d}t/t_c, \quad \bar{v} = \int_0^{t_c} v\mathrm{d}t/t_c \tag{8.24}$$

8.1.2 Experimental Measurement and Comparison with Model Prediction

Particle Image Velocimeter (PIV) has been widely applied to the measurement of velocity distribution of flow field since it is able to carry out the simultaneous nonintrusive optical measurement of fluid flow at all points in an illuminated region by recording the light scattering particles. Based on the traditional PIV, we improve it by means of the video technique accompanied with Digital Image Correlation Method (DICM), and construct a digitized PIV. An important advantage of the video-based cross-correlation technique is easily to use for flow velocity measurements due to the absence of the photographic and optical mechanical processing steps inherent in the non-video-based PIV technique.

Theoretically, the measured velocities of the particles are not exactly equal to that of the fluid elements, because of the inertial effect resulted by the density between the particles and fluid. In order to minimize the velocity difference, we choose polystyrene spheres, 1–5 μm in diameter and 1.05 g cm^{-3} in density, as the tracer particles, so that the relative velocity approaches to unity. As a result, the velocities of the particles can be considered to be those of the fluid elements.

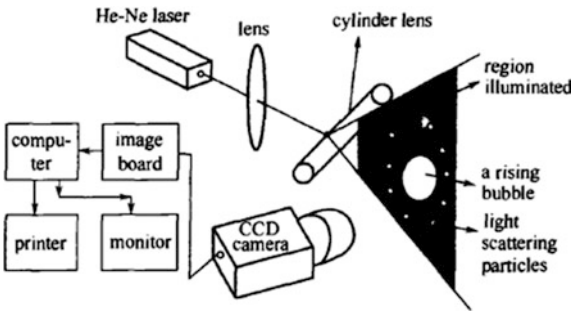

Fig. 8.5 Schematic diagram of experimental setup

The experimental setup (Fig. 8.5) is composed of an illumination system and a system of image capturing and processing. The illumination is a laser light sheet of 0.5 mm in thickness, provided by a helium–neon laser beam passing through a cylindrical lens. The sequential image system includes a CCD camera (coupled charge device, 512 × 512 pixels), an image processor (DC32, 512 × 512 pixels) at the framing rate of 50 Hz and a computer software for calculating the velocity distribution. The video image is first transformed into the digital image (2^8 bites) by DC32 processor in gray degrees, or light density distribution, from 0 to 255. The digital image is stored rapidly in the hard disk of a computer for computing the cross-correlation coefficients of the sequential images.

In order to improve the accuracy of measurement, all digitized images were divided into several subsample images in the size of 32 by 32 pixels, and each subsample image retains the spatial distribution pattern of the tracer particles in the sampled region at a given time. Let $f(m,n)$ be a distribution function, which is defined by the pattern of pixels distribution with different gray degrees, representing the tracer particle spatial distribution pattern in a subsample region in a image taken at t_0. Then, it is chosen as a reference pattern, and compared with those of all subsamples of the image taken at $t_0 + \Delta t$, by line-by-line scan, in order to search the full matching region with distribution function $g(m^*, n^*)$. The $f(m,n)$ and $g(m^*, n^*)$ are the distribution functions of two subsamples (32 by 32 pixels) in two images at t_0 and $t_0 + \Delta t$, respectively. The discrete cross-correlation function, or cross-correlation coefficient $\mathrm{Sim}(m,n)$, which represents the similarity between the sampled regions $f(m,n)$ and $g(m^*, n^*)$, is defined by Eq. (8.25) according to the statistical technique of spatial cross-correlation [7].

$$\mathrm{Sim}(m,n) = \sum_{i=-N}^{N}\sum_{j=-N}^{N} f(i,j)\cdot g(i-m, j-n) \Bigg/ \sqrt{\sum_{i=-N}^{N}\sum_{j=-N}^{N} f^2(i,j)\cdot \sum_{i=-N}^{N}\sum_{j=-N}^{N} g^2(i,j)} \tag{8.25}$$

If the two patterns fully match each other, $\mathrm{Sim} = 1$; if they are completely unmatched, $\mathrm{Sim} = 0$, and in general, $0 \le \mathrm{Sim} \le 1$. Consequently, $\mathrm{Sim} = 1$ implies that a fluid element with the pattern $f(m,n)$ at t_0 is also found at $t_0 + \Delta t$. This

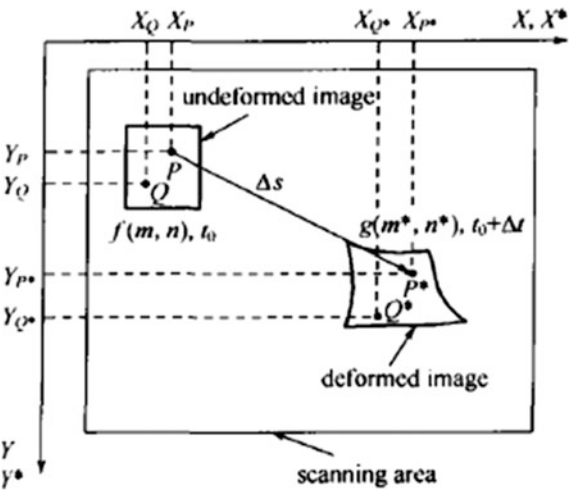

Fig. 8.6 Schematic diagram of spatial shift and contour of the sequential digital images (reprinted from Ref. [7], Copyright 2005, with permission from Elsevier)

equally implies that the fluid element is moved to form the location with pattern $f(m,n)$ to the location of pattern $g(m^*,n^*)$ after a time interval Δt. The distance between these two locations can be known as the average displacement of the fluid element in the sampled region. The displacement is then divided by the timescale Δt to give the average velocity vector of the motion of the fluid element.

However, the particle patterns $g(m^*,n^*)$ are usually deformed due to the particles moving out of the laser light illumination region and the high gradients of velocities. Hence, in practice, the highest value of the coefficients is considered to represent the best match of particle images of $f(m,n)$ and $g(m^*,n^*)$, as shown in Fig. 8.6. To acquire higher degree of similarity, in general, we suggest that the density of 10–15 particles in a subsample is proper in experiment. Once the

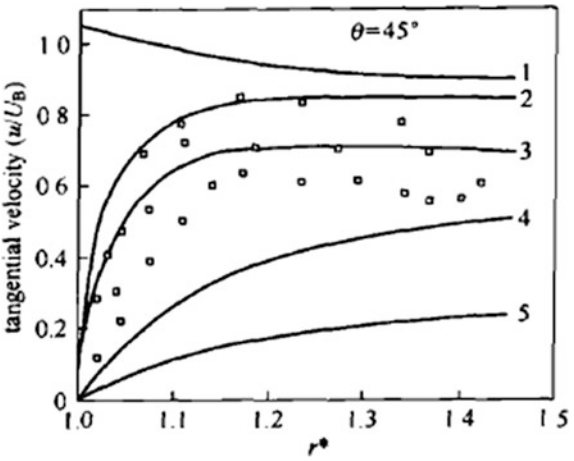

Fig. 8.7 Tangential velocity on the surface of a bubble at $\theta = 45°, Re_B = 376$ (*1* potential flow model, *2* Schultz flow model [11], *3* present flow model, *4* Dobby et al. [10] flow model, *5* stokes flow model, and *open square* experimental point)

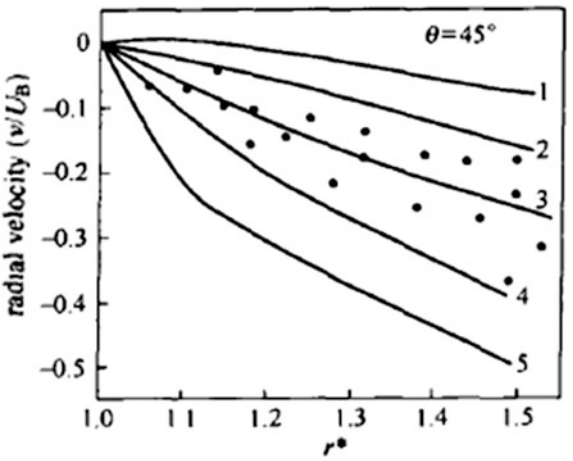

Fig. 8.8 Radial velocity on the surface of a bubble at $\theta = 45°, Re_B = 376$ (*1* potential flow model, *2* Schultz flow model [11]; *3* present flow model, *4* Dobby et al. [10] flow model; *5* stokes flow model, and *filled circle* experimental point)

maximal value of cross-correlation coefficients is determined, the displacement and the velocity vectors of the particles are obtained. The experimental results are plotted in Figs. 8.7 and 8.8.

The results calculated by the present model are plotted in Figs. 8.7 and 8.8, in which predictions by other published models such as potential flow, Stokes flow, and intermediate flow [8, 9] are also given. The comparison between experimental measurement and prediction by different models is also shown in Figs. 8.5 and 8.6. As seen, the prediction by present model is better than the others and in rough agreement with experimental measurement.

8.2 Concentration Field Around a Bubble [7, 8]

8.2.1 Concentration at Bubble Interface

Experimental installation

An experiment of CO_2 single bubble absorption was carried out, in which the laser holographic interference technique was used to determine CO_2 concentration near the interface and the thickness of concentration boundary layer under various liquid velocities. Figure 8.9 shows the experiment setup. The laser beam from a He–Ne laser source is split into two coherent beams, one (objective beam) passes through the bubbling simulator at a point near the interface of a rising bubble, while the other (reference beam) bypassed the simulator. These two beams intersect at the photographic plate to form a hologram by interference. The two beam amplifying lens 6 and 9 should be carefully chosen and adjusted to obtain satisfactory view of interference fringes within the thin concentration boundary layer [5].

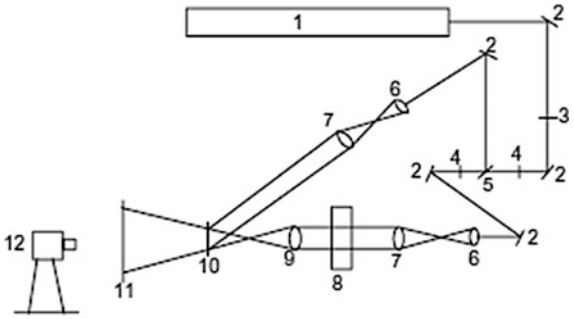

Fig. 8.9 Optical schema of single source laser interferometer (*1* He–Ne laser, *2* mirror, *3* shutter, *4* half-water plate, *5* separate prim, *6* beam amplifying lens, *7* lens, *8* simulator, *9* amplifying lens, *10* holographic plate, *11* frosted glass, and *12* camera) (reprinted from Ref. [7], Copyright 2005, with permission from Elsevier)

Figure 8.10 is the schematic diagram of gas–liquid flow simulator, in which a bubble is kept stationary and exposed to a countercurrent downflow of liquid so that to make the interfacial measurement steady. The liquid was pumped to the top of a vertical rectangular channel 1, which is made of optical glass, and flows downward to the bottom. The incoming liquid was introduced through a horizontal perforated tube to ensure uniform distribution. The gas phase was injected into the channel by syringe 7 and the bubble size was carefully controlled by the rate of gas being injected. A small metal mesh was installed in the channel to keep the rising bubble

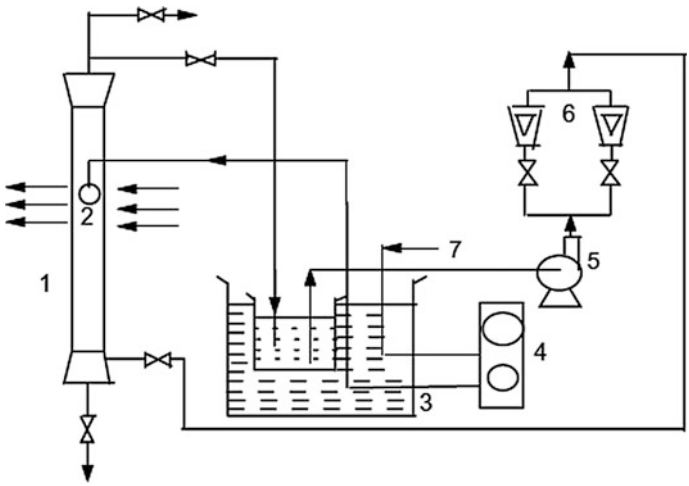

Fig. 8.10 Schematic diagram of experimental setup (*1* bubbling simulator, *2* captured bubble, *3* thermostat, *4* controller, *5* pump, *6* flow meter, *7* CO_2 injector, and *8* laser beam) (reprinted from Ref. [7], Copyright 2005, with permission from Elsevier)

in stationary position against the downward current of liquid. By means of thermostat 3, the gas and liquid phase were kept at the same temperature.

The typical holograms for the absorption of CO_2 by different absorbents are shown in Figs. 8.11, 8.12 and 8.13, where the interference fringes are clearly seen. By carefully measuring the curvature of the fringes, the concentration profile around the interface and the bulk liquid can be calculated by the following formula:

$$\frac{n^2+2}{n^2-1} = A + Bx, \tag{8.26}$$

where n is the refractive index of the liquid which is a function of λ and x; λ is the wavelength of the laser; x is the concentration in mole fraction; A and B are constants which can be determined by an experimental n versus x plot. Equation (8.26) is valid only for the mass transfer of a component from a bubble to a pure liquid absorbent.

For the study of concentration field in the bubbling process of binary absorbent, an interferometer with two laser beams of different wavelengths should be used

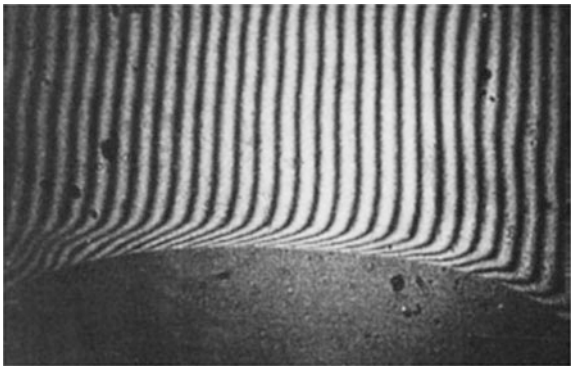

Fig. 8.11 The hologram of CO_2 absorbed by methanol (reprinted from Ref. [7], Copyright 2005, with permission from Elsevier)

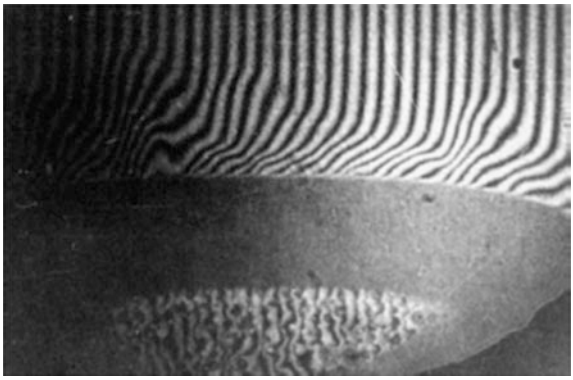

Fig. 8.12 The hologram of CO_2 absorbed by ethanol (reprinted from Ref. [7], Copyright 2005, with permission from Elsevier)

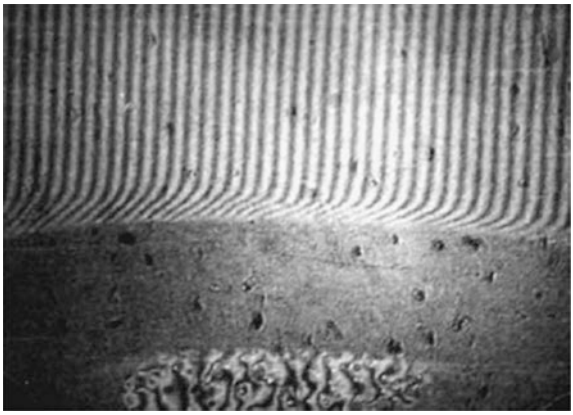

Fig. 8.13 The hologram of CO_2 absorbed by *n*-propanol (reprinted from Ref. [7], Copyright 2005, with permission from Elsevier)

instead of single laser beam. For this purpose, a duo-laser source interferometer with magnification power up to 200 has been specifically designed and constructed as the second step of research work. The wavelength of laser generated from a He–Ne source and an Ar^+ source are 6328 nm (red) and 4800 nm (green) laser beams, respectively. Since the interferometer fringes are different for the red and green laser beams, the change of concentration in the binary absorbent can be computed by setting up two independent equations similar to Eq. (8.26) and being solved by the aid of fringe measurement. The optical setup of duo-source interferometer is shown schematically in Fig. 8.14. The two laser beams are adjusted precisely to meet exactly coaxial at compound lens 5, then they are split into two beams again in a spectroscope lens 7. The object beam passes through the simulator 11 and is projected to the holographic plate 13 to form a hologram with two sets of fringes. In order to separate the fringes from the red and green laser beams, an optical

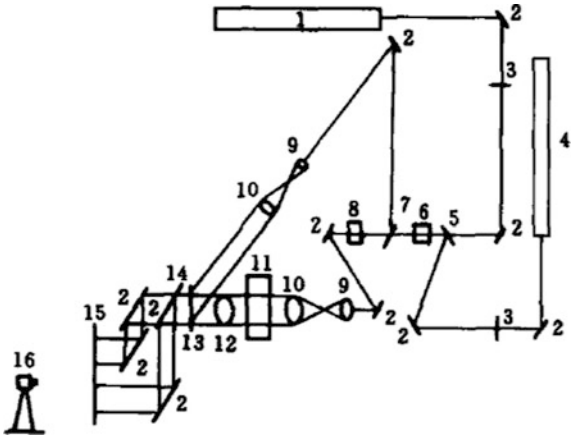

Fig. 8.14 Optical schema of duo-source holographic interferometer (*1* He–Ne laser source, *2* mirror, *3* half-wave plate, *4* Ar+ laser source, *5* compound lens, *6* shutter, *7* separate prism, *8* multiwavelength rotation, *9*-beam amplifying lens, *10* lens, *11* bubbling simulator, *12* amplifying lens, *13* holographic plate, *14* separation filter, *15* frosted glass, and *16* camera)

resolving lens 14 was placed and two sets of fringes were displayed separately on the frosted glass 15.

Experimental results

The thickness of concentration boundary layer δ_c can be determined from the fringe at a point where the concentration is substantially equal to the bulk. The δ_c is measured from the hologram at the frontal part of the bubble as shown in Fig. 8.15 at different fluid velocities. It is found that the thickness in the frontal part of a bubble is relatively steady, but that in the bubble wake is nonuniform, decreasing from the center $r' = 0$ to the edge ($r' = 1$) as shown in Fig. 8.15.

Furthermore, the δ_c gets thinner with increasing liquid bulk velocity as shown in Fig. 8.16. The thickness of the concentration boundary layer and the concentration distribution inside the concentration boundary layer are displayed respectively in Figs. 8.17 and 8.18.

Some experimental results of concentration profile in the frontal area of the liquid phase are shown in Fig. 8.18, in which the concentration distributions of various system along the distance Y from the interface ($Y = 0$) of frontal bubble to the near 1.5 mm under the condition of $u = 4.3$ m s^{-1}, bubble diameter $d_e =$ 0.65 cm and t = 298.15 K are displayed.

Figure 8.19 shows the concentration distribution close to the frontal bubble under the conditions of $u = 4.3$ cm s^{-1}, $d_e = 0.65$ cm, and $T = 298.15$ K. It can be seen that concentration profiles in the vicinity very close to the interface can be obtained by the experiment.

Some experimental results of CO_2 concentration at about 10^{-2} mm from the interface in the process of absorption of stationary CO_2 bubble by various solvents are shown and compared with the thermodynamic equilibrium value in Table 8.1.

As seen in Table 8.1, the CO_2 concentration near the interface in any of these mass transfer processes is significantly lower than its thermodynamic equilibrium value even at 0.01 mm from the interface. If thermodynamic equilibrium between

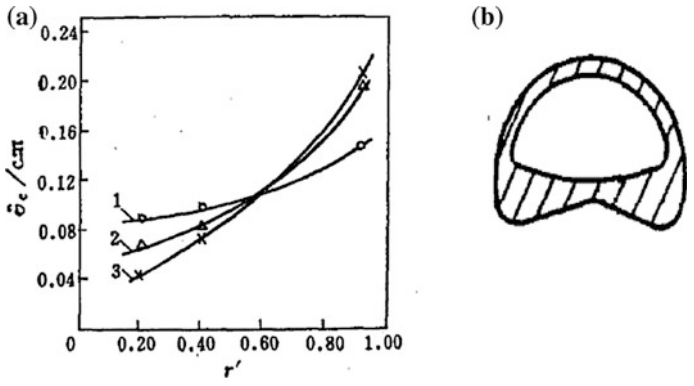

Fig. 8.15 The variation of concentration boundary layer thickness in the wake of a bubble with $d_e = 0.42$ cm (for the liquid velocity u_c (cm s^{-1}), *1* $u_c = 4.4$, *2* $u_c = 11.3$, *3* $u_c = 18.2$). **a** Experimental data, **b** conceptual form of the boundary layer (reprinted from Ref. [5], Copyright 1992, with permission from CIESC)

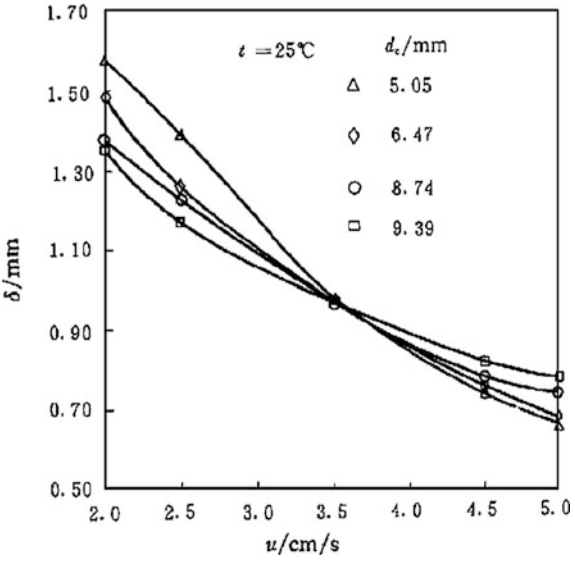

Fig. 8.16 The concentration boundary layer thickness at different bubble diameter and fluid velocity for CO_2 absorption by isopropanol

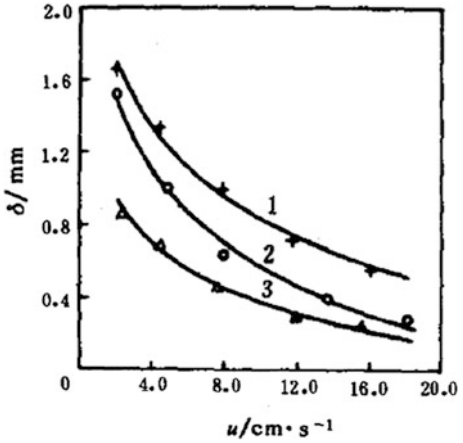

Fig. 8.17 Concentration boundary thickness versus bulk fluid velocity (*1* methanol–propanol–CO_2, *2* methanol–ethanol–CO_2, and *3* ethanol–propanol–CO_2)

phases can be established at the interface, as conventionally postulated in nonequilibrium mass transfer models, the foregoing experimental results suggest that there should exist a sharp concentration drop near or in the interface.

The concentration profile in a bubble is shown in Fig. 8.20.

It was found that the concentration near interface is affected by the fluid velocity as shown experimentally in Fig. 8.21. As seen, when the fluid velocity u is small, less than 4 cm s^{-1}, both concentration near interface and concentration boundary layer are decreased sharply due to the reduction of vapor–liquid contacting time and the interruption of concentration boundary layer by the flowing fluid. When the fluid velocity is high enough, the effect is approaching equilibrium and the concentration as well as the layer becomes stable.

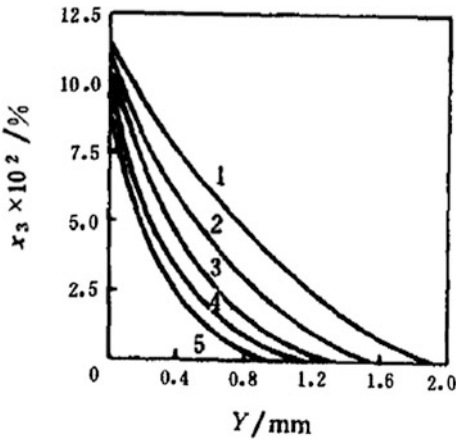

Fig. 8.18 Concentration profile of CO_2 in concentration boundary layer for the MeOH–EtOH–CO_2 system for d_e = 0.65 cm (Y is the distance from the interface in mm, for the values of r', *1* r' = 0.9, *2* r' = 0.7, *3* r' = 0.5, *4* r' = 0.3, and *5* r' = 0.1)

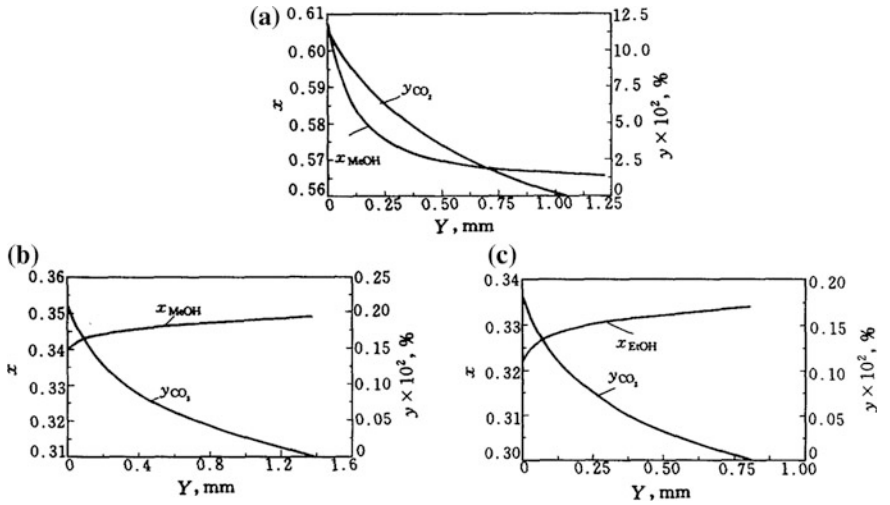

Fig. 8.19 Experimental concentration profiles in frontal area along the distance from interface of a bubble (u = 4.3 m s^{-1}) for the absorptions of CO_2 by various binary mixtures. **a** in mixture MeOH–EtOH, with an initial x_{MeOH} = 0.5657; **b** in MeOH–PrOH, with an initial x_{MeOH} = 0.3447; and c in EtOH–PrOH, with an initial x_{EtOH} = 0.3318

The experimental observation also showed repeatedly that under zero velocity, the bubble interface appeared disturbed as shown in Fig. 8.22. Such disturbance disappeared soon and the fringes remain stable. It indicated that the interfacial mass transfer is unstable at the beginning because of perturbation from the fluid and kept constant afterward.

Table 8.1 Comparison of measured close interface concentration with thermodynamic equilibrium value

System	Absorbent	Measured CO_2 concentration at 0.01 mm (mol. frac.)	Equilibrium CO_2 concentration (mol. frac.)
1	MeOH	0.001016	0.006277
2	EtOH	0.001799	0.007149
3	PrOH	0.001987	0.008484
4	MeOH+EtOH	0.001011	0.007989
5	MeOH+PrOH	0.002128	0.006421
6	EtOH+PrOH	0.001687	0.007326

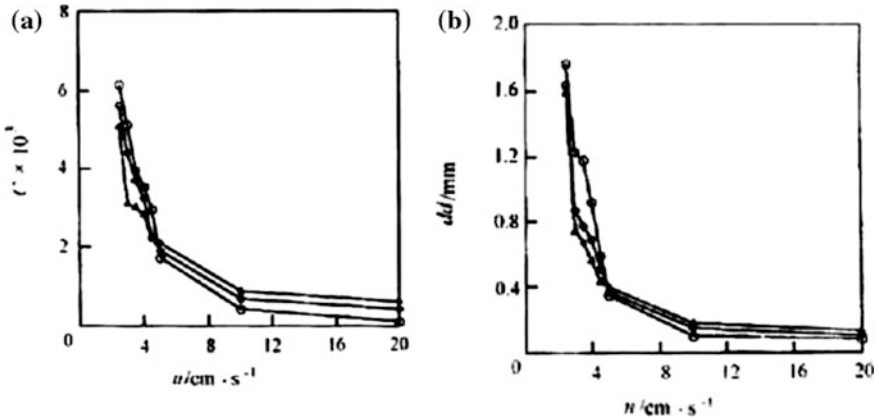

Fig. 8.21 Effect of fluid velocity on concentration. **a** concentration profile near interface and **b** concentration profile in boundary layer

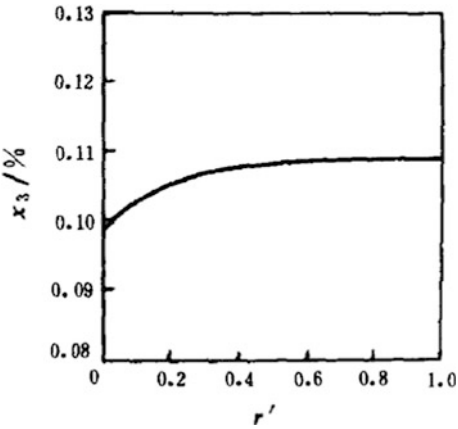

Fig. 8.20 The CO_2 (x_3) concentration profile in the bubble

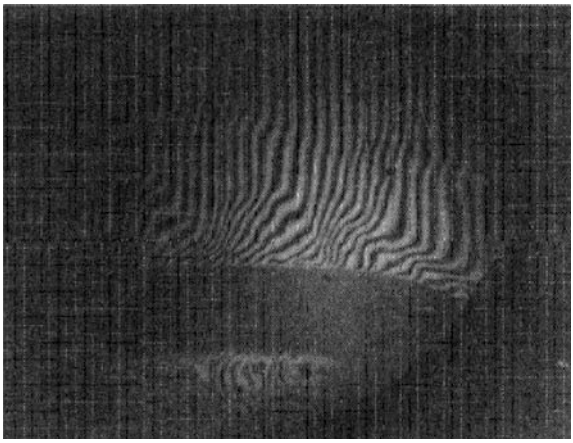

Fig. 8.22 The interfacial disturbance by fluid perturbation observed on an interfered fringes graph, the gas–liquid system is CO_2-ethanol

8.2.2 Interfacial Mass Transfer [9]

The gas–liquid interfacial mass transfer has been considerably studied since the early work of Whitman in 1923. In recent years, due to the development and extensive application of the laser Doppler holographic interference and computer online technique, much attention has been paid to the study of the mechanism of interfacial process. Most proposed models about gas–liquid interfacial mass transfer are based on the two-film theory with a basic assumption that the gas and liquid are in thermodynamic equilibrium at the interface. However, such assumption has not been proved experimentally. Therefore, molecular thermodynamic method may be used to study the molecule interacting with the solvent according to some potential law, for instance Lenard-Jones pairwise potential.

Take gas absorption as an example, the gas molecules transfer to the liquid can be postulated by undergoing the following steps in sequence:

(1) Gas molecules of solute diffuse to the interface from bulk gas phase;
(2) Gas molecules combine with the liquid molecules at the interface forming the solvation, in which the following steps are consisted:
    (i) The creation of a cavity in solvent of suitable size to accommodate the solute molecule;
    (ii) The solute molecule enters into the cavity and interacts with the solvent according to some potential law, for instance the Lenard-Jones pairwise potential.
(3) Solvated molecules transfer to the bulk liquid phase.

According to the Maxwell–Stefan diffusion equation

$$\frac{x_i \nabla_{T,p} \mu_i}{RT} = \sum_{\substack{k=1 \\ k \neq i}}^{n} \frac{x_i J_k - x_k J_i}{c_t D_{ik}},$$

where c_t is the total molar concentration. For the system of absorbed solute 2 (subscript 2 refers to the solute) only, the foregoing equation can be written as:

$$\frac{x_2 \nabla_{T,p} \mu_2}{RT} = -\frac{x_1 J_2}{c_t D_M} = -\frac{(1-x_2) J_2}{c_t D_M}, \tag{8.27}$$

where D_M is the Maxwell–Stefan diffusivity. In the case of dilute absorbent, $x_2 \ll 1$. The foregoing equation becomes

$$J_2 = \frac{c_t D_M}{RT} \frac{d\mu}{dy}$$

or after integrating yields

$$J_2 = \frac{c_t D_M}{RT} \frac{\Delta \mu_2}{\delta}$$

where $\Delta \mu_2 = \mu_g - \mu_l$, δ is the thickness of concentration boundary layer on the liquid side. By substituting the thermodynamic relationship $\mu = RT \ln \gamma x$ where γ is the activity coefficient and $\gamma = 1$ for ideal solution. In the case of very small x_2, D_M is equal to Fick law diffusivity D_F, the foregoing equation takes the following form for calculating the interfacial mass transfer of the solute, i.e., the mass transfer from interface to the bulk:

$$J_2 = \frac{c_t D_M}{\delta} \ln \frac{x_2^*}{x_2} \tag{8.28}$$

In order to test the valid age of foregoing equation, an experiment of CO_2 single bubble absorption was carried out, in which the laser holographic interference technique was used to determine the CO_2 concentration near the interface and the thickness of the concentration boundary layer under various liquid velocity. The experimental result is shown in Table 8.2. The experimental conditions are T = 298.15 K, p = 101.325 kPa, $d_e = 0.42$ cm.

Table 8.2 Measured result of CO_2 absorption

No.	u (cm s^{-1})	Methanol		Ethanol		n-Propyl alcohol	
		δ (cm)	$x_2 \times 10^4$	δ (cm)	$x_2 \times 10^4$	δ (cm)	$x_2 \times 10^4$
1	1.5	0.110	1.79	0.090	5.57	0.085	4.88
2	4.0	0.078	1.63	0.075	4.69	0.074	4.80
3	8.0	0.056	1.47	0.050	4.16	0.057	4.65
4	11.0	0.051	1.39	0.047	3.98	0.052	4.58
5	16.0	0.041	1.30	0.040	3.51	0.050	4.42

Table 8.3 Comparison of calculated mass transfer flux with experiment measurements

No.	u (cm s^{-1})	Methanol		Ethanol		n-Propyl alcohol	
		$J_{cal} \times 10^9$ (mol cm^{-2} s^{-1})	$J_{exp} \times 10^9$ (mol cm^{-2} s^{-1})	$J_{cal} \times 10^9$ (mol cm^{-2} s^{-1})	$J_{exp} \times 10^9$ (mol cm^{-2} s^{-1})	$J_{cal} \times 10^9$ (mol cm^{-2} s^{-1})	$J_{exp} \times 10^9$ (mol cm^{-2} s^{-1})
1	1.5	5.33	6.28	10.78	11.54	6.06	5.76
2	4.0	7.02	7.15	11.63	11.88	6.89	6.75
3	8.0	9.06	8.54	16.15	15.98	8.76	8.90
4	11.0	9.56	10.23	16.70	16.56	9.50	10.14
5	16.0	11.31	12.56	18.05	18.25	9.66	10.28

Another experiment of mass transfer of single bubble (d_e = 0.42 cm) absorption was made to verify Eq. (8.28). Table 8.3 shows the comparison of calculated results of mass transfer flux J_{cal} by Eq. (8.28) with the experimental measurements J_{exp}. The agreement between them is satisfactory.

The mass transfer between two fluid phases must go through the interface. Due to the existence of surface tension gradient on the interface and the density gradient between the interface and the main fluid, the fluid dynamic instability or bifurcation may appear under certain conditions, which always significantly influence the process efficiency.

8.3 Discussion

The experimental measurements repeatedly reveal that the main resistance of mass transfer is on a very thin layer attached to the boundary of interface causing very sharp concentration gradient. Such deductive inference is based on the experimental result that there is a very sharp concentration drop very close, say 10^{-2} of a millimeter, to the interface. The thin layer may be called as "transfer barrier" layer. The resistance of this layer may come from the molecular retarding force for keeping the mass molecule in interface and the molecular repelling force for refusing the mass molecule entering the fluid phase. Such thin layer is similar but not equal to Gibbs adsorption layer.

According to experimental result, an interfacial theory may be proposed that the concentration boundary consists of two parts: the "transfer barrier" layer and the diffusion layer. The "transfer barrier" layer takes the major part of mass transfer resistance. The increase of fluid velocity enables to reduce the thickness of diffusion layer to achieve the increase of mass transfer coefficient up to onefold, but it cannot affect the "transfer barrier" layer. The lowering of the resistance of "transfer barrier" layer can be realized by the measures of increasing the mass potential at interface, such as by creating interfacial Marangoni convection, which can raise the mass transfer coefficient by several folds. Thus, the effect of process intensification by interfacial means is more pronounced than that by changing the operating condition.

8.4 Summary

(1) By solving the continuity equation and momentum conservation equation, the velocity field around a bubble can be obtained. The calculated result is compared with experimental measurement in both tangential and radial velocities and shows better than the others in literature.

(2) The concentration field near the vapor bubble is measured by using holographic interferometer. The measured result shows that the concentration at distance about 10^{-2} mm from the bubble surface is far from the thermodynamic equilibrium value. If vapor–liquid interface is under thermodynamic equilibrium, that means there exists a very sharp concentration drop or high mass transfer resistance near the interface. Thus it is reasonable to deduce that there exists a "transfer barrier" layer attached to the interface creating the main resistance of interfacial mass transfer. However, further investigation is needed regarding this finding.

References

1. Whitman WG (1923) The two-film theory of gas absorption. Chem Metall Eng 29(4): 146–149
2. Higbie R (1935) The rate of absorption of a pure gas into a still liquid during short periods of exposure. Trans AIChE 31:365–377
3. Danckwerts PV (1951) Significance of liquid-film coefficients in gas absorption. Ind Eng Chem 43(6):1460–1467
4. Miao R, Wang S, Yu G (1992) Micro behavior and hydrodynamic structure near interface of a moving turbulent bubble by laser technique. CIESC J. 43(5):570–573
5. Miao R, Wang S, Yu G (1992) Concentration fields and mass transfer behaviors near a moving bubble interface by laser technique. CIESC J 43(5):635–637
6. Cheng H, Zhou M (2002) Prediction of fluid velocity distribution near a rising bubble. Chin J Chem Eng 10(5):545–549
7. Ma YG, Yu KT, Li HZ (2005) Note on the mechanism of interfacial mass transfer of adsorption process. Inter J Heat Mass Transfer 48:3454–3459
8. Ma YG, Cheng H, Yu KT (1999) Measurement of concentration fields near the interface of a rising bubble by holographic interference technique. Chin J Chem Eng 7(4):363–367
9. Cheng H (1997) Study on enhancement of fine adsorbent particles on gas-liquid mass transfer and its mechanism. PhD dissertation, Tianjin University, Tianjin, China (in Chinese)
10. Ma YG, Feng HS, Xu SC, Yu KT (2003) The mechanism of interfacial mass transfer in gas absorption process. Chin J Chem Eng 11(2):227–231

Chapter 9
Simulation of Interfacial Effect on Mass Transfer

Abstract The mass transferred from one phase to the adjacent phase must diffuse through the interface and subsequently may produce interfacial effect. In this chapter, two kinds of important interfacial effects are introduced and discussed: Marangoni effect and Rayleigh effect. The theoretical background and method of computation are described including origin of interfacial convection, mathematical expression, observation, theoretical analysis (interface instability, on-set condition), experimental and theoretical study on enhancement factor of mass transfer. The details of interfacial effects are simulated by using CMT differential equations.

Keywords Interfacial mass transfer · Marangoni effect · Rayleigh effect · Interfacial concentration gradient · Interfacial convection · Mass transfer enhancement

Nomenclature

Bi	Biot number
c	Mass concentration, kg m^{-3}
$c^{\mathbf{i}}$	Interfacial concentration, kg m^{-3}
c^*	Interfacial concentration in equilibrium with the bulk concentration, kg m^{-3}
Cr	Crispation number
d	Liquid layer thickness, m
D	Diffusivity of solute, m^2 s^{-1}
F	Enhancement factor
g	Acceleration of gravity, m s^{-2}
j	Mass transfer flux, mol s^{-1} m^{-2}
k	Coefficient of mass transfer, m s^{-1}; wave number
k_H	Coefficient of mass transfer calculated by penetration theory, m s^{-1}
l, L	Characteristic length, m
Le	Lewis number
Ma	Marangoni number

K.-T. Yu and X. Yuan, *Introduction to Computational Mass Transfer*,
Heat and Mass Transfer, DOI 10.1007/978-981-10-2498-6_9

N	Mass transfer flux, mol s^{-1} m^{-2}
P	Pressure, kg m^{-1} s^{-2}
Ra	Rayleigh number
Re	Reynolds number
S	Source term
Sc	Schmidt number
Sh	Sherwood number
t	Time, s
T	Temperature, K
$\overline{T}$	Residence time of fluid cell, s
u, v, w	Velocity component, m s^{-1}
U, V, W	Dimensionless velocity component
U_s	Velocity at interface, m s^{-1}
x, y, z	Coordinate
X, Y, Z	Dimensionless distance
β_c	Concentration gradient in x direction, $\frac{\partial c}{\partial x}$
β'_c	Concentration gradient in z direction, $\frac{\partial c}{\partial z}$
β_T	Temperature gradient in x direction, $\frac{\partial T}{\partial x}$
β'_T	Temperature gradient in z direction, $\frac{\partial T}{\partial z}$
R_T	Coefficient of surface tension change with temperature, $\frac{\partial \sigma}{\partial T}$
R_c	Coefficient of surface tension change with concentration, $\frac{\partial \sigma}{\partial c}$
α	Thermal diffusivity, m^2 s^{-1}
μ	Viscosity, kg m^{-1} s^{-1}
ν	Kinematic viscosity, m^2 s^{-1}
σ	Surface tension, kg s^{-2}
τ	Dimensionless time
ψ	Amplitude of velocity disturbance
Φ	Amplitude of concentration disturbance
Θ	Amplitude of temperature disturbance
ρ	Density, kg m^{-3}
ω	Increasing rate of disturbance

Superscript

$'$	Disturbance
$-$	Average

Subscript

cr	Critical
exp	Experimental
h	Heat transfer
G	Gas phase

log Logarithmic average
L Liquid phase
surf Surface
theo Theoretical

The mass transfer between two fluid phases must go through the interface. Due to the existence of surface tension gradient on the interface and the density gradient between the interface and the main fluid, the fluid-dynamic instability or bifurcation may appear under certain conditions, which can significantly influence the process efficiency.

9.1 The Interfacial Effect

In the course of interfacial mass transfer, from molecular point of view, the process is stochastic; that means some local molecules may undergo the mass transfer in advance than the others, so that small concentration gradient $\frac{\partial c}{\partial x_i}$ (where $i = x, y, z$) are established at the interface. As the surface tension σ is function of concentration, it follows that the surface tension gradient $\frac{\partial \sigma}{\partial x_i}$ is also created at the interface. If $\frac{\partial \sigma}{\partial x_i}$ is increased up to a critical point, the fluid-dynamic instability will appear to induce the interfacial convection as well as the formation of orderly structure at the interface. At the same time, the rate of mass transfer may be enhanced or suppressed depending on the properties of the mass transfer system concerned; such phenomena is generally regarded as interfacial effect.

In the middle of eighteen century, Marangoni described and investigated such interfacial convection [1], which afterward was called Marangoni convection and its effect was also regarded as Marangoni effect.

Further increase of $\frac{\partial \sigma}{\partial x_i}$ after the critical point will continue to magnify (if not to depress) the interfacial effect until the interface structure becomes blurred and the orderly structure gradually turns to the disordered or chaotic state. At this time, the process is approaching to the turbulent state of mass transfer.

The Marangoni convection, induced by surface tension gradient $\frac{\partial \sigma}{\partial x_i} = \frac{\Delta \sigma}{\Delta x}\Big|_{\Delta x \to 0}$ or by concentration gradient $\frac{\partial c}{\partial x_i} = \frac{\Delta c}{\Delta x}\Big|_{\Delta x \to 0}$ at the same time, can be represented by a dimensionless group, denoted as Marangoni number Ma, as given below. The greater Ma number means more intense interfacial convection:

$$Ma = \frac{R_c \Delta c L}{\mu D} \tag{9.1}$$

where $R_c \left(R_c = \frac{\partial \sigma}{\partial c}\right)$ is the rate of surface tension increase with respect to the concentration of the transferred species; D and μ are respectively the diffusivity and

viscosity of the transferred species; L is the characteristic length. In the literature, L and Δc can be expressed in specified form according to the process concerned.

When Ma number reaches its critical value Ma_{cr} and beyond, i.e. $Ma \geq Ma_{cr}$, the mass transfer system is under instability and Marangoni convection is induced; when $Ma < Ma_{cr}$, the system is stable and the convection is suppressed.

The Marangoni number Ma may be positive or negative dependent on the value of R_c and Δc. For instance, if CO_2 is absorbed by ethanol, the Δc of CO_2 in ethanol is positive and R_c is negative, then Ma is negative. Otherwise, if CO_2 is desorbed from CO_2 saturated ethanol, both R_c and Δc are negative, thus Ma is positive. In multi-component mass transfer process, since more than one component is transferred, the sign of Ma is dependent on their coupling result.

According to the sign of Ma, the mass transfer processes can be classified into:

(1) Positive Ma process ($Ma > 0$): Marangoni convection is promoted.
(2) Negative Ma process ($Ma < 0$): Marangoni convection is inhibited.
(3) Neutral Ma process ($Ma = 0$): Marangoni convection is absent. Generally, this class also refers to the case that $\Delta\sigma$ is less than 1–2 dyn/cm.

Marangoni convection is also influential to many other transfer processes, such as crystallization, metallurgical and drug productions as well as the transport behaviors in the space [2].

Since Marangoni convection is induced by surface tension gradient on the interface, the creation of such gradient is caused not only by having concentration gradient but also by temperature gradient $\frac{\partial T}{\partial x_i}$. The intensity of Marangoni convection created due to the temperature gradient on interface can be represented by Ma_h as follows:

$$Ma_h = \frac{R_h \Delta T d}{\mu D} \tag{9.2}$$

where R_h represents the rate of surface tension increase with respect to the temperature, $R_h = \frac{\partial \sigma}{\partial T} = \frac{\Delta \sigma}{\Delta T}\Big|_{\Delta T \to 0}$; ΔT and d are respectively the temperature difference and the characteristic length, which are usually specified by different investigators to suit different processes.

Furthermore, the interfacial convection and the renewal of interface can also be promoted by the vertical convective circulation between interface and main fluid due to the density difference $\Delta\rho$. Such convection is called Rayleigh convection [3, 4] or Rayleigh-Bénard convection. The intensity of Rayleigh convection can be represented by the Rayleigh number Ra as follows:

$$Ra = \frac{g \Delta \rho L^3}{D \mu} \tag{9.3}$$

Table 9.1 The sign of *Ma* and *Ra* for the absorption and desorption of CO_2 by different absorbents

Absorbent	CO_2 absorption		CO_2 desorption	
	Ma	*Ra*	*Ma*	*Ra*
Methanol	−	+	+	−
Ethanol	−	+	+	−
Chlorobenzene	−	−	+	+
Trichloroethylene	−	−	+	+

where L is the characteristic length, and generally refers to the distance from interface to the bulk fluid; g is the acceleration of gravity. Similar to *Ma*, the Rayleigh convection appears only after reaching its critical value.

In short, the Marangoni convection induced by surface tension gradient and the Rayleigh convection induced by density gradient are the two main interfacial effects. Marangoni convection displays on the interface and underneath (the depth of Marangoni convection underneath is about 10^{-4} m in our observation); and the Rayleigh convection appears vertically from interface to the bulk fluid with accompanied action of interfacial renewal. When the critical point of each convection is reached, the interfacial effect will be initiated.

In fact, the gradients of concentration, temperature and density are all giving contributions to the interfacial convection and forming coupling effect. For instance, when CO_2 is desorbed from CO_2 saturated ethanol, the Marangoni convection is positive ($Ma > 0$), but if the Rayleigh convection is negative ($Ra < 0$), it will depress the Marangoni convection. On the contrary, when CO_2 is desorbed from CO_2 saturated chlorobenzene, both *Ma* and *Ra* are positive, the Marangoni convection will be strengthened. The sign of *Ma* and *Ra* for the absorption and desorption of CO_2 by different absorbents are listed in Table 9.1

9.2 Experimental Observation of Interfacial Structure Induced by Marangoni Convection

Since last century, many researchers have undertaken the observation of Marangoni convection, especially using the laser Schlieren technique. In this section, Some results of our experimental study on interface structure are presented for illustration [5–9]. The experimental installation is shown in Fig. 9.1. The experiment was undertaken at constant temperature so that the temperature induced Marangoni convection can be eliminated. The liquid–gas contactor (Fig. 9.2) can be placed in horizontal position for horizontal liquid–gas flow, or in vertical position for falling liquid film and uprising gas flow. The mass transfer process to be study is either absorption or desorption of CO_2 by various kinds of absorbent. Nitrogen is served as CO_2 carrier. The liquid phase can be in either stagnant or countercurrent flow with the gas phase.

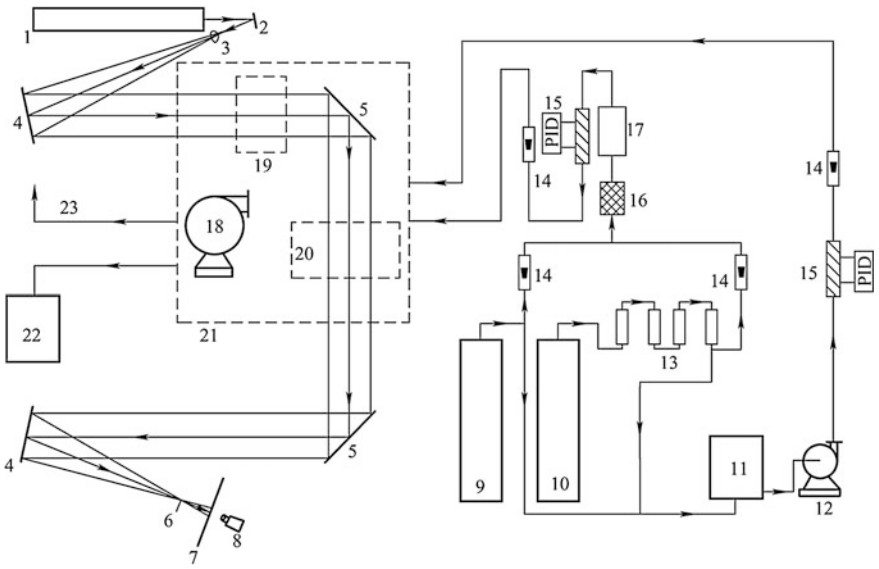

Fig. 9.1 Experimental installation for the observation of interfacial structure (*1* He–Ne laser, *2* reflecting mirror, *3* expanding lens, *4* concave mirror, *5* mirror, *6* blade, *7* screen, *8* CCD camera, *9* N_2 cylinder, *10* CO_2 cylinder, *11* absorbent vessel, *12* pump, *13* CO_2 purifier, *14* Rotameter, *15* PID controlled heater, *16* mixer, *17* bubbling vessel, *18* blower, *19* falling film liquid-gas contactor, *20* horizontal flow liquid-gas contactor, *21* air conditioning zone, *22* solvent recovery vessel, *23* flue gas exit) [1]

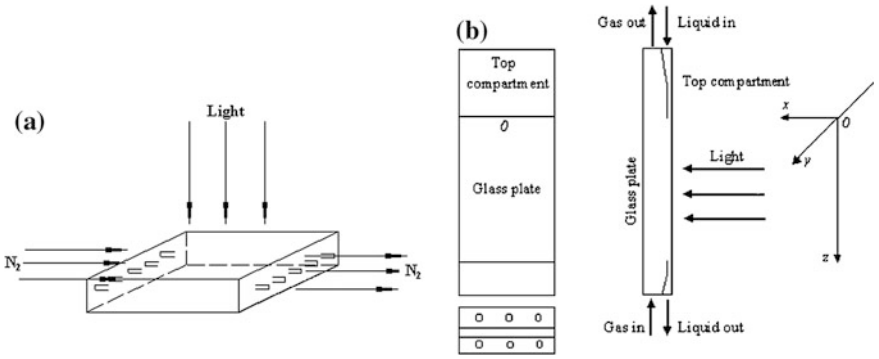

Fig. 9.2 Liquid–gas contactors **a** horizontal contactor, **b** vertical (falling film) contactor

9.2.1 Stagnant Liquid and Horizontal Gas Flow

(1) ***Desorption of CO_2 from CO_2 saturated ethyl acetate***
In this case, $Ma > 0$, $Ra < 0$, the Marangoni convection is induced after the surface tension gradient is reaching to the critical value. The interface was

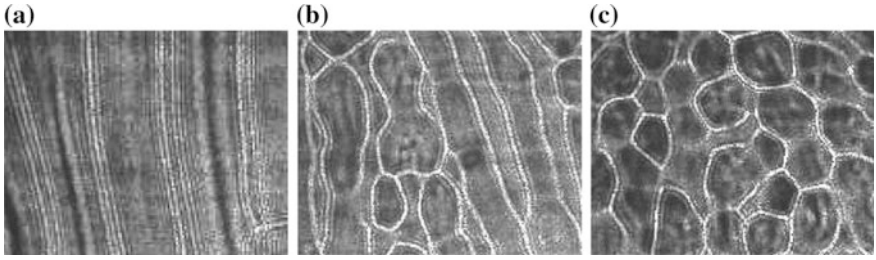

Fig. 9.3 Interfacial structure of CO_2 desorption from stagnant ethyl acetate at 17 °C and N_2 rate of 0.1 m^3/h [1] **a** beginning of formation, **b** development, **c** stable structure

photographed for the whole desorption process until stable picture was obtained. The liquid-gas contactor is schematically shown in Fig. 9.3a.
Under the condition of 17 °C, nitrogen flow rate 0.1 m^3/h and liquid thickness 5 mm, the interface image displayed not so clear roll structure at the beginning as seen in Fig. 9.3a, and afterward turned to polygonal like structure (b), and finally reached stable clear polygonal cell structure (c).

(2) ***Absorption of CO_2 by ethyl acetate***
In this case, $Ma < 0$, $Ra > 0$, although the Marangoni convection is negative, yet the density gradient between interface and the bulk liquid induced the Rayleigh convection to renew the interface so as to establish concentration gradient with the depleted local point and formed interfacial convection as seen in Fig. 9.4. As seen in this figure, when the liquid thickness is 2 mm, the interface displayed polygonal like structure but without order. When thickness of liquid was increased to 5 mm, mixed roll and cellular structure was appeared. Further increased of liquid thickness to 10 mm, the interface showed the enlargement of the mixed structure and more intense convection. It demonstrated that the Rayleigh effect was strengthened by deeper liquid thickness to increase the density gradient. It is also shown that the interfacial structure is dependent on the coupling effect of Marangoni and Rayleigh convections.

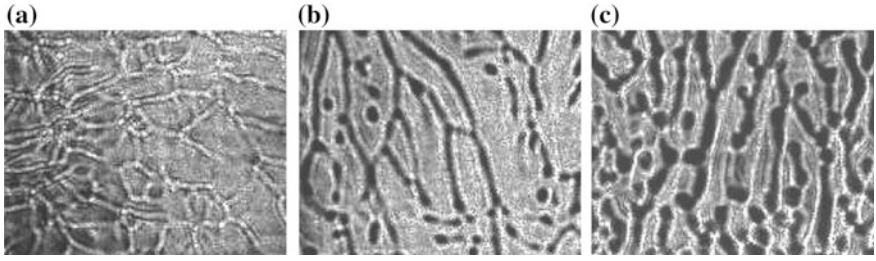

Fig. 9.4 Interfacial structure of CO_2 absorption by stagnant ethyl acetate at 17 °C and gas rate of 0.04 m^3/h [1] **a** liquid thickness 2 mm, **b** liquid thickness 5 mm, **c** liquid thickness 10 mm

Fig. 9.5 Image of convection perpendicular to the interface for the absorption of CO_2 by stagnant ethyl acetate [1]

The Rayleigh convection was also photographed from vertical view (perpendicular to the interface) as shown in Fig. 9.5. The inverted mushroom shape of convection penetrates from the interface to the main body of liquid.

9.2.2 Horizontal Concurrent Flow of Liquid and Gas

(1) ***Desorption of CO_2 from CO_2 saturated ethanol***
In this case ($Ma > 0$, $Ra < 0$), under the condition of liquid thickness 4.6 mm, ethanol velocity 6.9×10^{-3} m s^{-1} and nitrogen rate 0.12 m^3 h^{-1}, Marangoni convection was induced as shown in Fig. 9.6a in the form of parallel roll structure. When nitrogen rate was increased to 0.16 m^3 h^{-1}, the roll became finer and smaller as shown in (b).

(2) ***Diffusion of aqueous ethanol to nitrogen in countercurrent flow***
In this case, two component, water and ethanol, was diffused to nitrogen in the liquid-gas concurrent flow and induced interfacial structure ($Ma > 0$, $Ra > 0$). Under the condition of liquid thickness 5.3 mm, aqueous ethanol rate

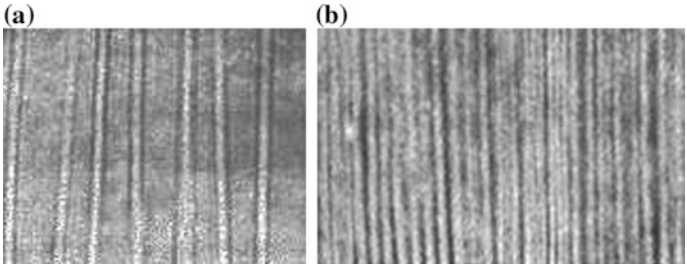

Fig. 9.6 Desorption of CO_2 in horizontal concurrent liquid-gas flow [1] **a** nitrogen rate 0.12 m^3/h, **b** nitrogen rate 0.16 m^3/h

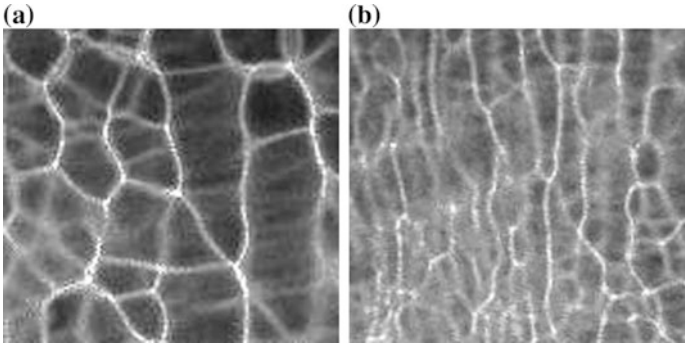

Fig. 9.7 Diffusion of aqueous ethanol to nitrogen in concurrent flow **a** nitrogen rate 0.12 m^3/h, **b** nitrogen rate 0.16 m^3/h (reprinted from Ref. [8], Copyright 2002, with permission from CIESC)

8.7×10^{-6} m s^{-1} and nitrogen rate 0.1 m^3 h^{-1}, the interface displayed clear cellular structure as shown in Fig. 9.7a. Under another condition of liquid thickness 4.3 mm, aqueous ethanol rate 1.1×10^{-5} m s^{-1} and nitrogen rate 0.16 m^3 h^{-1}, the cellular structure was not so clear and likely to have tendency of becoming roll as seen in (b). Thus the interfacial structure is also affected by the flowing condition of liquid and gas.

9.2.3 *Vertical (Falling Film) Countercurrent Flow of Liquid and Gas*

Two cases of chemical absorption are taken for illustration.

(1) ***CO_2 absorption by aqueous diethanolamine***
In this case, 28 mol% of aqueous diethanolamine was used to absorb CO_2 ($Ma > 0$, $Ra > 0$) in the falling film liquid–gas countercurrent contactor as shown in Fig. 9.4b. Under the condition of liquid thickness 0.12 mm, liquid rate 3.22×10^{-2} m s^{-1} and CO_2 rate 0.016 m^3 s^{-1}, the interface displayed mixed structure of roll and cell as shown in Fig. 9.8a. At higher CO_2 rate of 0.1 and 0.2 m^3 s^{-1}, the roll structure was dominated although some cells was appeared locally as seen in (b) and (c).

(2) ***CO_2 absorption by aqueous NaOH***
In this case, under the condition of falling film thickness 0.13 mm, liquid rate 2.76×10^{-2} m s^{-1} and the countercurrent CO_2 rate respectively 0.08, 0.1, 0.16, 0.2, 0.3 m^3 s^{-1}, the interface structure is shown in Fig. 9.9a–d. At low gas rate, cellular structure appeared locally; while at higher gas rate, the roll structure involving cells was developed with tendency to becoming all roll structure.

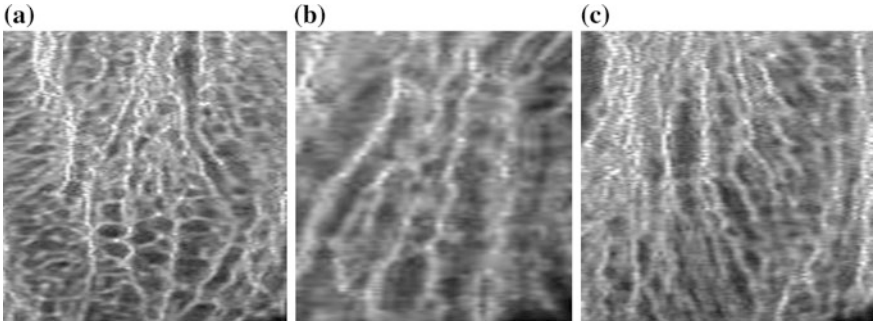

Fig. 9.8 Falling film absorption of CO_2 by diethanolamine [1] **a** CO_2 flow rate 0.016 $m^3\ h^{-1}$, **b** CO_2 flow rate 0.1 $m^3\ h^{-1}$, **c** CO_2 flow rate 0.2 $m^3\ h^{-1}$

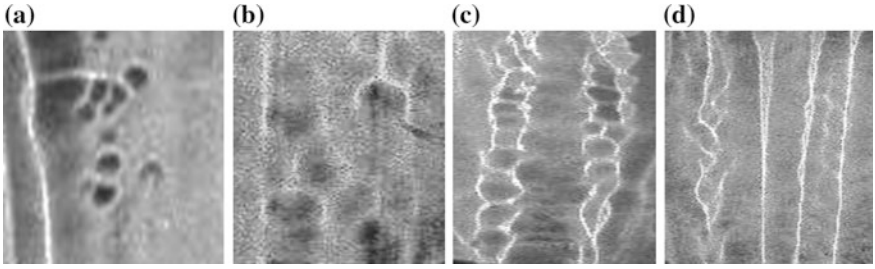

Fig. 9.9 Falling film absorption of CO_2 by NaOH [1] **a** CO_2 rate 0.08 $m^3\ h^{-1}$, **b** CO_2 rate 0.1 $m^3\ h^{-1}$, **c** CO_2 rate 0.16 $m^3\ h^{-1}$, **d** CO_2 rate 0.3 $m^3\ h^{-1}$

9.3 The Condition for Initiating Marangoni Convection

The appearance of Marangoni convection in the liquid-gas interface means that the system can not retains the stable state and turns to induce interfacial flow and accompany with the formation of orderly structure. In other words, the Marangoni convection is initiates at the point where the stability of a mass transfer process is broken down and led to the non-equilibrium phase transition to the orderly structure.

The condition of initiating Marangoni convection can be found by analysing the stability of a mass transfer process, i.e. answering the question: under what condition the stable state is interrupted. The process chosen for this study is desorption of falling desorbent (aqueous acetone) by the countercurrent flowing gas (nitrogen) as shown in Fig. 9.10.

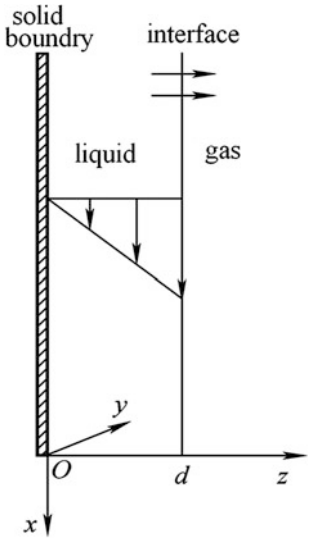

Fig. 9.10 Mass transfer model of falling film and countercurrent gas flow

Sha simulated and analyzed this process with the following model [10, 11]:

Assumptions

(1) The thickness of falling film is small; the density difference between interface and the film in the direction perpendicular to the interface is negligible so that the effect of Rayleigh convection can be neglected. Also the process is isothermal and the Marangoni convection is only due to interfacial concentration difference.
(2) The interface is flat, no deformation.
(3) All physical properties are constant except surface tension.
(4) Both the rate of falling film and uprising gas flow are low, and the frictional force between liquid and gas is neglected.
(5) The amount of desorbed species (acetone) transferred is small, so that the density of desorbent is practically remained constant.

9.3.1 Model Equations

The mass transfer process is desorption where desorbed species (acetone) is transferred from aqueous liquid phase to the gas phase. The surface tension is changed linearly with the concentration as follows:

$$\sigma = \sigma_0 + R_c(c - c_0)$$

where σ_0 is the surface tension at the interfacial desorbent (aqueous acetone) concentration c_0; $R_c = \frac{\partial \sigma}{\partial c}$ is the rate of surface tension change with respect to the concentration; c is the desorbent concentration in aqueous liquid phase.

For the desorption of aqueous acetone to the nitrogen, the concentration of acetone is decreased as the liquid phase flowing down, the concentration gradient $\frac{\partial c}{\partial x}$ is negative. Since R_c is negative in this case, thus $R_c \Delta c$ as well as Ma is positive and Marangoni convection can be induced under appropriate condition. The following interacted liquid phase (aqueous acetone) model can be established:

$$\frac{\partial u}{\partial x_i} = 0$$
$$\frac{\partial u}{\partial t} + u\frac{\partial u}{\partial x_i} = -\frac{1}{\rho}\frac{\partial p}{\partial x_j} + \frac{\mu}{\rho}\frac{\partial^2 u}{\partial x_i^2} + S$$
$$\frac{\partial c}{\partial t} + u\frac{\partial u}{\partial x_i} = D\frac{\partial^2 c}{\partial x_i}$$
$$\boldsymbol{S} = -\left(0, \frac{\rho' g}{\rho}\right)$$
$$\boldsymbol{u} = (u, v, w)$$

where c is the mass concentration of the desorbed species (acetone) in desorbent (kg m^{-3}); D is the molecular diffusivity (m^2 s^{-1}); $\boldsymbol{S}$ is the source term (gravity); t is the time.

The boundary conditions are:

At $z = 0$ (wall), $u = v = w = 0$, $\frac{\partial c}{\partial z} = 0$.

At $z = d$ (liquid–gas interface), solute is diffused from liquid phase to the gas phase, the rate of which can be represented by the following equation:

$$-D\frac{\partial c}{\partial z} = k_L(c - c_I)$$

where k_L is the liquid film coefficient of mass transfer; c_I is the solute concentration at the interface.

Dimensionless model equations

For the convenience of solving the model equation, the method of dimensionless is used to reduce the number of variables. Let d, $\beta_c R_c d/\mu$, $\beta_c R_c$, $\beta_c d$, $\mu/\beta_c R_c$ are respectively the dimensionless length, velocity, pressure, concentration and time, i.e.

$$U = \frac{u\mu}{\beta_c R_c d}, \quad V = \frac{v\mu}{\beta_c R_c d}, \quad W = \frac{w\mu}{\beta_c R_c d}, \quad X = \frac{x}{d}, \quad Y = \frac{y}{d},$$
$$Z = \frac{z}{d}, \quad C = \frac{c}{\beta_c d}, \quad \tau = \frac{t\beta_c R_c}{\mu}, \quad P = \frac{p}{\beta_c R_c}$$

Substitute the foregoing dimensionless variables to the model equations to yield the following equations:

$$\frac{\partial \boldsymbol{U}}{\partial x_i} = 0$$

$$Re\left[\frac{\partial \boldsymbol{U}}{\partial \tau} + \boldsymbol{U}\frac{\partial \boldsymbol{U}}{\partial \boldsymbol{x_i}}\right] = -\frac{\partial P}{\partial \boldsymbol{x_j}} + \frac{\partial^2 \boldsymbol{U}}{\partial \boldsymbol{x_i}}$$

$$Ma\left[\frac{\partial C}{\partial \tau} + \boldsymbol{U}\frac{\partial C}{\partial x_i}\right] = \frac{\partial^2 C}{\partial x_i^2}$$

$$\boldsymbol{U} = (U, V, W)$$

The dimensionless boundary conditions are:
At $Z = 0$,

$$U = V = W = \partial C/\partial Z = 0$$

At $Z = 1$,

$$W = 0$$

$$\frac{\partial U}{\partial Z} = -\frac{\partial C}{\partial X}$$

$$\frac{\partial V}{\partial Z} = -\frac{\partial C}{\partial Y}$$

$$-\frac{\partial C}{\partial Z} = Bi(C - C_{\mathrm{I}}) + S$$

where the dimensionless group are:

$$Re = \frac{\rho \beta_{\mathrm{c}} R_{\mathrm{c}} d^2}{\mu^2}, \quad Sc = \frac{\mu}{\rho D}, \quad Bi(M, L) = \frac{k_{\mathrm{L}} d}{D}, \quad Ma = \frac{\beta_{\mathrm{c}} R_{\mathrm{c}} d^2}{\mu D},$$

$$C - C_{\mathrm{I}} = \frac{c - c_{\mathrm{I}}}{\beta_{\mathrm{c}} d}, \quad C = \frac{c - c_0}{\beta_{\mathrm{c}} d}, \quad S = \frac{S_{\mathrm{G}}}{\beta_{\mathrm{c}} D}$$

where $Bi(M, L)$ is the Biot number for liquid phase; the (M, L) is omitted in subsequent section.

9.3.2 Stability Analysis

Since the inhomogeneity of surface tension at the interface is the cause of initiating the Marangoni convection, the surface tension gradient $\frac{\partial \sigma}{\partial x_i}$ can be considered as an external force acting to the system. When this external force is not great enough to overcome the viscous shearing force of the fluid, the system remains stable. If this

external force is just equal to the viscous shearing force of the fluid, the system is said to be in the critical condition. The Marangoni number at this point is denoted as critical Marangoni number Ma_{cr}. Thus we may apply a small disturbance as external force to study the stability of the system.

The small disturbance acting on the variables concerned can be represented as follows:

$$(U, V, W, P, C) = (\bar{U}, \bar{V}, \bar{W}, \bar{P}, \bar{C}) + (\delta u, \delta v, \delta w, \delta p, \delta c)$$

where superscript "–" denotes stable state. If the disturbance system follows single normal mode, the disturbance term (δu, δv, δw, δp, δc) is expressed by two-dimensional (x, y) exponential form as follows:

$$(\delta u, \delta v, \delta w, \delta p, \delta c) = (\hat{u}(Z), \hat{v}(Z), \hat{w}(Z), \hat{p}(Z), \hat{c}(Z)) \exp\left[ik_x x + ik_y y + \omega t\right]$$

where k_x and k_y are respectively the wave number in x and y direction; ω is the increasing rate of disturbance; superscript ^ represents the amplitude of the disturbed variable; x, y are the dimensionless coordinates.

Under neutral condition, ω is equal to 0. If the disturbance appears in x direction, $k_y = 0$. Substituting the disturbance expression to the dimensionless model equation and the boundary condition, we have:

$$\begin{aligned} \left(\widetilde{D}^2 - k_x^2\right)\hat{u} &= MaSc^{-1}\hat{w} \\ \left(\widetilde{D}^2 - k_x^2\right)^2 \hat{w} &= 0 \\ \left(\widetilde{D}^2 - k_x^2\right)\widehat{C} &= -Ma(\hat{u} + MaZ^2\hat{w}/2) \end{aligned} \tag{9.4}$$

At $Z = 0$, $\widehat{u} = \widehat{w} = \widehat{D}\widehat{w} = \widehat{D}\widehat{C} = 0$

At $Z = 1$时, $\widetilde{D}\widehat{u} = \widehat{w} = \widetilde{D}^2\widehat{w} + k_x^2\widehat{C} = \widetilde{D}\widehat{C} + Bi\widehat{C} = 0$.

where $\widetilde{D}$ is differential operator.

If the system is stable, the foregoing dimensionless equations have zero solution; if the system is unstable, there should have solution. Direct integration of foregoing dimensionless equations yield the solutions for $\hat{u}$, $\hat{w}$ and $\widehat{C}$ with eight unknown integration constants in which the Ma, Bi, Sc, k_x are involved. Substituting to the boundary condition, eight linear equations are obtained. In this equation set, if the coefficients of 8 × 8 determinant equal to zero, the dimensionless equations can be solved. Mathematically speaking, the necessary and sufficient condition of system under instability is the foregoing 8 × 8 determinant is equal to zero. It follows that we have:

$$f(Ma,\ Bi,\ Sc,\ k_x) = 0$$

The left hand side of the equation represents the relationship between Ma, Bi, Sc, k_2 obtained by setting the 8 × 8 determinant equal to zero. In other words, the

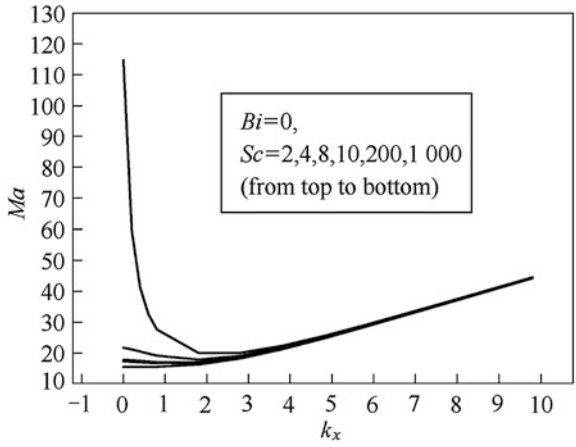

Fig. 9.11 *Ma* and *k* relationship at $Bi = 0$ and different *Sc*

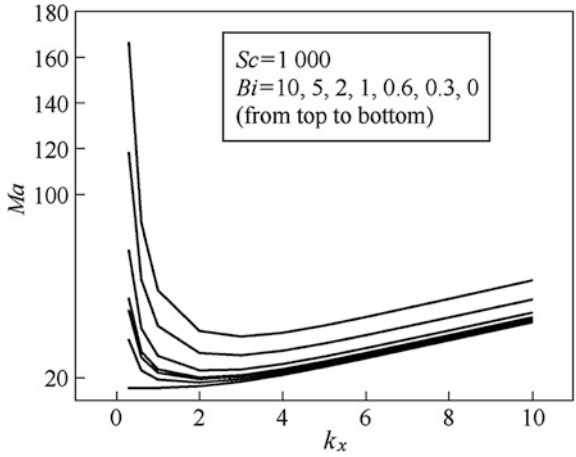

Fig. 9.12 *Ma* and *k* relationship at $Sc = 1000$ and different *Bi*

foregoing system is unstable if its reasonable values of *Ma*, *Bi*, *Sc*, k_x are fulfill the condition of $f(Ma,\ Bi,\ Sc,\ k_x) = 0$.

By setting different *Sc* and *Bi*, the relationship between *Ma* and k_x can be obtained from $f(Ma,\ Bi,\ Sc,\ k_x) = 0$ as shown by the curves in Figs. 9.11–9.14. In these figures, any points above the curve are unstable and induce Marangoni convection; while any points below are stable without Marangoni convection. The minimum point of the curve represents the critical Marangoni number Ma_{cr}. It is also seen from Fig. 9.11 through 9.14 that Ma_{cr} is affected by both *Sc* and *Bi* of the process.

Sha performed the experiment on the falling film desorption of acetone from its aqueous solution [10, 11] and found the Ma_{cr} as given in Table 9.2. In comparison with the calculated Ma_{cr}, the error is less than 10 %.

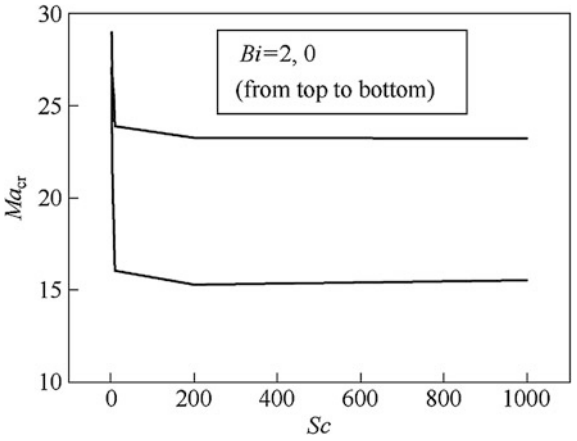

Fig. 9.13 Ma_{cr} and Sc relationship at Bi = 2, 0

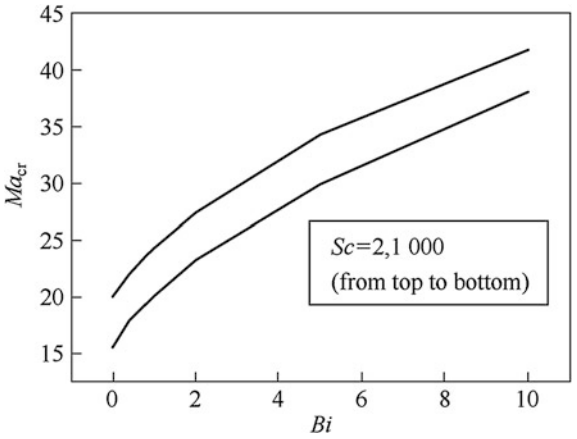

Fig. 9.14 Ma_{cr} and Bi relationship at Sc = 2, 1000

Table 9.2 Comparison of calculated and experimental Ma_{cr} (gas phase N_2, Re = 446)

Liquid rate × 10^5 (m^3 s^{-1})	Film thickness × 10^4 (m)	Bi	Sc	Experimental Ma_{cr}	Calculated Ma_{cr}	Error (%)
1.11	2.78	1.655	714	26.92	24.86	8.29
1.67	3.18	2.168	714	28.67	26.24	9.26
2.22	3.5	2.62	714	29.86	27.43	8.97
2.78	3.77	3.05	714	31.24	28.56	9.4

9.4 Mass Transfer Enhancement by Marangoni Convection

As stated in previous section, the mass transfer process can be enhanced by the presence of Marangoni convection. Xiao analyzed the mass transfer condition under $Ma > Ma_{cr}$ to find the enhancement factor as follows [12].

Starting from the equation of steady diffusion,

$$u\frac{\partial c}{\partial x} + w\frac{\partial c}{\partial x} = D\frac{\partial^2 c}{\partial z^2} \tag{9.5}$$

and the direct integration of continuity equation:

$$w = -z\frac{\partial u}{\partial x} \tag{9.6}$$

Substituting Eq. (9.5) to Eq. (9.4), we have:

$$u\frac{\partial c}{\partial x} - z\frac{\partial u}{\partial x}\frac{\partial c}{\partial z} = D\frac{\partial^2 c}{\partial z^2} \tag{9.7}$$

The boundary conditions are:

$$\begin{cases} z = d & c = c_I \\ z = 0 & c = c_0 \\ x = 0 & c = c_0 \end{cases}$$

where c_I and c_0 are respectively the concentration at the interface and bulk fluid.

If the thickness of the boundary layer at point x is $h(x)$, let

$$\eta = \frac{z}{h(x)}$$

Substituting to Eq. (9.6) yields:

$$\frac{1}{D}\left(\frac{u}{2}\frac{\mathrm{d}h^2}{\mathrm{d}x} + h^2\frac{\mathrm{d}u}{\mathrm{d}x}\right)\eta\frac{\mathrm{d}c}{\mathrm{d}\eta} + \frac{\mathrm{d}^2 c}{\mathrm{d}\eta} + \frac{\mathrm{d}^2 c}{\mathrm{d}\eta^2} = 0 \tag{9.8}$$

Let

$$\frac{1}{D}\left(\frac{u}{2}\frac{\mathrm{d}h^2}{\mathrm{d}x} + h^2\frac{\mathrm{d}u}{\mathrm{d}x}\right) = l \tag{9.9}$$

Equation (9.7) becomes

$$l \cdot \eta \frac{\mathrm{d}c}{\mathrm{d}\eta} + \frac{\mathrm{d}^2 c}{\mathrm{d}\eta^2} = 0 \tag{9.10}$$

From the boundary condition, at $x = 0$, $h = 0$, integrating Eq. (9.8) and Eq. (9.9) and combining with the boundary condition, we get:

$$c = c_0 - \sqrt{\frac{2l}{\pi}}(c_\mathrm{I} - c_0) \int_0^\eta \mathrm{e}^{-\frac{1}{2}\eta^2} \mathrm{d}\eta \tag{9.11}$$

or:

$$\frac{\partial c}{\partial z} = \frac{\partial c}{\partial \eta}\frac{\partial \eta}{\partial z} = \frac{1}{h}\sqrt{\frac{2l}{\pi}}(c_0 - c_\mathrm{I})\mathrm{e}^{-\frac{1}{2}\eta^2} \tag{9.12}$$

Let N be the mass flux transferred, which is given by:

$$N = D\frac{\partial c}{\partial z}\bigg|_{z=0} = \mathbf{k_p}(c_0 - c_\mathrm{I})$$

In connection with Eqs. (9.10) and (9.11), we have:

$$\mathbf{k_p} = \sqrt{\frac{D}{\pi}} \frac{u}{\left(\int_0^x u \mathrm{d}x\right)^{\frac{1}{2}}}$$

where $\mathbf{k_p}$ is the local mass transfer coefficient at point p. Thus the liquid phase mass transfer coefficient covering the length x_0 of the process can be considered as the averaged $\mathbf{k_p}$:

$$\begin{aligned} \mathbf{k} &= \frac{1}{x_0}\int_0^x \mathbf{k_p}\mathrm{d}x = \sqrt{\frac{D}{\pi}}\frac{1}{x_0}\int_0^{x_0} \frac{u}{\left(\int_0^x u \mathrm{d}x\right)^{\frac{1}{2}}}\mathrm{d}x \\ &= 2\sqrt{\frac{D}{\pi x_0}}\left[\frac{1}{x_0}\int_0^{x_0} u \mathrm{d}x\right]^{\frac{1}{2}} \end{aligned} \tag{9.13}$$

If u in the foregoing equation is replaced by the average velocity u_0, it becomes Higbie penetration model. Here we considered a disturbance velocity δu is added to u_0 as follows:

$$u = u_0 + \delta u$$

and

$$\delta u = -\int \frac{\partial \delta w}{\partial z} \mathrm{d}x = -\int DW \exp(ik_x x + \omega t)\mathrm{d}x$$

The W can be expressed as function of z:

$$W = Af(z)$$

where A is a constant to be determined. Then we have:

$$\delta u = \frac{i}{k_1} Af(z) \exp(ik_x x + \omega\, t)$$

Substituting ∂u to the force balance equation at the interface gives:

$$\begin{aligned}\frac{\partial \sigma}{\partial x} &= \mu\left(\frac{\partial \delta u}{\partial z} + \frac{\partial \delta w}{\partial x}\right) \\ &= \mu A\left[\frac{i}{k_2} f(z) + ikf(z)\right] \exp(ik_x x + \omega t)\end{aligned}$$

Integrating foregoing equation from 0 to x_0 yields:

$$\Delta\sigma = \mu A\left[\frac{1}{k^2} f(z) + f(z)\right] \exp(ik_x x + \omega t)\big|_0^{x_0} = \theta A$$

where $\Delta\sigma$ is the liquid phase surface tension difference of the element in contact with the gas phase at the interface after traveling through distance x_0. Substituting $\Delta\sigma$ to the definition of Ma and rearranging, we have:

$$A = \frac{\Delta\sigma}{\theta} = \frac{\mu D}{d^2\theta} Ma = BMa$$

Substitute δu and A to the following velocity equation yields:

$$u = u_0 + \delta u = u_0 + \frac{i}{k} BMa f'(z) \exp(ik_x x + \omega t)$$

Then we have:

$$\begin{aligned}\mathbf{k} &= 2\sqrt{\frac{D}{\pi x_0}}\left[u_0 + \frac{1}{k_x^2} BMa f'(z) \exp(ik_x x + \omega t)\big|_0^{x_0}\right]^{\frac{1}{2}} \\ &= 2\sqrt{\frac{D}{\pi(x_0/u_0)}}\left[1 + \frac{1}{u_0 k_x^2} BMa f'(z) \exp(ik_x x + \omega t)\big|_0^{x_0}\right]^{\frac{1}{2}} \\ &= \mathbf{k}_{\mathrm{H}}[1 + EMa]^{\frac{1}{2}}\end{aligned}$$

Obviously, $\mathbf{k}_H$ is the mass transfer coefficient given by penetration theory; E can be considered as a constant. Then we have the ratio of the mass transfer coefficients with surface disturbance to that of penetration theory as follows:

$$F = \frac{\mathbf{k}}{\mathbf{k_H}} = (1 + EMa)^{\frac{1}{2}} = \left(\frac{1}{Ma} + E\right)^{\frac{1}{2}} Ma^{\frac{1}{2}}$$

where the ratio F is the enhancement factor. When Ma is sufficient large, the foregoing equation can be simplified to:

$$F = E^{\frac{1}{2}} Ma^{\frac{1}{2}}$$

The F is proportional to square root of the Ma. As seen from foregoing equation, the mass transfer can be enhanced by Marangoni convection, although it should be verified by experimental evidence as shown in subsequent section.

Sun [13, 14] derived from dimensionless disturbance equation to obtain F to be:

$$F = \left[1 + a\left(\frac{Ma - Ma_{cr}}{Ma_{cr}}\right)\right]^{\frac{1}{2}}$$

where a is a constant. When Ma is sufficient large, it becomes:

$$F = a^{\frac{1}{2}}\left(\frac{Ma}{Ma_{cr}}\right)^{\frac{1}{2}}$$

when $Ma = Ma_{cr}$, $F = 1$, we obtain $a = 1$; the equation also takes the form of:

$$F = \left(\frac{Ma}{Ma_{cr}}\right)^{\frac{1}{2}}$$

For a mass transfer process, the Ma_{cr} is a fixed value, the foregoing equation can be written as $F = b(Ma)^{\frac{1}{2}}$.

9.5 Experiment on the Mass Transfer Enhancement by Interfacial Marangoni Convection

9.5.1 Absorption of CO_2 by Horizontal Stagnant Solvent

Sun performed the experiment of CO_2 absorption by methanol, toluene and chlorobenzene in a horizontal liquid-gas contactor at different liquid thickness h as shown in Fig. 9.16 for investigating the progress of Marangoni effect [13, 14]. The

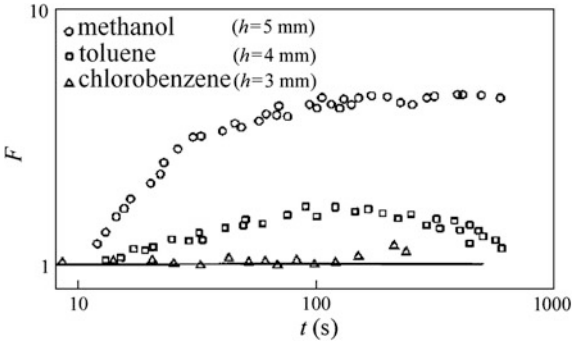

Fig. 9.15 *F-t* curve of CO_2 absorption by various horizontal stagnant absorbent (reprinted from Ref. [14], Copyright 2002, with permission from American Chemical Society)

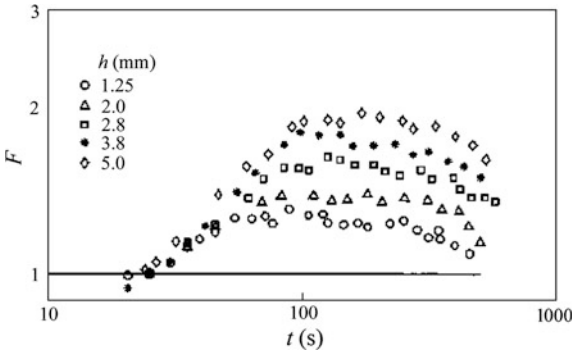

Fig. 9.16 *F-t* curve of CO_2 absorption by horizontal stagnant isopropanol at different liquid thickness (reprinted from Ref. [14], Copyright 2002, with permission from American Chemical Society)

development of enhancement factor F with time of the unsteady absorption is given in Fig. 9.15.

As seen from Fig. 9.15, the enhancement factor F at the beginning is increased with time where the rate of absorption by ethanol is faster than that by toluene. While the absorption by chlorobenzene shows no enhancement effect $(F = 1)$ due to both the *Ma* and *Ra* numbers are negative. Figure 9.16 shows the *F-t* curve of CO_2 absorption by isopropanol at different liquid thickness.

As seen in Fig. 9.16, the F increases with increasing liquid thickness because the higher the liquid thickness the more intense Rayleigh effect. It dominstrates that the coupling effect of Rayleigh and Marangoni makes greater increase of the enhancement factor.

Sun proposed that the *F-t* curve is composed with three stages [14]: (1) ascending stage where the interfacial disturbance is gradually intensified and F is increased; (2) transition stage where the interfacial disturbance and F becomes relatively stable; (3) descending state where the absorption is approaching saturation so that the driving force of mass transfer is lowered and F is gradually declined.

In the ascending stage, the F factor can be regressed by the following equation:

$$F = \left(\frac{Ma}{Ma_{\mathrm{cr}}}\right)^{n}$$

9.5.2 Desorption of CO_2 by Falling Film Solvent

Zhou performed the experiment of steady falling film mass transfer process to investigate the effect of Marangoni convection on the mass transfer coefficient [5, 7, 15]. The choice of falling film is to eliminate the Rayleigh effect. The experimental setup is the same as shown in Figs. 9.1 and 9.2b. The process is desorption of aqueous desorbent by nitrogen. The inlet composition of aqueous desorbent was changed for every run in order to study the influence of mass transfer coefficient on the effect of Marangoni convection. Pure nitrogen was used as gas absorbent for desorption. The composition of desorbent in the outlet gas phase can be calculated by:

$$c_{\mathrm{Gout}} = \frac{Q_{\mathrm{L}}(c_{\mathrm{Lin}} - c_{\mathrm{Lout}})}{Q_{\mathrm{G}}}$$

where c_{Lin} is the desorbent concentration at the inlet (mol m^{-3}); c_{Lout} and c_{Gout} are respectively the desorbate (species to be desorbed, called solute hereafter) concentration at the outlet liquid and gas phases; Q_{L} and Q_{G} are respectively the volumetric flow of liquid and gas phases.

The overall coefficient of mass transfer can be calculated by the following equation:

$$K_{\mathrm{Lexp}} = \frac{Q_{\mathrm{L}}(c_{\mathrm{Lin}} - c_{\mathrm{Lout}})}{A(c_{\mathrm{L}} - c_{\mathrm{L}}^{*})_{\log}}$$

$$(c_{\mathrm{L}} - c_{\mathrm{L}}^{*})_{\log} = \frac{(c_{\mathrm{Lin}} - c_{\mathrm{Gout}}/m) - c_{\mathrm{Lout}}}{\log\frac{c_{\mathrm{Lin}} - c_{\mathrm{Gout}}/m}{c_{\mathrm{Lout}}}}$$

where A is the liquid–gas contacting area; $(c_{\mathrm{L}} - c_{\mathrm{L}}^{*})_{\log}$ is the logarithmic average driving force of mass transfer between liquid inlet and outlet; c_{L}^{*} is the desorbate (solute) concentration in liquid phase in equilibrium with that in gas phase; $m = c_{\mathrm{G}}^{*}/c_{\mathrm{L}}$; c_{G}^{*} is the solute concentration in equilibrium with the partial pressure of solute concentration c_{L} in the bulk liquid phase.

In this case, the Δc in Marangoni number, which represents the intensity of Marangoni convection, can be expressed by the interfacial solute concentration difference per unit length of interface as follows:

$$\Delta c = \frac{\Delta c_{\mathbf{Lf}}}{l} = \frac{c_{\mathbf{Lf(out)}} - c_{\mathbf{Lf(in)}}}{l}$$

where $c_{\mathbf{Lf}}$ is the solute concentration at interface. The $\frac{\Delta c_{\mathbf{Lf}}}{l}$ can be regarded as the driving force per unit interfacial length. The $c_{\mathrm{Lf(in)}}$ and $c_{\mathrm{Lf(out)}}$ can be calculated as follows [16]:

$$c_{\mathrm{Lf(in)}} = \frac{c_{\mathrm{Gout}} + c_{\mathrm{Lin}}\sqrt{\frac{D}{D_G}}}{m + \sqrt{\frac{D}{D_G}}}$$

$$c_{\mathrm{Lf(out)}} = \frac{c_{\mathrm{Lout}}\sqrt{\frac{D}{D_{\mathrm{G}}}}}{m + \sqrt{\frac{D}{D_{\mathrm{G}}}}}$$

where D and D_{G} are respectively the diffusivity of solute in liquid phase and gas phase.

Under the condition of no Marangoni convection, the mass transfer on falling film is only by diffusion. Zhang [16] and Bird [17] derived the following equation of overall mass transfer coefficient K_{Ltheo} based on the penetration theory:

$$\frac{1}{K_{\mathrm{Ltheo}}} = (\pi T)^{0.5}\left(D^{-0.5} + D_{\mathrm{G}}^{-0.5} \times m\right)/2$$

Under the condition of existing Marangoni convection, the enhancement factor F can be expressed as:

$$F = \frac{K_{\mathrm{Lexp}}}{K_{\mathrm{Ltheo}}}$$

From the experimental F factor obtained under different $\frac{\Delta c_{\mathbf{Lf}}}{l}$, we can judge the intensity of Marangoni effect.

(1) ***The increase of K_{Lexp} with $\frac{\Delta c_{\mathbf{Lf}}}{l}$***

(A) *Desorption of ethyl ether in nitrogen stream*
Under the condition of N_2 1.5 $m^3\ h^{-1}$, aqueous ethyl ether 10 L h^{-1}, the overall liquid phase mass transfer coefficient K_{Lexp} versus driving force per unit interfacial length $\frac{\Delta c_{\mathbf{Lf}}}{l}$, is shown in Fig. 9.17. Different $\frac{\Delta c_{\mathbf{Lf}}}{l}$ are established by changing the inlet composition of aqueous ethyl ether.

(B) *Desorption of ethanol in nitrogen stream*
Under the condition of N_2 1.5 m^3/h, aqueous ethanol 10 L/h, the overall liquid phase mass transfer coefficient K_{Lexp} versus driving force unit length $\frac{\Delta c_{\mathbf{Lf}}}{l}$ is shown in Fig. 9.18.

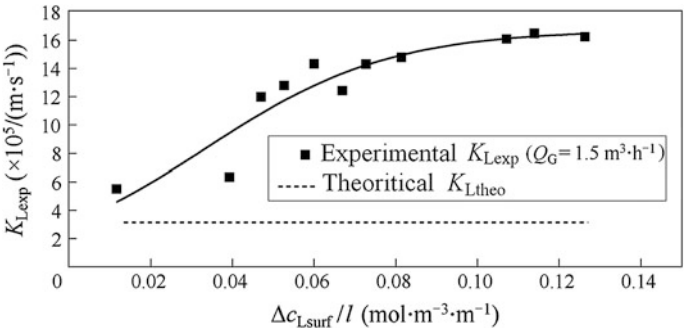

Fig. 9.17 The K_{Lexp} versus $\Delta c_{Lf}/l$ curve for the desorption of aqueous diethyl ether

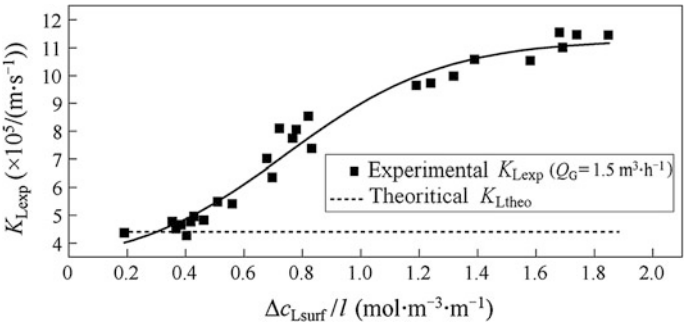

Fig. 9.18 The K_{Lexp} versus $\Delta c_{Lf}/l$ curve for the desorption of aqueous ethanol

As seen from Figs. 9.17 and 9.18, the overall mass transfer coefficient K_{Lexp} is increased with increasing $\frac{\Delta c_{Lf}}{l}$ because the Marangoni convection is intensified. When $\frac{\Delta c_{Lf}}{l}$ is further increased, the Marangoni convection is too strong to approaching turbulence and desorption is gradually turning to the stable turbulent mass transfer. The enhancement factor is found about 1.5–4.0.

(2) ***The increase of enhancement factor F with Ma number***

The $\Delta c_{Lsurf}/l$ can be converted to the *Ma* number by Eq. (9.1). The increase of *F* with *Ma* number at different liquid and gas rates is shown in Fig. 9.19 [18]. As seen in the figure, the liquid rate is much influential on *F* factor than the gas rate.

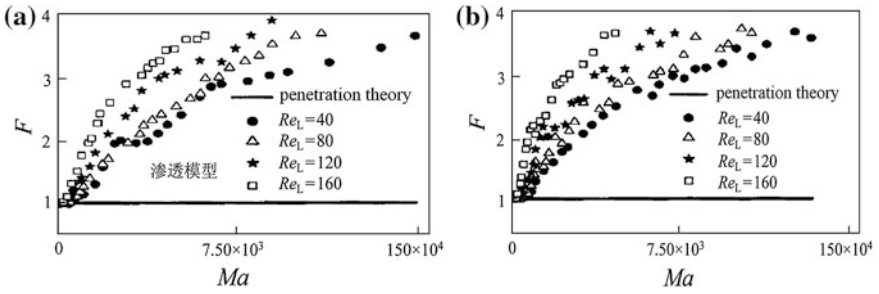

Fig. 9.19 The F versus Ma curve for the desorption of aqueous ethanol **a** $Re_G = 230$, **b** $Re_G = 460$ (reprinted from Ref. [9], Copyright 2006, with permission from Tianjin University)

9.6 The Transition of Interfacial Structure from Order to Disorder

For the falling film mass transfer process as shown in Fig. 9.3, when the Ma number exceeds the critical value Ma_{cr}, the linear stability analysis is not valid, and the non-linear disturbance should be considered. Xiao solved the following non-linear disturbance equation for the process with heat and mass transfer as follows [12]:

$$\frac{\partial \delta u}{\partial t} + \delta u \cdot \frac{\partial \delta u}{\partial x_i} = -\frac{1}{\rho}\frac{\partial \delta P}{\partial x_j} + v\frac{\partial^2 \delta u}{\partial x_i}$$

$$\frac{\partial \delta T}{\partial t} + \delta u \frac{\partial \Delta T}{\partial x_i} = \delta w + \alpha \frac{\partial^2 \delta T}{\partial x_i^2}$$

$$\frac{\partial \delta C}{\partial t} + \delta u \frac{\partial \delta C}{\partial x_i} = \delta w + D\frac{\partial^2 \delta C}{\partial x_i^2}$$

$$\frac{\partial \delta u}{\partial x_i} = 0$$

The foregoing equation set involves unknown δu, δw, δp, δT and δC. Eliminating δp from the velocity equation, we have:

$$\frac{\partial \varphi}{\partial t} + \delta \boldsymbol{u} \cdot \nabla \varphi = v\nabla^2 \varphi$$

where

$$\varphi = \frac{\partial \delta u}{\partial z} - \frac{\partial \delta w}{\partial x}$$

The boundary conditions are:
At z = 0 (wall surface):

$$\delta u = 0$$
$$\frac{\partial \delta C}{\partial z} = Bi_{\mathrm{m}}^{0} \delta C$$
$$\frac{\partial \delta T}{\partial z} = Bi_{\mathrm{h}}^{0} T \delta T$$

where $Bi_{\mathrm{m}}^{0} = \frac{k_{\mathrm{L}}^{0} d}{D}$ is the Biot number for mass transfer; $Bi_{\mathrm{h}}^{0} = \frac{h_{\mathrm{L}}^{0} d}{\alpha}$ is the Biot number for heat transfer; superscript 0 denotes at the solid wall.

At z = 1 (interface):

$$\delta w = 0$$
$$\frac{\partial \delta T}{\partial z} = Bi_{\mathrm{h}}^{\mathrm{I}} \delta T$$
$$\frac{\partial \delta C}{\partial z} = Bi_{\mathrm{m}}^{\mathrm{I}} \delta C$$
$$\frac{\partial \delta u}{\partial z} + \frac{\partial \delta w}{\partial x} = \frac{Ma_{\mathrm{h}}}{Le} \frac{\partial \delta T}{\partial x} + Ma \frac{\partial \delta C}{\partial x}$$

where the superscript I denotes the interface.

For solving the unknown δu, δw, δT, δC, the tau method developed from Gelerkin method were used. The energy spectrum function P is defined as [12]:

$$P(f) = \sum_{k=1}^{N} C_k \exp(2\pi f k \sqrt{-1}/N$$

where f is the frequency; k is the wave number; N is the number of terms taken in the expansion series of disturbance. Figures 9.19 (no heat transfer, $Ma_{\mathrm{h}} = 0$) and 9.20 (with heat transfer, $Ma_{\mathrm{h}} = 34$) show the energy spectrum for desorption of aqueous methanol at different Ma/Ma_{cr} and Ma_{h}.

From the energy spectrum at different Ma/Ma_{cr}, it is seen that when Ma/Ma_{cr} between 3 and 12, clear peak is found indicating periodic motion (ordered convection); but when Ma/Ma_{cr} up to about 13, obvious noise is appeared indicating the periodic motion being interrupted and turned to disorder (chaos). Thus the transition point, which can be found from interfacial order to disorder structure, is about Ma/Ma_{cr} = 13. Nevertheless, upon careful study of Figs. 9.20 and 9.21, some small noise yet be seen; it means that some small disorder is always accompanied with the major part of the ordered interfacial structure.

From the solution of foregoing differential equation set, Zhou [15] also obtained the relationship between mass flux (represented by Sherwood number Sh, $\left(Sh = \frac{k_c l}{D} = \frac{j_c l}{D \Delta c}\right)$ and Ma/Ma_{cr}. The calculated results are compared with

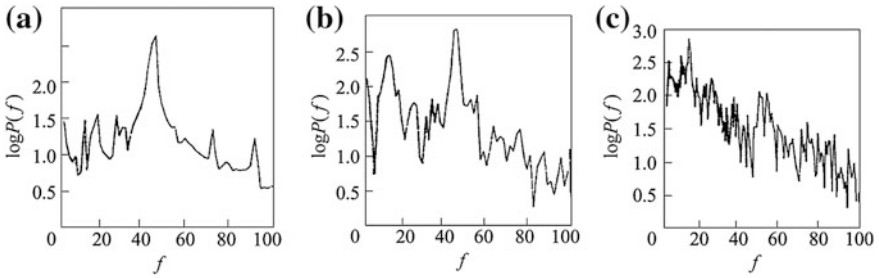

Fig. 9.20 Energy spectrum of aqueous methanol desorption ($Ma_h = 0$) **a** $Ma/Ma_{cr} = 2$, **b** $Ma/Ma_{cr} = 12$, **c** $Ma/Ma_{cr} = 13$

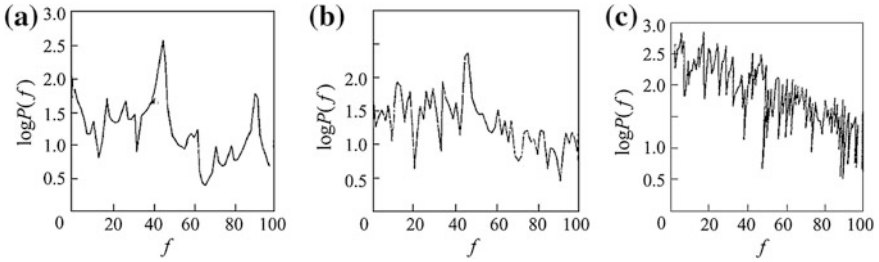

Fig. 9.21 Energy spectrum of aqueous methanol desorption ($Ma_h = 34$) **a** $Ma/Ma_{cr} = 2$, **b** $Ma/Ma_{cr} = 12$, **c** $Ma/Ma_{cr} = 13$

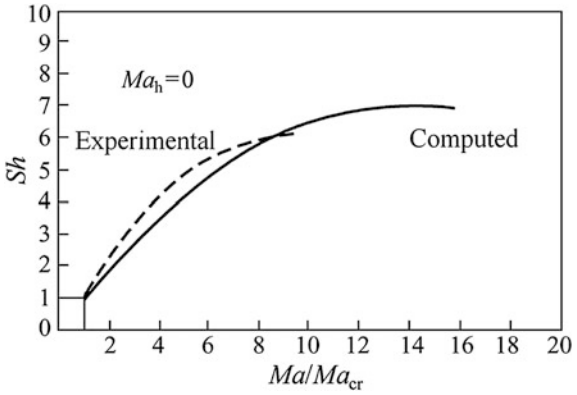

Fig. 9.22 *Sh* versus Ma/Ma_{cr} for aqueous methanol desorption

experimental data on desorption of aqueous methanol and acetone under nitrogen stream as shown in Figs. 9.22 and 9.23. When *Ma* exceed critical value ($Ma/Ma_{cr} = 1$), *Sh* goes up sharply, and then slow down as *Ma* further increases. Finally *Sh* becomes almost constant which indicates that the chaos or turbulent state is reached.

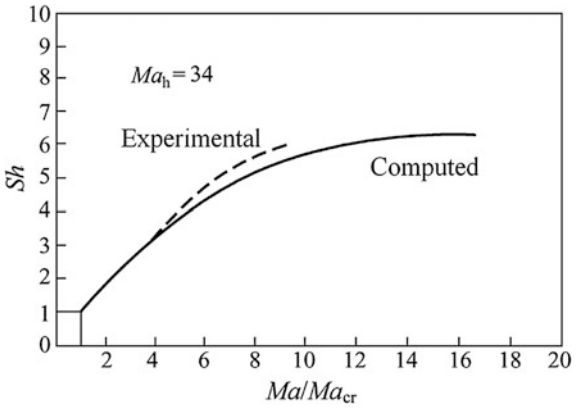

Fig. 9.23 *Sh* versus Ma/Ma_{cr} for aqueous acetone desorption

9.7 Theory of Mass Transfer with Consideration of Marangoni Effect

In the study of mass transfer, the fluid element (microcell) can be used to describe the behaviors of the process. Under the condition of no Marangoni effect, according to the penetration theory, the fluid element flows randomly from fluid phase to the interface and stays there within residence time $\overline{T}$ for unsteady mass transfer and then go back to the bulk fluid. The liquid phase mass transfer coefficient k_H is given by:

$$k_H = 2\sqrt{\frac{D}{\pi \overline{T}}}$$

When Marangoni convection appears, the interfacial flow and accompanied underneath circulation promotes the renewal of interface. The residence time of fluid element is then shortened.

Based on this viewpoint, Sha modified the penetration theory [10, 19] with consideration that the residence time of fluid element should be changed to t instead of $\overline{T}$ $(t < \overline{T})$ when Marangoni convection occurs. The mass transfer coefficient $\mathbf{k}_c$ at the presence of Marangoni convection becomes:

$$k_c = 2\sqrt{\frac{D}{\pi t}}$$

The enhancement factor F can be calculated by the following ratio:

$$F = \frac{k_c}{k_H} = \sqrt{\frac{\overline{T}}{t}} \quad (t < \overline{T})$$

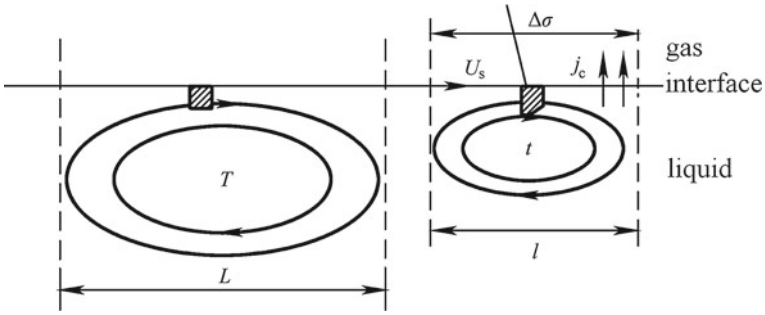

Fig. 9.24 Renewal of interfacial fluid element **a** no Marangoni convection, **b** with Marangoni convection (reprinted from Ref. [19], Copyright 2003, with permission from CIESC)

Since the F factor is generally about 2–5, the residence time of fluid element is then reduced by 4–25 folds. The shorter residence time means the faster the fluid circulation and quicker the interfacial mass renewal. The circulations of the fluid element without Marangoni convection and with Marangoni convection are shown schematically in Fig. 9.24. It is seen that by the help of Marangoni convection the path of circulation is smaller ($l < L$) and the residence time is shorten ($t < \bar{T}$) because the renewal of interfacial concentration is faster. Nevertheless, the l and t are statistic average length and time, which are still unknown.

Sha postulated that the dimensionless time $\frac{t}{\bar{T}}$ and length $\frac{l}{L}$ satisfy the exponential relationship as follows:

$$\frac{t}{\bar{T}} = \left(\frac{l}{L}\right)^m \tag{9.14}$$

where $0 < \frac{t}{\bar{T}} < 1$ and $0 < \frac{l}{L} < 1$ as seen in Fig. 9.25; m is a constant and $0 < m < 1$. The value of m will be given later.

At the critical point of initiating Marangoni convection ($Ma = Ma_{cr}$), the interfacial flow is a result of establishing the following force balance at the interface:

$$\mu \frac{\partial u}{\partial y} = \frac{\partial \sigma}{\partial c} \frac{\partial c}{\partial x}$$

Let the local interfacial velocity u be the average convective velocity at interface U_s, the vertical distance y be the penetration depth of the Marangoni convection δ_y, the following approximated relationship is obtained from foregoing equation:

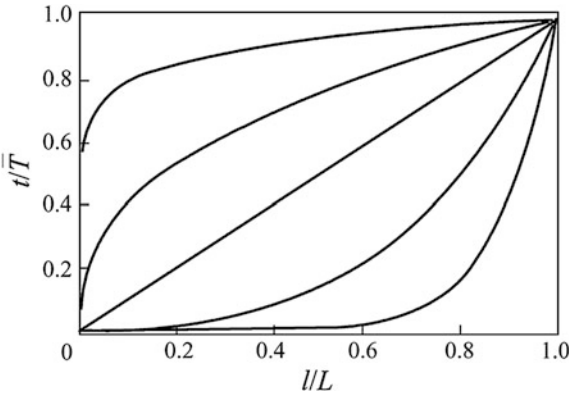

Fig. 9.25 $t/\bar{T}$ versus l/L at different m (*from upper to lower curves in sequence* m = 0.2, 0.4, 1, 3, 8) (reprinted from Ref. [19], Copyright 2003, with permission from CIESC)

$$\mu \frac{U_s}{\delta_y} \sim \frac{\partial \sigma}{\partial c} \frac{\Delta c}{l}$$

Substituting $U_s \sim l/t$, $\delta_y \sim \sqrt{vt}$, where v is the kinematic viscosity, one yields:

$$\frac{l^2}{t^{\frac{3}{2}}} \sim \frac{1}{\mu} \frac{\partial \sigma}{\partial c} \Delta c v^{1/2}$$

Combining with Eq. (9.14),

$$\frac{L^2}{\bar{T}^{\frac{2}{m}}} \frac{1}{t^{\frac{3m-4}{2m}}} \sim \frac{1}{\mu} \frac{\partial \sigma}{\partial c} v^{1/2} \Delta c$$

and after simplifying, the residence time t can be expressed by:

$$\frac{1}{t^{\frac{3m-4}{2m}}} \sim \frac{1}{\mu} \frac{\partial \sigma}{\partial c} v^{1/2} \Delta c \frac{\bar{T}^{\frac{2}{m}}}{L^2}$$

or

$$\frac{1}{t^{\left(-\frac{1}{2}\right)\frac{4-3m}{m}}} \sim \frac{1}{\mu} \frac{\partial \sigma}{\partial c} \Delta c \frac{L}{D} \frac{D_L}{L} v^{1/2} \frac{\bar{T}^{\frac{2}{m}}}{L^2}$$

Substituting the definition of Ma,

$$Ma = \frac{1}{\mu} \frac{\partial \sigma}{\partial c} \Delta c \frac{L}{D}$$

the following relationship is obtained:

$$\frac{1}{t^{\left(-\frac{1}{2}\right)\frac{4-3m}{m}}} \sim MaDv^{1/2}\frac{\bar{T}^{\frac{2}{m}}}{L^3}$$

$$t^{-\frac{1}{2}} \sim \left(MaDv^{1/2}\frac{\bar{T}^{\frac{2}{m}}}{L^3}\right)^{\frac{m}{3m-4}}$$

For unsteady diffusion, the mass flux j_c can be expressed by penetration theory:

$$j_c \sim \Delta c\sqrt{\frac{D}{t}}$$

Substitute the expression for t to have

$$j_c \sim \Delta c D^{\frac{1}{2}}\left(MaDv^{1/2}\frac{\bar{T}^{\frac{2}{m}}}{L^3}\right)^{\frac{m}{3m-4}}$$

The Sherwood number Sh is defined as:

$$Sh = \frac{k_c l}{D} = \frac{j_c l}{D\Delta c}$$

Substitute j_c to yield

$$Sh \sim D^{-\frac{1}{2}}\left(MaDv^{1/2}\frac{\bar{T}^{\frac{2}{m}}}{L^3}\right)^{\frac{m}{3m-4}} l$$

and eliminate l by Eq. (9.14), the following relationship is obtained:

$$Sh \sim D^{-\frac{1}{2}}\left(MaDv^{1/2}\frac{\bar{T}^{\frac{2}{m}}}{L^3}\right)^{\frac{m-2}{3m-4}}\frac{L}{\bar{T}^{\frac{1}{m}}}$$

As all variables are constant except Sh, Ma and Sc $\left(Sc = \frac{\nu}{D}\right)$ in the foregoing equation, it can be simplified as follows:

$$Sh \propto Ma^{\frac{m-2}{3m-4}}Sc^{\frac{1}{2}\left(\frac{m-2}{3m-4}\right)}$$

or:

$$Sh \propto Ma^n Sc^{\frac{1}{2}n}, \quad n = \frac{m-2}{3m-4}$$

The exponent $\frac{m-2}{3m-4}$ is not continuous as shown in Fig. 9.26.

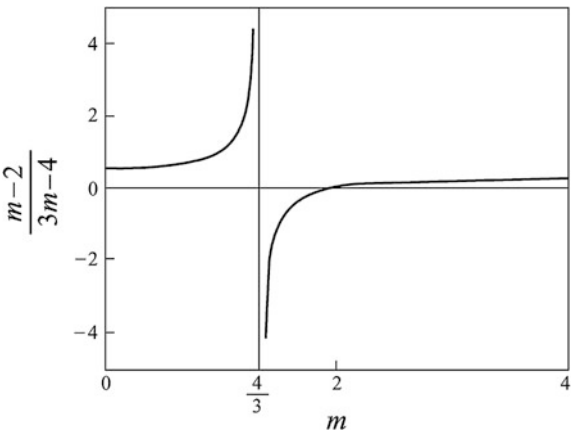

Fig. 9.26 Relationship between $\frac{m-2}{3m-4}$ and m (reprinted from Ref. [19], Copyright 2003, with permission from CIESC)

According to Eq. (9.14), m should be greater than 0 and less than 1, therefore the exponent n is between 0.5 and 1.

At the critical point, where $t = \bar{T}$, $l = L$ and $m = 0$, the Sh and Ma relationship becomes

$$Sh = Ma^{0.5} Sc^{0.25}$$

Or express generally as

$$Sh = Ma^{n} Sc^{a}$$

It indicates that the exponent n of Ma is 0.5 at the beginning of Marangoni convection appearance, and n is gradually increased with increasing Ma as t and l becoming smaller to make m larger. Note that the extent of n increase is dependent on the nature of the process concerned.

The exponent n is affected by many factors, such as Re_L of liquid phase, Re_G of gas phase, physical property of the system, structure of the equipment, depth of the liquid (Ra effect), concentration and temperature (Ma and Ma_h effect) etc. For instance, the falling film experiment of desorption by Yu indicated that the value of n is varied with the Reynolds number Re_L of the flowing liquid [18]. Thus different values of n were reported in literature by different authors under their specific experimental conditions.

Zhou gave $n = 0.452$ [15] for desorption of falling aqueous isopropanol, ether and acetone in uprising nitrogen; Sun reported $n = 0.5 \pm 0.05$ [13, 14]; Imaishi obtained $n = 0.6$ [20] for acetone desorption under short liquid-gas contacting time and $Re = 80$. Brian reported $n = 0.5$, $n = 1.01$ [21] and also n between 0.25 and 0.5 [22, 23] under different conditions. Hozawa presented $n = 0.4 \pm 0.1$ [24] for desorption of aqueous methanol, ether, acetone and triethanolamine. Golovin considered n was between 1/3 and 1 [25, 26]. Fujinawa obtained $n = 1.05$ [27] in

agitation system with Re = 10,000. Olander [28] and Sawistowski [29] reported n = 1 from their experiment of extraction with agitation.

Although the exponent n reported is quite different, it can be considered that n is about 0.45–0.6 for desorption process. In the process with agitation, n can be around 1 as it is in the chaos (highly turbulent) condition.

Sun gave the following relationship by solving the dimensionless disturbance equation [13, 30] for the roll cell convection at interface:

$$Sh = 1 + 2AI\left(\frac{Ma - Ma_{\mathrm{cr}}}{Ma_{\mathrm{cr}}}\right)$$

and for the hexagonal cell convection:

$$Sh = 1 + 12B^2 I\left[1 + \frac{A}{B^2}\left(\frac{Ma - Ma_{\mathrm{cr}}}{Ma_{\mathrm{cr}}}\right)\right]^{\frac{1}{2}} + 12B^2 I\left[1 + \frac{A}{2B^2}\left(\frac{Ma - Ma_{\mathrm{cr}}}{Ma_{\mathrm{cr}}}\right)\right]$$

where the parameters A, B and I are function of Bi and $\frac{Ma}{Ma_{\mathrm{cr}}}$, which can be obtained by the regression of experimental data.

9.8 Simulation of Rayleigh Convection

9.8.1 Mathematical Model

As observed from experimental work, the mass transfer through horizontal interface is affected by the Rayleigh convection created by the density difference between interface and the main fluid.

Sha established the mathematical model and analyzed the results of simulation for the gas absorption with Rayleigh effect [10, 31]. The simulated object is shown in Fig. 9.27.

Assumptions

(1) The Marangoni number of the liquid-gas mass transfer is negative, $Ma < 0$;
(2) All physical properties except density are constant;
(3) Linear relationship between absorbed species (solute) concentration and density;
(4) The interface is flat, no deformation;
(5) The rate of mass transfer is small.

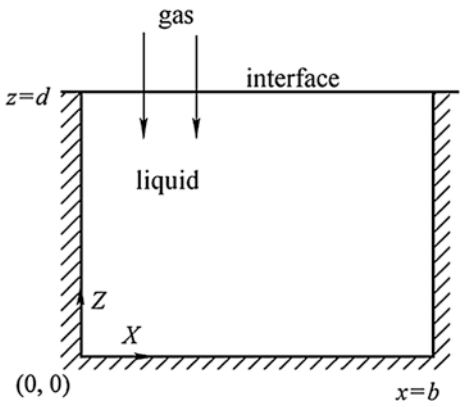

Fig. 9.27 Rayleigh convection simulation

Model equations

$$\frac{\partial u}{\partial x_i} = 0$$

$$\frac{\partial u}{\partial t} + u\frac{\partial u}{\partial x_i} = -\frac{1}{\rho}\frac{\partial p}{\partial x_j} + \frac{\mu}{\rho}\frac{\partial^2 u}{\partial x_i^2} + \boldsymbol{S}$$

$$\frac{\partial c}{\partial t} + u\frac{\partial u}{\partial x_i} = D\frac{\partial^2 c}{\partial x_i}$$

$$\boldsymbol{u} = (u, w)$$

$$\boldsymbol{S} = -\left(0, \frac{\rho' g}{\rho}\right)$$

$$\rho' = \rho(1 + R_\rho(c - c_0))$$

where u and w are respectively the liquid velocity (liquid element or cluster motion) component in x (horizontal, parallel to the interface) and z directions (vertical, perpendicular to the interface); D is the diffusivity of solute in liquid phase; c is the solute concentration in liquid phase; c_0 is the solute concentration in main liquid; g is gravitational acceleration; ρ' and ρ are respectively the density of liquid with concentration c and c_0; $R_\rho = \frac{1}{\rho}\left(\frac{\partial \rho}{\partial c}\right)_{p,T}$ is a constant.

Combining the static pressure of the fluid to the pressure term, the following two-dimensional flow and mass transfer equation set is established:

$$\frac{\partial u}{\partial x}+\frac{\partial w}{\partial z}=0$$

$$\frac{\partial u}{\partial t}+u\frac{\partial u}{\partial x}+w\frac{\partial u}{\partial z}=-\frac{1}{\rho}\frac{\partial p}{\partial x}+v\left(\frac{\partial^2 u}{\partial x^2}+\frac{\partial^2 u}{\partial z^2}\right)$$

$$\frac{\partial w}{\partial t}+u\frac{\partial w}{\partial x}+w\frac{\partial w}{\partial z}=-\frac{1}{\rho}\frac{\partial p}{\partial z}+\frac{\mu}{\rho}\left(\frac{\partial^2 w}{\partial x^2}+\frac{\partial^2 w}{\partial z^2}\right)-gR_\rho(c-c_0)$$

$$\frac{\partial c}{\partial t}+u\frac{\partial c}{\partial x}+w\frac{\partial c}{\partial z}=D\left(\frac{\partial^2 c}{\partial x^2}+\frac{\partial^2 c}{\partial z^2}\right)$$

The initial and boundary conditions are:

At $t = 0$, $u = w = 0$, $c = c_0$;

When $t > 0$, no slip and solute penetration conditions are applied to the solid wall:

At $x = 0$, $u = w$=0, $\frac{\partial c}{\partial x}=0$

At $x = b$, $u = w$=0, $\frac{\partial c}{\partial x}=0$

At $z = 0$, $u = w$=0, $\frac{\partial c}{\partial z}=0$

At interface, $z = d$, $w = 0$, $\frac{\partial u}{\partial z}=0$

The solute transferred from gas phase to liquid phase should go through Gibbs adsorption layer (see Sect. 9.11), the boundary condition is:

$$-D\frac{\partial c}{\partial z}=k_{\mathrm{G}}(p_{\mathrm{c}}-mc_I)+S_{\mathrm{Gibbs}}$$

where k_{G} is the gas phase film mass transfer coefficient; p_{c} is the partial pressure of solute in gas phase; c^{I} is the solute concentration at interface; m is the Henry constant ($m=\frac{p_{\mathrm{c}}^*}{c_{\mathrm{I}}}$, p_{c}^* is the partial pressure of the solute in equilibrium with c_{I}); S_{Gibbs} is the source term representing the influence of Gibbs adsorption layer to the mass transfer, which can be neglected due to small rate of mass transfer.

The foregoing equation set can be generalized to dimensionless for the convenience of solution and analysis.

Let d, $\frac{\mu}{\rho d}$, $\frac{c_\infty}{m}-c_0$, $\frac{d^2\rho}{\mu}$, $\frac{\mu^2}{\rho d^2}$ be the scalar length, velocity, concentration, time pressure; the following dimensionless parameters can be formed:

$$U=\frac{ud\rho}{\mu},W=\frac{wd\rho}{\mu},X=\frac{x}{d},Z=\frac{z}{d},$$

$$C=\frac{c}{(c_{\mathrm{I}}/m)},\tau=\frac{t\mu}{\rho d^2},P=\frac{pd^2\rho}{\mu^2},P_{\mathrm{c}}=\frac{p_{\mathrm{c}}d^2\rho}{\mu^2}$$

The dimensionless equation set and boundary conditions are obtained as follows:

$$\frac{\partial U}{\partial X}+\frac{\partial W}{\partial Z}=0$$

$$\frac{\partial U}{\partial \tau}+U\frac{\partial U}{\partial X}+W\frac{\partial U}{\partial Z}=-\frac{\partial P}{\partial X}+\left(\frac{\partial^2 U}{\partial X^2}+\frac{\partial^2 U}{\partial Z^2}\right)$$

$$\frac{\partial W}{\partial \tau}+u\frac{\partial W}{\partial X}+w\frac{\partial W}{\partial Z}=-\frac{\partial P}{\partial Z}+\left(\frac{\partial^2 W}{\partial X^2}+\frac{\partial^2 W}{\partial Z^2}\right)-\frac{Ra}{Sc}C$$

$$\frac{\partial C}{\partial \tau}+U\frac{\partial C}{\partial X}+W\frac{\partial C}{\partial Z}=\frac{1}{Sc}\left(\frac{\partial^2 C}{\partial X^2}+\frac{\partial^2 C}{\partial Z^2}\right)$$

The initial and boundary conditions are:

At $\tau=0, \quad U=W=0, \quad C=0$

At $\tau>0, \quad X=0, \quad U=W=0, \quad \dfrac{\partial C}{\partial X}=0$

$$X=b/d, \quad U=W=0, \quad \frac{\partial C}{\partial X}=0$$

$$Z=0, \quad U=W=0, \quad \frac{\partial C}{\partial Z}=0$$

$$Z=1, \quad W=0, \quad \frac{\partial U}{\partial Z}=0 \quad -\frac{\partial C}{\partial Z}=Bi_{\mathrm{m}}(P_c-mC^*)+S$$

The dimensionless groups *Ra*, *Sc*, *Bi* in the equation set are:

$$Ra=\frac{g(c^*-c_0)\beta_{\mathrm{c}}d^3}{\nu D}, \quad Sc=\frac{\mu}{\rho D}, \quad Bi_{\mathrm{m}}=\frac{k_{\mathrm{G}}d}{D}$$

where Bi_{m} is the *Bi* for mass transfer in gas phase, the subscript *m* will be omitted in Sect. 9.8.2.

9.8.2 *Result of Simulation and Analysis [10, 31]*

The dimensionless equation set involves three dimensionless groups *Ra, Sc* and *Bi*. By designating the values of these three dimensionless groups for a specific mass transfer process, the Rayleigh convective flow and the solution of model equations can be obtained. In industrial equipment, the corresponding *Ra* number is usually large and far from the critical Ra_{cr}. Thus we chose larger *Ra* for investigation. As the mass transfer is also affected by the condition of gas phase, different *Bi* is adopted for study its effect.

(1) **Rayleigh-convection and interface renewal**

Take the absorption of CO_2 by ethanol as an example. The dimensionless groups chosen are *Bi* = 1, *Sc* = 200 and *Ra* = 10^8 which is far from Ra_{cr}. The simulated

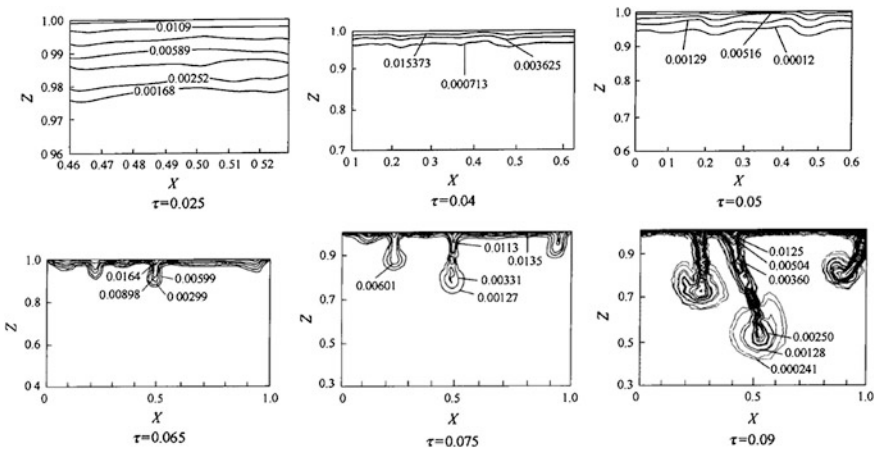

Fig. 9.28 The solute concentration contour at different time for the absorption of CO_2 by ethanol (Bi = 1, Ra = 10^8, Sc = 200) (reprinted from Ref. [31], Copyright 2002, with permission from CIESC)

results are shown in Figs. 9.28 and 9.29, the former displays dimensionless CO_2 contours at different dimensionless time, and the latter displays the dimensionless velocity contours at different dimensionless time.

As seen from Fig. 9.28, at the beginning ($\tau < 0.005$) of mass transfer, the concentration contour is almost flat as the mass transfer is only by molecular diffusion. At $\tau = 0.065$, sudden change is seen at the interface due to the formation of individual Rayleigh convection to force some local interfacial fluid cells moving downward. The corresponding velocity contour of individual Rayleigh convection is shown in Fig. 9.29 ($\tau < 0.005$). As seen in the figure, the couples of opposite eddy flow (small Rayleigh convection) carry the local aqueous solute cells apart from interface; the vacancy at the interface is refilled instantly by the flash bulk fluid cells. The moving downward interfacial cells are interacting with the Rayleigh fluid convection to form inverted mushroom shape of concentration vortex as seen in Fig. 9.28 at $\tau = 0.09$. Compared with Fig. 9.5, the simulated result is similar with the Schlieren picture where the line of reflective index is equivalent to the concentration contour.

The renewal of interfacial cells demonstrates the effect of Rayleigh convection in enhancing the mass transfer and promoting the mixing of the interfacial fluid with the bulk liquid. Obviously, the enhancement factor F of mass transfer is increased with increasing Rayleigh convection or Ra number.

(2) **Analysis of interfacial concentration**

Under the condition of $Bi = 1, Sc = 200, Ra = 10^8$, the variation of dimensionless concentration with time at the central point of interface is given in Fig. 9.30.

At the beginning of CO_2 absorption by ethanol ($\tau = 0$), the solute absorbed is accumulated at the interface to raise the interfacial concentration ($\tau = 0.06$).

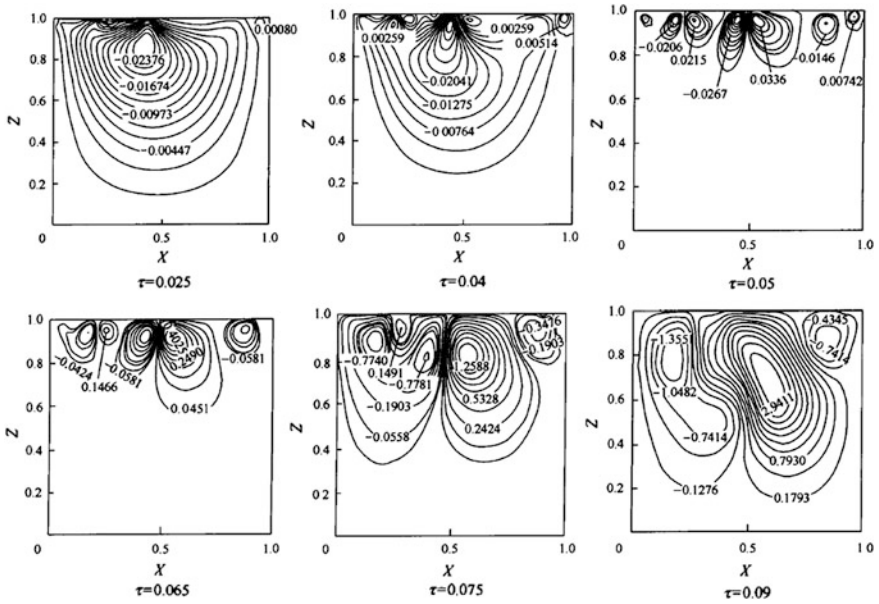

Fig. 9.29 The contour of liquid cell moving velocity at different time for the absorption of CO_2 by ethanol ($Bi = 1$, $Ra = 10^8$, $Sc = 200$) (reprinted from Ref. [31], Copyright 2002, with permission from CIESC)

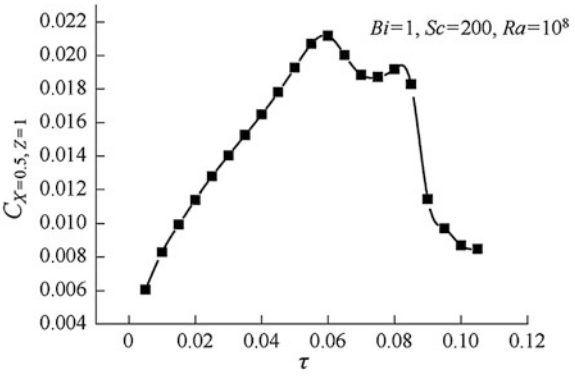

Fig. 9.30 Variation of solute concentration at the center of interface for CO_2 absorption by ethanol [10]

Following the initiation of Rayleigh convection, some interfacial cells are carrying down to the bulk liquid by the convection stream so as to lower the interfacial concentration as seen Fig. 9.30 at $\tau = 0.06$. At this time, the supplement of fresh fluid to renew the interface is insufficient. The lowering of interfacial concentration means the greater driving force of transferring solute, then the interfacial concentration is raised again slightly. After $\tau = 0.08$, the Rayleigh convection is gradually established to increase the renewval of interfacial cells but not yet sufficient to compensate the solute depletion. At $\tau = 0.1$ the interface is almost renewed and the

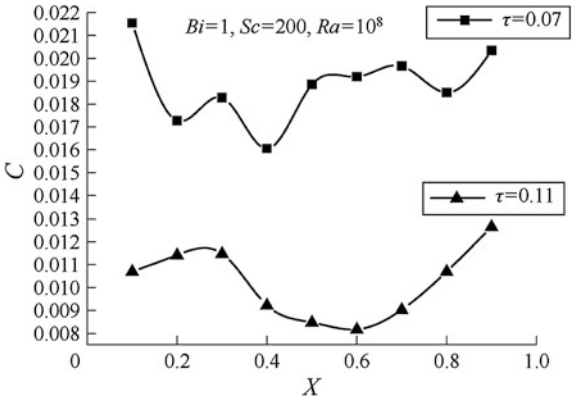

Fig. 9.31 Solute concentration at different position of interface and at different time for CO_2 absorption by ethanol (reprinted from Ref. [31], Copyright 2002, with permission from CIESC)

interfacial concentration lowering is suppressed or even begin to raise up. Thus the interfacial concentration is oscillating up and down.

The oscillating variation of interfacial concentration by the action of Rayleigh convection is stochastic, thus at different positions of interface, the $C - \tau$ curve (concentration-time) is different. Figure 9.31 give the solute concentration at

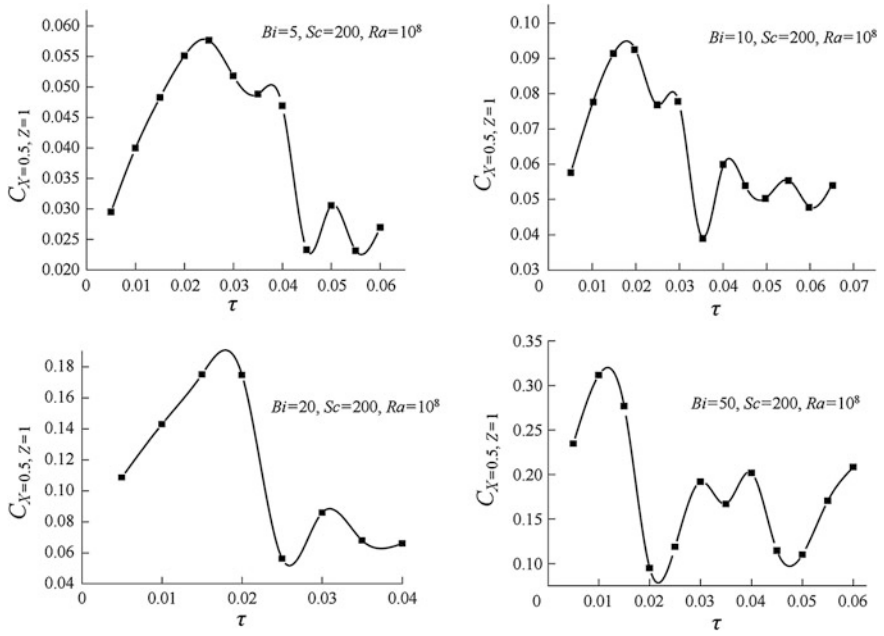

Fig. 9.32 Solute concentration at the center of interface and at different *Bi* for CO_2 absorption by ethanol [10]

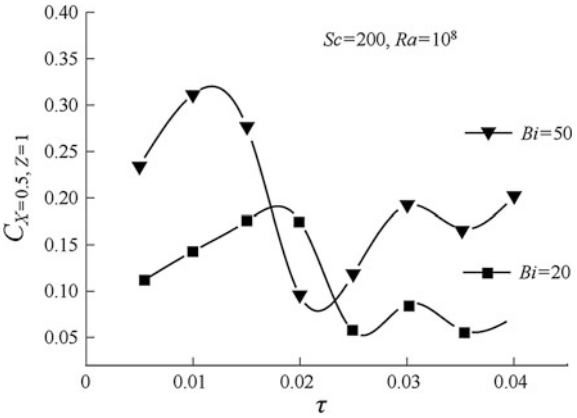

Fig. 9.33 Solute concentration at the center of interface and Bi = 20, 50 for CO_2 absorption by ethanol (reprinted from Ref. [31], Copyright 2002, with permission from CIESC)

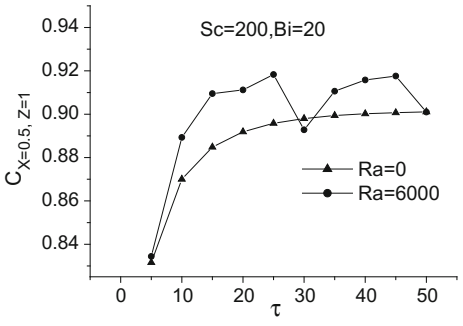

Fig. 9.34 Solute concentration at center of interface at different Ra number for CO_2 absorption by ethanol

different position of interface and at different time. It demonstrates that the interfacial concentration in non-uniform in position and changing with time.

The transfer of solute from gas to liquid depends on the resistance of both sides which can be represented by the Biot number $\left(Bi = \frac{k_G d}{D}\right)$. The influence of interfacial concentration by Bi number is shown in Fig. 9.32 by the $C - \tau$ curve at the center of interface under Bi = 5, 10, 20, 50. As seen in the figure that maximum interfacial concentration is lowered with increasing Bi number, although their concentration oscillating shape are similar. For more detailed comparison, the $C - \tau$ curve is drawn for Bi = 20, 50 in the same coordinate as shown in Fig. 9.33. At high Bi, the gas phase resistance is low to facilitate the solute transfer, so that the average interfacial concentration is higher.

The intensity of Rayleigh convection, which is represented by Ra number, is another influential factor to the interfacial concentration. Figures 9.34 and 9.35 shows the variation of solute concentration at the center of interface with different Ra number. With increasing Ra, the intense Rayleigh convection promotes the interface renewal so that the solute concentration at the interface is increased with increasing Ra. In Fig. 9.34, the point representing Ra = 6800 at $\tau = 30$ is obviously in error.

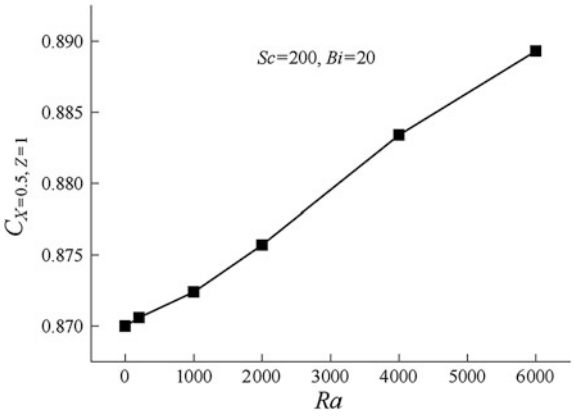

Fig. 9.35 Solute concentration at center of interface versus *Ra* number for CO_2 absorption by ethanol

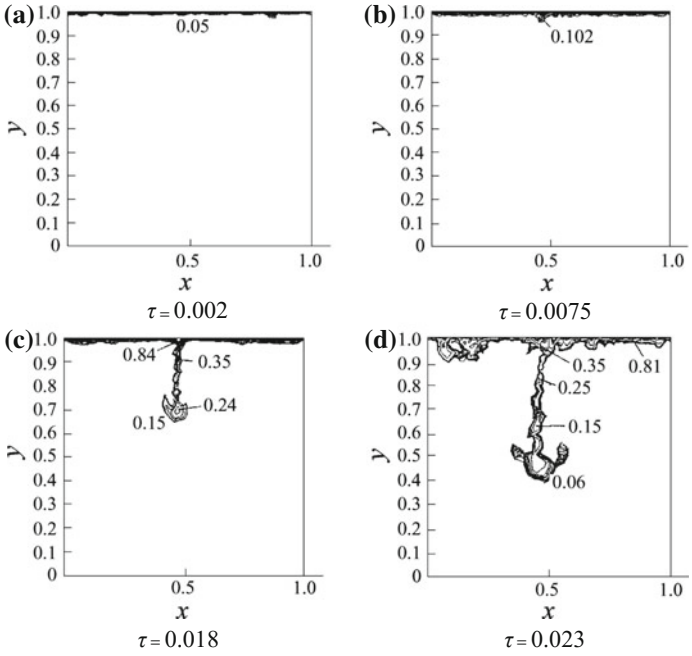

Fig. 9.36 Contour of solute concentration at different time for CO_2 absorption by ethanol ($Ra = 10^8$, $Sc = 200$, $Bi = \infty$) **a** $\tau = 0.002$, **b** $\tau = 0.0075$, **c** $\tau = 0.018$, **d** $\tau = 0.023$

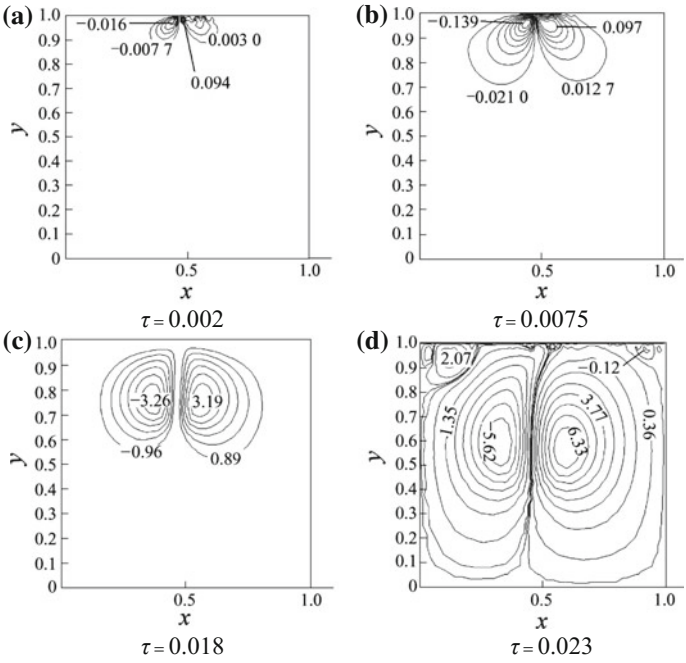

Fig. 9.37 Contour of liquid phase convection velocity at different time for CO_2 absorption by ethanol ($Ra = 10^8$, $Sc = 200$, $Bi = \infty$) **a** $\tau = 0.002$, **b** $\tau = 0.0075$, **c** $\tau = 0.018$, **d** $\tau = 0.023$

(3) **Rayleigh-convection at** $Bi = \infty$

For the case of $Bi \to \infty$, it is worthy to mention. Under such condition, the mass transfer from gas phase to the interface will be no resistance, thus the interfacial concentration will remain at constant and in equilibrium with the partial pressure of gas phase. For this case, the boundary conditions of the model equations in Sect. 9.8.1 for mass transfer should be changed to $c = c^*$ at $z = d$, where c^* is the interfacial solute concentration in equilibrium with the partial pressure of gas phase. The simulated results of dimensionless solute concentration and convection velocity at $Ra = 10^8$ and $Sc = 200$ are shown respectively in Figs. 9.36 and 9.37. They are similar to Figs. 9.34 and 9.35 except the early appearance of Rayleigh convection because the interfacial concentration at the beginning is c^* and not need any time for transferring solute from gas phase to the interface. Besides, small Rayleigh convection is also appear near the wall due to the wall effect.

9.9 Experimental Measurement of Rayleigh Convection

Chen used particle image velocimeter (PIV) to measure and study Rayleigh convection [32]. The experimental setup is shown in Fig. 9.38.

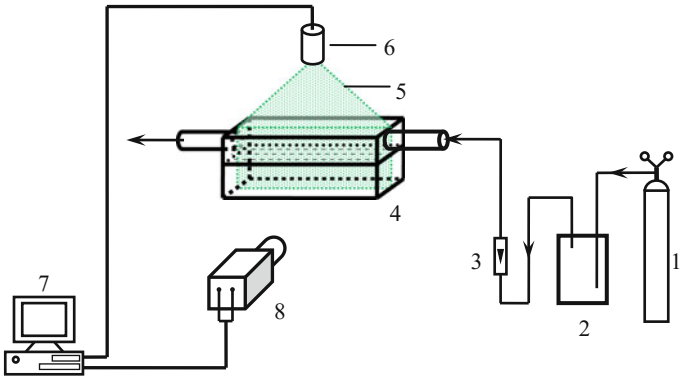

Fig. 9.38 Experimental setup for the measurement of Rayleigh convection (*1* nitrogen vessel, *2* gas purifier and presaturator, *3* rotameter, *4* interfacial mass transfer simulator, *5* laser sheet, *6* laser head, *7* computer, *8* CCD camera)

The PIV system used in this study were made by a double cavity Nd-YAG laser with a maximum energy of 200 mJ and a wavelength of 532 nm as the light source. The laser beam, with a 10 ns duration of the pulsed illumination, had a variable pulse frequency up to 15 Hz. The laser was also equipped with a lens system to produce a diverging laser sheet with a thickness not exceeding 1 mm. A CCD camera with resolution of 1376 × 1040 pixels was used to capture the images, and was equipped with a filter with a wavelength of 532 nm to capture only the light scatted from the laser lightened particles. Hollow glass microspheres with diameters of 8–12 μm were seeded in the liquid as tracer particles. The laser was run at 4 Hz and the measurement time was 30 s. The PIV system grabbed and processed the digital particle images utilizing the cross-correlation approach of the FlowMaster software to give the measured velocity vector.

The interfacial mass transfer simulator was made of quartz glass with an inner size of 200 mm in length, 20 mm in width and 40 mm in height. The liquid was initially quiescent in the simulator with a thickness of 10 mm. Nitrogen gas successively passed through activated carbon, silica gel and molecular sieve to remove the impurities and water, and then pre-saturated by the solvent in a tank in order to reduce the influence of solvent evaporation. The liquid was likewise pre-saturated by nitrogen gas to avoid the gas absorption into the liquid. The liquid concentrations near the gas inlet and outlet positions of the simulator were measured by the gas chromatography.

The experimental system is desorption of acetone from the binary solution of acetone and ethyl acetate under nitrogen stream. Part of the experimental results are given below [32].

(1) **Velocity vector of Rayleigh convection**

The convection velocity can be obtained by measuring the velocity of tracer particle by the PIV installation at different time as shown in Figs. 9.39 and 9.40.

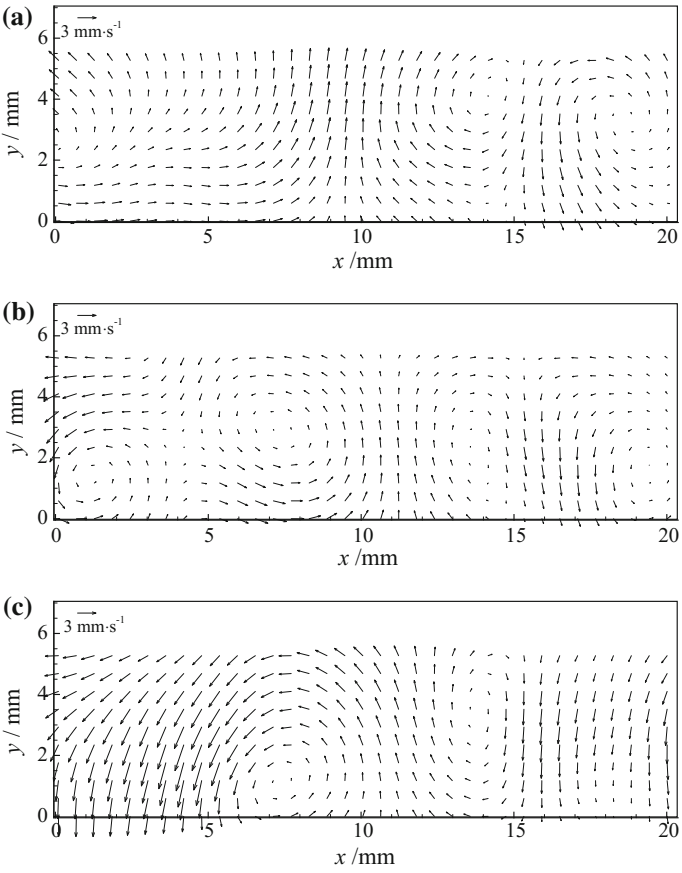

Fig. 9.39 Velocity vector distributions at different times measured by PIV for $Ra = 2.66 \times 10^8$, $Re_G = 13.78$ at different time for the desorption of acetone **a** 5 s, **b** 15 s, **c** 25 s

Figures 9.39 and 9.40 display the velocity distributions perpendicular to the interface of the liquid at different time, Re_L and Re_G of the acetone desorption process. As seen in the figures at $t = 5$ s, two-cell symmetrical convection is clearly formed near the interface (Fig. 9.39a). Following at $t = 15$ s the convection cells are developed and merged into the bulk liquid. At $t = 25$ s, the large convection cells are dissipated, and new smaller convection cells are generated.

Comparing (a–c) in Fig. 9.40, it can be seen that following the increase of Ra and Re_G the scale of velocity vortex becomes larger and the convective vortexes turns to slightly chaos. The convection patterns shown in Fig. 9.40 are found to be in good agreement with the simulated result for Rayleigh convection in previous section.

The velocity distributions shown in Figs. 9.39 and 9.40 are not only due to the Rayleigh convection but also imply the bulk flow convection from the incoming

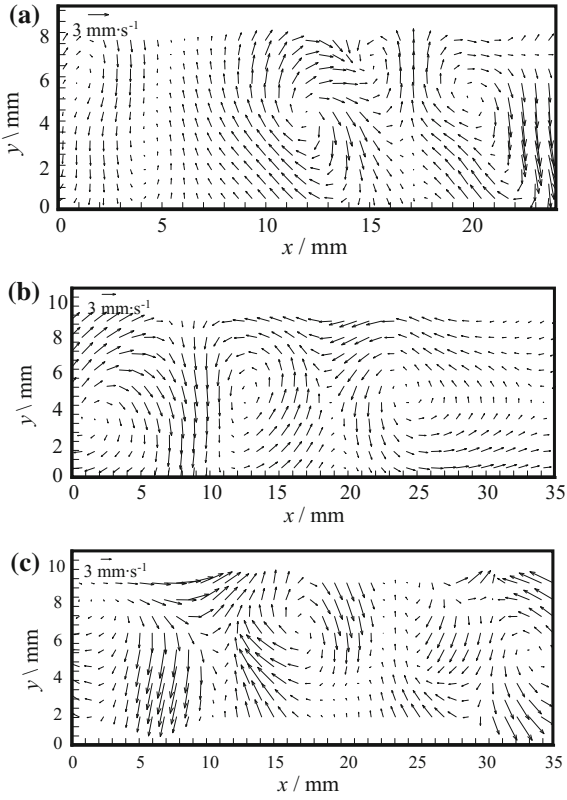

Fig. 9.40 The measured velocity vector by PIV under different conditions for the desorption of acetone **a** $Ra = 8.6 \times 10^6$, $Re_G = 86.25$, **b** $Ra = 8.3 \times 10^7$, $Re_G = 86.25$, **c** $Ra = 8.3 \times 10^7$, $Re_G = 172.5$

liquid, i.e. the small surface flow induced by gas sweeping over the interface and the influence by Marangoni convection. In other words, the Rayleigh convection from interface to the bulk liquid is always accompanied with the convection induced by incoming liquid flow, gas sweeping and the Marangoni convection. However, Rayleigh convection is dominant in the large scale convective flow between interface and the bulk liquid; the other effects are relatively small and uninfluential.

According to the concept of convective flow, the large vortexes formed from the bulk flow and carried the flow energy are soon convert to small scale vortices (eddies) which dissipate afterward in counteracting with the viscous force of the fluid. Thus large eddy simulation (LES) decomposition [33] was employed to filter out the velocity of smaller scale. According to LES decomposition, the measured velocity can be decomposed into a filtered average velocity u_{avg} that forms large eddies and velocity u' that forms small eddies, i.e. $u = u_{avg} + u'$, as shown in Fig. 9.41:

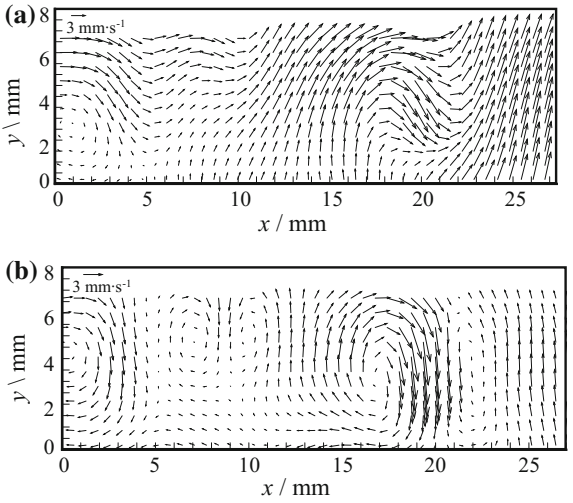

Fig. 9.41 LES decomposition of the velocity field for the desorption of acetone **a** velocity vector field of large scale velocity u_{avg}, **b** velocity vector field of small scale velocity u'

Average convection velocity

As Rayleigh convection caused by the density gradient play the dominant role in the gravitational direction (y direction). Therefore, the time-space averaged velocity in y direction is employed to characterize the Rayleigh convection.

Figure 9.42 shows the time-space averaged vertical velocity u_{avg} versus Ra with different Re_G. The reason that u_{avg} is increased with increasing Re_G is due to the gas flow can renew the solute concentration of gas phase at the interface and promote the convection. Therefore, both high liquid concentration and gas flow rate can enhance the volatilization of acetone.

Average characteristic length

The characteristic scale can be defined as the size of the largest Rayleigh vortex which can be obtained by velocity vector measurement as shown in Fig. 9.40. The characteristic scale L can be decompounded into $L_{u,x}$, $L_{v,x}$, $L_{u,y}$ and $L_{v,y}$, where the

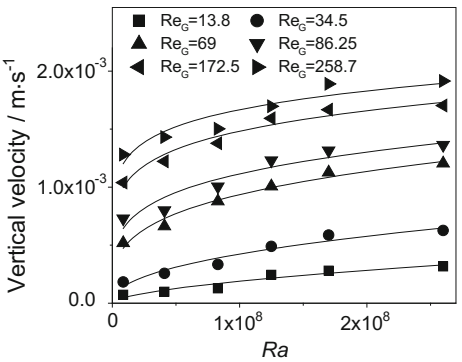

Fig. 9.42 Time-space averaged vertical velocity under different conditions

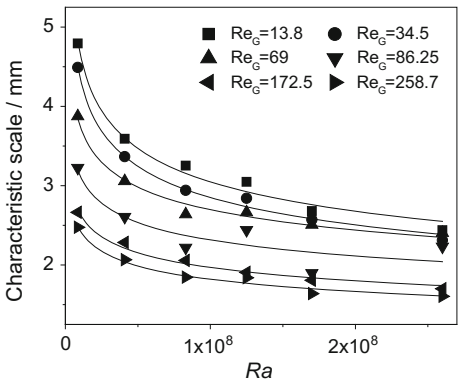

Fig. 9.43 Characteristic scale of Reyleigh vortex under different conditions

first subscript is the u or v velocity components and the second subscript means along the x or y coordinates [34]. Finally, L can be calculated by orthogonal synthesis of $L_{u,x}$, $L_{v,x}$, $L_{u,y}$ and $L_{v,y}$. The time-space averaged characteristic scale L_{avg} is obtained under different Ra and Re_{G} as shown in Fig. 9.43.

From Fig. 9.43, it is found that L_{avg} is decreased exponentially with the increasing of Ra and also decreased with the increasing Re_{G}. Besides, the calculated characteristic scale of the system could be further used to compute the surface residence time for the penetration mass transfer model.

The enhancement factor by Rayleigh convection

The mean mass transfer coefficient during 30 s interval can be obtained for the acetone desorption from acetone-ethyl acetate solution. The measured average mass transfer coefficient $K_{\text{L,exp}}$ can be calculated by the following equation:

$$K_{\text{L,exp}} = \frac{V_{\text{L}}(C_{\text{L},\,0} - C_{\text{L},\,t})/t}{A\overline{(C_{\text{L}} - C_{\text{L}}^{\text{i}})}_{\text{log}}}$$

where V_{L} is the liquid volume; $C_{\text{L,0}}$ is the initial solute concentration of the solution at $t = 0$; $C_{\text{L},\,t}$ is the solute concentration at $t = 30$ s which is estimated by averaging the solute concentrations at the inlet and outlet of the simulator; A is the mass transfer area; $\overline{(C_L - C_{\mathbf{L}}^{\mathbf{i}})}_{\mathbf{log}}$ is the logarithmic average mass transfer driven force between t = 0 s and t = 30 s, i.e.

$$(C_{\text{L}} - C_{\text{L}}^{\text{i}})_{\text{log}} = \frac{(C_{\text{L,in}} - C_{\text{L,in}}^{\text{i}}) - (C_{\text{L,out}} - C_{\text{L,out}}^{\text{i}})}{\ln \frac{(C_{\text{L,in}} - C_{\text{L,in}}^{\text{i}})}{(C_{\text{L,out}} - C_{\text{L,out}}^{\text{i}})}}$$

where superscript i represents the interfacial condition.

For mass transfer process, Zhang derived a model for the overall liquid phase mass transfer coefficient $K_{\text{L,theo}}$ based on the Higbie penetration theory: [28]

$$\frac{1}{K_{\mathrm{L,theo}}} = \frac{1}{2}(\pi\tau)^{0.5}(D_{\mathrm{L}}^{-0.5} + mD_{\mathrm{G}}^{-0.5})$$

where τ is the surface residence time.

In the actual mass transfer process, the liquid mass transfer coefficient is enhanced by the interfacial convection, usually represented by the enhancement factor F as described in previous section. The F factor calculated by Chen [32] for acetone desorption at different Ra and Re_{G} as given in Fig. 9.44. As seen in the

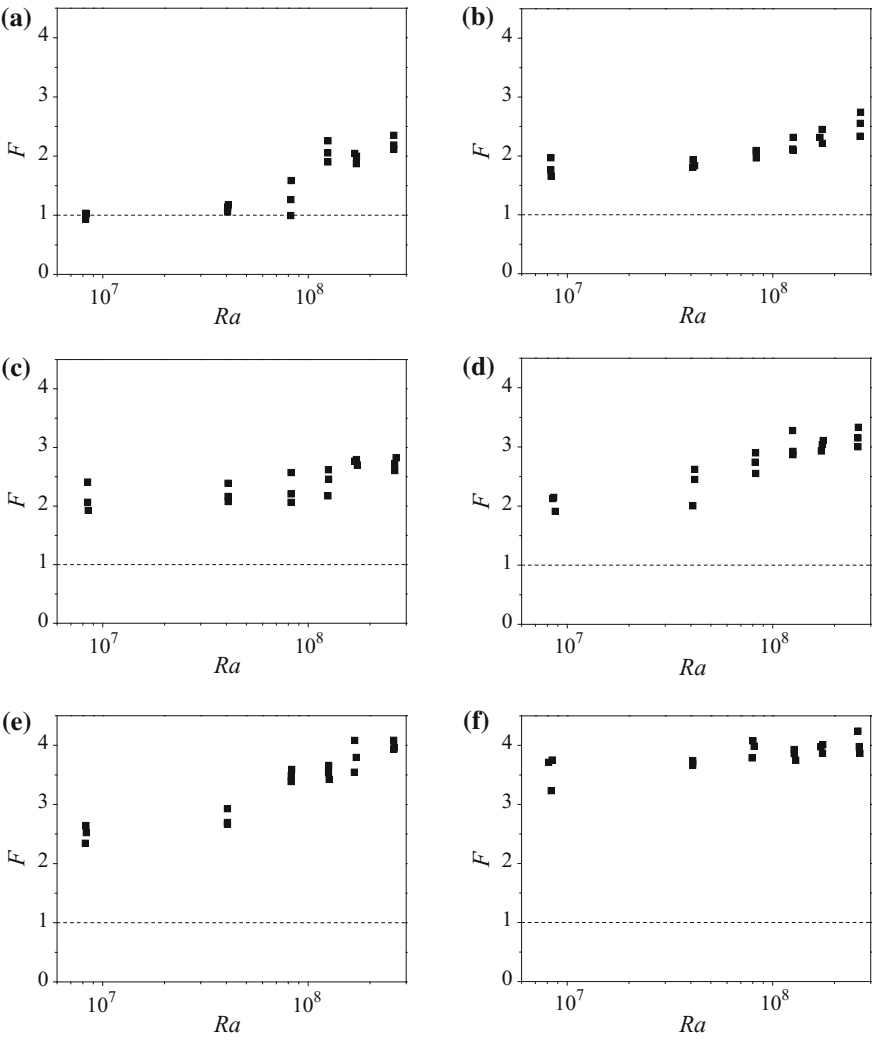

Fig. 9.44 Enhancement factors F for different conditions **a** Re_{G} = 13.78, **b** Re_{G} = 34.45, **c** Re_{G} = 68.90, **d** Re_{G} = 86.12, **e** Re_{G} = 172.25, **f** Re_{G} = 258.4

figure, the F factor increases with increasing Ra and Re_G. The corresponding critical Ra (Ra_{cr} at $F = 1$) is seen around 10^7 at $Re_G = 13.78$.

Figure 9.44 dislays the relationship between enhancement factor F and Ra at different Re_G. It can be seen that, F increased firstly with Ra and Re_G, and became flat when F was up to about 4. This result indicates that the Rayleigh convection can promote the liquid surface renewal and intensify the mass transfer significantly only to a certain limit, which is in consistent with the experimental measurement in Sect. 9.5.2.

The simulated (predicted) mass transfer coefficient

It is difficult to obtain the surface residence time of the liquid for mass transfer processes by experimental measurement. Yet we may consider that the resident time of a solute particle at the interface equal to the traveling time of a solute particle from bulk fluid to the interface in order to avoid solute accumulation or depletion and keep constant solute concentration at the interface. Thus the interfacial residence time of the solute can be computed by the average interfacial velocity and the average characteristic scale. Characteristic scale was referred to the largest turbulent eddy in the fluid as defined in previous section. On the assumption that the interfacial solute renewal is controlled by the large scale vortex ranging from bulk liquid to the interface, the surface residence time can be obtained by the following relationship:

$$\tau = L_{avg}/u_{avg}$$

where u_{avg} and L_{avg} are given respectively in Figs. 9.42 and 9.43.

With the computed surface residence time by foregoing equation, the liquid mass transfer coefficient of liquid phase can also be obtained by applying the Higbie penetration theory as follows:

$$k_L = \sqrt{\frac{4D_L}{\pi\tau}}$$

The computed mass transfer coefficient [32] is shown in Fig. 9.45.

The predicted mass transfer coefficients by applying Higbie penetration theory are seen to be in rough agreement with the experimental data. As seen in the figure, the computed mass transfer coefficients based on the calculated surface residence time are well in agreement with the experimental data for low Re_G number, but the deviations became greater with the increasing Re_G. For low Re_G, the sweeping effect of the gas flow on the liquid surface is weak, and the solute resident time at liquid surface is mainly attribute by Rayleigh convection. While for high Re_G, the gas flow might promote the removal of the solute acetone so that the Rayleigh convection becomes faster to fill up the solute depletion. Thus the simulated results deviate from experimental data at high Re_G is due to ignoring the gas sweeping effect.

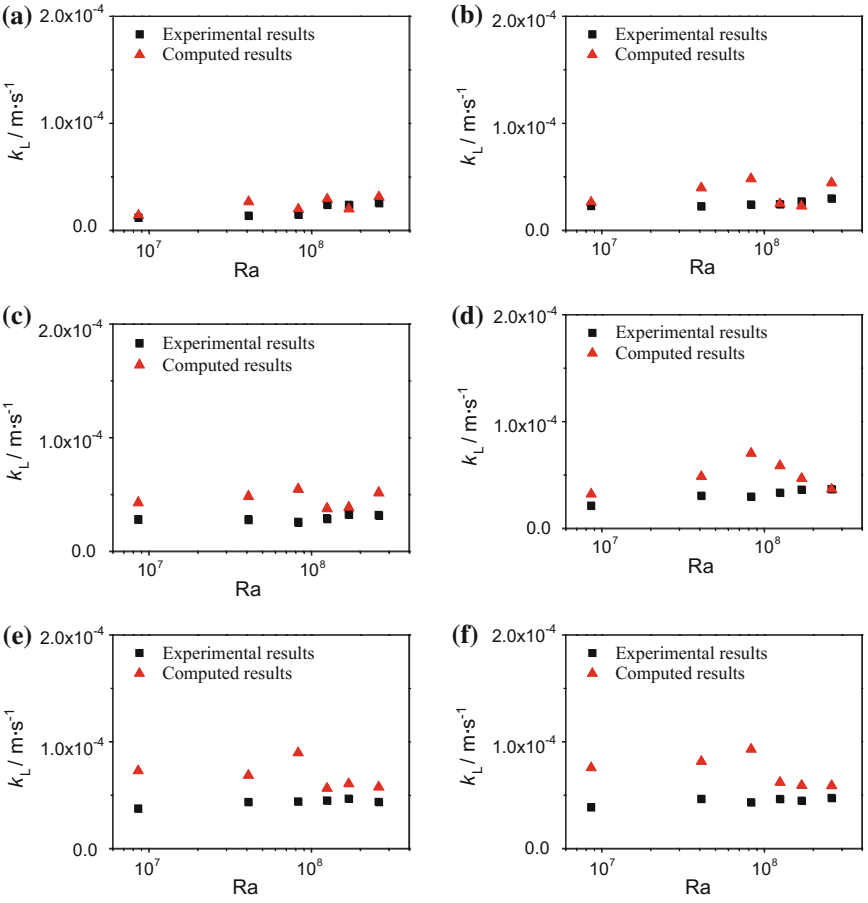

Fig. 9.45 Predicted and measured value of mass transfer coefficient under different conditions **a** Re_G = 13.78, **b** Re_G = 34.45, **c** Re_G = 68.90, **d** Re_G = 86.12, **e** Re_G = 172.25, **f** Re_G = 258.4

9.10 Simulation and Observation of Two-Dimensional Solute Convection at Interface

9.10.1 Simulation of Two-Dimensional Interfacial Concentration

In the foregoing sections, the analysis of interfacial concentration is based on the x-z plane where x and z are respectively the coordinates of interface and perpendicular to the interface. That means the study is on a cross section of the interface in x direction with no concern on y direction. In this section, the study on interface is

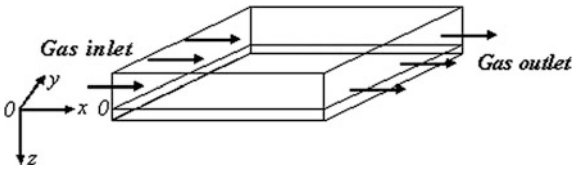

Fig. 9.46 Desorption model of horizontal stagnant liquid by gas stream

considered two dimensional in x and y directions. In this section, the study on interface is considered two dimensional in x and y directions.

Yu simulated the desorption of aqueous ethanol in horizontal manner and the physical model is as shown in Fig. 9.46, with unsteady three-dimensional model [7] to obtain the solute distribution on x-y and x-z planes. Some of the simulated results are given below.

9.10.1.1 Model Equations

The assumption of model simulation is similar to that in Sect. 9.8.1. The model equations are as follows:

$$\frac{\partial \mathbf{u}}{\partial x_i} = 0, \quad u = (u, v, w)$$

$$\frac{\partial \mathbf{u}}{\partial t} + \mathbf{u}\frac{\partial \mathbf{u}}{\partial x_i} = \frac{1}{\rho_{\mathrm{L}}}\left[-\frac{\partial p}{\partial x_j} + \mu_L\left(\frac{\partial^2 \mathbf{u}}{\partial x_i}\right) + S_{\mathrm{F}}\right]$$

$$S_{\mathrm{F}} = (F_{\mathrm{LG}}, F_{\mathrm{LG}} + g)$$

$$\frac{\partial c}{\partial t} + \mathbf{u}\frac{\partial c}{\partial x_i} = D\frac{\partial^2 c}{\partial x_i}$$

where S_{F} is the source term representing the liquid–gas interfacial shearing force in x, y, z directions.

In order to transform the model equation to dimensionless, let length, velocity, time and concentration be d_{L}, D/d_{L}, d_{L}^2/D and C; where d_{L} is the thickness of the liquid layer (10 mm in present simulation).

The initial and boundary conditions as well as the calculation of source term can be found from Ref. [7].

The object of simulation is the desorption of ethanol (solute) from aqueous ethanol by nitrogen stream. It is an unsteady process. For the convenience of expression, dimensionless time $\tau' = t\frac{D}{d_{\mathrm{L}}^2}$ is adopted in the subsequent figures. The simulation is ranging from very short time at the beginning $(\tau' = 1.0 \times 10^{-8})$ to the very long time $(\tau' = 3.5 \times 10^{-2})$.

9.10.1.2 Simulated Results

(A) **Interfacial velocity and solute concentration distributions**

Figures 9.47 and 9.48 display respectively the simulated distributions of liquid velocity and solute concentration on *x*-*y* plane.

At the beginning of desorption ($\tau' = 1.0 \times 10^{-8}$), few small scale velocity eddies appear and no appreciable vortex is formed. It follows that only few concentration eddies are displayed, indicating that the surface tension difference established at the interface is not sufficient to initiate Marangoni convection.

Following the time progress to $\tau' = 3.0 \times 10^{-7}$, some local circular convection is formed by the combination of neighboring small eddies, indicating the evolution of local disturbance. Further development of the local disturbance will promote the formation of Maragoni convection.

At $\tau' = 2.5 \times 10^{-5}$, the local convection grows up to form large circular flow indicating the appearance of Marangoni convection and interfacial structure. The concentration eddies are in different scale distributed at the interface.

After sufficient long time, $\tau\prime > 2.5 \times 10^{-2}$, the ethanol in the stagnant liquid is depleted by desorption, the interfacial ethanol concentration as well as the

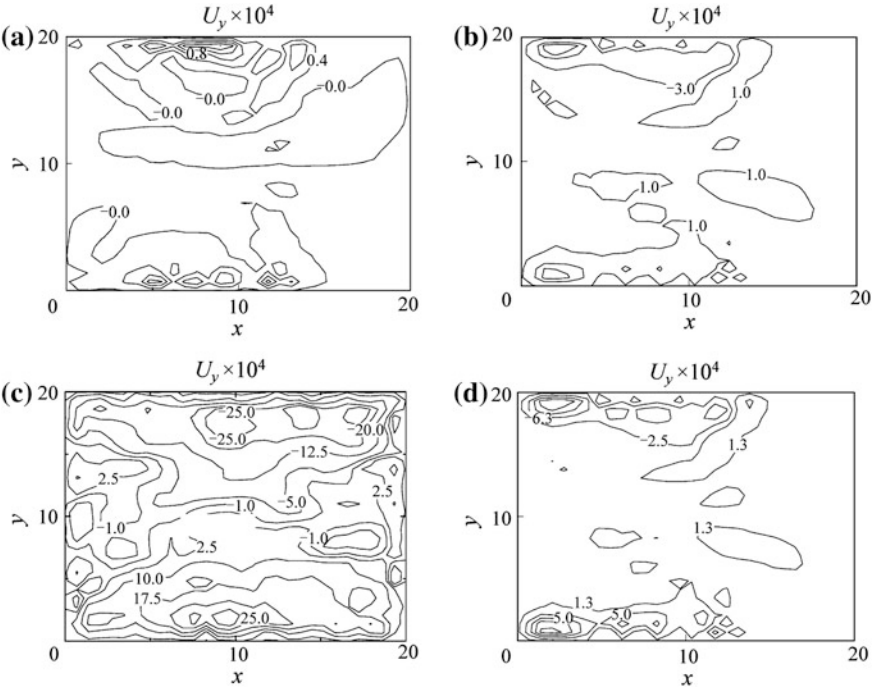

Fig. 9.47 Interfacial liquid velocity contours for horizontal desorption of aqueous ethanol ($Re_G = 20$, $c_0 = 0.5$ mol m^{-3}). **a** $\tau' = 1.5 \times 10^{-8}$, **b** $\tau' = 3.0 \times 10^{-7}$, **c** $\tau' = 2.5 \times 10^{-5}$, **d** $\tau' = 1.2 \times 10^{-2}$ (reprinted from Ref. [35], Copyright 2008, with permission from Elsevier)

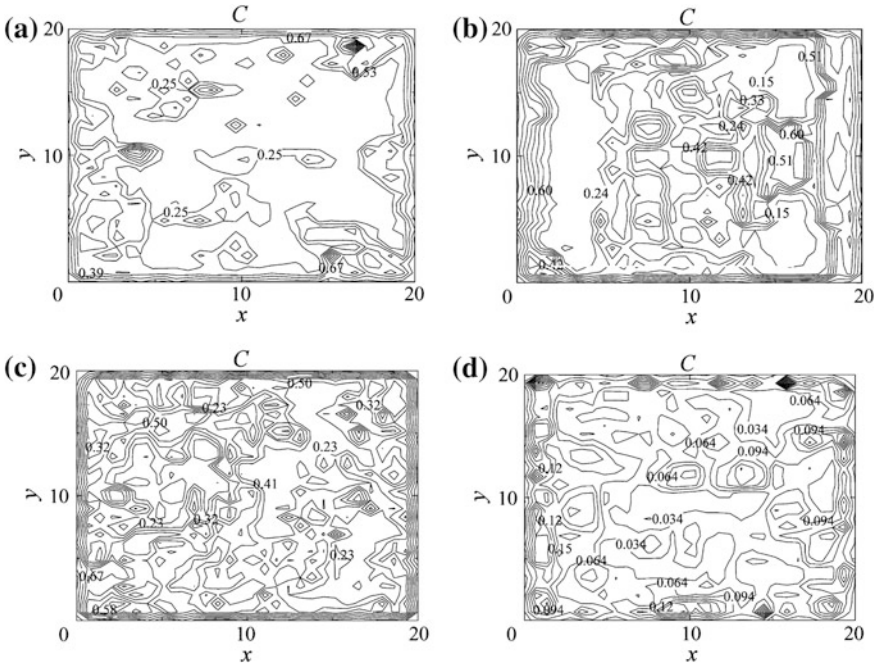

Fig. 9.48 Interfacial solute concentration contours for horizontal desorption of aqueous ethanol ($Re_G = 20$, $c_0 = 0.5$ mol m^{-3}) **a** $\tau' = 1.5 \times 10^{-8}$, **b** $\tau' = 3.0 \times 10^{-7}$, **c** $\tau' = 2.5 \times 10^{-5}$, **d** $\tau' = 1.2 \times 10^{-2}$

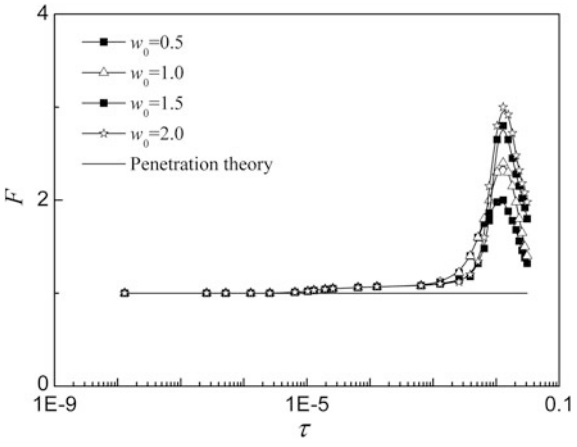

Fig. 9.49 Enhancement factor at different time for the desorption of stagnant aqueous ethanol

local Δc is decreased so that the Marangoni convection is depressed and gradually vanished.

(B) **Enhancement factor**

The calculated enhancement factor F at different time for the desorption of stagnant aqueous ethanol in nitrogen stream is shown in Fig. 9.49.

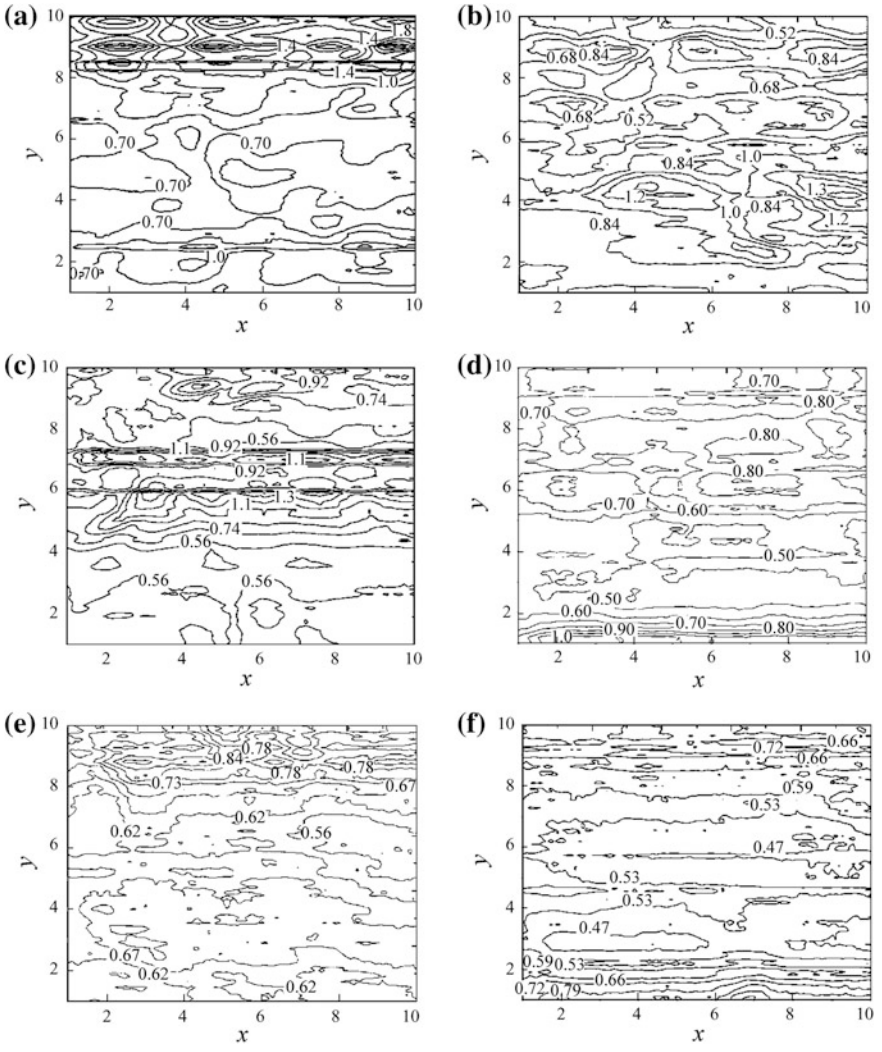

Fig. 9.50 Experimental observation of interfacial solute concentration gradient for aqueous acetone desorption at different time **a** ~0 s, **b** 30 s, **c** 60 s, **d** 90 s, **e** 120 s, **f** 150 s (reprinted from Ref. [35], Copyright 2008, with permission from Elsevier)

At the beginning stage before dimensionless time $\tau' = 1 \times 10^{-5}$, the local surface tension difference Δc is not great enough to create Marangoni convection and therefore $F = 1$. The critical point is seen to appear around $\tau' = 1 \times 10^{-5}$ and F is increased afterward until reaching the maximum at

$\tau' = 1 \times 10^{-2}$. Then due to the continuous depletion of ethanol to make the interfacial ethanol concentration decreasing, which tends to lowering the Δc and dropping the F factor. Such tendency is in agreement with the works published in literature [36, 37].

9.10.2 *Experimental Observation of Interfacial Concentration Gradient*

Besides mathematical simulation, Liu obtained the interfacial concentration gradient by analysing the light intensity distribution of the Schlieren image on *x*-*y* plane for the desorption of acetone from its aqueous solution under nitrogen stream as shown in Fig. 9.50 [35].

As seen from Fig. 9.50, at the beginning period of desorption, the interface displays instantly some disordered concentration gradients in small scale which are not great enough to induce Marangoni convection. Following the progress of desorption, the concentration gradient is increased to form some larger concentration vortex, although these figures is not so clear.

In brief, both simulation and observation in this section indicate that, for the $Ma > 0$ liquid–gas mass transfer process, the velocity and concentration gradients always occur at the interface to form velocity and concentration eddies in large or smalls scales; they are developed and vanished in alternation until sufficient surface tension is established to initiate the interfacial Marangoni convection.

9.11 Marangoni Convection at Deformed Interface Under Simultaneous Mass and Heat Transfer

In the foregoing sections, the interface is considered as a horizontal or vertical plane without deformation. Actual observation reveals that in the liquid-gas flowing process the contacting interface is always in wavy or ripply form. Such condition is considered in this section.

For simplifying the problem, the simulated object is the liquid-gas contacting falling film with wavy interface as shown in Fig. 9.51. The simulation is on the two dimensional *x*-*z* plane. Xiao established the model equation and give the simulated results as follows [12].

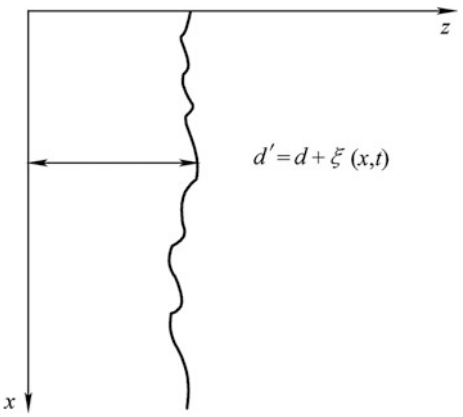

Fig. 9.51 Falling film with wavy interface

9.11.1 Model Equations

Assumptions

- The mass and heat transfer are taken place simultaneously in the direction between the wall and the interface (z direction in the figure) in order to avoid the Rayleigh convection. Thus the gravitational influence (Rayleigh convection) can be ignored;
- The velocity of both liquid and gas is low so that the drag force between gas and falling liquid is neglected;
- The mass of liquid phase is substantially constant as the amunt of mass transfer is small.

(1) **Basic equations**

$$\frac{\partial \boldsymbol{u}}{\partial x_i} = 0$$

$$\frac{\partial \boldsymbol{u}}{\partial t} + \boldsymbol{u}\frac{\partial \boldsymbol{u}}{\partial x_i} = \frac{1}{\rho} - \frac{\partial p}{\partial x_i} + \frac{\mu}{\rho}\frac{\partial^2 \boldsymbol{u}}{\partial x_i^2} + \mathbf{S}$$

$$\frac{\partial T}{\partial t} + \boldsymbol{u}\frac{\partial T}{\partial x_i} = \alpha\frac{\partial^2 T}{\partial x_i^2}$$

$$\frac{\partial c}{\partial t} + \boldsymbol{u}\frac{\partial c}{\partial x_i} = D\frac{\partial^2 c}{\partial x_i^2}$$

where $\boldsymbol{u} = (u,w)$ and source term $\boldsymbol{S}$ (gravity) is neglected by assumption.

Since the mass and heat transfer is considered in horizontal (z) direction, the change of liquid temperature and solute concentration with respect to the liquid thickness in z direction can be represented by the following equation:

$$T = T_0 - \beta'_{\mathrm{T}} z$$
$$c = c_0 - \beta'_{\mathrm{c}} z$$

where subscript 0 denotes the condition at $z = 0$, β'_{T} and β'_{c} represent respectively the temperature gradient $\left(\frac{\partial T}{\partial z}\right)$ and concentration gradient $\left(\frac{\partial c}{\partial z}\right)$.

(2) **Disturbance equations**

Let δu(δu,δw), δT, δc, δp are the infinitesimal small disturbance of velocity, temperature, concentration and pressure, we have after disturbance,

$$\boldsymbol{u}' = \boldsymbol{u} + \delta \boldsymbol{u}$$
$$T' = T + \delta T$$
$$c' = c + \delta c$$
$$p' = p + \delta p$$

Substituting $\boldsymbol{u}'$, T', c' and p' to the model equation and neglecting the non-linear term, the following linear disturbance equations are obtained:

$$\begin{aligned}
\frac{\partial \delta \mathbf{u}}{\partial x_i} &= 0 \\
\frac{\partial \delta \boldsymbol{u}}{\partial t} &= -\frac{1}{\rho}\frac{\partial \delta p}{\partial x_j} + \frac{\mu}{\rho}\frac{\partial^2 \delta \mathbf{u}}{\partial x_i^2} \\
\frac{\partial \delta T}{\partial t} &= \alpha \frac{\partial^2 \delta T}{\partial x_i^2} + \beta_T \delta w \\
\frac{\partial \delta c}{\partial t} &= D\frac{\partial^2 \delta c}{\partial x_i^2} + \beta' \delta w
\end{aligned} \tag{9.15}$$

Eliminating δp from Eq. (9.15) and after rotational transformation, we have in z direction,

$$\frac{\partial}{\partial t}\left(\frac{\partial^2 \delta w}{\partial x_i^2}\right) = \frac{\mu}{\rho}\frac{\partial^4 \delta w}{\partial x_i^4}$$

(3) **The effect of interface deformation**

Under the condition of interface deformation, the surface tension σ can be represented by:

$$\sigma = \sigma_f + \frac{\partial \sigma}{\partial T}(T - T_f) + \frac{\partial \sigma}{\partial c}(c - c_f) \tag{9.16}$$

where subscript f denotes the condition of no deformation.
Suppose the quantity of interfacial deformation is $\xi(x,t)$, the thickness of the liquid layer is changed from d to d', then we have:

$$d' = d + \xi(x,t)$$

The temperature and concentration at interface after disturbance become

$$T' = T + \delta T = T_0 - \beta'_{\mathrm{T}} d' + \delta T = T_0 - \beta'_{\mathrm{T}}(d + \xi) + \delta T = T_f - \beta_T \xi + \delta T$$
$$c' = c + \delta c = c_f - \beta'_{\mathrm{c}} \xi + \delta c$$

Substituting to Eq. (9.15) yields:

$$\sigma = \sigma_f + \frac{\partial \sigma}{\partial T}(\delta T - \beta'_{\mathrm{T}} \xi) + \frac{\partial \sigma}{\partial c}(\delta c - \beta'_{\mathrm{c}} \xi) \tag{9.17}$$

(4) **Boundary conditions**

(a) At $z = 0$ (solid wall), the condition of no slip is applied

$$\delta w = 0$$

and from continuity equation gives

$$\frac{\partial \delta w}{\partial z} = 0$$

Take heat balance to yield

$$\lambda \frac{\partial \delta T}{\partial z} = h_{\mathrm{L}}^{\mathrm{S}} \delta T$$

The left hand side of above equation represents the heat transferred by conduction to the solid wall surface at $z = 0$; the right hand side represent the heat transferred between solid wall surface and the bulk liquid; λ is the thermal conductivity; $h_{\mathrm{L}}^{\mathrm{S}}$ is the film coefficient of heat transfer between solid wall surface and bulk liquid.
As no mass is transferred between solid wall and the liquid, it is obvious that $\frac{\partial \delta c}{\partial z} = 0$.

(b) At $z = 1$ (liquid-gas interface), since the interface is deformed, the disturbance velocity should satisfy the following relationship:

$$\delta w = \frac{\partial \xi}{\partial t}$$

In normal direction the force causing interfacial deformation is equal to the force acting by the bulk liquid to the interface [38], that is:

$$\sigma \frac{\partial^2 \xi}{\partial x^2} = -\delta p + 2\mu \frac{\partial \delta w}{\partial z}$$

Substituting Eq. (9.15) to eliminate δp, we get

$$\frac{\partial \delta u}{\partial t} = \frac{\sigma}{\rho} \frac{\partial^3 \xi}{\partial x^3} + \frac{\mu}{\rho} \left(\frac{\partial^2 \delta u}{\partial z^2} - 3 \frac{\partial^2 \delta w}{\partial x \partial z} \right)$$

Similarly, in tangential direction when interfacial convection is initiated, the surface tension is equal to shearing force acting to the interface by the bulk liquid as follows

$$\frac{\partial \sigma}{\partial x} = \mu \left(\frac{\partial \delta u}{\partial z} + \frac{\partial \delta w}{\partial x} \right)$$

where σ can be obtained from Eq. (9.17).
Take heat balance at the interface and consider the deformation ξ, we yield

$$\lambda \frac{\partial \delta T}{\partial z} = -h_{\mathrm{L}} (\delta T - \beta \xi)$$

where h_{L} is the film coefficient of heat transfer.

(c) At interface, according to thermodynamics, the interfacial liquid concentration c_{L}^* and the interfacial gas concentration c_{G}^* are coexisted and in equilibrium. For the explanation of interfacial behaviors, Gibbs in 1878 proposed the theory of adsorption layer by considering the interface was an imaginary layer with no thickness.

Take desorption as an example, the quantity of mass transferred from bulk liquid to the interface is undergoing the following steps in sequence:

(1) Solute diffuse to the interface from bulk liquid;
(2) Accumulation of solute in the adsorption layer;
(3) Diffusion of solute in the adsorption layer.
(4) Diffusion of solute from the interface (adsorption layer) to the gas phase.

Mathematically, the mass balance of foregoing steps can be expressed as follows:

$$-D\frac{\partial c}{\partial Z} = k_{\mathrm{L}}\Delta c + \frac{\partial \Gamma}{\partial t} - \left[\frac{\partial u\Gamma}{\partial x} + \frac{\partial w\Gamma}{\partial z} - D_{\mathrm{S}}\left(\frac{\partial^2 \Gamma}{\partial x^2} + \frac{\partial^2 \Gamma}{\partial z^2}\right)\right] = k_{\mathrm{L}}\Delta c + S_{\mathrm{G}}$$

where k_{L} and Δc are respectively the film coefficient of mass transfer and solute concentration difference between bulk liquid and interface; Γ is the excess quantity in the adsorption layer, that is the accumulated solute per unit interfacial area; D_{S} is the solute diffusivity in adsorption layer, which is considered equal to the diffusivity of solute in bulk liquid D.

The excess quantity (solute) Γ can be expressed as the sum of fixed Γ and disturbance quantity $\delta\Gamma$:

$$\Gamma = \Gamma + \delta\Gamma$$

Substituting to the mass balance equation and considering the disturbance of concentration and velocity as well as the interfacial deformation, the following equation is obtained after neglecting the high order infinitesimal terms:

$$-D\frac{\partial c}{\partial Z} = k_L\left(\delta c - \beta'_c\xi\right) + \frac{\partial \delta\Gamma}{\partial t} - D\left(\frac{\partial^2 \delta\Gamma}{\partial x^2} + \frac{\partial^2 \delta\Gamma}{\partial z^2}\right)$$

From Gibbs theory, we have the following relationship:

$$\Gamma = -\frac{1}{RT}\left(\frac{\partial \sigma}{\partial c}\right)c = d_{\mathrm{G}}c$$

If surface tension σ is linear with concentration, then $d_{\mathrm{G}} = -(1/RT)(\partial\sigma/\partial c)$ becomes a constant and having the dimension of length, which is commonly defined as "adsorption layer thickness".

Combining the foregoing equations, we have the boundary condition at interface to be:

$$-D\frac{\partial \delta c}{\partial z} = k_{\mathrm{L}}(\delta c - \beta'\xi) + d_{\mathrm{G}}\frac{\partial(\delta c - \beta'_{\mathrm{c}}\xi)}{\partial t} - d_{\mathrm{G}}D\left[\frac{\partial^2(\delta c - \beta'_{\mathrm{c}}\xi)}{\partial x^2} + \frac{\partial^2(\delta c - \beta'_{\mathrm{c}}\xi)}{\partial z^2}\right]$$

If the mass transfer process is absorption, similar boundary condition is also established.

9.11.2 Generalization to Dimensionless

For the generalization of foregoing equations and boundary conditions to dimensionless, let the bulk liquid thickness d be the length scale, d^2/D be the time scale, $\beta'_{\mathrm{T}}d$ be the temperature scale, $\beta'_{\mathrm{c}}d$ be the concentration scale, i.e.

$$t = \frac{d^2}{D}\tau$$
$$\boldsymbol{u} = \frac{D}{d}\boldsymbol{U}$$
$$(\xi, x, z) = d(\xi_1, x_1, z_1)$$
$$T = \beta'_{\mathrm{T}} d\bar{T}$$
$$c = \beta'_{\mathrm{c}} dC$$

where τ, $\boldsymbol{U}$, $\bar{T}$, C are dimensionless. Substituting to the foregoing model equations, we have:

$$\frac{\partial}{\partial\tau}\left(\frac{\partial^2\delta w}{\partial x_i^2}\right) = \frac{\mu}{\rho D}\left(\frac{\partial^4\delta w}{\partial x_i^4}\right)$$
$$\frac{\partial\delta\boldsymbol{U}}{\partial x_i} = 0$$
$$\frac{\partial\delta C}{\partial\tau} = \frac{\partial^2\delta C}{\partial x_i^2} + \delta w$$
$$\frac{\partial\delta\bar{T}}{\delta\tau} = \frac{\alpha}{D}\frac{\partial^2\delta\overline{T}}{\partial x_i^2} + \delta w$$

Boundary conditions:
At $z = 0$ (wall):

$$\frac{\partial\delta\mathbf{U}}{\partial x_i} = 0$$
$$\frac{\partial\delta W}{\partial z} = 0$$
$$\frac{\partial\delta C}{\partial z} = Bi^0\delta C$$
$$\frac{\partial\delta\bar{T}}{\partial z} = Bi_{\mathrm{h}}^0\delta\bar{T}$$

where $Bi^0 = k_{\mathrm{L}}d/D_{\mathrm{L}}$ is the liquid phase Biot number for mass transfer; $Bi_{\mathrm{h}}^0 = h_{\mathrm{L}}d/\alpha$ is the Biot number for heat transfer; superscript 0 denotes the value at $z = 0$.

At $z = 1$(interface):

$$\begin{aligned}
\delta W &= \frac{\partial \xi}{\partial \tau} \\
\frac{\partial \delta \bar{T}}{\partial z} &= Bi_{\mathrm{h}}^{1}(\delta \bar{T} - \xi) \\
\frac{\partial \delta C}{\partial z} &= Bi^{1}(\partial C - \xi) - G\frac{\partial(\partial C - \xi)}{\partial \tau} + \widehat{S}\frac{\partial^2}{\partial x_i^2}(\delta C - \xi) \\
\frac{\partial \delta U}{\partial \tau} &= \frac{Sc}{Cr}\frac{\partial^3 \xi}{\partial x^3} + Sc\left(\frac{\partial^2 \delta U}{\partial z^2} - 3\frac{\partial^2 \delta W}{\partial x \partial z}\right) \\
\frac{\partial \delta U}{\partial z} + \frac{\partial \delta W}{\partial x} &= \frac{Ma_{\mathrm{h}}}{Le}\left(\frac{\partial \delta \bar{T}}{\partial x} - \frac{\partial \xi}{\partial x}\right) + Ma\frac{\partial(\delta C - \xi)}{\partial x}
\end{aligned}$$

where $Sc = \frac{\mu}{\rho D}$; $Le = \frac{D_{\mathrm{L}}}{\alpha}$; $\widehat{S} = Bi^{1}\frac{d_{\mathrm{G}}c^{*}}{d^2\beta_{\mathrm{c}}'}$; $Ma = \frac{\partial \sigma}{\partial c}\frac{\beta' d^2}{\mu D}$; $Ma_{\mathrm{h}} = \frac{\partial \sigma}{\partial T}\frac{\beta d^2}{\mu \alpha}$; $G = \frac{d_{\mathrm{G}}}{d}$; d_{G} is the adsorption layer thickness; c^{*} is the interfacial solute concentration; β_{c}' is the concentration gradient in the bulk liquid, superscript 1 denotes the value at $z = 1$. Dimensionless group $Cr = \mu D/(\sigma d)$ represents the influence of surface tension to the interfacial deformation, and is called crispation number [33].

9.11.3 Stability Analysis

Similar to the stability analysis in Sect. 9.3, let the small disturbance follows the following form:

$$\begin{aligned}
\delta W &= \Psi(z)\exp(\mathrm{i}k_x x + \omega t) \\
\delta T &= \Theta(z)\exp(\mathrm{i}k_x x + \omega t) \\
\delta c &= \Phi(z)\exp(\mathrm{i}k_x x + \omega t)
\end{aligned}$$

where Ψ, Θ, Φ are respectively the disturbance amplitude of velocity, temperature and concentration; k_x is the wave number in direction x; ω is the increasing rate of disturbance.

Similar to the Sect. 9.3, let

$$\begin{aligned}
\frac{\partial^2}{\partial x^2} &= -k_x^2 \\
\nabla^2 &= \frac{\partial^2}{\partial x^2} + \frac{\partial^2}{\partial z^2} = \frac{d^2}{dz^2} - k_x^2 = \widetilde{D}^2 - k_x^2
\end{aligned}$$

The dimensionless disturbance equation can be written in the following form:

$$\left(\widetilde{D}^2 - k_x^2\right)^2 \psi = 0$$
$$(\widetilde{D}^2 - k_x^2)^2 \Theta = -Le\Psi$$
$$\left(\widetilde{D}^2 - k_x^2\right)\Phi = -\Psi$$

The boundary conditions are:
At $z = 0$:

$$\Psi = 0 \quad \widetilde{D}\Psi = 0$$
$$\widetilde{D}\Theta - Bi_{\mathrm{h}}^0 \Theta = 0$$
$$\widetilde{D}\Phi - Bi^0 \Phi = 0$$

At $z = 1$:

$$\Psi = 0$$
$$\widetilde{D}\Theta + Bi_{\mathrm{h}}^1(\Theta - \eta) = 0$$
$$\widetilde{D}\Phi + Bi^1(\Phi - \eta) - \widehat{S}\left(\widetilde{D}^2 - k_x^2\right)(\Phi - \eta) = 0$$
$$\left(\widetilde{D}^2 + k_x^2\right)\Psi + \frac{Ma_{\mathrm{h}}}{Le}k^2(\Theta - \eta) + Mak_x^2(\Phi - \eta) = 0$$

where dimensionless group $\widehat{S} = Bi^1 \frac{d_G c^*}{d^2 \beta_c'}$, β' is the temperature gradient in bulk liquid.

Simulated results

In order to find the instability of foregoing model equations enabling to induce interfacial convection, no zero solution is necessary. Similar to the method used in Sect. 9.3.2, by letting the coefficients of the corresponding determinant equal to zero, the following equation can be established:

$$f(Ma, Ma_{\mathrm{h}}, k_x, Cr, Bi_{\mathrm{h}}^1, Bi^1, Bi_{\mathrm{h}}^0, Bi^0, \widehat{S}) = 0$$

If reasonable value of Cr, Bi_{h}^1, Bi^1, $\widehat{S}$, Ma_{h} are given, the relationship between Ma and k_x is obtained, from which the critical Ma number, Ma_{cr}, can be found.

(1) **The influence of Ma_{h} on Ma_{cr}**
Figure 9.52 shows the Ma-k_x curve calculated under designated condition at different Ma_{h}. The area underneath the curve represents the system in stable state, and that above the curve is in the unstable state for the corresponding condition. The minimum point of the curve represents the smallest Ma which is the bordering point between the system in stable state and unstable state, in other words, it represents the critical Ma number, or Ma_{cr}. If Ma_{cr} ploted

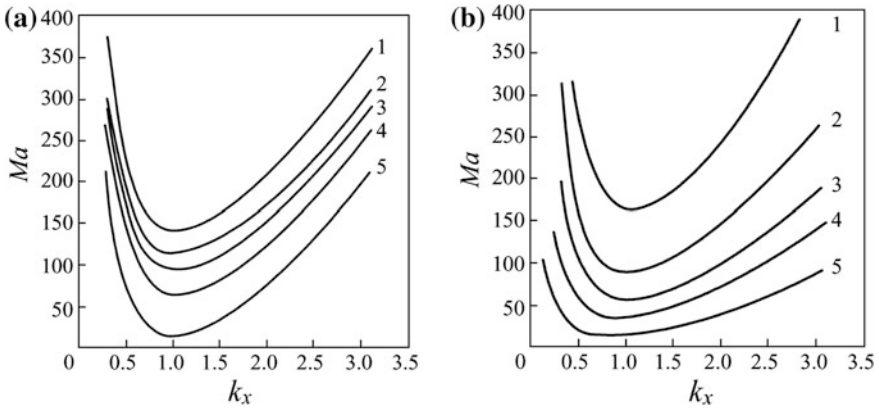

Fig. 9.52 The *Ma-k* curves at different Ma_h. **a** $Cr = 0$, $\widehat{S} = 0$, $Bi_h^0 = Bi^0 = 0$, $Bi_h^1 = Bi^1 = 10$, **b** $Cr = 0.001$, $\widehat{S} = 0.01$, $Bi_h^0 = Bi^0 = 5$, $Bi_h^1 = Bi_l^1 = 15$ (Curve: *1* $Ma_h = -50$; *2* $Ma_h = 0$; *3* $Ma_h = 20$; *4* $Ma_h = 50$; *5* $Ma_h = 100$)

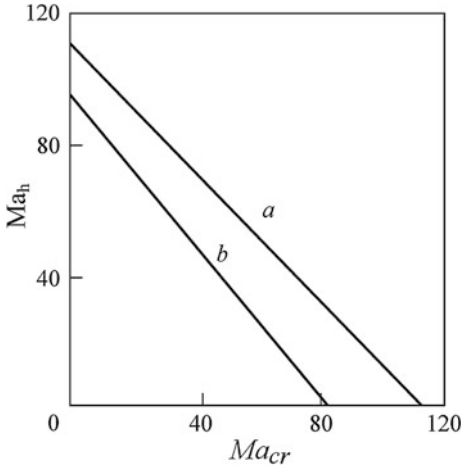

Fig. 9.53 Critical Ma_{cr} at different Ma_h for simultaneous mass and heat transfer (*line a* $Cr = 0$, $\widehat{S} = 0$, $Bi_h^0 = Bi^0 = 0$, $Bi_h^1 = Bi^1 = 10$, *line b* $Cr = 0.001$, $\widehat{S} = 0.01$, $Bi_h^0 = Bi^0 = 5$, $Bi_h^1 = Bi_l^1 = 15$)

agianst Ma_h as seen from Fig. 9.53, the Ma_{cr} is decreased with increasing Ma_h; Fig. 9.53 demonstrates more clearly the effect of Ma_h on Ma_{cr}.

(2) **The influence of *Cr* on Ma_{cr}**

The dimensionless crispation number, $Cr = \mu D/(\sigma d)$, represents the influence of surface tension on interface deformation. Figure 9.54 shows the Ma_{cr} at different Cr for various systems. The influence of Cr on Ma_{cr} is obvious as seen at higher Cr.

(3) **The influence of interfacial adsorption on Ma_{cr}**

The effect of interfacial adsorption can be represented by the dimensionless group [22] $\widehat{S} = Bi^1 \frac{d_G c^*}{d^2 \beta_c^\gamma}$ where d_G is the thickness of adsorption layer. The $\widehat{S}$ is

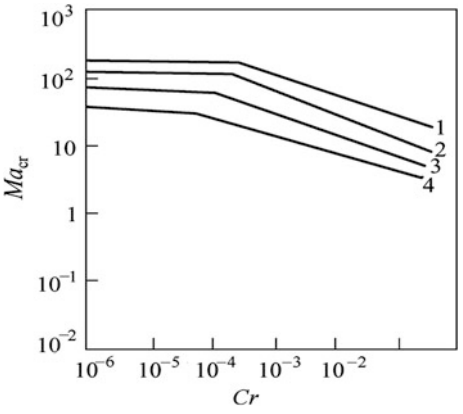

Fig. 9.54 The influence of Cr on Ma_{cr} (*1* $Ma_h = -20$, $B_h^0 = 20$, $B_h^1 = Bi^1 = 100$, $\dot{S} = 0$, *2* $Ma_h = 0$, $Bi_m^1 = 100$, $\dot{S} = 0$, *3* $Ma_h = 40$, $B_h^0 = 20$, $B_h^1 = Bi^1 = 100$, $\dot{S} = 0.01$, *4* $Ma_h = 100$, $B_h^0 = 20$, $B_h^1 = Bi^1 = 100$, $\dot{S} = 0.05$)

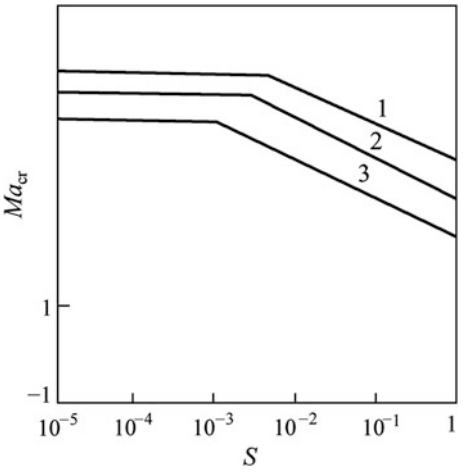

Fig. 9.55 The influence of $\widehat{\mathbf{S}}$ on Ma_{cr} (*1* $Ma_h = -20$, $B_h^0 = 20$, $B_h^1 = Bi^1 = 10$, $Cr = 0$, *2* $Ma_h = 0$, $Bi^1 = 10$, $Cr = 0$, *3* $Ma_h = 50$, $B_h^0 = 20$, $B_h^1 = Bi^1 = 10$, $Cr = 0.01$)

also reflects the influence of Bi^1. Figure 9.55 shows that Ma_{cr} is lowered at higher $\widehat{S}$, it means the appearance of Marangoni convection can be promoted earlier by interfacial adsorption.

Form the simulated results of foregoing sections, the interfacial effect is influenced by many factors, such as Marangoni convection, Rayleigh convection, heat transfer, interface deformation, physical properties of the process and others. Each factor may be positive or negative; the overall effect depends on their coupling result. For the flowing system, it is also in connection with the behaviors of fluid-dynamics.

9.12 Summary

The mass transferred from one phase to the adjacent phase must diffuse through the interface and subsequently produces interfacial effect. The behaviors of interfacial effect can be summarized briefly as follows:

(1) From the molecular viewpoint, the transfer of mass at the interface is stochastic and subsequently produces local concentration difference Δc from which the surface tension difference $\Delta\sigma$ is also established so as to induce interfacial circulation; it is called Marangoni convection. Furthermore, due to the density at the interface is different from that of the bulk fluid by $\Delta\rho$, circulation between interface and the bulk fluid is also induced, which is called Rayleigh convection. Nevertheless, the creation of $\Delta\sigma$ may be also due to the interfacial local temperature difference ΔT and the $\Delta\rho$ may be achieved due to the temperature difference between interface and the bulk. Thus there are ΔT based besides Δc based Marangoni convection and Rayleigh convection.

(2) Generally speaking, the Marangoni convection exists at the interface and slightly underneath, while the Rayleigh convection appears between interface and the bulk. The coupling effect of these two convections may be positive (enhance mass transfer) or negative (suppress mass transfer). The enhancement factor may be up to above 5.

(3) The intensity of Marangoni convection and Rayleigh convection can be represented by the Marangoni number *Ma* and Rayleigh number *Ra*. The onset of convection and orderly interfacial structure only when *Ma* and *Ra* reach its critical value Ma_{cr} and Ra_{cr}. When *Ma* and *Ra* number further increase to a certain extent, the system turns to stable at fully turbulence or chaos state.

(4) The interface in most cases is not flat but deformed. Thus the effect of crispation number *Cr* should be considered.

References

1. Marangoni C (1871) Ueber die ausbreitung der tropfeneiner flüssigkeit auf der oberfläche einer anderen. Ann Phys 219(7):337–354
2. Sha Y, Cheng C, Yu KT (2003) Interfacial effect of mass and heat transfer. Prog Chem 15 (1):9–11
3. Rayleigh L (1916) On the convection currents in a horizontal layer of fluid when the higher temperature is on the under side. Phil Mag 32:529–535
4. Bénard H (1901) Les tourbillons cellulaires dans une nappeliquide. Rerue Gén Sci Pures Appl 11:1261–1271
5. Yu YH (2003) Interfacial disturbance in gas liquid mass transfer process. MS dissertation, Tianjin University, Tianjin, China (in Chinese)
6. Yu YH, Sha Y, Cheng H (2003) Observation of interfacial structure on single component diffusion. Chem Eng J Chin Univ 17(2):212–215 (in Chinese)

7. Yu LM (2005) The study of Marangoni effect on the gas liquid mass transfer process. PhD dissertation, Tianjin University, Tianjin, China (in Chinese)
8. Yu YH, Sha Y, Cheng H (2002) Observation of interfacial structure on binary mass transfer process. Chem Eng Prog 137–141 (in Chinese)
9. Yu LM, Zeng AW, Yu GC (2006) The effect of Marangoni convection in gas-liquid system. Trans Tianjin Univ 12(6):391–398
10. Sha Y (2002) Study on Rayleigh-Benard-Marangoni convection driven by the mass transfer. PhD dissertation, Tianjin University, Tianjin, China (in Chinese)
11. Sha Y, Chen H, Yu LH (2003) Stability analysis of falling film mass transfer process. Chem Eng J 54(10):1361–1368 (in Chinese)
12. Xiao FZ (1991) Stability of heat and mass transfer on a deformable gas-liquid interface. PhD dissertation, Tianjin University, Tianjin, China (in Chinese)
13. Sun ZF (1998) Study on the non-equilibrium phase transition in mass transfer process. PhD dissertation, Tianjin University, Tianjin, China (in Chinese)
14. Sun ZF, Yu KT (2002) Absorption and desorption of carbon dioxide in and from organic solvent: effects of Rayleigh and Marangoni instability. Ind Eng Chem Res 41:1905–1913
15. Zhou CF (2005) The influence of Marangoni effect on the mass transfer coefficient. MS dissertation, Tianjin University, Tianjin, China (in Chinese)
16. Zhang SH, Wang ZM, Su YF (1990) Mass transfer and interfacial turbulence in a laminar film/study of transferring two solutes separately and simultaneously through liquid-liquid interface. Trans IChemE 68:84–92
17. Bird RB, Stewart WE, Lightfoot EN (1994) Transport phenomena. Wiley, New York
18. Yuen CK, Fraser D (1986) Digital spectral analysis. CSIRO/Pitman, Melbourne
19. Sha Y, Cheng H, Yuan XG, Yu KT (2003) Dynamics of mass transfer with Marangoni effect. Chem Eng J 54(11):1518–1523 (in Chinese)
20. Imaishi N, Suzuki Y, Hozawa M, Fujinawa K (1982) Interfacial turbulence in gas-liquid mass transfer. Intern Chem Eng 22:659–665
21. Brian PLT, Vivian JE, Mayr ST (1971) Cellular convection in desorbing surface tension-lowering solutes from water. Ind Eng Chem Fundam 10:75–83
22. Brian PLT, Ross JR (1972) The effect of Gibbs adsorption on Marangoni Instability in penetration mass transfer. AIChE J 18:582–591
23. Brian PLT, Smith KA (1972) Influence of Gibbs adsorption on oscillatory Marangoni instability. AIChE J 18:231–233
24. Hozawa M, Komatsu N, Imaishi N, Fujinawa K (1984) Interfacial turbulence during the physical absorption of carbon dioxide into non-aqueous solvents. J Chem Eng Jpn 17: 173–179
25. Golovin AA (1992) Mass transfer under interfacial turbulence: kinetic regularities. Chem Eng Sci 47:2069–2080
26. Golovin AA, Nepomnyashchy AA, Pismen LM (1995) Pattern formation in large-scale Maranoni convection with deformable interface. Physica D 81:117–147
27. Fujinawa K, Hozawa M, Imaishi N (1978) Effects of desorption and absorption of surface tension lowering solutes on liquid phase mass transfer coefficients at a turbulent gas-liquid interface. J Chem Eng Jpn 11:107–111
28. Olander DR, Reddy LB (1964) The effect of concentration driving force on liquid-liquid mass transfer. Chem Eng Sci 19:67–73
29. Sawistowski H, Goltz GE (1963) The effect of interface phenomena on mass transfer rates in liquid-liquid extraction. Trans Instn Chem Engrs 41:174–181
30. Sun ZF, Yu KT (2006) Rayleigh-Bénard-Marangoni convection: expressions for heat and mass transfer rate. Chem Eng Res Des 84(A3):185–191
31. Sha Y, Hong C, Yu Y (2002) The numerical analysis of the gas-liquid absorption process accompanied by Rayleigh convection. Chin J Chem Eng 10(5):539–544
32. Chen W (2010) Experimental measurement of gas–liquid interfacial Rayleigh-Bénard—Marangoni convection and mass transfer. Ph.D. thesis, Tianjin University, Tianjin, China

33. Scriven LE (1960) Dynamics of a fluid interface equation of motion for newtonian surface fluids. Chem Eng Sci 12(2):98–108
34. Zhang ZS, Cui GX, Xu CX (2005) Theory and modeling of turbulence. Tsinghua University Press, Beijing
35. Liu CX, Zeng AW, Yuan XG, Yu GC (2008) Experimental study on mass transfer near gas-liquid interface through quantitative Schlieren method. Chem Eng Res Des 86(2): 201–207
36. Agble D, Mendes-Tatsis MA (2000) The effect of surfactants on interfacial mass transfer in binary liquid–liquid systems. Int J Heat Mass Transf 43(6):1025–1034
37. Agble D, Mendes-Tatsis MA (2001) The prediction of Marangoni convection in binary liquid-liquid systems with added surfactants. Int J Heat Mass Transf 44:1439–1449
38. Scriven LE, Sternling CV (1964) On cellular convection driven by surface-tension gradients: Effects of mean surface tension and surface viscosity. J Fluid Mech 19(3):321–340

Chapter 10
Simulation of Interfacial Behaviors by the Lattice-Boltzmann Method

Abstract In this chapter, the mesoscale computational methodology, lattice-Boltzmann Method (LBM) is introduced for the simulation of the interfacial Marangoni and Rayleigh effects as described and discussed in Chap. 8. The fundamentals of LBM are briefly introduced and discussed. By the simulation using the LBM, some mechanisms and phenomena of the interfacial effect are studied, including the patterns of the interfacial disturbance for inducing the interfacial convections, conditions of initiating interfacial instability and interfacial convection as well as the effect on interfacial mass transfer.

Keywords Lattice-Boltzmann method · Simulation of interfacial mass transfer · Solutal-induced interfacial convection · Marangoni convection · Rayleigh convection

Nomenclature

A_i	Interfacial area, m^2
b	Number of particle streaming directions; number of discrete particle velocity
c	Lattice velocity, m/s
C	Solute concentration, kg/m^3
C_i	Interfacial solute concentration, kg/m^3
C_S	Saturation concentration, kg/m^3
C_0	Initial concentration of solute, kg/m^3
C_s	Sound velocity of simulated object, m/s
c_s	Sound speed of lattice model, m/s
c_k	Solute concentration of component k, kg/m^3
D_k	Mass diffusivity of component k, m^2/s
E	Internal energy, J
e_α	Discrete velocity (α = 1, 2, 3, …, b), m/s
F	Volumetric external force, kg m/s^2
f_α	Distribution function
f_α^{eq}	Equilibrium distribution function
G_α	Concentration distribution function
G_α^{eq}	Equilibrium concentration distribution function

K.-T. Yu and X. Yuan, *Introduction to Computational Mass Transfer*,
Heat and Mass Transfer, DOI 10.1007/978-981-10-2498-6_10

g Internal energy density distribution function
$\boldsymbol{g}_0$ Gravitational force, kg m/s^2
H Thickness of liquid, m
L Characteristic length of simulated object, m
l Characteristic length of lattice model, m
Ma Marangoni number
n_α Number of particles along direction α, 0 or 1
R Gas constant, J/mol k
Ra Rayleigh number
Re Reynolds number
S Source term
Sc Schmidt number
T Temperature, K
T_i Temperature distribution function
T_i^{eq} Equilibrium temperature distribution function
t Time, s
U Characteristic velocity of the simulated object, m/s
u^* Macroscopic velocity in equilibrium distribution function, m/s
u Macroscopic velocity, m/s
V Volume of liquid, m^3
x Space position
α Thermal diffusivity, m^2/s
μ Viscosity, kg/m s
μ_{t} Turbulent viscosity, kg/m s
v Kinematic viscosity, m^2/s
v^* Kinematic viscosity the simulated object, m^2/s
P Macroscopic density, kg/m
σ Ratio of specific heat between solid wall and fluid
τ Single relaxation time
τ_0 Relaxation time, s
τ_{e} Single relaxation time in internal energy distribution function
τ_{h} Single relaxation time in heat transfer model
τ_k Single relaxation time in mass transfer model
Ω Collision operator
ω Weight coefficient

In the foregoing chapters, the simulation is based on the macroscopic point of view that the fluid is continuous medium and its physical properties, such as density, velocity, and pressure, are function of time and space. Thus the Navier–Stokes equation can be employed as modeling equation in the mathematical simulation. In this chapter, we turn to the mesoscopic point of view and use the lattice-Boltzmann (LB) method for simulating the interfacial phenomena. The LB method is based on such postulation that the fluid is composed of large number of particles which obey

the law of mechanics and exhibit the macroscopic behaviors by means of statistical methodology. This method has been applied to various fields since the eighties of last century.

In 1986, Frisch simulated the two-dimensional Navier–Stokes equation by using lattice gas automation, and called it as lattice gas method [1]. At the same time, Wolfram used this method for simulating the flowing fluid behaviors [2]. Chen [3] and Qian [4] further developed this method by combining with the work of Bhatnager [5] to establish a new method called lattice-Boltzmann BGK method (LBGK), or simply lattice-Boltzmann method (LBM). This method has been received wide attention by the researchers and applied to multiphase flow, heat transfer, convection, reaction, and many other fields. The LBM is still developing and serving as a new method in the computational methodology.

In this chapter, the LBM is used for simulating the interfacial behaviors of mass transfer. The fundamentals of LBM are briefly introduced in subsequent section as the basic knowledge for understanding this method.

10.1 Fundamentals of Lattice-Boltzmann Method

10.1.1 From Lattice Gas Method to Lattice-Boltzmann Method

The lattice gas method was developed from cellular automaton for simulation purpose. Cellular automaton is a method that automatically repeats the designated process to approaching the desired goal. The simulation of flow field by lattice gas method is based on the viewpoint that the fluid is composed of large amount of microparticles with mass and zero volume. The macroscopic motion of the fluid is the result of the collective behaviors of the microparticles. The detail of mutual interaction of particles is not important as it influence only the fluid parameters and does not affect the mass, momentum, and energy conversation laws of the fluid. Thus the lattice gas method is employing the model of simple regular particle motion for simulating the complicated real process.

The basic idea of lattice gas method is to discrete the fluid and its occupied space into lattices. The microparticle of fluid at the nodes of the lattice is moving synchronously to the neighboring node with velocity $\boldsymbol{e}_\alpha(\alpha = 1, 2, 3, \ldots, b)$ where b represents the number of possible moving directions, including stationary (no direction). In each moving direction, either one particle or no particle is allowed. Since the particles at the neighboring nodes are moving toward the other nodes, collision of particles is happened. Therefore at the time interval Δt_1, the following events take place:

(1) Streaming of particles: The particles at a node are moving to the neighboring nodes with velocity $\boldsymbol{e}_\alpha$;

(2) Collision of particles: When different particles reach to the same node, collision happened and changed the moving direction; such collision obeys the conservation laws of mass, momentum, and energy.

Following next time interval Δt_2, the propagation of particle and collision are repeated; such cyclic evolution goes on again and again for all particles at increasing time intervals to realize the simulation of the fluid motion.

Let $n_\alpha(\boldsymbol{x}, t)$ denotes the number of particles at node x moving along α direction with velocity $\boldsymbol{e}_\alpha$ within time interval Δt, the whole process can be expressed mathematically as follows:

$$n_\alpha(\boldsymbol{x} + \boldsymbol{e}_\alpha \Delta t, t + \Delta t) - n_\alpha(\boldsymbol{x}, t) = \boldsymbol{\Omega}_\alpha(\boldsymbol{x}, t), \quad \alpha = 1, 2, 3, \ldots, b \tag{10.1}$$

where $\boldsymbol{\Omega}_\alpha(\boldsymbol{x}, t)$ is the collision term representing the rate of change of the particle distributions due to collisions. Some researchers, like McNamara, used Fermi–Dirac distribution function f_α to replace n_α for simulating the flow pattern [6].

10.1.2 Basic Equations of Lattice-Boltzmann Method

(1) **The model equation**

The LBM is established on the basis of lattice gas method. The difference between them is that the LBM is dealing with average character of the particles in the system instead of single particle.

The Boltzmann equation, derived from molecular motion and collision, expresses the relationship between distribution function of molecular density f, time t, molecular velocity $\boldsymbol{e}$, and space position x. In LBM, the molecule is considered to be the particle and the molecular velocity is identical with the particle velocity, then the Boltzmann equation can be written as follows:

$$\frac{\partial f}{\partial t} + \boldsymbol{e} \cdot \nabla f = \Omega_{\mathrm{C}} + \Phi \tag{10.2a}$$

where f is the distribution function of particles; $\boldsymbol{e}$ is the particle velocity; Ω_{C} is the collision term; Φ represents the influence of external force (such as gravitational force) on f.

According to the H theorem and BGK model, the nonequilibrium system always tends to approach the state of equilibrium. Thus the collision of particles can be considered as a process intended to reach the equilibrium state; the rate of the process approaching equilibrium is proportional to $\left[f_\alpha(\boldsymbol{x}, t) - f_\alpha^{\mathrm{eq}}(\boldsymbol{x}, t)\right]$. The Ω_{C} can be expressed as

$$\Omega_{\mathrm{C}}(\boldsymbol{x},t) = -\frac{1}{\tau_0}\left[f_\alpha(\boldsymbol{x},t) - f_\alpha^{\mathrm{eq}}(\boldsymbol{x},t)\right], \quad \alpha = 1,2,3,\ldots,b$$

where $f_\alpha(\boldsymbol{x},t)$ is the distribution function of single molecule, or the probability of a particle at node x and time t moving along α direction with velocity $\boldsymbol{e}_\alpha$; $f_\alpha^{\mathrm{eq}}(\boldsymbol{x},t)$ is the f_α when equilibrium is reached; τ_0 is a proportionality constant with dimension of time, called relaxation time. In the LBM, Chen [3, 7] and Qian [4] employed Maxwell–Boltzmann distribution function to replace the Fermi–Dirac distribution function. Substituting foregoing equation to Eq. (10.2a) under the condition of no external force ($\Phi = 0$), the following equation is obtained:

$$\frac{\partial f}{\partial t} + \boldsymbol{e}\cdot\nabla f = -\frac{1}{\tau_0}\left[f_\alpha(\boldsymbol{x},t) - f_\alpha^{\mathrm{eq}}(\boldsymbol{x},t)\right] \tag{10.2b}$$

After discretization at Δt and distance x, the foregoing equation becomes

$$f_\alpha(\boldsymbol{x} + \boldsymbol{e}_\alpha\Delta t, t+\Delta t) - f_\alpha(\boldsymbol{x},t) = -\frac{1}{\tau_0/\Delta t}\left[f_\alpha(\boldsymbol{x},t) - f_\alpha^{\mathrm{eq}}(\boldsymbol{x},t)\right]$$

or

$$f_\alpha(\boldsymbol{x} + \boldsymbol{e}_\alpha\Delta t, t+\Delta t) - f_\alpha(\boldsymbol{x},t) = -\frac{1}{\tau}\left[f_\alpha(\boldsymbol{x},t) - f_\alpha^{\mathrm{eq}}(\boldsymbol{x},t)\right] \tag{10.3}$$

where τ is dimensionless proportional constant, $\tau = \frac{\tau_0}{\Delta t}$, called single relaxation time, which controls the rate of approach to equilibrium. Equation (10.3) is commonly called LBGK equation.

(2) **The lattice model**

For the implementation of LBM to the simulation of fluid behavior, the simulated object should be first divided into lattice. The objective fluid is discrete and represented by the particles at the nodes. The two-dimensional (denoted by 2D) 9 directions (denoted by Q9) square lattice model is shown by Fig. 10.1.

The particle at the node may be moving toward any one of the nine directions as indicated in the figure including zero direction (stationary). At time interval Δt, the particle moves with velocity $\boldsymbol{e}_\alpha(\alpha = 0,1,2,3,\ldots,8)$ to the neighboring nodes and happens collision. Let Δx be the length of the square lattice, the ratio of $\frac{\Delta x}{\Delta t} = c$ is called lattice velocity. The ratio c can be letting $c = 1$ or $c = \sqrt{3RT} = \sqrt{3}c_{\mathrm{s}}$ where R is gas constant, T is the absolute temperature and $c_{\mathrm{s}} = \sqrt{RT}$ is customary called speed of sound (see Appendix 4). The particle velocity in the diagonal directions is $\sqrt{2}$ times that in x direction; the nine particle velocity $\boldsymbol{e}_\alpha$ is given below

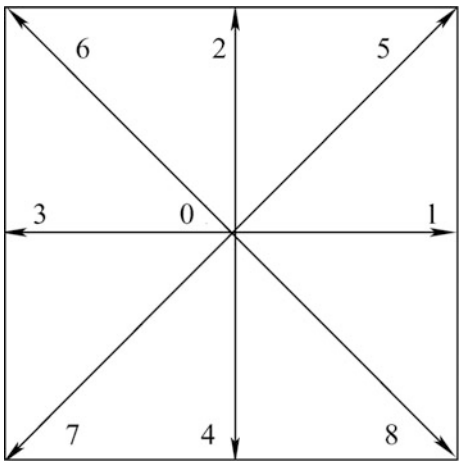

Fig. 10.1 D2Q9 lattice model

$$\boldsymbol{e}_\alpha = \begin{cases} (0,0), & \alpha = 0 \\ \left[\cos\left(\frac{\alpha-1}{2}\pi\right)c, \quad \sin\left(\frac{\alpha-1}{2}\pi\right)c\right], & \alpha = 1,2,3,4 \\ \left[\sqrt{2}\cos\left(\frac{\alpha-5}{2}\pi+\frac{\pi}{4}\right)c, \quad \sqrt{2}\sin\left(\frac{\alpha-5}{2}\pi+\frac{\pi}{4}\right)c\right], & \alpha = 5,6,7,8 \end{cases} \tag{10.4}$$

From statistical mechanics, the Maxwell–Boltzmann distribution function for single particle in equilibrium state can be expressed as

$$f^{\mathrm{eq}} = \frac{\rho}{(2\pi RT)^{D/2}} \exp\left[-\frac{(\boldsymbol{e}-\boldsymbol{u})^2}{2RT}\right] \tag{10.5}$$

where $\boldsymbol{u}$ is the macroscopic fluid velocity (vector); ρ is macroscopic density. Using Taylor expansion and Chapman–Enskog expansion technique, the equilibrium distribution function of single particle for D2Q9 lattice model is obtained as follows (see Appendix 4 or Ref. [4]).

$$f^{\mathrm{eq}} = \rho\omega_\alpha\left[1 + \frac{\boldsymbol{e}_\alpha\cdot\boldsymbol{u}}{c_{\mathrm{s}}^2} + \frac{(\boldsymbol{e}_\alpha\cdot\boldsymbol{u})^2}{2c_{\mathrm{s}}^4} - \frac{\boldsymbol{u}^2}{2c_{\mathrm{s}}^2}\right] \tag{10.6}$$

where the weight coefficient ω_α is

$$\omega_\alpha = \begin{cases} \frac{4}{9}, & \alpha = 0 \\ \frac{1}{9}, & \alpha = 1,2,3,4 \\ \frac{1}{36}, & \alpha = 5,6,7,8 \end{cases}$$

The relationship between macroscopic quantities and f_α is as follows

$$\begin{aligned}\rho &= \sum_{\alpha=0}^{8} f_\alpha(\boldsymbol{x}, t) \\ \rho \boldsymbol{u} &= \sum_{\alpha=0}^{8} \boldsymbol{e}_\alpha f_\alpha(\boldsymbol{x}, t)\end{aligned} \tag{10.6a}$$

Besides two-dimensional lattice, there are many three-dimensional lattice models that can be chosen as shown in Fig. 10.2 [8]. Three-dimensional lattice model has more discrete velocity to give more accurate simulation, yet the computer load becomes heavy and requires parallel computation.

The suitability of using LBM to the simulation of fluid flow can be proved by converting Eq. (10.3) to Navier–Stokes equation under some specified conditions (see Appendix 5 or Ref. [4, 9]). In other words, any fluid process, which can be modeled by Navier–Stokes equation, is suitable to use LBM for process simulation.

For D2Q9 lattice model, the following specified condition should be satisfied for applying LBM (see Appendix 5):

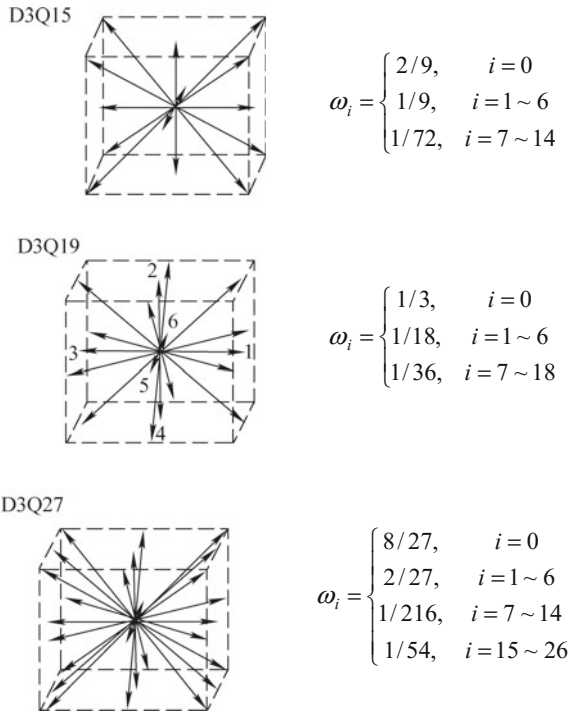

Fig. 10.2 Several three-dimensional lattice models

$$v = \frac{c^2 \Delta t}{3}\left(\tau - \frac{1}{2}\right) \tag{10.7}$$

where v is kinematic viscosity, $v = \frac{\mu}{\rho}$ for lamina flow and $v = \frac{\mu + \mu_t}{\rho} \approx \frac{\mu_t}{\rho}$ for turbulent flow; $c = \sqrt{3RT}$. If v is known for the fluid concerned, the unknown parameter τ can be obtained by Eq. (10.7). Obviously, τ cannot be less than $\frac{1}{2}$.

(3) **Boundary conditions**

There are several boundary conditions can be chosen for the distribution function f under different conditions. The details can be found in Refs. [10–13].

(1) Bounce-back boundary condition
This is the simplest condition by considering that the particle impacts the solid wall and bounce back with the same velocity but opposite in direction. If f and f' denote, respectively, the distribution function before and after the impact, then $f' = f$. This boundary condition is easy to apply, but the degree of accuracy is low.

(2) No slip boundary condition
Since the slip of particle appears during the impact to the wall, a negative distribution function f_{-1} is introduced to eliminate the effect of slip. The accuracy of simulation by this method is better than that by bounce-back.

(3) Extended boundary condition
Refer to Fig. 10.3, if the boundary of simulation is located on the line 391 (denoted as layer 0) and the underneath neighboring nodes of the fluid are 748 (denoted as layer 1), an virtual (extended) layer with nodes 625 (denoted as layer −1) is imagined, then the boundary nodes 391 are considered as the nodes of the fluid in the computation. The condition of the imaginary nodes may bounce back or others. Satisfactory accuracy is obtained by this method.

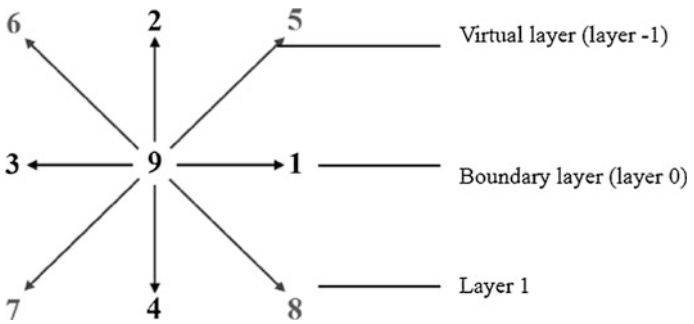

Fig. 10.3 Extended boundary layer

(4) Periodic boundary condition
In case of simulating flowing fluid, the periodic boundary condition is frequently used by considering the distribution function in the inlet and outlet is equal.

(4) Procedure of computation

(1) Select lattice model, for instance, D2Q9, and evaluate τ, Δx, Δt according to Eq. (10.7);
(2) Give the initial value of distribution function f_α, ρ and u;
(3) Calculate equilibrium distribution function f_α^{eq} by Eq. (10.6);
(4) Calculate the distribution function $f_\alpha(\boldsymbol{x},t)$ for all nodes at time t and direction α;
(5) Calculate the new distribution function $f_\alpha(\boldsymbol{x} + \boldsymbol{e}_\alpha \Delta t, t + \Delta t)$ at $t + \Delta t$ by Eq. (10.3);
(6) According to the boundary conditions chosen, calculate the distribution function at the boundary;
(7) Renew ρ and u according to Eq. (10.6a) to be the initial value for next iteration. Go back to step (3) and repeat the procedure again and again until the simulation is satisfied.

(5) The lattice-Boltzmann equation with external force

In the presence of external force, its action on the molecules should be considered, the Boltzmann equation can be expressed by one of the following form:

(1) Retaining the source term Φ

The Φ term in Eq. (10.2a) is retained and written as S_F in more general sense, that is

$$\frac{\partial f}{\partial t} + e \cdot \nabla f = \Omega_{\mathrm{C}} + \boldsymbol{S}_F \tag{10.8}$$

where $\boldsymbol{S}_F$ is the source term representing the action of external force in general. After discretization, Eq. (10.8) becomes

$$f_\alpha(\boldsymbol{x} + \boldsymbol{e}_\alpha \Delta t, t + \Delta t) - f_\alpha(\boldsymbol{x}, t) = \Omega_\alpha(\boldsymbol{x}, t) + \boldsymbol{S}_\alpha(\boldsymbol{x}, t), \quad \alpha = 1, 2, 3, \ldots, b \tag{10.8a}$$

Substituting the expression for $\Omega(\boldsymbol{x}, t)$, one yields

$$f_\alpha(\boldsymbol{x} + \boldsymbol{e}_\alpha \Delta t, t + \Delta t) - f_\alpha(\boldsymbol{x}, t) = -\frac{1}{\tau}\left[f_\alpha(\boldsymbol{x}, t) - f_\alpha^{\mathrm{eq}}(\boldsymbol{x}, t)\right] + \boldsymbol{S}_\alpha(\boldsymbol{x}, t), \quad \alpha = 1, 2, 3, \ldots, b \tag{10.9}$$

The source term $\boldsymbol{S}_F$ is evaluated for the specified object of simulation. For instance, He [14] proposed a lattice-Boltzmann model for simulating the influence of gravity on the nonideal fluid, the $\boldsymbol{S}_F$ is given below

$$\boldsymbol{S}_F = -\frac{(\boldsymbol{e}-\boldsymbol{u})\cdot(\boldsymbol{F}_\mathrm{e}+\boldsymbol{g}_0)}{\rho RT} f^\mathrm{eq}$$

where $\boldsymbol{F}_\mathrm{e}$ is the effective intermolecular acting force; $\boldsymbol{g}_0$ is gravitational force; R is gas constant.

Another example is the model proposed by Dixit for simulating the high Reynolds number convection created by heating, where the source term $\boldsymbol{S}_F$ is given below [15]:

$$\boldsymbol{S}_F = \frac{\boldsymbol{F}\cdot(\boldsymbol{e}-\boldsymbol{u})}{RT} f^\mathrm{eq}$$

where $\boldsymbol{F}$ is external force acting on the system per unit mass, which is related to many factors, such as density, coefficient of thermal expansion, local and average temperature of the system concerned.

(2) Modifying the particle velocity

The external force per unit volume $\left(\frac{1}{\mathrm{m}^3}\cdot\frac{\mathrm{kg\cdot m}}{\mathrm{s}^2}\right)$ acting on the particle can be expressed by $\boldsymbol{F} = \rho\frac{\boldsymbol{u}^*-\boldsymbol{u}}{\tau_0} = \rho\frac{\boldsymbol{u}^*-\boldsymbol{u}}{\tau\Delta t}$, where $\boldsymbol{u}^*$ and $\boldsymbol{u}$ are, respectively, the particle velocity in the equilibrium distribution function after and before modification; ρ is the density of the particle. The modified $\boldsymbol{u}^*$ is expressed as

$$\boldsymbol{u}^* = \boldsymbol{u} + \frac{\boldsymbol{F}\tau}{\rho}\Delta t$$

(6) **The scale-up of lattice-Boltzmann model**

The simulated object generally is in large scale, such as the fluid behaviors in industrial equipment. Nevertheless, the dimension of lattice Δx is very small, the number of lattice for the full-scale simulation is tremendous to make the computer load too heavy. In practice, the model equations are established aiming to the reduced size of the equipment, and then use the principle of similarity to adjust the parameters in the model so that the simulated results are applicable to the large dimension equipment.

For example, Let L, U, and v^* are, respectively, the characteristic length, velocity, and turbulent viscosity of the large simulated object, and l, u, and v are the corresponding parameters of the small-scale lattice model.

The Reynolds number for the simulated object (large-scale) is then given by $\mathrm{Re} = \frac{LU}{v^*}$. By letting the corresponding Reynolds number of the lattice-Boltzmann model (small-scale) Re' be equal to Re, or $\frac{LU}{v^*} = \frac{lu}{v}$, then we have $v = v^*\frac{l}{L}\cdot\frac{u}{U}$, in

which the velocity ratio $\frac{u}{U}$ can be considered equal to the ratio of sound speeds $\frac{c_s}{C_s}$, and then the viscosity of lattice-Boltzmann simulation model should be modified to

$$v' = v^* \frac{l}{L} \cdot \frac{c_s}{C_s}$$

where c_s and C_s are, respectively, the speed of sound at lattice-Boltzmann model and at the actual object; the ratio C_s/c_s can be set equal to 1. By using v' instead v in the lattice-Boltzmann model, the simulated results are applicable to the behaviors of the large object at the Reynolds number *Re*.

It should be emphasised that the similarity principle is not applicable to more than one dimensionless group. For instance, under the condition of *Re* is equal for both the object and model simulation, the corresponding dimensionless group *Eu* may not be equal. Therefore only the dominated dimensionless group is used to modify the scaling up simulation. Obviously, the application of such method of scale-up is restricted.

10.1.3 Lattice-Boltzmann Method for Heat Transfer Process

(1) Scalar temperature model

The discrete LBGK equation for heat transfer can be expressed below if the source term is ignored [16]:

$$T_\alpha(\boldsymbol{x} + \boldsymbol{e}_\alpha \Delta t, t + \Delta t) - T_\alpha(\boldsymbol{x}, t) = -\frac{1}{\tau_h}\left[T_\alpha(\boldsymbol{x}, t) - T_\alpha^{\mathrm{eq}}(\boldsymbol{x}, t)\right] \tag{10.10}$$

where T_α is the temperature distribution function; τ_h is the single relaxation time for heat transfer. The equilibrium T_α is given below:

$$T_\alpha^{\mathrm{eq}} = \omega_\alpha T\left[\frac{\boldsymbol{e}_\alpha \cdot \boldsymbol{u}}{c_s^2} + \sigma\right]$$

where $\boldsymbol{e}_\alpha$ and ω_α for D2Q9 model are referred to Eq. (10.6) with lattice velocity $c = \frac{\Delta x}{\Delta t} = \sqrt{3RT} = \sqrt{3}c_s$. The τ_h is calculated by

$$\alpha = \sigma c_s^2\left(\tau_h - \frac{1}{2}\right)\Delta t$$

where α is thermal diffusivity. The simulated temperature and velocity distributions of the process can be obtained by solving simultaneously Eq. (10.10) with fluid dynamic equations (10.9) and (10.6).

(2) Heat energy model

He proposed a model considering the heat energy and heat flux can be expressed in terms of internal energy distribution function [17]. On this basis, Dixit suggested a simplified model [15], in which the internal energy distribution function is given by

$$g(\boldsymbol{x},\boldsymbol{e},t)=\frac{(\boldsymbol{e}-\boldsymbol{u})^2}{2}f$$

The internal energy is calculated by

$$E(\boldsymbol{x},t)=\frac{1}{\rho(\boldsymbol{x},t)}\int g(\boldsymbol{x},\boldsymbol{e},t)\mathrm{d}\boldsymbol{e}$$

Similar to the Boltzmann equation, the equation of internal energy can be expressed in the form of approaching to the equilibrium as follows:

$$\frac{\partial g}{\partial t}+\boldsymbol{e}\cdot\nabla g=-\frac{g-g^{\mathrm{eq}}}{\tau_{\mathrm{e}}}$$

where τ_{e} is the single relaxation time for internal energy distribution function.

The foregoing equation can be discrete as follows:

$$g_\alpha(\boldsymbol{x}+\boldsymbol{e}_\alpha\Delta t,t+\Delta t)-g_\alpha(\boldsymbol{x},t)=-\frac{1}{\tau_{\mathrm{e}}}\left[g_\alpha(\boldsymbol{x},t)-g_\alpha^{\mathrm{eq}}(\boldsymbol{x},t)\right] \tag{10.11}$$

For D2Q9 model, the g_α^{eq} is given by

$$g_\alpha^{\mathrm{eq}}=\begin{cases}-\frac{2}{3}\rho E\frac{\boldsymbol{u}^2}{RT}, & \alpha=0\\ \frac{\rho E}{9}\left[\frac{3}{2}+\frac{3\boldsymbol{e}_\alpha\cdot\boldsymbol{u}}{2RT}+\frac{9(\boldsymbol{e}_\alpha\cdot\boldsymbol{u})^2}{4(RT)^2}-\frac{3\boldsymbol{u}^2}{2RT}\right], & \alpha=1,2,3,4\\ \frac{\rho E}{36}\left[3+6\frac{\boldsymbol{e}_\alpha\cdot\boldsymbol{u}}{RT}+\frac{9(\boldsymbol{e}_\alpha\cdot\boldsymbol{u})^2}{2(RT)^2}-\frac{3\boldsymbol{u}^2}{2RT}\right], & \alpha=5,6,7,8\end{cases}$$

The macroscopic quantities are calculated by

$$\rho=\sum_\alpha f_\alpha$$

$$\rho\boldsymbol{u}=\sum_\alpha \boldsymbol{e}_\alpha f_\alpha$$

$$\rho E=\sum_\alpha g_i$$

For the calculation of τ_e, He and Dixit gave the following equation [15] for D2Q9 lattice model:

$$\alpha = \frac{2}{3}c^2\left(\tau_e - \frac{1}{2}\right)\Delta t = 2c_s^2\left(\tau_e - \frac{1}{2}\right)\Delta t$$

where $c = \sqrt{3RT}$; $c_s = \sqrt{RT}$.

The simulated temperature and velocity distributions of the heat transfer process can be obtained by simultaneous solution of Eq. (10.11) and fluid dynamic equations Eqs. (10.9) and (10.6).

10.1.4 Lattice-Boltzmann Method for Mass Transfer Process

The following mass transfer (species conservation) equation can be derived from lattice-Boltzmann equation after Chapman–Enskog expansion [18] (also see Appendix 5).

$$\frac{\partial c_k}{\partial t} + \boldsymbol{u}\frac{\partial c_k}{\partial x_i} = \frac{\partial}{\partial x_i}\left(D_k\frac{\partial c_k}{\partial x_i}\right)$$

where c_k is the concentration of component species k; D_k is the diffusivity of species k. Thus the LBM is applicable to the simulation of mass transfer process.

The foregoing equation can be discrete as follows:

$$G_\alpha^k(\boldsymbol{x} + \boldsymbol{e}_\alpha\Delta t, t + \Delta t) - G_\alpha^k(\boldsymbol{x}, t) = -\frac{1}{\tau_k}\left[G_\alpha^k(\boldsymbol{x}, t) - G_\alpha^{k,\mathrm{eq}}(\boldsymbol{x}, t)\right] + \boldsymbol{S}_\alpha^k \qquad (10.12)$$

where G_α^k is the concentration distribution function of component species k; τ_k is the single relaxation time for the mass transfer; $\boldsymbol{S}_\alpha^k$ is the source term for component species k. It is noted that the foregoing equation can be written for each component species.

For the mass transfer process accompanied with chemical reaction, each mode can be considered as a complete mixing reactor, the concentration change of component species k at Δt can be calculated from the equation of reaction kinetics. The $G_\alpha^{k,\mathrm{eq}}$ is given below for D2Q9 model

$$G_\alpha^{k,\mathrm{eq}} = \omega_\alpha c_n\left[1 + \frac{\boldsymbol{e}_\alpha\cdot\boldsymbol{u}}{RT} + \frac{(\boldsymbol{e}_\alpha\cdot\boldsymbol{u})^2}{2(RT)^2} - \frac{\boldsymbol{u}^2}{2RT}\right]$$

The concentration of component species k is calculated by

$$c_k = \sum_{\alpha} G_{\alpha}^{k}$$

The relaxation time τ_k, which is related with D_k, can be determined by the relationship

$$D_k = c_s^2 \left(\tau_k - \frac{1}{2} \right) \Delta t$$

The concentration distributions of component species k and the fluid velocity can be obtained by the simultaneous solution of Eq. (10.12) and fluid dynamic Eqs. (10.9) and (10.6).

10.2 Simulation of Solute Diffusion from Interface to the Bulk Liquid

The simulated object is the absorption of CO_2 through horizontal interface in a container by the ethanol as shown in Fig. 10.4.

The density difference between interface and the bulk liquid is considered as external force F. The influence of the external force on the simulation by LBM is realized by modifying macroscopic velocity $\boldsymbol{u}$ by $\boldsymbol{u}^*$ as follows:

$$\boldsymbol{u}^* = \boldsymbol{u} + \frac{\boldsymbol{F}\tau}{\rho}\Delta t = \boldsymbol{u} + \frac{\left(\frac{\partial \rho}{\partial c_k}\right)(c_{k,i} - c_k)\boldsymbol{g}}{\rho}\tau \Delta t$$

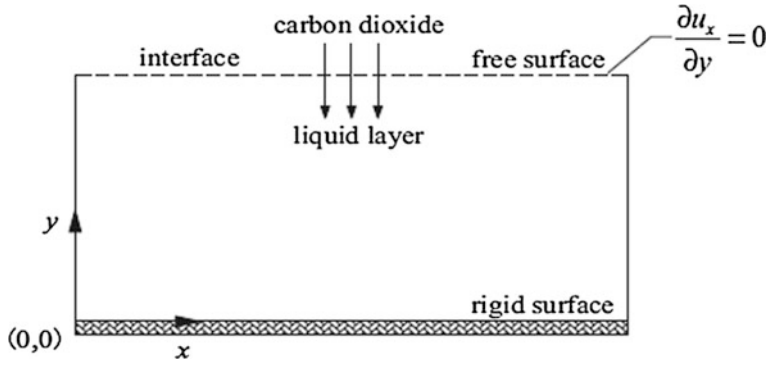

Fig. 10.4 Simulation domain of Rayleigh convection

where $c_{k,i}$ and c_k are, respectively, the concentration of component species k at the interface and in the bulk liquid.

The model equations are shown below

The LBGK equation for solvent particles

$$f_\alpha(\boldsymbol{x}+\boldsymbol{e}_a\Delta t, t+\Delta t) - f_\alpha(\boldsymbol{x},t) = -\frac{1}{\tau}\left[f_\alpha(\boldsymbol{x},t) - f_\alpha^{\mathrm{eq}}(\boldsymbol{x},t)\right], \quad \alpha = 0,1,2,\ldots,8$$

$$f_\alpha^{\mathrm{eq}} = \omega_\alpha \rho\left[1 + \frac{\boldsymbol{e}_\alpha\cdot\boldsymbol{u}^*}{RT} + \frac{(\boldsymbol{e}_\alpha\cdot\boldsymbol{u}^*)^2}{2(RT)^2} - \frac{\boldsymbol{u}^{*2}}{2RT}\right]$$

$$\rho = \sum_{\alpha=0}^{8} f_\alpha(\boldsymbol{x},t)$$

$$\rho\boldsymbol{u}^* = \sum_{\alpha=0}^{8} \boldsymbol{e}_\alpha f_\alpha(\boldsymbol{x},t) + \tau_0 \boldsymbol{F}$$

$$v = c_s^2\left(\tau - \frac{1}{2}\right)\Delta t$$

The LBGK equation for solute particles

$$G_\alpha^k(\boldsymbol{x}+\boldsymbol{e}_\alpha\Delta t, t+\Delta t) - G_\alpha^k(\boldsymbol{x},t) = -\frac{1}{\tau_n}\left[G_\alpha^k(\boldsymbol{x},t) - G_\alpha^{k,\mathrm{eq}}(\boldsymbol{x},t)\right], \quad \alpha = 0,1,2,\ldots,8$$

$$G_\alpha^{k,\mathrm{eq}} = \omega_\alpha c_n\left[1 + \frac{\boldsymbol{e}_\alpha\cdot\boldsymbol{u}^*}{RT} + \frac{(\boldsymbol{e}_\alpha\cdot\boldsymbol{u}^*)^2}{2(RT)^2} - \frac{\boldsymbol{u}^{*2}}{2RT}\right]$$

$$c^k = \sum_\alpha G_\alpha^k$$

$$D_k = c_{\mathrm{s}}^2\left(\tau_k - \frac{1}{2}\right)\Delta t$$

The profiles of concentration and velocity of the gas–liquid interfacial diffusion process can be obtained by the simultaneous solution of the model equations.

Boundary conditions

The bounce-back boundary condition is applied to the solid bottom of the container, the bounce-back or periodic boundary conditions can be employed to the left and right walls according to the model condition.

In the gas–liquid mass transfer process, such as absorption, the interface can be considered as composed of numerous number of local solute concentration points. Due to the fluctuation of solute concentration and stochastic local absorption, the interfacial solute concentration cannot be remained uniform and inevitably appear some local points with higher solute concentration. For instance, in the gas absorption process, some solvent points at the gas–liquid contacting interface may absorb the solute prior to the others to form higher solute concentration so as to create solute concentration gradient. The higher solute concentration point diffuses

instantly from interface to the bulk liquid and at the same time the solute concentration is being lowered. If the depleted solute is not renewed in time, the priority of diffusion will shift to the neighboring point with higher solute concentration. The diffusion of interfacial local solute points is thus competitive and stochastic.

The appearance of solute concentration gradient at interface (as well as the accompanied surface tension, density and temperature gradients) may produce interfacial instability or disturbance, by which the Marangoni and Rayleigh convections are induced, the former is acting mainly around the interface and the latter between the interface and the bulk liquid. Thus the description of concentration distribution at interface, which may be regarded as interface model, should be designated, for which the following models are given in subsequent sections.

- Fixed point interfacial disturbance model
- Random point interfacial disturbance model
- Self-renewable interface model

10.3 Fixed Point Interfacial Disturbance Model

The gas–liquid mass transfer process of CO_2 absorbed by quiescent ethanol is Rayleigh unstable ($Ra > 0$) and Marangoni stable ($Ma < 0$). The absorption process is initiated at some local points to create concentration gradient at the interface and also establish the density gradient between interface and the bulk liquid. Thus the condition of specified disturbance points (higher concentration points) at the interface is necessary as shown in following sections.

10.3.1 Single Local Point of Disturbance at Interface

The study of local single point diffusion is helpful to understand the development of mass transfer from gas to the liquid phase. Fu employed LBM to investigate the point diffusion process of solute from interface to the bulk liquid and the influence by Rayleigh convection [19]. The object of simulation is the absorption of CO_2 (solute) by ethanol (solvent) in a container. The physical properties of the solute and the solvent are given in Table 10.1.

Table 10.1 Physical properties of solute and solvent

v/(m^2 s^{-1})	D_k/(m^2 s^{-1})	ρ/(kg m^{-3})	C_{sat}/(kg m^{-3})	$\partial\rho/\partial C$	Sc	Ra
1.52×10^{-6}	3.42×10^{-9}	788.9	5.15	0.214	444.44	3.19×10^{5}

Note v is the kinematic viscosity of ethanol; D_k is the diffusivity of CO_2 in ethanol; C is the concentration of CO_2 in ethanol; C_{sat} is the saturated concentration of CO_2 in ethanol; ρ is the density of ethanol

Assumptions

(1) The gas phase resistance of mass transfer is neglected and the diffusion is liquid film control. The liquid phase is pure ethanol;
(2) The absorption is low, and the heat of absorption can be neglected;
(3) The interface is horizontal and flat without deformation.

The simulated domain is 5 × 5 mm square flow field with 100 × 100 grids. Extended boundary condition is applied to the upper gas–liquid interface; periodic and bounce-back boundary conditions are chosen, respectively, for the two side walls and solid bottom. The simulated scale is $\Delta x = 5 \times 10^{-5}$ m and $\Delta t = 5 \times 10^{-5}$ s. An uniform distributed higher solute concentration is set in the width of 1 mm at the interface at $t = 0$. During the diffusion process, both Marangoni and Rayleigh convections are simultaneously coupling; the former is created at the surface and the latter is formed perpendicular to the interface. Figure 10.5 give the simulated results at different time:

Figure 10.5 shows at $t = 1$ and $t = 5$ s the solute diffuse freely from the concentrated point and no Rayleigh convection is found in the vertical direction. At $t = 10$ s, the solute diffusion cell is squeezed by the new born Rayleigh convection to form cylindrical shape. Later at $t = 20$ s, the further influence by the two symmetrical Rayleigh convections (see Fig. 10.6) is obvious, which squeeze the diffusion cell to the shape of inverted mushroom with long rod. Afterward the circulating Rayleigh convections become stronger and lead the mushroom top to be in anchor shape. Figure 10.6 displays clearly the symmetrical Rayleigh convection, it moves gradually downward with stronger circulation.

10.3.2 *Influence of Physical Properties on the Solute Diffusion from Interface*

Under the conditions of fixed interfacial local point of disturbance and linear relationship between concentration and density, the influence of kinematic viscosity and diffusivity of solute on the interfacial diffusion was studied by Fu [21] as given below.

The simulated conditions (size of simulated object, grid network and interfacial concentration) are identical with Sect. 10.3.1 except the physical properties as given in Table 10.2. The simulated profiles of solute concentration at $t = 20$ and $t = 30$ s for various physical properties of solvent are shown in Figs. 10.7 and 10.8.

Figures 10.7 and 10.8 indicate that at constant v and increasing D_k, the solute diffusion is intensified by Rayleigh convection. At constant D_k and increasing v, the Rayleigh convection is depressed. Also, in Fig. 10.8, by comparing Fig. 10.7d

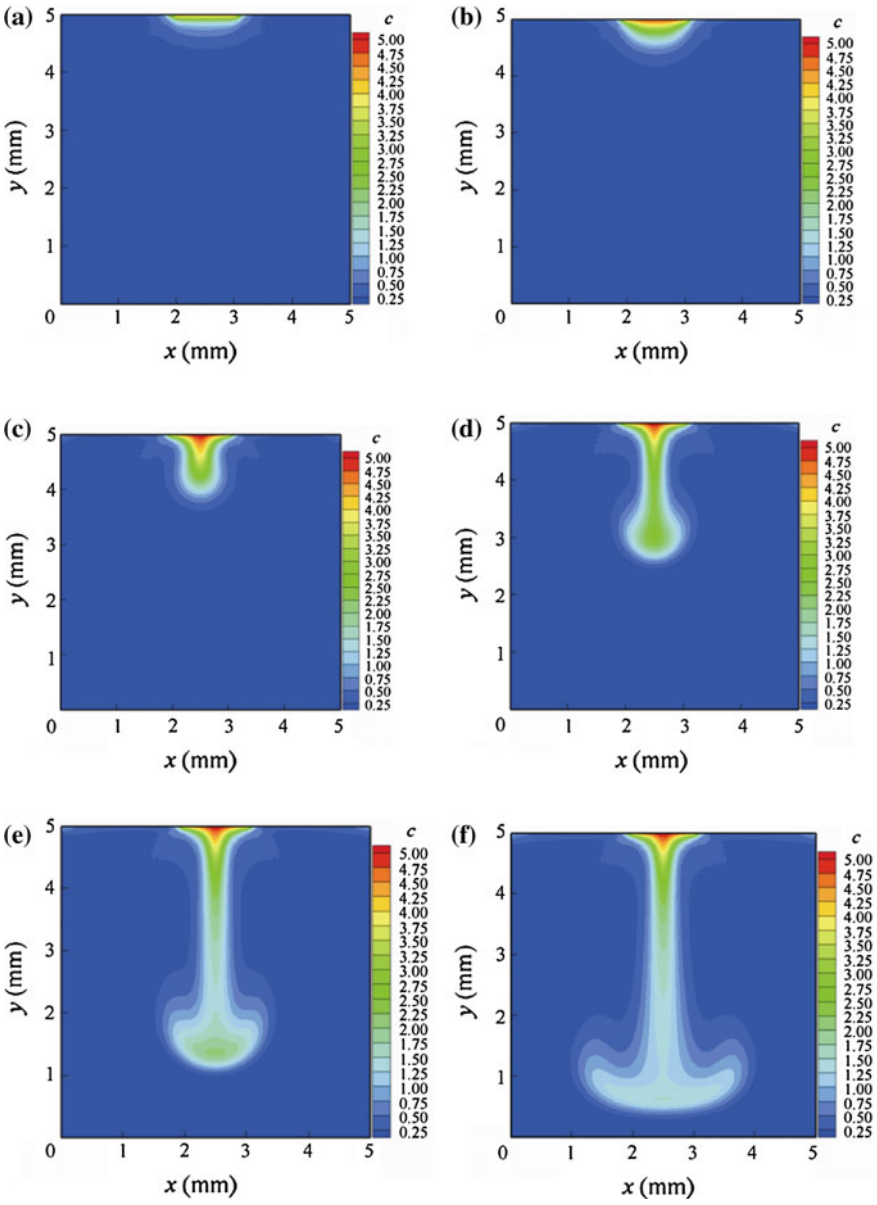

Fig. 10.5 Solute distribution profile at different time. **a** t = 1.0 s, **b** t = 5.0 s, **c** t = 10 s, **d** t = 15 s, **e** t = 20 s, **f** t = 25 s

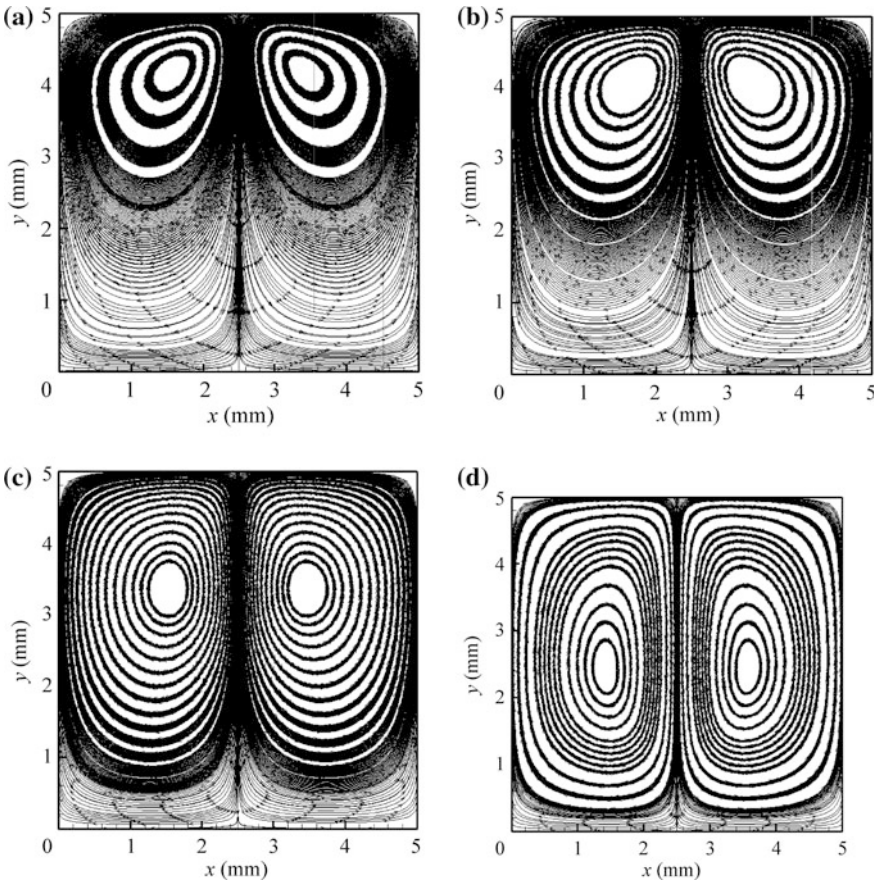

Fig. 10.6 Contours of Rayleigh convection at different time. **a** t = 5 s, **b** t = 10 s, **c** t = 15 s, **d** t = 20

Table 10.2 Different conditions of simulation

Serial marks	v (m^2/s)	D_k (m^2/s)	$\partial\rho/\partial C$	ρ (kg/m^3)	Sc	Ra
a	2×10^{-6}	1×10^{-9}	0.214	1000	2000.0	6.55×10^5
b	2×10^{-6}	2×10^{-9}	0.214	1000	1000.0	3.28×10^5
c	2×10^{-6}	3×10^{-9}	0.214	1000	666.7	2.18×10^5
d	2×10^{-6}	4×10^{-9}	0.214	1000	500.0	1.64×10^5
e	1×10^{-6}	2×10^{-9}	0.214	1000	500.0	6.55×10^5
f	3×10^{-6}	2×10^{-9}	0.214	1000	1500.0	2.18×10^5
g	4×10^{-6}	2×10^{-9}	0.214	1000	2000.0	1.64×10^5

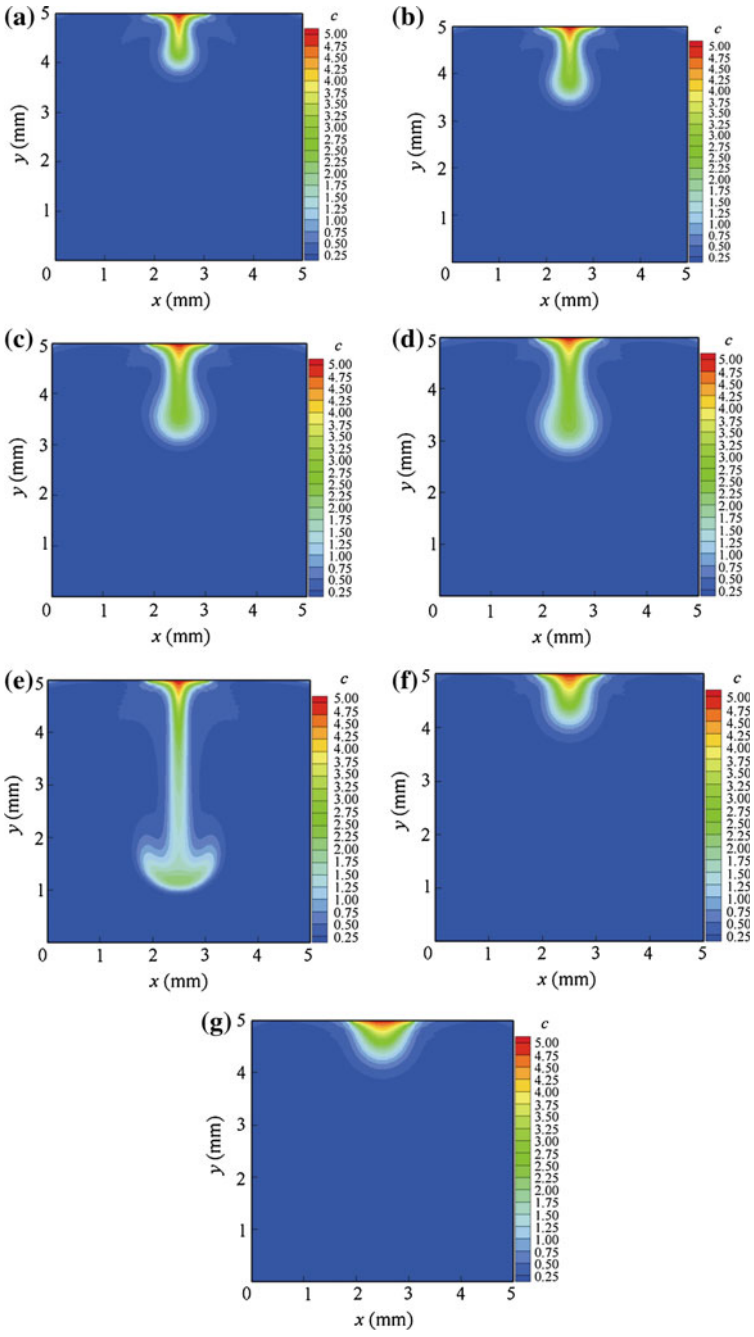
(a)
(b)
(c)
(d)
(e)
(f)
(g)
c
5.00
4.75
4.50
4.25
4.00
3.75
3.50
3.25
3.00
2.75
2.50
2.25
2.00
1.75
1.50
1.25
1.00
0.75
0.50
0.25
y (mm)
x (mm)
0
1
2
3
4
5

◀ **Fig. 10.7** The solute concentration profiles under different diffusivities (**a**–**d**) and kinematic viscosities (**e**–**g**) at $t = 20$ s. **a** $\nu = 2 \times 10^{-6}$ m^2 s^{-1}, $D_k = 1 \times 10^{-9}$ m^2 s^{-1}, **b** $\nu = 2 \times 10^{-6}$ m^2 s^{-1}, $D_k = 2 \times 10^{-9}$ m^2 s^{-1}, **c** $\nu = 2 \times 10^{-6}$ m^2 s^{-1}, $D_k = 3 \times 10^{-9}$ m^2 s^{-1}, **d** $\nu = 2 \times 10^{-6}$ m^2 s^{-1}, $D_k = 4 \times 10^{-9}$ m^2 s^{-1}, **e** $\nu = 1 \times 10^{-6}$ m^2 s^{-1}, $D_k = 2 \times 10^{-9}$ m^2 s^{-1}, **f** $\nu = 3 \times 10^{-6}$ m^2 s^{-1}, $D_k = 2 \times 10^{-9}$ m^2 s^{-1}, **g** $\nu = 4 \times 10^{-6}$ m^2 s^{-1}, $D_k = 2 \times 10^{-9}$ m^2 s^{-1}

($Sc = 500$) and Fig. 10.7g ($Sc = 2000$) at constant Ra, the solute diffusion is stronger at smaller Sc number. On the other hand, by comparing (a, $Ra = 6.55 \times 10^5$) and (g, $Ra = 1.64 \times 10^5$) at constant Sc, the Rayleigh convection is promoted by greater Ra number.

10.3.3 Uniformly Distributed Multi-points of Disturbance at Interface

Similar to Sect. 9.3.2, Fu simulated the absorption of CO_2 by ethanol with 19 points of disturbance at the interface [20]. The periodic boundary condition is employed for the left and right sides of the container with $\Delta x = 1 \times 10^{-4}$ m and $\Delta t = 1 \times 10^{-4}$ s. Figure 10.9 gives the solute distribution profiles at $t = 30$ s for $n = 1, 2, 3, 4, 5, 7, 9, 19$.

In Fig. 10.9, when the number of concentration point is small ($n < 5$), the concentration profile is clearly in anchor shape. When the number of concentration points is larger ($n < 5$), the diffusion at the center of interface is suppressed and restricted to a small region by the strong upward symmetrical Rayleigh convection as seen in Fig. 10.8d. When the concentration point is further increased ($n = 19$), the diffusion at the central part of interface is almost stopped by the Rayleigh convection and only appeared round the region near the wall.

Figure 10.10 displays the velocity vector diagram of $n = 5$ at different time. At $t = 1$ s, small convection is seen at every designated interfacial points. At $t = 10$ s, Rayleigh convection structure is appeared. At $t = 30$ s, strong Rayleigh convection is clearly seen with the tendency of developing large convection.

If n is very large to approach infinite, that means the solute concentration is uniformly distributed at the interface, the progress of diffusion is shown in Fig. 10.11.

As seen in Fig. 10.11a, b, the interfacial disturbance starts firstly around the two sides of container wall, it may be due to the numerical perturbation in model computation. However, following the Rayleigh convection, the solute concentration there is being lowered, and create concentration gradient with the neighboring points so that to induce more Rayleigh convections as seen in Fig. 10.11c. After that, four mushroom type convections are formed toward the bottom and soon combined to large convective flow as shown in Fig. 10.11h–l. It demonstrates that the large Rayleigh convection is created from the mutual interaction of small convections; such phenomenon is consistent with the experimental observation.

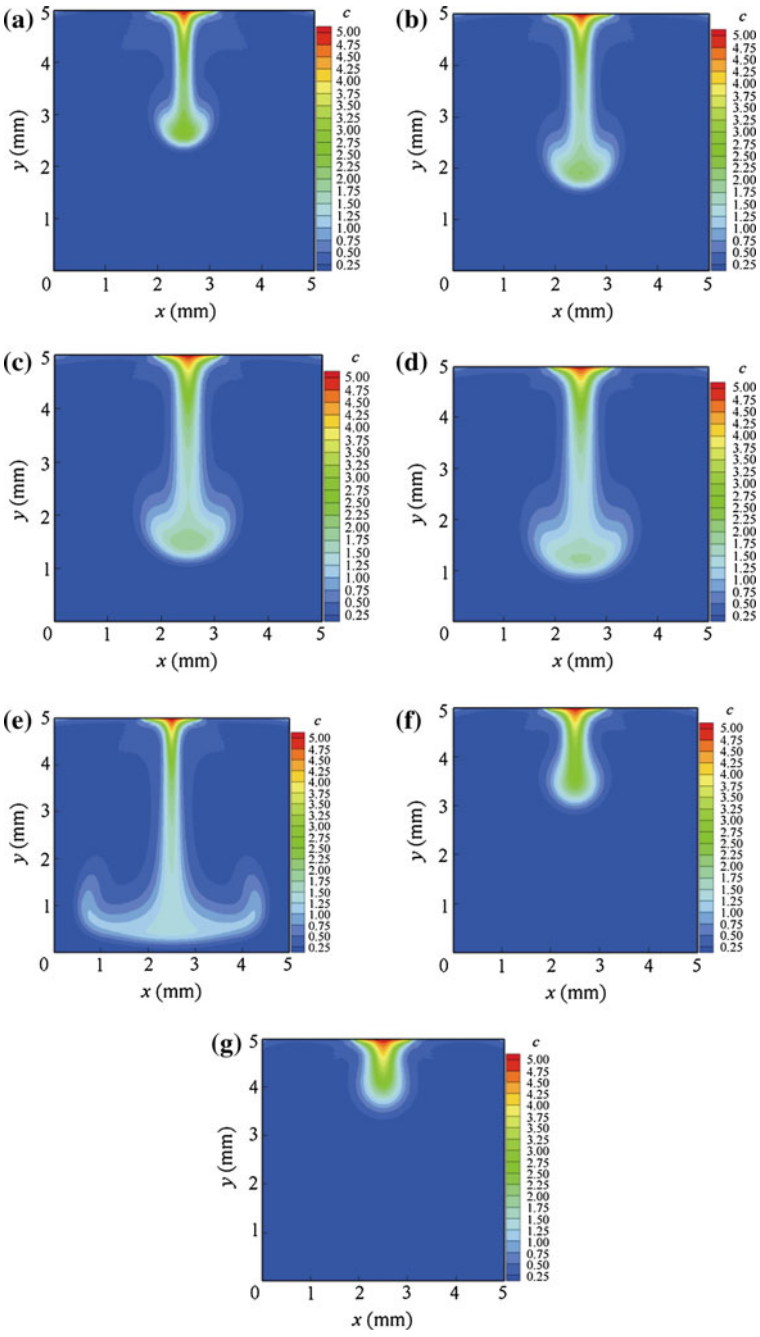
(a)
(b)
(c)
(d)
(e)
(f)
(g)
c
5.00
4.75
4.50
4.25
4.00
3.75
3.50
3.25
3.00
2.75
2.50
2.25
2.00
1.75
1.50
1.25
1.00
0.75
0.50
0.25
y (mm)
x (mm)
0
1
2
3
4
5

◀ **Fig. 10.8** The solute concentration profiles under different diffusivities (**a**–**d**) and kinematic viscosities (**e**–**g**) at $t = 30$ s. **a** $\nu = 2 \times 10^{-6}$ m^2 s^{-1}, $D_k = 1 \times 10^{-9}$ m^2 s^{-1}, **b** $\nu = 2 \times 10^{-6}$ m^2 s^{-1}, $D_k = 2 \times 10^{-9}$ m^2 s^{-1}, **c** $\nu = 2 \times 10^{-6}$ m^2 s^{-1}, $D_k = 3 \times 10^{-9}$ m^2 s^{-1}, **d** $\nu = 2 \times 10^{-6}$ m^2 s^{-1}, $D_k = 4 \times 10^{-9}$ m^2 s^{-1}, **e** $\nu = 1 \times 10^{-6}$ m^2 s^{-1}, $D_k = 2 \times 10^{-9}$ m^2 s^{-1}, **f** $\nu = 3 \times 10^{-6}$ m^2 s^{-1}, $D_k = 2 \times 10^{-9}$ m^2 s^{-1}, **g** $\nu = 4 \times 10^{-6}$ m^2 s^{-1}, $D_k = 2 \times 10^{-9}$ m^2 s^{-1}

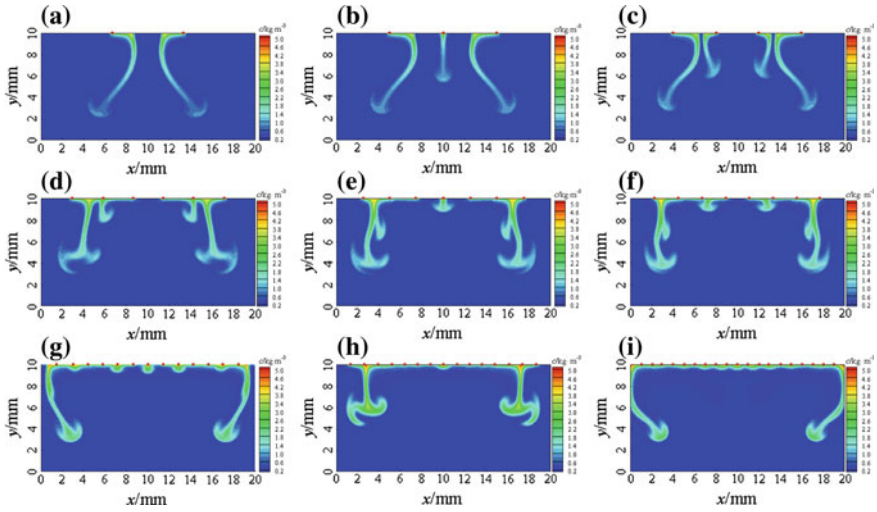

Fig. 10.9 The transient contours of solute concentration at $t = 30$ s for different n ($P = 10^{-4}$, $\beta = 10^{-8}$). **a** $n = 2$, **b** $n = 3$, **c** $n = 4$, **d** $n = 6$, **e** $n = 7$, **f** $n = 8$, **g** $n = 13$, **h** $n = 15$, **i** $n = 19$

10.3.4 Nonuniformly Distributed Multi-points of Disturbance at Interface

In the case that the distribution of local disturbance points is nonuniform, Figs. 10.12 and 10.13 show separately the concentration and velocity profiles for $n = 1$ and unevenly distributed $n = 2$ and $n = 3$ at $t = 35$ s.

As seen in Fig. 10.12, similar to the previous section, the shape of concentration profile is significantly influenced by the position of local points as well as Rayleigh convection and the wall effect. In Fig. 10.12c, d, the position of the three local points is different, so as to show different concentration profiles. The influence of Rayleigh convection and wall effect on the concentration profiles is also clearly seen by the velocity profiles shown in Fig. 10.13. The renewal of interfacial concentration is demonstrated in these figures by the convective circulation of the outer velocity contour of Rayleigh convection.

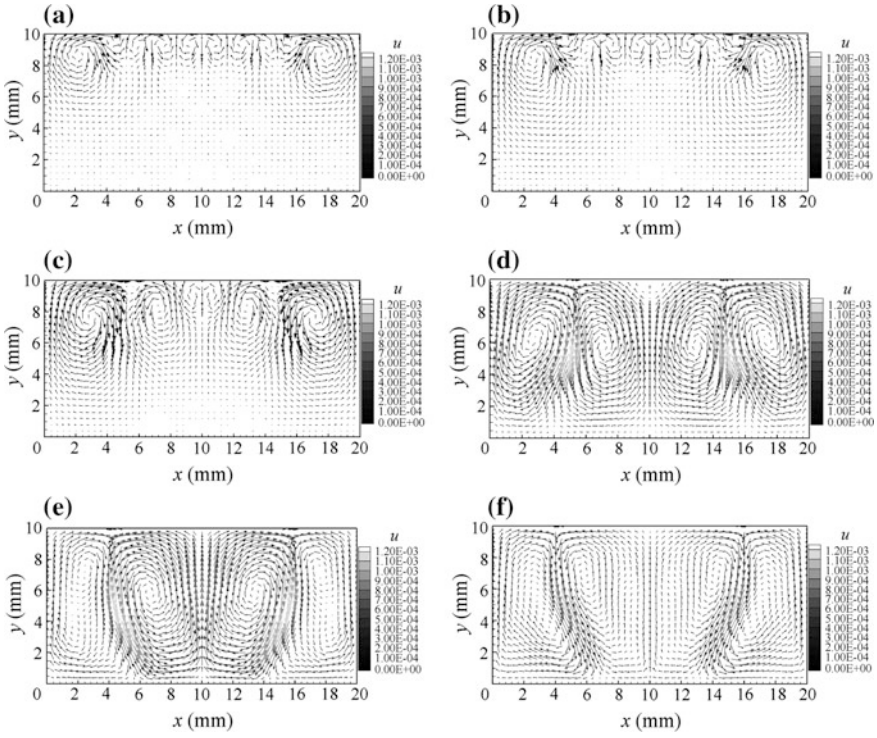

Fig. 10.10 Velocity vector diagram for $n = 5$ at different time. **a** $t = 1$ s, **b** $t = 10$ s, **c** $t = 20$ s, **d** $t = 30$ s, **e** $t = 40$ s, **f** $t = 50$ s

10.4 Random Disturbance Interfacial Model

Fu [21] proposed a random disturbance model by using P to represent the probability of concentration point at the interface with concentration higher than the average, denoted by C_D, and their suitable values are $0.05 \le P < 0.3$ and $10^{-15} < C_D \le 10^{-9}$ kg m^{-3}. For instance, let $P = 0.06$ and concentration $C_D = 10^{-12}$ kg m^{-3}. For instance, $P = 0.06$ means that there are 6 % randomly distributed concentration points out of every 100 points at the interface with concentration higher than the average interfacial concentration by 10^{-12} kg m^{-3}. For the absorption of CO_2 by ethanol as shown in Sect. 10.3.1, the concentration contours at $P = 0$ (no high concentration point) and $P = 0.06$ are given in Figs. 10.14 and 10.15 for comparison.

As shown in Fig. 10.14, if there is no disturbance at the interface ($P = 0$), no Rayleigh convection is found in spite of having concentration (density) difference between interface and the bulk liquid, and meanwhile only molecular diffusion of solute from interface occurs. Under the condition of disturbance at the interface with $P = 0.06$ and $\mathbf{C_D} = 10^{-12}$ kg m^{-3}, a slight deformation of the concentration

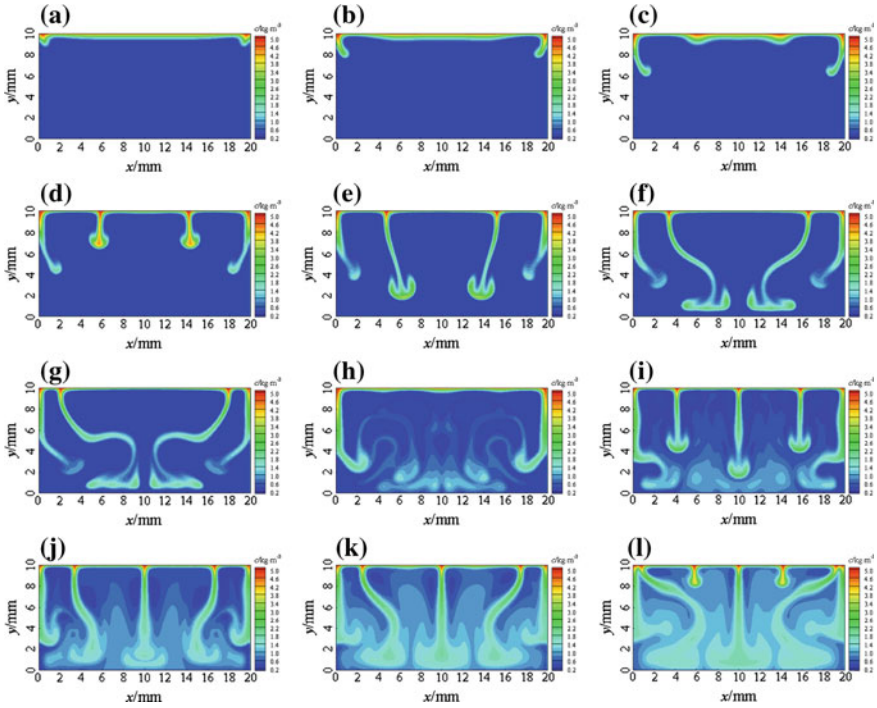

Fig. 10.11 The transient contours of solute concentration for $n = \infty$ at different times. **a** t = 40 s, **b** t = 20 s, **c** t = 30 s, **d** t = 35 s, **e** t = 40 s, **f** t = 45 s, **g** t = 50 s, **h** t = 70 s, **i** t = 90 s, **j** t = 110 s, **k** t = 130 s, **l** t = 150 s

contours is found at the left side near the wall at about t = 50–54 s, from where the Rayleigh convection initiates. The concentration cell is fully developed at t = 65 s and it is squeezed by two symmetrical Rayleigh convective fluid vortexes on both sides (not shown in the figure) so as forming the invert mushroom shape.

By this model, the simulated results of the transient fields of concentration and velocity vector under P = 0.06, $C_D = 10^{-12}$ are shown in Figs. 10.16 and 10.17.

As seen from Fig. 10.16, the interface display some unstable indication at 52 s (A) and then develop randomly to nearby local points. At the same time the developed concentration cells move downward to the bulk liquid. At 62 s, as seen in Fig. 10.17a, the velocity cell by Rayleigh convection has been formed to squeeze the concentration cell to become mushroom shape until reaching the bottom turning to anchor shape. It is noted that the circulating velocity of the velocity cell is about 10^{-3}–10^{-4} m s^{-1} which is consistent with the experimental measurement by Chen [23] and Fu [24]. The foregoing simulation demonstrates the velocity circulation promotes the renewal of concentration around interface so as to enhance the mass transfer by Rayleigh convection.

To test the effect of P on mass transfer, the quantity of instantaneous mass transferred N (kg m^{-2} s^{-1}) can be calculated for comparison. During the gas–liquid

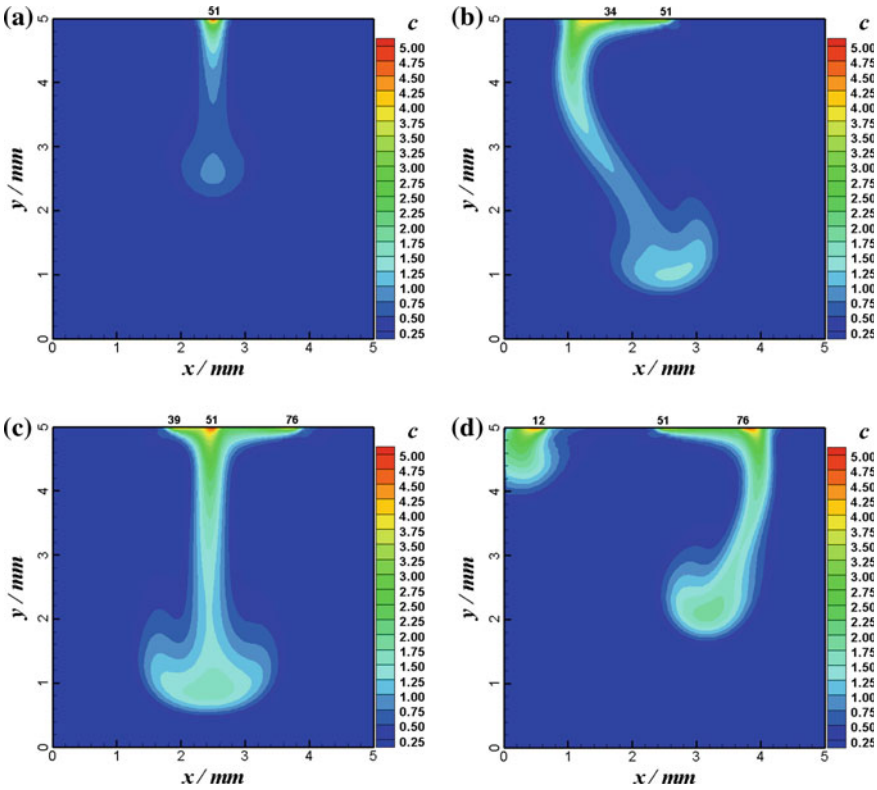

Fig. 10.12 Solute concentration profile for $n = 1$ and unevenly distributed $n = 2$ and $n = 3$ at $t = 35$ s. **a** $n = 1$, **b** $n = 2$, **c** $n = 3$, **d** $n = 3$

contacting time Δt, the instantaneous simulated $N_{\text{ins},t}$ can be calculated by the following equation between t and $t + \Delta t$:

$$N_{\text{ins},t} = \frac{[C(t+\Delta t) - C(t)] \cdot V}{\Delta t \cdot A_i} = \frac{[C(t+\Delta t) - C(t)] \cdot H}{\Delta t} \tag{10.13}$$

where C is the solute mass concentration; V is the volume of liquid; A_i is the area of the flat gas–liquid contacting interface; H is the thickness of the liquid.

Under the condition of no Rayleigh convection, the unsteady interfacial mass transferred N_{pen} can be calculated from penetration theory by the following equation:

$$N_{\text{pen}} = (C_i - C_0)\sqrt{\frac{D}{\pi t}} \tag{10.14}$$

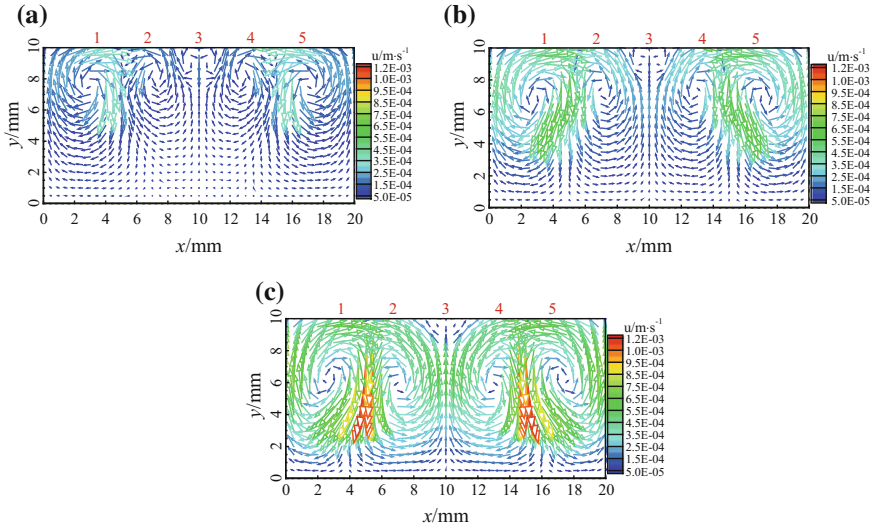

Fig. 10.13 The transient velocity vector distributions of flow field for $n = 5$ (uniformly distributed) at different times. **a** $t = 20$ s, **b** $t = 25$ s, **c** $t = 30$ s

where C_i is the interfacial concentration; C_0 is the solute concentration in the solvent.

With consideration of the Rayleigh convection, the simulated concentration profiles of CO_2 absorption by ethanol at interfacial solute concentration of 5 kg m^{-3} as shown in Fig. 10.16. From such profile, the values of $N_{\text{ins},t}$ during $C(t)$ and $C(t+\Delta t)$ is obtained by the summation of solute concentration counting in each lattice (discrete elements in computation) at time t and $t+\Delta t$. The calculated $N_{\text{ins},t}$, denoted by N_{sim}, is given in Fig. 10.18, in which the N_{pen} by penetration theory is also shown for comparison. In this figure, the onset of Rayleigh convection is found at about 50–54 s so that the mass flux N is increased sharply. After that, the wavy fluctuation of N_{sim} is due to the alternative action of depletion and renewal of solute at the interface as result of Rayleigh convection. Following the accumulation of solute in the liquid bulk by absorption, the driving force of mass transfer $(C_i - C_0)$ is gradually lowered to reduce both N_{sim} and N_{pen}. When the depletion of solute is compensated and renewed by Rayleigh convection, the N_{sim} goes up again. Such action is repeated alternatively forming a wavy curve.

The influence of P on the mass flux N_{sim} is given in Fig. 10.19 in which showing the onset time of Rayleigh convection is faster for greater P. After 120 s the N_{sim} is almost independent of P.

The influence of C_D on the mass flux N_{sim} is also given in Fig. 10.20 where the onset time of Rayleigh convection is faster for smaller C_D; the difference of simulations at different C_D are not obvious.

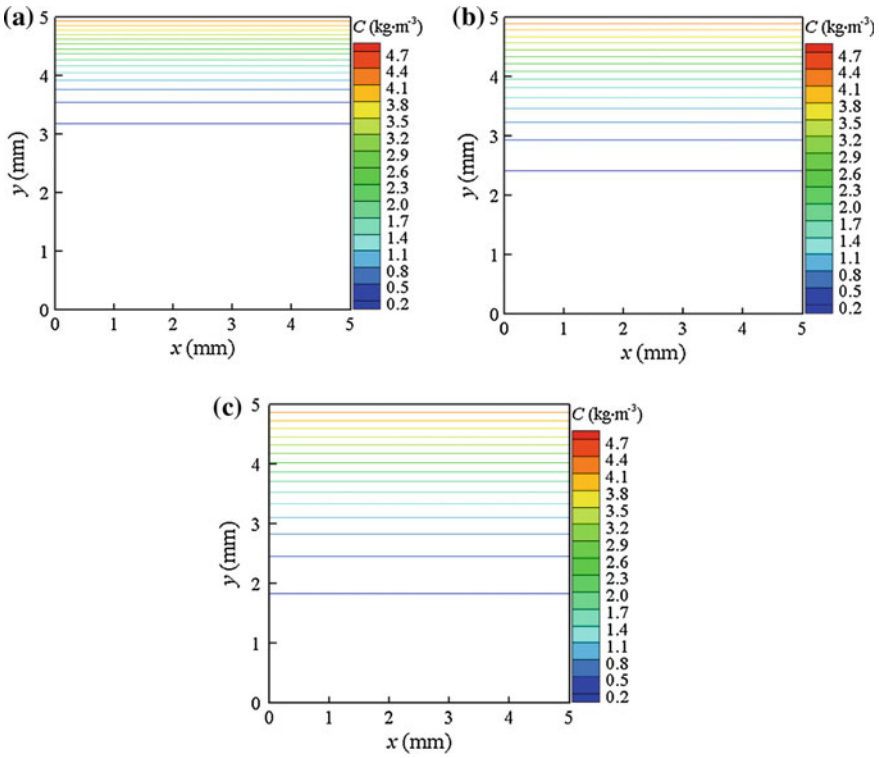

Fig. 10.14 Concentration profiles of CO_2 concentration without interfacial disturbance ($P = 0$, $C_D = 0$) at different times for CO_2 absorption by ethanol. **a** $t = 100$ s, **b** $t = 200$ s, **c** $t = 200$ s (Reprinted from Ref. [22], Copyright 2013, with permission from Elsevier)

The instantaneous mass transfer enhancement factor $F_{\text{ins},t}$ can also be calculated from the N curve by the equation:

$$F_{\text{ins},t} = \frac{N_{\text{ins},t}}{N_{\text{pen},t}}$$

where $N_{\text{pen},t}$ is the N by penetration theory.

The instantaneous mass transfer coefficient at time t, denoted by $k_{\text{ins},t}$, can be computed by the following equation:

$$k_{\text{ins},t} = \frac{(C_{t+\Delta T} - C_t)V}{A_i \Delta T (C_i - C_0)_{\text{av}}} = \frac{(C_{t+\Delta T} - C_t)H}{\Delta T (C_i - C_0)_{\text{av}}} \tag{10.15}$$

where C_i is the interfacial solute concentration; $(C_i - C_0)_{\text{av}}$ is the average of the driving force of mass transfer during Δt; Δt is the time interval which is set to be 0.1 s. The computed enhancement factor $F_{\text{ins},t}$ at different interfacial solute

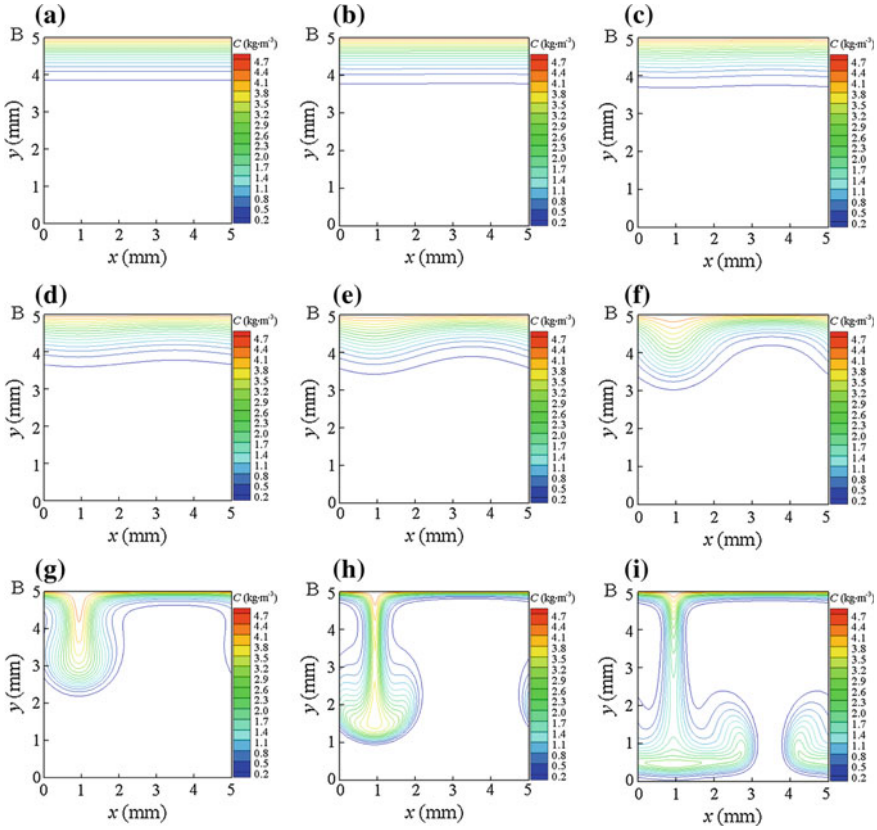

Fig. 10.15 CO_2 concentration profiles under $P = 0.06$, $C_D = 10^{-12}$ kg m^{-3} at different time for the process of CO_2 absorption by ethanol. **a** $t = 40$ s, **b** $t = 45$ s, **c** $t = 50$ s, **d** $t = 52$ s, **e** $t = 54$ s, **f** $t = 56$ s, **g** $t = 58$ s, **h** $t = 60$ s, **i** $t = 65$ s (Reprinted from Ref. [22], Copyright 2013, with permission from Elsevier)

concentration for different absorption processes are given in Figs. 10.21 and 10.22. As indicated in the figures, the onset time (the durations for $F = 1$) is quite different for different solvents.

As seen from Fig. 10.23, the variations of $k_{ins,t}$ for different interfacial concentration C_i have similar trend with those of the enhancement factor.

Fu further proposed more precise random disturbance model [22] by considering the position, size, and duration of concentration disturbance should be randomly varying in the real gas–liquid mass transfer process. In this model, a probability P and a coefficient of disturbance size β are introduced to express randomness of concentration disturbance at the liquid surface. The probability P at any point in the interface represents the probability of the occurrence of concentration disturbance at that point. The distribution size C_R is proportional to the degree approach (denoted

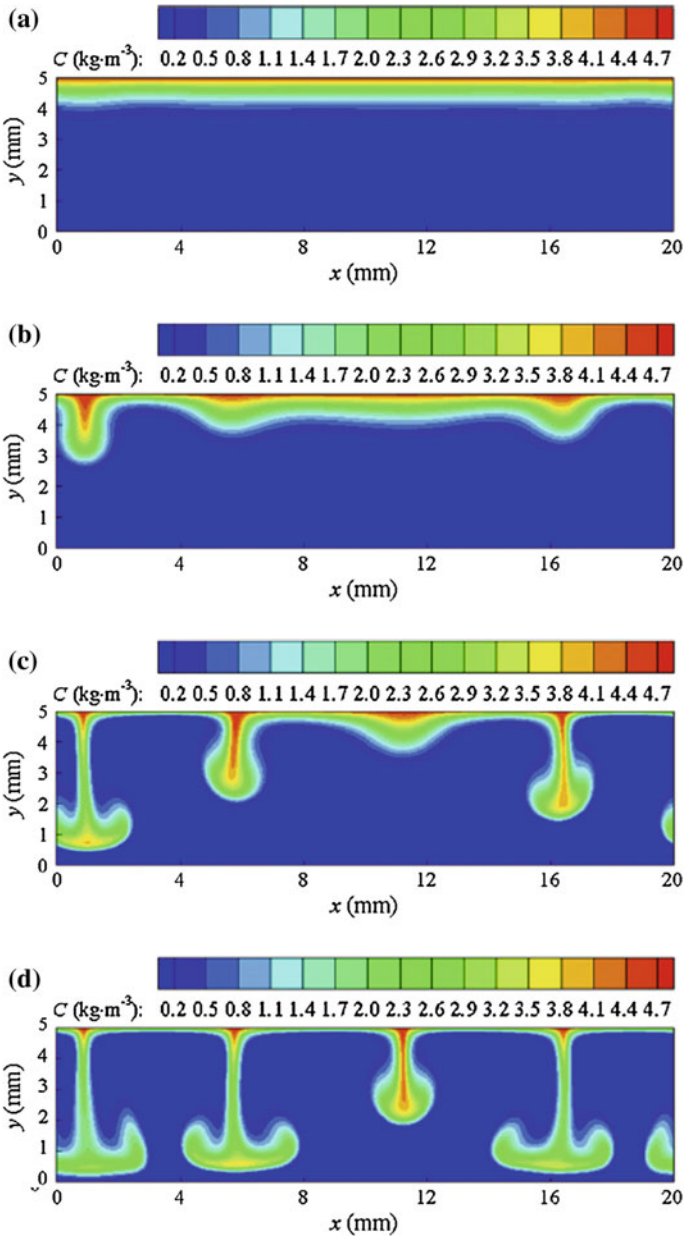

Fig. 10.16 Transient concentration fields of CO_2 at 52 s (**a**) 58 s (**b**), 62 s (**c**) and 66 s (**d**) for CO_2 absorption by ethanol (P = 0.06, $C_D = 10^{-12}$) (Reprinted from Ref. [22], Copyright 2013, with permission from Elsevier)

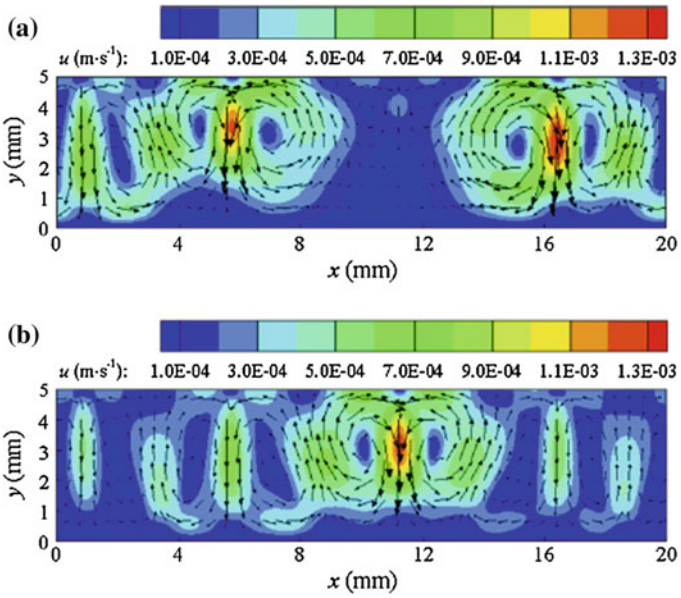

Fig. 10.17 Transient velocity vector field at 62 s (**a**) and 66 s (**b**) for CO_2 absorption by ethanol ($P = 0.06$, $C_D = 10^{-12}$) (Reprinted from Ref. [22], Copyright 2013, with permission from Elsevier)

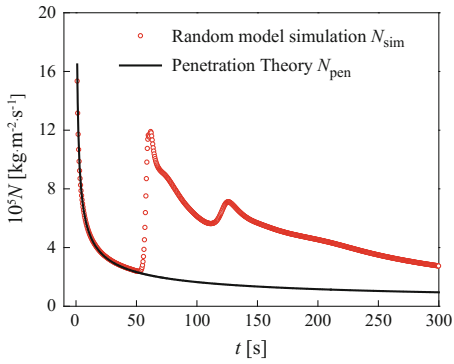

Fig. 10.18 Simulated N_{sim} by random disturbance model ($P = 0.06$, $C_D = 10^{-12}$ kg m^{-3}) and N_{pen} by penetration theory at different time (Reprinted from Ref. [22], Copyright 2013, with permission from Elsevier)

by β) of interfacial concentration C_i to the concentration of saturated liquid C_S as follows:

$$C_R = \beta(C_S - C_i)$$

Figure 10.24 is an example where the solute points with higher concentration are changing randomly at different time. As seen in the figure the evolution of the concentration contour is stochastic without definite pattern.

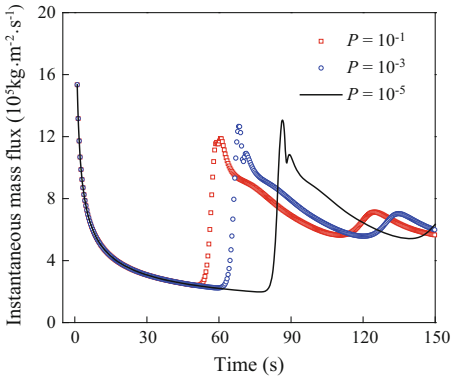

Fig. 10.19 Influence of P on N at $C_D = 10^{-12}$ kg m^{-3} in CO_2 absorption by ethanol

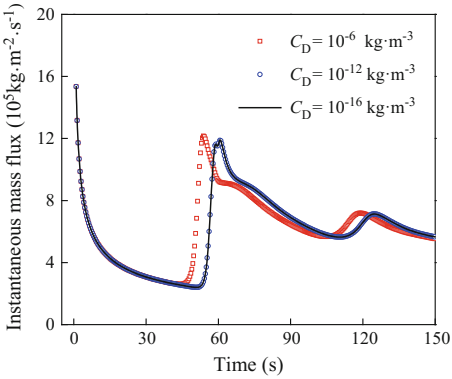

Fig. 10.20 Influence of C_D on N at $P = 0.1$ for CO_2 absorption by ethanol

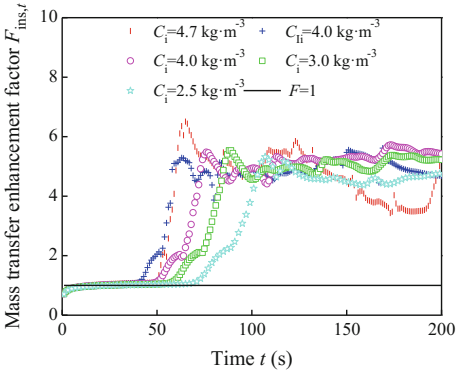

Fig. 10.21 Instantaneous mass transfer enhancement factor for different interfacial concentration for the process of CO_2 absorption by ethanol

As seen in Fig. 10.25, velocity of Rayleigh convection and mutual interaction is increased with time. The random characters of both velocity and concentration are obvious.

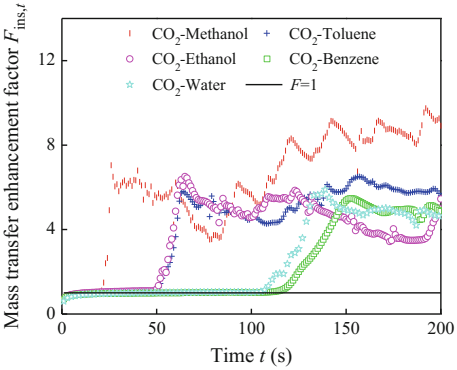

Fig. 10.22 Variation of instantaneous mass transfer enhancement factor with time for the process of CO_2 absorption by various solvents

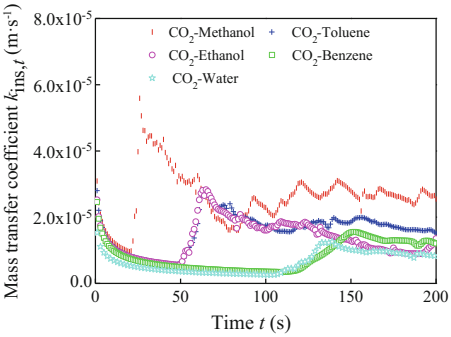

Fig. 10.23 Variation of instantaneous mass transfer coefficient with time for CO_2 absorption by various solvents

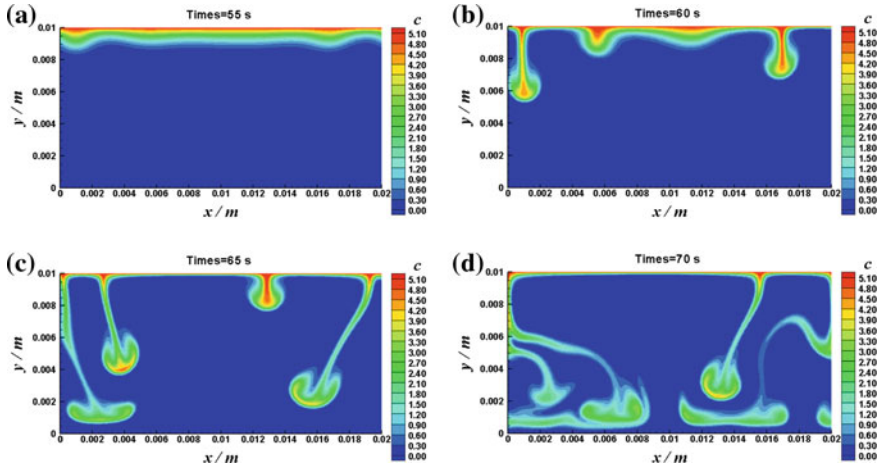

Fig. 10.24 Concentration profiles of random disturbance interfacial diffusion at different time ($P = 10^{-4}$, $\beta = 10^{-8}$). **a** t = 55 s, **b** t = 60 s, **c** t = 65 s, **d** t = 70 s

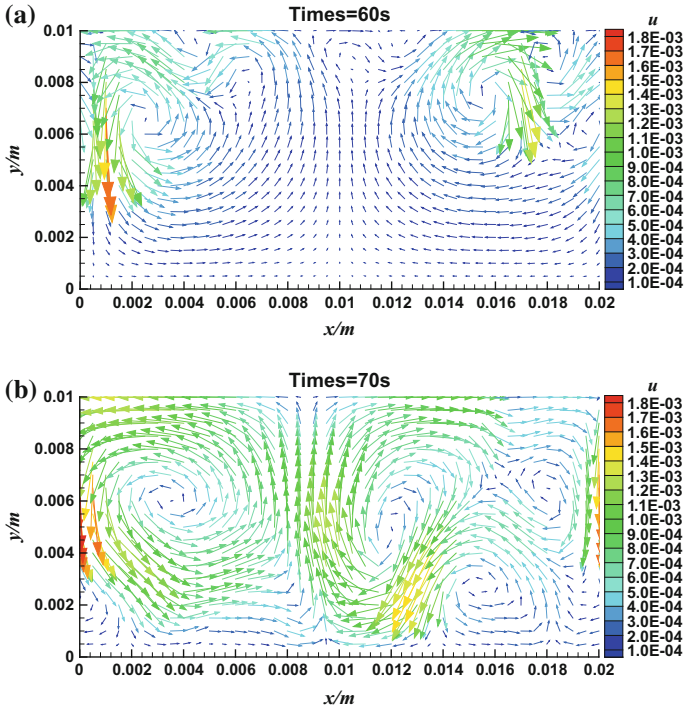

Fig. 10.25 Velocity vector of random interfacial diffusion at different time. **a** t = 60 s, **b** t = 70 s

10.5 Self-renewable Interface Model

For the self-renewable interface model, the simulated domain as shown in Fig. 10.25 consists of two parts: the quiescent gas and liquid phases. The evolutions of concentration distributions in both gas and liquid phases are simulated and the disturbance is maintained by the evolution of the interfacial concentration distribution. For this purpose, a zone of gas phase is imposed between the liquid and gas phases as shown in Fig. 10.25 where both gas and liquid phases are quiescent and the mass transfer in gas phase is only by molecular diffusion. This approach was developed based on the implementations of the gravity/buoyancy and surface tension forces, and an interfacial perturbation model, namely, the self-renewal interface model.

Chen [25] implemented this model by considering an instantaneous nonuniform concentration distribution of gas phase at the interface due to the localizing mass transfer from the interface to be the source of disturbance. The nonuniform distribution of concentration in the gas phase at the interface leads to different driving force of mass transfer and the instantaneous depletion of solute enhance the nonuniformity of the interfacial concentration so as to promote the Rayleigh

convection. Moreover, in LBM, the numerical accuracy and stability are strongly dependent on the relaxation time τ see Sect. 10.1.4) which should be greater than 0.5. Nevertheless, as Servan-Camas pointed out [26], the computed accuracy drops down after $\tau \approx 0.789$. In CO_2 absorption, the liquid phase Sc is in the order of 10^2 and therefore the τ_c is out of the 0.5–0.789 satisfactory range. To overcome this difficulty, Chen employed a hybrid model for computation in which the velocity field is computed according to BGK equation and the concentration field is calculated by using finite different method (FDM).

The governing equation of concentration field C_k is as follows:

$$\frac{\partial C_k}{\partial t} + \boldsymbol{u}\frac{\partial C^k}{\partial x} = D_k \frac{\partial^2 C_k}{\partial x^2}$$

In order to simply the model, the following assumptions are made:

(a) The mass transfer in the gas phase is only by means of molecular diffusion;
(b) Gas and liquid phases are in equilibrium at the interface;
(c) No mass is accumulated at the interface.

For the boundary conditions, bounce-back is applied for the solid walls. Constant concentration is implemented at the gap of upper wall as seen in Fig. 10.26. The sizes of domains A (gas) and B (liquid) in the figure are 100 mm × 5 mm ($L \times H_G$) and 100 mm × 30 mm ($L \times H_L$), respectively, and the gap of the upper wall has a width of 4 mm.

The initial condition for CO_2 absorption is $C_{0,G} = 0$ kg m^{-5},$C_{\mathbf{0,L}} = 0$ kg m^{-5}, $C_{\mathbf{gap}} = 1,7$ kg m^{-3}, u_L = 0 m s^{-1}. The hybrid LBM-FDM method is used.

The hybrid LBM-FDM method is used for the simulation, the convection term is discretized by upwind weighted scheme and the diffusion term is discretized by central difference scheme Runge–Kutta scheme is employed for time stepping.

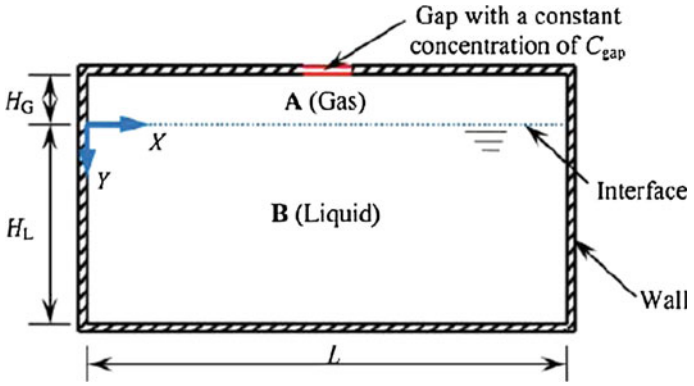

Fig. 10.26 Schematic computational domain (Reprinted from Ref. [27], Copyright 2012, with permission from American Chemical Society)

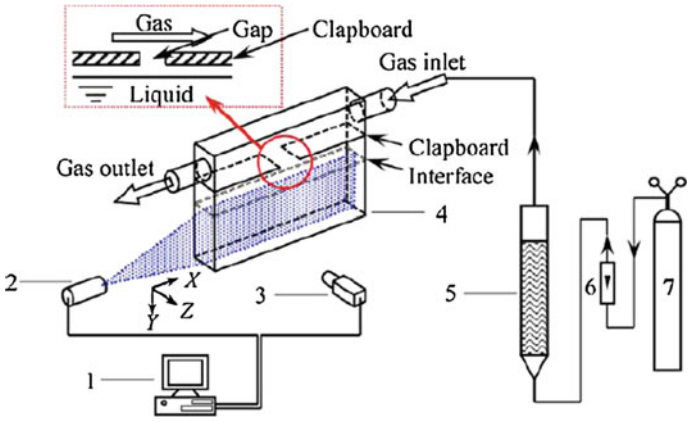

Fig. 10.27 Schematic diagram of the experimental setup (*1*—computer; *2*—laser source; *3*—camera; *4*—optical cell; *5*—presaturator; *6*—rotameter; *7*—gas cylinder) (Reprinted from Ref. [27], Copyright 2012, with permission from American Chemical Society)

For testing the accuracy of simulation, Chen also performed the experimental under the simulated condition. The experimental setup is shown in Fig. 10.27.

The experimental results are shown in Fig. 10.28a. As seen, in the beginning one pair of vortex is found around the center of the interface, which then further develops and influences the fluid near the wall. This pattern may be as a result of faster absorption at the center of interface due to higher concentration at the gap of the upper wall so that the concentration around the center of interface is higher than the others by faster absorption. Figure 10.28b shows similar pattern by simulation as well as in (c) where concentration development from two interfacial points and penetration to the bulk liquid is seen. In Fig. 10.29, symmetric peaks in average velocity distributions in X direction are found in both experimental and simulated results, which are corresponding to the vortex shown in Fig. 10.28. The peaks move toward the left and right walls with time before 50 s due to the diverging flow induced by surface concentration gradient.

From Figs. 10.28 and 10.29, it can be found that both the simulated and experimental results show the following tendency:

(a) The maximum velocity appears at the liquid surface and the average velocity decreased rapidly in the direction perpendicular to the liquid surface;
(b) The convection was centered in a region of $Y = 0$–0.01 m. The simulated average velocity at the liquid surface is higher than the experimental measurement. The deviation may be due to the simulation is two-dimensional and the experiment is under three-dimensional performance.

As seen in Fig. 10.29 the velocity of Rayleigh convection and mutual interaction is increased with time. The random characters of both velocity and concentration are obvious.

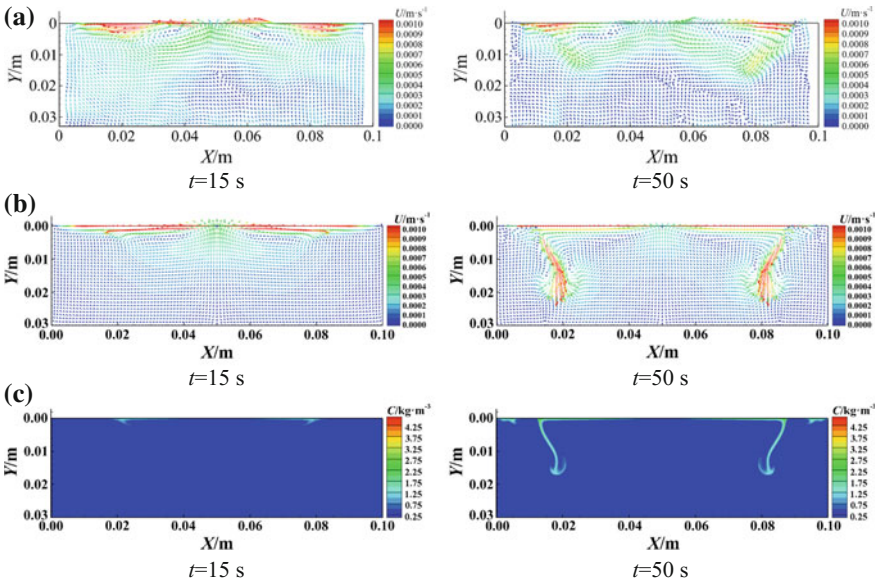

Fig. 10.28 Results of CO_2 absorption at t = 15 and 50 s for CO_2 absorption. **a** experimental velocity distribution, **b** simulated velocity distribution, **c** simulated concentration distribution (Reprinted from Ref. [27], Copyright 2012, with permission from American Chemical Society)

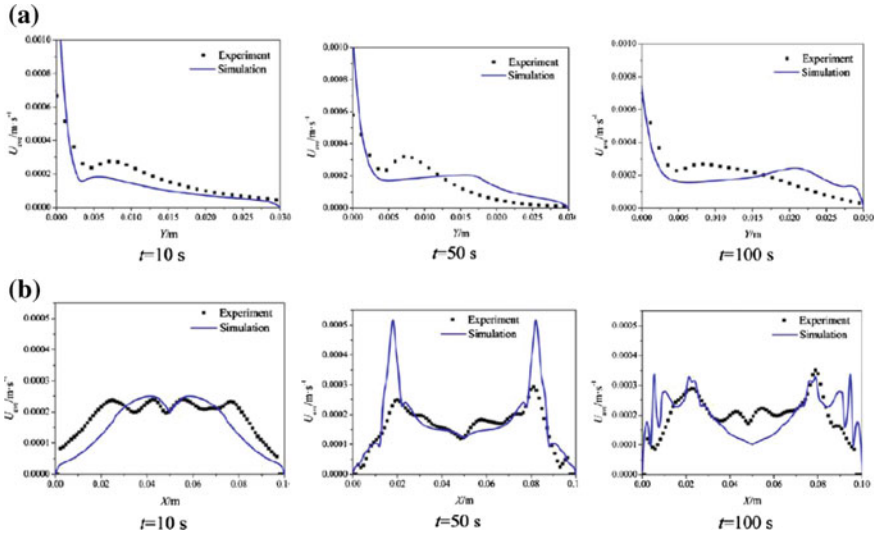

Fig. 10.29 Simulated and experimental results on average velocity distributions for CO_2 absorption at different time. **a** along Y (*vertical*) direction, **b** along X (*horizontal*) direction (Reprinted from Ref. [27], Copyright 2012, with permission from American Chemical Society)

10.6 Summary

In short, any disturbance on concentration or temperature at interface may initiate the Marangoni or Rayleigh convections if the interfacial surface tension gradient or the density gradient develop near the interface; the former is mainly acting around interface and the latter is circulated between interface and the bulk fluid.

The influence of Marangoni convection and Rayleigh convection on the mass transfer is significant as seen by the increase of enhancement factor by simulations and experimental measurement as described in this chapter and Chap. 9. The necessary conditions for initiating Rayleigh or Marangoni convection are first the *Ra* or *Ma* number should exceed their critical value, respectively; second the interfacial should be disturbed at least one point to initiate the interfacial instability.

The location of the disturbed points is stochastic and can be described by employing different interfacial models. It is noted that, in the course of simulation, the numerical disturbance may affect the simulated result. For instance, in the absorption process as shown in Fig. 10.13, since the bounce-back boundary condition is applied, numerical disturbance is arising from the two sides of the container wall to make the Rayleigh convection appeared primo near the wall as seen in Figs. 10.10 and 10.24. Such convection promotes the instability of neighboring interfacial concentration points and induces subsequent Rayleigh convections. Nevertheless, by using the LBM-FDM method of computation, the Rayleigh convection first appear away from the wall as shown in Fig. 10.27. However, in spite of the location of the initial disturbance, the appearance of both convections are developing with time and spreading out to the whole fluid body so as to promote the interface renewal and enhance the mass transfer until the process reaches stable state.

References

1. Frisch U, Hasslacher B, Pomeau Y (1986) Lattice-gas automata for the Navier-Stokes equation. Phys Rev Lett 56(14):1505–1508
2. Wolfram S (1986) Cellular automaton fluids 1: basic theory. J Stat Phys 45:471–526
3. Chen SY, Chen HD, Martinez D, Matthaeus W (1991) Lattice Boltzmann model for simulation of magnetohydrodynamics. Phys Rev Lett 67(27):3776–3780
4. Qian YH, D'Humieres D, Lallemand P (1992) Lattice BGK model for the Navier-Stokes equation. Europhys Lett 17(6):479–484
5. Bhatnagar PL, Gross EP, Krook M (1954) A model for collision processes in gases. I. Small amplitude processes in charged and neutral one-component systems. Phys Rev 94(3):511–525
6. McNamara GR, Zanetti G (1988) Use of the Boltzmann equation to simulate lattice-gas automata. Phys Rev Lett 61(20):2332–2335
7. Chen HD, Chen SY, Matthaeus WH (1992) Recovery of the Navier-Stokes equation using a lattice-gas Boltzmann method. Phys Rev A 45(8):5339–5342
8. Wagner AJ (2008) A practice introduction to lattice Boltzmann method. North Dakota State University, North Dakota

9. Hou S, Zou Q, Chen SY, Doolen GD, Cogley AC (1995) Simulation of cavity flow by the lattice Boltzmann method. J Compt Phys 118:329–347
10. Chen SY, Martinez D, Mei RW (1996) On boundary conditions in lattice Boltzmann methods. Phys Fluid 8(9):2527–2536
11. Skordos PA (1993) Initial and boundary conditions for the lattice Boltzmann method. Phys Rev E 48(6):4823–4842
12. Maier RS, Bernard RS, Grunau DW (1996) Boundary condition for the lattice Boltzmann method. Phys Fluids 8(7):1788–1801
13. Inamuro T, Yoshino M, Ogino F (1995) A non-slip boundary condition for lattice Boltzmann simulations. Phys Fluids 7(12):2928–2930
14. He XY, Chen SY, Zhang RY (1999) A lattice Boltzmann scheme for incompressible multiphase flow and its application in simulation of Rayleigh-Taylor instability. J Compt Phys 152:633–642
15. Dixit HN, Babu V (2006) Simulation of high Rayleigh number natural convection in a square cavity using the lattice Boltzmann method. Int J Heat Mass Transfer 49:727–739
16. Guo ZL, Zhao TS (2005) Lattice Boltzmann simulation of natural convection with temperature-dependent viscosity in a porous cavity. Prog Comput Fluid Dyn 5:110–117
17. He XY, Chen SY, Doolen GD (1998) A novel thermal model for the lattice Boltzmann method in incompressible limit. J Compt Phys 146:282–300
18. Dawson SP, Chen S, Doolen GD (1993) Lattice Boltzmann computations for reaction-diffusion equation. J Chem Phys 98(2):1514–1523
19. Fu B, Yuan XG, Liu BT, Yu GC, Chen SY (2010) Simulation of Rayleigh convection in gas-liquid mass transfer using lattice Boltzmann method. In: The 13th Asia Pacific confederation of chemical engineering congress, 2010
20. Fu B, Yuan XG, Chen SY, Liu BT, Yu GC (2011) Lattice-Boltzmann method for Rayleigh convection and its influence on interfacial mass transfer. CIESC J (Huagong Xuebao) 62 (11):2933–3000
21. Fu B (2012) Rayleigh convection and its effect on interfacial mass transfer based on lattice-Boltzmann method. Ph.D. dissertation, Tianjin University, Tianjin, China
22. Fu B, Liu BT, Yuan XG, Chen SY, Yu KT (2013) Modeling of Rayleigh convection in gas–liquid interfacial mass transfer using lattice Boltzmann method. Chem Eng Res Des 91: 437–447
23. Chen W (2010) Experimental measurement of gas–liquid interfacial Rayleigh-Bénard-Marangoni convection and mass transfer. Ph.D. dissertation, Tianjin University, Tianjin, China
24. Fu B, Yuan XG, Liu BT, Chen SY, Zhang HS, Zeng AW, Yu GC (2011) Characterization of Rayleigh convection in interfacial mass transfer by lattice Boltzmann simulation and experimental verification. Chin J Chem Eng 19:845–854
25. Chen SY, Fu B, Yuan XG, Zhang HS, Chen W, Yu KT (2012) Lattice Boltzmann method for simulation of solutal interfacial convection in gas-liquid system. Ind Eng Chem Res 51:10955–10967
26. Servan-Camas B, Tsai FTC (2008) Lattice Boltzmann method with two relaxation times for advection-diffusion equation: third order analysis and stability analysis. Adv Water Resour 31 (8):1113–1126
27. Chen SY, Fu B, Yuan XG, Zhang HS, Chen W, Yu KT (2012) Lattice Boltzmann method for simulation of solutal interfacial convection in gas–liquid system. Ind Eng Chem Res 51:10955–10967